



International Union  
of Theoretical and Applied Mechanics

## IUTAM Symposium

Poitiers - Futuroscope - France  
August 31 - September 4, 1998

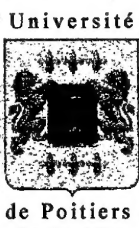
# Advanced Optical Methods and Applications in Solids Mechanics

Editor : Prof. A. LAGARDE

DISTRIBUTION STATEMENT

Approved for public release  
Distribution Unlimited

TOME 1



PROGRAMME  
com'Science  
CONSEIL REGIONAL  
POITOU-CHARENTES

CYRS



19990126 037



PSA  
PEUGEOT  
CITROËN

**Scientific Committee**

A. Lagarde, Chairman, University of Poitiers France

J. W. Dally, University of Maryland, College Park USA

J. Engelbrecht (ex officio), Institut of Cybernetics, Tallinn Estonia

J.F. Kalthoff, Ruhr University, Bochum Germany

A.S. Kobayashi, University of Washington, Washington USA

V.P. Kutovoy, Siberian State Transport Academy, Novosibirsk Russia

J. Stupnicki, Inst. Aeron & Appl. Mech., Varszawa Poland

M. Takashi, Aoyama Gakuin University, Tokyo Japan

C.A. Walker, University of Strathclyde, Glasgow U.K.

**Local Organizing Committee**

A. Lagarde (Chairman)

M. Cottron (Secretary)

F. Brémand

J.C. Dupré

V. Valle

### *Acknowledgments*

We wish to thank profusely the international , national and regional organisations emphasing the essential part of the regional supports. Their financial assistance as well as those of societies have been indispensable for the proper preparation and the fonctionning of the symposium but also for the subsidies given to permit the participation. Our aknoledgments are applied to :

International Union of Theoretical and Applied Mechanics, European Research Office, Délégation Générale à l'Armement, Centre National de la Recherche Scientifique, Association Universitaire de Mécanique, Université de Poitiers, Faculté des Sciences Fondamentales et Appliquées de Poitiers, Mairie de Poitiers, Conseil Général du Département de la Vienne, Conseil Régional du Poitou-Charentes, Peugeot Citroën, Kluwer Academic Publishers.

July 1998

**Alexis Lagarde**

Chairman of the Scientific Committee  
IUTAM Symposium

Preliminary program for the IUTAM Symposium

**Advanced optical methods and applications in solid mechanics**

	8H30	9H20	10H30	11H20	14H00	14H50	16H25
	9H20	10H10	11H20	12H35	14H50	16H05	18H05
Mo 3/8	9H OPENING SESSION	GL1	GL2	moiré	photoelasticity	dynamic measurement	Poster Session
Tu 1/9	GL3	hybrid methods L9-L10	GL4	L1-L2-L3	L4-L5	L6-L7-L8	P1 to P12
We 2/9	GL6	photorefractive materials L17-L18	GL7	image analysis L11-L12-L13	GL5	crack tip stresses L14-L15-L16	Poster Session P13 to P24
Th 3/9	GL9	new optical tools GL10	GL11	thermomechanics L19-L20-L21	GL8	FUTUROSCOPE VISIT	A
Fr 4/9	GL14	shearography L30-L31	GL15	strain&displacement measurement L22-L23-L24	GL12	speckle interferometry L25-L26-L27	optical diagnostic L28-L29
				shear bands and crack propagation L32-L33-L34	GL16	holography interferometry L35-L36-L37	CONCLUSION

A: Tuesday evening : Poitiers City Hall Reception

B: Thursday evening : Symposium Dinner

GL : General Lecture

L : Regular Lecture

P : Poster Presentation

# TOME 1

## MONDAY - August 31, 1998

### **GL1: Lagarde A.**

Static and dynamic strain measurement on a plane surface. Tridimensional photoelasticity

### **GL2: Walker C.A., Mc Kenzie P.**

High sensitivity moiré and applications

### **L1: Mc Kelvie J., Collin G.,**

Temperature-insensitive moiré interferometry: a quantitative investigation

### **L2: Sciammarella C.A., Sciammarella F.M.**

An extension of holographic-moiré to micromechanics

### **L3: Read D. T., Dally J. W.**

Theory of moiré fringe formation with an electron beam

### **L4: Allison I.M., Acito M.**

Determining stress components on selected sections in photoelastic models.

### **L5: Miyano Y., Kunio T., Sugimori S.**

A study on stress freezing method based on time and temperature dependent photoviscoelastic behavior

### **L6: Huntley J.M., Coggrave C.R.**

High speed measurement of discontinuous surface profile

### **L7: Valle V., Cottron M., Lagarde A.**

High speed local strain determination from grating diffraction

### **L8: Yoneyama S., Takashi M.**

Transient stress analysis under low velocity impact by white light photoviscoelastic technique

### **P1: Monneret S., Laubère V., Corbel F.**

Stereophotolithography and micromechanics

### **P2: Aben H., Ainola L.**

Interference blots in integrated fringe patterns

### **P3: Plouzennec N., Dupré J. C. , Lagarde A.**

Visualisation of photoelastic fringes within three dimensional specimens using an optical slicing method

### **P4: Zenina A., Dupré J. C. , Lagarde A.**

Optical approaches of a photoelastic medium for theoretical and experimental study of the stresses in a three dimensional specimen

### **P5: Oi T., Takashi M.**

An approach to general 3-D stress analysis by multidirectional scattered light technique

### **P6: Quiroga J.A., Gonzalez-Cano A.**

Phase measurement method for stress analysis from photoelastic data

### **P7: Umezaki E., Nanka Y.**

Generalised phase-shifting method for measuring photoelastic fringe parameters and its applications

### **P9: Akhmetzyanov M., Albaut G., Baryshnikov V.,**

Solution of fracture problems by non-linear photoelastic methods under significant elastic and plastic strains

### **P10: Optasanu V., Bonneau D.**

Optical investigation of a connecting-rod big end bearing model under dynamic loads

### **P11: Li Z., Liu X., Wang W.**

Application of dynamic orthotropic photoelasticity

**TUESDAY - September 1, 1998**

**GL3: Takashi M., Mawatari S.**

Hybrid stress analysis by construction of approximate analytical solution

**L9: Rowlands R. E.**

Hybridizing optical methods with analytical and computational techniques for stress analysis

**L10: Aben H., Ainola L.**

Hybrid stress analysis with integrated photoelasticity

**GL4: Morimoto Y., Fujigaki M.**

Digital image processing by phase shifting method using Fourier transform

**L11: Berka L., Klima J., Druckmüller M., Sova M.**

Digital image comparator for experimental analysis of deformations

**L12: Küchel M. F.**

Precise and robust phase measurement algorithms

**L13: Zenina A., Dupré J. C. , Lagarde A.**

Plotting of isochromatic and isostatic patterns of slice optically isolated in a three-dimensional photelastic model

**GL5: Kobayashi A.S.**

Experimental fracture mechanics: a moiré interferometry analysis

**L14: Suzuki S., Inayama I., Arai N., Mizuta T.**

Stress field measurement at bifurcation of fast propagating cracks by high-speed interferometry

**L15: Chona R.**

The stress field around two parallel cracks in a finite geometry : a hybrid study combining high-density geometric moiré and photoelasticity with the Westergaard approach and local collocation methods

**L16: Fang J. Xiong C. Y., Yao, X. F.**

Study of interaction between stress wave and cracks by optical method combining dynamic photoelasticity and dynamic caustics

**P13: Li K.**

Residual stress measurement with optical strain rosettes

**P14: Cincinelli V., Pappalettre C., Sun W. M., Surace L.**

Application of geometric moiré to the analysis of large deformation in three-dimensional models

**P16: Denis S., Bremand F.**

Development of a stereoscopic optical strain measurement technique : application of maize roots

**P18: Berthaud Y. , Calloch S., Collin F. , Hild F, Ricotti Y.**

Analysis of the degradation mechanisms in composite materials through a correlation technique in white light

**P19: Cavallo N., Morestin F., Jullien J.F.**

Measurement of residual deformations induced by high temperature load

**P20: Sakagami T., Ogura K., Kubo S., Farris T. N.**

Application of infrared thermography for contact problems

**P21: Ferber F., Herrmann K.P., Linnenbrock K.**

Applications of optical methods of stress analysis to study fracture phenomena

**P22: Shimamoto A., Furuya Y., Umezaki E.**

Active control of stress intensity factor K under mixed mode stress in the SMA-FEC

**P24: Dadkhah M.S.**

Mechanical/thermal integrity of MCM technology for RF PA applications

STATIC AND DYNAMIC STRAIN MEASUREMENT ON A PLANE SURFACE.  
TRIDIMENSIONAL PHOTOELASTICITY

A. LAGARDE

*Laboratoire de Mécanique des Solides,  
Université de Poitiers,  
Unité Mixte de Recherche CNRS 6610  
SP2MI - Téléport 2 - BP 179, 86960 FUTUROSCOPE CEDEX, FRANCE*

**Abstract**

For small or large strains, using two orthogonal gratings marked upon a plane measure base, we determine, in its plane, the rotation of the rigid solid and the algebraic values of principal extensions. An optical setting gives the measure by optical diffraction, without contact and at a distance, within  $10^{-5}$  accuracy by introducing quasi-heterodyne detection. The holographic record permits the extension of the measure to the whole of a plane surface. For the dynamic event, the grating interrogation by beam laser with angular coding gives not only strains for local measure base but also rigid motions. In photoelasticity, the optical slicing method is recalled; then, we bring up a new implementing with a C.C.D. camera which permits to obtain quickly isoclinics and isochromatics and also the isostatics for one model slice limited by two parallel plane laser beams.

**1 Introduction**

It is well known that the advent of the laser has permitted a spectacular development of the photomechanics.

The means of digitalization of the images, their acquisition and their treatment by computer offer new possibilities.

We havé selected to present you works of our side about two implement basis in experimental mechanic : the measurement of strains and three-dimensional photoelasticity.

The measurement of strain on a small plane base uses numerical or optical spectral analysis of orthogonal grating marked on surface. Means to increase the precision are given in the two cases. The optical set up for measurement of strain giving this possibility is also insensible to the out of plane displacement of the piece. The recourse to holography allows to extend the measure to quasi-plane surface. The lecture point by point is executed in differred time. In dynamic the position of the diffracted spots permits the determination of the strains and the motion of the local measurement base.

In three-dimensional photoelasticity we briefly recall the present practice and the possibilities of non-destructive optical slicing method, the one point-wise and the other in whole field. We also recall fundamental results on wave light propagation in weakly anisotropic environment and their importance for the analysis of thin slice and the new conception of the modelisation. The whole field optical slicing method is then presented in its recent developments.

## 2 Small and large strains measurement

The idea to realise grids at the surface of a specimen in order to accede to its strains is not new. This idea has been introduced by Rayleigh [1] in 1874 suggesting the use of moiré phenomenon which has been developed by Dantu [2] in 1957. This technique gives the field of displacements which has been also obtained using orthogonal grids.

The coherent radiation of the laser has permitted the development of the interferometric moiré [3] which offers a higher accuracy. Always, in view to increase the accuracy, let us notice the numerous works dealing with the interpolation between fringes and the multiplication of the fringes [4] and other technics [5]. The strains are obtained by the help of a derivation process.

The direct measurement of strains has been realised from the local observation of circle marked on the surface. Orthogonal grids have also been employed. With a smaller pitch the information has been extracted from the grating by optical diffraction either locally [6] or along a line using filtering [7]. The use of an optoelectronic device [8] has allowed an automatic calculation of strain distribution. With the recent development of C.C.D. cameras and image processings, these methods are being revived [9-10].

Our purpose is, on an area which can be of very small dimension, the determination of algebraic values of the principal extensions for large and small strains with a good accuracy and on a whole-field.

### 2.1 LOCAL MEASUREMENT OF STRAINS

#### 2.1.1. PRINCIPLE

We use tangent linear application [11] to study deformations of an orthogonal grating of pitch  $p$  which is engraved or marked on the local plane surface of a specimen submitted to loadings. This grating is supposed to follow perfectly the displacements in each point. Thus (Fig. 1) an interior point  $M(X, Y)$  is transformed to  $m(x, y)$  by the following transformation :

$$\begin{cases} x = \frac{a_1}{p} \cos \alpha_1 X + \frac{a_2}{p} \cos \alpha_2 Y \\ y = \frac{a_1}{p} \sin \alpha_1 X + \frac{a_2}{p} \sin \alpha_2 Y \end{cases}$$

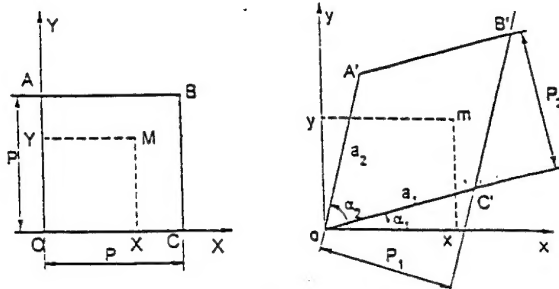


Fig. 1 - Deformation of a square

The gradient of the transformation tensor  $F$  is constant inside the parallelogram.

The Cauchy-Green's right tensor  $C = {}^tFF$  has the following matrix :

$$C = \begin{pmatrix} \left(\frac{a_1}{p}\right)^2 & \frac{a_1 a_2}{p^2} \cos(\alpha_2 - \alpha_1) \\ \frac{a_1 a_2}{p^2} \cos(\alpha_2 - \alpha_1) & \left(\frac{a_2}{p}\right)^2 \end{pmatrix}$$

Using the polar decomposition of  $F$  we can express the rigid-body rotation of the solid,  $R$ :

$$\tan R = \frac{a_2 \cos \alpha_2 - a_1 \sin \alpha_1}{a_2 \sin \alpha_2 + a_1 \cos \alpha_1}$$

We assume the strains are uniform on the measurement base. Thus we obtain the orientation and the value of the principal extensions and the rigid body rotation from a knowledge of four parameters (two pitches  $p_1$  and  $p_2$  and two angles  $\alpha_1$  and  $\alpha_2$ ). These values are experimentally obtained either by optical Fourier Transform or by numerical Fourier Transform.

The first procedure gives the strain with an accuracy of  $10^{-3}$  (sec. 2.1.3). For better performances we use the phase shifting technique (sec. 2.2.1). The second procedure requires an adapted interpolation process (sec. 2.2.1).

## 2.1.2. GRATING REALISATION

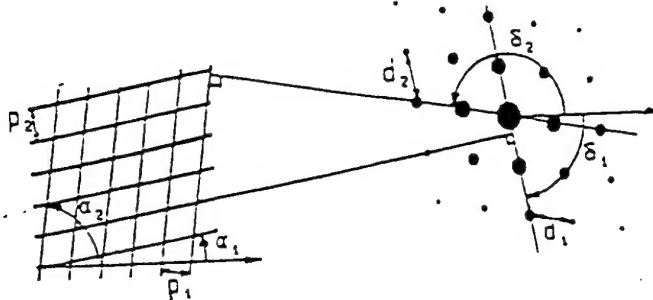
We use [12] the interferences of two beams laser for the exposure of a photosensitive coating used directly for diffraction. The repeat of these interferences allows direct engraving at the surface of the material (epoxy, steel, ...) with the help of a yag laser. We use also the Post replication technic to obtain phase grating. All technics give grating which are disturbed when large strains appear. We develop a technic to make small viscoelastic pavements. Other ways to realise grating with lines or points consist to use print, transfer, inking pad, mold, point or issued from the specimen structure clothes, sails. The choice depend of the size of the measurement base and the nature of the problem.

## 2.1.3. MEASUREMENT BY OPTICAL DIFFRACTION

The diffraction phenomena of a parallel beam of coherent light passing through a plane grating is well known.

We have represented in Fig. 2 the diffraction image by a grating of parallel crossing lines. We notice that the direction formed by the diffraction points is perpendicular to the orientation of the family of corresponding lines. It is now easy to describe  $p_1, p_2, \alpha_1, \alpha_2$  as functions of  $d_1, d_2, \delta_1, \delta_2$  : (L : distance between the grating and the screen)

$$p_1 = \frac{\lambda \sqrt{L^2 + d_1^2}}{d_1}, \quad p_2 = \frac{\lambda \sqrt{L^2 + d_2^2}}{d_2}, \quad \alpha_1 = \delta_1 + \frac{\pi}{2}, \quad \alpha_2 = \delta_2 - \frac{\pi}{2}$$



*The figure 2 gives an idea of the decreasing of the spots intensities from zero order using blots with decreasing areas. In fact, on the screen, all the spots have the same diameter.*

Fig. 2 - Diffraction image by a grating

The diffraction image is recorded by a C.C. D. camera, and the centroid ( $x, y$ ) of the spots computed from an intensity analysis.

The grating analysis using the optical diffraction allows measurements at distance and is very convenient for strain determination in hostile environment. For example, we give the evolution of longitudinal and transversal strains determined by this way on a specimen in epoxy resin and subjected to an uniaxial test at the frozen temperature. The measure base was  $0,5 \times 0,5 \text{ mm}^2$  and the line density 300 by millimeter.

From this test we can evaluate the strain accuracy to  $10^{-3}$ .

Let us notice that the method has been adapted in dynamics [13] and also, in statics, to studies of cylindrical specimens [14].

#### 2.1.4. MEASUREMENT BY SPECTRAL ANALYSIS

The crossed grating is recorded by C.C.D. camera and an algorithm of bidimensional DFT is used.

The location of the 5 peaks of the spectrum (central order and 4 peaks order  $\pm 1$ ) gives searched parameters as for the optical analysis.

#### 2.2. IMPROVEMENT OF ACCURACY

##### 2.2.1. THE TOOLS OF THE ACCURACY

**The quasi-heterodyne or phase shifting method [15]**

Now, this method is very well known. We note it for memory.

**The spectral interpolation method [16] [17]**

Let us consider  $f(x)$  periodic function,  $F(N)$  his Fourier Transform (F.T.),  $x$  and  $N$  are reciprocal variables respectively spatial and spectral. Let  $T$  the period of sampling, satisfying the Shannon condition,  $M$  the number of discretisation points,  $MT$  the wideness of the window limiting the sampling function.

We use the DFT (noted  $F_k$ ) with  $nT$  and  $k/MT$  the reciprocal variables respectively spatial and spectral. The frequencies of the spectrum of  $f(nT)$  are calculated with the peaks of the square modulus of  $F_k$ . If the number  $M$  of points of discretisation is one multiple of the period of the signal, the DFT is equal in these points to the continuous F.T. The most important peak of coordinate  $k'$ , corresponds to the principal frequency of the signal  $N = k'/MT$ . In practical case,  $M$  is not one multiple of the period of the signal. We show that the principal frequency is given by the relations ship.

$$N = \frac{k_s + \beta}{MT} , \quad \beta = \text{Re} \frac{F_{k_s-1} - F_{k_s+1}}{2F_{k_s} - F_{k_s-1} - F_{k_s+1}}$$

where  $k_s$  is the integer value of the coordinate the nearest of the principal peak.

### 2.2.2. THE DEVICE

Using a numerical Fourier transform of the grating image or the optical transform by laser beam diffraction, an out of plane translation between the reference state and the deformed state of the specimen leads to an error in the strain determination. We present a measurement method at distance insensitive to the translations and with better accuracy by the use of quasi-heterodyne detection [17-18].

We consider in normal incidence the diffraction of a laser beam by a parallel equidistant lines grating. The optical device (Fig. 3) is made by a cylindrical mirror having the same axis as the incident beam. After reflecting, the two diffracted beams of the order  $\pm 1$  interfere on the level of the axis of the cylinder. The interference field is composed of parallel fringes and its analysis allows to characterize the geometry of the grating bounded to the piece. The interference field has a depth of several millimeters, function of the transverse dimension of the diffracted beams where the geometry of the fringes is identical. There is so no problem of focusing and an out of plane displacement of the piece and therefore of the interference zone does not lead to an error measurement. To be free from the translation in the plane of the grating, we use a dimension of grating superior to the diameter of the incident beam.

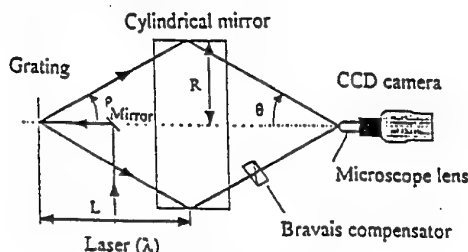


Fig. 3 - Optical device

The interference field can be analysed using the numerical spectral interpolation. We have shown that the use of the quasi-heterodyne technique gives better results than the previous one. We applied this by modulating the phase of one of the diffracted beam using a Bravais compensator. For an unidimensional signal this technique consists of the use of three dephasing  $\psi^k$  (calculated by Fourier transform) for the determination of the phase  $\phi(x)$  and so of the value of the period of the signal. The same procedure is applied for a two-dimensional signal. In order to show the performances of the developed optical device, we give results [19] from an uniaxial traction test on a plexiglas specimen submitted to step of strain of  $2 \times 10^{-5}$ .

### 2.3. WHOLE FIELD STRAINS MEASUREMENT

We have developed a whole field strain measurement method [20] which uses the recording of the grating by holography (Fig. 4). The image of the crossed grating illuminated in normal incidence is formed in an optical device that realises successively two Fourier transforms. We obtain so in the second Fourier plane the interferences of the diffracted beams which create a new grating. A filter located in the first Fourier plane allows to eliminate the zero order and the orders superior to  $\pm 1$ . Few different orientations of the reference beam are generated to record so many object states on the same holographic plate.

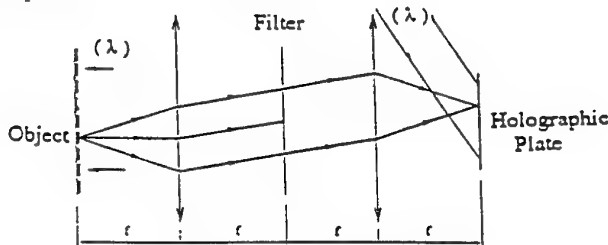


Fig. 4 - Holographic recording device

The figure 5 shows the optical device for the recording of the image of the grating. This device allows to generate 4 different reference beams.

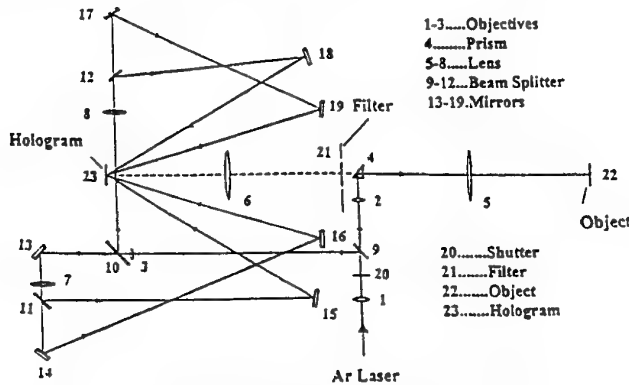


Fig. 5 - Set up for the holographic recording device

At the reconstruction, the illumination of the holographic plate using the reference beam gives the order  $\pm 1$  in each point of the plate, image of an object point. The analysis of the reconstructed grating using the device with a phase shifting procedure gives the determination point by point of the strain components in the whole-field. It is also possible for the strain determination to employ the set-up for the recording procedure. This method has been used for a ductile fracture investigation.

#### 2.4. HIGH SPEED LOCAL STRAINS DETERMINATION

The diameter of the plane measurement base is about 1 mm. The crossed grating, marked on the surface, has a density equal to 200 lines by millimeter.

The method is always based on the interrogation of a crossed grating from diffraction phenomenon and we use the five diffracted beams  $0 ; \pm 1$  order. To separate the spots on the recording (with film or C.C.D. camera) during the dynamic event, we use the angular coding. At each sampled time one cylindrical beam with diameter of about 1 cm light the crossed grating figure 6.

Generally, the unknown quantities are :

- 4 parameters characteristic for the measure base orientations and pathes of the two grating taking into account the pure strains and the rotation of the rigid solid in the plane of that base.
- 2 angular parameters for the orientation of the base.
- 5 distances from the measure reference to the position of the spots in the screen.

That is to say 14 unknown quantities.

At each time, one experimental data is the orientation of the incident beam. The measured positions on the screen of the corresponding 5 spots lead to 15 equations.

It can be proved that at each sampled time, the unknown quantities are the solutions of one nonlinear system of fifteen equations characteristic for the five considered beams. Taking into account the given diffraction spots is therefore sufficient to solve the problem.

It is to notice that the method gives not only the strain components tensor on the measure base but also the displacements and the rotations of the measure referent. One lecture will deal with it and will precise its performances.

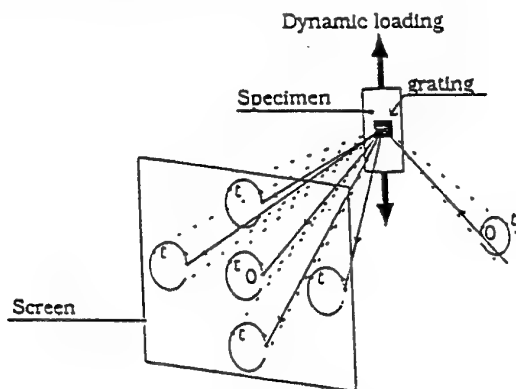


Fig. 6 - Schema of a part of the optical recording device

### 3 THREE-DIMENSIONAL PHOTOELASTICITY

#### 3.1. PRESENT PRACTISE AND NEW POSSIBLE WAY

Photoelasticity still give subjects to searchers. It is the case for the study of the residual stresses in glass specially by means of integrated photoelasticity. So it is with the use of the isodynies in view of taking into account the three dimensional local effects.

These fields are particular ones. We deal with the study of elasto-static problems about pieces having complex geometry. In this way, with the help of the well known stress frozen technic, photoelasticity is still often used in the test and research laboratories of motor vehicle and aeronautic industries.

This situation proves the efficiency of the photoelastic study ; this efficiency is due to the fact that the model being worked out with the loading elements then the real boundary conditions are taken into account. In the last ten years, photoelasticity and numerical simulation have been used sometimes in parallel.

The process consists in first adjusting the boundary conditions in order to get the obtained numerical values identify to the experimental values, the mechanical parameters being those corresponding to the frozen temperature. Then, the stress distribution inside the prototype as obtained with its own mechanical parameters. So, we become free from difficulty due to the quasi incompressibility of the model material at the frozen temperature.

Let us notice a recent progress : the original, necessary to make the mould, can be realised from C.A.O. data by means of the stereolithography. Now, it is even possible to directly realise the model with frozenable resin.

The exploitation of the frozen model is executed by mechanical slicing into plane sheets with a thickness from 2 to 4 mm. Each sheet polished roughly and analysed in linear and circular polariscope like in plane photoelasticity. Let us notice that slicing and analysing of one serie of parallel sheets require one qualify personal working during one week. The time of work is reduce if the use of immension thank because is not necessary to polish roughly the slices. The aim is to determine the parameters of interest for Ingeneers : the angle  $\alpha$  and the difference  $\sigma' - \sigma''$  of the secondary principal stresses. These quantities obtained for three series of mutually orthogonal planes make possible, using well known relations, to integrate the equilibrium equations with known boundary, conditions. Then, the most general study, scarcely done, requires the making and the slicing of three models. Pratically, most often, we restrict ourself in determining only the above quantities in principal planes in order to optimiste the shape of the model.

Over fifteen years ago, we have developped and used two optical slicing methods of the model ; one point wise [21 to 25], the other whole field [24 to 27]. In a three-dimensional medium, these two methods give a non destructive way of investigation, based on the scattering light phenomenon. This phenomenon is intensified by introducing fine particles of silice in the epoxy resine.

The point wise method of optical slicing offers the possibility to use the light scattering phenomenon as polarizer or as analyser. This method with a linear detection of parameters is automatized in order to facilitate the use ; it permits a precise determination, in every point of the sheet, of the three optical parameters leading in general to the determination of  $\alpha$  and  $\sigma' - \sigma''$  (sec. 3.2.2.). Let us notice that a number

of methods have been developed to determine the three optical parameters, more particularly for the thick medium located between the sheet and the model boundary ; it is analysed in the book of Srinath [28]. Let us mention the iterative process and the ones using polarizer and analyser rotations and compensator [29].

For example, we have determined the stress tensor along a line in a prismatic bar, under torsion, the cross section of which being an equilateral triangle. The values of the stresses are normalised by the maximum value of the shear of the cross section. So, in the base of a turbine blade, we could determine the values of the equivalent stress in the Von Mises sense at various points for a tensile load [23] [25].

The whole field optical slicing method is based on limitation of a sheet by two parallel beams emitted from a laser.

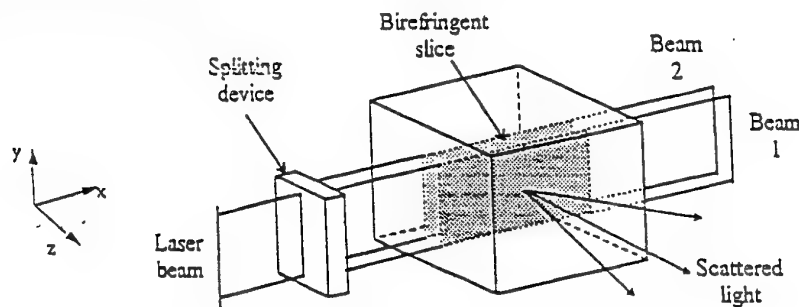


Fig. 7 - Isolation of a slice with two plane laser beams

Then, the model is analysed slice by slice. The scattered radiations interfere (Rayleigh's law) on the image plane of the middle of the sheet. They make into account the different polarizations that depend of optical characteristics of the sheet. Two methods are been developed (sec. 3.4.). The aim of this part is to demonstrate that it is possible to obtain the isoclinic and isochromatics fringes and to plot the isostatic patterns. It is the new possible way.

Before presenting the method principles, we shall give the new conception of the modelisation of the light waves propagation in three dimensional medium having low anisotropy.

### 3.2. PROPAGATION OF THE LIGHT WAVE THROUGH PHOTOELASTIC MEDIUM

To define the light propagating direction in a photoelastic medium a basic hypothesis consist in assuming the medium to be isotropic (indeed current photoelastic materials are slightly anisotropic). It follows that for a ray light propagating along  $\vec{z}$  direction, the wave planes ( $x, y$ ) are orthogonal to  $\vec{z}$ .

It can be shown that the secondary principle directions of the indice tensor and that of the stress tensor coincide and that we have the following relationship.

$$\begin{aligned} n' - n_0 &= c_1 \sigma' + c_2 (\sigma'' + \sigma_z) \\ n'' - n_0 &= c_1 \sigma'' + c_2 (\sigma' + \sigma_z) \end{aligned}$$

where  $n'$  and  $n''$  denote the secondary principal indices in the wave-plane ( $x, y$ ) and  $\sigma', \sigma''$  are corresponding secondary principal stresses ;  $c_1, c_2$  are constants for a photoelastic material.

### 3.2.1. THE CLASSICAL SCHEME

In three-dimensional photoelasticity it is usually assumed that the directions of secondary principal stresses and their values are constant through the thickness  $dz$  of a slice having its parallel face normal to  $\bar{z}$ . This assumption allows to consider this slice as a birefringent plate characterized with the two following parameters.

- secondary principal angle  $\alpha = (\sigma', \sigma'')$       - angular birefringence  $\phi = \frac{2\pi\delta}{\lambda}$ ,

$$\delta = dz(n', n'') = C(\sigma', \sigma'') dz \quad C = c_1 - c_2 \quad (C \text{ being a photoelastic constant}).$$

### 3.2.2. ABEN SCHEMATISATION

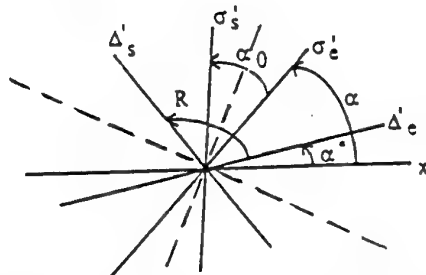


Fig. 8 - Orientation of the characteristic  $\Delta'$  directions and the  $\sigma'$  directions at the entrance and the emergence

Aben in 1966 showed that when rotation of secondary principal axes was present, there were always two pairs of perpendicular conjugate « characteristic directions » (Fig. 8). He distinguished the primary characteristic directions at the entrance of light ( $\Delta'_e, \Delta''_e$ ), and the secondary characteristic directions ( $\Delta'_s, \Delta''_s$ ) for the light emerging from the medium. The light linearly polarized at the entrance along one of the primary directions emerges as linearly polarized along the conjugate secondary direction. We will denote by  $R$  the angle determinated by two such directions,  $R = (\Delta'_e, \Delta'_s)$  and by  $\alpha^*$  the angle  $(x, \Delta'_e)$ .

The characteristic directions are generally different from the secondary principal directions of the stress tensor (or those of index tensor). At the entrance we have  $(\sigma'_e, \sigma''_e)$  and at emergence we have  $(\sigma'_s, \sigma''_s)$  from the medium. We denote  $\alpha_0 = (\sigma'_e, \sigma'_s)$ .

### 3.2.3. HYPOTHESIS FOR A THIN SLICE

For the case where  $dx/dz$  and  $\sigma' - \sigma''$  are constant through a thickness, important conclusions follow [30 - 31] :

- The bisecting lines for the angles formed by two associated « characteristic directions » coincide with those for the angles formed by the associated secondary principal directions at the entrance and at the exit, (Fig. 8).

Remark : The bisectors mentioned correspond to the secondary principal directions (mechanical or optical) at mid thickness ; so their directions are defined by the angles  $\pm R/2$  from the characteristic directions :

- The phase difference  $\phi^*$  characteristic to the medium traversed by the light wave along two characteristic orthogonal directions is generally different from the angular birefringence which would result in the absence of rotation  $R$ . The values  $R, \alpha^*, \phi^*$  and  $\alpha, \alpha_0, \phi$  are linked [23 - 27].

About the torsion strain, in a bar of equilateral triangular section, let us recall that the Aben schematisation gives good concordance between calculated and experimental results for slices inclined at an angle of  $\pi/4$  from the axis of the model with the thickness of the slices being only 2 mm for classical size of model [23].

### 3.2.4. DISCRETE ANALYSIS INTO THIN SLICES

This technique approaches the thick medium, in the direction  $\bar{z}$  of light propagation, by  $n$  plane thin slices perpendicular to  $\bar{z}$  [31 - 32]. This approach gives more realistic images in comparison with experimental images : in this case, we have variation of the stresses difference along the thickness ; the Aben's hypothesis does not respect this condition. One poster is devoted to this discrete analysis and shows this interest, in particular simplicity and good connexion with finite element method.

About the behaviour of slightly anisotropic medium, with a large thickness, crossed by light, the Poincaré's theorem permits us the representation by birefringent plate followed by a rotatory power (or by the inverse position, of the value of the rotatory power)

### 3.3. WHOLE-FIELD ANALYSIS WITH A PLANE POLARISCOPE

Here, the analysis with a light-field polariscope is presented as it corresponds to the whole-field method of optical slicing. One can conduct an analogous study for a dark polariscope.

Let us examine a slice (which should be obtained by freezing and slicing) in a plane light-field (rectilinear) polariscope. In each point the slice is represented by a birefringent plate and a rotatory power. Let  $I_0$  designate uniform light-field illumination and  $x$  the polarizing axis of the polarizer. Then the light intensity is :

$$I = I_0 [\cos^2 R - \sin 2\alpha^* \sin 2(\alpha^* + R) \sin^2 \phi^*/2]$$

The extremum values for intensity distribution correspond to :

$$\alpha^* = R/2 + k\pi/4, \quad k = 0, 1, 2, \dots$$

In order to specify the condition of analysis of fringe patterns we plotted the variations of  $I_{max}$  and  $I_{min}$ . Versus  $\phi$  for different values of  $\alpha_0$  obtained following the relationships given in sect. 3.2.3. As example, curves were plotted for  $\alpha_0 = \pi/9$  in Fig.9.

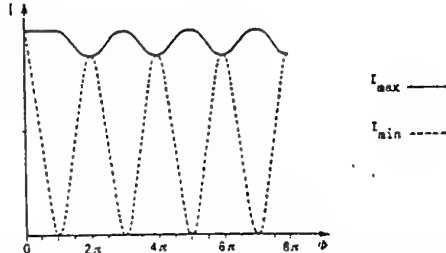


Fig. 9 - Variation of  $I_{\max}$  and  $I_{\min}$  as a function of  $\phi$  ( $\alpha_0 < \pi/9$ )

The foregoing analysis indicates that for small values of  $\alpha_0$  ( $\alpha_0 < \pi/9$ ) the maximum intensity  $I_{\max}$  shows a reduced modulation. Thus, it characterizes an isoclinic zone which permits one to locate the secondary principal stress directions (or those of the indices) in the median plane of a slice. This zone corresponds to  $\alpha^* = R/2 \bmod \pi/2$  (remark sect. 3.2.3.). The orientation of the polarizer then coincides with one of the secondary principal directions in the median plane. This interesting result is analogous to the one established by Hickson [33] for a dark-field polariscope.

It should be emphasized, that in order to avoid errors during the numerical integration procedure, the discritization points should lie on the median plane of a slices.

If  $\alpha_0$  increases, the  $I_{\max}$  modulation increases and it becomes very pronounced for  $\alpha_0 = \pi/3$ . In this case the isoclinic zone disappears although it should be noticed that the isoclinics are discernible till  $\alpha_0$  value of  $\pi/6$ .

The term  $I_{\min}$  which is strongly modulated for  $\alpha_0$  close to  $\pi/6$ , characterizes the isochromatic pattern. The extremum values occur for  $\phi = k\pi$  ( $k = 1, 2, \dots$ ) and it follows that localization of fringes is practically independent of the rotation of secondary principal axes.

We can now conclude by noting result: investigation of a slice within the plane (rectilinear) polariscope allows one to determinate the secondary principal stress directions in the median plane (without resorting to rotatory power measurements) and the angular birefringence  $\phi$  for the multiple  $\pi$ -values when the rotation of the secondary principal axes is less than  $\pi/6$ .

We should point out that the condition on the orientation of the secondary principal axis is not very limiting since one is able to choose the slice-thickness for the non-destructive optical slicing method.

### 3.4. WHOLE-FIELD OPTICAL SLICING METHOD

We have developped two methods using the limitation of the sheet by two parallel plane beams emitted from a laser. The scattered radiations interfere (Rayleigh's law) in the image plane of the middle of the sheet. The informations concerning isoclinic and isochromatics patterns of the sheet are obtained from the square of the correlation factor  $\gamma$  of the two speckle fields.

We show that the illumination of the speckle field is the following basement relation

$$I(x, y) = I_1(x, y) + I_2(x, y) + 2\sqrt{I_1 I_2} \gamma \cos(\psi_2 - \psi_1 - \eta)$$

$$\text{with } \gamma^2 = \cos^2 R - \sin 2\alpha^* \sin 2(\alpha^* + R) \sin \phi^*/2$$

$\psi_1, \psi_2$  random variables,  $\eta$  function of  $\alpha^*, \phi^*, R$ .

The speckle fields interfere in amplitude for  $\gamma = 1$ ; they add in energy for  $\gamma = 0$  (it is said that they interfere in energy).

### 3.4.1. METHOD BASED ON THE CONTRAST MEASUREMENT OF ONE RECORDING INTENSITY FIELD

This method, that uses only one recording with holographic film, is purely optical of one recording interesting field.

We note  $\langle \rangle$  the average spatial.

The static study of the speckle field gives from basement relation

$$\sigma^2 = \langle [I - \langle I \rangle]^2 \rangle = \langle I_1 \rangle^2 + \langle I_2 \rangle^2 + 2\gamma^2 \langle I_1 \rangle \langle I_2 \rangle$$

As the contrast  $\rho_i = \frac{\sigma_i}{\langle I_i \rangle}$  is unit for the two speckle fields, we have for the variance

$$\sigma^2 = \sigma_1^2 + \sigma_2^2 + 2\gamma^2 \langle I_1 \rangle \langle I_2 \rangle$$

We suppose  $\langle I_1 \rangle = \langle I_2 \rangle$  then the square contrast  $\rho^2$  of the recording speckle is

$$\rho^2 = \frac{1 + \gamma^2}{2}. \text{ Therefore the maximum of contrast of the fringes is } 1/3.$$

To increase the contrast of the fringes, we use a polychromatic laser (laser with variable wave length) [34]. In the regions of the image with  $\gamma = 1$ , the grain of the speckle are channeled. One pass band filtering gives theoretically a unit contrast. In practice, the noise of the film tempers somewhat these results.

This method was successfully used in the context of linear fracture mechanics to determine the characteristic parameters  $K_1$  and  $\sigma_{on}$  for a semi-elliptical surface crack loaded in opening made in a bar in tension [35].

### 3.4.2. METHOD BASED ON THE VARIANCE MEASUREMENT OF THE COMBINATION OF THREE RECORDING INTENSITY FIELDS [36 - 37]

The idea to use a C.C.D. camera instead holographic film was motived by the consideration of the density of isochromatic patterns. It is possible to use more big size of speckle grain. Then C.C.D. is available.

To take into account, one background intensity due to the fluorescence phenomenon of the material and a part of the scattered light not polarized, we add  $I_{1B}, I_{2B}$  to the values  $I_{1S}$  and  $I_{2S}$  corresponding to Rayleigh laws

$$I_1 = I_{1B} + I_{1S} \quad I_2 = I_{2B} + I_{2S}$$

$$\text{and we suppose } k = \frac{\langle I_{1S} \rangle}{\langle I_1 \rangle} = \frac{\langle I_{2S} \rangle}{\langle I_2 \rangle}$$

In these conditions, the basement relation becomes

$$I = I_1 + I_2 + 2\sqrt{I_{1S}} \sqrt{I_{2S}} \gamma \cos(\psi_1 + \psi_2 + \eta)$$

and the variance  $\sigma^2$  of  $I - I_1 - I_2$  is  $\sigma^2 = 2k^2 \gamma^2 \langle I_1 \rangle \langle I_2 \rangle$

The recording of the three fields  $I$ ,  $I_1$ ,  $I_2$  and the determination of one variance give a value proportional to  $\gamma^2$ .



Previous method with  
holographic film and optical filtering



New method with C.C.D.  
camera and image processing

Fig. 10 - For torsion strain in a bar of square section and a plane slice inclined at an angle of  $\pi/4$  from the axis, thickness 8 mm : comparison of the two methods.

### 3.5. SEPARATION OF ISOCLINIC AND ISOCHROMATIC PATTERNS OF THE SLICE. ISOSTATICS PLOTTING

We recall that the properties of polarization of the scattered light (Rayleigh's law) permits to realize, with two plane parallel laser beams, the optical slicing giving the analysis of the slice in light-field polariscope.

In the plane of the slice, we change the orientation of the beams and we record several images of the field (for example sixteen for a variation of  $\pi/2$ ).

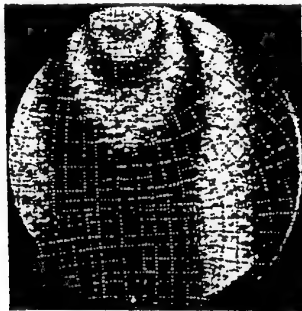


Fig. 11 - Isostatics and isochromatics patterns for one 4mm thickness slice  
Then we have sufficient information characterising a periodic phenomenon and it is possible to calculate in each pixel the Fourier transform of the correlation factor. The filtering in Fourier plane of the zero order gives the isochromatics and the same operation for the 1 order gives the isoclinic patterns.

When the isoclinic patterns are determined, the isostatics can be plotted to obtain the visualization of the orientations of the secondary principal stress directions.

The figure 11 shows the results for optical slice in model loaded by concentrated force. This process is important for the optimization of the design of the shape in mechanical construction.

#### 4 Conclusion and perspectives

The optical method based on the grating interrogation on the local plane surface, can make measurement at large distance without contact and without difficulties linked to the use of electrical alimentation of the electrical strain-gages. This is convenient for the control and the measurement in hostile environment. The accuracy is smaller  $10^{-5}$  against  $10^{-6}$  for the strain gage but the size of the measurement base can be more reduced than that necessary for rosette strain gage. The recourse to holography allows to extend the measure to quasi-plane surface.

The measurement of the large strains is only limited by the quality of the markage. This optical method can allow to extend the metrology in extensometry to domains badly adapted to use the electrical strain gage (banded joints, rack, sails, soft materials). For one dynamic event, the local grating interrogation gives not only the strains but also the rigid motions of the measurement base. Present technical means should permit the extension to large plane surface.

Our works, for optical slicing method in three-dimensional photoelasticity with the C.C.D. camera and the means of image processing, show, in statics, that it is easy and rapid to determine isochromatics and isostatics of a model slice.

In next future, it should be good to be able to determine the stress tensor in statics and dynamics.

#### References

1. Rayleigh, "Sur la production et la théorie de réseaux de diffraction" Phil. Mag. 47 (81) 193-(1874).
2. Dantu M.P., "Utilisation des réseaux pour l'étude des déformations" Annales de l'I.T.B.T.P., n° 12 (reprend une conférence du 5 mars 1957) 1958.
3. Post D., "High Sensitivity Displacement Measurement by Moiré Interferometry" Pro. 7<sup>th</sup>. Int. Conf. Exp. Stress Analysis Haïfa Israël 1982.
4. Sciammarella C.A., "Technique of fringe interpolation in Moiré patterns" Exp. Mech., pp. 19 A-29 A 7 (11) Novembre 1967.
5. Fu-Pen Chiang, "Techniques of optical spatial filtering applied to the processing of Moiré Fringe Patterns" Exp. Mech. pp. 525-526, November 1969.
6. Bell J.F., 1959, "Diffraction grating strain gage" S.E.S.A. Proceeding XVIII (2) 51-64.
7. Boone P.M., "A method for directly determining surface strain - Fields using diffraction grating" Exp. Mech. 11, Noll (1971).
8. Sevenhuijsen P.J., 1978 "The development of a laser grating method for the measurement of strain distribution in plane, opaque surfaces, V.D.I. Berichte, N°313, pp. 143-147.
9. Brémand F., Lagarde A., "Méthode optique de mesure des déformations utilisant le phénomène de diffraction". C.R. Acad. Sciences. Paris, 303, série II, 1986, p. 515-520.
10. Brémand F., Lagarde A., "Optical Method of Strain Measurement on a Small Size Area Application" IUTAM Symposium on Yielding, Damage and Failure of Anisotropic Solids, Villars de Lans, Août 1987.
11. Brémand F., Dupré J.C., Lagarde A., "Non-contact and non disturbing local strain measurement methods I Principle", Eur. J. Mech. A/Solids 11 n°3, pp. 349-366, 1992.
12. Cottron M., Brémand F., Lagarde A., "Non-contact and non-disturbing local strain measurement methods II Applications", Eur. J. Mech. A/Solids 11 n°3, pp. 367-379.
13. Valle V., Cottron M., Lagarde A., "A new optical method for dynamic strain measurement". 10<sup>th</sup> International Conference on Experimental Mechanics Lisbon 1994.
14. Meva'a L., Brémand F., Lagarde A., "Optical methods of strain measurement of cylindrical specimen submitted to uniaxial load". 10<sup>th</sup> International Conference on Experimental Mechanics Lisbon 1994.
15. Cloud G.L., "Optical methods of engineering analysis" Cambridge University Press, pp. 447-491.

16. Rajaona D.R., Sulmont P., "A method of spectral analysis applied to periodic and pseudo-periodic signals", *Jour. Comput. Phys.*, Vol. 61, n°1, pp. 186-193, October 1985.
17. Dupré J.C., "Traitement et analyse d'images pour la mesure de grandeurs cinématiques, déplacements et déformations à partir de la granularité laser et de réseaux croisés, et pour l'étude de couplage thermomécaniques". Thèse de Doctorat de l'Université de Poitiers, 1992.
18. Dupré J.C., Lagarde A., "Optical method of the measurement at distance of local strains", XVIII<sup>th</sup> International Congress of Theoretical and Applied Mechanics, Haifa, Israël, August 22-28, 1992.
19. Dupré J.C., Cottron M., Lagarde A., "Méthode indépendante des petites translations de l'objet, pour la mesure locale et à distance avec quasi-hétérodynage de l'état de déformations", *C.R. Acad. Sci. Paris*, Tome 315, Série II, n°4, pp. 393-398, 1992.
20. Wang S.B., Cottron M., Lagarde A., "An holographic grid technic for a whole strain measurement and application to elastoplastic structure". 10<sup>th</sup> International Conference on Experimental Mechanics Lisbon 1994.
21. Brillaud J., Lagarde A., "Ellipsometry in scattered light and its application to the determination of optical characteristics of a thin slice in tridimensional photoelasticity". Symposium IUTAM "Optical Methods in Mechanics of Solids", Poitiers, septembre 1979, (Sijhoff Noordhoff).
22. Brillaud J., Lagarde A., "Méthode ponctuelle de photoélasticité tridimensionnelle". R.F.M. n° 84, 1982.
23. Brillaud J., "Mesures des paramètres caractéristiques en milieu photoélastique tridimensionnel. Réalisation d'un photoélasticité automatique. Applications". Thèse de Doctorat d'Etat, Poitiers, 1984.
24. Lagarde A., "Non-obstructive Three Dimensional Photoelasticity -Finite strains Applications Photoelasticity". M. Nisida, K Kawata Springer Verlag 1986. Nisida M., Kawata K., Springer Verlag "Photo-elasticity Proceeding" of the International Symposium on Photoelasticity, Tokyo, 1986.
25. Lagarde A., "Dynamic Photoelasticity and Caustics Recent Developments", Springer Verlag, 1987.
26. Desailly R., Lagarde A., "Sur une méthode de photoélasticité tridimensionnelle à champ complet". *Journal de Mécanique Appliquée*. Vol. 4, n° 1, 1980.
27. Desailly R., "Méthode non-destructive de découpage optique en photoélasticité tridimensionnelle - Application à la mécanique de la rupture". Thèse d'Etat n°336, Poitiers, 1982.
28. Srinath L.S., Torta Mc Graw-Hill, "Scattered Light Photoelasticity". Publishing Company.
29. Srinath L.S., Keshavan S.Y., "A simple method to determine the complete photoelastic parameters using scattered light", *Mechanics Research Communications*, 5(2), 1978, pp. 85-90.
30. Aben H., "Optical phenomena in photoelastic models by the rotation of principal axes". *Expr. Mechanics*, Vol. 6, n° 1, 1966.
31. Aben H., Josepson J., "Strange interference blots in the interferometry in inhomogeneous birefringent objects", *Applied Optics*, vol. 36, n°28, pp. 7172-7179, Oct. 1997.
32. Zénina A., Dupré J.C., Lagarde A., "Découpage optique d'un milieu photoélastique épais pour l'étude des contraintes dans un milieu tridimensionnel", 13<sup>ème</sup> Congrès Français de Mécanique, Poitiers, France, Vol. 4, pp. 447-450, Sept. 1997.
33. Hickson V.M., "Errors in stress determination at the free boundaries of "Frozen stress" photoelastic model". *J. Appl. Phys.*, Vol. 3, n°6, p. 176-181, 1952.
34. Desailly R., Froehly C., "Whole field method in three dimensional photoelasticity : improvement in contrast fringes". Symposium IUTAM "Optical Methods in Mechanics of Solids", Poitiers, september 1979. Sijhoff Noordhoff.
35. Desailly R., Lagarde A., "Surface Crack Analysis by an Optical Slicing Method of Three Dimensional Photoelasticity" Experimental Stress Analysis Haifa Israël, août 1982.
36. Dupré J.C., Plouzennec N., Lagarde A., "Nouvelle méthode de découpage optique à champ complet en photoélasticité tridimensionnelle utilisant des moyens numériques d'acquisition et d'analyse des champs de granularité en lumière diffusée", *C.R. Acad. Sci. Paris*, t, 323, Série II b, pp. 239-245, 1996.
37. Dupré J.C., Lagarde A., "Photoelastic analysis of a three-dimensional specimen by optical slicing and digital image processing", *Experimental Mechanics*, Vol. 37, n°4, pp. 393-397, Dec. 1997.

*Other references can be found in Lagarde A. "Progress in photomechanics". General Lecture 10<sup>th</sup> International Conference on Experimental Mechanics. Lisbon 1994.*

### **The assessment of the $T^*$ fracture parameter during creep relaxation**

*The limitations of experimental measurement and advantages of a hybrid approach to the problem.*

Colin Walker and Peter MacKenzie  
Department of Mechanical Engineering,  
University of Strathclyde,  
Glasgow, UK

#### **Abstract**

While most fracture mechanics investigations are concerned with crack growth, there is a class of behaviour that occurs during creep relaxation where the plastic zone develops in a regime of reducing stress and near-zero crack growth. This behaviour has been measured in the aluminium alloy 7075 T6, using moiré interferometry at 190 °C, and the experimental data have been used to investigate the  $T^*$  integral fracture parameter as a function of time and creep deformation

It was found that under time-dependent deformation conditions  $T^*$  could be measured successfully. For a fuller investigation of  $T^*$  as a function of the deformation a finite element model of the specimen was calibrated using experimental data.

#### **Introduction**

While the use of the J-integral has become widespread in fracture mechanics, progress has been slow towards a new parameter that will be valid for conditions where J is by definition outside its area of relevance. New fracture parameters such as the  $T^*$  integral have been enunciated (1), and investigated by means of computational models, the difficulties in carrying out valid experiments have meant that few studies have attempted to correlate theory, computation and experimental measurements (2,3). It is only by such means that confidence may be established, and the new formalisms pass into routine use.

In a previous study the authors have shown how strain field data from a crack growth experiment may be analysed, to show that in reality J and to  $T^*$  are indeed equal in situations of modest crack growth as would be expected (3). The main conclusion from this work was a validated routine for assessing  $T^*$  from the strain field components around the crack tip as visualised by moiré interferometry . The next phase in the investigation of  $T^*$  is to evaluate it in a situation where either extensive plasticity or crack growth occur or where time dependent deformation takes place. This study is

concerned with time-dependent deformation.

The particular situation investigated it is one of stress relaxation where the specimen is held on a fixed grip configuration at a load sufficient to cause creep at the test temperature ( $190^{\circ}\text{C}$  for the aluminium alloy 7075 T6). In this experiment, the load steadily reduced as the specimen deformed. The crack in essence did not extend which meant that the data analysis was a simple matter compared to that for an extending crack.

#### T\* Integral Fracture Parameter

The  $\text{T}^*$  integral may be defined following the notation in Figure 1 as

$$\text{T}^* = \int_{\Gamma_i} [Wn_1 - T_i u_{i,1}] ds$$

$\text{T}^*$  may also be defined as a summation along the loading history of the incremental form:  $\Delta T^*$  viz.

$$\Delta T^* = \int_{\Gamma} [\Delta W \delta_{ij} - (T_i + \Delta T_i) \Delta u_{i,1} - \Delta T_i - u_{i,1}] ds$$

The path  $\Gamma$  should be taken as small as possible but still contain (and avoid) the process zone, where intense microcracking will take place, and the strain field parameters will not be well defined.

By suitable manipulation, one may derive

$$\begin{aligned} \Delta T^* &= \int_{\Gamma} [\Delta W \delta_{ij} - (\sigma_{ij} + \Delta \sigma_{ij}) \Delta u_{i,1} - \Delta \sigma_{ij} u_{i,1}] n_j ds \\ &\quad - \int_{v-v_s} \int \{ \Delta \epsilon_{ij} (\sigma_{ij} + \frac{1}{2} \Delta \sigma_{ij}),_1 - \Delta \sigma_{ij} (\epsilon_{ij} + \frac{1}{2} \Delta \epsilon_{ij}),_1 \} dV \end{aligned}$$

Where  $\text{T}^*$  may now be calculated from the strain field parameters alone, with a knowledge of the constitutive relations for the material.

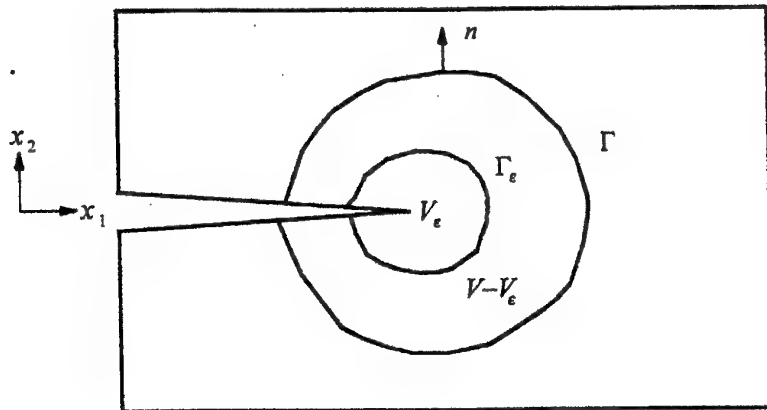


Figure 1. Integration contours for calculation of a path integral in a cracked body

- $n$  = outward normal
- $\Gamma$  = outer integration contour
- $\Gamma_\epsilon$  = inner integration contour
- $V_\epsilon$  = volume defined by  $\Gamma_\epsilon$
- $V - V_\epsilon$  = volume defined by  $\Gamma$
- $x_1, x_2$  = coordinate system

#### Integration Path

In the summation of  $\Delta T^*$  along the loading history, the path  $\Gamma$  stays stationery in relation to the cracked tip i.e. the  $\Gamma$  moves with the crack tip.

This implies that data needs to be recorded ahead of the track tip for use eventually as the crack propagates. This is the one feature of the grating method that is highly attractive, as the whole crack-tip field is recorded as a unity. Given that no crack growth was intended in this study, a fixed contour could be used. (Dimensions are given in Figure 2)

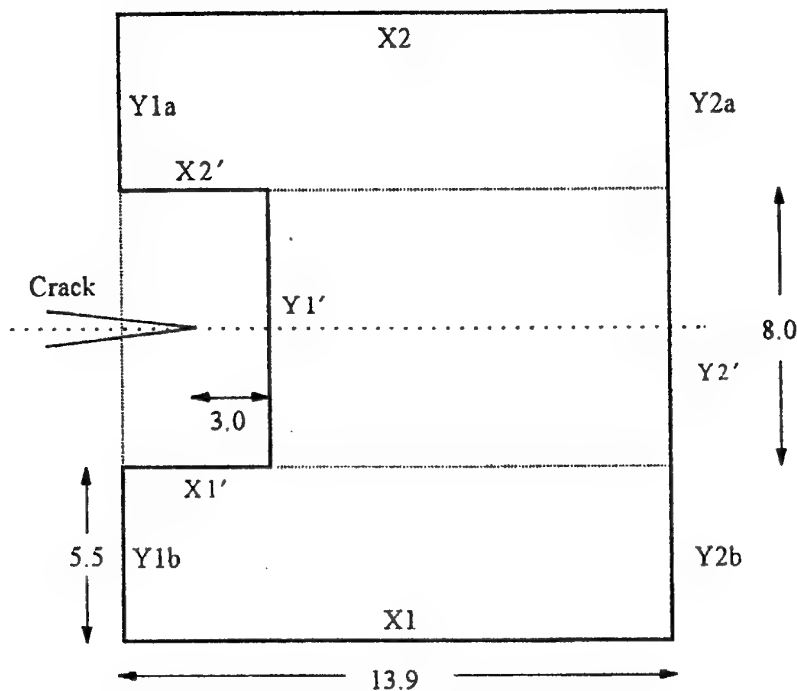


Figure 2. Path of integration (distances in mm)

#### Experimental Procedure

The specimen material was a high strength aluminium alloy (7075 T 6), in the shape of a compact tension fracture specimen (Figure 3). The starter crack was fatigue precracked from a machined notch, although, in fact, due to the degree of creep deformation envisaged, this precaution was probably unnecessary. After precracking a 500line/mm

cross grating was cast on to the area around the crack tip. An epoxy resin was used, although at 190°C, this was close to the upper operational limit for epoxy gratings. Perceptible degradation took place in the gratings over the period of the test (24 hours)

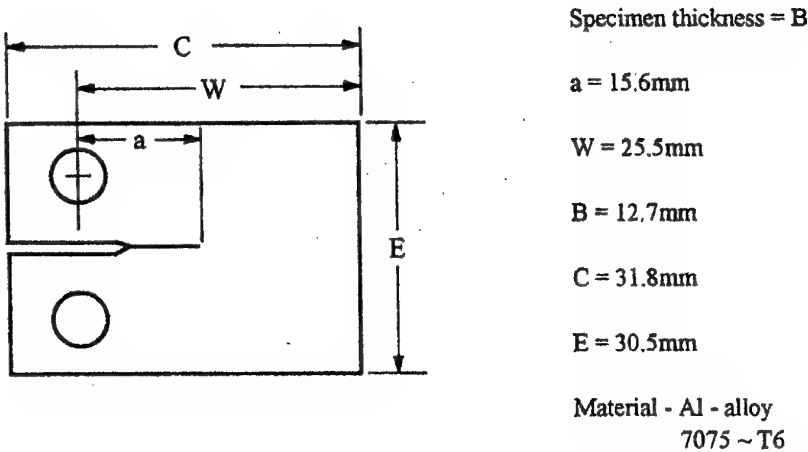


Figure 3. Specimen details

A servo hydraulic test frame applied the initial load of 12.5 kN and thereafter the displacement was held constant. An oven with a low-expansion glass window of optical quality maintained the temperature of the test. A shroud to minimise convection currents surrounded the window. With this system, it was found that high quality interferograms could be recorded using a moiré interferometer that has been previously described (4). The system is largely immune to ambient vibration; interferograms were recorded in three directions (0, 90, 45) so that a complete record of deformation was available for any point in the field for the times recorded ( $t=0, 3, 8, 15, 23, 79, 283, 1318$  minutes). (Sample interferograms are shown in Figure 3). Over the period of the tests, the load relaxed to 5. 3kN - i.e. to less than 50 per cent of its original level.

#### Fringe Analysis

Each interferogram was overlain by the outline of the contour of integration. It will be seen that there is a region around the crack tip when no fringes are visible (Figure 4). While the basic cause of this is the intense deformation that causes the surface to dimple, fringes are actually formed in this region, but the surface rotation directs the diffracted light out of the system. For convenience, then, the inner contour was defined outside of this zone (Figure 2). Fringe analysis was then carried out using a graphics-digitising

tablet as input to an analysis programme (5). The volume integration was accomplished by decomposing the area between the contours into horizontal and vertical stripes (6). Only the bottom half of the area was digitised, in view of the symmetry about the crack. As a check to insure that the near-field path remained within the elastic regime, a test of the principal stresses was included in the  $T^*$  evaluation using the von Mises criterion. No evidence of yielding was found for times up to 23 minutes.

### Results

The calculated values for  $t=0$  to  $t=23$  minutes are shown in Table 2. Up to this point, the creep zone evolved close to the crack tip. Beyond this time, the creep zone spread beyond the integration contour. It is possible to calculate  $T^*$  in this regime, if the creep rates are known as a function of time at each position, and one is able to presume that the deformation is primarily creep. An interpolation of the creep rates from 79 to 1318 minutes showed unstable results. The fact remains that there are two simple situations - one where the creep zone is limited, and the other where creep is dominant throughout the specimen; in the transition between the these two neither elastic nor creep deformations are dominant, and the strain field cannot be easily measured experimentally. In order to decouple plasticity and creep, one could unload the specimen periodically, removing the elastic component (which is time-dependent due to the reducing load and the spreading creep field). Alternatively, the moire data could be used to validate an elastic - plastic finite-element model of the specimen. This option was adopted (7), and with the model, the spread of the creep zone (defined as a 0.1 per cent creep strain) from a small area around the crack at 15 minutes to a zone extending to the uncracked border by 203 minutes was analysed and predicted (Figure 5)

### Conclusion

In a creep - relaxation experiment, it has been shown that  $T^*$  may be measured solely from the strain field parameter so long as the creep strains are limited to a zone close to the crack tip. When the creep zone grows beyond the inner integration contour, and establishes dominance across a specimen, the elastic and plastics strains need to be decoupled. This may conveniently be accomplished with an elastic - plastic finite element model of the specimen.

It should be noted that the results achievable with a combined approach are greater than with either of the techniques on its own, since the FE model gained its credibility from the comparison with the experimental data.

### References:

- 1) Atluri, SN and Nakagaki, M An incremental path independent integral in inelastic and dynamic fracture mechanics. *Engineering Fracture Mechanics*, 20, 1984, 209-244.
- 2) Atluri, SN et al.  $T^*$ -Integral Analysis of Fracture Specimens, Proc ESDA 1996, Montpellier, 76, 89-94.(ASME)

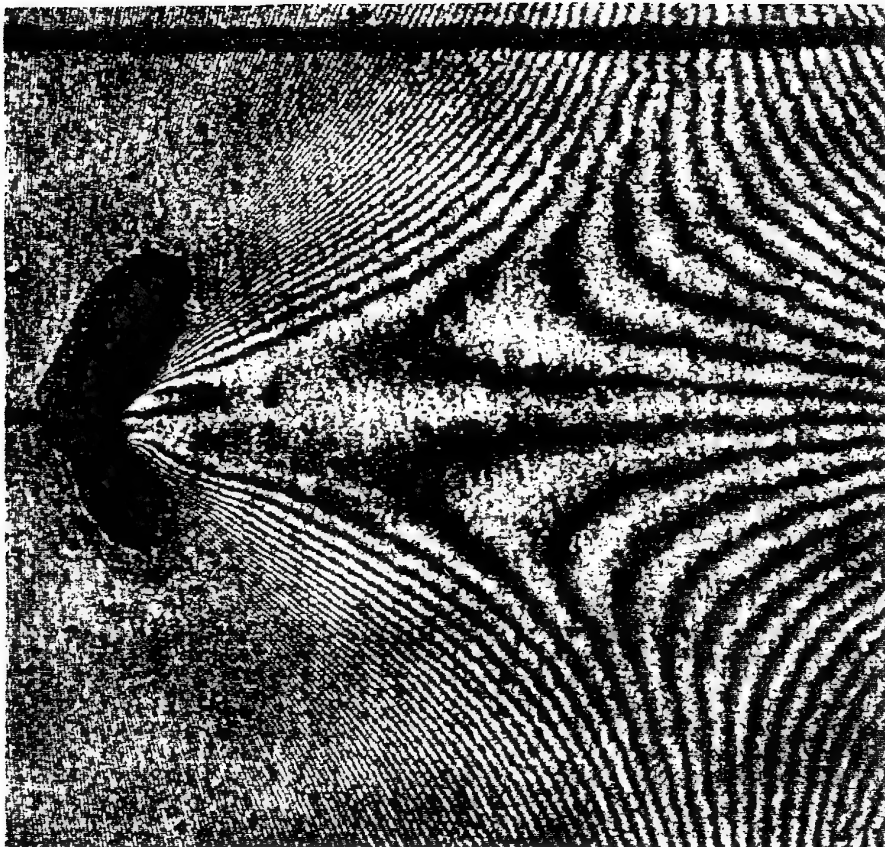


Figure 4a  
Deformation Contours around the crack tip after 3minutes  
(deformation contour interval – 1.05 micron, linear magnification 8.5x)

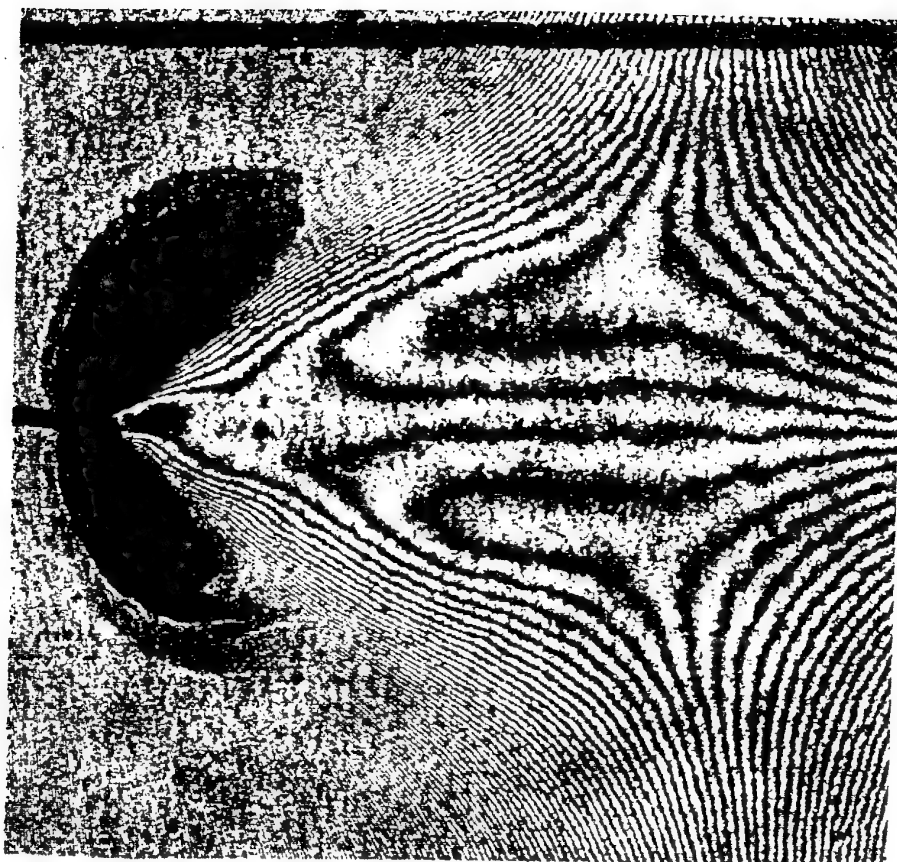


Figure 4b  
Deformation Contours around the crack tip after 24 hours  
(deformation contour interval = 1.05 micron, linear magnification 8.5x)

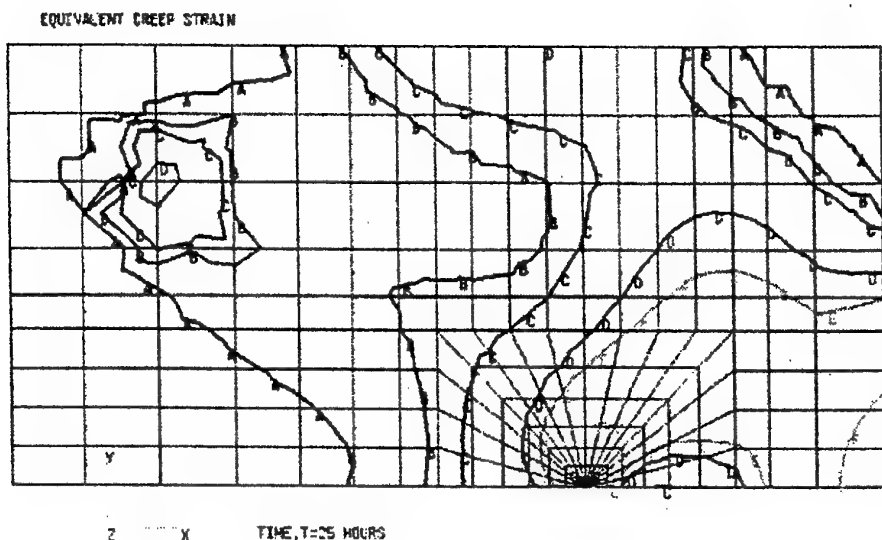


Fig.5

Predicted creep contours after 25h

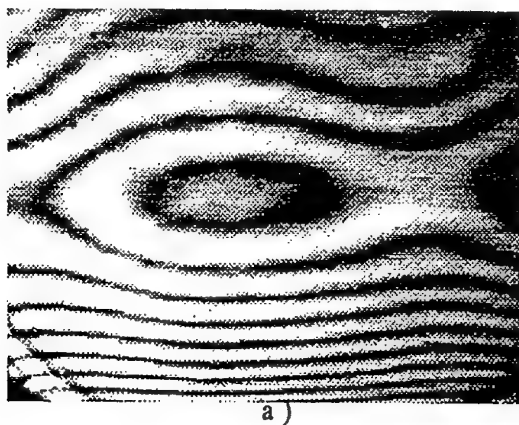
TEMPERATURE INSENSITIVE MOIRÉ INTERFEROMETRY: A QUANTITATIVE INVESTIGATION.

J. MCKELVIE AND G. COLLIN,  
*Dept of Mechanical Eng., University of Strathclyde, Glasgow, Scotland*

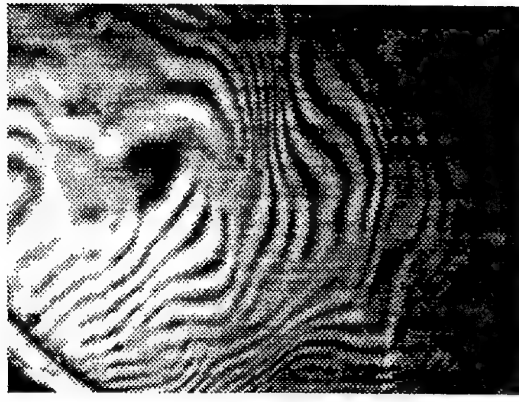
ABSTRACT: Fringe patterns produced in an allegedly thermally-immune moiré interferometry arrangement, through severely thermally disturbed air, have been analysed quantitatively. It is found that the spurious strains are generally less than  $30\mu\epsilon$ .

1. Introduction

Coherent-optical interferometric methods of strain measurement (holography, speckle and moiré) have been usefully employed for almost thirty years now, but one of their limitations in common has been the effect of thermal non-uniformity in the medium through which the beams pass.



a )



b)

Fig. 1

The resulting disturbance of the phase of the light, and concomitantly of the pattern of the interference fringes, has generally meant that the methods have been employed only for investigations at ambient temperature; (but including, importantly, cases where the object has been heated and then cooled again, - a circumstance in which there is no thermal disturbance of the beams).

An example of a moiré interferogram is shown in Fig 1a, and the effect of disturbing one of the beams using the turbulent air ahead of a small blow-torch flame is shown in Fig 1b.

A notable exception to this general avoidance of non-ambient work has been the work of Kang et al. ([1] & [2]). In that work, moiré interferometry was used for live investigations of specimens under load in ovens at temperatures up to 1100°C, with the light passing into and out of the oven through quartz windows, with no particular precautions being taken to obviate or quantify any thermal disturbance. The resulting interferograms published in that work are quite astonishingly good, considering the conditions, but in any such environment there must always be a measure of doubt as to the value of the information extracted. Even the absence of fringe movement is not a sufficient condition for confidence, since the existence of steady-state disturbance due to, for example, thermal gradients, cannot be discounted.

A more considered approach to the problem is that of Hyer et al.[3], in which the two illuminating beams of a moiré interferometer are created very near to the specimen by using a suitable prism beam splitter in very close proximity, with single-beam illumination. Any phase disturbance of the single beam up to the prism creates compensating disturbances in both incident beams. However, any thermal gradient that exists within the prism will cause phase disturbances that are not mutually compensating, although it is conceivable to monitor the extent of such gradients.

In McKelvie, [4], there was presented an optical arrangement for moiré interferometry that is of its nature immune to thermal disturbance for the purpose of strain measurement (but, importantly not for more general displacement measurement). The efficacy was demonstrated purely qualitatively in that work by illustrating an interferogram undisturbed and then disturbed, where it could be seen that although there was major change of the fringe spacing in the direction parallel to the grating lines, the spacing perpendicular to them (which is the quantity of major interest) appeared to be hardly affected.

There was, however, no quantification of the disturbance, which is what this current work addresses.

## 2. The Extent of the Problem

A simple experiment was carried out to determine how serious the general problem might be. A raw He-Ne laser beam was set to pass through a small tube furnace held at 1100°C. The position of the spot at a distance of 1 metre was monitored on a screen. In steady conditions the spot moved approximately 1mm, with a little obvious perturbation. In a typical moiré interferometer (1200 lines/mm) such an angle of deflection of 0.06° would correspond to a spurious strain of 900 $\mu\epsilon$ , or 2500 $\mu\epsilon$  for the 600 lines/mm grating used by Kang. However, when a fan was used to blow air past the exit of the furnace tube, the deflection changed rapidly and erratically, and more severely, up to 4mm, corresponding to spurious strains of some 3,600 $\mu\epsilon$  and 10,000 $\mu\epsilon$  respectively for the two grating frequencies.

By comparison, using a grazing incidence angle of 88.5° (and the appropriate grating frequency of 1580 l/mm), the corresponding spurious strains are 28 $\mu\epsilon$  and 112 $\mu\epsilon$  for the 0.06° and 0.24° deviations, respectively.

In the context of typical engineering strains encountered at these temperatures, such error, as an outside limit, is very acceptable.

### 3. The Optical Arrangement

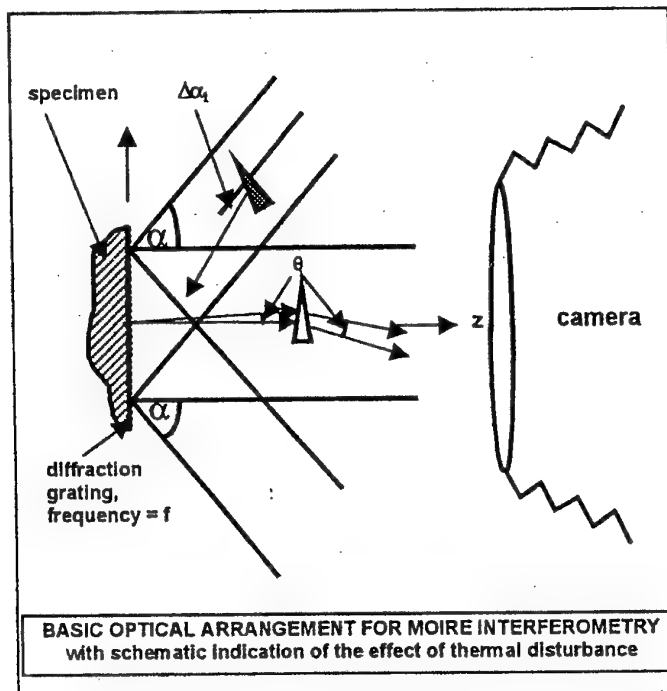
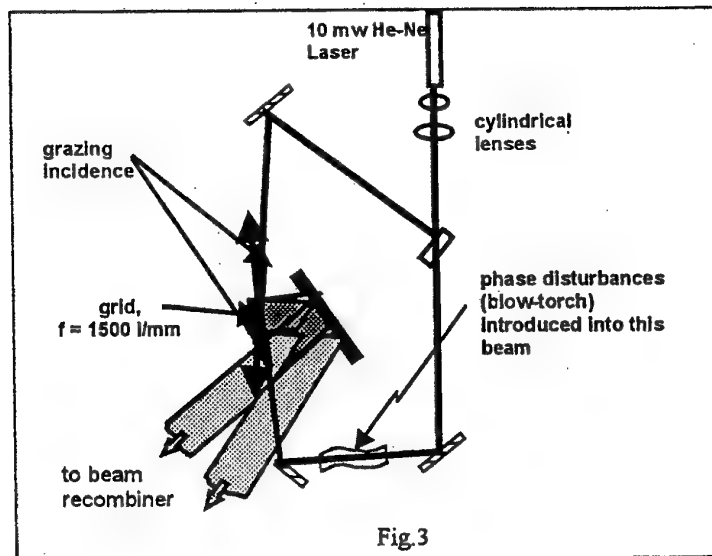


Fig. 2



For the sake of completeness, the generic optical arrangement for moiré interferometry is shown in Fig 2. There is some degree of immunity to thermal disturbance, imparted by virtue of the fact that two emerging diffracted rays that are brought together in the plane of the image pass through essentially the same intervening space, (because their angle of divergence is very small)..

Their phases will be altered to the same degree therefore, so that there results a very substantial immunity to thermal disturbance in that space between specimen and camera, as is easily demonstrated. The difficulty arises in the two illuminating beams, whose phases will be altered the one quite independently from the other. These effects are indicated schematically by the actions of the prisms in Fig 2

The essence of the solution is in arranging that the angles of incidence of the illuminating beams are close to 90° (i.e. grazing incidence). An analysis explaining the immunity is presented in McKelvie, 1997.

Fig 3 shows the particular layout for the experimental work. Because no grating was to hand that corresponded to grazing incidence together with normal emergence for the He-Ne wavelength, the emergent beams actually diverged, as indicated, but were brought to interference using a beam recombiner. The thermal disturbance was introduced in one of the input beams by means of the blow-torch as used in generating Fig 1b. A video was taken, and three frames are illustrated as Figs 4a, 4b, 4c. What appears to be the worst case, Fig 4c, was chosen for detailed comparison with the undisturbed original "zero" condition, shown in Fig 1a.

#### 4. The Fringe Analysis

The fringes were manually digitised by estimating the y-positions of their centres along vertical lines spaced at 20mm intervals (the prints being 240mm long) in the x-direction. The fringe values, N, at these positions were entered into a Stanford Graphics package, and 6<sup>th</sup> order polynomials  $N=f(y)$  were fitted to the data. Values of fringe order N on a matrix

$$x = 0 \text{ to } 240 \text{ (20mm intervals)}$$

$$y = 0 \text{ to } 180 \text{ (10mm intervals)}$$

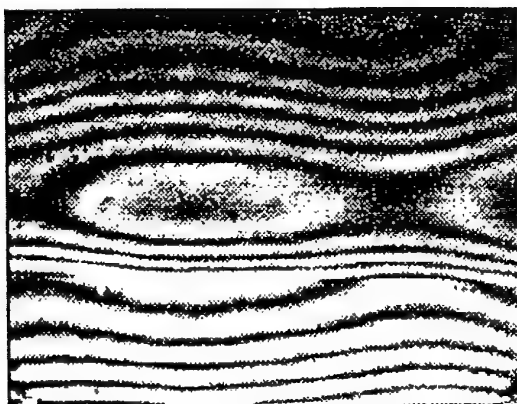
were calculated. Contours of the constant N are shown as Fig 5, corresponding to Fig 1a. The agreement is seen to be generally good, but for the purpose of determining strains, fitting with a two-dimensional polynomial was found to be not sufficiently accurate. Instead, the values on individual columns ( $y=\text{constant}$ ) were fitted with 4<sup>th</sup>

order polynomials,  $N=f(x)$ , from which the derivative  $\frac{\partial N}{\partial x}$  was calculated. For the

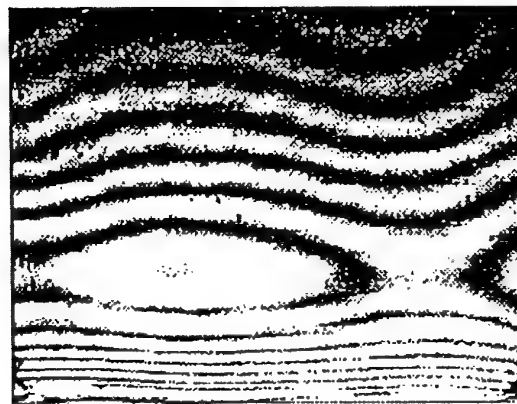
"deformed" case, (Fig 4c), it was not possible to fit  $N=f(x)$  for the whole y- range from 0 to 180 due to a particularly powerful disturbance that can be seen running across the field, approximately half way up. Instead, the curve-fitting was done up to  $y=100\text{mm}$ , and then separately from  $y=100$  upwards (with a small overlap region). The fringe contour interval was 1/3000mm, (grating frequency 1500 lines/mm). Knowing that, and the magnification (from frames in which the blow-torch appeared), the connection

between  $\frac{\partial N}{\partial x}$  in the space of the print and  $\frac{\partial u}{\partial x}$  in the space of the grating is known.

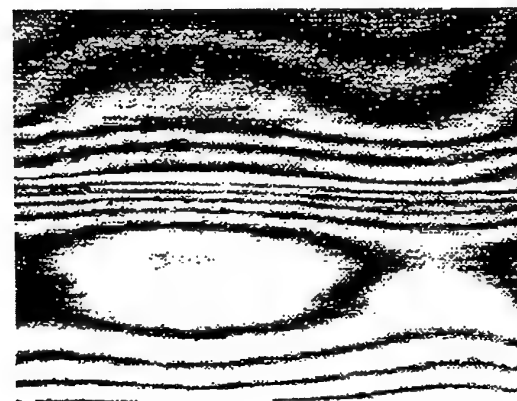
Since  $\varepsilon_x = \frac{\partial u}{\partial x}$  it was straightforward to generate estimates of the x-strains for each interferogram, and thus their differences, by differentiation of the fitted polynomials.



a)



b)



c)

Fig. 4

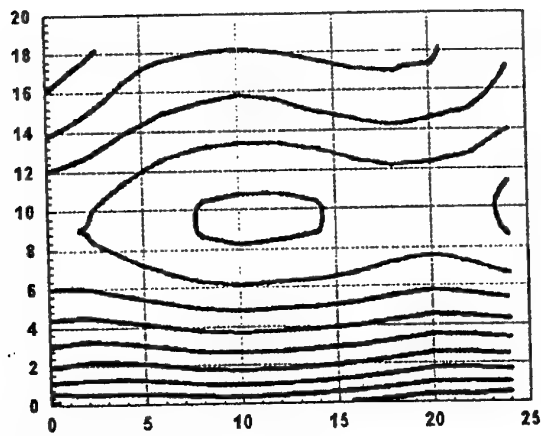


Fig. 5

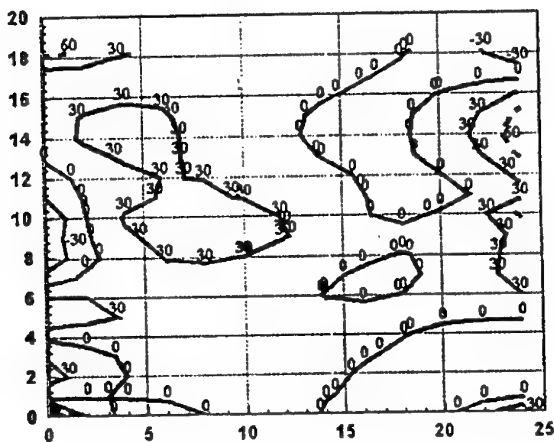


Fig. 6

The resulting "errors" – that is the apparent strain field introduced by the very violent thermal disturbance – are plotted as Fig 6. It can be seen that generally the error rarely exceeds  $30\mu\epsilon$  except near edges, where the value may rise to over  $60\mu\epsilon$ . (The highest error recorded was  $137\mu\epsilon$ , occurring in the extreme left-hand bottom corner, where, in fact, there is no information at all in the undisturbed field).

At edges of course, – and especially at corners – the curve-fitting algorithms would be rather more prone to error than elsewhere.

### 5. Possible Application in Other Coherent Systems

There are systems, in holographic and speckle interferometry, that are sensitive essentially to in-plane displacements, using two conjugate collimated illuminating beams - as in moiré interferometry. Grazing incidence will endow the same degree of immunity on the incident beams in these systems as for the moiré system, but the emergent beams present a different problem. That is because the interference that produces the displacement fringes arises not only between two beams, but, in effect, four, - the two in the first exposure and the two in the second - so that any change in the relative phases across the space in the interval between the exposures will cause distortion of the fringes. Any application must therefore employ rapid double-exposure, so that the thermal distribution has no time to alter, - but such circumstances would also obviate the need for grazing incidence anyway.

### 6. Conclusion

It has been demonstrated quantitatively that the use of grazing incidence in the illuminating beams renders moiré interferometry immune within typical engineering acceptability, to the effects of even quite violent thermal disturbance of the surrounding space. The stratagem would not be of benefit in the analogous systems using holographic or speckle interferometry.

### 7. References

1. Kang, B.S.-J., Zhang, G.Z., Jenkins, M.G., Ferber, M., & Ifju, P. 1993. Development of Moiré Interferometry for In-situ Material Surface Deformation Measurement at High Temperature. *Proc. SEM Spring Conf. on Experimental Mechanics*, Dearborn, MI, 964-976.
2. Kang, B.S.-J., Zhang, G.Z., Manohar, E., & Liu, P., 1994. Creep Crack Growth of Inconel 718 Superalloy at Elevated Temperature Using Moiré Interferometry. *Proc. SEM Spring Conf. on Experimental Mechanics*, Baltimore, MD, 904-912.
3. Hyer, W.M., Herakovich, C.T., & Post, D. 1982, Thermal Expansion of Graphite Epoxy. *Advances in Aerospace Structures and Materials*, ASME 1982.
4. McKelvie, J. 1997. Thermal-insensitive Moiré Interferometry. *Opt. Lett.*, 22, 1, 55-58.

## AN EXTENSION OF HOLOGRAPHIC MOIRÉ TO MICROMECHANICS

C.A. SCIAMMARELLA

F.M. SCIAMMARELLA

*Illinois Institute of Technology*

*Dept. of Mechanical Materials and Aerospace Engineering*

*10 West 32<sup>nd</sup> St. E1 bldg. Chicago IL, 60616 U.S.A.*

### Abstract

The electronic Holographic Moiré is an ideal tool for micromechanics studies. It does not require a modification of the surface by the introduction of a reference grating. This is of particular advantage when dealing with materials such as solid propellant grains whose chemical nature and surface finish makes the application of a reference grating very difficult. Traditional electronic Holographic Moiré presents some difficult problems when large magnifications are needed and large rigid body motion takes place. This paper presents developments that solves these problems and extends the application of the technique to micromechanics.

### 1. Introduction

In [1] one of the authors presented a method to measure displacements and to obtain strains in the microscopic range by using electronic holography. This method can only be used in static problems. The method is based on repeated measurements of a specimen under the same conditions. This paper presents a different approach. A similar optical arrangement is utilized but the actual data processing method has been changed so that dynamic measurements can be performed.

### 2. Review of the Foundations of the Method

Recording holographic interference patterns via a CCD camera and the reconstruction of those patterns by electronic means are referred to in the literature as holographic TV, electronic holography, electronic speckle pattern interferometry. The patterns are recorded in the same way as in conventional lens holography with an almost in line reference beam. The fringe interpretation is the same as in conventional holographic interferometry. The basic equation of holographic interferometry is valid,

$$\phi = \frac{2\pi}{\lambda} (\mathbf{d} \cdot \mathbf{S}) \quad (1)$$

where  $\phi$  is the phase angle corresponding to a point in the region of analysis,  $\lambda$  is the wavelength of the illuminating light,  $\mathbf{d}$  is the displacement vector of the considered point and  $\mathbf{S}$  is the sensitivity vector. In most of the currently utilized systems, the recovery of the displacement information is done by a method that is very similar to the method proposed initially by Leendertz [2] in speckle interferometry. This technique is based on the correlation of the speckle patterns corresponding to the initial or unloaded condition and the final or loaded condition. A complete description of this technique and examples of its application can be found in [3]. A computer version of this technique has been given in [4]. In [5] a different approach is presented. In [6] a procedure based on the precise relocation of a specimen by a control system, via fiducial marks is presented.

## 2.1. HOLOGRAPHIC MICROSCOPY

The use of holography in microscopy has been the object of extensive studies. Holographic microscopy has also been applied to many different technical and scientific fields. The different applications show the versatility of holography as a tool in microscopy, but at the same time they reveal the enormous difficulties there are to obtain optimum conditions. Most of the effort has been placed on eliminating the speckles to get adequate resolution. In the application that we are analyzing the information is encoded in the speckles, therefore we must preserve them. The resulting image will be of poor quality, thus the problem has to be approached in the following way. A white light image of the region of interest must be recorded to obtain the features of interest. The images to measure the displacements must be recorded with coherent light. Afterwards the displacement field must be related to the surface features. The speckle visibility must be optimized to obtain the displacement information with optimum signal to noise ratio. The speckle visibility depends on many variables and requires a complex statistical analysis. However, an elementary analysis can be employed to get an insight on the main variables controlling fringe visibility. The equation

$$I(r') = \left[ \int_A k(r, r') A(r) e^{i\phi(r)} dA \right]^2 \quad (2)$$

expresses the intensity in the image plane of the recording lens system. In (2),  $r$  is the polar coordinate of a point in the object plane and  $r'$  is the coordinate of the same point in the image plane, the term  $A(r) e^{i\phi(r)}$  represents the object field and  $k(r, r')$  represents the spread function of the imaging system. The spread function defines the area of the object that contributes to the image at a given point of the image. The other factor defines the amplitude and phase of the region of influence determined by the spread function. The amplitude variations depend on the changes in reflectivity and phase of the surface. In turn, these quantities depend on the statistical properties of the surface. The larger the changes of phase and reflectivity are in the area of influence of the point under observation, the greater are the changes of intensity in the image, causing speckles with more contrast.

### 2.1.1. Basic Properties of the Microscope

The basic properties of interest are:

- a) Displacement resolution
- b) Spatial resolution
- c) Magnification
- d) Depth of focus

The displacement resolution depends on the configuration of the optical system. We are interested in the in-plane displacements consequently the double illumination technique is used. Since we have two beams that act as reference beams to each other, no additional reference beam is necessary. Calling  $\theta$  the angle of the beams with the normal to the surface that at the same time is the direction of observation we get,

$$\Delta d = \frac{\lambda}{2 \sin \theta} \quad (3)$$

One important consideration in making microscopic measurements is the fact that since the region under observation is small, even if the strains are high, the displacements will also be small. We can see that the sensitivity is limited by  $\theta$  and by the wavelength of the light. The spatial resolution  $\Delta s$  is related to the numerical aperture (NA) of the lens system through a relationship of the form,

$$\Delta s \propto NA^{-1} \quad (4)$$

The above equation indicates that to get the best resolution possible the NA must be increased. There is another requirement, depth of focus  $\Delta z$ ,

$$\Delta z \propto NA^{-2} \quad (5)$$

This implies that if we increase the NA to get the best resolution possible we lose depth of focus. The transversal size of the speckle is given by,

$$\Delta \rho \propto NA^{-1} \quad (6)$$

and the longitudinal size  $\Delta l$ ,

$$\Delta L \propto NA^{-2} \quad (7)$$

### 3. Techniques to Obtain Displacement Information

As shown in Fig. 1 we have a specimen that is illuminated coherently by four symmetrically oriented beams. The microscope focuses the surface of the specimen onto the CCD camera sensor. If we consider a region within the area of influence

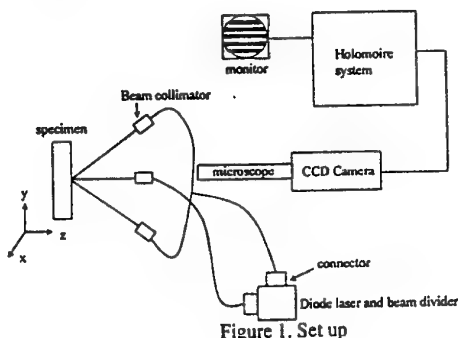


Figure 1. Set up

defined by equation (2), the total light amplitude reaching this region is made out of four components. We have four beams, two in the x-direction and two in the y-direction.  $E_{1x} = E_{1x} e^{i\phi_x}$ ,  $E'_{1x} = E_{1x} e^{-i\phi'_x}$  in the x-direction and  $E_{2y} = E_{2y} e^{i\phi_y}$ ,  $E'_{2y} = E_{2y} e^{-i\phi'_y}$  in the y-direction. In these equations the E's represent the amplitudes of the illumination beams, and the  $\phi$ 's represent the phases in the same region. If we assume that the two orthogonal systems of illumination are non coherent (direction of polarization orthogonal to each other), the intensity gathered in the region will be,

$$I_{1T}(x, y) = I_o + 2I_{1x} \cos \psi_x(x, y) + 2I_{2y} \cos \psi_y(x, y) \quad (8)$$

where  $I_{1x} = (E_{1x})^2$ ,  $I_{2y} = (E_{2y})^2$ ,  $\psi_x(x, y) = \phi_x - \phi'_x$ ,  $\psi_y(x, y) = \phi_y - \phi'_y$ . Let us assume that a deformation has been applied to the specimen and that this deformation leaves the E's substantially unchanged and only causes phase changes. The second exposure results in an intensity distribution,

$$I_{2T}(x, y) = I_o + 2I_{1x} \cos [\psi_x(x, y) + \Delta\phi_x] + 2I_{2y} \cos [\psi_y(x, y) + \Delta\phi_y] \quad (9)$$

where,

$$\Delta\phi_x = 2\pi f_p u(x, y) \quad (10)$$

$$\Delta\phi_y = 2\pi f_p v(x, y) \quad (11)$$

In the above equations  $f_p = 2\pi \sin \theta/\lambda$  and  $u, v$  are the components of displacement parallel to the x and y directions respectively. The intensities are converted into voltages, and without loss of generality can be considered proportional to the received voltages. A non-linear recording will produce [7] additional harmonics that can be removed by spatial filtering. By subtracting the signals to remove the background term we obtain,

$$V(x, y) = K \{ 2I_{1x} [\cos \psi_x(x, y) - \cos [\psi_x(x, y) + \Delta\phi_x]] \\ + 2I_{2y} [\cos \psi_y(x, y) - \cos [\psi_y(x, y) + \Delta\phi_y]] \} \quad (12)$$

Expanding the difference of the cosines, and taking the Fourier transform of (12), calling  $\xi$  and  $\eta$  the coordinates in the frequency space with the notations,

$$\bar{V}(\xi, \eta) = FT[V(x, y)] \quad (13)$$

$$A_x(\xi, \eta) = FT \left[ \sin \left[ \psi_x(x, y) + \frac{\Delta\phi_x}{2} \right] \right] \quad (14)$$

$$D_x(\xi, \eta) = FT \left[ \sin \frac{\phi_x}{2} \right] \quad (15)$$

And similar definitions for  $A_y(\xi, \eta)$  and  $D_y(\xi, \eta)$  we get,

An Extension of Holographic Moiré to Micromechanics

$$\bar{V}(\xi, \eta) = 4K \{ I_{1x} [A_x(\xi, \eta) \otimes D_x(\xi, \eta)] + I_{2y} [A_y(\xi, \eta) \otimes D_y(\xi, \eta)] \} \quad (16)$$

where  $\otimes$  indicates convolution. The quantities in brackets are the FT of random signals (speckles) convolved with a deterministic function that contains the displacement information. Our purpose is to separate the spectra of the functions that contain the displacement information from other spectral components. The approach presented here is to re-establish the correlation between the unloaded and the loaded images by a procedure that is a generalization of the optical technique described in [5].

With the notations,

$$F_{ix} = 2K I_{1x} \cos \psi_x(x, y) \quad (17)$$

$$F_{dx} = 2K I_{1x} \cos [\psi_x(x, y) + \Delta\phi_x] \quad (18)$$

$$F_{iy} = 2K I_{2y} \cos \psi_y(x, y) \quad (19)$$

$$F_{dy} = 2K I_{2y} \cos [\psi_y(x, y) + \Delta\phi_y] \quad (20)$$

we can write equation (12) assuming that a displacement  $d_x$  is given to the loaded recording,

$$V(x, y) = F_{ix} \otimes \delta(x, y) - F_{dx} \otimes \delta(x + \Delta x, y) + F_{iy} \otimes \delta(x, y) - F_{dy} \otimes \delta(x + \Delta x, y) \quad (21)$$

If we take the FT (the FT is indicated by the bar quantities) of (21), and replace the subtraction by the addition with a phase change of  $\pi$  we obtain,

$$\bar{V}(\xi, \eta) = \bar{F}_{ix} + \bar{F}_{dx} e^{i\gamma} + \bar{F}_{iy} + \bar{F}_{dy} e^{i\gamma} \quad (22)$$

if we neglect the effect of the displacements caused by the deformations  $\Delta x = d_x$  and the argument  $\gamma$  is,

$$\gamma = 2\pi d_x \xi + \pi \quad (23)$$

Then by squaring (22),

$$[\bar{V}(\xi, \eta)]^2 = H(\xi, \eta)[1 + C \cos \gamma] \quad (24)$$

where,

$$H = |\bar{F}_{ix} + \bar{F}_{iy}|^2 + |\bar{F}_{dx} + \bar{F}_{dy}|^2 \quad (25)$$

and

$$C = \frac{|\bar{F}_{ix} + \bar{F}_{iy}| |\bar{F}_{dx} + \bar{F}_{dy}|}{|\bar{F}_{ix} + \bar{F}_{iy}|^2 + |\bar{F}_{dx} + \bar{F}_{dy}|^2} \quad (26)$$

$H(\xi, \eta)$  is a random function (speckle pattern) and  $C$  is a visibility term that provides the visibility of the fringes formed in the frequency space [8]. If we take the FT of (24),

$$\overline{|V(\xi, \eta)|^2} = \overline{H(\xi, \eta)} \delta(0,0) + \overline{|CH(\xi, \eta)|} \delta(d_x, 0) \quad (27)$$

To illustrate the formation of fringes in the frequency space the orthogonal patterns shown in Fig.2 were created. An initial image was recorded and then separately two recordings were made with shifts in the  $x$  and  $y$  directions. The FT's of the subtracted images were computed and then added bringing forth Fig. 2. If we take the FT of the pattern in Fig. 2 we get the spectrum of the fringes in the frequency space, Fig. 3. The

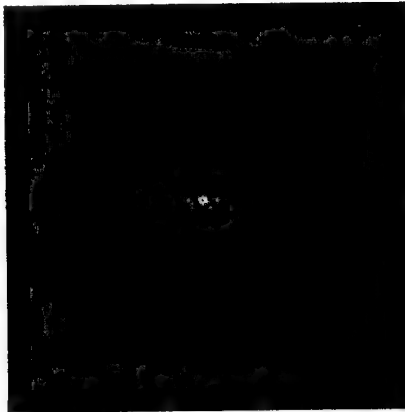


Figure 2. Fringes in FT space.

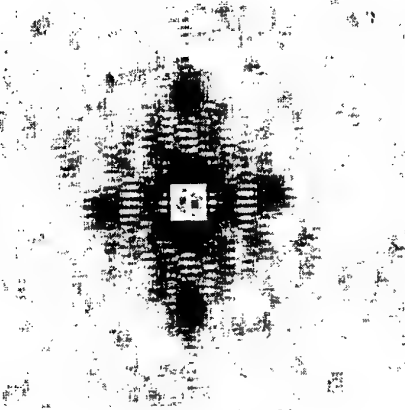


Figure 3. Spectrum of the fringes.

distances of the spectrum peaks in the x and y directions to the origin of coordinates provide the displacements  $d_x$  and  $d_y$ . If the image in Fig. 2 is filtered, we get Fig. 4 that displays the pattern of fringes without the background noise. Each time that the fringes have a minimum, for example in the x-direction,

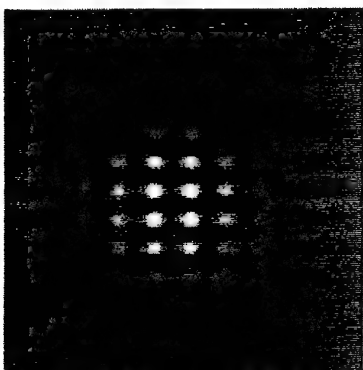


Figure 4. Filtered system of fringes.

$$\xi = \frac{2 n - 1}{2 d_x} \quad (28)$$

the patterns in the initial and in the loaded conditions are re-correlated as it can be concluded from equation (22). When the following relationship is satisfied, Fig. 5,

$$f_o = \xi_o = \frac{1}{2 d_x} \quad (29)$$

where  $f_o$  is the central frequency of the spectrum of the displacement fringes, the spectrum is located in its correct position. At any other minimum the fringe pattern will be shifted of a certain frequency shift  $\Delta\xi$  with respect to the central frequency  $f_o$  as shown in Fig. 6. If we select a displacement such that the correlation occurs at the frequency  $\xi_1$ , then we filter the spectrum at this frequency we get,

$$V(x, y) = F_{lx} - F_{dx} e^{2\pi i \Delta\xi x} \quad (30)$$

and

$$V(x, y) = 2K I_{lx} [\cos \psi_x(x, y) - \cos [\psi_x(x, y) + \Delta\phi_x + 2\pi \Delta\xi x]] \quad (31)$$

Calling  $\beta = \Delta\phi_x + 2\pi \Delta\xi x$ , after squaring we get the signal displayed in the monitor,

$$V^2(x, y) = 8K^2 I_{lx}^2 \sin^2 \left[ \psi_x(x, y) + \frac{\Delta\beta}{2} \right] [1 - \cos \beta] \quad (32)$$

If we integrate the speckle pattern in the x-direction and use the notation

$$I = 4K^2 I_{lx}^2 \quad (33)$$

the signal has the form,

$$V^2(x, y) = I [1 - \cos \beta] \quad (34)$$

We have a pattern of fringes that contains the displacement information in the x-direction and have a visibility of one. The fringes will have minima at points where  $\beta = 2n\pi$  and maxima every time that  $\beta = (2n+1)\pi$ . These fringes contain a carrier frequency and to remove it one must know the central frequency of the spectrum of the fringes. If one has an estimate of the central frequency one can use two frequencies  $f_1$

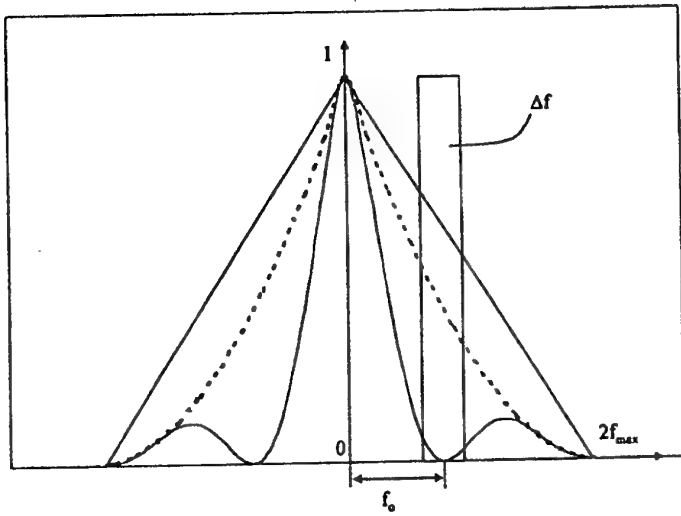


Figure 5. Filtering in the FT space.

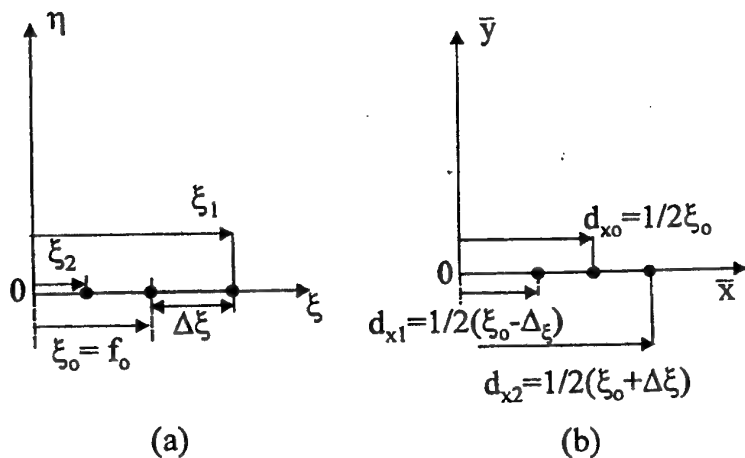


Figure 6. (a) Frequency space. Spectrum corresponding to the fringe in the physical space. (b) FT of the frequency space. Spectrum corresponding to the displacements in the physical space.

## An Extension of Holographic Moiré to Micromechanics

9

and  $f_2$  above and below the central frequency and by successive steps reach  $f_0$  taking into consideration that the phase will remain stationary at  $f_0$ .

### 3.1. ALTERNATIVE TECHNIQUE TO RECOVER THE DISPLACEMENT INFORMATION

In the preceding sections, the spectrum of the displacement fringes was recovered by shifting the loaded image with respect to the unloaded of a given amount. An alternative technique for recovering displacement information can be used in the case when large magnifications are utilized and the individual speckles cover several pixels. This technique is carried out by means of fiducial marks. These marks allow the two images to be re-positioned within one pixel, and thus the recovery of the displacement information can be achieved. The phases of the individual speckles in the unloaded and the loaded positions are determined [9]. The subtraction of these phases will yield,

$$[\psi_x(x+y) + \Delta\phi_x(x,y)] - \psi_x(x,y) = \Delta\phi_x(x,y) \quad (35)$$

The phase differences are encoded on a carrier,

$$V(x,y) = V_o \{ 1 + \cos[2\pi f_{cx}x + \Delta\phi_x] \} \quad (36)$$

where  $f_{cx}$  is the carrier frequency in the x-direction. The spectrum of the displacement fringes is encoded in the fringes and can be recovered by filtering and removing the carrier.

## 4. Applications

Our example deals with strain measurements carried out on propellant grain tensile specimens. A system for testing tensile specimens was designed and built. The system consists of Fig. 1: a) a loading frame with micrometric motions in three orthogonal directions, b) an optical fiber interferometer, c) a microscope connected to an electronic system. The fiber optics interferometer consists of a solid state laser whose output goes to four fibers that produce four collimated beams to measure displacements in two orthogonal directions. The fibers are not polarization preserving fibers but light polarization was adjusted by bending the fibers and separately matching the polarization of the horizontal beams and of the vertical beams. The observation system uses a microscope and it is possible to perform measurements in the range of few hundreds of microns up to 3 mm, maximum size of the area illuminated by the fiber optics system. The basic characteristics of the illumination system are as follows: a) angle of illumination  $\theta = 45^\circ$ , b) wavelength of laser  $\lambda = 0.635 \mu\text{m}$ , c) displacement sensitivity  $\Delta d = 0.447 \mu\text{m}$ . Fiducial marks on the specimen surface were used to restore the position of the loaded image. Many measurements were carried out on these specimens. For this paper, we are going to concentrate on the micromechanics measurements.

Propellant grains are a mixture of a rubber matrix with crystalline particles embedded in it. A binder is added to the particles to insure the adherence of the particles to the matrix. The surface of the propellant is extremely rough and the numerical aperture of the lens (NA) in the measurements carried out in this work was limited by this circumstance. The large particles in the propellant are about  $400 \mu\text{m}$  in size and of prismatic shape. Measurements were carried out at two different magnifications. In the first magnification the pixel size in the y-direction was  $\Delta y = 1.83 \mu\text{m}$  and in the second magnification applied  $\Delta y = 0.834 \mu\text{m}$ . The NA for the second group of measurements was  $NA = 0.0253$ . The speckle size was determined in three ways, directly by measurements in the image plane, by computation and by measuring the diameter of the halo in the frequency space. The three determinations yielded very close numbers around  $15 \mu\text{m}$  for the pixel diameter. For this study, measurements were performed in a region of a tensile specimen where a particle was present. Since the particle has Young's modulus that is four orders of magnitude bigger than the rubber matrix, the particle can be considered as rigid. During the computation of the strains, the particle was considered as an internal boundary. Fig. 7a shows the strains in the axial directions for the image filtered at the central frequency determined by successive approximations, for the stress level in the tensile specimen of  $\sigma = 78 \text{ KPa}$ . Fig. 7b shows the results of the same measurement by re-correlating the image using a displacement that satisfies equation (29). Fig. 8a shows the strains determined by introducing a displacement that moves the spectrum of the signal to the 12 harmonic. Fig. 8b shows the strains when the spectrum is displaced to the 16<sup>th</sup> harmonic. In view of the difficulties involved in performing micromechanics measurements, the different patterns agree reasonably well. Fig. 9a shows the region around the particle for the stress level  $\sigma = 39 \text{ Kpa}$ . The strains in this region were determined by re-correlating the spectra of the unloaded and the loaded recordings, obtained with the magnification yielding  $\Delta y = 1.83 \mu\text{m}$ . Fig. 9b shows the strains in the same region obtained with a different magnification ( $\Delta y = 0.834 \mu\text{m}$ ). The two strain distributions agree well. To get the strain distribution shown in Fig. 9b the phases of the unloaded and the loaded images were computed, subtracted and then the phase difference was encoded in a carrier. The strains were obtained by differentiating the carrier [9] and removing the strain equivalent to the carrier frequency. In all the previous cases of fringe analysis the region of the gradients between the matrix and the particle are poorly resolved. It is not possible with the equipment at hand to have a broader view of a region and at the same time to obtain accurate spatial resolution if a steep gradient is present. The CCD camera has sensors at a given distance, so the frequency resolution in the frequency space depends on the size of the regions analyzed. To illustrate this point two regions of the particle-matrix boundary are analyzed. At the side of the particle the strain parallel to the particle (axial strain), must be zero at the surface of the particle and then it should build up to the value in the field. In Fig. 9 b the analyzed section is shown. Fig. 10 shows the first  $50 \mu\text{m}$  of the boundary of the particle matrix. Fig. 11 shows the strains along the indicated cross-sections. At the end of the particle there is continuity of the stress and therefore the strain must jump to the prevailing value of the matrix, Fig. 9b shows the area that is analyzed. Fig. 12 shows the details of the region and Fig. 13 shows three cross sections.

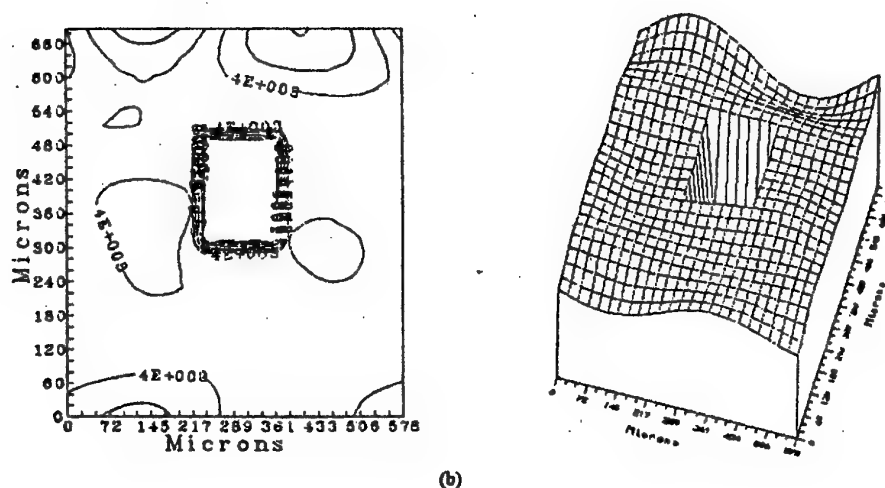
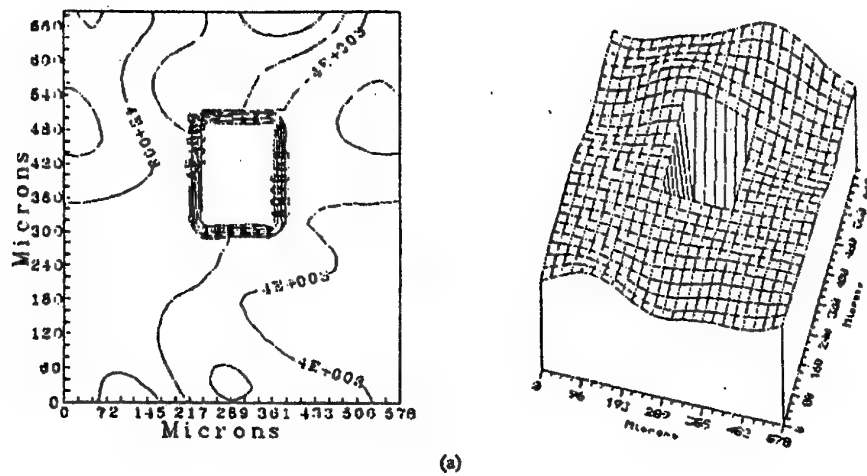


Figure 7. Strains in the  $y$ -direction (longitudinal direction)  
in a region of a particle embedded in a rubber matrix.  
(a) Filtered image at the frequency  $f_0 = 8$  harmonic.  
(b) Filtered image (shifted 30 pixels)  $f_{01} = 8$  harmonic.

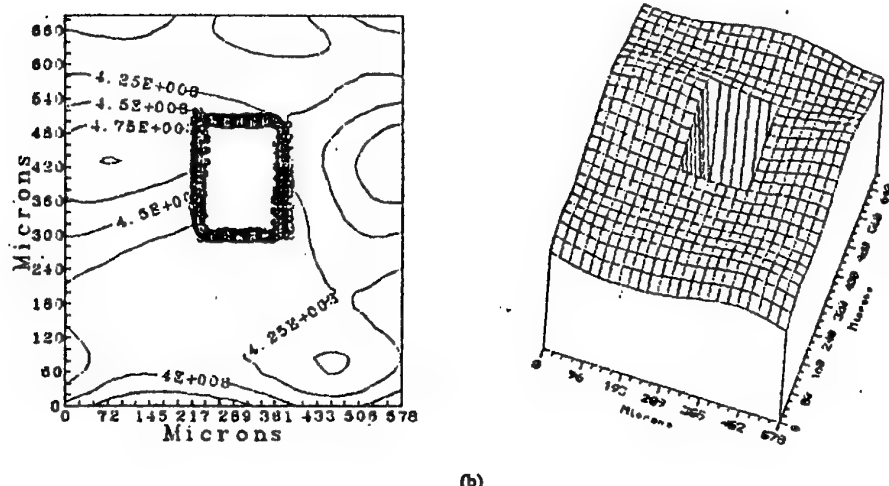
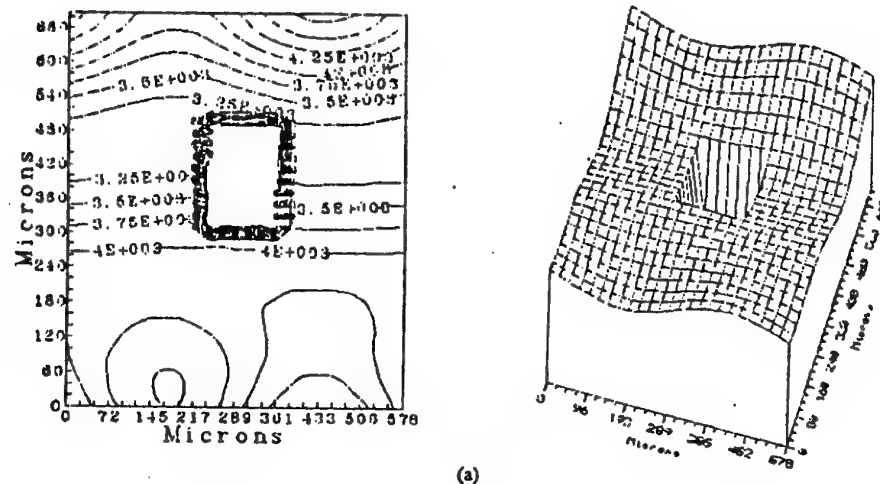


Figure 8. (a) Filtered image (shifted 20 pixels)  $f_3 = 12$  harmonic and removing the carrier fringe with (4<sup>th</sup> harmonic) to obtain  $f_e = 8$  harmonic.

(b) Filtered image (shifted 15 pixels)  $f_3 = 16$  harmonic and removing the carrier fringe with (8<sup>th</sup> harmonic) to obtain  $f_e = 8$  harmonic.

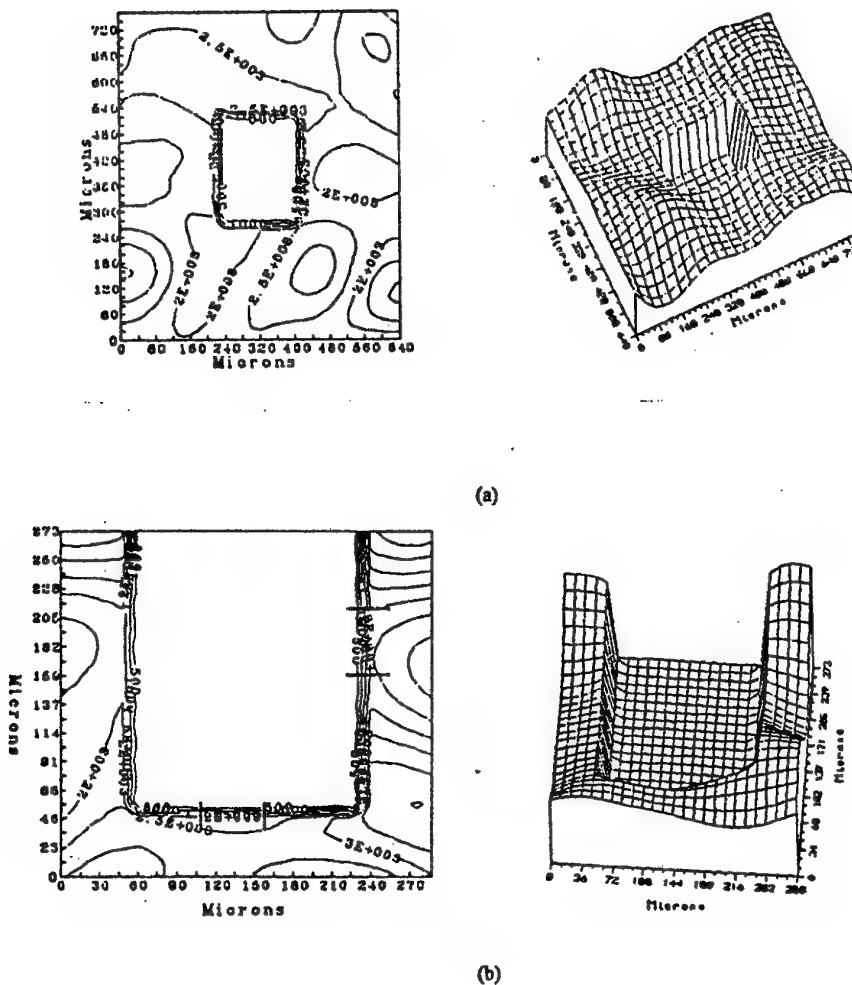


Figure 9. Strains in the y direction  $\alpha_y = 39 \text{ kPa}$   
 a) Obtained by recorrelation and filtering  $\Delta y = 1.83 \mu\text{m}$ .  
 b) Obtained by speckle phase subtraction and filtering  
 $\Delta y = 0.847 \mu\text{m}$ .

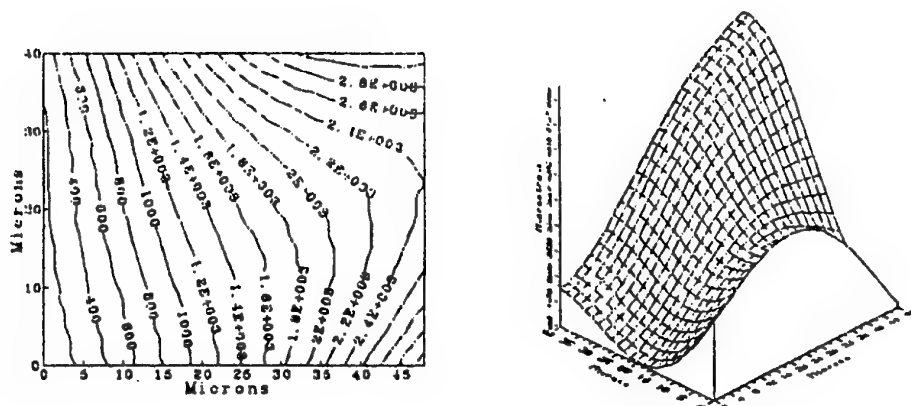


Figure 10. Strains at the right boundary of the particle region shown in Fig. 9b.

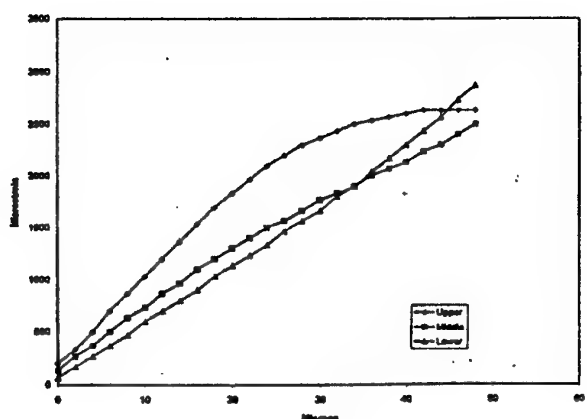


Figure 11. Cross sections of the strain distributions shown in Fig. 10.

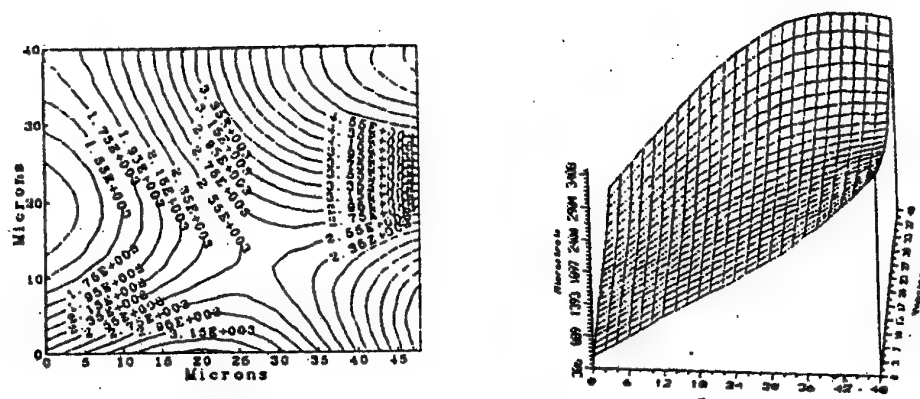
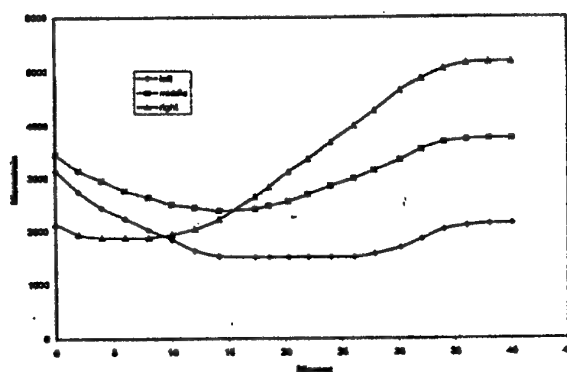


Figure 12. Strains at the lower boundary of the particle section shown in Fig. 9b.



**Figure 13.** Cross sections of the strains shown in Fig. 12.

### 5. Discussion and Conclusions

The presence of large speckles in the field has a significant impact on the data processing particularly if the speckles have low modulation or if there are sudden changes of phase. These features introduce phase errors that are averaged by the filtering process. More work needs to be done to introduce standard procedures required to overcome the different problems that are encountered. In spite of all the obstacles that are posed by the characteristics of the propellants surface, valuable micromechanics information has been gathered and some of the obtained results are confirmed through data obtained by other means.

### 6. Acknowledgments

The application work presented in this paper has been supported by the United States Airforce. The authors would like to give special thanks to Dr. C.T. Liu of the Phillips Laboratory for his support.

### 7. References

1. Sciammarella, C.A., Bhat, G., Longinow, N., Zhao, M. (1989) A High Accuracy Micromechanics Displacement Measurement Optical Technique, in W.N. Sharpe, Jr. (editor), *Micromechanics: Experimental Techniques*, ASME, New York, pp. 121-132.
2. Leendertz, J.A. (1970) Interferometric Displacement Measurement on Scattering Surfaces Utilizing the Speckle Effect, *J. Phys. Series E: Scientific Instruments* 3, 214-218.
3. Rastogi, P.K. (1979) *Visualization et Measure des Déplacements Tangentiels, et de Déformations Associées, par Moiré Holographiques et Interférométrie Speckle*, Doctoral Thesis France, L'Université de Franche-Comté, Besançon, 49-51.
4. Ahmadshahi M.A., Krishnaswamy, S., Nemat-Naser, S. (1991) Dynamic Two-Beam Interferometry, in Fu Pen Chiang (editor), *Proceedings of the Second International Conference in Photomechanics and Speckle*, SPIE, Bellingham, Wa, 1554A, 620-627.
5. Archbold, E., Burch, J.M., Ennos, A.E. (1970) Recording of in-plane Displacement by Double Exposure Speckle Photography, *Optica Acta*, 17(12), 883-898.
6. Sciammarella, C.A., Bhat, G., Bayeux, P. (1993) A portable electro-optical interferometer, *Proceedings of the Conference on Advanced Technology in Experimental Mechanics*, The Japan Society of Mechanical Engineers, Tokyo, 155-160.
7. Sciammarella, C.A., Doddington, C.W. (1967) Effect of photographic-film nonlinearities on the Processing of moiré-fringe data, *Experimental Mechanics*, 7, 398-402.
8. Burch, J.M., Tokarski, M.J. (1968) Production of Multiple beam fringes from photographic scatters, *Optical Acta*, 15(2), 102-111.
9. Sciammarella, C.A., Bhat, G. (1991) Computer assisted techniques to evaluate fringe patterns, in Rysard J. Pryputniewicz (editor), *Laser Interferometry IV: Computer Aided Interferometry*, SPIE, Bellingham, Wa, 1553, 252-262.

## THEORY OF MOIRÉ FRINGE FORMATION WITH AN ELECTRON BEAM<sup>1</sup>

David T. Read

*National Institute of Standards and Technology  
Boulder, Colorado 80303, USA*

James W. Dally

*University of Maryland  
College Park, MD 20742, USA*

### Abstract

When a specimen surface carrying a high-frequency line grating is examined under a scanning electron microscope (SEM), moiré fringes are observed at several different magnifications. The fringes are characterized by their spatial frequency, orientation, and contrast. These features depend on the spatial frequency mismatch between the specimen grating and the raster scan lines, the diameter of the electron beam, and the detailed topography of the lines on the specimen.

A mathematical model of e-beam moiré is developed that depicts the spatial dependence of the SEM image brightness as a product of the local intensity of the scanning beam and the local scattering function from the specimen grating. Equations are derived that show the spatial frequency of the moiré fringes as functions of the microscope settings and the spatial frequency of the specimen grating. The model also describes the contrast of several different types of moiré fringes observed at different magnifications. The different types of fringe patterns are divided into categories including: natural fringes, fringes of multiplication, and fringes of division.

### 1. Introduction

When a specimen surface that carries a regular array of lines is examined under a scanning electron microscope (SEM), moiré fringes can be observed at several different magnifications. Some confusion can arise in the interpretation of the different fringe patterns, because the spatial frequency of the moiré fringes changes with mismatch, rotation, a multiplication phenomena, and a division phenomena. In this paper, we first demonstrate these different fringe patterns and then explain their formation based on a Fourier series representation.

---

<sup>1</sup> Contribution of the U. S. National Institute of Standards; not subject to copyright in the U. S.

Optical moiré fringes, either geometric or interferometric, are widely employed in experimental mechanics. The classical treatments of geometric moiré by Parks[1], Durelli and Parks[2], and Theocaris[3], and the descriptions of interferometric moiré by Post [4], Graham [5], and McKelvie [6] are most helpful in interpreting fringe pattern formation in e-beam moiré. However, certain features of the phenomenon of electron beam moiré were not anticipated in these classic treatments of optical moiré. These features occur because no actual reference grating exists in electron beam moiré. Instead, the electron beam raster scan replaces the reference grating.

The e-beam raster scan is similar in many respects to the video raster scan employed by Morimoto [7] in forming moiré fringes using low frequency specimen gratings. Kishimoto [8] recognized the similarity between the video and SEM raster scans and was the first to report the use of e-beam moiré fringes for experimental mechanics. However, neither Morimoto nor Kishimoto discussed the many fringe patterns that may be observed when scanning lines are employed as the reference grating. With the controls available on a typical SEM, it is possible to vary the e-beam diameter, the pitch of the raster scan, and the angle between the scan lines and the grating lines. All affect the fringe pattern.

We develop a mathematical model of e-beam moiré fringe formation that allows us to reproduce and extend certain results previously derived for optical moiré. The model is based on two postulates used in treatments of optical moiré [5]:

1. The spatial dependence of both the pattern of the scan lines and the specimen grating can be described using Fourier series.
2. The SEM image can be represented numerically as a set of intensity values given by the product of the scattering power of the specimen grating and the intensity of the scanning lines. The spatially extended interaction of the e-beam with the near-surface region of the specimen, due to back-scattered and secondary electrons, is incorporated as a contribution to the width of the scanning lines.

Based on these postulates, a model is derived that concisely describes natural moiré fringes, fringes of multiplication and fringes of division. Experimental examples are demonstrated. The model is well-suited to determine the fringe contrast and the fringe shape as functions of the raster scan pitch, the scan line width and specimen grating parameters.

## 2. Observation of Specimen Gratings and e-Beam Moiré Fringes

Several high-frequency gratings (2.5 to 10 line/ $\mu\text{m}$ ) were written on a brass specimen using the methods described in [9]. A macroscopic view of the small areas written with different frequencies and different e-beam exposures is presented in Figure 1. A line grating with a frequency  $f_g = 5 \text{ line}/\mu\text{m}$  at 55,000X is presented in Figure 2. Depending on the effectiveness of the process used to fabricate such lines, they may appear in the SEM display as high-contrast stripes of black and white, as shown in Figure 2, or as low

contrast stripes represented by intensity modulations in a gray field. Local imperfections in the specimen surface and in the grating produce irregularities in the brightness of the image. Additional imperfections are generated by the imaging process even though the SEM image is recorded at a slow scan rate.

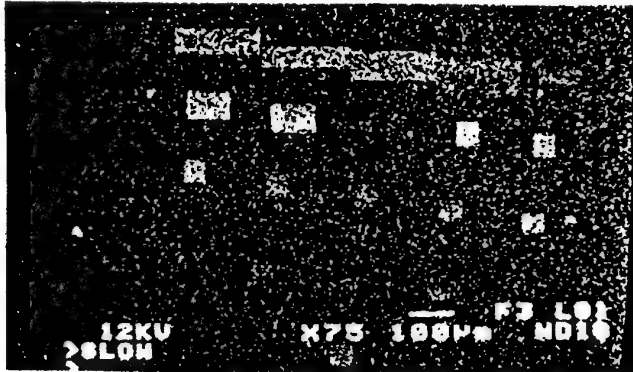


Figure 1 Several line gratings written with different frequencies and exposures on a brass specimen.

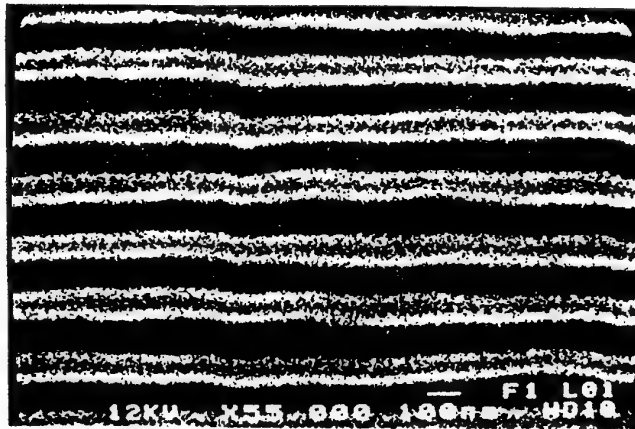


Figure 2 SEM image of a line grating with  $p_s = 220$  nm at a magnification of 55,000X.

When a grating with  $f_g = 5$  line/ $\mu\text{m}$  is observed, moiré fringes appear at several different magnifications from 300 to 3000 X. Typical moiré patterns are illustrated in Figs. 3 to 5. We have divided these fringe patterns into three categories based on the relative sizes of the spatial frequency of the specimen grating and the raster scan. Moiré fringes of division, where  $f_g > f_b$ , are presented in Figure 3. Natural moiré fringes, where  $f_g \approx f_b$ , are shown in Figure 4. Moiré fringes of multiplication, first observed optically by Post [8], are also generated with e-beam moiré when  $f_b > f_g$ . Multiplication

by a factor of three is depicted in Figure 5.

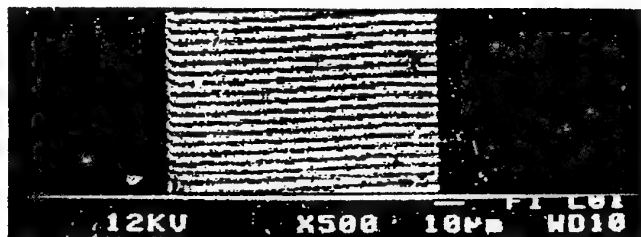


Figure 3 Moiré fringes of division with  $p_s = 200$  nm at a magnification of 500.

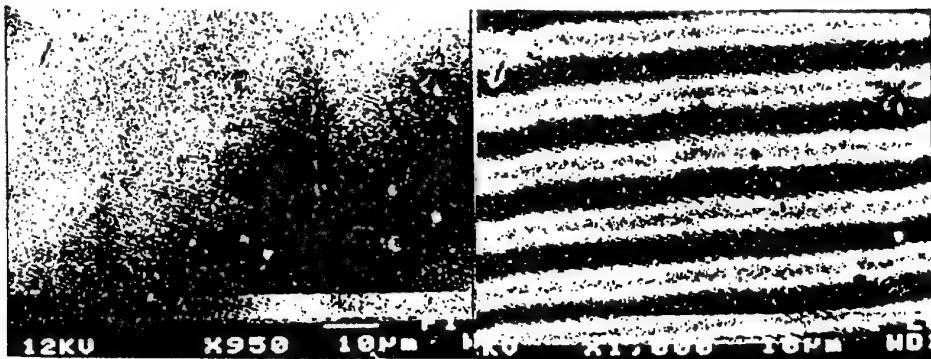


Figure 4 Natural moiré fringes with  $p_s = 200$  nm at magnifications of 950 and 1000.

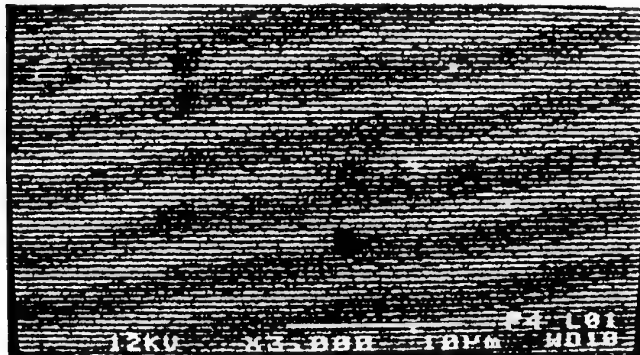


Figure 5 Moiré fringes of multiplication with  $p_s = 200$  nm at a magnification of 3000.

### 3. Theory of e-Beam Moiré Fringe Formation

We introduce a theory to describe the formation of the several different types of moiré fringes observed in a SEM. The theory is similar to that used to describe the formation of fringes in optical geometric moiré. Fourier series representations describe the SEM raster scan, the specimen line grating, and the moiré fringes. The results are interpreted

to explain the occurrence of fringes classified as natural, multiplied, and divided.

### 3.1 THE SEM RASTER SCAN SYSTEM

The image observed in a SEM is produced by scanning the specimen grating with an e-beam raster scan. We locate a point in this image by its coordinates ( $x, y$ ). The e-beam is scanned continuously across the imaged field in the  $x$  direction. The e-beam scan lines are equally spaced, with pitch  $p_b$  in the  $y$  direction. The magnified image, viewed on the CRT display, has a nominal size of 90 mm in the  $y$  direction which is related to the size of a common photomicrograph. In a SEM the raster pattern is always aligned with the viewing screen and the camera frame, so the  $x$ -axis is horizontal and the  $y$ -axis is vertical in all SEM images.

The specimen carries an array of lines extending in the  $\pm x$  direction, spaced equally with pitch  $p_s$  in the  $y$ -direction. The reciprocal of  $p_s$  is  $f_g$ , the spatial frequency. The e-beam and specimen coordinates may be rotated with respect to one another by a control on the SEM.

The number of scan lines used to form the image can be set at various values. Typical nominal settings are 500, 1000, or 2000 scans to produce an image. The images in Figs. 3 to 5 were made with 500 lines. Possible magnification values range from 10 to 300,000. Because of the design of most SEMs, only discrete values of the magnification are available. As a consequence, it is usually not possible to achieve a null-field moiré fringe pattern.

The pitch of the electron beam raster scan lines,  $p_b$ , depends on the magnification,  $M$ , the nominal image size,  $S$ , and the number of raster scans  $R$  forming the image:

$$p_b = S / MR \quad (1)$$

For example, with 500 lines per image, a nominal image height of 90 mm, and a magnification of 1900, the scan pitch  $p_b$  is 95 nm.

The effective width of the electron beam scan lines depends on the actual e-beam diameter and the interaction of the beam with the specimen surface. Beam diameters of 5 to 20 nm are reported in the literature and in the specifications for a typical SEM. Attainment of very small beam diameters (10 nm) requires very low beam currents, a well-aligned microscope, a small aperture and extremely sharp focussing. The interaction zone diameter depends on the specimen material and the electron beam energy (accelerating voltage). We believe a value of 15 to 30 nm is typical for the effective width of the raster scan lines used in this study.

The specimen gratings are formed by etching thin slits in a polymeric film about 100 nm thick. The frequencies obtained vary from 2.5 to 10 line/ $\mu\text{m}$ . The lines (slits) appear as dark stripes in the image and the flats between the slits appear as light stripes. In our densest gratings, the width of the slits and the flats is approximately equal. A  $y$ -direction trace of the image intensity shows a profile with gradual, rather than abrupt, changes in the image intensity. It appears that our gratings are between "phase grating" and an "amplitude grating" according to the usage of these terms in optical moiré.

### 3.2 FOURIER REPRESENTATIONS OF THE GRATING AND SCANNING LINES

We follow the approach introduced by Sciamarella [8] for optical moiré, and assume the local intensity of the image proportional to the product of the local scattering power of the specimen grating and the local intensity of the e-beam scan line. The scattering function  $G(y)$  for the specimen grating is represented by a Fourier series:

$$G(y) = \frac{g_0}{2} + \sum_{n=1}^{\infty} g_n \cos(2\pi n f_g y) \quad (2)$$

where the  $g_n$  are Fourier coefficients and  $f_g$  is the spatial frequency of the grating lines. After deformation, the specimen grating frequency  $f_g$  can vary with position over the specimen. However, in this treatment we simplify the analysis by considering only deformation fields that produce constant strain over the local region of interest. The frequency  $f_g$  represents the current value at the time of image formation, which is usually different from the original value.

The intensity of the e-beam scan lines  $B(y)$  is also represented by a Fourier series:

$$B(y) = \frac{b_0}{2} + \sum_{m=1}^{\infty} b_m \cos(2\pi m f_b y) \quad (3)$$

where the  $b_m$  are Fourier coefficients and  $f_b$  is the spatial frequency of the raster lines.

The moiré pattern  $M(y)$  is represented as the product of the raster function and the grating function:

$$M(y) = B(y) G(y) \quad (4)$$

Substituting Eqs. (2) and (3) into Eq. (4) and arranging the products of the cosine terms into sum and difference cosine functions gives a relation of the form:

$$M(y) = C + F(y) + S(y) + D(y) \quad (5)$$

where  $C = g_0 b_0 / 4$  is a constant. The functions:

$$\begin{aligned} F(y) &= (b_0/2) \sum g_n \cos(2\pi n f_g y) + (g_0/2) \sum b_m \cos(2\pi m f_b y) \\ S(y) &= \sum \sum (g_n b_m / 2) \cos 2\pi (n f_g + m f_b) y \end{aligned}$$

exhibit a frequency that is too high to be observed. The difference function:

$$D(y) = \sum \sum (g_n b_m / 2) \cos 2\pi (n f_g - m f_b) y$$

is the term in the double series expansion that produces the image observed and identified as the moiré fringe pattern. We simplify Eq. (5) to give:

$$M(y) = C_1 + \sum_{m=1}^{\infty} \sum_{n=1}^{\infty} g_n b_m \cos [2\pi(n f_g - m f_b)y] \quad (6)$$

where  $C_1 = C + F(y) + S(y)$  is the intensity of the background.

The result is similar to that obtained in optical moiré. When the magnification yields moiré fringes, the grating lines cannot be clearly imaged. The coefficients  $g_n$  in the specimen grating function  $G(y)$  decrease rapidly with  $n$  because of the topography of the grating. The coefficients  $b_m$  of the scanning beam raster function  $B(y)$  do not decay as rapidly with increasing order  $m$  of the expansion.

### 3.3 NATURAL MOIRÉ FRINGES

The simplest condition for fringe formation in optical moiré is the near-match condition when  $f_g \approx f_b$ . In e-beam moiré, we refer to fringes formed under this near-match condition as natural fringes. Because only discrete values of magnification are available on our SEM, it was not possible to achieve a perfect null field, where  $f_g = f_b$  and the pitch of the moiré fringes  $p_m$  becomes infinite.

The frequency  $f_m$  of the moiré fringe function  $M(y)$  is determined by considering the first term in Eq. (6) ( $n = m = 1$ ) for the near match condition.

$$f_m = f_g - f_b \quad (7)$$

In Eq. (7), negative values of the moiré fringe frequency are allowed, because moiré fringes are formed both for  $f_g > f_b$  and for  $f_g < f_b$ .

Consider small uniform longitudinal strains along the  $y$  direction, relative to the ideal initial condition where  $f_g = f_b$  and  $\theta = 0$ . Equation 7 implies that the tensile strain  $\epsilon$  is given by

$$\epsilon = -\frac{f_m}{(f_b + f_m)} \quad (8)$$

The periodic form of Eqs. (2) to (6) permits us to adopt a vast body of previous developments to interpret e-beam moiré fringes. Some familiar wave phenomena have analogs in SEM images of line gratings. For example, it is clear from Eq. (7) that the moiré fringes are analogous to the beat frequency due to two pure sound tones of slightly different frequencies.

The contrast of the natural moiré fringes is determined primarily by the amplitude term  $g_1 b_1 / 2$  although higher order terms also affect the contrast. Higher order harmonics of the fringe frequency occur for  $m = n = 2, 3, \dots$  etc. These harmonics distort

the pure sinusoid of the fundamental and degrade the contrast of the image. Other higher order terms occur when  $n \neq m$  and produce signals with a very high frequency which can be disregarded except for their detrimental effect on contrast.

### 3.4 FRINGES OF MULTIPLICATION

Post [11] showed that fringe multiplication occurred in optical moiré when the spatial frequency of the reference grating was a near multiple of the spatial frequency of the specimen grating. The same fringe multiplication occurs in e-beam moiré. We express the spatial frequency of the scan lines, following the notation introduced by Post [11] as:

$$f_b = \beta (1 + \lambda) f_s \quad (9)$$

where  $\beta$  is a positive integer and  $\lambda$  is a small fraction. Substituting Eq. (9) into Eq. (7) shows that the spatial frequency of the moiré fringes is:

$$f_m = [n - m\beta(1 + \lambda)] f_s = [(n - \beta m) - m\lambda\beta] f_s \quad (10)$$

Moiré fringes may be observed when  $n = \beta m$ ; then  $f_m$  becomes:

$$f_m = -m\lambda\beta f_s \quad (11)$$

The amplitude of the moiré fringe terms in Eq. (6) is given by  $g_n b_m / 2$ . Since  $\beta$  is typically an integer from 2 to 5,  $n = \beta m$  is always greater than one. Maximum contrast requires  $m = 1$ ; hence, fringes of multiplication occur when we match the fundamental frequency of e-beam raster scan with the second, third, etc. harmonics of the grating function. Difficulties in obtaining high contrast in attempts to employ fringe multiplication are due to the use of decreasing Fourier amplitudes of higher harmonics of the grating function. To illustrate this important result, let  $\beta = 2$  and consider a specimen grating that is represented by a symmetric square wave (a grating with bar width equal to space width). Since  $g_2 = 0$ , the coefficient of the second harmonic for a square wave, contrast vanishes and these fringes of multiplication cannot be observed.

These results show the importance of the grating scattering function for the contrast of fringes of multiplication. A grating with narrow lines and wide spaces exhibits stronger even harmonics than a balanced grating with equally wide lines and spaces. However, for all shapes, except the periodic delta function, the general rule is that the coefficients  $g_n$  decrease rapidly with increasing order of the harmonic.

### 3.5 FRINGES OF DIVISION

Moiré fringes of division also occur when the specimen grating frequency is a multiple of the scan line frequency. Fringes of division are commonly observed at low magnification settings on the SEM, when  $p_b$  is larger than  $p_s$ . The formation of the fringes of division and their contrast is evident from Eq. (6). Consider an observation in

the SEM with a frequency relation given by

$$f_b = (I + \Lambda) f_s / \beta \quad (12)$$

The frequency of the resulting moiré fringe pattern is obtained from Eq. (6) as:

$$f_m = [(n - m/\beta) - m\Lambda/\beta] f_s \quad (13)$$

The moiré pattern can be observed when  $n = m/\beta$  and Eq. (13) reduces to:

$$f_m = -m\Lambda f_s / \beta \quad (14)$$

Since  $\beta$  is an integer typically from 2 to 5,  $m = \beta n$  is always greater than one. This fact shows that moiré fringes of division are formed by combining the fundamental frequency component of the specimen grating with higher harmonics of the e-beam raster pattern. The e-beam scan lines that are produced at low magnification have relatively high coefficients  $b_n$  for  $n$  as large as 10.

#### 4. Conclusions

The formation of e-beam moiré fringes in a SEM can be described with a model based on a Fourier series representation of the specimen grating line function  $G(y)$  and the raster scan line function  $B(y)$ . The moiré function  $M(y)$  is the product of these two functions. The model describes the variation in the spatial frequency  $f_m$  of the moiré fringes with the magnification used in producing the image. It also provides a means for estimating the contrast of different moiré fringe patterns that are observed in the SEM. The spatial frequency  $f_m$  can be used to measure the spatial frequency  $f_g$  of the specimen grating to determine displacements.

The sensitivity and resolution of measurements made with e-beam moiré are limited by the frequency of the specimen grating. Fringes of multiplication offer enhanced displacement sensitivity per fringe, but require that the specimen grating be fabricated with a slit-ridge ratio that produces substantial higher order Fourier components. Fringes of division are observed as easily as natural moiré fringes because the raster scan lines at low magnifications exhibit significant Fourier coefficients for the higher order terms in the expansion. Fringes of division are useful because they permit a larger field of observation.

#### REFERENCES

1. Parks, Vincent J., "Geometric Moiré," in *Handbook on Experimental Mechanics*, edited by Albert S. Kobayashi, Prentice-Hall, Englewood Cliffs, New Jersey, 1987, pp. 282-313.
2. Durelli, A. J. and Parks, V. J., *Moiré Analysis of Strain*, Prentice-Hall, Englewood Cliffs, New Jersey, 1970.

3. Theocaris, P. S., Moiré Fringes in Strain Analysis, Pergamon Press, Elmsford, N.Y., 1969.
4. Post, Daniel, "Moiré Interferometry," in [1].
5. Graham, S. M., "Sensitivity and Resolution Limitations of Various Moiré Methods," Optics and Lasers in Engineering 12, 119-133, 1990.
6. McKelvie, J., "On the Limits to the Information Obtainable from a Moiré Fringe Pattern," in Proceedings of the 1986 SEM Spring Conference on Experimental Mechanics, SEM, 1986.
7. Morimoto, Y. and Hayashi, T. "Deformation Measurement During Powder Compaction by a Scanning Moiré Method," Experimental Mechanics, Vol. 24, pp. 112-116, 1984.
8. Kishimoto, S. Egashira, M. and Shina, N., "Measurements of Grain Boundary Sliding and Observation of Microgrids for High Temperature Use," Journal of Society for Materials Science Japan, Vol. 40, No. 452, pp. 637-641, 1991 (in Japanese).
9. Dally, J. W. and Read, D. T., "Electron Beam Moiré," Experimental Mechanics, 33, 270-277, 1993.
10. Sciamaralla, C. A., "Basic Optical Law in the Interpretation of Moiré Patterns Applied to the Analysis of Strains—Part I," Experimental Mechanics 5, 154-160, 1965.
11. Post, D., "Sharpening and Multiplication of Moiré Fringes," Experimental Mechanics 28, 329-335, 1988.
12. Read, D. T. and Dally, J. W., "Theory of Electron Beam Moiré," Journal of Research NIST, 101, 47-61, 1996.

## A STUDY ON STRESS FREEZING METHOD BASED ON TIME AND TEMPERATURE DEPENDENT PHOTOVISCOELASTIC BEHAVIORS

Y. MIYANO

*Professor, Materials System Research Laboratory,  
Kanazawa Institute of Technology,  
Yatsukaho Matto, 924-0838, Japan*

T. KUNIO

*Professor, Kanazawa Institute of Technology, Japan  
Professor Emeritus, Keio University, Japan*

S. SUGIMORI

*Professor, Kanazawa Technical College,  
Hisayasu Kanazawa, 921-8601, Japan*

### 1. Introduction

The stress freezing (SF) method has been widely known as a simple and useful photoelastic technique applicable to various kinds of experimental stress analysis problem, particularly for three-dimensional problems.

To accomplishment of complete SF method, more careful attention should be paid to the temperature conditions of SF cycle, because their thermoviscoelastic effects during heating and cooling process leading the non-uniformity of the temperature distribution in the whole model are very serious, since the model made from polymeric materials has generally remarkable time and temperature dependent characteristic properties. Additionally, the strain sensitivity of the optical property of thermosetting resin used for SF model is considerably small in rubbery state than in glassy state. Therefore, SF model should be much more distorted comparing with the general photoelastic model. Thus, SF method may lead finally to experimental analysis error, and gives considerably large effect upon accuracy of three-dimensional stress analysis using the SF method.

By the way, the thermosetting resin used in SF method is very soft but has high stress sensitivity at higher temperature than the glass transition temperature, whereas in the range of temperature below the glassy transition temperature, the polymeric resin is very hard and has low stress sensitivity. Furthermore, not only the mechanical but also optical properties of resin in the vicinity of glass transition temperature show a remarkable time and temperature dependence, that is, so-called photoviscoelastic behavior.

This paper intends to propose a new technique for finding the most suitable holding SF temperature and optimizing the freezing cycle with an aim to improve SF method, based on the quantitatively character of linear-photoviscoelastic behavior<sup>1-3</sup> of model material. Thus, the estimating functions including the strain sensitivity mentioned above, are newly defined from view points of the photoviscoelastic behaviors of the material. And, their availability will be verified theoretically, together with experimental results obtained from 4-point bending test of epoxy resin beam.

## 2. Estimate Functions for the Stress Freezing Method

Figure 1(a) shows two kinds of ordinary temperature cycle regarding SF cycle, where both maximum temperatures  $T_h$  are higher than glassy transition temperature  $T_g$ , and  $T_c$  is the room temperature. Figure 1(b) shows the principal stress difference  $\sigma_1 - \sigma_2$ , produced in a model due to application of a constant load. Similarly, Fig. 1(c) and (d) are respective changes of the principal strain difference  $\epsilon_1 - \epsilon_2$  and of birefringence  $n$ . As easily understood, the principal stress difference at any point in the model, which was caused by applied loading, disappear at removal of this applied load. However, both principal strain difference  $\epsilon_1 - \epsilon_2$  and fringe order  $n$  per unit path of light still show time dependent variations with time as seen in Fig. 1(c) and (d). Therefore, even after finishing one cycle of SF procedure, then removing a constant applied loading, not only the frozen birefringence  $n_f$ , but also frozen principal strain difference are left in the model. This is basic concept of Stress Freezing method, in which the values  $n_f$  of frozen fringe are used in analysis of stress or strain similar to fringe order from an ordinary

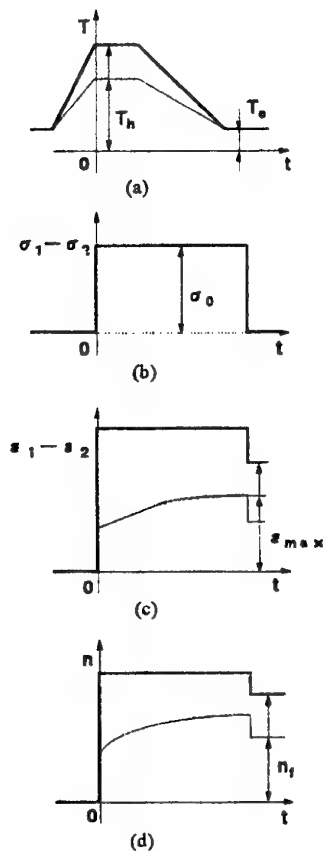


Fig. 1 Stress freezing procedure

### STRESS FREEZING METHOD ON PHOTOVISCOELASTICITY

photoelasticity. Thus, by use of SF method, experimental analysis of three-dimensional problems become possible.

Now, let us discuss the effect of SF temperature as to the following two cases. The first case is shown as the thick lines in the Fig. 1(a)-(d), in which the model used is loaded at a sufficiently higher temperature  $T_h$  than the glass transition temperature  $T_g$  of the material, and then is cooled down very slowly to the room temperature lower than  $T_g$ , at which the model material is in the glassy state. In this case, stress and strain fields at all point in the model make response for a given loading without any time lapse, so that magnitudes of both principal stress difference  $\sigma_1 - \sigma_2$  and strain difference  $\epsilon_1 - \epsilon_2$  are of time independence. The similar situations may be said as for birefringence  $n$  produced in the model. Since the external loading for SF is removed from the model when SF procedure is complete, both the principal strain and birefringence somewhat may get down as seen in the Fig. 1(c) and (d), because of balance of external loading. In ordinary SF method, the principal stress difference  $\sigma_1 - \sigma_2$  by loading is experimentally analyzed by using the  $n_f$ .

In the second case shown as the thin lines in Fig. 1, the holding temperature  $T_h$  is in so-called time and temperature dependent viscoelastic region. Both the principal strain difference  $\epsilon_1 - \epsilon_2$  and the birefringence  $n$  increase due to creep with time even for constant loading to the model. And it can be also found that the  $\epsilon_{\max}$  as well as the frozen birefringence  $n_f$  reduced after finish of SF procedure may be changed to some extent.

It is very essential that, to make improvement of high accuracy in the SF method, the model material used has linear relations between stress, strain and birefringence is held even during all procedure. Also, it is a matter of course that it has a large ultimate strain strength in the viscoelastic region. Furthermore, besides these requisites, the following three items should be needed for improving the accuracy of SF method.

(1) The frozen birefringence produced should be as large as possible within limit of allowable distortion of model.

(2) The constant applied load  $\sigma_0$  leading to the principal stress difference  $\sigma_1 - \sigma_2$  produced wants to be as large as possible under the condition of the above item (1).

(3) The frozen birefringence should be as large as possible to make the analysis easy with better accuracy.

The above requisites are not always possible to be satisfied simultaneously, so that careful choice of which items should be taken preferentially is most essential, although their preference bases depend upon aims of experimental circumstances. To do this, introduction of the following three "estimation functions" are very useful, which are defined as,

$$k_1 = \frac{n_f}{\epsilon_{\max}} \quad (1)$$

$$k_2 = \frac{\sigma_0}{\epsilon_{\max}} \quad (2)$$

$$k_3 = \frac{n_f}{\sigma_0} \quad (3)$$

Among of them, the first function  $k_1$  represented by equation (1) has been known as "Figure of Merit", which has widely been used for the three-dimensional stress analysis by SF method, but the rest two functions  $k_2$  and  $k_3$  are newly defined and proposed ones in this paper.

### 3. Theoretical Consideration of New Functions Based Photoviscoelasticity

Assume that the model material shows a linear-photoviscoelastic behaviors and behaves thermo-rheologically simple, and at the same time, has the same time-temperature superposition principle is held for the both optical and mechanical characteristics.

A three-dimensional model body made by the linear- photoviscoelastic material is held for sufficiently long time without any constraint at a high holding temperature  $T_h$  at which the material shows viscoelastic behavior. At this period, no stress, no strain and no birefringence exist. The load is applied to this body at time  $t=0$ , then cooling down very slowly to the cooling temperature  $T_c$ , at which the material is in glassy state. Therefore, there is no temperature distribution in the model during cooling process. The initial loading is kept through this cooling. The stress distribution due to a constant load will not change with time and also the directions of principal stress, principal strain and polarization of light coincide completely with each other at any point in the model and do not change with time.

In this case, the fundamental equations between stress-strain-birefringence of the two-dimensional photoviscoelastic body of which the temperature changes uniformly with time, can be expressed by the following hereditary integral equation by using the linear photoviscoelastic theory and the time-temperature superposition principle.

$$\varepsilon_1(x, t) - \varepsilon_2(x, t) = \int_0^t D_c(t' - \tau', T_0) \frac{d}{d\tau} [\sigma_1(x, \tau) - \sigma_2(x, \tau)] d\tau \quad (4)$$

and

$$n(x, t) = \int_0^t C_c(t' - \tau', T_0) \frac{d}{d\tau} [\sigma_1(x, \tau) - \sigma_2(x, \tau)] d\tau \quad (5)$$

where  $t'$  is reduced time calculated by the following relation

$$t' = \int_0^t \frac{du}{a_{T_0}[T(x, u)]} \quad (6)$$

in which  $T_0$  is the reference temperature,  $a_{T_0}$  is the time-temperature shift factor with respect to  $T_0$ , and  $D_c(t')$ ,  $C_c(t')$  are creep birefringence-strain coefficient and creep compliance, respectively, both of which should be experimentally determined by mechanical and optical characterization. The transient uniform temperature  $T(t)$  and load  $W(x, t)$  are loaded in photoviscoelastic model used. The pulse shaped principal stress difference  $\sigma_0$  is applied to any point in model shown in Fig. 1(b). And the principal strain difference  $\varepsilon_1 - \varepsilon_2$  and birefringence  $n$  are produced at this point. From equations (4), (5) and (6), the maximum strain  $\varepsilon_{max}$  and the frozen birefringence  $n_f$  are given by

$$\varepsilon_{max} = D_c(t', T_0) \sigma_0 \quad (7)$$

## STRESS FREEZING METHOD ON PHOTOVISCOELASTICITY

$$n_f = (C_c(t', T_0) - C_c(0, T_0)) \sigma_0 \quad (8)$$

Therefore, the estimate functions  $k_1$ ,  $k_2$  and  $k_3$  can be expressed from equations (1), (2) and (3) as follows,

$$k_1 = \frac{C_c(t', T_0) - C_c(0, T_0)}{D_c(t', T_0)} \quad (9)$$

$$k_2 = \frac{1}{D_c(t', T_0)} \quad (10)$$

$$k_3 = C_c(t', T_0) - C_c(0, T_0) \quad (11)$$

If two photoviscoelastic coefficients  $D_c$  and  $C_c$  are obtained previously before SF procedure, then it is able to find out theoretically the most suitable temperature and loading condition in SF method, by using three estimate functions.

#### 4. Theoretical and Experimental Verification

By using epoxy resin of which two photoviscoelastic coefficients were obtained, the optimizing of the SF method is analyzed theoretically and is clarified experimentally by four-points bending test of this epoxy beam.

##### 4.1. THEORETICAL VERIFICATION OF OPTIMIZING METHOD

The mechanical and optical properties of epoxy resin are tabulated in Table 1 and shown in Fig. 2 and 3. Figure 2 shows the master curves of creep compliance  $D_c(t, T_0)$  and creep birefringence-strain coefficient  $C_c(t, T_0)$  of the resin used. Figure 3 shows the time-temperature shift factor with respect to  $T_0$  of these master curves.

This resin shows a glassy behavior in the region of short reduced time where both coefficients  $D_c$  and  $C_c$  keep low constant values, and this region shows rubbery behavior in the region of long reduced time, where these two coefficients keep high constant values. In the region of the intermediate reduced time, this region shows viscoelastic behavior where both coefficients  $D_c$  and  $C_c$  increase remarkably.

Table 1 Mechanical and optical properties

Item	Glassy	Rubbery
Young's modulus	1.31 GPa	0.0124 GPa
Poisson's ratio	0.35	0.5
Strain sensitivity	$116 \times 10^3 \text{ fr/m}$	$40.6 \times 10^3 \text{ fr/m}$
Coefficient of thermal expansion	$61 \times 10^{-6} \text{ }^\circ\text{C}^{-1}$	$166 \times 10^{-6} \text{ }^\circ\text{C}^{-1}$
Glass transition temperature	132°C	

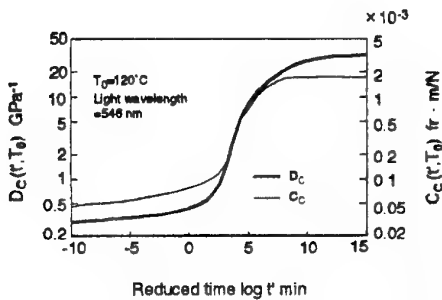


Fig. 2 Master curves of photoviscoelastic coefficients

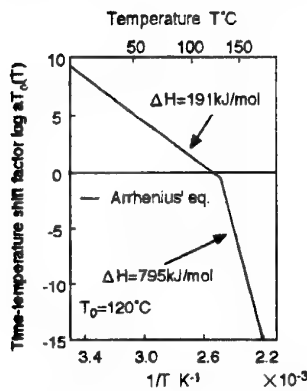


Fig. 3 Time-temperature shift factor  $a_{T_0}(T)$

Three estimate functions  $k_1$ ,  $k_2$  and  $k_3$  with respect to the reduced time  $t'$  can be theoretically calculated by using the photoviscoelastic coefficients of this resin and equations (9), (10) and (11). The theoretical values shown in Fig. 4, 5 and 6 were obtained from the master curves shown in Fig. 2.

First,  $k_1$ , the ratio of  $n_f$  to  $\epsilon_{max}$ , has peak value near  $t'=10^4$  min and keeps constant value in at long reduced time regions seen Fig. 4. This means that the frozen birefringence  $n_f$  by the stress freezing from viscoelastic region is rather larger than that from rubbery region, in the case that the maximum frozen strain  $\epsilon_{max}$  is fixed.

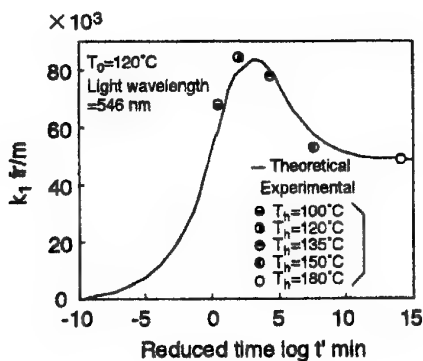
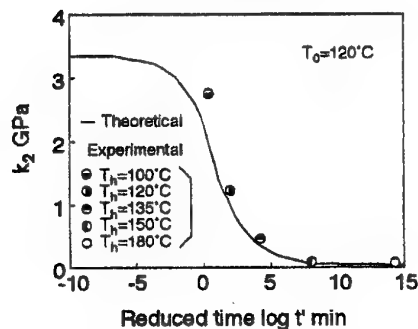
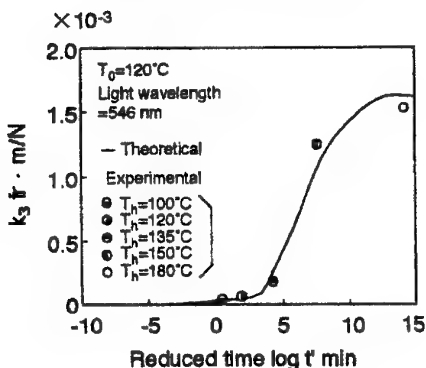
Secondly,  $k_2$ , the ratio of  $\sigma_0$  to  $\epsilon_{max}$ , decreases monotonously as the reduced time  $t'$  increases as shown in Fig. 5. This means that the large stress can be loaded, in the case that the stress freezing is done from the short reduced time.

Finally,  $k_3$ , the ratio of  $n_f$  to  $\sigma_0$ , increases monotonously as  $t'$  increase as shown in Fig. 6. This means that the large frozen birefringence can be obtained in the vicinity of rubbery state, in the case that the stress  $\sigma_0$  is fixed.

#### 4.2. EXPERIMENTAL VERIFICATION OF OPTIMIZING METHOD

A specimen for 4-point bending test made from the epoxy resin mentioned previously was

## STRESS FREEZING METHOD ON PHOTOVISCOELASTICITY

Fig.4 Estimate function  $k_1$ Fig.5 Estimate function  $k_2$ Fig.6 Estimate function  $k_3$ 

used. Gauge marks for measuring the deformation and strain were drawn on the surfaces of the specimen. As the glass transition temperature is 132 °C, five temperatures, 100 °C, 120 °C, 135 °C, 150 °C and 180 °C, were adapted as the holding temperature  $T_h$ . The loads  $W$  at each  $T_h$  were determined using the master curve of creep

compliance.

Specimen was held for a sufficiently long time at each constant temperature  $T_h$  in the heating chamber without loading and W was loaded on the specimen at time  $t=0$  and was kept for 30 min, then gradually cooling down to room temperature  $T_c (=20^\circ\text{C})$  at a cooling speed of approximately  $0.5^\circ\text{C}/\text{min}$ . After cooling, the maximum strain  $\epsilon_{\max}$  was obtained by measuring gauge marks of the loaded specimen. Then, the load of specimen was removed and the maximum frozen birefringence  $n_f$  at the edge of the specimen was obtained from the frozen fringe pattern recorded. Finally, experimental values of  $k_1$ ,  $k_2$  and  $k_3$  were obtained by substituting these values into the equations (1), (2) and (3).

Experimental results are indicated in Fig. 4, 5 and 6, comparing with the theoretical results. Experimental results of  $k_1$ ,  $k_2$  and  $k_3$  agree well with the theoretical results of  $k_1$ ,  $k_2$  and  $k_3$  for each experimental conditions.

In an ordinary SF method, SF procedure is determined to hold  $k_3$ , the ratio of  $n_f$  and  $\sigma_0$ , as large as possible. But, in some case, it is need to hold  $k_1$  or  $k_2$  as large as possible. For example, the stress freezing from the high temperature at which the material is in a rubbery state, large frozen birefringence can be obtained, but  $\epsilon_{\max}$  becomes considerably large. On the other hand, the evident was proofed that, if the strain limit is small, the SF from the temperature range at which the material is in viscoelastic state results in rather large frozen birefringence and larger frozen stress than the ordinary SF.

## 5. Conclusion

The results are summarized as follows. A new concept for finding the most suitable holding SF temperature and optimizing the freezing cycle in order to improve this technique, based on the quantitatively character of linear-photoviscoelastic behavior of model material. Thus, the estimation functions including the strain sensitivity mentioned above, are defined for practical SF method, based on the photoviscoelastic behaviors of the material. And, their availability was proved theoretically, together with experimentally.

## References

1. Kunio, T. and Miyano, Y.(1968) Photoviscoelastic analysis by use of polyurethane rubber, Applied Mechanics(Proceeding 12th International Congress Applied Mechanics) 269-276.
2. Arenz, R. J., Ferguson, C. W. and Williams, M. L.(1967) The mechanical and optical characterization of a Solithane composition, Experimental Mechanics 7, 183-188.
3. Sugimori, S., Miyano, Y. and Kunio, T.(1984) Photoviscoelastic analysis of thermal stress in a quenched epoxy beam, Experimental Mechanics 24(2), 150-156.

## HIGH SPEED MEASUREMENT OF DISCONTINUOUS SURFACE PROFILES

J. M. HUNTLEY AND C. R. COGGRATE

*Loughborough University*

*Department of Mechanical Engineering,*

*Loughborough, LE11 3TU, UK*

**Abstract.** The measurement of surface profile by projecting phase-stepped fringe patterns at an angle to the observation direction is well known. Ambiguous range data results, however, when the object has discontinuities in its profile. The ambiguities can be prevented by projecting fringes of varying spatial frequency. In this paper we describe an approach which combines high accuracy and reliability. The spatial frequency is reduced exponentially from the maximum value. The sequence of phase values at a given pixel is then unwrapped independently of the other image pixels, and all the intermediate phase values contribute in a least squares sense to the final range estimate for the pixel. The algorithm has been implemented on a pipeline image processing system. The fringe patterns are projected at 30 frames s<sup>-1</sup> using a high resolution data projector. Images are acquired and analysed in real time, at the same framing rate. A total acquisition and processing time of 0.75 s has been achieved for a maximum spatial frequency of 16 fringes across the field of view.

### 1. Introduction

Projected fringes have been used over many years for measuring surface profiles [1-3]. The fringes are usually created by imaging a fixed or programmable mask, having a sinusoidal density profile, onto the object. Interference patterns from a coherent light source can also be used, resulting in an extended depth of field, but with more speckle noise and greater sensitivity to environmental disturbance. If the projection direction is different from the observation direction, the phase distribution of the measured fringe pattern includes information on the surface height profile of the object.

The fringe phase distribution is normally calculated from the images either by Fourier transformation or by phase-stepping of the fringe patterns. Both methods result in phase maps which are wrapped onto the range  $-\pi$  to  $+\pi$ . When the object surface is continuous, the phase map can be unwrapped (i.e. the  $2\pi$  phase discontinuities removed) by a spatial comparison of neighbouring pixels. When the object has surface discontinuities, however, this process will fail and it then becomes necessary to project

fringe patterns of varying spatial frequency [4-8]. The resulting sequence of phase values at each pixel can be unwrapped over time ("temporal phase unwrapping") to give an absolute phase value independent of the other pixels in the image.

In this paper we describe an optimised version of this approach in which the fringe spatial frequency is reduced from a maximum value down to zero by an exponentially growing decrement[9,10]. Intermediate phase values are included in a least squares sense to reduce the random errors in the calculated range values. The so-called "reversed exponential" algorithm has been implemented on a pipeline image processor with the aim of calculating range data at rates in excess of  $10^5$  coordinates s<sup>-1</sup>. The system hardware and preliminary results are described in section 3.

## 2. Temporal phase unwrapping: reversed exponential method

Figure 1 shows the standard set up used for shape measurement by projected fringes. The projector fills a region of space with a three-dimensional sinusoidal intensity distribution. The fringe normals are assumed to lie in the plane of the page. To apply the "forward exponential" temporal unwrapping method, the fringe spatial frequency is increased exponentially over time. Initially ( $t = 1$ ), a single fringe is projected, so that the fringe phase ranges from  $-\pi$  on one side to  $+\pi$  on the other side of the field of view. For subsequent measurements ( $t = 2, 4, 8, \dots, s$ ) the number of fringes is set equal to  $t$  so that the phase range increases to  $(-t\pi, t\pi)$ . For each  $t$  value, a number (typically 4) of phase-stepped images,  $I(k, t)$  (where  $k = 1, 2, 3, 4$  for the four frame algorithm), is acquired. The situation depicted in Figure 1 corresponds to the case  $t = 2$ .

The phase change  $\Delta\Phi_w(i, j)$  occurring at a given pixel due to a change in fringe frequency from  $t = i$  to  $t = j$  is calculated from the two sets of intensity values using the formula:

$$\Delta\Phi(i, j) = \Phi(i) - \Phi(j) \quad (1)$$

where

$$\Phi(t) = \tan^{-1} \left[ \frac{\Delta I_{42}(t)}{\Delta I_{13}(t)} \right] \quad (2)$$

and

$$\Delta I_{kl}(t) = I(k, t) - I(l, t). \quad (3)$$

The phase values calculated by Eqn. (2) lie in the range  $(-\pi, \pi)$  and therefore the incremental phase changes calculated by Eqn. (1) lie in the range  $(-2\pi, 2\pi)$ . It is convenient to rewrap these back into the range  $(-\pi, \pi)$  using the unwrapping operator  $U\{\Phi_1, \Phi_2\}$ :

$$\Delta\Phi_w(i, j) = U\{\Delta\Phi(i, j), 0\} \quad (4)$$

where

$$U\{\Phi_1, \Phi_2\} = \Phi_1 - 2\pi \text{NINT}\left[\frac{\Phi_1 - \Phi_2}{2\pi}\right] \quad (5)$$

and NINT[...] denotes rounding to the nearest integer. The subscript *w* denotes a wrapped phase value (i.e., one lying in the range  $(-\pi, \pi)$ ), and subscript *u* will be used to denote an unwrapped phase value (i.e., adjusted by addition of the correct integral multiple of  $2\pi$ ).

The sequence of measured phase values, for a pixel receiving light from a scattering point on plane P of Figure 1, is illustrated in Figure 2(a).  $\Delta\Phi_w(1, 0)$  and  $\Delta\Phi_w(2, 1)$  are both equal to the corresponding unwrapped phase changes, because in each case the number of projected fringes is increased by just one, and they can therefore be added to give  $\Delta\Phi_u(2, 0)$ .  $\Delta\Phi_w(4, 2)$  will in general contain phase wraps, but can be unwrapped by noting that  $\Delta\Phi_u(4, 2)$  should be equal to  $\Delta\Phi_u(2, 0)$ . The sum  $\Delta\Phi_u(4, 2)$  and  $\Delta\Phi_u(2, 0)$  then results in  $\Delta\Phi_u(4, 0)$ . This process can be repeated with an exponentially growing sequence of fringe densities. The final unwrapped phase value,  $\Psi$ , then defines the plane on which the scattering point lies.

The accuracy of the range value can, however, be improved by least squares fitting a line to the phase values. The gradient  $\omega$ , rather than the unwrapped value  $\Psi$ , is used to define the plane on which the scattering point lies. The problem with the forward exponential sequence is that most of the phase values lie at the low-*t* end of the  $\Phi$ -*t* graph. Low *t* values do not provide reliable estimates of the gradient, and so do not contribute significantly to the least-squares fit. However, the algorithm can be modified by starting at the maximum fringe density (*t* = *s*), and reducing the number of fringes by 1, 2, 4, 8...*s*/2. This ensures that the measured phase values are now clustered at the high-*t* end of the  $\Phi$ -*t* graph. The least-squares estimator for  $\omega$  is given by [9,10]

$$\hat{\omega} = \frac{s\Phi_u(s) + \sum_{v=0}^{\log_2 s-1} (s - 2^v)\Phi_u(s - 2^v)}{s^2 + \sum_{v=0}^{\log_2 s-1} (s - 2^v)^2} \quad (6)$$

and the standard deviation of the range value is reduced by a factor of approximately  $\sqrt{\log_2 s}$ , compared with that from the basic temporal unwrapping algorithm.

### 3. Real-time implementation of reversed exponential algorithm

A commercial pipeline processing system has been used to implement the reversed exponential algorithm in real-time. The Datacube MaxTD system consists of two

MaxVideo250 image processing boards with the addition of one Advanced Processor module.

During the initialisation period a lookup table (LUT) is created which contains the projected fringe pattern data. Each row of the LUT can be expanded at run-time using the pipeline hardware to create a complete projection image as illustrated in Figure 3. Hence, a reversed exponential sequence of phase stepped images starting with 16 fringes (ie.  $t=16, 15, 14, 12, 8$ ) requires a LUT with 20 rows of pixel data. In this way projected images are generated at a rate of 30 frames s<sup>-1</sup> and projected onto the test object using a Proxima DLP SVGA projector.

A digital CCD camera (EEV16) is synchronised to the projector and acquires the intensity maps into virtual surface image memories (VSIM) on the MaxVideo boards. Multi-buffering of the dual-ported memories is employed to allow the data to be processed during the acquisition period. Hence, at any given time during the experiment four operations occur in parallel: (i) generation of the fringe pattern image; (ii) transfer of the fringe pattern image to the projector; (iii) acquisition of the intensity map from the camera; and (iv) processing the acquired data.

Implementing the processing algorithm using pipeline processing hardware dictates that the arithmetic is performed using fixed point arithmetic. Furthermore the intermediate results that are stored on VSIMs must have 8 or 16 bit resolution to make efficient use of available resources so some rounding of results is inevitable. The propagation of these errors has been minimised by scaling all intermediate values such that the full dynamic range of the register stores are utilised.

The processing algorithm can be divided into four sections as illustrated in Figure 4, each of which can be performed in one frame period. Hence, the updated phase gradient estimate ( $\omega$ ) is computed every four frame periods which corresponds to the time taken for one acquisition cycle. The first step computes a 16 bit wrapped phase value ( $\Phi_w$ ) from the acquired 8 bit intensity maps ( $I(1,t) \dots I(4,t)$ ) according to equation (2). The intermediate results ( $\Delta I_{42}$  and  $\Delta I_{13}$ ) are rounded to 8 bits and used as inputs to a 16 bit x 16 bit LUT which performs the atan2() function. The second step derives the change in wrapped phase ( $\Delta\Phi_w$ ) according to equation (1) and generates the unwrapped phase using a running sum of unwrapped phase value ( $\Sigma\Phi_u$ ). Step 3 then adds the new unwrapped phase value to the running total. Step 4 updates the running phase gradient estimate  $\omega$  with a weighted sum of the unwrapped phase value.

The final stage is the calculation of a surface height value from each  $\omega$  value. This is done using pre-determined values of calibration constants following the procedure described in [6].

#### 4. Results

Figures 5 and 6 show results obtained from a test object containing surface steps. Figure 5 is the wrapped phase map from the highest fringe density (16 fringes across the field of view). From this map alone it is impossible to determine the relative heights of the surface steps. In addition, holes and shadowed regions would cause difficulties for most spatial unwrapping algorithms. A reversed exponential sequence with a maximum

of 16 fringes was used to illuminate the sample. A projection and acquisition rate of 30 frames s<sup>-1</sup> was employed, with the resulting (512x508) depth matrix available in 0.75 s. This is shown as a surface plot in Figure 6. Despite the problem areas the profile is reconstructed correctly in the regions where valid data is available. Shadowed regions are detected automatically by thresholding a modulation map so as to create a binary mask. The mask is generated at run time and can be toggled on or off as required by the user.

## 5. Conclusions

When measuring surface profile by the method of phase-shifted projected fringes, the use of fringes of varying pitch combined with temporal phase unwrapping allows unique range data to be calculated at each camera pixel. The optimal approach described in the paper involves decreasing the number of fringes exponentially to zero from the maximum value,  $s$ . This method combines a superior unwrapping reliability, a reduction in data acquisition and processing time by a factor  $(\log_2 s)/s$  and a decrease in measurement error of  $\sqrt{\log_2 s}/s$ , compared with the basic temporal unwrapping method (in which the number of fringes increases linearly from 1 to  $s$ ). It is the most appropriate of the methods in situations where the emphasis is on achieving a high measurement speed with reasonable accuracy.

A shape measurement system has been built based on this algorithm in which fringe patterns are projected, and images acquired, at 30 frames s<sup>-1</sup>. The images are analysed in real time on a pipeline processor. The entire process of projecting the patterns, acquiring the images, calculating and unwrapping the phase maps, generating the valid-data mask, performing the least squares fitting along the time axis, and converting the data to height values takes under 0.8 s for ca. 250,000 coordinates. Depth measurement accuracies of ca. 1 part in 1500 have been achieved to date with the current fringe density of 16 across the field of view. Such a system is likely to find application in areas such as high speed quality control and robot vision systems.

## 6. Acknowledgments

This work was supported by the Royal Society and by the Engineering and Physical Sciences Research Council under research grant GR/K67274.

## 7. References

1. Brooks R E and Heflinger L O *Appl. Opt.* **8** (1969) 935-939.
2. Indebetouw G *Appl. Opt.* **17** (1978) 2930-2933.
3. Srinivasan V, Liu H C and Halioua M *Appl. Opt.* **23** (1984) 3105-3108.
4. Zhao H, Chen W and Tan Y *Appl. Opt.* **33** (1994) 4497 - 4500.
5. Saldner H O and Huntley J M *Appl. Opt.* **36** (1997) 2770 - 2775.

6. Saldner H O and Huntley J M *Opt. Eng.* **36** (1997) 610-615.
7. Nadeborn W, Andrä P and Osten W *Opt. Lasers Eng.* **24** (1996) 245-260.
8. Xie X, Atkinson J T, Lalor M J and Burton D *Opt. Lasers Eng.* **27** (1997) 247-257.
9. Huntley J M and Saldner H O *J. Opt. Soc. Am. A* **14** (1997) 3188-3196.
10. Huntley J M and Saldner H O *Proc. SPIE* **3100** (1997) 185-192.
11. Huntley J M and Saldner H O *Appl. Opt.* **32** (1993) 3047-3052.
12. Creath K in *Interferogram Analysis* D. W. Robinson and G. T. Reid, eds. (Bristol: Institute of Physics) 1993.
13. Huntley J M and Saldner H O *Meas. Sci. Technol.* **8** (1997) 986-992.

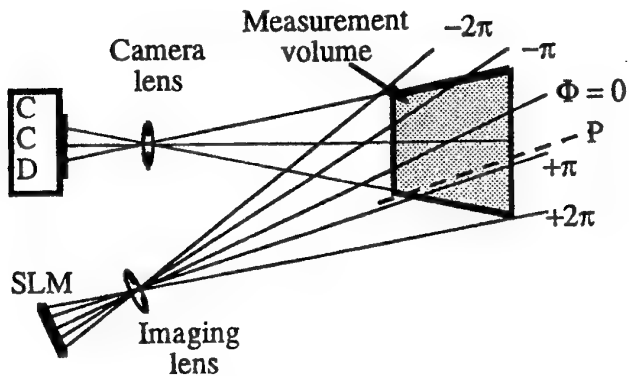


Figure 1. Set-up used to measure the surface shape of an object within the measurement volume. The dashed line is the cross-section through plane  $P$  referred to in the text.

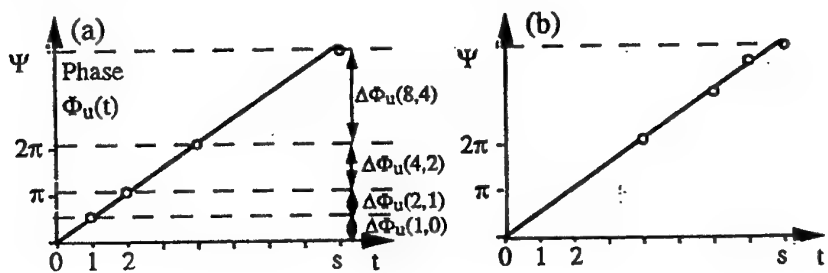


Figure 2. Time-varying unwrapped phase for a given pixel: forward and reversed exponential methods (a) and (b), respectively.

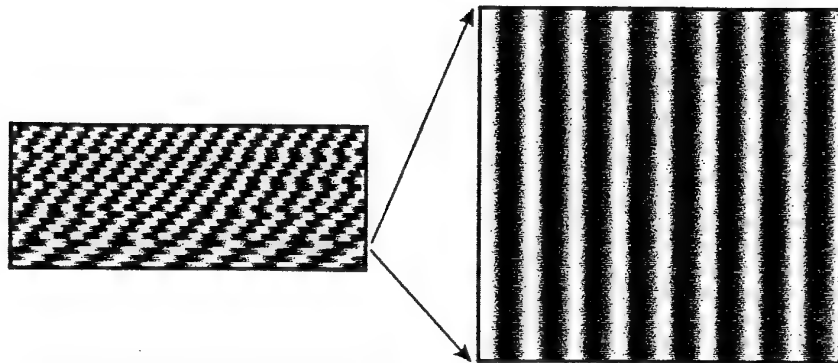


Figure 3. Pipeline processing hardware generates each fringe pattern image from one row of the LUT.

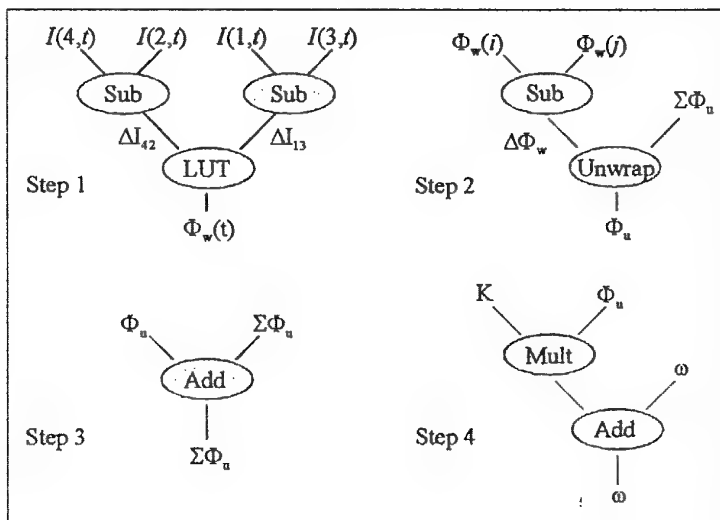


Figure 4. Pipeline image processing operations for the four steps referred to in section 3.

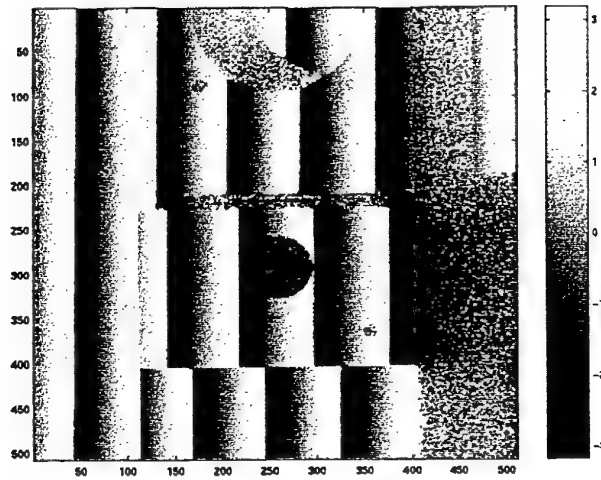


Figure 5. Wrapped phase map for a plate with surface steps. Black and white represent phase values of  $-\pi$  and  $+\pi$ , respectively.

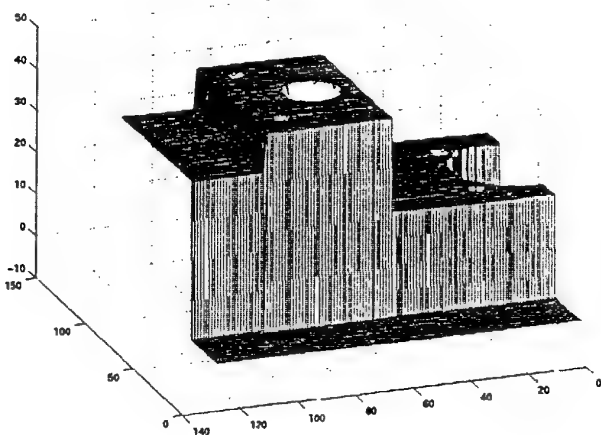


Figure 6. Surface profile for the plate shown in Figure 5 as measured by the high speed system described in this paper. Units for the axes are mm.

## HIGH SPEED LOCAL STRAIN DETERMINATION FROM GRATING DIFFRACTION

V. VALLE

*LMS, Université de Poitiers, CNRS UMR 6610  
SP2MI - Téléport 2 - BP 179, 86960 FUTUROSCOPE CEDEX, FRANCE*

M. COTTRON

*LMS, Université de Poitiers, CNRS UMR 6610  
SP2MI - Téléport 2 - BP 179, 86960 FUTUROSCOPE CEDEX, FRANCE*

A. LAGARDE

*LMS, Université de Poitiers, CNRS UMR 6610  
SP2MI - Téléport 2 - BP 179, 86960 FUTUROSCOPE CEDEX, FRANCE*

### Abstract

The spectral analysis of grating allows, for static loading, the direct measurement of local strains at the surface of a body. This grating analysis is achieved by two ways (optical diffraction phenomenon or numerical Fourier transform) in order to determine at each step of load pitches and orientations of crossed grating. Our purpose is to extend this strain measurement method to investigate dynamic problems. The grating interrogation is performed using optical diffraction of a laser beam with an oblique incidence. In order to separate the diffracted beams during the dynamic event, we associate with each strain state a specific angle of the incident laser beam. This procedure allows to record 23 strain states at a maximum frequency equal to 1 MHz. The diffracted spots can be stored by two ways (film and CCD camera) and their analysis gives a strain sensitivity of  $2.10^4$ .

### 1. Introduction

The measurement of mechanical quantities without contact, without destruction of the specimen or in hostile environment can be achieved by the optical investigations. The grid method [1], one of these, allows to determine the magnitude and the orientation of the principal strain as well as the rigid body rotation [2]. This is achieved by the comparison between the geometry of a deformed crossed grating (pitch and orientation

of each direction of grating) with the geometry of the same grating in the initial state. The analysis of the grating is obtained for static investigations by an optical Fourier transform or a numerical one [3][4]. This method is performed for the measurement of small and large strains with a sensitivity comparable to the one obtained by strain gauge [5].

Investigations of dynamic problems from grating analysis have been performed [6] few decades ago. The easy use of laser and the recent development of numerical tools like CCD camera allows the elaboration of modern and simplify experimental devices. This new method is based on an interrogation of a crossed grating from diffraction phenomenon under the oblique incidence.

## 2. recording and analysis device

### 2.1. OBLIQUE DIFFRACTION PHENOMENON

By associating with each strain state a specific angle of the incident laser beam, we can separate the diffracted beams during the dynamic event. We have so to take account of the diffraction phenomenon in oblique incidence [7]. We present on the Figure 1 the oblique diffraction phenomenon for an uni-directional grating of pitch  $p$  analysed on reflection by a laser beam.

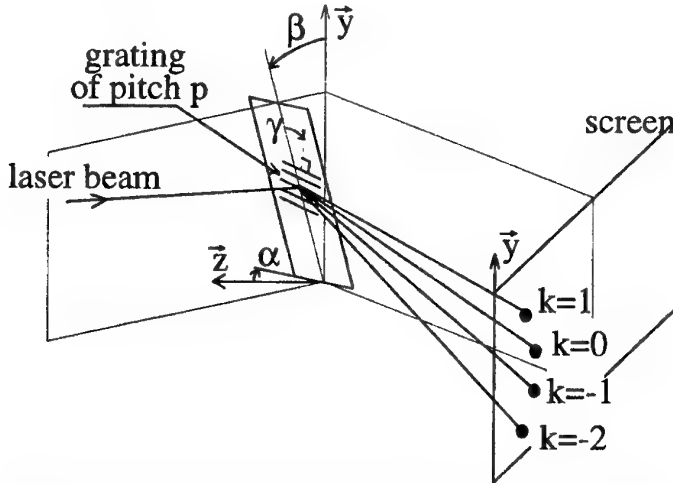


Figure 1 : Oblique diffraction of a laser beam from an uni-directional grating

We can see on Figure 2 the geometrical distribution of the diffracted spots (experimentally realised with an oblique incidence of  $\alpha=30^\circ$ ) given by a crossed grating.

HIGH SPEED LOCAL STRAIN DETERMINATION

3

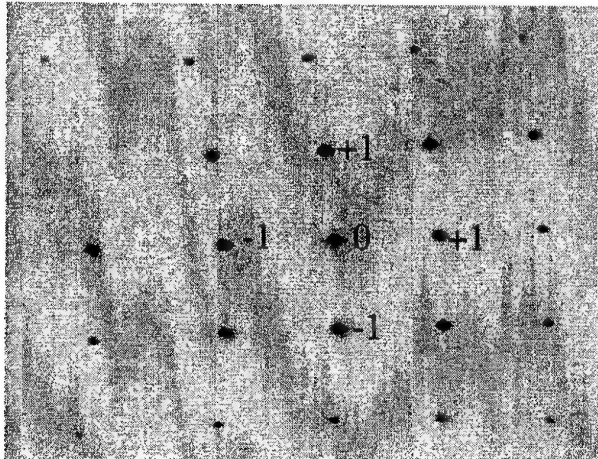


Figure 2 : Photography realised from the diffraction in oblique incidence of a laser beam through a crossed grating

The recording and the localisation of +1, 0 and -1 orders of diffraction give not only the 4 geometrical characteristics of the crossed grating, but also the 2 angular positions and the 3 components of the position of the measurement base. The comparison of these 9 parameters with the quantities in the initial state gives the strain tensor, the rigid body rotation and the rigid body displacement [8].

## 2.2. RECORDING DEVICE

The variation of the orientation of the incident laser beam is experimentally achieved by the used of acousto-optics deflectors [9][10] (Figure 3 and Figure 4). These elements allow the recording of 23 sequential information during the dynamic event at a maximum frequency near 1 MHz.

An acousto-optic shutter authorises exposure time equal to 30 ns and an optical element constituted of 48 mirrors permits to move each beam in the direction of the measurement base.

A study of the optical efficiency of this experimental device shows that the use of a recording film of 400 ASA sensitivity or a direct recording on CCD camera with a 250 mW laser power gives a minimum exposure time equal to 0.1  $\mu$ s. This value, ten percent of the maximum frame rate, is correct to have instantly information.

In these conditions, the developed device can be applied for a strain measurement during a dynamic loading of a minimal duration equal to 23  $\mu$ s.

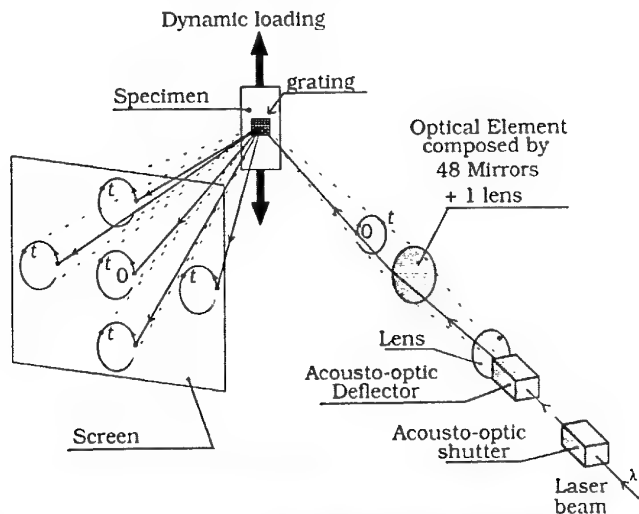


Figure 3 : Schema of the optical recording device

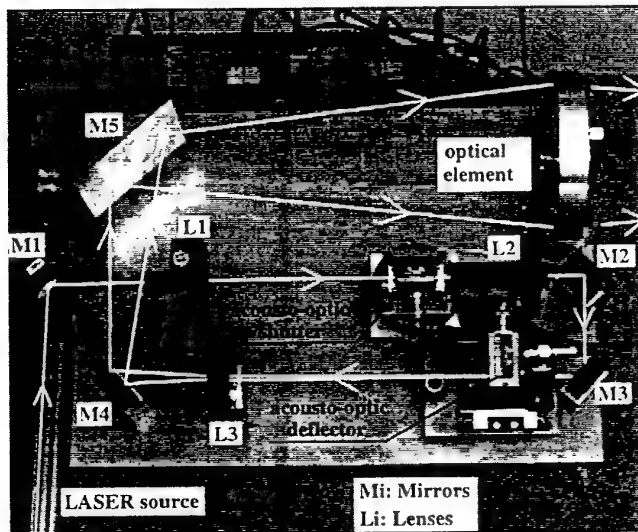


Figure 4 : Photography of the optical recording device

The small dimension of this recording device, about  $300 \times 500 \times 200 \text{ mm}^3$ , allows the use of this technique on most experimental or industrial site.

### 2.3. STORAGE ON PHOTOGRAPHIC FILM

For a photographic storage of the diffraction picture we replace the screen of the Figure 3 by a 9x12 cm photographic film (400 ASA). An adapted analysis device has been

## HIGH SPEED LOCAL STRAIN DETERMINATION

5

developed to determine the position of the 115 spots (5 orders of diffraction x 23 states of loading) recorded on the photographic film. This device consists of a XY displacement table (Figure 5) with 10  $\mu\text{m}$  sensitivity for moving the film, and a CCD camera for the acquisition of the spots

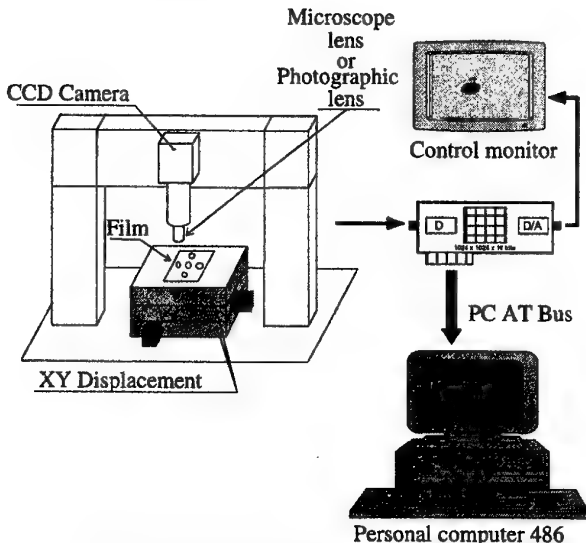


Figure 5 : Experimental device for photographic film analysis

In a first time we create a XY file containing the spots localisation obtained by a global analysis of the film. This analysis is achieved by mounting a photographic lens on the CCD camera. In a second time, we use the XY file to move the film with a motorised displacement table. The diffraction picture is then analysed spot by spot mounting a microscope lens on the CCD camera. By this way, we virtually multiply the number of pixels of the CCD camera (1024x1024 pixels to 8000x8000 pixels with 10  $\mu\text{m}$  resolution of the XY displacement). After 10 minutes of photographic film analysis, we obtain a strain sensitivity of approximately  $2.10^4$ .

The maximum strain rate depends on the strain sensitivity and on the minimum exposure time. this is obtained by dividing the strain sensitivity by the exposure time. For example, a dynamic event analysed with a sensitivity of  $2.10^4$  and an exposure time of 0.1  $\mu\text{s}$  authorises a maximum strain rate of  $2000 \text{ s}^{-1}$ . We can have a better strain rate of  $20000 \text{ s}^{-1}$  if the strain sensitivity is equal to  $2.10^3$ .

#### 2.4. DIRECT STORAGE ON CCD CAMERA

For a CCD storage of the diffraction picture we replace the screen of the Figure 3 by a CCD camera with 1024x1024 pixels on 10 bits. The storage of the diffracted spots is obtained by synchronisation of the CCD camera acquisition with the dynamic loading.

This device is more simple but the pitch of the CCD grid (larger than the film grain) induces a smaller strain sensitivity. In our case the strain sensitivity reaches to  $10^{-3}$ .

The optical efficiency of this experimental device gives the same performances than the first (20  $\mu$ s of minimum loading time with 0.1  $\mu$ s of exposure time and 250 mW of laser power). The maximum strain rate is equal to  $10000 \text{ s}^{-1}$ .

### 3. Tests

For all the experimental investigations, the diameter of the measurement base is of about 1 mm. The crossed grating is realised by a replication technique [11] and their density is equal to 200 lines per millimetre. The tests are realised with a CCD camera of 1024x1024 pixels for the direct technique and a 400 ASA film of 9x12 cm for the photographic one. On our figures, we compare the strain optically measured and those obtained by a classical extensometry using a strain gauge.

#### 3.1. PHOTOGRAPHIC RECORDING

We give (Figure 6) a compression test using the impact of a mass on the mobile grip of the specimen. The storage of the optical data is realised on a photographic film. For this impact of 600  $\mu$ s duration, we have chosen the frame rate equal to 35 kHz and an exposure time of 2.8  $\mu$ s.

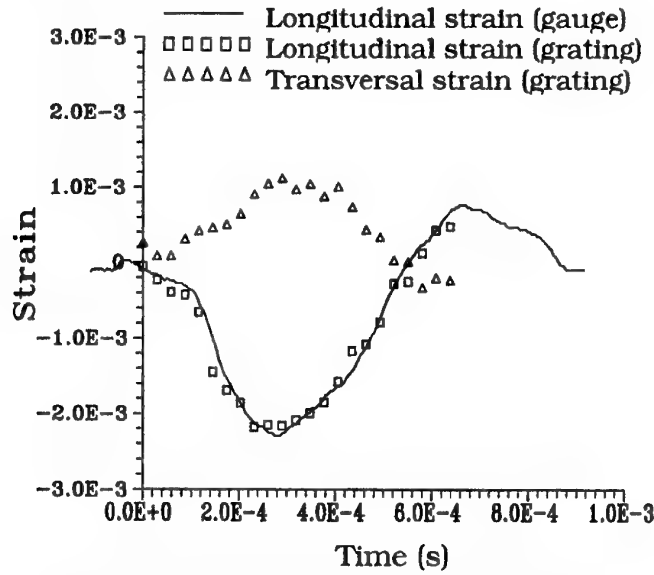


Figure 6 : Dynamic compression test with photographic acquisition

## HIGH SPEED LOCAL STRAIN DETERMINATION

7

## 3.2. CCD CAMERA RECORDING

On Figure 7 we present a compression test performing with a Hopkinson bar loading. We have adjusted the framing rate to 1 MHz according to the duration of the loading ( $20 \mu\text{s}$ ). In this test, the exposure time is 10% of the framing rate ( $0.1 \mu\text{s}$ ).

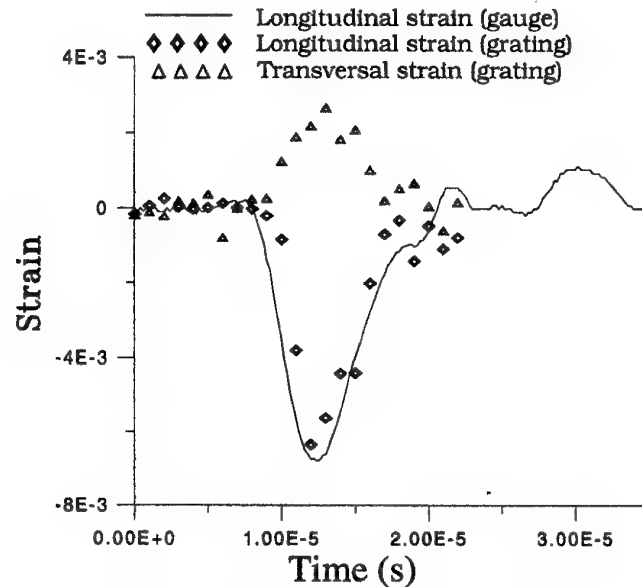


Figure 7 : Dynamic compression test with CCD acquisition.

These two dynamic tests give a good idea of the performances of this method. The accordance between longitudinal strains optically determined and classically measured demonstrates the efficiency of the developed method.

## 4. Conclusion

This measurement method performed by an interrogation of the grating using the optical diffraction with an oblique incidence allows to determine not only the strain tensor given by the optical diffraction in normal incidence but also the six rigid motions of a measurement base of 1 mm.

The use of acousto-optic components allows to separate easily the information during a dynamic or a static loading [12] and to record 23 states of the specimen at up to 1,000,000 frames per second.

The recording of the diffraction image can be achieved by two ways : the acquisition on a photographic film analysed by specific device composed by a digital image processing using a CCD camera - the direct acquisition on CCD camera. These two procedures give different strain sensitivity and maximum strain rate.

The direct determination of strains without any contact is well adapted to the analysis of impact loadings with the measurement directly obtained from the specimen, to the study of behaviour laws in static and dynamic loading or to the control of structures under vibratory regimes.

### References

1. Sevenhuijsen, P.J. 1989. Grid method : a new future. Proceeding of SEM Spring Conference.
2. Brémand, F. and A. Lagarde (1988) Analyse spectrale bidimensionnelle d'un réseau de traits croisés. Application à la mesure des grandes et petites déformations. C.R. Académie des Sciences. t 307. serie II 683-688.
3. Brémand, F., J.C. Dupré and A. Lagarde (1992) Non-contact and non disturbing local strain measurement methods. I - Principle. European Journal of Mechanics. A/Solids. Vol.11 3:349-366.
4. Cardenas-Garcia, J.F. and M.S. Wu (1989) Further development of the video optical diffractometer for strain measurement. Proceeding of the SEM Spring Conference.
5. Dupré, J.C., M. Cottron and A. Lagarde (1994) Phase shifting technique for local measurements of small strains by grid method. Proceedings 10th International Conference on Experimental Mechanics.
6. Bell, J. F. (1956) Determination of dynamic plastic strain through the use of diffraction gratings. Journal of Applied Physics. Vol.27 1109-1113.
7. Valle, V., M. Cottron and A. Lagarde (1995) Utilisation du phénomène de diffraction sous incidence oblique d'un faisceau laser par un réseau croisé pour la mesure locale en statique et dynamique des déformations et des mouvements de solide. Mechanics Research Communications. Vol 22. 2 103-107.
8. Valle, V., M. Cottron and A. Lagarde (1994) A new optical method for dynamic strain measurement. proceeding 10<sup>th</sup> International Conference on Experimental Mechanics :549-553.
9. Brillouin, L. (1921). Ann. de Phys. **17** 103.
10. Debye, P. and F.W. Sears (1932) Proc. Nat. Acad. Sci., Washington **18** 409.
11. Post, D. (1982) Developments in moire interferometry. Optical Engineering, **21** :458-467.
12. Valle, V., M. Cottron & A. Lagarde (1996) Grating diffraction for local strain determination under dynamic loading. ESDA 96. 4 69-74.

## TRANSIENT STRESS ANALYSIS UNDER LOW VELOCITY IMPACT BY WHITE LIGHT PHOTOVISCOELASTIC TECHNIQUE

S. YONEYAMA AND M. TAKASHI

*Aoyama Gakuin University*

*6-16-1 Chitosedai, Setagaya, Tokyo 157-8572, Japan*

**Abstract.** This paper discusses a new method for determining fringe order and the principal direction of birefringence from a single image in practical photoviscoelastic analysis. Using an elliptically polarized white light and color image processing, fringe pattern at each instant is analyzed from three monochromatic images obtained with a single shot. It will be emphasized that no repetition of experiment under the same condition nor multiple images acquisition is necessary, which is usually adopted in the current techniques. An example problem in the case of a plate subjected to low velocity impact is successfully analyzed by use of the method proposed, then the time variation of stress around the point of impact is traced taking the constitutive equations of photoviscoelasticity into account.

### 1. Introduction

From the viewpoint of experimental analysis of time-dependent stress and strain in a viscoelastic material, photoviscoelastic technique [1-4] is a very useful tool. In the currently available fringe analysis techniques such as phase-shifting methods with a monochromatic light [5, 6], multiple images are inevitably required to determine both fringe order and the principal direction of birefringence. Namely, multiple measurements are required assuming the same stress and strain state involving their history could arise under repeated experiments. Thus, the current techniques cannot be applied to the problems in which the good repeatability of experiment is not expected. In order to analyze stresses in a viscoelastic body, it is required to determine both of fringe order and the principal direction of birefringence from an image data obtained with a single shot at each instant.

The objective of this study is to develop a method, using photoviscoelastic technique, for studying time-variant stress distributions. In the previous

paper, the authors [7] have proposed a photoelastic method for determining both fringe order and the principal direction of birefringence from a single color image using an elliptically polarized white light. Applying the method proposed to sequential color photoviscoelastic image data, time-dependent fringe order and the principal direction of birefringence distributions at each instant can be determined, and the following time-dependent stress and strain analysis can be performed using the constitutive equations of photoviscoelasticity. In this paper, the theory of the proposed fringe analysis method is described briefly. Then, the successful application of the method to a photoviscoelastic analysis is demonstrated in the case of a plate subjected to low velocity impact.

## 2. Optical Constitutive Equations of Photoviscoelasticity

In two-dimensional linearly photoviscoelastic analysis, the time-dependent differences of principal stresses  $\sigma_1(t) - \sigma_2(t)$  and strains  $\epsilon_1(t) - \epsilon_2(t)$  as well as the angle  $\beta(t)$  of the principal stress direction and the angle  $\gamma(t)$  of the principal strain direction can be calculated by measuring isochromatic fringe order per unit thickness of a specimen  $n(t) = N(t)/h$  (where  $h$  is the thickness of the specimen) and the principal direction of birefringence  $\alpha(t)$  which change with time  $t$ . The 2-D photoviscoelastic constitutive relations are expressed by the following equations [2-4].

$$\begin{aligned} \{\sigma_1(t) - \sigma_2(t)\} \cos 2\beta(t) &= C_{\sigma r}^{-1}(t)n(0) \cos 2\alpha(0) \\ &+ \int_0^t C_{\sigma r}^{-1}(t-\tau) \frac{dn(\tau) \cos 2\alpha(\tau)}{d\tau} d\tau \quad (1) \end{aligned}$$

$$\begin{aligned} \{\sigma_1(t) - \sigma_2(t)\} \sin 2\beta(t) &= C_{\sigma r}^{-1}(t)n(0) \sin 2\alpha(0) \\ &+ \int_0^t C_{\sigma r}^{-1}(t-\tau) \frac{dn(\tau) \sin 2\alpha(\tau)}{d\tau} d\tau \quad (2) \end{aligned}$$

$$\begin{aligned} \{\epsilon_1(t) - \epsilon_2(t)\} \cos 2\gamma(t) &= C_{\epsilon c}^{-1}(t)n(0) \cos 2\alpha(0) \\ &+ \int_0^t C_{\epsilon c}^{-1}(t-\tau) \frac{dn(\tau) \cos 2\alpha(\tau)}{d\tau} d\tau \quad (3) \end{aligned}$$

$$\begin{aligned} \{\epsilon_1(t) - \epsilon_2(t)\} \sin 2\gamma(t) &= C_{\epsilon c}^{-1}(t)n(0) \sin 2\alpha(0) \\ &+ \int_0^t C_{\epsilon c}^{-1}(t-\tau) \frac{dn(\tau) \sin 2\alpha(\tau)}{d\tau} d\tau \quad (4) \end{aligned}$$

where  $C_{\sigma r}^{-1}(t)$  denotes the inverse relaxation stress-birefringence coefficient and  $C_{\epsilon c}^{-1}(t)$  is the inverse creep strain-birefringence coefficient, which are material properties and must be measured and determined beforehand.

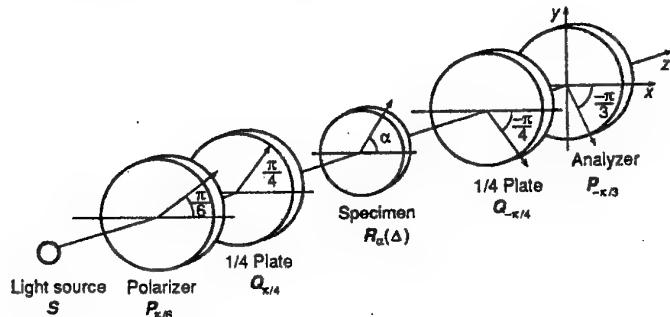


Figure 1. Arrangement of the optical elements.

### 3. Fringe Analysis Using Elliptically Polarized White Light

#### 3.1. FRINGE ORDER DETERMINATION

When a color CCD camera is used to record fringe pattern with white light, a digitized color image data consists of three monochromatic images corresponding to the three primary colors, i.e., red, green and blue, and each of three monochromatic images has its own intensity level and distribution. The brightness distribution of the photoviscoelastic image through a polariscope arranged as shown in Figure 1 is expressed as [7]

$$I_i = \frac{1}{16} \frac{1}{\lambda_{i2} - \lambda_{i1}} \int_{\lambda_{i1}}^{\lambda_{i2}} I_0 F_i \sin^2 \frac{\delta\pi}{\lambda} (9 + \cos 2\varepsilon + 5 \cos 4\alpha + \cos 2\varepsilon \cos 4\alpha + 4\sqrt{3} \sin \varepsilon \sin 4\alpha) d\lambda \quad (i = r, g, b) \quad (5)$$

where  $I_0$  ( $= I_0(\lambda)$ ) expresses the spectral distribution of the light used,  $i = r, g, b$  denotes red, green and blue colors,  $\lambda_{i1}$  and  $\lambda_{i2}$  are the lower and upper limits of the spectrum of the filters in the camera,  $F_i$  ( $= F_i(\lambda)$ ), the spectral responses of the red, green and blue filters,  $\delta$ , retardation,  $\alpha$ , the principal direction of birefringence,  $\varepsilon$ , the quarter-wave plate error [8], respectively.

By comparing the light intensity values at each data point with the corresponding values in a calibration table which connects fringe order with the light intensity values, fringe order can be determined in a good accuracy. Different from the data-base-search method proposed by Ajovalasit et al. [9], to eliminate the effect of the principal direction of birefringence  $\alpha$  of the image data, the gray levels have to be normalized before comparing these values from the model and the calibration table in the proposed method. Fringe order can be determined by means of an error function  $E_j$  as

$$E_j = \left( \frac{R_j}{X_j} - \frac{R_m}{X_m} \right)^2 + \left( \frac{G_j}{X_j} - \frac{G_m}{X_m} \right)^2 + \left( \frac{B_j}{X_j} - \frac{B_m}{X_m} \right)^2 \quad (6)$$

where  $R_m$ ,  $G_m$  and  $B_m$  are the digitized values of light intensities  $I_r$ ,  $I_g$  and  $I_b$ , i.e., the gray levels of a image data at each point, and  $R_j$ ,  $G_j$  and  $B_j$  are also digitized in the calibration table, respectively.  $X_m$  and  $X_j$  are the sum of the intensity levels, i.e.,

$$X_m = R_m + G_m + B_m, \quad X_j = R_j + G_j + B_j \quad (7)$$

Fringe order at a point can be determined by searching index  $j$  which minimize the error function  $E_j$ . If the variation of the fringe order in the calibration beam is linear and the first pixel of the calibration table could be zero fringe order, the fringe order  $N_j$  corresponding to the pixel index  $j$  is expressed as [9]

$$N_j = N_m \frac{j}{j_m} \quad (8)$$

where  $N_m$  is the maximum fringe order in the calibration table and  $j_m$  is the number of the values stored in the calibration table.

### 3.2. PRINCIPAL DIRECTION OF BIREFRINGENCE DETERMINATION

If the retardation error  $\varepsilon$  could be treated as a constant for each color, Equation (5) can be rewritten as

$$I_i = Y_i \cdot Z_i \quad (9)$$

where

$$Y_i = 9 + \cos 2\varepsilon_i + 5 \cos 4\alpha + \cos 2\varepsilon_i \cos 4\alpha + 4\sqrt{3} \sin \varepsilon_i \sin 4\alpha \quad (10)$$

$$Z_i = \frac{1}{16} \frac{1}{\lambda_2 - \lambda_1} \int_{\lambda_{i1}}^{\lambda_{i2}} I_0 F_i \sin^2 \frac{\delta\pi}{\lambda} d\lambda \quad (i = r, g, b) \quad (11)$$

Here,  $\varepsilon_i$  represents the retardation errors of the quarter-wave plates at the center wavelengths of the spectrums captured by each sensor in the color camera. In the following, Equation (9) is adopted for the calculation of the principal direction of birefringence.

The value of Equation (11) can be obtained from the digitized intensity values in the calibration table if the calibration test is performed with the polarization angle 0 rad. Thus, using the light intensity values in the calibration table, the following equation is derived [7].

$$X_m - Y_r \cdot \frac{8}{7 + \cos \varepsilon_r} \cdot R_t - Y_g \cdot \frac{8}{7 + \cos \varepsilon_g} \cdot G_t - Y_b \cdot \frac{8}{7 + \cos \varepsilon_b} \cdot B_t = 0 \quad (12)$$

where  $R_t$ ,  $G_t$  and  $B_t$  are the gray levels stored in the calibration table, i.e., they are corresponding to Equation (11). Equation (12) is a non-linear equation with respect to the principal direction of birefringence  $\alpha$ . The value of  $\alpha$  can be obtained by solving Equation (12), numerically.

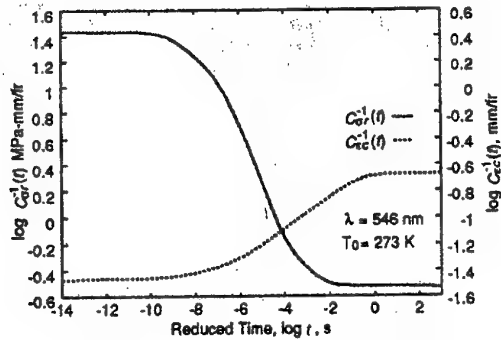


Figure 2. Master curves of  $C_{\sigma r}^{-1}(t)$  and  $C_{\epsilon c}^{-1}(t)$  of the material.

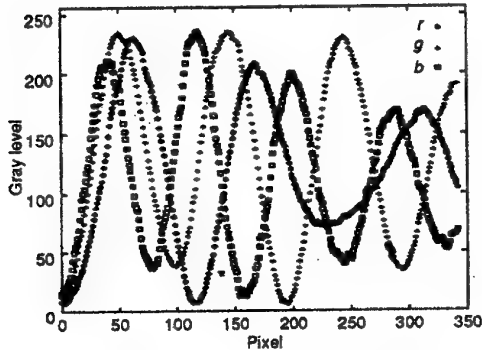


Figure 3. Calibration table (Gray level distributions of the calibration beam).

#### 4. Material Properties and Experimental Procedure

The material used in this study is a polyurethane rubber [2]. This material is linearly viscoelastic, thermorheologically simple and birefringent, and exhibits excellent light transmission properties. Its glass transition temperature was measured as  $T_g = 223 \text{ K}$ . Figure 2 shows the photoviscoelastic characteristics of the material, i.e., the master curves of the inverse relaxation stress-birefringence coefficient  $C_{\sigma r}^{-1}(t)$  and the inverse creep strain-birefringence coefficient  $C_{\epsilon c}^{-1}(t)$ . Details of the experimental procedure for determining photoviscoelastic coefficients are given in Ref [1].

The calibration test to make up the calibration table linking the digitized light intensity levels with fringe order was performed using a beam specimen made of the same material (polyurethane rubber). A beam specimen, 40 mm height, 140 mm width and 10 mm thickness, was subjected to a tension-bending load. The color fringe pattern around the center of

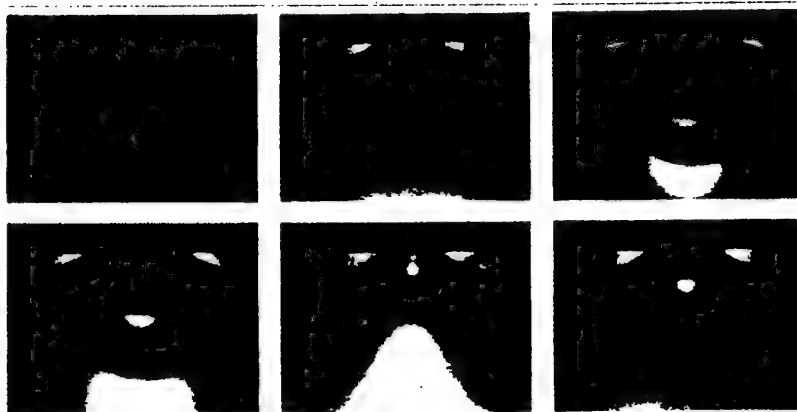


Figure 4. Series of 6 consecutive photoviscoelastic fringe patterns; camera speed—1000 frames per sec (Note that these are color images).



Figure 5. An example set of the distributions of fringe order and the principal direction of birefringence.

the beam was acquired and the light intensity levels at each pixel along the transverse section of the calibration beam were stored in an ascending order array with fringe order for the wavelength 546 nm as the calibration table, as shown in Figure 3.

A plate specimen made of polyurethane rubber, 150 mm width, 50 mm height and 10 mm thickness, was subjected to low velocity impact of 1.64 kg disk type weight falling from a height of 10 mm. The photoviscoelastic fringe patterns were recorded by a color video camera operated at a speed of 1000 frames per sec. The constant temperature  $T = 237$  K was carefully maintained during the whole experiment within  $\pm 0.5$  K. At this temperature the material shows a remarkably viscoelastic behavior.

## 5. Results and Discussion

Figure 4 shows the first 6 frames of the photoviscoelastic fringe pattern. Note that the color images are expressed by gray levels, here. The attenua-

## WHITE LIGHT PHOTOVISCOELASTIC TECHNIQUE

7

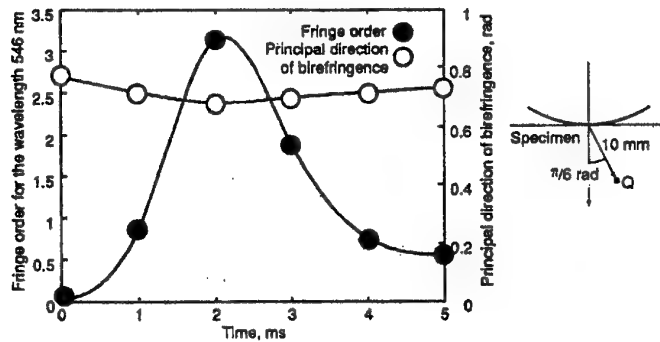


Figure 6. Time variations of the fringe order and the principal direction of birefringence.

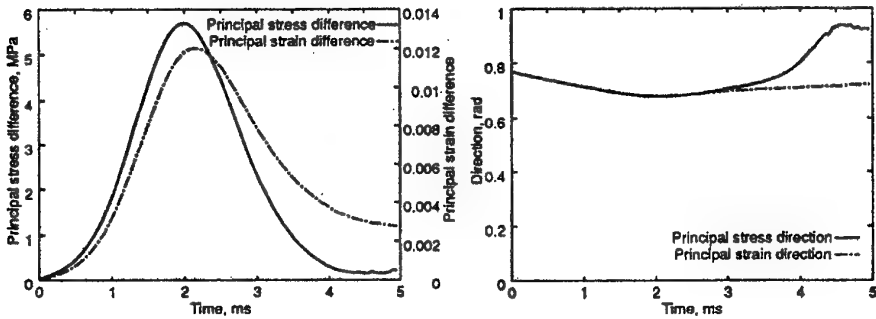


Figure 7. Time variations of the differences of principal stresses and strains, and their directions

tion of fringes due to the ellipticity of the light used is obviously seen. The fringe patterns look significantly different from static ones [10] or Hertz elastic contact [11] where maximum fringes appear inside a specimen. The distributions of the fringe order and the principal direction of birefringence at each instant were determined by the method proposed. Figure 5 shows an example set of the distributions of the fringe order and the principal direction of birefringence. Here, the values are expressed in 10 steps contour maps. Figure 6 shows the time variations of the fringe order and the principal direction of birefringence at an example point Q shown in this figure. The principal direction of birefringence varies with time reflecting the nonproportional loading condition. The time variations of the differences of the principal stresses and strains as well as their directions were calculated using the optical constitutive equations of photoviscoelasticity as shown in Figure 7. Reflecting the viscoelastic properties of the material, not only  $\sigma_1(t) - \sigma_2(t)$  and  $\epsilon_1(t) - \epsilon_2(t)$  but  $\beta(t)$  and  $\gamma(t)$  show different

time variations each other.

### 6. Concluding Remarks

This study discussed a new method for determining fringe order and the principal direction of birefringence from a single image using an elliptically polarized white light and color image processing for practical photoviscoelastic analysis. Using the method proposed, the time variation of fringe order and the principal direction of birefringence in a plate subjected to low velocity impact were determined without the repetition of experiment. Also, the time variations of the differences of the principal stresses and strains as well as their directions were evaluated using the optical constitutive equations of photoviscoelasticity.

It is pointed out that time-varying problems in which good repeatability of experiments is not expected can be analyzed by the method proposed.

### Acknowledgment

This work was partly supported by the Center for Science and Engineering Research Institute, Aoyama Gakuin University.

### References

1. Williams, M.L. and Arenz, R.J.: The engineering analysis of linear photoviscoelastic materials, *Exp. Mech.* **4** (1964), 249-262.
2. Kunio, T. and Miyano, Y.: Photoviscoelastic analysis by use of polyurethane rubber, in *Applied Mechanics (Proc. 12th Int. Cong. Appl. Mech.)*, H. Hetenyi and W. Vincenti (eds), Springer-Verlag, Berlin (1969), 269-276.
3. Gotoh, J., Horie, H., Misawa, A. and Takashi, M.: Photoviscoelastic method for time-dependent stress and strain analysis under non-proportional loading, in *Proc. SEM Spring Conf. Exp. Mech.*, Grand Rapids (1995), 234-241.
4. Yoneyama, S., Ayame, D., Gotoh, J. and Takashi, M.: Photoviscoelastic stress and strain analysis around a surface groove under rolling contact load, *JSME Int. J., Ser. A* **40** (1997), 44-50.
5. Patterson, E.A. and Wang, Z.F.: Towards full field automated photoelastic analysis of complex components, *Strain* **27** (1991), 49-56.
6. Mawatari, S., Takashi, M., Toyoda, Y. and Kunio, T.: A single valued representative function for determination of principal stress direction in photoelastic analysis, in *Proc. 9th Int. Conf. Exp. Mech.*, Copenhagen (1990), 2069-2078.
7. Yoneyama, S. and Takashi, M.: A new method for photoelastic fringe analysis from a single image using elliptically polarized white light, *Submitted for Publication in Optics and Lasers in Engineering*.
8. Redner, A.S.: Photoelastic measurements by means of computer-assisted spectral-content analysis, *Exp. Mech.* **25** (1985), 148-153.
9. Ajovalasit, A., Barone, S. and Perucci, G.: Towards RGB photoelasticity: full-field automated photoelasticity in white light, *Exp. Mech.* **35** (1995), 193-200.
10. Yoneyama, S., Gotoh, J. and Takashi, M.: Tricolor photoviscoelastic technique and its application to moving contact, *Accepted for Publication in Exp. Mech.*
11. Johnson, K.L.: *Contact Mechanics*, Cambridge University Press, Cambridge, 1985.

## STEREOLITHOGRAPHY AND MICRO-MECHANICS

Serge MONNERET, Serge CORBEL, Virginie LOUBERE  
*Département de Chimie Physique des Réactions  
UMR 7630 CNRS-INPL  
Ecole Nationale Supérieure des Industries Chimiques de Nancy  
1 rue Grandville - BP 451 - 54001 Nancy Cedex  
FRANCE*

**Abstract :** Laser stereolithography deals with the manufacture of three-dimensional objects that are made by space-resolved laser-induced polymerization. In order to obtain three dimensional microobjects, we developed a new microstereolithography apparatus based on the use of a dynamic mask-generator which allows the manufacture of a complete layer by only one irradiation, the part being manufactured layer by layer. This process uses a broad-band visible light source, that leads to the elimination of speckle effects resulting from the conventional use of a laser beam. A lateral resolution of  $2 \mu\text{m} * 2 \mu\text{m}$  has been demonstrated with this new process.

### Introduction

All started, as regards microtechnologies, a few centuries ago with the watch-making industry. The manufacturing of clock components has been a constant way to make progress in the design of new mechanisms as well as in the development of new technologies. Such a domination of mechanics as regards miniaturization and precision continued until the recent appearance of microelectronics, about 30 years ago : microelectronics technologies have been developed to improve miniaturization, in order to manufacture higher density integrated electronic components. This leads to a higher functional frequency due to shorter displacements of charges carriers inside the structures.

Nowadays, the same microfabrication processes are beginning to be applied to the manufacture of integrated mechanical systems on silicon chips. Such microsystems are called Micro Electro Mechanical systems (MEMs) and can lead to many applications such as micromotors, microsensors, microactuators, micropositioning systems [1-4]...

But the main limitation of these processes is that they can be only adapted to manufacture planar components presenting a maximal thickness of about 20 micrometers. Then, several recent processes have been developed to manufacture thick micro-parts. The most successful is the so-called LIGA process, based on deep-etch x-ray lithography and subsequent replication processes like electroforming and molding [5]. However, the use of a synchrotron source leads to

limitations because of its expense and availability constraints. Then, a new negative-tone near-UV resist (IBM SU-8) has been recently designed specifically for ultrathick, high-aspect-ratio MEMS-type applications, based on a low-cost LIGA-type process [6]. But, because they are lithography-based, the main limitation of these LIGA-type processes is that complex shapes can not be made easily, in particular with curved surfaces or an important number of layers.

That is why, applying stereolithography (SL) to the field of micro-fabrication appears to be an attractive alternative process to the manufacture of real three-dimensional microobjects with complex shapes.

After reminding the principles of the SL technique, we briefly present previous works concerning applications of SL to microtechnics. At last, we describe a new apparatus of micro-SL, which is based on the use of a broad-band visible light source.

## 2. The Stereolithography technique

The stereolithography technique [7] is a process which has been performed to manufacture three-dimensional objects, mainly for rapid prototyping applications.

The basic principle is a space-resolved light-induced polymerization, consisting in a liquid/solid phototransformation. Current machines work by laying down a thin layer of resin and shining the proper wavelength of light on it in a pattern that describes the two-dimensional shape of a single cross section of the object to be built. Once a single cross section is built in this way, a new layer of resin is applied and the process is repeated. Then thin layers made of solidified photopolymer are stacked from bottom to up to create complicated three dimensional shapes, leading to true 3D microparts obtained quickly and with no assembly. At last, a scraper is also used to ensure a homogeneous thickness of the new liquid resin layer, each time the process is repeated.

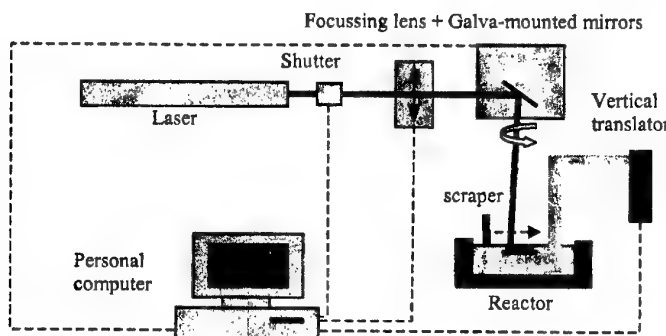


Figure 1. The conventional SL process

Once the object to be built is designed (generally using Computer Aided Design processes), it is then numerically sliced to define the different cross sections of the object to be manufactured. Then, the numerical data defining each of the sections are sequentially sent to the machine, in order to built them.

Two principal kinds of SL processes can be distinguished up to now, depending on the way to build a cross section. The first one, which can be considered as conventional, is based on the vectorial tracing of every layer of the object by moving a focalized laser beam on the surface of the resin (Fig. 1). Galva-mounted mirrors are then used, and the light is occulted by a mechanical shutter during jumps of the laser beam between different polymerized segments, or when a new layer of liquid monomer is made. A dynamic focusing lens is also used to ensure the laser beam to be exactly focused on the resin surface, at any place on it. The second kind of process allows to built a complete layer by only one irradiation, by imaging directly its pattern with a masked lamp. But this needs to define a mask each time the pattern is changed, and to use a much more stronger intensity of the laser beam.

When compared to the conventional machining techniques, SL has the advantages to need neither moulds nor tools and the parts have almost any shape. It principally concerns the rapid prototyping field, and the manufacturing industries which are already using this technology include automotive, aerospace, and medical industries. The manufactured objects have a typical volume of about a few dm<sup>3</sup> with a spatial resolution of 100 μm.

### 3. Extension to micro-Stereolithography

To improve the accuracy obtained by the SL technique for manufacturing three dimensional microobjects, several processes have been studied [8,9]. In order not to introduce moving elements which can cause a loss of resolution, no galva-mounted mirrors nor dynamic focusing lens to deflect and focalize the light beam are used. The focus point of the light beam then remains fixed on the surface of the resin, while an x-y positioning stage moves the resin reactor in which the object is made. But the reactor must be translated very slowly to ensure the required stability of the surface of the liquid resin during the polymerization step. The main limitation of this process is the much more important time to manufacture a layer, compared to the use of galva-mounted mirrors.

That is why a new process of micro-stereolithography (μ-SL) technique has been developed in our laboratory [10], which allowed to manufacture a complete layer by only one irradiation, the three-dimensional microobject being still manufactured layer by layer. As already given in Ref. [10], this type of μ-SL process presents a number of advantages, that will be rapidly described now.

First, the limitation to only one moving operating element leads to a good stability during the curing step. Moreover, the light flux density on the surface of the resin is low compared to that is used with vectorial processes, which are based on very fast displacements of a strongly focussed laser beam on the surface of the resin.

As a consequence, thermal-induced problems can be considered as negligible. At last, the process has the potential of being much faster than classical vectorial processes, since the irradiation of an entire layer is enacted simultaneously.

But the major disadvantage of this process comes from the liquid crystal matrix that presents a bad transmission to ultraviolet (UV) light. So, it is necessary to use a light source emitting in the visible spectrum and consequently to use a photochemical mixture which is photosensitive to these wavelengths [11].

A first apparatus has been achieved using a coherent and visible light source (Ar+ laser emitting at 515 nm). It used a liquid crystal display (LCD) as a dynamic mask generator [10].

Complex objects have then been obtained with a resolution of 5  $\mu\text{m}$  in the three directions of space [11]. Prototypes of microactuators having a distributed elasticity and made of multiple imbricated springs have also been realized. As an example, Fig. 2 shows such a microactuator, which was moved by using shape memory alloy (SMA) wires in the clamping areas [12].

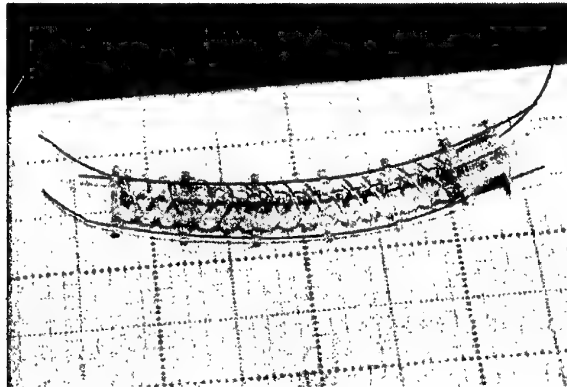


*Figure 2. Photograph of a distributed elasticity microactuator after SMA wire assembly [12]*

#### 4. Micro-Stereolithography using a dynamic mask generator and a non coherent light source

We are now developing a new  $\mu\text{SL}$  apparatus still based on the use of a dynamic mask generator, but using a non coherent broad-band halogenure light source. There are in fact several tradeoffs between using a masked enlarged laser beam versus a masked lamp to cure the layers of photopolymer resin :

- A laser is potentially more energy efficient, since a lamp generates a lot of useless light outside the range of frequencies to which any particular resin is photosensitive.
- There is some evidence that monochromatic light, as generated by a laser, yields more uniform-in-depth curing for thicker layers. But the gaussian

intensity distribution of such a laser beam leads to a non uniform curing in the covered mask area.

- The coherence of a laser beam leads to a strong local inhomogeneity of the projected image, due to speckle effects.
- The broad spectrum of a lamp makes it more flexible in the resins it can use, whereas a laser must be used with resins specifically tuned to its frequency.
- The use of a lamp strongly decreases the production cost of the microparts.

Thus, it may be attractive to conceive a new  $\mu$ -SL machine from a broad-band visible light source.

#### 4.1. EXPERIMENTAL SETUP

The experimental setup of the process is given in figure 3. The beam is issued from a conventional halogenure light source (dataprojector-based). After its propagation through the computer-controlled liquid crystal display (L.C.D) which contains the pattern of the layer, the beam is then reduced and focused on the surface of the photocurable resin. As in Ref. [10], a LCD is then used as a dynamic mask generator. By connecting a computer to this device, every pixel can be set either to its transparent or to its opaque state by changing the orientation of molecules, it is made of. So, the pixels in their dark state stop the light, in contrast to those which are in their transparent state. The contrast ratio of about 1:100 of the LCD is sufficient to use it also as a shutter (all the pixels are then in their dark state).

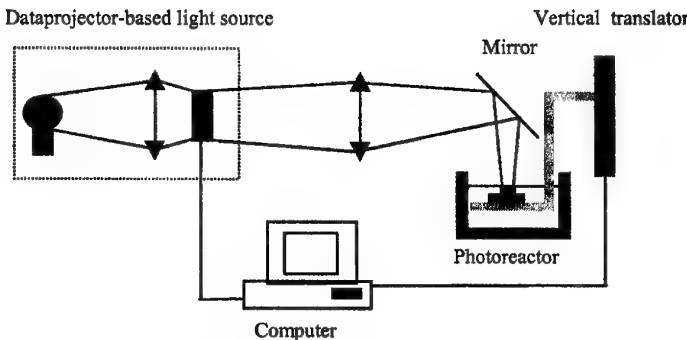


Figure 3.  $\mu$ SL device using a mask-generator display and a non coherent light source

Contrary to the conventional SL process, no scraper can be used to add a layer of reactive medium on the surface of the part being manufactured because such a kind of device could damage the microobjects during their manufacture. So, the time to obtain each new horizontal fresh layer of resin depends mainly on its rheological properties. As a result, only low viscosity photocurable resins have to be used.

## 4.2. SPATIAL RESOLUTION

### 4.2.1. Longitudinal resolution measurement

As in Ref. [11], longitudinal resolution has been evaluated by measuring the depth of a single layer polymerized beam, manufactured in the real operating conditions of the apparatus. As a remark, the cured depth has to be a little more important than the real thickness of the layers that form the object, in order to allow a partial overlapping of the layers so that they could be joined together.

The polymerized beam has been inserted in a simple object with a « U » shape (Fig. 5). Such an object can be manipulated without fear of breaking the polymerized beam.

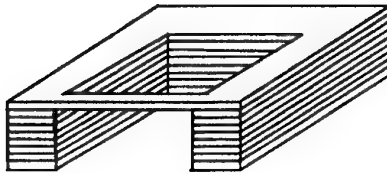


*Figure 4. Supported beam to measure the longitudinal resolution*

The experimental results are presented on Fig. 5. They give the evolution of the cured depth versus the irradiation time, showing clearly that the cured depth increases with irradiation time.

We have chosen to work with sufficiently large polymerized depths in order to manipulate the thread without breaking it. In fact, during the last step consisting in taking it away, there are strong strains on the beam due to the effect of capillarity-type forces between the surface of the liquid resin and the object. However, during the normal manufacturing of multilayer 3D objects, the thickness of each layer can decrease to 5 µm because the object is never removed from the resin during the process.

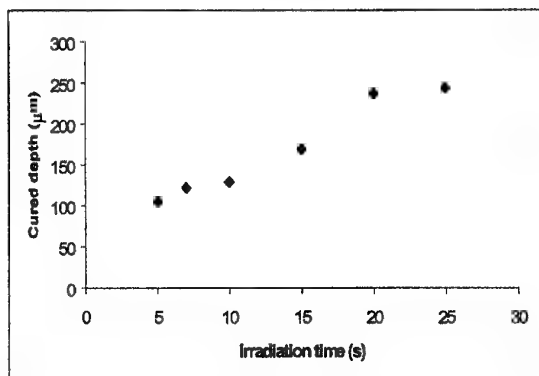


*Figure 5. Cured depth versus the irradiation time*

The experimental results seem to be correct even if the washing operations, using solvents, needed before the measurement of the beam depth can damage it or cause deformations. However, the damage that can be caused by washing operations is strongly reduced when manufacturing complex objects. This is due to the overlapping of the layers, which gives a better mechanical quality to the part.

#### 4.2.2. Transversal resolution measurements

In order to make transversal resolution measurements, we used an optical microscope that allows to obtain the size of pixels that are contained in the image. For instance, the minimal obtained size of pixels is  $2 \mu\text{m} \times 2 \mu\text{m}$ . Fig. 6 gives an image of a single layer object and a detail of this object, showing the transversal resolution and the reliability of the process.

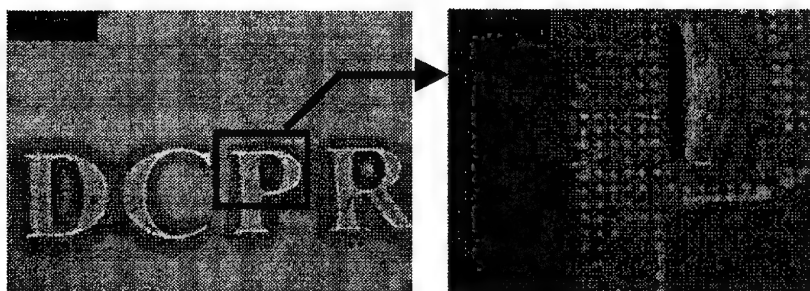


*Figure 6. Example of a single layer object manufactured by the new process ; images obtained by an optical microscope.*

### 5. Conclusion

We proposed a new apparatus using a mask-generator display and a broad-band visible light source. It seems to be a very interesting process allowing to manufacture small, complex in shape 3D micro-objects.

Nowadays, we are beginning to produce different small 3D objects made of a very large number of layers. The insertion of shape memory alloy wires in particular 3D polymer structures will allow the manufacture of new types of microactuators for microrobotic applications.

### References

1. Mandle, J., Lefort, O., and Migeon, A. : A new macromachined silicon high-accuracy pressure sensor, *Sensors and Actuators A* **46-47**, (1995), 129-132.
2. Müllenborn, Dirac, Petersen, and Bouwstra : Fast three-dimensional laser micromachining of silicon for microsystems, *Sensors and Actuators A* **52**, (1996), 121-125.
3. Moore, Daniel, and Walker : Nano and micro technology applications of focused ion beam processing, *Microelectronics Journal* **28**, (1997), 465-473.
4. Kussul, E., Rachkovskij, D., Baidyk, T., and Talayev, S. : Micromechanical engineering : a basis for the low-cost manufacturing of mechanical microdevices using microequipment, *J. Micromech. Microeng.* **6**, (1996), 410-425.
5. Lehr, H., Ehrfeld, W., Schmidt, M., Kallenbach, E., and Thuan, H. : Application of the LIGA technique for the development of microstructures based on electromagnetic principles, *J. Micromech. Microeng.* **2**, (1992), 229-233.
6. Despont, M., Lorenz, H., Fahrni, N., Brugger, J., Renaud, P., and Vettiger, P. : High-aspect ratio, ultrathick, negative-tone near-UV photoresist for MEMS applications, *IEEE* (1997), 518-522.
7. André, J.C., Corbel, S. (1994) *Stéréolithographic Laser*, Polytechnia Ed. Paris France.
8. Ikuta, K., Hirowatari, K., and Ogata, T. Three dimensional micro integrated fluid system fabricated by stereolithography, *Proc. IEEE MEMS'93, (Fort Lauderdale, FL, Feb)* 42-47.
9. Nakamoto, T., Yamaguchi, K., Abraha, P., and Mishima, K. : Manufacturing of three-dimensional micro-parts by UV laser induced polymerization, *J. Micromech. Microeng.* **6**, (1996), 240-253.
10. Bertsch, A., Zissi, S., Jézéquel, J.Y., Corbel, S., and André, J.C. : Microstereolithography using a liquid crystal display as dynamic mask-generator, *Microsystem Technologies* **3**, (1997), 42-47.
11. Bertsch, A., Jézéquel, J.Y., and André, J.C. : Study of the spatial resolution of a new 3D microfabrication process : the microstereophotolithography using a dynamic mask-generator technique, *Journal of Photochemistry and Photobiology A* **107** (1997), 275-281.
12. Bertsch, A., Zissi, S., Calin, M., Ballandras, S., Bourjault, A., Hauden, D., and André, J.C. : Conception and realization of miniaturized actuators fabricated by Microstereophotolithography and actuated by shape memory alloys, *Proc. 3rd France-Japan Congress on Mechatronics, Besançon, vol 2* (October 1996), 631-634.

## INTERFERENCE BLOTS IN INTEGRATED FRINGE PATTERNS

H.ABEN AND L.AINOLA

*Institute of Cybernetics,  
Tallinn Technical University, 21 Akadeemia tee,  
EE0026 Tallinn, Estonia*

**Abstract.** By experiments in integrated photoelasticity it has been observed that besides the usual interference fringes, interference blots may appear. The latter are areas where interference fringes have low contrast or even vanish totally. It has been shown that the cause of the interference blots is rotation of the principal stress axes. Since an arbitrary inhomogeneous birefringent medium is optically equivalent to a system of two birefringent plates, in this paper conditions of the appearance of the interference blots and of the dislocation of integrated fringes is studied using this simple model. Computer generated fringe patterns are compared with the experimentally recorded ones.

### 1. Introduction

In integrated photoelasticity, a 3-D transparent birefringent specimen is placed in an immersion bath and investigated in a transmission polariscope. Since in the general case both the values of the principal stresses and their directions vary on the light rays, the principle of superposition of birefringence is not valid. Actually, the specimen is an inhomogeneous twisted birefringent medium [1]. Therefore, optical phenomena are much more complicated than in 2-D photoelasticity and can be described by the theory of characteristic directions [1-5].

In the case of strong birefringence, integrated fringe patterns can be recorded. Sometimes these fringe patterns exhibit peculiar features. Figure 1a shows the integrated fringe pattern of a diametrically loaded sphere in a light-field circular polariscope. Near the points where the load is applied, one can observe dark areas that are similar to fringes but somewhat wider and that cross the basic system of fringes. These are the interference blots.

As another example, Fig. 1b shows the integrated fringe pattern of the wall-to-bottom region of a tempered drinking glass. One can observe inter-

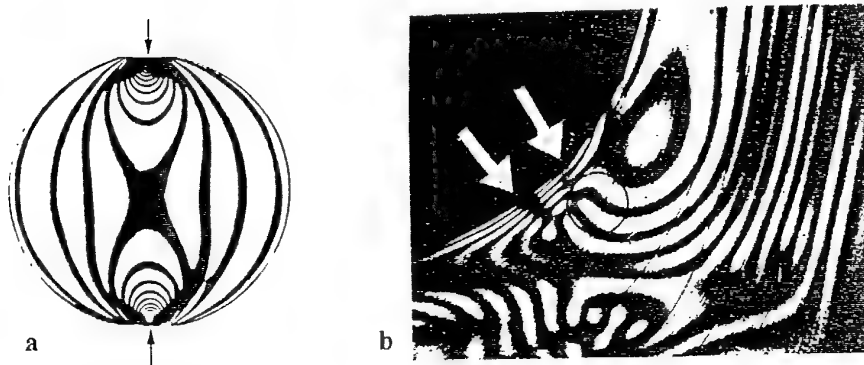


Figure 1. Integrated fringe patterns of a diametrically loaded sphere (a) and of the wall-to-bottom region of a tempered drinking glass (b) in a light-field circular polariscope.

ference blots (shown by arrows) that cross the main fringe system, dislocation of the fringes, etc.

Fringe patterns in Fig. 1 contradict to the conventional theory of fringes in birefringent objects. According to the latter, fringes of different order can never intersect one another, and between the adjacent dark fringes there is always a bright fringe.

Preliminary analysis of the integrated fringe patterns is presented in Refs. 6, 7 and 8. The aim of the present paper is to study in greater detail the reasons of the peculiarities in integrated fringe patterns. This problem is important not only in photoelasticity but also in interferometry and optical tomography of inhomogeneous birefringent phase objects.

According to the Poincaré equivalence theorem [9], an arbitrary inhomogeneous birefringent medium is optically equivalent to a system containing only two birefringent plates, the principal optical axes of which form an angle. Therefore, in this paper the analysis of the interference blots and of fringe dislocations in an inhomogeneous birefringent medium is mostly based on this simple model.

## 2. Theory of the Fringe Pattern Formation

It is known that the main reason of the complicated optical phenomena in integrated photoelasticity is rotation of the secondary principal stress directions. If the secondary principal stress directions are constant on the ray, integrated optical retardation  $\Delta$  is expressed through the integral Wertheim law

$$\Delta = C \int (\sigma_1 - \sigma_2) ds, \quad (2.1)$$

INTERFERENCE BLOTS IN INTEGRATED...

3

where  $C$  is photoelastic constant and  $\sigma_1, \sigma_2$  are secondary principal stresses.

Light intensity in a dark field circular polariscope is determined by

$$I_1 = I_0 \sin^2 \frac{\Delta}{2}, \quad (2.2)$$

and in a light field circular polariscope by

$$I_2 = I_0 \cos^2 \frac{\Delta}{2}. \quad (2.3)$$

If in the specimen distribution of stress is continuous, integrated fringe patterns determined by Eqs. (2.2) or (2.3) are also continuous, light intensity between fringes varies between 0 and  $I_0$ , and no peculiarities in the fringe pattern will occur.

In the case of rotation of the secondary principal directions, in formulas (2.2) and (2.3) instead of  $\Delta$  appears the characteristic optical retardation  $\Delta_*$ . The latter is not determined by Eq. (2.1) due to the effect of rotation of the axes, and is related to the stress distribution on the ray in a complicated manner [1,2]. That is the reason of the curious optical phenomena we observe in integrated fringe patterns.

Considering a system of two birefringent plates with optical retardations  $\Delta_1$  and  $\Delta_2$ , and  $\beta$  the angle between the principal axes of the plates, the characteristic retardation can be written as

$$\cos \Delta_* = \cos(\Delta_1 + \Delta_2) \cos^2 \beta + \cos(\Delta_2 - \Delta_1) \sin^2 \beta. \quad (2.4)$$

In rectangular coordinates  $x$  and  $y$  we have  $\Delta_1 = \Delta_1(x, y)$ ,  $\Delta_2 = \Delta_2(x, y)$ ,  $\beta = \beta(x, y)$ , and  $\Delta_* = \Delta_*(x, y)$ . Coordinates  $x$  and  $y$  are perpendicular to the direction of the wave normal.

If an inhomogeneous birefringent model is investigated in a dark-field circular polariscope, then the light intensity is determined by

$$I_1 = \frac{1}{2} I_0 (1 - \cos \Delta_*), \quad (2.5)$$

and in a light-field circular polariscope by

$$I_2 = \frac{1}{2} I_0 (1 + \cos \Delta_*). \quad (2.6)$$

Consequently, formation of the fringe pattern is completely determined through the function  $\cos \Delta_*$ . From Eq. (2.4) follows that the function  $\cos \Delta_*$  is a complicated function of periodic trigonometric functions of in general aperiodic functions  $\Delta_1, \Delta_2$  and  $\beta$ .

The distinct fringe structure occurs in regions where one or two of the functions  $\Delta_1, \Delta_2$  and  $\beta$  change more rapidly than others. Figure 2 shows

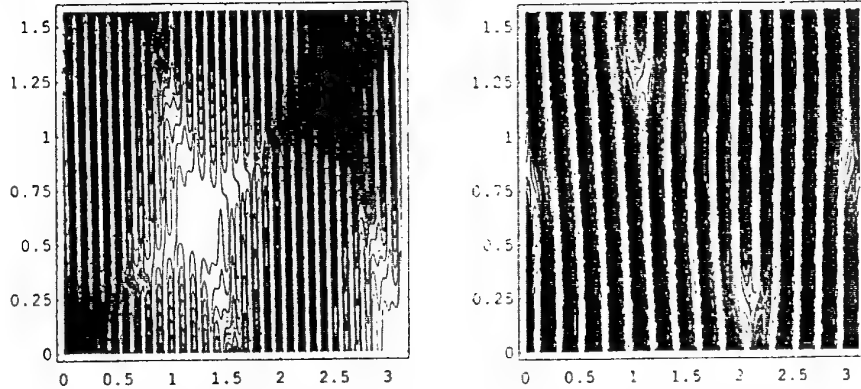


Figure 2. Computer-generated fringe patterns of an optical system containing two birefringent plates: left:  $\beta = 30x + y$ ,  $\Delta_1 = x - 2y$ ,  $\Delta_2 = 2x + y$ ; right:  $\beta = x + y$ ,  $\Delta_1 = x - 2y$ ,  $\Delta_2 = 30x + y$ .

computer-generated fringe patterns in a dark-field circular polariscope in the cases of different change rates of the functions  $\Delta_1$ ,  $\Delta_2$  and  $\beta$ . The distinct fringe patterns can be distorted by two types of irregularities: interference blots [6-8,10] and fringe dislocations [11-13].

### 3. Interference Blots

We define the interference blot as a region in the fringe pattern where the contrast of fringes is diminished or vanishes completely. This is a region where  $\cos \Delta_\star$  changes slowly.

Consider the neighborhood of the line  $\beta(x, y) = \pi/2$ :

$$\beta(x, y) = \pi/2 + \eta(x, y), \quad (3.1)$$

where  $|\eta(x, y)| \ll 1$ .

In this region we have

$$\begin{aligned} \cos \beta &= -\sin \eta \approx -\eta, \\ \sin \beta &= \cos \eta \approx 1 - \frac{\eta^2}{2}. \end{aligned} \quad (3.2)$$

Therefore, we can write Eq. (2.4) as

$$\cos \Delta_\star \approx \cos(\Delta_2 - \Delta_1) - 2\eta^2 \cos \Delta_1 \cos \Delta_2. \quad (3.3)$$

Let us write  $\Delta_2 - \Delta_1$  in the form

$$\Delta_2 - \Delta_1 = \pm 2n\pi + \mu(x, y), \quad (3.4)$$

where  $|\mu(x, y)| \ll 1$ .

Then Eq. (3.3) reveals

$$\cos \Delta_* \approx 1 - \frac{\mu^2}{2} - 2\eta^2 \cos^2 \Delta_1. \quad (3.5)$$

From Eqs. (2.12) and (3.5) we have

$$I_1 \approx I_0 \left( \frac{1}{4} \mu^2 + \eta^2 \cos^2 \Delta_1 \right). \quad (3.6)$$

In the same way we obtain

$$\begin{aligned} \Delta_2 - \Delta_1 &= (1 \pm 2n)\pi + \mu, \\ I_2 &\approx I_0 \left( 1 - \frac{1}{4} \mu^2 - \eta^2 \cos \Delta_1 \right). \end{aligned} \quad (3.7)$$

Consequently, in the neighborhood of the points  $(x, y)$  determined by equations

$$\beta(x, y) = \pi/2, \quad \Delta_2(x, y) = \Delta_1(x, y) \pm 2n\pi, \quad (3.8)$$

or

$$\beta(x, y) = \pi/2, \quad \Delta_2(x, y) = \Delta_1(x, y) + (1 \pm 2n)\pi, \quad (3.9)$$

dark or bright areas must appear. The same holds for the neighborhood of the points  $(x, y)$  determined by Eqs. (3.8) and (3.9) if  $\beta(x, y) = \pi/2 + n\pi$ .

Interference blots are seen in Fig. 2 on the left.

#### 4. Fringe Dislocations

Fringe dislocation is an imperfection of the fringe pattern where the normal pattern is distorted by the interposition of one or more extra fringes [11-13]. Using the analogy with crystal structure we can describe the fringe dislocation in terms of the Burgers circuit [11,14]. The Burgers circuit is any fringe-to-fringe path in the fringe pattern containing fringe dislocation which forms a closed loop (Fig. 3a). If the same fringe-to-fringe sequence is made in a dislocation-free pattern, the circuit does not close (Fig. 3b). The Burgers vector required to close the circuit describes the magnitude and direction of the slip in the fringe pattern. Notice that to the distance between fringes corresponds the phase shift  $2\pi$ . Therefore, to the Burgers vector corresponds the phase shift  $\pm n2\pi$ .

Let us show that fringe dislocations are induced by beat of fringes.

The right side of Eq. (2.4) can be considered as a composite fringe complex which is formed by two sets of fringes (waves) with different frequencies. If we assume that  $\Delta_1 \ll \Delta_2$  then the frequencies of the waves are close to each other. In that case the beat phenomena of fringes occurs.

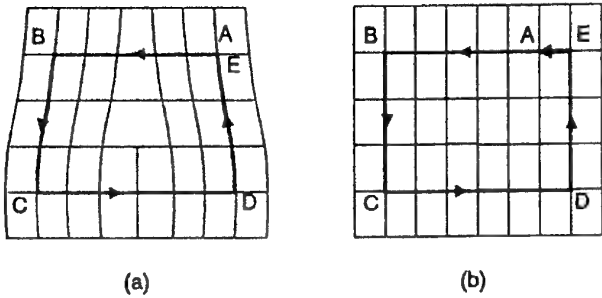


Figure 3. Burgers circuit ABCDE around a fringe dislocation (a); Burgers circuit in a perfect fringe pattern (b).

Equation (2.4) can be written as

$$\cos \Delta_* = A \sin(\Delta_2 + \varphi). \quad (4.1)$$

Here the amplitude and the phase of the composite wave are given by

$$A = \sqrt{\cos^2 2\beta \sin^2 \Delta_1 + \cos^2 \Delta_1}, \quad (4.2)$$

and

$$\tan \varphi = -\frac{\cos \Delta_1}{\cos 2\beta \sin \Delta_1}. \quad (4.3)$$

The amplitude  $A$  describes an envelope as a curved surface enclosing the surfaces of fringes (waves). The beat phenomena originate from the low frequency of this envelope.

If in Eq. (4.3)  $\cos^2 \beta = \cos \Delta_1 = 0$ , we have

$$\tan \varphi = \frac{0}{0}, \quad (4.4)$$

i.e. the phase  $\varphi$  is indeterminate and dislocation of fringes occurs (Fig. 2, right).

### 5. Boussinesq Problem

Let us consider now optical phenomena in the case of a classical problem of the elasticity theory, the Boussinesq problem, when a vertical concentrated load acts on the surface of a half-space. Integrated fringe patterns in an epoxy cube of  $40 \times 40 \times 40$  mm in a light-field circular polariscope for

## INTERFERENCE BLOTS IN INTEGRATED...

7

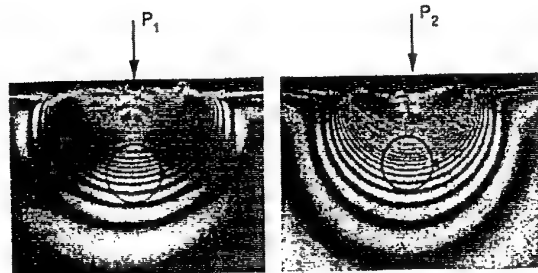


Figure 4. Experimental integrated fringe patterns in a light-field circular polariscope in the case of the Boussinesq problem,  $P_2 > P_1$ .

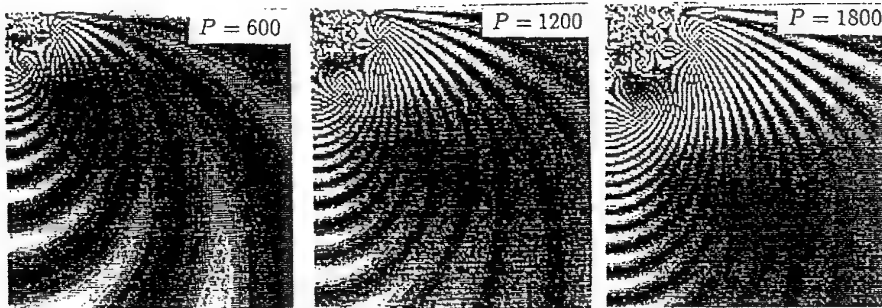


Figure 5. Computer-generated fringe patterns for the Boussinesq problem in a light-field circular polariscope for various loads  $P$  (in relative units).

different loads are shown in Fig. 4. In the case of  $P_1$ , interference blots are clearly visible. In the case of  $P_2$ , interference blots have vanished because of high birefringence. Note that, owing to difficulties in effectuating experimentally a point load, the stress distribution in Fig. 4 deviates to a certain extent from the theoretical one.

To establish the dependence of the interference blots on the load (or value of the birefringence), integrated fringe patterns for the Boussinesq problem were generated on the computer for different load values (Fig. 5).

In Fig. 5 we see both interference blots and fringe dislocations, similar to those generated above for the optical system containing two birefringent plates. In the fringe pattern for  $P = 1800$ , the Burgers vector is  $4\pi$ .

## 6. Conclusions

If has been shown both experimentally and numerically that in integrated fringe patterns interference blots and dislocation of fringes may appear. Due to that the fringe order may be ambiguous.

## 7. Acknowledgements

The authors are thankful to Walter Schumann for his valuable comments and suggestions. Support of the Estonian Science Foundation by grant 2248 is gratefully acknowledged.

## References

1. Aben, H.: Characteristic directions in optics of twisted birefringent media, *J. Opt. Soc. Am. A* **3** (1986), 1414-1421.
2. Aben, H.: *Integrated Photoelasticity*, McGraw-Hill, New York *et al.*, 1979.
3. Aben, H.K., Josepson, J.I., and Kell, K-J.E.: The case of weak birefringence in integrated photoelasticity, *Optics and Lasers in Eng.* **11** (1989), 145-157.
4. Aben, H., Jdnurim, S., and Puro, A.: Integrated photoelasticity in case of weak birefringence, In: *Proc. of the Ninth Internat. Confer. Exp. Mech.*, Copenhagen. Aahy Tryk, Copenhagen, 1990, **2**, pp. 867-875.
5. Aben, H., and Guillemet, C.: *Photoelasticity of Glass*, Springer-Verlag, Berlin *et al.*, 1993.
6. Josepson, J.: Curious optical phenomena in integrated photoelasticity, In: J.F. Silva Gomes, *et al.* (eds.), *Recent advances in Experimental Mechanics*, A.A. Balkema, Rotterdam, 1994, **1**, pp. 91-94.
7. Aben, H., and Josepson, J.: Nonlinear optical phenomena in integrated photoelasticity, In: *Proc. Internat. Symp. on Advanced Technology in Exp. Mech.*, The Japanese Society of Mechanical Engineers, Tokyo, 1995, pp. 49-54.
8. Aben, H., and Josepson, J.: Strange interference blots in the interferometry of inhomogeneous birefringent objects, *Appl. Optics* **36** (1997), 7172-7179.
9. Poincaré, H.: *Théorie mathématique de la lumière II*. Paris, 1892.
10. Aben, H., Anton, J., and Josepson, J.: Ambiguity of the fringe order in integrated photoelasticity. In W. Jüptner, W. Osten (eds.), *Proc. 3rd Internat. Workshop on Automatic Processing of Fringe Patterns*, Bremen. Akademie Verlag, Berlin, 1997, pp. 309-317.
11. Nye, J.F., and Berry, M.V.: Dislocations in wave trains, *Proc. Royal Soc. London A* **336** (1974), 165-190.
12. Coullet, P., Gil, L., and Rocca, F.: Optical vortices, *Optics Comm.* **73** (1989), 403-408.
13. Il'yenkov, A.V., Khiznyak, A.I., Kreminskaya, L.V., Soskin, M.S., and Vasnetsov, M.V.: Birth and evolution of wave-front dislocations in a laser beam passed through a photoreactive LiNbO<sub>3</sub>: Fe crystal, *Appl. Phys. B* **62** (1996), 465-471.
14. Hull, D., and Bacon, D.J.: *Introduction to Dislocations*, Butterworth-Heinemann, Oxford, 1984.

## VISUALISATION OF PHOTOELASTIC FRINGES WITHIN THREE DIMENSIONNAL SPECIMENS USING AN OPTICAL SLICING METHOD

N. Plouzennec, J-C. Dupré and A. Lagarde

Université de Poitiers, Laboratoire de Mécanique des Solides, UMR 6610  
Bd 3 - Téléport 2 - BP179  
86960 FUTUROSCOPE CEDEX - FRANCE

### Abstract

We show a non destructive method to obtain the isochromatic and isoclinic fringes in three dimensional photoelastic specimens. The basic idea is to delimit a slice between two plane laser beams. The properties of polarization of the scattered light (Rayleigh law) and the interference possibilities of the diffused beams are used. By introducing speckle pattern properties, the correlation factor of the two scattered beams is similar to the illumination given in a plane polariscope for the investigation of a slice (in a classical frozen-stress technique). We use a monochromatic laser beam, a CCD camera and a PC. As we can not obtain directly the correlation factor, we do a statistical analysis of the speckle patterns. The variance (function of the correlation factor) is computed from the light intensities of three images corresponding to the speckle pattern for plane 1 alone, plane 2 alone, and both planes together.

### 1. Introduction

The experimental study of stresses in three dimensional models under solicitation still remains a problem. The method usually employed is the frozen stress technique coupled with a mechanical slicing and a two dimensional analysis of each slice in a classical polariscope. But the mechanical slicing of models in different planes takes a lot of time and imposes to manufacture several models for a general study.

To avoid these difficulties, we have developed a non destructive method of optical slicing using the properties of polarization of the light scattered by a photoelastic material (Rayleigh law). This phenomenon was used by R. Weller [1] and by many authors for punctual methods [2]-[6]. Our method is based upon a whole field technique developed in our laboratory several years ago [7]-[9]. But this technique using holographic film, polychromatic laser beam, spectroscope and optical filtering was very complex which greatly limits its domains of application. So we have developed a method much simpler and faster using numerical recording and analysis.

## 2. Principle

### 2.1 INTRODUCTION

The basic idea is to use the properties of polarisation of the scattered light (Rayleigh law). If one observe along the  $\vec{Z}$  vector, perpendicular to the direction of the propagated light beam  $\vec{X}$ , the scattered light is polarised rectilinear along  $\vec{Z} \wedge \vec{X}$  (fig. 1).

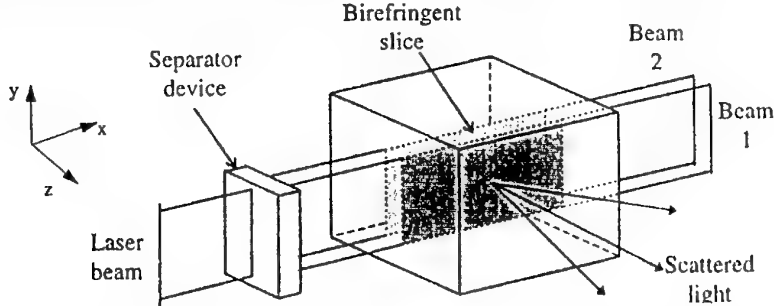


Figure 1. Isolation of a slice with two plane laser beams

The principle of the method is to isolate a slice of the photoelastic model between two parallel plane laser beams (fig. 1). The speckle field observed in the direction perpendicular to the plane of the two illuminated sections is due to the interferences between the light scattered by each section. Their possibilities of interferences depend on the birefringence of the isolated slice. But experimentally, the direct visualisation of the photoelastic fringes is impossible. To obtain this information, the characteristics of the scattered light are studied.

### 2.2 EXPRESSION OF THE SCATTERED LIGHT

The photoelastic model is lighted by only one beam (1 or 2), then by both. The scattered light intensities are respectively named  $I_1$ ,  $I_2$  and  $I$ . These images are recorded thanks to a CCD camera. The values in grey level of the intensities along one line of these images is plotted on fig. 2.

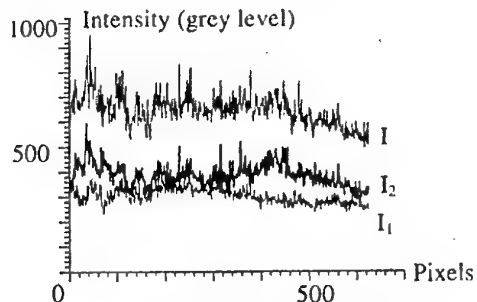


Figure 2. Light intensities profile

### PHOTOELASTIC FRINGES USING OPTICAL SLICING METHOD 3

By studying one intensity profile (for example  $I_1$ ), we observe that the speckle field is coupled with a background intensity due to the fluorescence phenomenon of the specimen and a part of the scattered light not polarized [10].

The light intensity  $I_i$  ( $i=1$  or  $2$ ) is expressed as :

$$I_i = I_{iB} + I_{is} \quad (1)$$

where  $I_{iB}$  is the background intensity,  $I_{is}$  is the speckle field intensity.

### 2.3 SUPERPOSITION OF THE TWO LIGHT FIELDS

The result of the superposition of the two light fields depend on their interference possibilities. If they can interfere in a coherent way, they superpose in amplitude. Otherwise, they superpose in intensity [11]. We studied the superposition of  $I_1$  and  $I_2$  using their interference possibilities and their statistical properties [12].

The light field  $I_{1S}$  and  $I_{2S}$  are due to coherent light. So they superpose in amplitude. The result is :

$$I_S = I_{1S} + I_{2S} + 2\sqrt{I_{1S}}\sqrt{I_{2S}} \cos(\psi_1 - \psi_2 + \eta) \quad (2)$$

where  $\gamma$  is the correlation factor of the two speckle fields,  $\psi_1$ ,  $\psi_2$  their random phases,  $\eta$  is function of the optical characteristics of the slice.

As the slice is represented by a birefringent plate and a rotatory power, the expression of the correlation factor  $\gamma$  is given by :

$$\gamma^2 = \cos^2 R - \sin 2\alpha \sin 2(\alpha + R) \sin^2 \frac{\varphi}{2} \quad (3)$$

where  $R$  is the rotatory power of the slice,  $\alpha$  the neutral lines,  $\varphi$  the angular birefringence.

This expression is similar to the one usually obtained when analysing an identical slice (done for example by frozen-stress technique and mechanical slicing) between two parallel polarisers. Thus thanks to the correlation factor, the isochromatic and isoclinic fringes of the isolated slice can be visualised.

In the case of thick slices and for a small rotation of the principal secondary stresses (less than  $30^\circ$ ), a low modulation of  $\gamma$  corresponds to a isoclinic line where a principal secondary direction is parallel to the polarisation direction and the isochromatic fringes appear with integer order for maximal values and half order for minimal values [11].

If the rotatory power is negligible (thin slice), equation 3 becomes :

$$\gamma^2 = 1 - \sin^2 2\alpha \sin^2 \frac{\varphi}{2} \quad (4)$$

The spatial average of  $I_S$  is calculated thanks to speckle properties [12] of the random variables  $I_{1S}$ ,  $I_{2S}$ ,  $\psi_1$  et  $\psi_2$  (ergodicity, stationary, independence of variables...).

$$\langle I_S \rangle = \langle I_{1S} \rangle + \langle I_{2S} \rangle \quad (5)$$

Using the same hypothesis, we calculate the variance of  $I_S$ .

$$\sigma_S^2 = \sigma_{1S}^2 + \sigma_{2S}^2 + 2\gamma^2 \langle I_{1S} \rangle \langle I_{2S} \rangle \quad (6)$$

The light field  $I_{1B}$  et  $I_{2B}$  are due to incoherent light. So they superpose in intensity. The result is :

$$I_B = I_{1B} + I_{2B} \quad (7)$$

We calculate the spatial average and the variance, and obtain :

$$\langle I_B \rangle = \langle I_{1B} \rangle + \langle I_{2B} \rangle \quad \text{and} \quad \sigma_B^2 = \sigma_{1B}^2 + \sigma_{2B}^2 \quad (8)$$

Also,  $I_B$  and  $I_S$  (or  $I_{1B}$  and  $I_{1S}$ ) (or  $I_{2B}$  and  $I_{2S}$ ) can not interfere, so we obtain :

$$I = I_B + I_S \quad \text{and} \quad \langle I \rangle = \langle I_B \rangle + \langle I_S \rangle \quad \text{and} \quad \sigma^2 = \sigma_B^2 + \sigma_S^2 \quad (9)$$

## 2.4 PROPERTIES OF THE RESULTING FIELD

Using the results obtained below, the expression of the global light intensity is :

$$I = I_1 + I_2 + 2 \gamma \sqrt{I_{1S}} \sqrt{I_{2S}} \cos(\psi_1 - \psi_2 + \eta) \quad (10)$$

Its spatial average is :  $\langle I \rangle = \langle I_1 \rangle + \langle I_2 \rangle \quad (11)$

and its variance :  $\sigma^2 = \sigma_1^2 + \sigma_2^2 + 2 \gamma^2 \langle I_{1S} \rangle \langle I_{2S} \rangle \quad (12)$

If we consider that the intensities of the two incident beams are equal and the average of scattered light are equivalent, we take:

$$\frac{\langle I_{1S} \rangle}{\langle I_1 \rangle} = \frac{\langle I_{2S} \rangle}{\langle I_2 \rangle} = k \quad (13)$$

$k$  is a factor, function to the scattered properties of the material. Experimentally we have to note that it is approximately equal to 1/10.

Equation 12 becomes :  $\sigma^2 = \sigma_1^2 + \sigma_2^2 + 2 k^2 \gamma^2 \langle I_1 \rangle \langle I_2 \rangle \quad (14)$

From this equation, we deduce equation 15, proportional to the correlation factor :

$$k^2 \gamma^2 = \frac{\sigma^2 - \sigma_1^2 - \sigma_2^2}{2 \langle I_1 \rangle \langle I_2 \rangle} \quad (15)$$

## 3. Experimental set-up

The experimental set-up (fig. 3) is composed by an argon laser, a separator device and a cylindrical lens in order to obtain two plane laser beams. A CCD camera (perpendicular to the laser beams) and a PC are used for the data acquisition and processing. A Babinet compensator is placed between the lens and the cylindrical lens to minimise the intensities of the Weller's fringes (the scattering phenomenon is used like analyser). These fringes have no influence on the results if their maximal intensities are less than 10 % of the global intensity (phenomenon studied by numerical simulations [13]).

A specific care must be taken to choose the CCD captor. Indeed the speckle field intensity is very low compared to the background intensity (Fig. 1). So a CCD camera with a low signal-noise ratio is chosen. Some tests are made with a classical camera with  $512 \times 512$  pixels coded by 256 grey levels. In taking care to have low electronic amplification which gives a ratio of 40 dB, we obtained good results. But the small sensitivity and resolution could limit the tests for all specimens. The CCD camera used for the presented tests, has a high resolution ( $1000 \times 1000$  pixels coded by 1024 grey levels) and a ratio of 50 dB.

## PHOTOELASTIC FRINGES USING OPTICAL SLICING METHOD

5

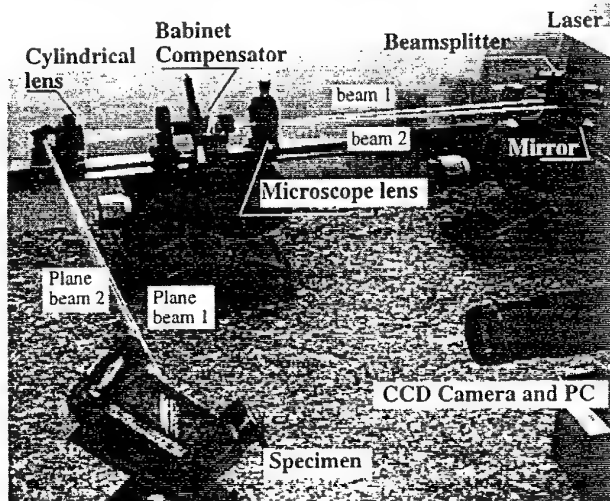


Figure 3. Experimental set-up

## 4. Obtention of the photoelastic fringes

The model is placed on the way of the laser beams which are oriented to isolate the slice to study. If the model is not in optical index liquid tank, the beams have to be perpendicular to the surface of the model to avoid refractions.

Three images  $I_1$ ,  $I_2$  and  $I$  corresponding to the speckle pattern for plane 1 alone, plane 2 alone, and both planes together are recorded thanks to the CCD camera and used to calculate a fourth image of  $k^2\gamma^2$  using equation 15.

To diminish the calculation time, it is also possible to calculate first :

$$I' = I - I_1 - I_2 \quad (16)$$

Then we calculate the variance of  $I'$  :  $\sigma'^2$ . And the expression of  $k^2\gamma^2$  becomes :

$$k^2\gamma^2 = \frac{\sigma'^2}{2 \langle I_1 \rangle \langle I_2 \rangle} \quad (17)$$

For each pixel  $(i,j)$ , the different coefficients appearing in equation 17 are calculated with a calculation area of  $(2N+1) \times (2N+1)$  pixels centred on  $(i,j)$ .

For  $i$  and  $j$  varying, the spatial average of  $I'$  is calculated thanks to equation 18.

$$\langle I'(i, j) \rangle = \left( \sum_{k=-N}^{k=+N} \sum_{l=-N}^{l=+N} I'(i+k, j+l) \right) / (2N+1)^2 \quad (18)$$

When the spatial average is calculated, we can obtain the variance :

$$\begin{aligned} \sigma'^2(i, j) &= \langle [I'(i, j) - \langle I'(i, j) \rangle]^2 \rangle \\ &= \left( \sum_{k=-N}^{k=+N} \sum_{l=-N}^{l=+N} [I'(i+k, j+l) - \langle I'(i+k, j+l) \rangle]^2 \right) / (2N+1)^2 \end{aligned} \quad (19)$$

Equation 18 is also used to calculate  $\langle I_1 \rangle$  and  $\langle I_2 \rangle$ , by replacing  $I'$  by  $I_1$  and  $I_2$ . Then, we use equation 17 to calculate  $k^2\gamma^2$  for each pixel  $(i,j)$ . Thus, we obtain the image of the isoclinic and isochromatic fringes. To eliminate a part of the speckle on the final image, a low-pass filter can be used.

The resolution of this image is function of the speckle depth and the size of the calculation area for the spatial average. Thanks to multiple simulations [13], we can show that with a speckle size of 1 pixel and an area of 3 by 3 pixels, the minimal visible period is about 15 pixels. This limitation becomes 30 pixels using a low pass filter (10 by 10 pixels).

## 5. Experimental results

The models used for the experimental tests are made in epoxy resin (photoelastic constant :  $30 \cdot 10^{-12} \text{ m}^2/\text{N}$ ).

The first experimental test is a torsion strain on a bar of square section ( $34 \times 34 \text{ mm}^2$ ). The images experimentally obtained correspond to slices inclined at an angle of  $\pi/4$  respect to the axis of the model (fig. 4). Thus the birefringence and the directions of the principal stresses vary along the observation direction.

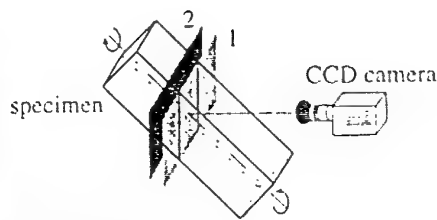
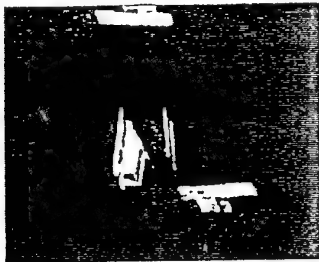


Figure 4.: Torsion strain on a bar of square section

Figure 5 shows the three recorded images  $I_1$ ,  $I_2$  and  $I$ , for a thickness of the slice equal to 6 mm. On figure 5-c, we slightly distinguish the Weller fringes. Their intensity is lower than 10% of the global intensity.

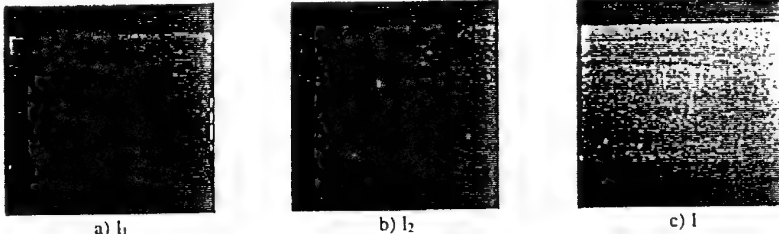


Figure 5.: Experimental speckle patterns

Using these images,  $k^2\gamma^2$  is calculated for an area of  $3 \times 3$  without low pass filter (fig. 6-a) and with low pass filter (fig 6-b). We observe two bright and large isoclinic zones and the isochromatic fringes. The fractional fringe order could be find with a manual procedure, but a full field automatic calculation seems to be still hard to develop.

## PHOTOELASTIC FRINGES USING OPTICAL SLICING METHOD

7

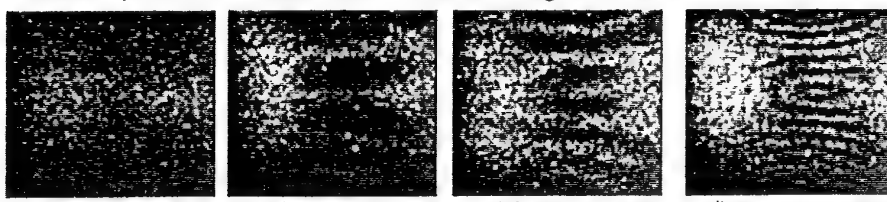


a) without low pass filter

b) with low pass filter

Figure 6.: Fringe pattern

Our experimental set up allows to record the images for thickness varying from 0,5 mm to 10 mm. A small thickness is interesting to study zones with high stress concentration. For the same loading, the slice thickness varies from the smaller to the higher value. Each time, the three images  $I_1$ ,  $I_2$  and  $I$  are recorded and the correlation factor calculated. These images are represented on figure 7. The number of isochromatic fringes increases with the thickness of the slice and the isoclinic fringe is constant except when the slice is thick (fig. 7-d). In this case, the isoclinic fringe disappears in the centre of the image where there is a large rotation of the stresses (we are not in the hypothesis of thin slice). So, we see continuous isochromatic fringes in the centre.



a) 0,5 mm

b) 2mm

c) 4mm

d) 10 mm

Figure 7. Experimental isochromatic and isoclinic fringes for several thickness of slice

The second test is a punctual loading on the top of a prismatic specimen (section =  $60 \times 45 \text{ mm}^2$  and length = 110 mm) (fig. 8). A quick scanning of the model has been realised with 2 mm of translation between each slice. In order to see a large number of fringes, we have chosen a test with slice thickness equal to 6 mm. It is possible to find the stress concentration area and to study a part of it (by zooming in and by a reduction of the thickness of the slice.)

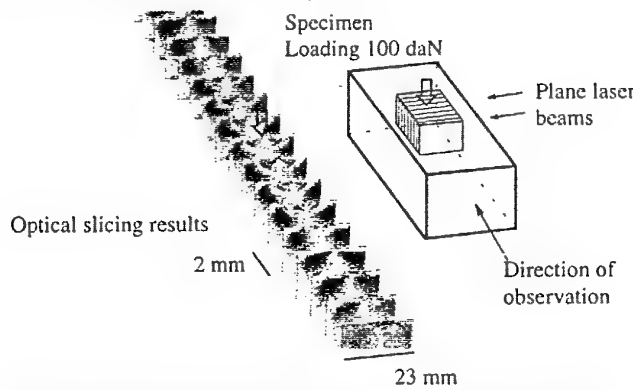


Figure 8. Scanning of a prismatic specimen submitted to a punctual loading

## 6. Conclusions

We present a new method using optical slicing coupled with a CCD camera and a PC to visualise rapidly isochromatics and isoclinic fringes of a slice, within a photoelastic material. The slice is delimited by two laser beams and the scattered light is numerically analysed to obtain the correlation factor. The experimental set up is easy to realise and once the images are recorded, the calculation are done in few seconds. Our slicing method takes into account the parameters inside the isolate slice but not the optical path through the specimen. The minimal slice thickness (because of the device) is about 0.5 mm and the maximal value is about 10 mm. In three dimensional photoelasticity, the rotation of the secondary principal stresses in the thickness of the studied slice can not be neglected. So the slice is represented by a photoelastic plate and a rotatory power. If the thickness is sufficiently small, the rotatory power has no effect on the isoclinic and isochromatic parameters. The largest studied field is about 150×150 mm<sup>2</sup> (0.15 mm/pixel) and the smallest 5×5 mm<sup>2</sup> which permits the study of contact zone. The model immersed in optical index liquid tank can be examined in different views. For a small size of image (128×128 pixels) a quasi-real time visualisation can been realised. A fast study of a specimen can be done in order to visualize the stresses concentration and the direction of the secondary principal stresses. So the first application, for an industrialist, could be the optimisation of the shape of models.

## 7. References

- 1 Weller, R., (1941) Three dimensional photoelasticity using scattered light, *Journal of Applied Physics*, 12, 610-616.
- 2 Robert, A. et Guillemet, E., (1963) Nouvelle méthode d'utilisation de la lumière diffusée en photoélasticité à trois dimensions, *Revue Française de Mécanique*, 147-157.
- 3 Robert, A. et Royer, J., (1980) Photoélasticité tridimensionnelle à lumière diffusée, *Journal de Mécanique Appliquée*, 4, 445-460.
- 4 Cheng, Y.F. (1967) A dual observation method for determining photoelastic parameters in scattered light, *Experimental Mechanics*, 7, 140-144.
- 5 Brillaud, J. et Lagarde, A., (1982) Méthode ponctuelle de photoélasticité tridimensionnelle. Application, *Revue Française de Mécanique*, 41-49.
- 6 Srinath, L.S., (1983) Scattered light Photoelasticity, Tata McGraw-Hill.
- 7 Desailly, R., Brillaud, J. et Lagarde, A., (1974) Enregistrement holographique de caractéristiques associées aux formes de lumière du rayonnement diffusé par les milieux transparents birefringents, *C.R.A.Sci.*, T. 279, Série B, 391-393.
- 8 Desailly, R. et Lagarde, A., (1977) Application des propriétés des champs de granularité à la photoélasticité tridimensionnelle, *C.R.A.Sci.*, T. 284, Série B, 13-46.
- 9 Desailly, R. et Lagarde, A., (1980) Sur une méthode de photoélasticité tridimensionnelle non destructive à champ complet, *Journal de Mécanique Appliquée*, 4, 3-30.
- 10 Brillaud, J. et Lagarde, A., (1975) Mesure des formes de lumière en diffusion et applications, *C.R.A.Sci.*, T. 281, Série B, 329-332.
- 11 Desailly, R. et Lagarde, A., (1984) Méthode de découpage optique de photoélasticité tridimensionnelle-Application, *Revue Française de Mécanique*, 47-55.
- 12 Dainty, J.C., (1975) Laser Speckle and related phenomena, *Topics in Applied Physics*, 9, Springer Verlag.
- 13 Dupré, J-C., Plouzennec, N. et Lagarde, A., (1996) Nouvelle méthode de découpage optique à champ complet en photoélasticité tridimensionnelle utilisant des moyens numériques d'acquisition et d'analyse des champs de granularité en lumière diffusée, *C.R.A.Sci.*, T 323, Série II b, 239-245.

**OPTICAL APPROACHES OF A PHOTOELASTIC MEDIUM FOR  
THEORETICAL AND EXPERIMENTAL STUDY OF THE STRESSES IN A  
THREE-DIMENSIONAL SPECIMEN**

A. ZENINA

*LMS, Université de Poitiers, CNRS UMR 6610*

*SP2MI - Téléport 2 - BP 179, 86960 FUTUROSCOPE CEDEX, FRANCE*

J.C. DUPRE

*LMS, Université de Poitiers, CNRS UMR 6610*

*SP2MI - Téléport 2 - BP 179, 86960 FUTUROSCOPE CEDEX, FRANCE*

A. LAGARDE

*LMS, Université de Poitiers, CNRS UMR 6610*

*SP2MI - Téléport 2 - BP 179, 86960 FUTUROSCOPE CEDEX, FRANCE*

**Abstract**

The aim of this study is to develop a procedure consisting in comparing real photoelastic fringes with the fringe pattern calculated with a theoretical or numerical stress field. This process can be used to validate for example the boundary conditions or mesh of a three-dimensional mechanical problem. We show three optical approaches of a three-dimensional specimen giving the classical photoelastic fringes (isochromatic and isoclinic patterns) from a theoretical stress distribution. So we used a new experimental technique for the study of stress fields in a three-dimensional medium. We show a comparison between these three formulations and experimental results obtained by our non-destructive method of optical slicing.

**1 Introduction**

The study of the stress state of a three-dimensional specimen may be effected by numerical means (like finite elements method). But for industrial problems, an experimental study is necessary to validate the theoretical and numerical approach as a boundary conditions, shape and mesh. Usually this is done by photoelasticimetry.

Let us remind that into a plane polariscope, a two-dimensional analysis of a beam, which can be mechanically sliced after stresses freezing, allows us to visualize two fringes patterns. The direction of principal stresses is obtained from isoclinic fringes, their difference is given by isochromatic fringes. We used in this paper an another experimental solution, developed in our laboratory. This technique is a non-destructive method of optical slicing giving the classical photoelastic fringes [Plouzennec, N., et al. 1998] [Dupré, J.C., et al. 1997] [Dupré, J.C., et al. 1996].

Many studies have been achieved to separate the stresses, their orientations and to integrate the equilibrium equations [Dally, J.W., et al. 1991] in order to compare them with the simulated results. However this method demands a high precision of measurement, a separation and an unwrapping of the isoclinic and isochromatic parameters. Then we present another solution avoiding most of these inconveniences. It consists in calculating the isoclinic and isochromatic fringes from a three-dimensional stress field obtained theoretically; for example by finite elements and in comparing them with experimental results. Nevertheless we have to correctly determine the optical parameters due to the stress fields. The aim of this work is to study three approaches of a thick medium and to compare them with experimental results.

## 2 Optical approaches of a three dimensional medium

We calculate the photoelastic fringes coming from a plane polariscope by three ways.

### 2.1 TWO-DIMENSIONAL APPROACH

In this case, the difference and direction of the stresses are constant along the thickness of the specimen.

The light intensity obtained in a plane polariscope is expressed by :

$$I = I_0 \left[ 1 - \sin^2 2\alpha \sin^2 \frac{\varphi}{2} \right] \quad (1)$$

$I_0$  is the light intensity when the model is unloaded,  $\alpha$  is the direction of one of the principal stresses. The birefringence  $\varphi$  is given by :

$$\varphi = \frac{2\pi C}{\lambda} (\sigma_1 - \sigma_2) e \quad (2)$$

$e$  represents the slice thickness shown in figure 1,  $(\sigma_1 - \sigma_2)$  is the difference of the principal stresses,  $C$  is the photoelastic constant and  $\lambda$  is the wavelength of the used light.

### 2.2 ABEN SCHEMATISATION

The Aben's works (1966) allow us to obtain the mechanical parameters  $\varphi$ ,  $\alpha$  from the knowledge of three physical parameters  $R$ ,  $\alpha^*$ ,  $\varphi^*$  with the hypothesis :  $(d\alpha/dz = \alpha_0)$  and  $(\sigma' - \sigma'')$ , the secondary principal stress difference, constant along the thickness of the specimen. The studied beam is schematized by a birefringent plate ( $\alpha^*$  and  $\varphi^*$ ) followed or preceded by a rotator power  $R$  (figure 2). The values  $R$ ,  $\alpha^*$ ,  $\varphi^*$  and  $\alpha$ ,  $\alpha_0$ ,  $\varphi$  are linked by the following relations [Brillaud, J., et al. 1983] [Desailly, R., et al. 1984] :

### OPTICAL APPROACHES OF A PHOTOELASTIC MEDIUM 3

or preceded by a rotator power  $R$  (figure 2). The values  $R$ ,  $\alpha^*$ ,  $\varphi^*$  and  $\alpha$ ,  $\alpha_0$ ,  $\varphi$  are linked by the following relations [Brillaud, J., et al. 1983] [Desailly, R., et al. 1984] :

$$\begin{aligned} \operatorname{tg} R &= \frac{\operatorname{tg} \alpha_0 - \frac{\alpha_0}{X} \operatorname{tg} X}{1 + \frac{\alpha_0}{X} \operatorname{tg} \alpha_0 \operatorname{tg} X}, & \cos \varphi^* &= 1 - \frac{\varphi^2}{2X^2} \sin^2 X \\ X &= \frac{\sqrt{\varphi^2 + 4\alpha_0^2}}{2}, & \alpha^* &= \alpha - \frac{R}{2} + \frac{\alpha_0}{2} \end{aligned} \quad (3)$$

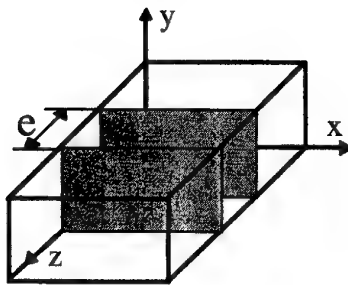


Figure 1 : The first approach

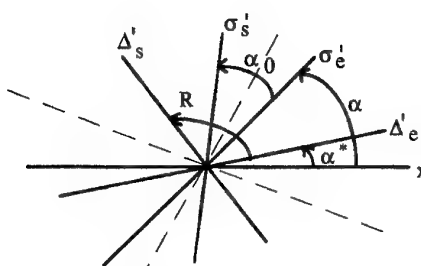


Figure 2 : Aben schematization

On figure 2, we show the optical parameters :  $(\Delta'_e, \Delta'_s)$  the characteristic directions of entrance and exit, and the mechanical parameters  $(\sigma'_e, \sigma'_s)$  the principal secondary directions. The light intensity coming from the plane polariscope [Desailly, R., et al. 1984] is then :

$$I = I_0 [\cos^2 R - \sin 2\alpha^* \sin 2(\alpha^* + R) \sin^2 \varphi^*/2] \quad (4)$$

#### 2.3 DISCRETE ANALYSIS INTO THIN SLICES

This technique consists in taking a thick beam and dividing it into  $n$  thin slices shown in figure 3. Every thin slice is characterized by  $\alpha_i$  and  $\varphi_i$  constant along the thickness (like the first approach) [Zenina, A., et al. 1997] [Aben, H., et al. 1997].

An iterative process has been developed for the numerical calculation of the light components after crossing the first slice from a direction of given polarization  $(x_0, y_0)$ . From these new components  $(x_i, y_i)$  the calculation is repeated again for the following beams until the last slice.

$$\begin{array}{c}
 \left( \begin{matrix} X_0 \\ Y_0 \end{matrix} \right)_{(x_0, y_0)} \xrightarrow{R\alpha_1} \left( \begin{matrix} X_0 \\ Y_0 \end{matrix} \right)_{(x_1, y_1)} \xrightarrow{S\varphi_1} \left( \begin{matrix} X_1 \\ Y_1 \end{matrix} \right)_{(x_1, y_1)} \xrightarrow{R\alpha_2} \dots \quad (5) \\
 \dots \xrightarrow{S\varphi_{n-1}} \left( \begin{matrix} X_{n-1} \\ Y_{n-1} \end{matrix} \right)_{(x_{n-1}, y_{n-1})} \xrightarrow{R\alpha_n} \left( \begin{matrix} X_{n-1} \\ Y_{n-1} \end{matrix} \right)_{(x_n, y_n)} \xrightarrow{S\varphi_n} \left( \begin{matrix} X_n \\ Y_n \end{matrix} \right)_{(x_n, y_n)}
 \end{array}$$

with :

$$R_{\alpha i} = \begin{bmatrix} \cos \alpha i & \sin \alpha i \\ -\sin \alpha i & \cos \alpha i \end{bmatrix} \quad S_{\varphi i} = \begin{bmatrix} 1 & 0 \\ 0 & (\cos \varphi i - j \sin \varphi i) \end{bmatrix} \quad (\text{for } i = 1, n)$$

The components of the light after the last slice are  $(x_n, y_n)$ . After crossing the analyzer (angle  $\beta$  figure 3), the light intensity is written as :

$$I = I_0 \left[ (Re(x_n) \cos \beta + Re(y_n) \sin \beta)^2 + (Im(x_n) \cos \beta + Im(y_n) \sin \beta)^2 \right] \quad (6)$$

$Re$  and  $Im$  are the real and the imaginary part.

Numerical simulations have shown that the ratio between  $\alpha_0$  and the number of the unitary beam is 1/3.

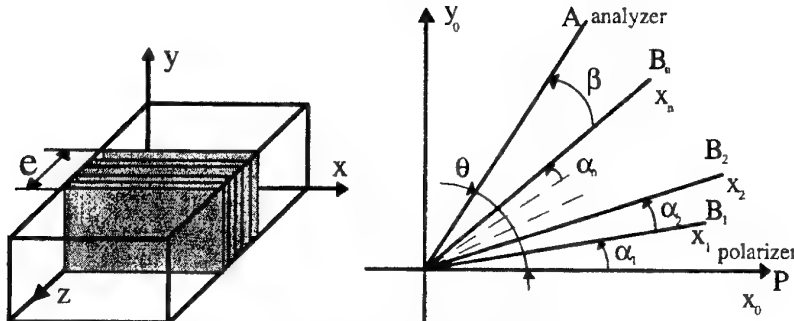


Figure 3 : Series of thin slices

## 2.4 COMPARISONS

We have numerically simulated the three approaches by varying  $\varphi$  from 0 to  $10\pi$  horizontally and  $\alpha$  from  $-\pi/4$  to  $\pi/4$  vertically and by applying different values of  $\alpha_0$ . A series of images obtained is presented in the figure 4.

The first image (figure 4A) corresponds to the first approach, the second one (figure 4B) corresponds to the Aben's formulation and the last (figure 4C) represents the discrete calculation of a series of thin slices.

We note that the image obtained by the first approach, which can not introduce a variation of the stresses along the thickness, is different than the other. The second and the third images are obtained for a variation  $\alpha_0$  of 30 degrees of the stresses direction.

## OPTICAL APPROACHES OF A PHOTOELASTIC MEDIUM      5

Furthermore the Aben's formulation can not be used for a variation of the stresses difference along the thickness.

We have to note that numerical problems appear in the Aben's schematization (paragraph 2.2). They are due to trigonometric calculation (equation 3), that is why this procedure is relatively complex.

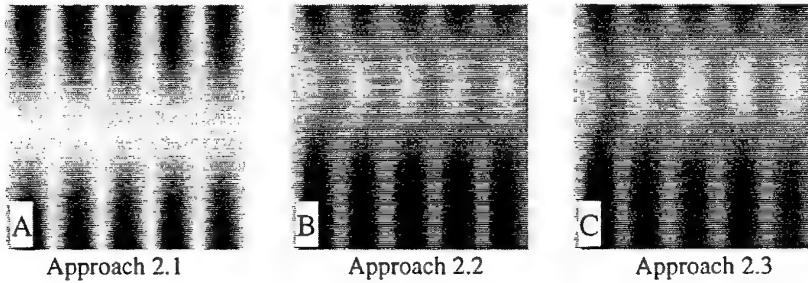


*Figure 4 : Simulations for  $\alpha_0 = 30^\circ$*

If we consider a variation of the stresses difference along the thickness of the specimen, we can apply only the third schematization (approach 2.3), for example we obtained this image.

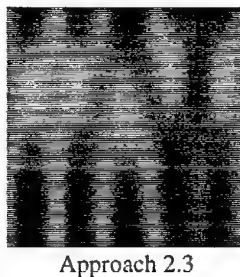


*Figure 5 : Simulations for  $\alpha_0 = 30^\circ$  with a variation of the stresses difference along the thickness*

### 3 Application

#### 3.1 EXAMPLE OF A TWO-DIMENSIONAL STUDY

The discrete calculation of a series of thin slices can be used from results obtained by finite elements method. In the following example (figure 6) of a plate of 10 mm of thickness submitted to the torsion - bending compound, we have calculated the stress field with a corresponding mesh formed by 90x20x5 cells. The third approach gives more realistic images and corresponds to experimental images obtained by a plane polariscope.

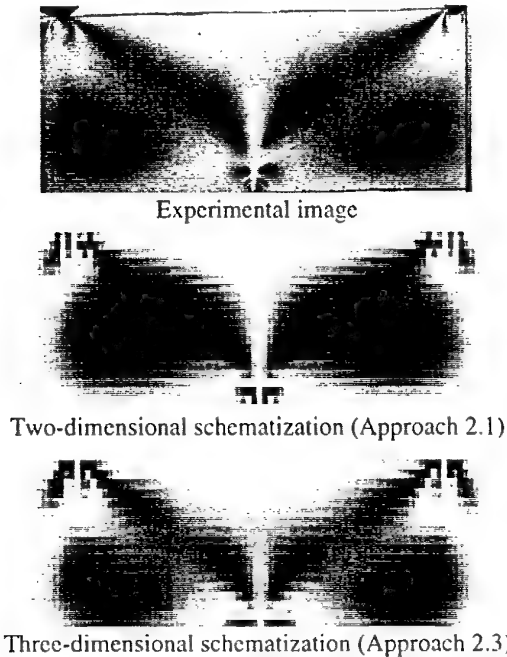


*Figure 6 : Comparison for a test of the torsion-bending compound*

### 3.2 EXAMPLE OF A THREE-DIMENSIONAL STUDY

If we study more complex problems, we must slice the specimens in several parts. The calculation of the fringes can be easily made by our approach (2-3) but for the experimental study we used a method developed in our laboratory. The photoelastic model is optically sliced by two plane laser beams. The analyze of the scattered light gives fringes equivalent to the ones obtained in a plane polariscope [Plouzennec, N., et al. 1998] [Dupré, J.C., et al. 1997] [Dupré, J.C., et al. 1996].

As we can modify the thickness of the slice : 0.5 mm to 10 mm, we used this technique in order to validate the presented approaches.

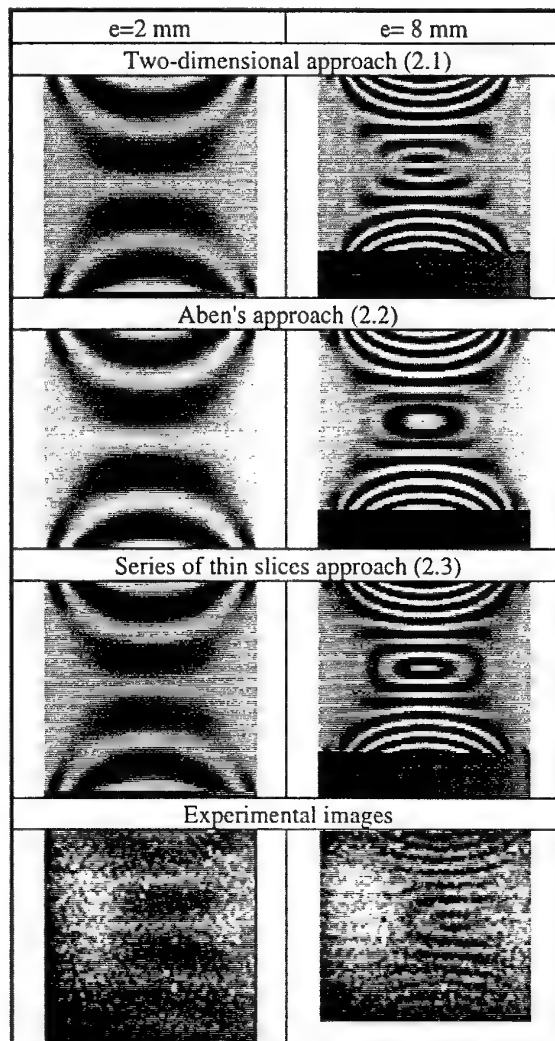
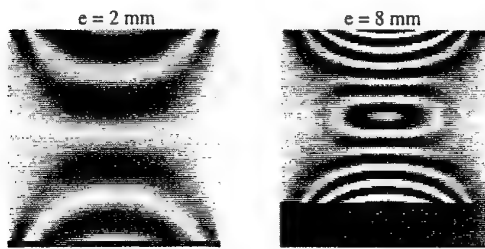
On figure 7, simulated and experimental results are presented for a torsion strain on a bar of square section. Using a theoretical expression of the stress field [Caignaert, G., et al. 1988] [Timoshenko, S., et al. 1961], we have simulated the different fringes pattern for the three shematizations (formula 1, 4 and 6).

The obtained images correspond to slices inclined at an angle of  $\pi/4$  respect to the axis of the model (figure 7). The experimental results show that the 2.3 and 2.2 design is more faithful to the reality than the first one (2.1), especially as for the disappearance of the isoclinic fringes. A difference appears between the two three-dimensional approaches because in this case we have an evolution of the stresses difference along the thickness. This condition is not respected by the Aben's theory.

In order to validate the boundary conditions, a difference on the rotation of 10% can be detected by comparing the figure 7 (approach (2.3)) and the figure 8.

## OPTICAL APPROACHES OF A PHOTOELASTIC MEDIUM

7

Figure 7 : Experimental and simulated fringes (imposed rotation  $4^\circ$ ).Figure 8 : Simulated fringes for a rotation equal to  $3.6^\circ$ .

#### 4 Conclusion

Our purpose is to compare real photoelastic fringes with the fringe pattern calculated with a theoretical or numerical stress field. This process allows us to validate a boundary conditions and mesh of a three-dimensional mechanical problem. We present three approaches of a photoelastic medium. The results obtained by the discrete approach of the three-dimensional medium by a series of thin slices present the best agreement with the experimental results.

The advantage of this method is its numerical simplicity and no hypothesis on  $\alpha$  and  $\varphi$  is made at the level of the thick beam. So we will use our process to compare the simulated fringes with the experimental fringes. A difference between both can be due to only a bad mechanical design. This technique associated with the optical slicing method can be used, in industry, for fast investigation and validation for specimens realized by molding or stereolithography. Nevertheless, the separation of the isoclinic and isochromatic parameters [Zénina, A., et al. 1998] and the calculation of the stress tensor is the next step of our work.

#### References

Aben, H., 1966, Optical phenomena in photoelastic models by the rotation of principal axes, *Experimental Mechanics*, vol. 6, n°1.

Aben, H., and Josepson, J., Oct. 1997, Strange interference blots in the interferometry of inhomogeneous birefringent objects, *Applied Optics*, vol. 36, n°28, pp. 7172-7179.

Brillaud, J., Desailly, R., and Lagarde, A., 1983, Paramètres optiques en photoélasticimétrie tridimensionnelle, *Revue Française de Mécanique*, n°1983-4.

Caignaert, G., and Henry, J.P., 1988, *Cours et exercices d'élasticité*, Dunod.

Dainty, J.C., 1975, *Laser Speckle and related phenomena*, Topics in Applied Physics, 9, Springer Verlag.

Dally, J.W., and Riley, F.W., 1991, *Experimental stress analysis*, McGraw-Hill, Inc.

Desailly, R., and Lagarde, A., 1984, Méthode de découpage optique de photoélasticimétrie tridimensionnelle, application, *Revue Française de Mécanique*, n°1984-1.

Dupré, J.C., Plouzennec, N., and Lagarde, A., 1996, Nouvelle méthode de découpage optique à champ complet en photoélasticimétrie tridimensionnelle utilisant des moyens numériques d'acquisition et d'analyse des champs de granularité en lumière diffusée, *C.R. Acad. Sci. Paris*, t, 323, Série II b, pp. 239-245.

Dupré, J.C., and Lagarde, A., Dec. 1997, Photoelastic analysis of a three-dimensional specimen by optical slicing and digital image processing, *Experimental Mechanics*, Vol. 37, No.4, pp. 393-397.

Plouzennec, N., Dupré, J.C., and Lagarde, A., Sept. 1998, Visualization of photoelastic fringes within three dimensional specimens using an optical slicing method, *Symposium I.U.T.A.M. « Advanced Optical Methods and Applications in Solid Mechanics »*, Poitiers, France.

Timoshenko, S., and Goodier, J.N., 1961, *Theory of elasticity*, Mc Graw-Hill, Inc, 2th edition.

Zénina, A., Dupré, J.C., and Lagarde, A., Sept. 1997, Découpage optique d'un milieu photoélastique épais pour l'étude des contraintes dans un milieu tridimensionnel, *13<sup>ème</sup> Congrès Français de Mécanique*, Poitiers, France, vol. 4, pp. 447-450.

Zénina, A., Dupré, J.C., and Lagarde, A., Sept. 1998, Plotting of isochromatics and isostatics patterns of slice optically isolated in a three dimensional photoelastic model, *Symposium I.U.T.A.M. « Advanced Optical Methods and Applications in Solid Mechanics »*, Poitiers, France.

**AN APPROACH TO GENERAL 3-D STRESS ANALYSIS  
BY MULTIDIRECTIONAL SCATTERED LIGHT TECHNIQUE**

Takahiro OI and Masahisa TAKASHI  
*Aoyama Gakuin University*  
6-16-1, Chitosedai, Setagaya-ku, Tokyo 157-8572, Japan  
Phone: +81-3-5384-1193, Fax: +81-3-5384-6311  
E-mail: ohi@shaqua.me.aoyama.ac.jp

**Abstract**

The scattered light photoelasticity has an excellent feature and advantage of the nondestructive analysis of stress components on a plane layer of incident light path. When analysing general three dimensional stress fields, however, the effect of birefringent axis rotation has to be taken into account. Because of difficulties of this type, the technique has been limited only in application to the case of plane stress or symmetrical stress distribution.

In this study, the authors propose a method for how to determine not only the secondary principal stress difference but also its direction using multiple image data obtained by combination of the angles of incident polarization light and observation. As an example, a sphere under a pair of diametrical compression is analysed to determine both the principal stress difference and direction in layers with or without the rotation of principal birefringent axis. Then, the results are compared with theoretical analysis and fairly good agreement was obtained between them.

**1. Introduction**

It is desirable to know precise and accurate distribution of stress perform optimum design on 3-D subject. However, there has not been developed reliable method for analysis of stress components inside 3-D body under load.

The scattered light photoelasticity has an excellent feature and advantage of the nondestructive analysis of stress components on a plane layer of incident light path. In general three dimensional stress fields, however, scattered photoelastic intensity superposes the effect of birefringent axis rotation due to change in the direction of secondary principal stress along the light path takes place. In addition, the intensity comes up by the integration of optical effects along the light path. It has not been

successful to separate its effects conveniently. Thus the technique has applied to limited cases such as the analysis of stress on symmetrical plane.

In this study, the authors propose a method how to determine not only the secondary principal stress difference but also its direction using multiple image data obtained by combination of the angles of incident polarization light and observation. As an example, a sphere under a pair of diametrical compression is analysed to determine the principal stress difference and direction in symmetrical and unsymmetrical layers. Then, the results are compared with theoretical results.

## 2. Intensity of Light Through a 3-D Model

From matrix calculation based on Stokes vector, the relation between optical devices and intensity of scattered light are derived. Referring to the arrangement of optical elements shown in Fig.1. The final Stokes vector  $S$  [1][2] observed by a camera in this optical setup is obtained as follows.

$$S = M_{\psi+\frac{\pi}{2}} M(\theta) M_\varphi(\delta) S_0 \\ = \frac{1}{2} \begin{bmatrix} 1 - \sin 2(\alpha - \varphi) \sin 2(\psi - \theta - \varphi) \cos \delta - \cos 2(\alpha - \varphi) \cos 2(\psi - \theta - \varphi) \\ -\cos 2\psi \{-\sin 2(\alpha - \varphi) \sin 2(\psi - \theta - \varphi) \cos \delta - \cos 2(\alpha - \varphi) \cos 2(\psi - \theta - \varphi)\} \\ -\sin 2\psi \{-\sin 2(\alpha - \varphi) \sin 2(\psi - \theta - \varphi) \cos \delta - \cos 2(\alpha - \varphi) \cos 2(\psi - \theta - \varphi)\} \\ 0 \end{bmatrix} \quad (1)$$

where,  $S_0$  is the Stokes vectors of polarized incident light,  $M_\varphi(\delta)$  the retarder of the specimen,  $M(\theta)$  the rotator of the specimen, and  $M_{\psi+\frac{\pi}{2}}$  the Stokes vector which shows observing direction. Thus, the intensity of scattered light is expressed as

$$I = \frac{1}{2} k A^2 \{1 - \sin 2(\alpha - \varphi) \sin 2(\psi - \theta - \varphi) \cos \delta - \cos 2(\alpha - \varphi) \cos 2(\psi - \theta - \varphi)\} \quad (2)$$

here,  $I$  : Intensity of observed scattered light from specimen,

$k$  : Light scattering coefficient,

$A^2$  : Amplitude of monochromatic incident light,

$\alpha$  : Azimuth of the axis of incident light,

$\varphi$  : Azimuth of the fast axis of the equivalent retarder,

$\psi$  : Observing direction,

$\theta$  : Characteristic angle of the equivalent rotator,

$\delta$  : Retardation of the equivalent retarder

In this equation,  $\theta + \varphi$  gives the secondary principal stress direction and  $\delta$  gives secondary principal stress difference. In order to eliminate the other parameters away, following combinations of  $\alpha$  and  $\psi$  are chosen. We denote intensities  $I_1$  under conditions of  $\alpha = \alpha_1$  and  $\psi = \psi_1$ , and  $I_2$  under conditions of  $\alpha = \alpha_2 = \alpha_1 + 45^\circ$  and  $\psi = \psi_2 = \psi_1 - 45^\circ$ , when selecting the same observation direction. Subtracting  $I_1$  from

**AN APPROACH TO GENERAL 3-D STRESS ANALYSIS  
BY MULTIDIRECTIONAL SCATTERED LIGHT TECHNIQUE**

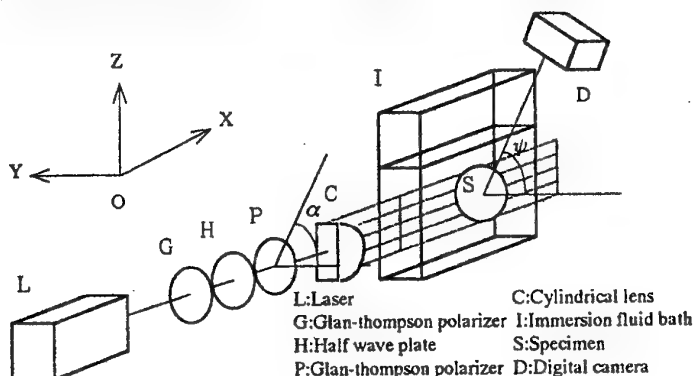


Fig.1 Experimental set up

$I_2$  and denoting it  $I_3$ , we have

$$I_3 = I_2 - I_1 = \frac{1}{2} kA^2 (1 + \cos \delta) \cos 2(\alpha_1 - \psi_1 + \theta) \quad (3)$$

In Eq.(3), for another combination of  $\alpha$  and  $\psi$ ,  $I_4$  under conditions of  $\alpha_1 - \psi_1 = 0^\circ$ , and  $I_5$  under conditions of  $\alpha_1 - \psi_1 = 45^\circ$  are chosen. Then,  $\theta$  and  $\delta$  are obtained as follows.

$$\theta = -\frac{1}{2} \tan^{-1} \left( \frac{I_5}{I_4} \right) \quad (4)$$

$$\delta = 2 \cos^{-1} \sqrt{\frac{I_4^2 + I_5^2}{kA^2}} \quad (5)$$

Again looking at Eq.(2),  $I_6$  under condition of  $\alpha = \alpha_6$  and  $\psi = \psi_6$ , and  $I_7$ , under condition of  $\alpha_7 = \alpha_6 + 45^\circ$  and  $\psi_7 = \psi_6 + 45^\circ$  are selected in order to separate  $\varphi$ . Taking  $I_8$  as

$$I_8 = I_7 - I_6 = \frac{1}{2} kA^2 (1 - \cos \delta) \{ \cos 2(\alpha_6 + \psi_6 - \theta - 2\varphi) \} \quad (6)$$

We can choose another set of combinations as follows. On Eq.(6), denoting  $I_9$  and  $I_{10}$  for the combinations of  $\alpha$  and  $\psi$  as  $\alpha_6 + \psi_6 = 90^\circ$  and  $\alpha_6 + \psi_6 = 180^\circ$ , respectively. We have,

$$\frac{I_{10}}{I_9} = \tan 2(-\theta - 2\varphi) \quad (7)$$

Then,

$$\therefore \varphi = \frac{1}{2} \left( -\theta - \frac{1}{2} \tan^{-1} \frac{I_{10}}{I_9} \right) = \frac{1}{4} \left( \tan^{-1} \frac{I_5}{I_4} - \tan^{-1} \frac{I_{10}}{I_9} \right) = \frac{1}{4} \tan^{-1} \left( \frac{I_5 I_9 - I_4 I_{10}}{I_4 I_9 + I_5 I_{10}} \right) \quad (8)$$

When looking at these calculations, it is necessary to obtain several image data under the combinations of  $\alpha$  and  $\psi$ .

$$I_4 \Rightarrow \alpha_1 = 22.5^\circ, \psi_1 = 22.5^\circ \text{ & } \alpha_2 = 67.5^\circ, \psi_2 = -22.5^\circ$$

$$I_5 \Rightarrow \alpha_1 = 67.5^\circ, \psi_1 = 22.5^\circ \text{ & } \alpha_2 = 112.5^\circ, \psi_2 = -22.5^\circ$$

$$I_9 \Rightarrow \alpha_6 = 112.5^\circ, \psi_6 = -22.5^\circ \text{ & } \alpha_7 = 157.5^\circ, \psi_7 = 22.5^\circ$$

$$I_{10} \Rightarrow \alpha_6 = 67.5^\circ, \psi_6 = -22.5^\circ \text{ & } \alpha_7 = 112.5^\circ, \psi_7 = 22.5^\circ$$

Using six image data (two image data are overlaped.), the secondary principal stress direction is obtained as,

$$\therefore \theta + \varphi = \frac{1}{2} \tan^{-1} \left( \frac{I_5}{I_4} \right) + \frac{1}{4} \tan^{-1} \left( \frac{I_5 I_9 - I_4 I_{10}}{I_4 I_9 + I_5 I_{10}} \right) \quad (9)$$

### 3. Experimental Procedures

#### 3.1 Experimental Setup

Fig.1 shows the experimental setup. A laser beam with small radius is polarized by Glan-Thompson polarizer and then the angle of polarization is adjusted by half wave plate. The light is polarized by second Glan-Thompson polarizer (angle  $\alpha$ ) again to make very assure the angle of polarization, then expanded to a thin layer of light by a cylindrical lens. The beam is inserted into the specimen placed in an immersion bath filled by the liquid of same refraction index with the specimen. Scattered light photoelastic image is taken into a picture by digital camera.

#### 3.2 3-D Photoelastic Model

A 3-D photoelastic sphere model adopted in this study is made of Araldite B-CT200 epoxy-resin cured with a hardener HT903. After removing residual stresses at high temperature and slow cooling process, stress was frozen in the specimen under diametrical load of 60N at the top and bottom of specimen as shown in Fig.2.

#### 3.3 Experimental and Analysis Procedures

A layer of incident light is inserted both on the meridian plane of the sphere specimen and a plane parallel to it as shown Fig.3(a), to investigate symmetrical and more general stress distributions. On the equator plane of the model and a plane parallel to it as shown Fig.3(b), the distribution of principal stress difference and its direction are also investigated. Fringe patterns on these plane are taken in pictures by digital camera. Using brightness distribution on four lines as shown Fig.4, the secondary principal stress difference and direction are calculated.

AN APPROACH TO GENERAL 3-D STRESS ANALYSIS  
BY MULTIDIRECTIONAL SCATTERED LIGHT TECHNIQUE

5

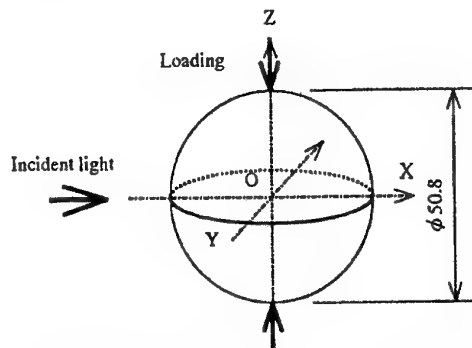
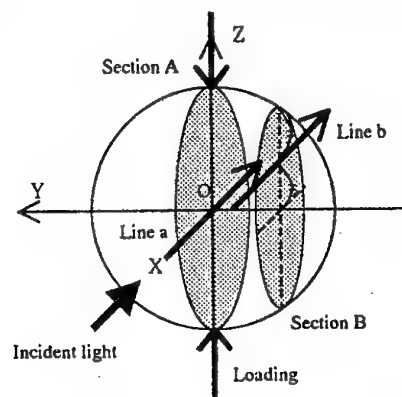
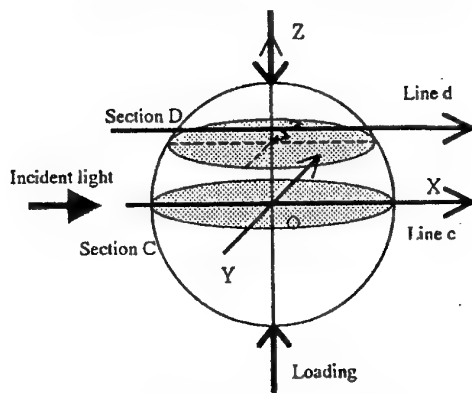


Fig 2 Geometry of specimen and loading condition



(a) the meridian plane and parallel to it



(b) the equator plane and parallel to it

Fig.3 Analyzed region

#### 4. Results and Discussion

Examples of scattered light image data are shown in Fig.4. In Fig.5(a)~(d), comparison of experimental with theoretical results [3] ~ [6] of the secondary principal stress difference are shown. And the secondary principal stress direction are compared in Fig.6(a) ~ (d). Let us discuss on the results of the secondary principal stress difference and direction separately.

1] On the secondary principal stress difference.

a) Experimental results show fairly good agreement with theoretical ones. However, some severe difficulties still remain particularly around the portion of high stress concentration.

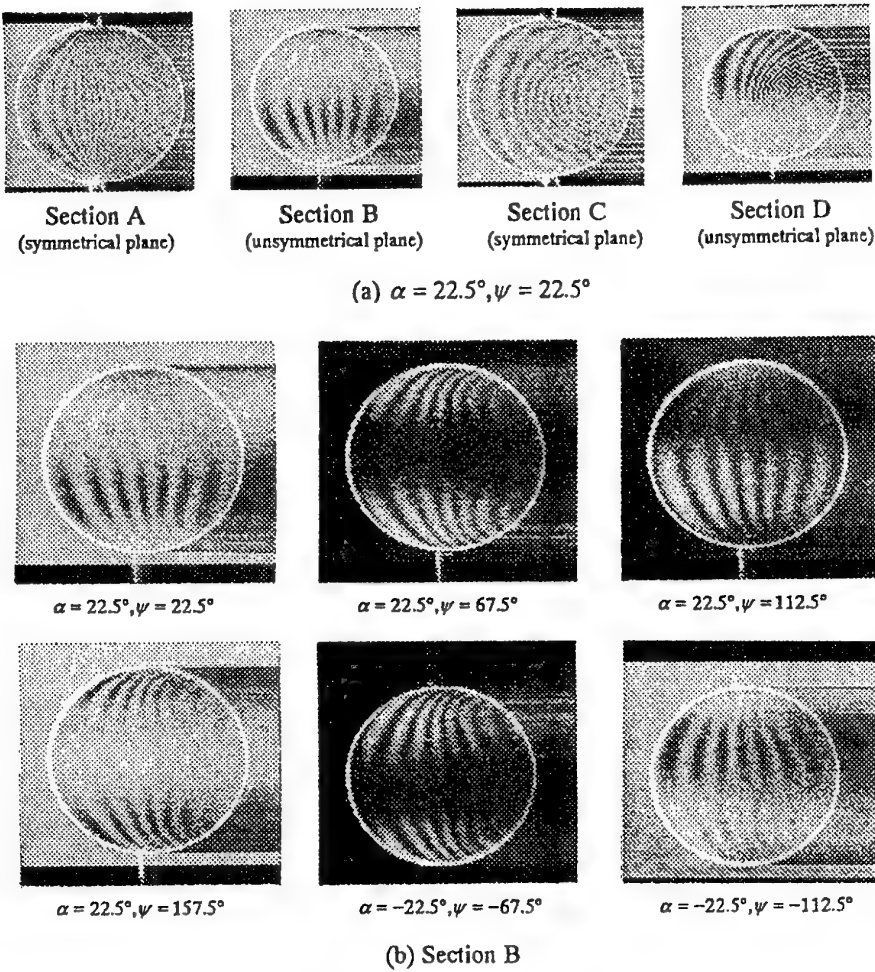


Fig.4 Examples of Image data

**AN APPROACH TO GENERAL 3-D STRESS ANALYSIS  
BY MULTIDIRECTIONAL SCATTERED LIGHT TECHNIQUE**

7

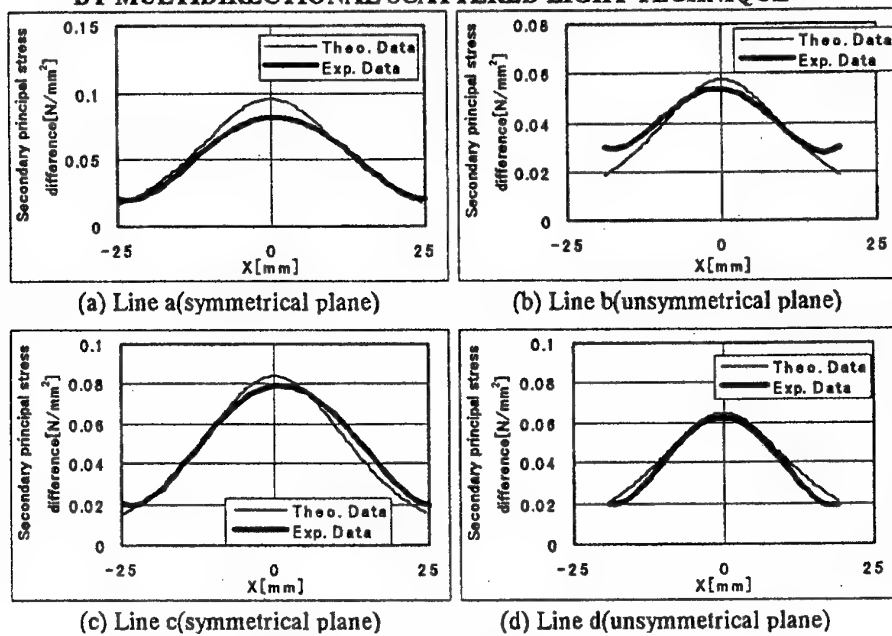


Fig.5 Secondary principal stress difference

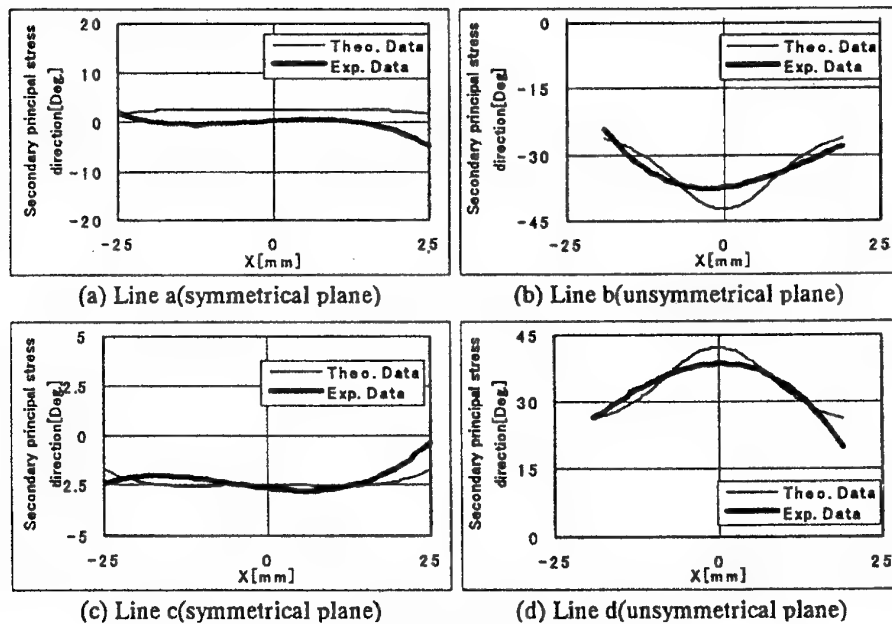


Fig.6 Secondary principal stress direction

b) Around regions where the difference of secondary principal stress becomes large, considerable errors between theoretical and experimental data are observed. This comes from the fact that the density of fringe vary rapidly, the resolution of camera is not sufficient in this region. So it would be necessary to choose a best fit camera for the density of fringe order.

2] On the secondary principal stress direction.

c) The error between experimental and theoretical value of the secondary principal stress direction is larger than the case of the secondary principal stress difference, because the influence of retardation of the equivalent retarder  $\delta$  on the intensity of scattered light is larger than the expectation in theory.

d) Experimental values show some degree of agreement with the theoretical results on the symmetrical layer. On the other hand, the experimental results on unsymmetrical layer show poorer agreement with theoretical results and the errors are much larger than that on the symmetrical layer. So, it is pointed out that both the azimuth of the fast axis of the equivalent retarder and the characteristic angle of the equivalent rotator on symmetrical planes is obtained much easier and more accurately than on unsymmetrical planes.

e) Since two solutions of the secondary principal stress direction obtained simultaneously in the calculation proposed, choice of proper solution from two is another problem in this method.

Similar level of accuracy on the meridian and the equator plane of sphere model are obtained, thus it can be expected that we will be able to improve the technique to get more accurate secondary principal stress distribution on every plane.

### 5. Concluding Remarks

The authors discussed a method for 3-D analysis of the direction and the difference of secondary principal stresses with a method based on the scattered light photoelastic technique. As an example, a sphere under a pair of diametrical compression is analysed. Then, comparing with theoretical results, good agreement was obtained on the place where the secondary principal stress difference and direction do not vary so much. Thus, effective clues were found for the development of a technique in general 3-D scattered light photoelastic stress technique.

### References

- [1] Thercaris, P.S. and Gdoutos, E.E. (1979) *Matrix Theory of Photoelasticity*, Springer Series in Optical Sciences, Berlin
- [2] Azzam, R.M.A.A. and Bashara, N.M. (1977) *Ellipsometry and Polarized Light*, North-Holland Personal Library, Elsevier
- [3] Sternberg, E. and Rosenthal, F. (1952) *J. Appl. Mech.*, 19-4, 413
- [4] Weber, C. (1952) *Z. AMM*, 32-6, 186.
- [5] Timoshenko, S.P. (1959) *Theory of Plates and Shells*, McGraw-Hill, 561
- [6] Ulitko, A.F. (1968) *Prikladnaya Mekhanika*, 4-5, 38

## PHASE MEASUREMENT METHOD FOR STRESS ANALYSIS FROM PHOTOELASTIC DATA

J.A. QUIROGA, A. GONZÁLEZ-CANO  
*Departamento de Óptica. Facultad de CC. Físicas.  
Universidad Complutense de Madrid  
Ciudad Universitaria s/n. 28040 Madrid (Spain).*

### Abstract

In recent years, phase measuring techniques have been applied to the problem of extracting information of photoelastic data. In this work, a complete method for stress analysis from photoelastic fringe patterns is presented.

The photoelastic phase maps are obtained with a circular polariscope. For the isoclinics calculation a four-step phase-shift algorithm is used. A white light source is used to avoid problems of low modulation in the fringe pattern. Isochromatics are calculated by a new algorithm developed by us with almost no influence of the isoclinics. The isochromatic parameter can be determined without sign ambiguity. We have also developed a method for the error analysis of the measurements produced by the errors of the elements of the polariscope. Finally, using the equilibrium equations, we can obtain the values of the main stresses in the sample from the isoclinic and isochromatic parameters.

### 1. Introduction

Photoelasticity is a well-established technique for stress analysis and has a wide range of industrial and research applications [1]. Recently, several methods of analyzing photoelastic fringe patterns by means of phase-measuring techniques have been presented [2-7]. The main goal of these techniques is the determination of the distributions of isoclinics and isochromatics in order to be able to perform an analysis of the stress distribution in the sample. To develop a complete, fully automated method of stress analysis from photoelastic data several difficulties must be faced.

First, we must adapt the usual phase-step algorithms to the kind of fringe patterns that appear in photoelasticity. The main problem is that the isoclinic and isochromatic fringe patterns are completely mixed. The modulation of the isoclinic phase map depends on the isochromatics, and vice versa. For that reason, the unwrapping of the corresponding phase maps is difficult because of the appearance of logical inconsistencies associated with low-modulation areas. The methods for the isoclinic calculation proposed in the

literature solve this problem adequately, by using of a white light source, instead of a monochromatic one. It is very different with isochromatics. The methods based on phase-measuring techniques that exist in the literature present several problems, the most important ones being sign ambiguity and dependence on isoclinics. We have developed a new algorithm that avoids sign ambiguity and whose performance is almost independent of the isoclinics, thus overcoming the inconsistencies associated to low-modulation areas produced by them.

Another point to take into account is the different error sources that influence the phase measurement. The error analysis of the phase-shifting algorithms [8,9] must be complemented with a specific study of the contributions of the errors associated to the polariscope. To quantify the errors produced in the determination of the isoclinics and the isochromatics due to this cause we have developed an error analysis method [10]. With this method, based on Jones calculus, we are also able to decide in a qualitative way the influence of the different errors in the final measurement.

Finally, we must be able to determine the values of the principal stresses at every point in the sample from the values of the isoclinics and isochromatics. This process is called *stress separation*. To perform this separation we must solve the so-called *equilibrium equations*. When we introduce photoelastic data in these equations we obtain a system of partial differential equations in which the right-hand side is a set of experimental values, which are of course discrete. In this way, the problem of stress separation is reduced to a problem of integration of pairs of difference equations. Different numerical methods have been applied to solve these kind of equations. We propose the use of a multigrid method that is well suited to deal with realistic, noisy sets of data. [11]

The combination of all these techniques (phase-measurement to determine isoclinics and isochromatics, error analysis and multigrid methods to solve the equations for stress separation) permit the complete evaluation of the stress state of a plane sample in few minutes.

## 2. Isoclinics and isochromatics calculation by phase-measuring techniques

For the isoclinics calculation a circular polariscope is used in the so-called *linear bright field* configuration. The output intensity of the polariscope in this configuration is given by

$$I = I_0 \sin^2 \frac{\delta}{2} (1 - \cos 4\alpha), \quad (1)$$

where  $\delta$  and  $\alpha$  are the isochromatic and isoclinic parameters respectively.  $I_0$  is the input intensity. We use a four-step phase-shift algorithm where the steps are introduced by rotating the whole polariscope by an angle  $\beta$ . Then, Eqn. (1) takes the form

$$I = I_B + m \cos[4(\alpha - \beta)] \quad (2)$$

where  $I_B$  is a background term and  $m$  is the modulation of the isoclinic fringes. Both  $I_B$  and  $m$  depend on the value of the isochromatic parameter and, because of this, of the wavelength of the used light source. However, the isoclinic parameter does not depend on wavelength. If we take four images with  $\beta_i = (i-1)\pi/8$ ,  $i=1,\dots,4$ , the wrapped isoclinic phase is calculated by

$$W[4\alpha] = \tan^{-1} \left( \frac{I_4 - I_2}{I_3 - I_1} \right) \quad (3)$$

where  $W$  is the so-called *wrapping operator*, that denotes modulo  $2\pi$ .

Eqn. (3) solves the problem of extracting the isoclinic parameter except in the cases where modulation is too low. Since  $m$  depends on  $\delta$ , the low-modulation areas depend on wavelength. If a monochromatic light source is used there will be several regions where the value of  $\delta$  makes  $m$  too small. However, this problem can be overcome by simply using a white light source, since then the low-modulation areas corresponding to a given wavelength will be regions of high modulation for another wavelength. Only in the so-called *zero-order isochromatic fringes*, corresponding to the loci of points of the sample for which  $\delta=0$ , the modulation is very low for every wavelength.

Once  $W[4\alpha]$  is determined in this way, we compute the value of the isochromatic parameter that depends on  $\alpha$ .

For isochromatics, as we have said, we present a new algorithm. We start now with a general configuration of the circular polariscope. The incident light on the sample is circularly polarized. The output intensity in this case is

$$I = 1 - \sin 2(\psi - \varphi) \cos \delta - \sin 2(\varphi - \alpha) \cos 2(\psi - \varphi) \sin \delta, \quad (4)$$

where  $\alpha$  and  $\delta$  are again the isoclinic and isochromatic parameters and the angles  $\psi$  and  $\varphi$  correspond to the orientation of the second quarter-wave plate and the analyzer of the polariscope, respectively.

We take eight images corresponding to different configurations of the circular polariscope, that appear in Table 1.

TABLE 1. Configurations of the polariscope

Configuration	Intensity output	Configuration	Intensity output
1. $P_{90}Q_{45}Q_{45}A_{-45}$	$I_1 = \frac{1}{2}(1 + \cos 2\alpha \sin \delta)$	5. $P_{-45}Q_{90}Q_{90}A_0$	$I_5 = \frac{1}{2}(1 + \sin 2\alpha \sin \delta)$
2. $P_{90}Q_{45}Q_{-45}A_{45}$	$I_2 = \frac{1}{2}(1 - \cos 2\alpha \sin \delta)$	6. $P_{-45}Q_{90}Q_0A_{90}$	$I_6 = \frac{1}{2}(1 - \sin 2\alpha \sin \delta)$
3. $P_{90}Q_{45}Q_{-45}A_0$	$I_3 = \frac{1}{2}(1 - \cos \delta)$	7. $P_{-45}Q_{90}Q_0A_{45}$	$I_7 = \frac{1}{2}(1 - \cos \delta)$
4. $P_{90}Q_{45}Q_{45}A_0$	$I_4 = \frac{1}{2}(1 + \cos \delta)$	8. $P_{-45}Q_{90}Q_{90}A_{45}$	$I_8 = \frac{1}{2}(1 + \cos \delta)$

Note: The notation used in the configuration is as follows:  $P$  stands for (*first*) polarizer,  $Q$  stands for quarter-wave plate and  $A$  stands for analyzer (*second polarizer*). The subscript corresponds to the orientation (in degrees) of the element with respect to the chosen  $x$ -axis. No reference to the sample (that is placed between the two quarter-wave plates) is included.

From these eight output intensity distributions, the (wrapped) isochromatic phase  $\delta$  is obtained by

$$W[\delta] = \tan^{-1} \left\{ \frac{(I_1 - I_2) \cos 2\alpha + (I_5 - I_6) \sin 2\alpha}{\frac{1}{2}[(I_4 - I_3) + (I_8 - I_7)]} \right\}. \quad (5)$$

The use of this expression permits to deal with the usual problems of isochromatic phase extraction, specifically with the problems arising from the existence of low-modulation areas due to isoclinics. From Table 1 we see that  $I_1 - I_2$  is modulated by  $\cos 2\alpha$  and  $I_5 - I_6$  by  $\sin 2\alpha$ . That means that any algorithm that uses only one of these differences, for instance, one based in the following equation:

$$W[\delta] = \tan^{-1} \left\{ \frac{(I_1 - I_2)}{(I_4 - I_3) \cos 2\alpha} \right\}, \quad (6)$$

would fail in the areas where the value of  $\cos 2\alpha$  is small, since both numerator and denominator would be very small, so there would appear big errors in the phase computation. Obviously, the case will be the same with  $I_5 - I_6$ , but then the low modulation areas will be associated to low values of  $\sin 2\alpha$ .

We see, then, that the low modulation areas corresponding to the considered differences are in quadrature. That means that if we use both differences, as in Eqn. (5), there will be no regions where both terms in the numerator are small because of the isoclinic parameter. In this way, the modulation of the isochromatic phase map calculated by (5) becomes independent of the value of  $\alpha$ , so that a complete separation of the information of isochromatics and isoclinics is achieved.

Another advantage of Eqn. (5) is that we work directly with the eight intensity distributions that are smooth functions, suitable to any filtering, in a way that the phase jumps are not affected by this filtering. This is not possible if we work instead with wrapped phases that are discontinuous by definition.

No sign ambiguity appears in the computation of  $\delta$ . The algorithm can deal with any number of isochromatic fringes in the field of view, as long as the spatial frequency of the fringes is below the Nyquist limit of the detector. The zero-order isochromatic fringe can be determined by studying the modulation of the isoclinic and isochromatic phase maps.

With this algorithm, both isoclinic and isochromatic wrapped phase maps are good enough for the use of any standard unwrapping algorithm. Unwrapping is necessary if we are going to perform a stress separation process.

### 3. Error analysis of phase-measuring algorithms applied to photoelasticity

There exists in the literature a considerable amount of papers that deal with the problem of error estimation in phase-measuring algorithms. These papers mainly study the effect in the phase calculation of errors in the phase steps, nonlinearities in the detector, additive noise, etc. When applied to photoelasticity, however, a new error source appears for this kind of algorithms, namely the errors associated to the configurations of the polariscope used to obtain the different intensity distributions upon which the phase-measuring algorithms are based. The theoretical expressions for the intensity distributions (e.g., those in Table 1) are valid only for definite orientations of the elements of the polariscope. That means that if we have an error in these orientations the real output intensity of the polariscope does not coincide with the one that is required to obtain the desired phase shifts between intensity distributions, which implies that the calculated phase (e.g., by Eqn. 5) will be affected of errors. The analytical expressions of these intensity distributions cannot be used as a basis of the analysis of the phase

error, since they are true only for the particular configurations of the polariscope for which they are calculated. Therefore, the usual method of error propagation cannot be directly applied to this case.

We have developed a different approach to the error analysis in phase-measuring algorithms applied to photoelasticity based in Jones calculus. To be able to perform in an easy way both qualitative and quantitative error analysis our method uses a linear approximation. Instead of using the exact Jones matrices of the error-affected elements, we associate to each element the Jones matrix of the error-free element plus a perturbation Jones matrix that depends linearly on the error. In this way we can calculate the Jones matrix of the whole polariscope, obtaining the Jones matrix of the error-free polariscope and a series of contributions of the different error sources. This "real" Jones matrix can then be used to obtain the output intensity of the error-affected polariscope.

The Jones matrix will be of the form

$$M^* = M + \sum_{j=1}^5 \varepsilon_j E_j, \quad (7)$$

where  $M$  is the "nominal" matrix of the polariscope (that means, the matrix if all the elements are free of errors)  $\varepsilon_j$  are the errors corresponding to each error source and  $E_j$  are matrices which can be analytically obtained that correspond to the "perturbations" introduced by the errors in the orientation of the elements or the retardation of the plates. Then we can use  $M$  to calculate the output intensity

$$I^* = (Ma)^+ Ma, \quad (8)$$

where  $a$  is the Jones vector of the initial beam.

We can then use the value of the perturbed intensities  $I^*$  in Eqn. (5) to obtain the errors in the isoclinics and the isochromatics. We have developed a procedure of error analysis based on the study of the histograms of the distribution of errors for the different values of isoclinics and isochromatics. We have checked the performance of the method by comparing it with experimental results.

#### 4. Stress separation

The determination of the values of the principal stresses at every point in a sample from any kind of direct experimental measurements is called *stress separation*. In photoelastic experiments it is not possible to obtain the values of the principal stresses in every point of the sample directly. What is obtained is the difference of the principal stresses (associated with isochromatics) and their orientations (associated with isoclinics). Therefore, some information must be added to photoelastic data to separate stresses. The method selected by us is the resolution of the *equilibrium equations*, which are relationships between the spatial variations of the Cartesian components of the stresses and the value of the shear stress at every point. The connecting point between photoelastic data and the equilibrium equations is shear stress, because it can be directly measured by photoelasticity.

In this way, if  $\sigma_x$  and  $\sigma_y$  are the components of the stress at a given point in a fixed Cartesian system of reference and  $\sigma_{xy}$  is the shear stress, the equilibrium equations, in the absence of body forces, are given by

$$\frac{\partial \sigma_x}{\partial x} + \frac{\partial \sigma_{xy}}{\partial y} = 0, \quad (9)$$

$$\frac{\partial \sigma_y}{\partial y} + \frac{\partial \sigma_{xy}}{\partial x} = 0. \quad (10)$$

The components  $\sigma_x$  and  $\sigma_y$  are related to the isoclinic and isochromatic parameters by

$$(\sigma_x - \sigma_y) = K\delta \cos 2\alpha, \quad (11)$$

$$\sigma_{xy} = \frac{1}{2} K\delta \sin 2\alpha, \quad (12)$$

where

$$K = \frac{\lambda}{2\pi d C}, \quad (13)$$

where  $\lambda$  is the wavelength of the light used,  $d$  is the thickness of the sample and  $C$  is its photoelastic constant.

From these equations we can obtain a relationship between the sum of stresses  $\sigma = \sigma_x + \sigma_y$  and the isoclinic and isochromatic parameters:

$$\frac{\partial \sigma}{\partial x} = -\frac{\partial \Phi}{\partial x} - \frac{\partial \Psi}{\partial y}, \quad (14)$$

$$\frac{\partial \sigma}{\partial y} = \frac{\partial \Phi}{\partial y} - \frac{\partial \Psi}{\partial x},$$

where

$$\Phi = K\delta \cos 2\alpha, \quad (15)$$

and

$$\Psi = K\delta \sin 2\alpha \quad (16)$$

We must then solve (14), a system of partial differential equations in which the right-hand side is a set of experimental values, which are of course discrete. We see that the problem of stress separation is reduced to a problem of integration of pairs of difference equations, which correspond to the discrete version of equation (14). Many numerical methods can be applied for this goal [12]. When dealing with stress separation these methods must be capable to work with arbitrarily shaped processing areas and to overcome the problems associated with the noise in the data. Noise problems are especially significant, since we measure  $\Phi$  and  $\Psi$  and then we calculate their partial derivatives and mix them, so the noise of the experimental data is amplified.

We have adopted a multigrid method to perform stress separation. [11] We can see that  $\sigma$  fulfills Laplace equation, which can be solved by the well-known Gauss-Seidel relaxation technique. Gauss-Seidel relaxation provides the high-frequency details of the function very fast, but it propagates this information very slowly, so low-frequency features of the function are difficult to obtain. For this reason, multigrid methods are well suited to improve the efficiency of the Gauss-Seidel relaxation scheme. The key idea of the multigrid approach is to transform the low-frequency components of the solution obtained by a Gauss-Seidel relaxation into high-frequency components of a coarser grid. In a coarser grid, Gauss-Seidel relaxation works very well and we only need to translate the results obtained to the finer grids. A set of grids, each with a double spacing between points can be used, and the information must be transferred first from finer to coarser and then from coarser to finer grids. This is accomplished by the action of two operators, *prolongation* and *restriction*. The algorithm performance is good

### 5. Experimental results

To show the performance of our method we have chosen a realistic sample, consisting of a plate with a hole and a cut joining the hole with the border (figure 1). A compressive force is applied as indicated in figure. In figures 2 and 3 we show the distribution of isoclinics and isochromatics respectively. In figure 4 the sum of principal stresses calculated by our method is shown. For comparison, we show in figure 5 this sum calculated by a method of finite elements. For the sake of clarity contour lines are included. In figure 6 profiles of the  $\sigma_1$  stress along line AB of figure 1, as calculated by our method (line) and the finite elements method (circles), are shown.

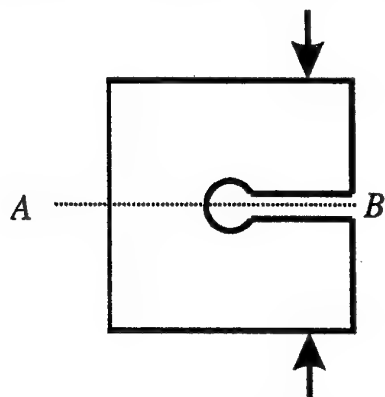


Figure 1. Schematic representation of the sample



Figure 2. Isoclinics

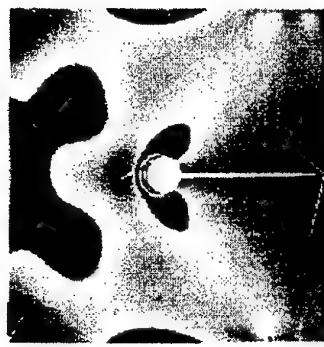
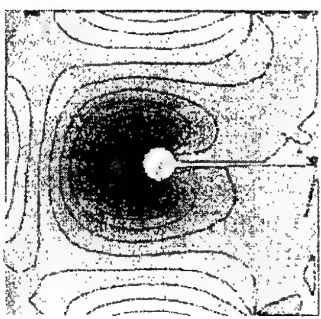
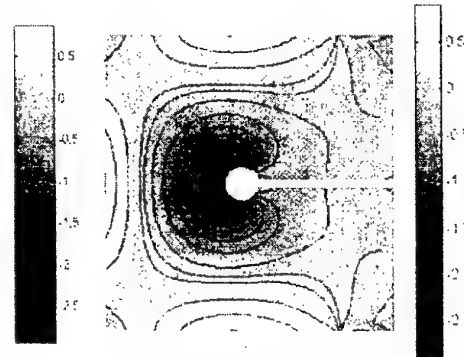


Figure 3. Isochromatics



**Figure 4.** Sum of principal stresses by our method



**Figure 5.** Sum of principal stresses by finite elements

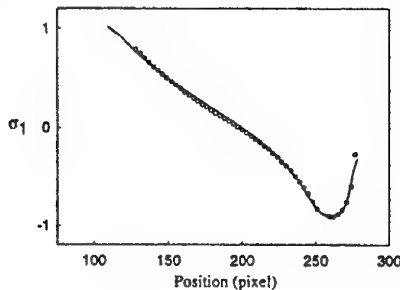


**Figure 6.** Profile of the  $\sigma_1$  stress along line  $AB$ .

## References

1. Frocht, M.M., *Photoelasticity*, 2 Vols., John Wiley and Sons, New York, 1941, 1948.
2. Morimoto, Y., Morimoto, Y. Jr., Hayashi, T., Separation of isochromatics and isoclinics using Fourier transform, *Exp. Techn.*, (Sept.-Oct. 1994), 13-16.
3. Buckberry, C., Towers, D., Automatic analysis of isochromatic and isoclinic fringes in photoelasticity using phase-measuring techniques, *Meas. Sci. Technol.*, **6** (1995), 1227-1235.
4. Franz, T., Maidhof, A., Sun, J., "Verfahren und Vorrichtung zur Bestimmung der Isochromatenwerte in der Spannungsoptik", German Patent DE-195 03 851 A1 (August, 10, 1995).
5. Nurse, A.D., Full-field automated photoelasticity by use of a three wavelength approach to phase stepping, *Appl. Opt.*, **36** (1997), 5781-5786.
6. Ng, T.W., Derivation of retardation phase in computer-aided photoelasticity by using carrier fringe phase-shifting, *Appl. Opt.*, **36** (1997), 8259-8263.
7. Quiroga, J.A., González-Cano, A., Phase measuring algorithm for extraction of isochromatics of photoelastic fringe patterns, *Appl. Opt.*, **36** (1997), 8397-8402.
8. Freischlad, K., Koliopoulos, C.L, Fourier description of digital phase-measuring interferometry, *J. Opt. Soc. Am. A* **7** (1990), 542-551.
9. Van Wingerden, K., Frankena, H.J., Smorenburg, C. Linear approximation for measurement errors in phase shifting interferometry, *Appl. Opt.*, **30** (1991), 2718-2729.
10. Quiroga, J.A., González-Cano, A., A method of error analysis for phase-measuring algorithms applied to photoelasticity, *Appl. Opt.*, in press
11. Quiroga, J.A., González-Cano, A., Stress separation from photoelastic data by a multigrid method, *J. Meas. Sci. Technol.*, in press.
12. Press, W.H., Teukolsky, S.A., Vetterling, W.T., Flannery, B.P., *Numerical recipes in C. The art of scientific computing*, 2<sup>nd</sup> ed., Cambridge University Press, Cambridge (UK), 1992.

## GENERALIZED PHASE-SHIFTING METHOD FOR MEASURING PHOTOELASTIC FRINGE PARAMETERS AND ITS APPLICATIONS

E. UMEZAKI and Y. NANKA

*Department of Mechanical Engineering, Nippon Institute of Technology*

*4-1 Gakuendai, Miyashiro, Saitama 345-8501, Japan*

*E-mail: umezaki@nit.ac.jp*

### Abstract

A generalized phase-shifting method was developed for reducing the influence of noise caused by the variation in light intensity of a light source and so on, and for automatically measuring photoelastic parameters, relative fringe orders and principal-stress directions, in the whole field. The fringe orders obtained using the method were used to measure the stress intensity factor, and the principal-stress directions to extract the zero points. Furthermore the zero points were used to design structural members with holes. The stress intensity factor in a beam with a crack on one side subjected to a three-point bending was accurately obtained from fringe loops multiplied using a technique for drawing a contour map of the fringe order values. The zero points in a T-shaped plate subjected to a compressive load were accurately extracted using a technique for judging the zero points, and were effective to design the plate with holes.

### 1. Introduction

The photoelastic method is one of the most effective methods for whole-field stress analysis. Photoelastic fringe parameters, fringe orders and principal-stress directions, in the whole field of a model are required in this analysis. There are many available methods for obtaining the fringe parameters[1-10]. Using these methods, the determination of the fringe parameters has been markedly improved. Among these methods, the phase-shifting method, which can be used to obtain the fringe parameters from a combination of several images taken by the rotation of optical components, is promising for the determination of fringe parameters in the whole field. This method has assumed that the time-series light intensity at any point obtained by the rotation of optical components lies exactly on a sinusoidal curve. Actually the light intensity does not lie exactly on such a curve because of noise caused by the variation in the intensity of a light source and by dust on optical components. Such noise has an adverse effect on the results obtained by the phase-shifting method[11]. A method based on Fourier transform[4] has been used to reduce the effect

of such noise on the separation of isochromatics and isoclinics from images obtained by rotating the crossed polaroids in a plane polariscope. However, fringe orders were not obtained by the Fourier transform method.

In this study, a generalized phase-shifting method was developed for suppressing such adverse effects and for automatically measuring photoelastic fringe parameters in the whole field, and the parameters were used to measure the stress intensity factors and extract the zero points in a structure member.

## 2. Generalized Phase-Shifting Method [6,10]

When the polarizer and analyzer in the dark field and light field are simultaneously rotated by  $\theta$  from a selected reference,  $R$ , the light intensities,  $I_d, I_l$ , at any point emerging from the dark-field and light-field plane polarisopes with the monochromatic light source are

$$I_d = I_0 \sin^2 2(\phi - \theta) + I_B \quad (1)$$

$$I_l = -I_0 \sin^2 2(\phi - \theta) + a^2 + I_B \quad (2)$$

where  $I_0 = a^2 \sin^2 \pi N$ ,  $a$  is the amplitude of polarized light transmitted through the polarizer,  $N$  is the fringe order,  $\phi$  is the direction of principal stress,  $\sigma_1$ , to  $R$ , and  $I_B$  is the background light intensity.

By applying the Fourier-series expansion to the time-series intensity data,  $I_{dk}$  ( $k=0, 1, 2, \dots, n$ ), obtained according to the rotation of the polaroids at every angle,  $\Delta\theta (= \theta/n)$ , from  $\theta=0$  to  $\theta=\pi/2$  in a dark-field plane polariscope at each point,  $I_0, I_B$  and  $\phi$  in eqs(1) and (2) can be calculated as

$$I_0 = 2 \sqrt{a_1^2 + b_1^2} \quad (3)$$

$$I_B = a_0 - \sqrt{a_1^2 + b_1^2} \quad (4)$$

$$\phi = \frac{1}{4} \left[ \frac{\pi}{2} - \tan^{-1} \left( \frac{b_1}{a_1} \right) \right] \quad (5)$$

where

$$a_0 = \frac{1}{n} \sum_{m=0}^{n-1} I_{dm} \quad (6)$$

$$a_1 = \frac{2}{n} \sum_{m=0}^{n-1} I_{dm} \cos \left( m \frac{2\pi}{n} \right), \quad b_1 = \frac{2}{n} \sum_{m=0}^{n-1} I_{dm} \sin \left( m \frac{2\pi}{n} \right)$$

In order to measure  $N$ ,  $a^2$  must be separated from  $I_0$ . By applying the Fourier-series expansion to the time-series intensity data,  $I_{lk}$  ( $k=0, 1, 2, \dots, n$ ), obtained according to the rotation of polaroids at every angle,  $\Delta\theta (= \theta/n)$ , from  $\theta=0$  to  $\theta=\pi/2$  in a light-field plane

## GENERALIZED PHASE-SHIFTING METHOD

3

polariscope at each point,  $a^2$  is obtained as

$$a^2 = \frac{I_0}{2} - I_B + \frac{1}{n} \sum_{m=0}^{n-1} I_{bm} \quad (7)$$

Hence the application of a half-angle relation to  $I_0 = a^2 \sin^2 \pi N$  gives the relative fringe orders,  $N$

$$N = \frac{1}{2\pi} \cos^{-1} \left( 1 - \frac{2I_0}{a^2} \right) \quad (8)$$

where  $0 \leq N \leq 0.5$ .

## 3. Application

## 3.1 MEASUREMENT OF STRESS INTENSITY FACTOR

The fringe orders obtained using the proposed method were used to measure the stress intensity factor in a rectangular plate with a crack at one side under 3-point bending as shown in Fig.1. This specimen was an epoxy resin plate (Arardite-CY230:Hardener-HY956=100:20 in weight ratio) 220 mm long, 50 mm width, 5.8 mm thick, and had a photoelastic sensitivity of 0.076 mm/N. It was subjected to a load of 125.4 N,  $P$ . The distance between supporting points was 200 mm. The crack length was 6.8 mm.

## 3.1.1 Measurement of Fringe Order

The fringe orders were obtained as follows. Figure 2 shows a polariscope system for measuring the fringe orders. The polarizer and analyzer were simultaneously rotated using the stepper motor driven by the number of pulses transmitted from a personal computer.

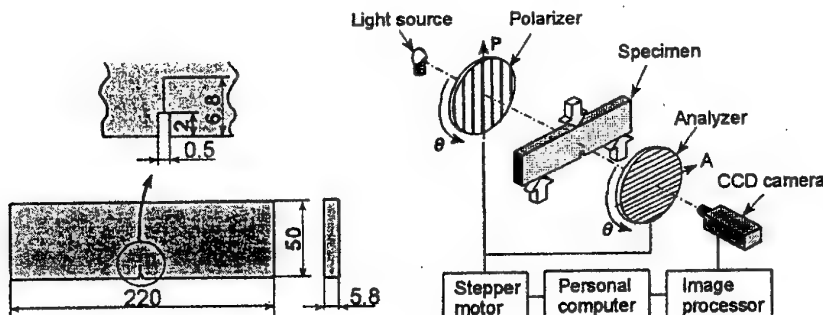


Figure 1. Specimen.

Figure 2. Computerized polariscope.

Images which included both isochromatics and isolinics were captured using the CCD camera, digitized into 8 bits (256 levels) using the image processor, and stored as a  $256 \times 256$  pixel array in a hard disk for each step of the rotation. In this study, the polarizer and analyzer were rotated with an interval about 0.7 deg, which was obtained by dividing 90 deg into 128 equal angles. As a result, 129 images in the dark and light fields were taken between 0 and 90 deg. A mercury lamp in a plane polariscope was used for obtaining fringe orders.

After the 129 images have been taken in each field, the time-series intensity data were made at each pixel using these images, and stored in a hard disk. The time-series intensity data were used to obtain fringe order at each pixel using the Fourier-series expansion.

Figure 3 shows the isochromatic fringes obtained in a dark-field circular polariscope. Figure 4 shows the relative fringe orders,  $N$ , obtained by the proposed method. In this figure, the black regions were assigned the value of  $N=0$ , and the white ones  $N=0.5$ . The regions changed from black to white as the value of  $N$  increased from 0 to 0.5.

### 3.1.2 Drawing of Fringe Loop

Fringe loops were drawn from an image with relative fringe orders as follows. First, an image with fringe orders at all pixels in a model, which was obtained using the generalized phase-shifting method, was partitioned into triangles with vertexes  $a$ ,  $b$ , and  $c$ , which were neighboring pixels. Second, the positions at which a fringe loop of a given fringe-order value was passed through on edges  $ab$ ,  $bc$ , and  $ca$  of each triangle were calculated on the basis of linear interpolation of fringe-order values  $N_a$ ,  $N_b$  and  $N_c$  at vertexes  $a$ ,  $b$ , and  $c$ . Third, line segments, which were parts of the fringe loop, were drawn between the positions. Finally, the fringe loops were drawn by connecting those line segments.

Figure 5 shows the isochromatic fringes, which were extracted at an interval of fringe order 0.05 between 0 and 0.5. In this figure, the absolute fringe orders were assigned to the extracted fringes. The fringes with integer orders of  $N=0, 1, 2, \dots$  and half orders of  $N=0.5, 1.5, 2.5, \dots$  were not extracted, because the values of  $N=0$  and 0.5 were seldom obtained at the points which were sampled as a  $256 \times 256$  pixel array and digitized into 256 levels used in this study.



Figure 3. Isochromatics.

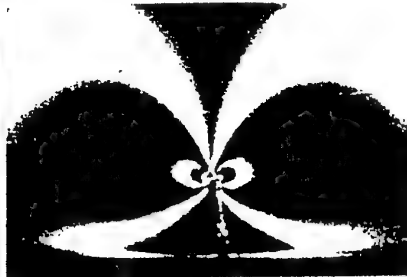


Figure 4. Relative fringe orders obtained using the proposed method.

### 3.1.3 Calculation of Stress Intensity Factor

The fringes shown in Fig.5 were used to calculate the stress intensity factor,  $K_{I(exp)}$ , by the Irwin method[12]. The theoretical stress intensity factor,  $K_{I(thy)}$ , in a rectangular plate with a crack at one side under 3-point bending[13].

Fringes in the vicinity of the crack tip must be used to calculate  $K_{I(exp)}$  accurately. However, fringes which were located extremely close to the tip were able to be used because they were not drawn accurately due to a large deformation near the tip. Hence, twenty-four fringes with fringe orders 0.85 (L/R), 0.9 (L/R), 0.95 (L/R), 1.05 (L/R), ..., 1.45 (L/R), where L/R indicated the fringes at the left and right of the crack shown in Fig.5, were selected to calculate  $K_{I(exp)}$ . Table 1 lists examples of  $K_{I(exp)}$  obtained by the proposed method. The error in  $K_{I(exp)}$  measurement decreased as the fringe order increased. The mean errors for four fringes with fringe orders 0.95 (L/R) and 1.05 (L/R) nearest to the 1st-order fringes, which were obtained by conventional techniques such as thinning, and for the twenty-four fringes were 4.3 % and 2.6 %, respectively. The mean error for eighteen fringes with fringe orders 1.05 (L/R), 1.1 (L/R), ..., 1.45 (L/R) was 0.9 %. The use of multiple fringes near the crack tip improved the accuracy of the measurement of the stress intensity factor.

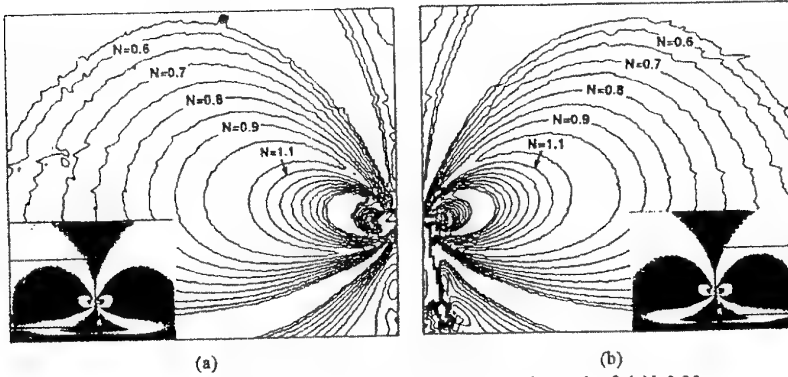


Figure 5. Contour maps of fringe order values drawn at intervals of  $\Delta N=0.05$ .

Table 1. Comparison between experimental and theoretical stress intensity factors,  $K_{exp}$  and  $K_{thy}$ .

Fringe used to calculate $K_{exp}$	$K_{exp}$ (MPa · mm <sup>1/2</sup> )	$K_{thy}$ (MPa · mm <sup>1/2</sup> )	Error (%) ( $=100 \cdot  K_{exp} - K_{thy}  / K_{thy}$ )
0.9(L/R)*	12.7		8.5
1.1(L/R)	11.9		1.7
1.2 (L/R)	11.7	11.7	0
1.3 (L/R)	11.7		0
1.4 (L/R)	11.7		0

\* L/R indicates the fringes at the left and right of the crack shown in Fig.5.

### 3.2 EXTRACTION OF ZERO POINT

The principal-stress directions obtained using the proposed method were used to extract the zero points in a T-shaped plate subjected to a compressive load,  $P$ , of 94IN, as shown in Fig.7. Furthermore, the zero points were used to design structural members with holes. This model was made of an epoxy resin plate of 6mm thickness,  $t$ , 3.6GPa Young's modulus,  $E$ , 0.36 Poisson's ratio,  $\nu$  and 0.1mm/N photoelastic sensitivity,  $\alpha$ .

#### 3.2.1 Measurement of Principal-Stress Direction

The principal-stress directions were obtained using the same technique as that described in Section 3.1.1 except for use of a white lamp instead of a mercury lamp.

Figure 8 is the image with the principal stress directions used for extracting zero points. In this figure, the black regions were assigned the value of  $\phi=0^\circ$ , and the white ones  $|\phi|=90^\circ$ . The regions changed from black to white as the value of  $|\phi|$  increased from  $0^\circ$  to  $90^\circ$ .

#### 3.2.2 Judgement of Zero Point

The extraction of zero points utilized the distribution of principal-stress directions around a zero point which differed from those around a regular point. To extract the positions of zero points, a window was moved on an image with the principal-stress directions, and the distribution around the center of the window was compared with a standard one at a zero point. If the distribution was similar to one of the standard ones, then the center was proposed to be a zero point[14].

Figure 9 shows the zero points superimposed on the isochromatics. The result shows that the location of the zero point extracted by the present method approximately agreed with that of the zero-order isochromatic. Table 2 lists the positions of the zero points extracted using the  $11 \times 11$  pixel window as well as that determined carefully by the naked eye with the aid of a graphic cursor moved on the image. The maximum difference between these coordinates was 1 pixel.

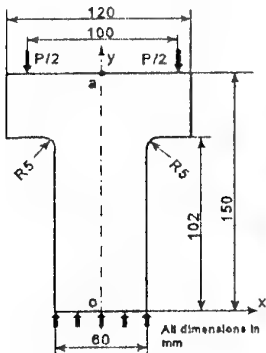


Figure 7. T-shaped plate subjected to compression load.

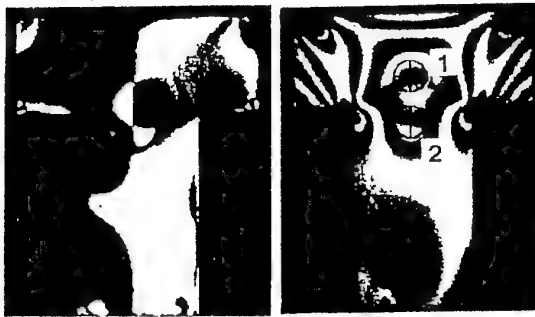


Figure 8. Principal-stress directions.

Figure 9. Zero points on isochromatics.

## GENERALIZED PHASE-SHIFTING METHOD

Table 2. CRT coordinates of zero points extracted using a window size of  $11 \times 11$  pixels and by the naked eye. (Unit:pixel)

Zero point no.	Position	
1	127,82	127,83*
2	127,111	127,111*

\* By naked eye

## 3.2.3 Application of Zero Points to Design of Structural Members

Holes are frequently made in structural members to decrease the weight of and to pass pipes and wires through these members with an external shape which cannot be changed. The holes should be made at locations at which the stresses in these members are lower than a required value. This is a kind of optimum design. In a plane stress problem, holes at positions where the normal stresses are equal, and the shear stress is zero are desirable. This point is just the zero point.

The stress distributions in structural members with different hole diameters at the zero and other points were analyzed by the finite-element method. The finite-element models had the same shape as that shown in Fig.7 without and with holes and the same material properties,  $E$  and  $\nu$ , and thickness,  $t$ , as the photoelastic one.

Figure 10 shows the positions of holes in the T-shaped plate. The holes at the zero points and the upper side were called Holes A, B and C, respectively. Hole diameters,  $D$ , of 3, 5, 10 and 15mm were used for each hole. The fringe orders,  $N$ , of the simulated isochromatics were obtained by multiplying  $(\sigma_1 - \sigma_2)$  obtained from the analysis and  $\alpha t$ .

Figure 11 is the relationship between the hole positions and the fringe orders around the holes. The fringe orders around the holes for Holes A and B were approximately constant. The maximum fringe order around the hole was in the case of Hole C. The compressive and tensile stresses alternated around the hole for Hole C, which were different from those in the case of Holes A and B. This implied that the original circular hole became an

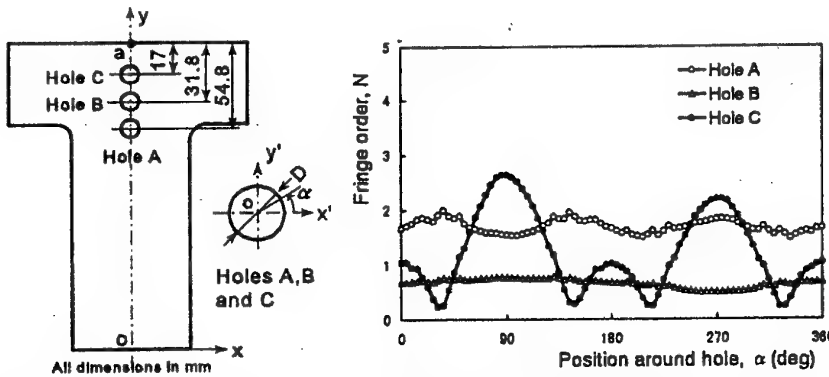


Figure 10. Positions of holes used in analytical models.

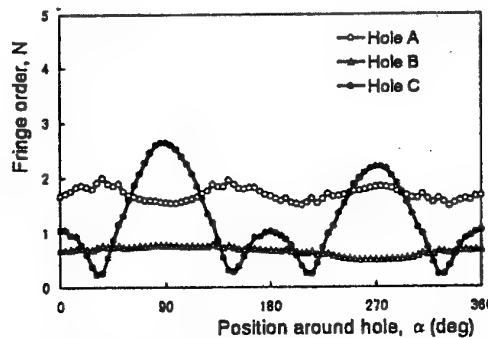


Figure 11. Comparison among fringe orders,  $N$  around Holes A, B and C with 3mm diameter.

elliptic one. The T-shaped plate with a hole at the zero point subjected to a compressive load was superior to those with holes at the other points.

The above results showed that the proposed method was effective in designing structural members with holes.

#### 4. Conclusions

A generalized phase-shifting method was developed for reducing the influence of noise caused by the variation in light intensity of a light source and so on, and for automatically measuring photoelastic parameters, relative fringe orders and principal-stress directions, in the whole field. The fringe orders obtained using the method was used to measure the stress intensity factor, and the principal-stress directions to extract the zero points. Furthermore the zero points were used to design structural members with holes. The stress intensity factor was accurately obtained from fringe loops multiplied using a technique for drawing a contour map of the fringe order values. The zero points were accurately extracted using a technique for judging the zero points, and were effective to design a plate with holes.

#### References

1. Umezaki, E., Tamaki, E., Shimamoto, A., and Takahashi, S.: Whole-field measurement of principal stress directions from photoelastic experiment using image processing system, in T.H. Hyde and E. Ollerton (eds.), *Applied Stress Analysis*, Elsevier Applied Science Publishers, London, 1990, pp.526-535.
2. Patterson, E.A., and Wang, Z.F.: Towards full field automated photoelastic analysis of complex components, *Strain*, 27-2 (1991), 49-56.
3. Haake, S.J., and Patterson, E.A.: Photoelastic analysis of frozen stressed specimens using spectral-contents Analysis, *Experimental Mechanics*, 32-3(1992), 266-272.
4. Morimoto, Y., Morimoto, Y. Jr, and Hayashi, T.: Separation of isochromatics and isoclinics using Fourier transform, *Experimental Techniques*, 18-5(1994), 13-17.
5. Ajovalasit, A., Barone, S., and Petrucci, G.: Toward RGB photoelasticity: full field automated photoelasticity in white light, *Experimental Mechanics*, 35-3(1995), 29-34.
6. Umezaki, E., Watanabe, H., and Shimamoto, A.: Automatic whole-field measurement of photoelastic fringe orders using generalized phase-shift method, *Post Conf. Proc. VIII Int. Cong. On Experimental Mechanics*, Nashville, 1996, pp.154-159.
7. Gotoh, J., Yoneyama, S., Mawatari, S., and Takashi, M.: Photoelastic analysis from a single piece of image with linearly polarized RGB lights, *Post Conf. Proc. VIII Int. Cong. On Experimental Mechanics*, Nashville, 1996, pp.160-166.
8. Ramesh, K., and Deshmukh, S.S.: Automation of white light photoelasticity by phase-shifting technique using colour image processing hardware, *Optics and Lasers in Engineering*, 28-1(1997), .47-60.
9. Hoy, D.E.P.: On the use of color imaging in experimental applications, *Experimental Techniques*, 21-4(1997), 17-19.
- 10 Umezaki, E., and Kawakami, T.: Measurement of principal-stress directions from photoelastic experiment using generalized phase-shift method, *Optical Review*, 4-2(1997), 249-252.
11. Umezaki, E., Koike, H., Shimamoto, A., and Watanabe, H.: Accuracy of measurement of photoelastic fringe orders and principal-stress directions using phase-shift method, *I. Japan Society for Non-Destructive Inspection* (in Japanese), 45-1(1996), 61-67.
12. Takahashi, S., and Nogata, F.: Application of photoelastic method to mechanical engineering (1), *Science of Machine* (in Japanese), 38-1(1986), 82-86.
13. Okamura, H.: *Introduction to linear fracture mechanics* (in Japanese), Baihukan, Tokyo, 1976, pp 218-219.
14. Umezaki, E., Watanabe, H., Sirichai, S., and Shimamoto, A.: Extraction of singular points from photoelastic experiment, in J.F.S. Gomes et al. (eds.) *Recent Advances in Experimental Mechanics*, A.A. Balkema, Rotterdam, 1994, pp. 107-112.

## SOLUTION OF FRACTURE PROBLEMS BY NON-LINEAR PHOTOELASTIC METHODS UNDER SIGNIFICANT ELASTIC AND PLASTIC STRAINS

MARAT AKHMETZYANOV, GALINA ALBAUT, VIKTOR  
BARYSHNIKOV  
*Novosibirsk State University of Architecture and Construction*

### Abstract

In this study the problems of fracture mechanics having geometrical and physical non-linearity were experimentally investigated by non-linear photoelastic methods. The strains changed in the range from -50% till +220% of relative lengthening. Changes in geometry and in thickness of the specimens were taken into consideration. Here, non-compressible optically active polyurethane rubber was applied. Two schemes of polarizative-optical tests were used: 1) through translucence of rubber specimens; 2) photoelastic coating method for the study of significant plastic strains in metals.

The main equations of the method evolved to verify experimental data are presented in this paper, and some elastic and plastic problems are studied as examples. Stress-strain state in rubber plates with cracks was determined, the cracks taking ellipse or round forms under deformation. The inclined crack affect upon stress concentration coefficients  $k_c$  and strain coefficients  $k_e$  at its tip was studied. Applying the photoelastic coating method, the behaviour of concentration coefficients  $k_c$  and  $k_e$  was investigated in the specimens made of middle steel and having cuts of different outlines and in the weldment of mild steel under plastic deformation. Common laws were ferreted out with respect to the distribution of stress fields in the prefailure zone near cracks, also, the tendency of functions  $k_c$  and  $k_e$  to change under the increasing strains for different outlines' specimens made of different sorts of steel was showed up.

### 1. Introduction

Structural design for new rubber-like or composite materials is mathematically hampered especially in view of concentrators or cracks. The same kind of thing applies to metal structural elements working at the prefailure stage under significant plastic strains. Some of the assumptions and hypotheses used in structural design must be experimentally tested and verified. The non-linear photoelastic method enables to solve similar problems through experiments.

## 2. General Relationships

When investigating significant plastic strains in rubber specimens, to measure stresses the true stress values were taken ( $\delta_1$  and  $\delta_2$  as the main components in the specimen's plane and  $\delta_3$  being equal to 0 along perpendicular); to measure strains in the specimen's plane the extents of lengthening  $\lambda_1$  and  $\lambda_2$  were exploited while  $\lambda_3$  evaluated the strains in specimen's thickness. By the study of large plastic strains carried out by means of photoelastic coating method the lengthening extents were converted into logarithmic strains according to Hencky ( $\varepsilon_i = \ln \lambda_i$ ,  $i=1,2,3$ ). Below there is a set of relations to treat the experimental data for SKU-6 polyurethane specimens: (1) non-changeable volume condition; (2) differential equilibrium equation for a plane problem; (3) stress-strain connection equation exploiting Bartenev-Khazanovitch's elastic potential; (4) the general law of non-linear photoelasticity; (5) the corresponding optic-strain relationship.

$$\lambda_1 \lambda_2 \lambda_3 = 1 ; \quad (1)$$

$$\frac{\partial(\lambda_3 \sigma_x)}{\partial x} + \frac{\partial(\lambda_3 \tau_{xy})}{\partial y} = 0 ; \quad \frac{\partial(\lambda_3 \sigma_y)}{\partial x} + \frac{\partial(\lambda_3 \tau_{yx})}{\partial y} = 0 ; \quad (2)$$

$$\sigma_1 = A(\lambda_1 - \lambda_3) ; \quad \sigma_2 = A(\lambda_2 - \lambda_3) ; \quad (3)$$

$$\sigma = C_\sigma \lambda_3 h_0 (\sigma_1 - \sigma_2) ; \quad (4)$$

$$\sigma = C_c \lambda_3 h_0 (\lambda_1 - \lambda_2) ; \quad (5)$$

when  $A$  is elastic constant,  $\sigma$  – optical path difference,  $C_\sigma$  and  $C_c$  – stress and strain optical constants,  $h_0$  – initial thickness [1].

Simple equations (3) are not universal, they approximate elastic properties of polyurethane SKU-6 quite well. Other kinds of rubber are advantageously characterised by relations (6) comprising 4 constants resulted from Mooney-Rivlin's theory of strains and the corresponding optic-strain relationship (7).

$$\begin{aligned} \sigma_1 &= 2(A_2 + B_2 \lambda_2^2)(\lambda_1^2 - \lambda_3^2) + 4(A_4 + B_4 \lambda_2^4)(\lambda_1^4 - \lambda_3^4) ; \\ \sigma_2 &= 2(A_2 + B_2 \lambda_1^2)(\lambda_2^2 - \lambda_3^2) + 4(A_4 + B_4 \lambda_1^4)(\lambda_2^4 - \lambda_3^4) ; \end{aligned} \quad (6)$$

$$\sigma = C_c h_0 \lambda_3 (2(A_2 + B_2 \lambda_3^2)(\lambda_1^2 - \lambda_2^2) + 4(A_4 + B_4 \lambda_3^4)(\lambda_1^4 - \lambda_2^4)) . \quad (7)$$

In this paper, the separation of stresses and strains is fulfilled by means of the method of numerical integration of equilibrium equations (2), with the subsequent use of the rest of the relations in the set (1)-(5) [2].

There have been worked out some other separation methods: measuring cross strain method, method of coating cutting, tilted translucence method, etc.

### 3. Stress-Strain State in Tensioned Rubber Plate With Crack

The investigation results of axial and biaxial tension of 3 polyurethane plates of different thickness (the upper specimen is of 3 mm thickness and the others are 1,2 mm thick) and having cracks that took the ellipse or round shapes under tension are presented in fig.1. One of the plates has several round holes at the tip of the crack and corresponds to the theoretical model. For all the specimens the fringe patterns were obtained, isoclinic fields were plotted and the complete separation of stresses and strains was fulfilled owing to the method of numerical integration of equilibrium equations (2) with due regard to thickness changes. For some vertical sections the stress sheets  $\sigma_x$ ,  $\sigma_y$  were plotted, biaxial tension was characterised by  $\sigma_x - \sigma_0$  epures. When studying these curves, one should notice that the maximum  $\sigma_y$  is marked not at the tip of the crack but inside a specimen, also, certain laws concerning stress distribution  $\sigma_x$  and  $\sigma_x - \sigma_0$  under axial and biaxial tension respectively are brought about there: the curves are waved and reverse the sign along the vertical axis, thus, the sum of projections of all forces on the x-axis is self-equilibrium.

Experimental data on how the inclined crack affects  $k_\sigma$  and  $k_e$  are presented for 4 initial slope values: 0°, 30°, 45°, 60° (fig.2). Fig.2 includes a loading scheme, fringe patterns, diagrams of changing slopes of ellipses axes as cracks take ellipse forms, diagrams demonstrating the behaviour of  $k_\sigma$  and  $k_e$  by increasing strains. Here, it should be mentioned that initial tips of the inclined cracks (points A in fringe patterns) do not coincide with the ellipses' tips, besides, the coefficients of stress and strain concentration decrease while increasing the nominal strains. All curves tend to some asymptotic values, for instance, the curve  $k_\sigma$  has the asymptote 2 when  $\alpha_0=0$ .

### 4. Determination of Stress Concentration in Steel Specimens Under Plastic Strain by Photoelastic Coating Method

Tests were carried out for 3 middle steel stripes having cuts of different forms: circular one, V-form and U-form (fig.3). Besides, the mild steel stripe with the weldment was exposed to tension (fig.4). Photoelastic coating presenting the combination of epoxy glue and polyurethane rubber covered the specimens at both sides. Fig.3, 4 represent the specimens' schemes, the fringe patterns in coating at several stages of loading, the

tension diagrams for the steel samples used and the graphs illustrating the behaviour of  $k_\sigma$  and  $k_e$  depending on the nominal value of logarithmic strains.

Studying the graphs  $k_\sigma$  and  $k_e$  for the specimens of different kinds of steel having the expressed yielding sections, one can ascertain general laws for the both graphs. When passing through the yielding section, all the graphs  $k_\sigma$  have the abrupt local minimum and those of  $k_e$  have the local maximum. Further, these graphs become quieter, but from the point of view of increase-decrease their behaviour can be regarded as reverse and satisfying H. Neuber's relationship  $k = \sqrt{k_\sigma \cdot k_e}$ , when  $k$  is concentration coefficient under insignificant strains. Judging by fig.4, this relationship is satisfied only for 3% strains.

### Conclusion

In this investigation, the methods of experimental stress-strain determination in prefailure zone are exploited, these are non-linear photoelastic methods. The experiments made revealed the facts that stresses were characterised as finite and defined, thus, they verified the theoretical crack model of Barenblatt-Khristianovich. Also, some general rules are noted for stress distribution near cracks.

The reliable method of determination of stress and strain concentration coefficients is offered and approved for non-linear problems under finite strains. Then, the paper proves that under significant strains the coefficients  $k_\sigma$  and  $k_e$  are the functions of the strain state. The experiments bring about the fact that Neuber's relationship considering  $k$ ,  $k_\sigma$  and  $k_e$  is valid for steel, but it doesn't work for rubber-like materials. Also, the tendency of smooth stress concentration coefficients to decrease at the cracks' tips, when strains increase both under great elastic and plastic strains, is observed. Investigations were sponsored by the Russian Fund of Fundamental Investigations (project No.98-01-00302).

### References

1. Albaut, G. and Baryshnikov, V.: *Investigation of Mechanics of Fracture Problems by Non-linear Photoelastic Method*. Proc. SPIE. Vol.2791, 1996, pp. 56-67.
2. Treloar, L.: *The Physics of Rubber Elasticity*. Oxford, 1949, p. 240.

## SOLUTION OF FRACTURE PROBLEMS

Isochromatic fringe patterns

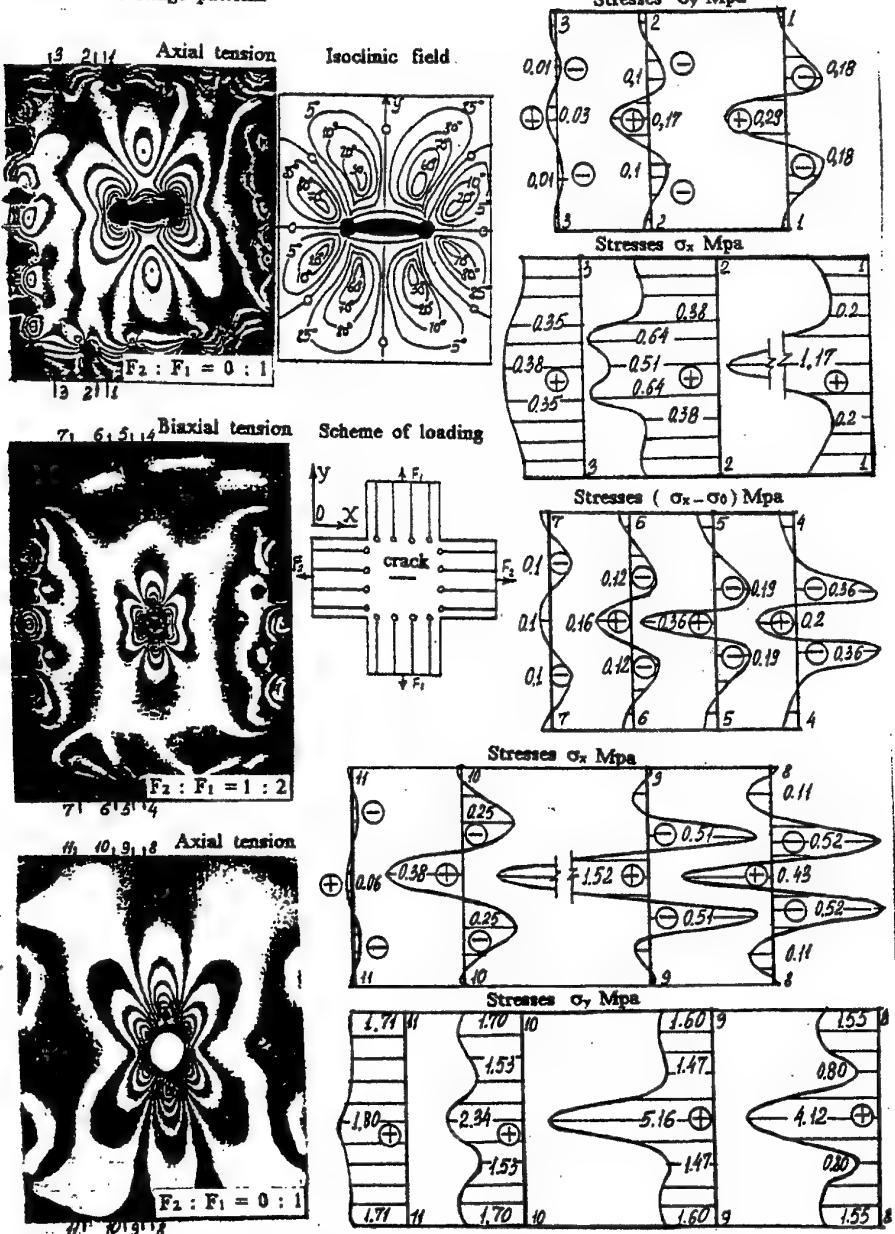


Figure 1. Stress determination in the rubber specimens with the crack

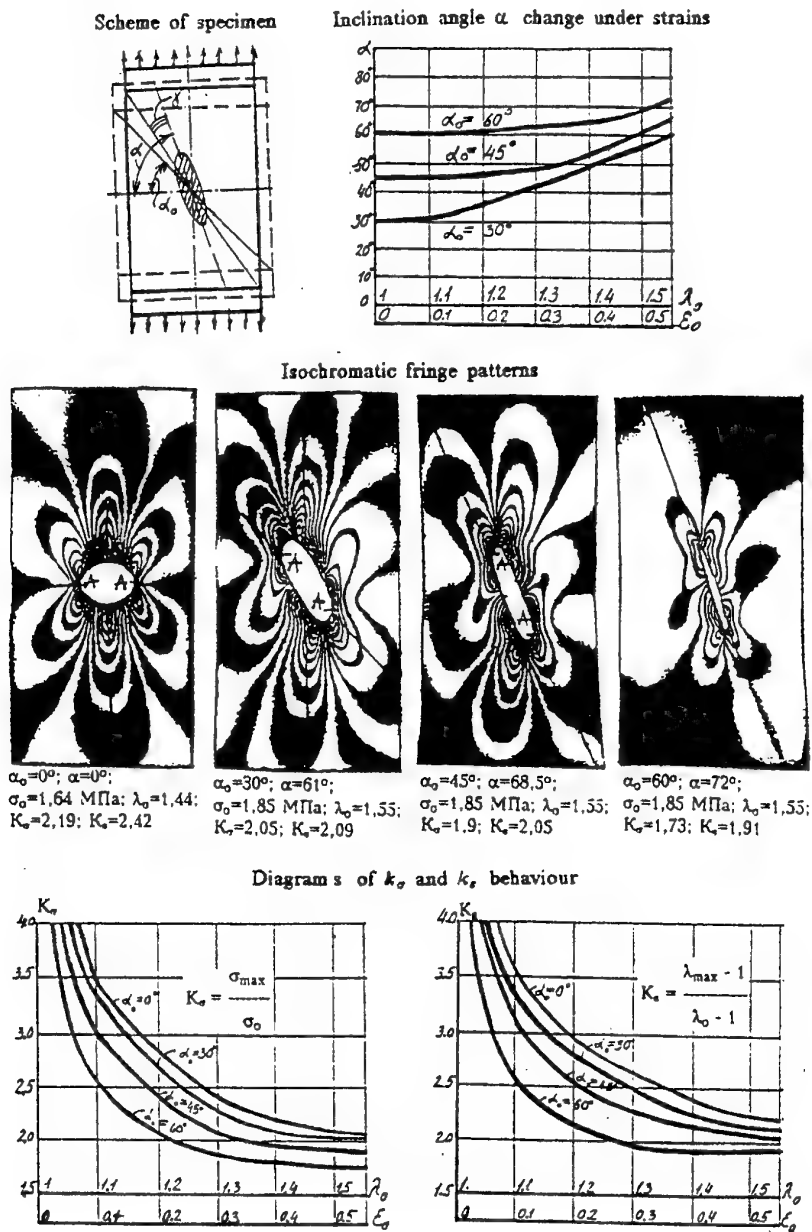


Figure 2. Inclined cracks affecting  $k_g$  and  $k_e$  behaviour under strains increase for rubber specimens

## SOLUTION OF FRACTURE PROBLEMS

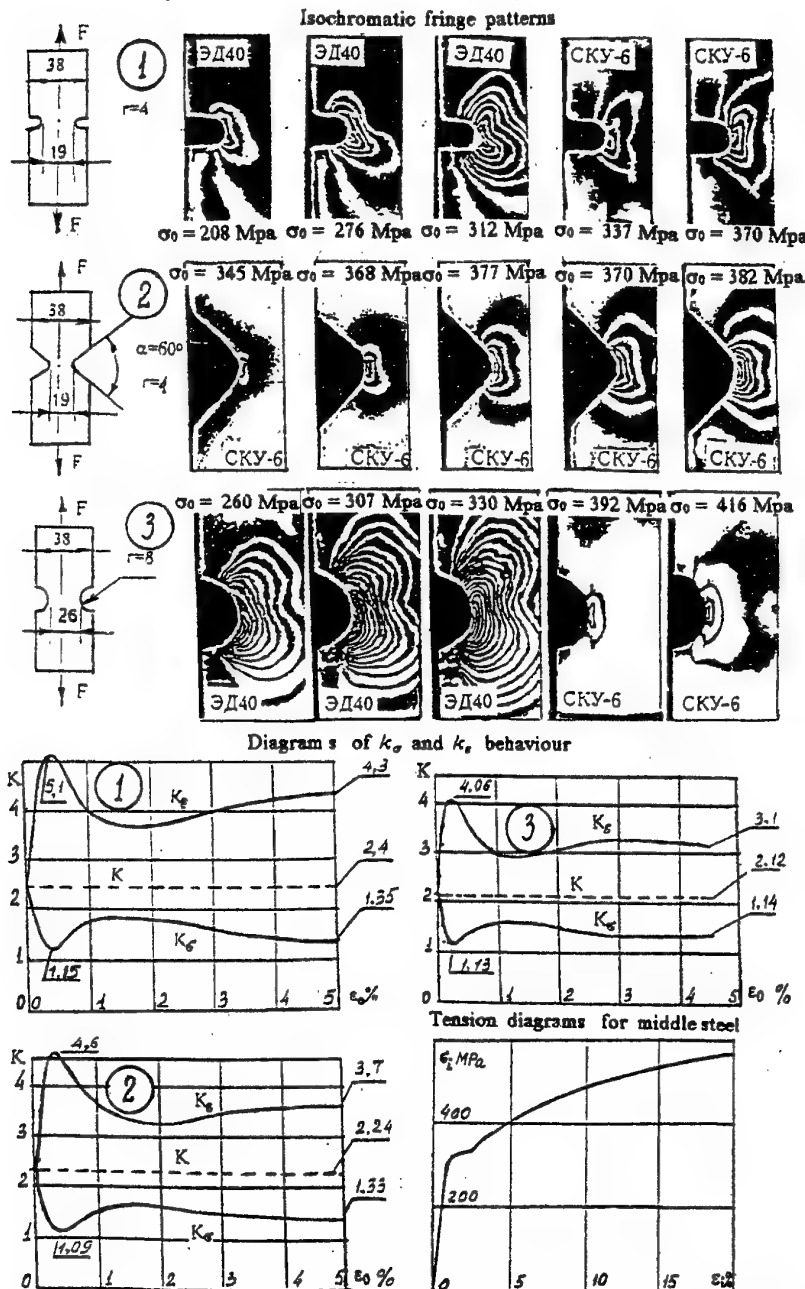


Figure 3. Study of  $k_\sigma$  and  $k_e$  behaviour for developed plastic strains in the steel specimens with different cuts by photoelastic coating method

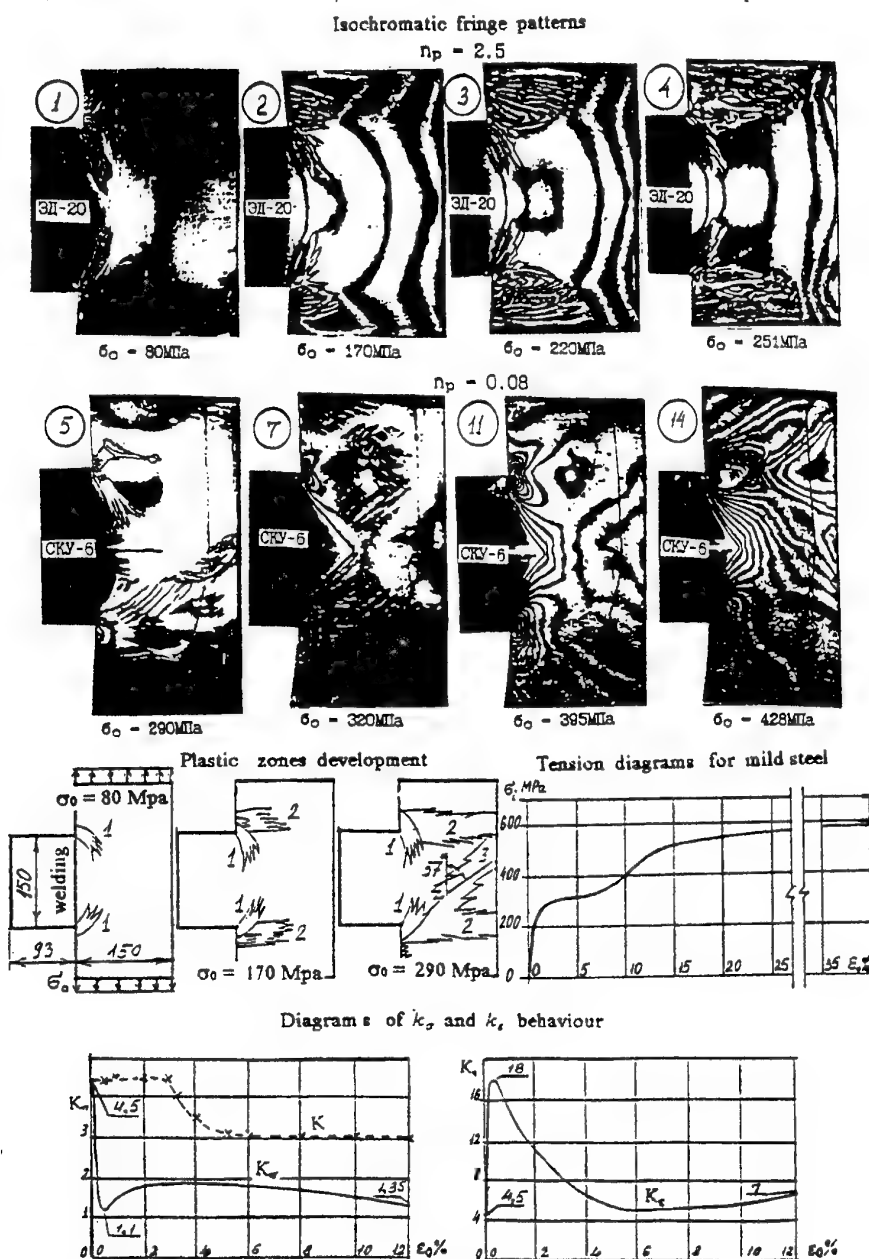


Figure 4. Study of  $k_\sigma$  and  $k_\epsilon$  behaviour for developed plastic strains in the steel welded specimens under tension by photoelastic coating method

## APPLICATION OF DYNAMIC ORTHOTROPIC PHOTOELASTICITY

LI Zheng  
LIU Haixiao  
WANG Wenyang  
*Department of Mechanics and Engineering Science  
Peking University, Beijing 100871, China*

### Abstract

A stress-optic law for dynamic orthotropic photoelasticity is developed from the static stress-optic law. Based on this law, the general dynamic photoelasticity has been successfully reformed for application to orthotropic composite material in this paper. Dynamic photoelastic stress analysis has been performed for an orthotropic plate with a hole, which is subjected to compressive impact with the direction of perpendicular and parallel to the reinforcement direction. Under the dynamic process the stress wave propagation is investigated from these orthotropic birefringent patterns recorded by a Cranz-Schardin type multiple sparks camera.

### 1. Introduction

Recently photoelasticity has been successfully formulated for application to orthotropic composite materials by several authors. They paid more attentions to develop the stress-optic law for the birefringent fiber-reinforced composite materials. Sampson (1970) proposed a stress-optic relation that is combined the components of the birefringence for plane-stress problems by using a Mohr circle. Dally and Prabhakaran (1971), using a micromechanical approach, developed a uniaxial stress-optic law based on simple stress-strain models. The biaxial-stress-optic law was verified experimentally by employing strain-gage rosettes on a unidirectionally reinforced circular disk under diameter compression (Prabhakaran, 1975). Along the other line, Pipes and Rose (1974) obtained a strain-optic law for a certain class of birefringent composites. Later, Prabhakaran (1975) derived a general strain-optic law for orthotropic model materials from the concept of Mohr circle of birefringence. Although these laws have successfully applied to some plane stress problems of orthotropic composite materials, there are still some differences between experimental and theoretical results due to the influences of residual stresses. Knight and Pih (1976) firstly gave the general treatment of anisotropic photoelasticity to include the effects of an arbitrary residual birefringence. Hahn and Morris (1978), Hyer and Liu (1984) further provided a more perfect stress-optic relation.

In this paper, a general dynamic photoelasticity is reformed to study stress wave

propagation in orthotropic birefringent materials. The development of stress-optic law is derived from the static Hyer and Liu law. The model materials are glass-fiber-reinforced materials with the glass fibers in only one direction, rendered transparent by carefully matching the refractive indices of the fibers and the matrix. Dynamic photoelastic stress analysis has been performed for an orthotropic plate with a hole, the specimen is contained 5% reinforcement by volume, and subjected separately to compressive impact with the perpendicular and parallel directions to the reinforcement direction. According to the stress-optic law for dynamic orthotropic birefringent materials, the stress wave propagation is investigated and calculated from these photoelastic patterns.

## 2. Stress-optic Law for Dynamic Case

For static situation, stress-optic law included the effects of residual birefringence is derived by Hyer and Liu, and has been accepted extensively. This law is suitable to investigate many plane-stress problems in the fields of orthotropic solid mechanics. According to the developmental process of general dynamic stress-optic law, we propose a dynamic stress-optic law for orthotropic composite materials based on the Hyer and Liu law. So, we give the stress-optic relation on the x, y coordinate system in the form

$$N_T = \left\{ \left( \frac{\sigma_x}{C_1} - \frac{\sigma_y}{C_2} + \frac{\tau_{xy}}{C_3} + N_R \cos 2\delta_R \right)^2 + \left[ 2 \left( \frac{\sigma_x - \sigma_y}{C_4} + \frac{\tau_{xy}}{C_5} \right) + N_R \sin 2\delta_R \right]^2 \right\}^{1/2}$$

where

$$\begin{aligned} \frac{1}{C_1} &= d \left( \frac{\cos^2 \theta - \sin^2 \theta}{f_1} \right), & \frac{1}{C_2} &= d \left( \frac{\cos^2 \theta - \sin^2 \theta}{f_2} \right) \\ \frac{1}{C_3} &= d \left( \frac{1}{f_1} + \frac{1}{f_2} \right) \sin 2\theta, & \frac{1}{C_4} &= -\frac{d \sin \theta \cos \theta}{f_{12}} \\ \frac{1}{C_5} &= \frac{d(\cos^2 \theta - \sin^2 \theta)}{f_{12}} \end{aligned}$$

$N_T$  is the total instantaneous fringe order of the orthotropic model,  $N_R$  and  $\delta_R$  separately indicate the fringe order and the isoclinic angle of residual birefringence,  $f_1$ ,  $f_2$  and  $f_{12}$  are three principal dynamic material-fringe values,  $d$  is model thickness,  $\theta$  is the angle between the fiber orientation and x-axis.  $N_R$  and  $\delta_R$  can be directly measured from the specimen under traction-free state. Direct measurements of the stress-optic coefficients and mechanical material properties in the law are achieved through tests of impact compressive specimens with fiber orientation parallel (0-degree), perpendicular (90-degree) and at 45° degree to the direction of the applied uniaxial stress.

Combining the tests of dynamic photoelasticity and electrical-resistance strain gages about the same specimen, the validity of proposed dynamic stress-optic law of orthotropic birefringent materials can be examined. Now, the uniaxial and biaxial specimens of orthotropic birefringent materials under impact compression have performed respectively along 0-degree, 90-degree and 45-degree orientations, and we get quite similar experimental results about these two kinds of methods.

### 3. Experimental Work

Transparent, unidirectional glass fiber/epoxy resin composite with about 5-volume-percentage glass, is prepared by carefully matching the refractive indices of the fibers and the matrix, and utilized for model. The experimental system is a general transmission arrangement of Cranz-Schardin type. The orthotropic plate 4.8mm in thick with a hole is loaded in impact compression with the loading direction parallel and perpendicular to the reinforcement direction. During the dynamic process orthotropic birefringent patterns are recorded by a Cranz-Schardin type multiple sparks camera, as shown in Fig. 1 and Fig. 2. Based on the stress-optic law for dynamic orthotropic birefringent materials, the stress wave propagation can be represented by these photoelastic patterns.

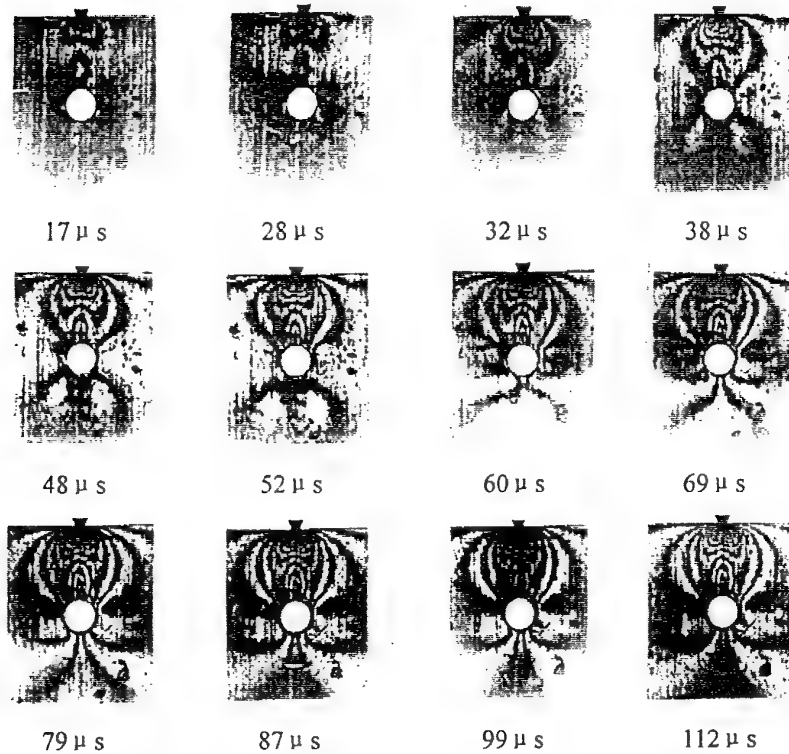


Fig. 1 A series isochromatic-fringe patterns about 0-degree specimen under impact load

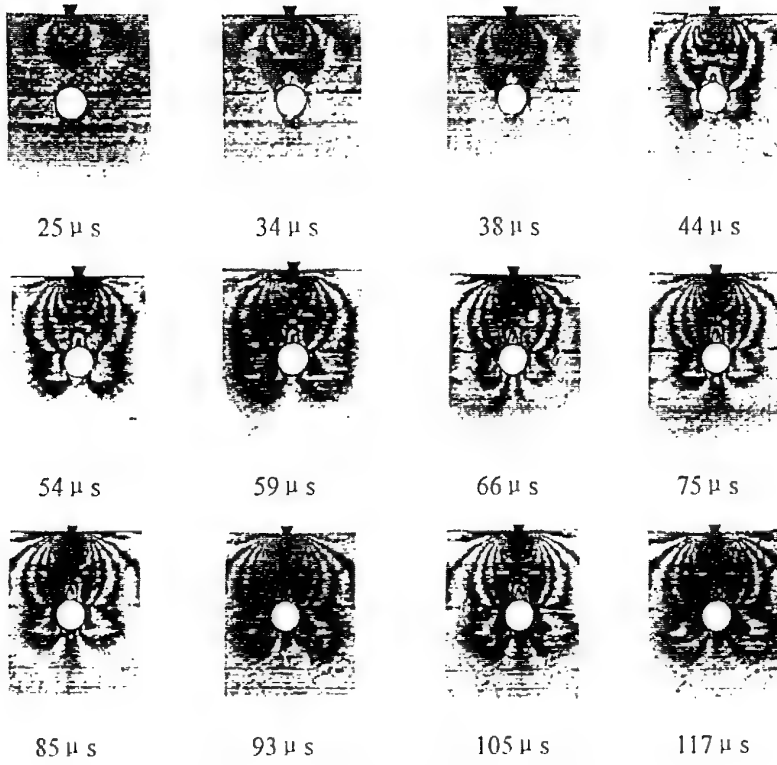


Fig. 2 A series isochromatic-fringe patterns about 90-degree specimen under impact load

#### 4. Results and Discussion

The dynamic photoelastic constants and other dynamic material coefficients of the anisotropic model are measured by presented in Section 2, as shown in table 1.

TABLE I. Dynamic material coefficients

$E_1$ (GPa)	$E_2$ (GPa)	$G_{12}$ (GPa)	$v_{21}$	$v_{12}$	$f_1$ (KN/m·fringe)	$f_2$ (KN/m·fringe)	$f_{12}$ (KN/m·fringe)
7.66	4.27	1.60	0.36	0.20	49.18	36.71	36.71

From these isochromatic-fringe patterns in Fig. 1 and Fig. 2, we can notice that the residual birefringent fringes are unavoidable for the orthotropic material, and the residual stresses are tensile stress along the reinforcement direction. By comparison with the dynamic isochromatic patterns of an isotropic specimen subjected to the same impact load (as shown in Fig. 3), it is obvious that the transient orthotropic fringes depends on the propagation direction of stress wave.

The reflection and propagation of stress wave around the circle hole can be clearly illustrated by these patterns. Furthermore, the transient stress distribution can be obtained from the stress-optic law by using material coefficients in table 1. The results indicate that for these three specimens the tensile stresses of the circle hole edge along

the diameter are very similar, but the compressive stresses on the both sides around the hole for 0-degree specimen are bigger than the other two specimens. Therefore, the dynamic orthotropic photoelasticity is a convenient method to study the dynamic response in orthotropic materials.

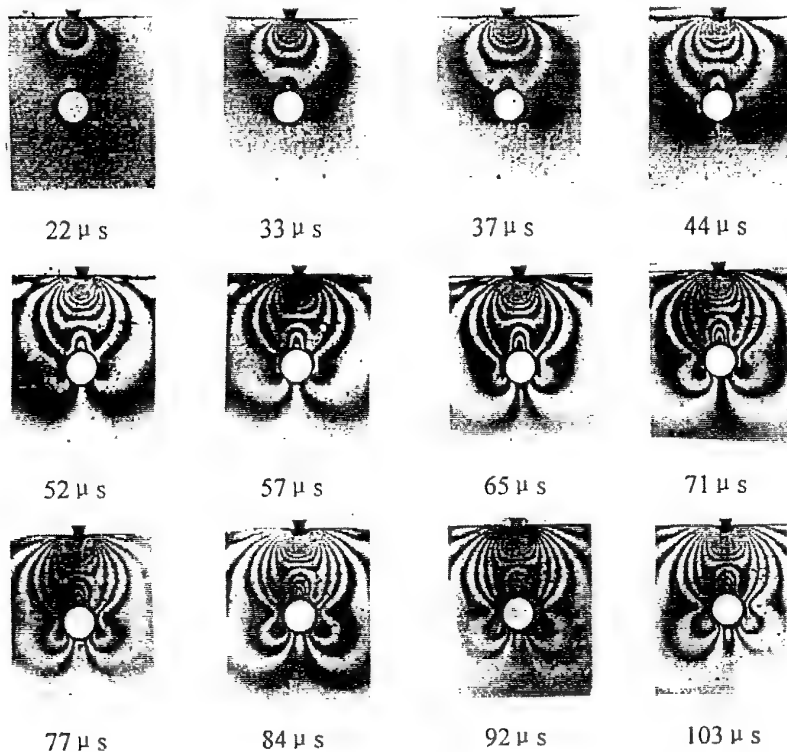


Fig. 3 A series isochromatic-fringe patterns about isotropic specimen under impact load

## References

Sampson, R.C. (1970) A stress-optic law for photoelastic analysis of orthotropic composites, *Experimental Mechanics* **10**, 210-215.

Dally, J.W. and Prabhakaran, R. (1971) Photo-orthotropic-elasticity, *Experimental Mechanics* **11**, 346-356.

Prabhakaran, R. (1975) On the stress-optic law for orthotropic-model materials in biaxial-stress fields, *Experimental Mechanics* **15**, 29-34.

Pipes, R.B. and Rose J.L. (1974) Strain-optic law for a certain class of birefringent composites, *Experimental Mechanics* **14**, 355-360.

Prabhakaran, R. (1975) Strain-optic law for orthotropic model materials, *AIAA Journal* **13**, 723-728.

Knight, C.E. and Pilh, H. (1976) Orthotropic stress-optic law for plane stress photoelasticity of composite materials, *Fibre Science and Technology* **9**, 297-313.

Hahn, H.T. and Morris, D.H. (1978) Anisotropic photoelasticity with application to composites, *Fibre Science and Technology* **11**, 113-125.

Iyer, M.W. and Liu D.H. (1984) An assessment of the accuracy of orthotropic photoelasticity, *NASA Rep. 3773*.

## HYBRID STRESS ANALYSIS BY CONSTRUCTION OF APPROXIMATE ANALYTICAL SOLUTION

Masahisa Takashi and Shizuo Mawatari  
Aoyama Gakuin University  
6-16-1 Chitosedai, Setagaya, Tokyo 157-8572, Japan

### 1. Introduction

Methods for elastic stress/strain analysis are broadly classified into the well known three categories, namely theoretical, experimental and computational analyses. Although some merits and demerits surely exist in all cases, there still exist some difficulties for each method in the categories to accomplish analysis by itself in closed form involving error estimation under general mechanical conditions. The authors have investigated for long time on a new hybrid method which reconstitutes together not only basic concepts but also various techniques involved in the three categories, in order to improve the accuracy and preciseness of 2-D and 3-D elastic stress/strain analysis. The fundamental concepts of the method have been already proposed in the previous paper [1]. In this paper, the authors discuss a method for the determination of unknown coefficients involved in the discretized representative function of analytical solution in Somigliana type.

### 2. Formal Solution of Displacement

#### 2.1. STRUCTURAL EQUATION OF DISPLACEMENT

It is well known that there are several types of formulation for the structural equation of elastic stress/strain analysis. In this paper, for convenience, the authors adopt the Navier equation in a closed bounded domain  $G \in R^n$  ( $n = 2$  or  $3$ ) having the piecewisely smooth boundary  $\partial G$ . The equation about displacement  $u$  is expressed as;

$$\Phi u(x) = \mu \Delta u(x) + (\lambda + \mu) \operatorname{grad} \operatorname{div} u(x) = -f(x) \quad (x \in G) \quad (2.1)$$

where  $\lambda$  and  $\mu$  are Lamé's constants,  $f(x)$  is body force on  $G$ .

## 2.2. DISTRIBUTION EXPRESSION OF DISPLACEMENT

Let  $\Gamma(x)$  be an elementary solution of Eq. (2.1). One of the distribution solutions of Eq. (2.1) is expressed as;

$$u(x) = - \int_G \Gamma(x-y) \Phi u(y) dy + \int_{\partial G} \left\{ \Gamma(x-y) \frac{du(y)}{dn} - \left\{ \frac{d\Gamma(x-y)}{dn_y} \right\} u(y) \right\} ds \quad (2.2)$$

where, in case of  $n = 2$ ,

$$\Gamma(x) = \frac{1}{8\pi\mu(1-\nu)} \begin{bmatrix} R_v + \frac{\partial r}{\partial x_1} \cdot \frac{\partial r}{\partial x_1} & \frac{\partial r}{\partial x_1} \cdot \frac{\partial r}{\partial x_2} \\ \frac{\partial r}{\partial x_2} \cdot \frac{\partial r}{\partial x_1} & R_v + \frac{\partial r}{\partial x_2} \cdot \frac{\partial r}{\partial x_2} \end{bmatrix}$$

$$\text{where } r = \sqrt{x_1^2 + x_2^2}, \quad R_v = (3-4\nu) \log \frac{1}{r}$$

and in case of  $n = 3$ ,

$$\Gamma(x) = \frac{1}{16\pi\mu(1-\nu)r} \begin{bmatrix} (3-4\nu) + \left( \frac{\partial r}{\partial x_1} \right)^2 & \frac{\partial r}{\partial x_1} \cdot \frac{\partial r}{\partial x_2} & \frac{\partial r}{\partial x_1} \cdot \frac{\partial r}{\partial x_3} \\ \frac{\partial r}{\partial x_2} \cdot \frac{\partial r}{\partial x_1} & (3-4\nu) + \left( \frac{\partial r}{\partial x_2} \right)^2 & \frac{\partial r}{\partial x_2} \cdot \frac{\partial r}{\partial x_3} \\ \frac{\partial r}{\partial x_3} \cdot \frac{\partial r}{\partial x_1} & \frac{\partial r}{\partial x_3} \cdot \frac{\partial r}{\partial x_2} & (3-4\nu) + \left( \frac{\partial r}{\partial x_3} \right)^2 \end{bmatrix}$$

$$\text{where } r = \sqrt{x_1^2 + x_2^2 + x_3^2}$$

## 3. EQUIVALENT TRANSFORMATION OF BOUNDARY CONDITION

Unknown function  $u(y)$  on  $\partial G$  in Eq. (2.2) has to be determined as to fit with boundary conditions.

### 3.1. PROBLEMS IN BOUNDARY CONDITIONS

Boundary condition is usually expressed with Dirichlet, Nuemann, Robin condition or their combination. Furthermore, since the original domain deforms under load, Euler or Lagrangian coordinate system has to be selected in order to discriminate the state before and after deformation, in a strict sense. However, since the shape of boundary after deformation and transformation formulae from one state to another is not known in advance, a certain consideration is necessary to handle boundary conditions.

### 3.2. UTILIZATION OF EXPERIMENTAL DATA

In order to avoid the difficulties mentioned above, the authors have proposed to utilize reliable experimental data in actual situation. Here, we pay attention to some data of fringe order of isochromatics in photoelasticity.

### 3.3. THEOREM OF RELATIVE FRINGE ORDER

The determination of fringe order of isochromatics is somewhat delicate in general. When we look at two different fringes, however, the difference of orders between them could be found easily, then the concept of relative fringe order comes up.

Let a domain  $D$  be a part of an isochromatics image pattern. Retardation  $\delta$  is connected with principal stress difference as

$$\delta = \frac{2\pi c}{\lambda} d(\sigma_1 - \sigma_2) \quad (3.1)$$

where  $\lambda$  is the wave length of incident light,  $c$ : photoelastic constant and  $d$ : specimen thickness. The brightness intensity of isochromatics in the dark field,  $I$ , is expressed as;

$$I = a^2 \sin^2 \left( \frac{\delta}{2} \right) \quad (3.2)$$

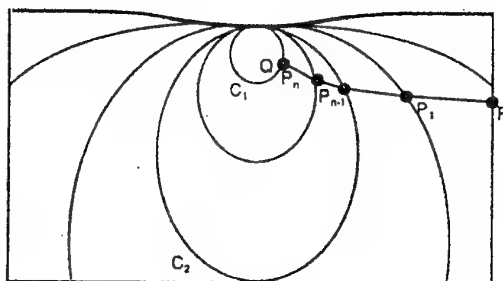


Figure 1. Schematic diagram of explanation for relative fringe order

Here, let us call a point at which  $\delta = m\pi$  ( $m$ : integer) as a fringe point. In Fig.1, curves  $C_i$  except a curve  $[P, P_1, \dots, P_n]$  and boundary lines show isochromatics schematically. On point  $P \in D$ , we denote the values of  $I$  and  $\delta$  as  $I(P)$  and  $\delta(P)$ , respectively. Taking another fringe point  $Q \in D$ , let us consider a continuous curve  $C \subset D$  which is connecting points  $P$  and  $Q$ ;

$$C : t \rightarrow C(t) \in D \quad (0 \leq t \leq 1), \quad C(0) = P \text{ and } C(1) = Q. \quad (3.3)$$

The point  $P$  is called as a regular point, when the following two conditions are satisfied. 1)  $\delta$  varies from  $P$  to  $Q$  on curve  $C$  monotonically, and 2) between  $P$  and  $Q$ , there exist at least one fringe point excluding themselves. Then, the point  $Q$  and the curve  $C$  are named as a fringe point and a curve subordinating to the regular point  $P$ .

Let  $P$  be the regular point and  $Q$  the subordinating point. A point array  $\{P_k\}_{k=1}^n$  is called as a fringe point resolution of the regular point  $P$ , when we can recognize the following facts such as; i)  $P_k = C(t_k)$  ( $0 = t_0 < t_1 \dots < t_n = 1$ ), ( $1 \leq k \leq n-1$ ) is all fringe points, and ii) there is no fringe point in an open interval  $(t_{k-1}, t_k)$ . In this context, the following relation is obtained;

$$\frac{1}{2}|\delta(P) - \delta(Q)| = \frac{1}{2}(n-1)\pi + \alpha \quad (3.4)$$

where

$$\alpha = \text{Sin}^{-1} \left[ \left\{ \frac{|I(P) - I(P_1)|}{|I(P_{n-1}) - I(P_n)|} \right\}^{\frac{1}{2}} \right]. \quad (3.5)$$

When  $P$  lies on a fringe point, the value of  $\alpha$  comes to  $\pi/2$ . We call here the right hand side in Eq. (3.4) the relative fringe order. Relative fringe order is equivalent to boundary condition within the domain governed by corresponding structural equation, namely an equivalent transformation of boundary condition. Thus, we can treat hereafter the relative fringe order as an alternative of boundary condition.

#### 4. Discretization of Representative Function in Terms of Stress Components

##### 4.1. THE FORM OF REPRESENTATION OF STRESS COMPONENTS

From Eq. (2.2) and the stress-displacement relation, we have;

$$\sigma_{ij}(x) = \int_{\partial G} D_{ij}^T(y, x) \zeta(y) ds_y \quad (x \in G) \quad (4.1)$$

where  $\zeta(y)$  is an unknown function on  $\partial G$  and a vector  $D_{ij}$  is expressed as follows;

$$D_{ij} = [D_{1ij}, D_{2ij}]^T \quad \text{for } n=2 \\ D_{ij} = [D_{1ij}, D_{2ij}, D_{3ij}]^T \quad \text{for } n=3 \quad (4.2)$$

and

$$D_{ij} = \frac{1}{4\alpha\pi(1-\nu)} \cdot \frac{1}{r^\alpha} [(1-2\nu)\{\delta_{kj}r_{ij} + \delta_{ij}r_{kj} - \delta_{jj}r_{kk}\} + \beta r_{ij}r_{kj}] \quad (4.3)$$

for  $n=2, k=1, 2; \alpha=1; \beta=2$

for  $n=3, k=1, 2, 3; \alpha=2; \beta=3$

Also, the function  $\zeta$  is called a density function. Attention should be paid to the following items. That is, (1) the integration in Eq. (4.1) is defined on every point in the original domain  $G$ , and (2) the integration in Eq. (4.1) involves the first kind discontinuity at  $x_0 \in \partial G$  where  $\zeta(x_0) \neq 0$ , and is continuous on any other points. Namely, we can denote as;

$$\hat{\sigma}_{ij}(x_0) - \check{\sigma}_{ij}(x_0) = 2\pi\zeta(x_0) \quad (4.4-1)$$

$$\sigma_{ij}(x_0) = \frac{1}{2} \{ \hat{\sigma}_{ij}(x_0) + \check{\sigma}_{ij}(x_0) \} \quad (\text{finitely determined}) \quad (4.4-2)$$

where  $\hat{\sigma}_{ij}(x_0) = \lim_{x \rightarrow x_0} \hat{\sigma}_{ij}(x)$  in  $G$ ,  $\check{\sigma}_{ij}(x_0) = \lim_{x \rightarrow x_0} \check{\sigma}_{ij}(x)$  in  $R^n - G$ .

#### 4.2. DISCRETIZATION

Utilizing photoelastic data, we can reconstruct the deformed boundary shape of specimen under load. Now, let us confine our discussion into the case of 2-dimension for convenience, hereafter. In a domain,  $\partial G = \{(y_1(t), y_2(t)): t \in [0, L]\}$ , let us put as;

$$\zeta(x) = \begin{bmatrix} w_1(x) \\ w_2(x) \end{bmatrix}. \quad (4.5)$$

Then, the unknown function  $\zeta(x)$  is approximated by use of spline function as follows;

$$\tilde{\xi}(y(t)) = \begin{bmatrix} \sum_{i=1}^m w_{1i} N_i(t) \\ \sum_{i=1}^m w_{2i} N_i(t) \end{bmatrix}, \quad y(t) \in \partial G, \quad \text{Supp}(N_i(t)) = [t_i, t_{i+1}] \quad (4.6)$$

Here, we have an approximation of Eq. (4.1) as;

$$\begin{aligned} \sigma_{ij}(x) &= \sum_{l=1}^m w_{1l} \left\{ \int_{t_l}^{t_{l+1}} D_{1ij}(y(t), x) N_i(t) g_1 dt \right\} \\ &\quad + \sum_{l=1}^m w_{2l} \left\{ \int_{t_l}^{t_{l+1}} D_{2ij}(y(t), x) N_i(t) g_1 dt \right\} \\ &= \sum_{l=1}^m v_l V_{ij}(x) \end{aligned} \quad (4.7)$$

where

$$\begin{cases} v_l = w_{1l}, & V_{ij}(x) = \int_{t_l}^{t_{l+1}} D_{1ij}(y(t), x) N_i(t) g_1 dt \\ v_{l+m} = w_{2l}, & V_{(l+m)ij}(x) = \int_{t_l}^{t_{l+1}} D_{2ij}(y(t), x) N_i(t) g_1 dt \end{cases} \quad (4.8)$$

(l = 1, 2, ..., m)

$$g_1 = g_1(t) = \left\{ \left( \frac{dx_1}{dt} \right)^2 + \left( \frac{dx_2}{dt} \right)^2 \right\}^{\frac{1}{2}} \quad (4.9)$$

## 5. Formulation of Density Function Determination Problem into mathematical Programming

### 5.1. SAMPLE POINT EXTRACTION BASED ON EQUIVALENT BOUNDARY CONDITION

To determine unknown coefficient  $v_l$  in Eq. (4.7), we select several fringes of which relative fringe order are known, and extract sample points on them appropriately as same as the number of unknown coefficient.

Now, recalling the relation between principal stresses and other stress components, we can obtain the following expression from Eq. (4.7),

$$\begin{aligned}
 (\sigma_1 - \sigma_2)^2 &= (\sigma_{11} - \sigma_{22})^2 + 4\sigma_{12} \\
 &= \left[ \sum_{l=1}^{2m} v_l \{V_{ll}(x) - V_{l2}(x)\} \right]^2 + 4 \left[ \sum_{l=1}^{2m} v_l V_{l2}(x) \right]^2 \\
 &= \sum_{k=1}^{2m} \sum_{l=1}^{2m} v_k v_l [\{V_{kk}(x) - V_{k2}(x)\} \{V_{ll}(x) - V_{l2}(x)\} + 4V_{kl}(x)V_{l2}(x)]
 \end{aligned} \tag{5.1}$$

When putting,

$$F_v(x) = \sum_{k=1}^{2m} \sum_{l=1}^{2m} v_k v_l [\{V_{kk}(x) - V_{k2}(x)\} \{V_{ll}(x) - V_{l2}(x)\} + 4V_{kl}(x)V_{l2}(x)], \tag{5.2}$$

we can evaluate the followings.

$$F(v, q_j) = F_v(q_j) - (v_{2m+1} + z_j)^2 \tag{5.3}$$

$$H(v) = \sum_{j=1}^{2m} \{F_v(q_j) - (v_{2m+1} + z_j)^2\}^2. \tag{5.4}$$

## 5.2. MATHEMATICAL PROGRAMMING FOR DETERMINATION OF DENSITY FUNCTION

The problem of determination of unknown coefficient  $v_l$  as that relative fringe order on sample points calculated by Eq. (5.2) fits to experimental data, is formulated into the following optimization problem as;

$$\begin{aligned}
 &\min H(v) \\
 \text{s.t. } &v \in R^{2m+1}
 \end{aligned} \tag{5.5}$$

## 6. Solution for Problems of Nonlinear Mathematical Programming

### 6.1. PROBLEMS IN NONLINEAR MATHEMATICAL PROGRAMMING

Since Eq. (5.5) is a type of nonlinear mathematical programming problems of degree four, local solution could be found by usual techniques such as Newton method or steepest decent method. However, there exist severe difficulties as follows [2].

#### 1) Selection of Initial Value for Global Optimum Solution

Eq. (5.4) has, in general, multiple local optimum solutions. The solution obtained by

starting from an arbitrary initial value is one of those local solutions. To find a global or true optimum solution, a suitable initial value has to be selected adequately. However, it is usually difficult to be attained.

## 2) Speed of Convergence

In cases that an optimum solution exists at the top/bottom of locally convex/concave surface, a step-by-step solution along the surface converges rapidly. However, since there often exist some ill points in a domain related to nonlinear optimization problem, the behavior of function value in the neighborhood of a local solution is so complicated that the value and the speed of convergence in step-by-step procedure are not known in advance.

## 6.2. IMPROVEMENT OF PROCEDURE TO SOLUTION

In order to overcome the difficulties and improve the solution, the authors developed a method of "Depth-First Homotopy."

### 1) Homotopy Method

Taking  $\mu$ -smooth functions  $F_k(v)$  ( $k = 1, 2, \dots, \mu$ ), we consider a  $\mu$ -dimensional vector function  $F(v)$  of which components are given by  $F_k(v)$ . Homotopy method is explained as follows. To solve the  $\mu$ -dimensional nonlinear equation  $F(v) = 0$ , settling an arbitrary point  $\bar{v}$  in the domain, the following equation in a domain  $(x, t) \in R^n \times [0, 1]$ ,

$$\Lambda(v, t) = F(v) + (t - 1)F(\bar{v}) = 0 \quad (6.1)$$

is translated into the following equation, by use of the implicit function theorem.

$$\begin{bmatrix} \frac{dv_1}{dt} \\ \frac{dv_2}{dt} \\ \vdots \\ \frac{dv_\mu}{dt} \end{bmatrix} = -J_F(v)^{-1} \begin{bmatrix} F_1(\bar{v}) \\ F_2(\bar{v}) \\ \vdots \\ F_\mu(\bar{v}) \end{bmatrix} \quad (v = \bar{v} \text{ when } t = 0) \quad (6.2)$$

Taking the Jacobian as follows;

$$J_F(v) = \begin{bmatrix} \frac{\partial F_1}{\partial v_1} & \frac{\partial F_1}{\partial v_2} & \dots & \frac{\partial F_1}{\partial v_\mu} \\ \frac{\partial F_2}{\partial v_1} & \dots & \dots & \dots \\ \dots & \dots & \dots & \dots \\ \frac{\partial F_\mu}{\partial v_1} & \frac{\partial F_\mu}{\partial v_2} & \dots & \frac{\partial F_\mu}{\partial v_\mu} \end{bmatrix}$$

In the numerical solutions of Eq. (6.2), the solution for  $t = 1$  is one of solutions we look for.

## 2) Depth -First Optimization

For a real value function  $\Phi(v)$  with  $\mu$ -variables defined in a domain  $D \subset R^\mu$ , the following algorithm is called as "Depth-First Optimization."

[1] Let us take as  $E=D$ .

- i) Divide  $E$  into  $m$ -pieces of subdomain,  $E_1, \dots, E_m$ , with a certain procedure.
- ii) From each subdomain, extract a sample point  $P_1, \dots, P_m$ .
- iii) On each sample point, find the minimum value of  $\Phi(v)$ . Here let us denote the point of minimum  $\Phi(v)$  as  $P_k$  and the subdomain as  $E_k$ .

[2] Repeat the above procedure, considering the subdomain  $E_k$  as a new domain  $E$ .

[3] Taking a certain stopping rule into account, [1] and [2] procedures are repeated.

## 3) Depth-First Homotopy Method

For the variables involved in Eq.(5.4), the variable  $v_{2m+1}$  holds different characteristics from other variables. Taking the fact into account, we construct an algorithm called "Depth -First Homotopy Method." To apply the Homotopy method to experimental data, a point  $x_0$  in Eq.(6.1) is selected arbitrarily and the initial value of  $\alpha$  is settled as zero, namely  $\alpha = 0$ .

- [1] For a given initial integer  $L$ , let us search the variable  $V_\mu$  within a finite closed interval of  $[\alpha - 9 \times 10^L, \alpha + 9 \times 10^L]$ .
- [2] Substituting the values  $\alpha - 9 \times 10^L, \alpha - 8 \times 10^L, \dots, \alpha + 8 \times 10^L, \alpha + 9 \times 10^L$  into  $V_\mu$ , other variables remained are solved by Homotopy method.
- [3] When the point at which the error  $H(v)$  in Eq.(5.4) comes to minimum is obtained as  $\alpha + k \times 10^L$ , we denote the solution by Homotopy method as  $\hat{v}$ .
- [4] Then, after decreasing the value of  $L$  by 1 and setting new values of  $\alpha$  and  $\bar{v}$  as to be  $\alpha + k \times 10^L$  and  $\hat{v}$ , repeat the procedures from [1] to [3].
- [5] According to a certain stopping rule, the same procedure is repeated within a designated times.

## 4) Discussion from Viewpoint of Mechanical Engineering

The solution obtained by the method of Depth -First Homotopy proposed in this paper is a local solution approved within a certain accuracy. On the other hand, since the variable  $V_\mu$  corresponds to the value of principal stress difference in the domain under consideration, it is expected that the value would not oscillate so steeply. Taking these into account, the solution obtained by the method proposed could be expected to be very close to the true optimum solution.

## 7. Example Application

Now, let us apply the method and algorithm to a photoelastic data in contact problem. The experimental conditions and the results obtained are shown as follows.

### 1) Experimental conditions

Fig.2 shows a schematic diagram of a rectangular plate specimen loaded by a concentrated contact force of 50 kN at the top surface. The bottom of the specimen is rested on a rigid bed. Dot marks on the boundary curve show the selected knots for the construction of basic spline function  $N_i(t)$  in Eq.(4.6). Two isochromatics are selected for sample points of relative fringe order.

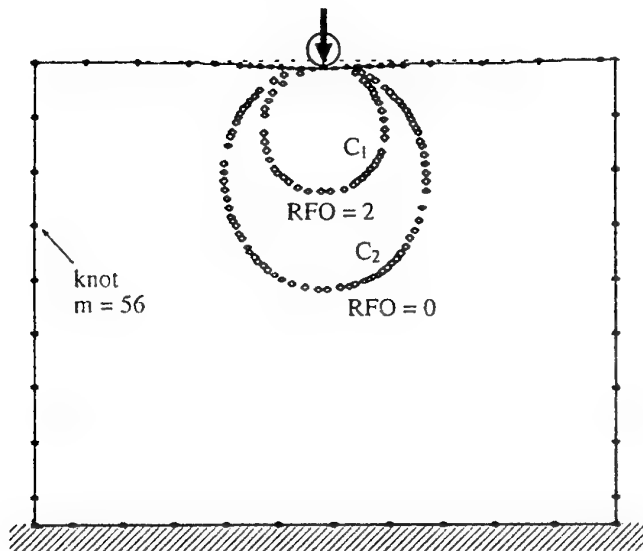


*Figure 2.* Schematic diagram of specimen and sample data selected.

## 2) Results obtained

Fig.3 shows the whole field distribution of photoelastic fringe obtained by the method proposed. Particularly around the contact point, fringes are successfully reconstructed. Not only around the contact region but on the free boundary and the bottom region, we can see fairly good reconstruction of fringe distribution in comparison with the original experimental data.



*Figure 3.* The whole field fringe pattern reconstructed by the method proposed.

## 8. Concluding Remarks

In this paper, the authors discussed on the determination of unknown coefficients involved in a representative function taking an example of the formulation of Navier equation. The method mentioned here is available if the distribution (hyperfunction) solution of displacement in linear elasticity is obtainable. Even in cases that it is difficult to obtain some formal solution, if a certain basic function that has similar characteristics with structural equations under consideration such as multi-harmonic nature, the procedures proposed will be applicable except the techniques in Chapter 2 and 4. Furthermore, the method mentioned is a part in the series of Hybrid Method for Stress Analysis that can include error estimation. From the viewpoint of the global system of the hybrid method, it is important to develop and complete the techniques and to increase examples of application.

## **References**

1. Takashi, M., Mawatari, S. and Omori, Y.: An Approach to Hybrid Method for Elastic Analysis Using Photoelastic Image Data, *Post Conference Proceedings of VIII International Congress on Experimental Mechanics*, Nashville, (1996) 1-7.
2. Host, R., Pardalos, P. M. and Thoai, N. V.: *Introduction to Global Optimization*, Kluwer Academic Press, Netherlands, 1995.

## HYBRIDIZING OPTICAL METHODS WITH ANALYTICAL AND COMPUTATIONAL TECHNIQUES FOR STRESS ANALYSIS

R. E. ROWLANDS  
*Mechanical Engineering*  
*University of Wisconsin*  
*Madison, WI 53706 USA*

### 1. Abstract

Contemporary needs involve effective, accurate and expedient nondestructive methods of stress analysis. Individual experimental, numerical or theoretical techniques are often less than ideal. Shortcomings of specific approaches include difficulties in obtaining stresses theoretically in finite shapes or for other than isotropic material, reliable numerical results when loading or geometry are not adequately known, and dependable measured data at geometric discontinuities where most serious stresses frequently occur. The typical need for many small elements when evaluating stress concentrations by conventional FEM increases computer storage demands and run times. This paper demonstrates synergizing experimental and numerical methods with theoretical concepts to stress analyze components fabricated from isotropic or orthotropic composite materials. Although thermoelastic data are emphasized, applications to moiré, isochromatics, isopachics, holography and finite elements are discussed.

### 2. Analytical Background

The classical analytical method of stress analyzing a component such as that in the lower portion of Figure 1 typically involves satisfying equilibrium and compatibility, subject to the boundary conditions. In terms of the Airy Stress Function  $F$ , for orthotropy one obtains the following compatibility equation [1]:

$$a_{22} \frac{\partial^4 F}{\partial x^4} - 2a_{26} \frac{\partial^4 F}{\partial x^3 \partial y} + (2a_{12} + a_{66}) \frac{\partial^4 F}{\partial x^2 \partial y^2} - 2a_{16} \frac{\partial^4 F}{\partial x \partial y^3} + a_{11} \frac{\partial^4 F}{\partial y^4} = 0, \quad (1)$$

where  $a_{ij}$  are compliances. The plane problem of classical elastic theory is now reduced to determining  $F$  throughout the component such that Equation (1) and the boundary conditions are satisfied. Considering  $F$  must be a real function of variables  $x$  and  $y$ , it can be expressed as follows:

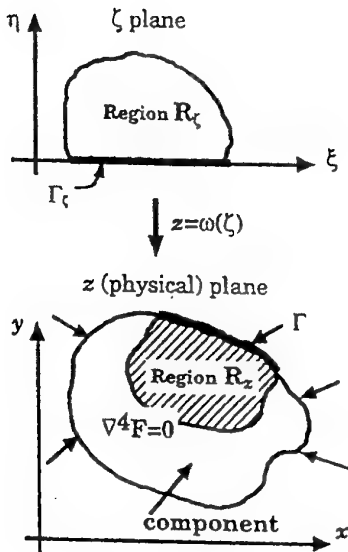


Fig. 1: Loaded component.

- In the case of different complex roots  $\mu_1$  and  $\mu_2$  :

$$F = 2 \operatorname{Re}[F_1(z_1) + F_2(z_2)] \quad (2)$$

- In the case of pairwise equal complex roots  $\mu_1$  and  $\mu_2$  :

$$F = 2 \operatorname{Re}[F_1(z_1) + \bar{z}_1 F_1'(z_1)], \quad (3)$$

where  $z_j = x + \mu_j y$ ,  $\mu_j$  are complex material properties whose values are obtained from the characteristic equation associated with Equation (1), and  $j = 1, 2$ . For isotropy,  $z_1 = z = x + iy$ ,  $\bar{z}_1 = \bar{z}$ . One can sometimes construct a representative stress function for a specific problem. On the other hand, many plane problems of elasticity can be solved by representing the stress function in terms of a truncated series, satisfying boundary conditions along only the edge adjacent to the region of interest, and combining the resulting equations with measured data.

For isotropy,  $E_{11} = E_{22} = E$ ,  $v_{12} = v_{21} = v$ ,  $G = E/2(1+v)$ ,  $a_{11} = a_{22} = 1/E$ ,  $a_{12} = -v/E$ ,  $a_{66} = 1/G$ ,  $a_{16} = a_{26} = 0$ ,  $\mu_1 = \mu_2 = i$  and the individual stresses can be written in terms of two analytical functions, i.e. [1, 2],

$$\begin{aligned} \sigma_x &= \operatorname{Re}\{2\phi'(z) - [\bar{z}\phi''(z) + \psi'(z)]\} \\ \sigma_y &= \operatorname{Re}\{2\phi'(z) + [\bar{z}\phi''(z) + \psi'(z)]\} \\ \tau_{xy} &= \operatorname{Im}[\bar{z}\phi''(z) + \psi'(z)] \end{aligned} \quad (4)$$

where the stress function of Equation (1) is

$$F = \operatorname{Re} \left[ \int^z \psi(z) dz + \bar{z} \phi(z) \right], \quad (5)$$

$\psi(z) = \chi'(z)$  and primes denote differentiation. The compatibility relationship of Equation (1) becomes

$$\nabla^4 F = \nabla^2(\sigma_x + \sigma_y) = \nabla^2(S) = 0. \quad (6)$$

Stresses of Equation (4) satisfy equilibrium and associated strains satisfy compatibility. One can therefore solve plane problems analytically by ensuring that the stresses associated with the stress functions  $\phi$  and  $\psi$  satisfy the boundary conditions. However, analytic solutions are generally only possible for problems having simple geometries. As an aid in analyzing plane problems having complicated shapes, conformal mapping techniques can be used to transform the complicated geometry of the physical plane into a simpler shape in a different plane, Figure 1. Moreover, at least for a region adjacent to a traction-free boundary, the individual stress functions  $\phi$  and  $\psi$  can be related to each other through the concept of analytic continuation.

Assume the function

$$z = \omega(\zeta) \quad (7)$$

maps the region  $R_\zeta$  of the  $\zeta(\zeta = \xi + i\eta)$ -plane into region  $R_z$  of the physical  $z$ -plane, Figure 1. Stress functions  $\phi(z) = \phi[\omega(\zeta)] \equiv \phi(\zeta)$  and  $\psi(z) = \psi[\omega(\zeta)] \equiv \psi(\zeta)$  of Equations (4) and (5) are analytic functions of  $\zeta$ . Analyticity of the mapping function  $\omega(\zeta)$  guarantees that equilibrium and compatibility equations are satisfied inside region  $R_z$ . For isotropy, combining Equations (4) through (7) gives

$$\begin{aligned} \sigma_x &= \operatorname{Re} \left\{ 2 \frac{\phi'(\zeta)}{\omega'(\zeta)} - \left[ \overline{\omega(\zeta)} \left( \frac{\phi''(\zeta)}{\omega'(\zeta)^2} - \frac{\omega''(\zeta)}{\omega'(\zeta)^3} \phi'(\zeta) \right) + \frac{\psi'(\zeta)}{\omega'(\zeta)} \right] \right\} \\ \sigma_y &= \operatorname{Re} \left\{ 2 \frac{\phi'(\zeta)}{\omega'(\zeta)} + \left[ \overline{\omega(\zeta)} \left( \frac{\phi''(\zeta)}{\omega'(\zeta)^2} - \frac{\omega''(\zeta)}{\omega'(\zeta)^3} \phi'(\zeta) \right) + \frac{\psi'(\zeta)}{\omega'(\zeta)} \right] \right\} \\ \tau_{xy} &= \operatorname{Im} \left\{ \overline{\omega(\zeta)} \left[ \frac{\phi''(\zeta)}{\omega'(\zeta)^2} - \frac{\omega''(\zeta)}{\omega'(\zeta)^3} \phi'(\zeta) \right] + \frac{\psi'(\zeta)}{\omega'(\zeta)} \right\}. \end{aligned} \quad (8)$$

For orthotropy, expressions for the stresses corresponding to Equations (8) can be written as

$$\begin{aligned} \sigma_x &= 2 \operatorname{Re} \left\{ \mu_1^2 \frac{\Phi'(\zeta_1)}{\omega'_1(\zeta_1)} + \mu_2^2 \frac{\Psi'(\zeta_2)}{\omega'_2(\zeta_2)} \right\} \\ \sigma_y &= 2 \operatorname{Re} \left\{ \frac{\Phi'(\zeta_1)}{\omega'_1(\zeta_1)} + \frac{\Psi'(\zeta_2)}{\omega'_2(\zeta_2)} \right\} \end{aligned} \quad (9)$$

$$\tau_{xy} = -2 \operatorname{Re} \left\{ \mu_1 \frac{\Phi'(\zeta_1)}{\omega'_1(\zeta_1)} + \mu_2 \frac{\Psi'(\zeta_2)}{\omega'_2(\zeta_2)} \right\}. \quad (9)$$

where

$$\Phi(z_1) = \frac{dF_1(z_1)}{dz_1} = \Phi[\omega_1(\zeta_1)] \equiv \Phi(\zeta_1) \text{ and } \Psi(z_2) = \frac{dF_2(z_2)}{dz_2} = \Psi[\omega_2(\zeta_2)] \equiv \Psi(\zeta_2). \quad (10)$$

The functions  $\Phi(z_1)$  and  $\Psi(z_2)$  are analytic in the complex  $z_1$ - and  $z_2$ -planes, respectively, where  $z_1 = x + \mu_1 y$  and  $z_2 = x + \mu_2 y$ . Substituting  $z_j = x + \mu_j y$  into Equation (7) yields the following induced mapping function in terms of  $\zeta_j (= \xi + \mu_j \eta)$ :

$$z_j = \omega_j(\zeta_j), \quad j = 1, 2. \quad (11)$$

Stress functions  $\Phi$  and  $\Psi$  are now analytic functions of  $\zeta_1$  and  $\zeta_2$ , respectively.

The classical stress analysis boundary-value problem entails satisfying equilibrium and compatibility throughout the entire engineering component (say bottom portion of Figure 1), subject to the boundary conditions. However, one can collect measured information in only the region of interest, say  $R_z$  of Figure 1, and then using relevant analytical and/or numerical tools, plus boundary information on the adjacent edge,  $\Gamma$ , evaluate the individual stresses throughout  $R_z$ . The region  $R_z$  might well involve a stress concentration. In some cases, because the measured data are unreliable on the edge  $\Gamma$ , experimental information is collected only away from the edge, although the final individual stresses are evaluated throughout the entire region  $R_z$ , including along the edge,  $\Gamma$ , of  $R_z$ . It may then only be necessary to map the edge  $\Gamma$  and its adjacent region  $R_z$  into the  $\zeta$  plane, Figure 1.

For a region  $R_z$  adjacent to a circular fillet or notch of radius  $R$ , the conformal transformation

$$z = \omega(\zeta) = i \operatorname{Re}^{-i\zeta} + z_c \quad (12)$$

maps the region  $R_\zeta$  of the  $\zeta$ -plane into the physical region  $R_z$  of the  $z$ -plane, Figures 1 and 2, where  $z_c$  is the center of the discontinuity [1, 2]. The circular boundary  $\Gamma$  in the physical  $z$ -plane is conformally mapped onto  $\Gamma_\zeta$ , a section of the real axis ( $\eta = 0$  surface) of the  $\zeta$ -plane. For orthotropy, one has the following induced mapping functions:

$$z_j = \omega_j(\zeta_j) = \frac{iR}{2} \left[ (1 - i\mu_j) e^{-i\zeta_j} - (1 + i\mu_j) e^{i\zeta_j} \right], \quad j = 1, 2. \quad (13)$$

The relationship between the two relevant stress functions of Equations (9) is

$$\Psi(\zeta_2) = \overline{B\Phi(\zeta_2)} + C\Phi(\zeta_2), \quad (14)$$

where

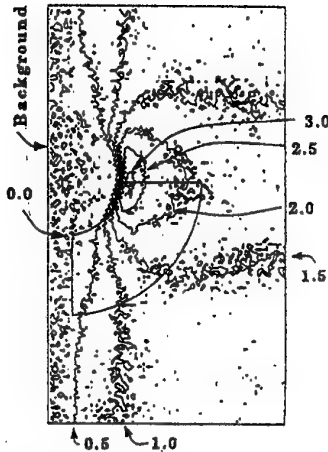


Figure 2: Thermoelastically measured  $S^*$  in vertically-loaded symmetrically notched (radius  $R$ ) composite strip.

$$B = \frac{\bar{\mu}_2 - \bar{\mu}_1}{\mu_2 - \bar{\mu}_2} \text{ and } C = \frac{\bar{\mu}_2 - \mu_1}{\mu_2 - \bar{\mu}_2}. \quad (15)$$

Traction-free conditions on the boundary of the physical  $z$ -plane are enforced by these relations which reduce the two stress functions into a single stress function, i.e.,  $\Phi$  for anisotropy. This is accomplished by introducing the conformal mapping function  $\omega(\zeta)$  which maps the traction-free physical boundary onto say the real axis ( $\eta = 0$  surface) of the  $\zeta$ -plane.

The representation of the stress function  $\Phi$  in the  $\zeta_1$ -plane can be approximated by a truncated power series,

$$\Phi(\zeta_1) = \sum_{j=0}^N \left\{ A_j (\zeta_1 - \zeta_0)^j \right\}. \quad (16)$$

Location  $\zeta_0$  is some point on the boundary  $\Gamma_\zeta$  ( $\eta = 0$  surface). From Equations (9), (14), (15) and (16), for orthotropy,

$$\begin{aligned} \sigma_x &= 2 \sum_{j=1}^N \operatorname{Re} \left\{ \left[ \frac{j\mu_1^2}{\omega'_1(\zeta_1)} (\zeta_1 - \zeta_0)^{j-1} + \frac{j\mu_2^2 C}{\omega'_2(\zeta_2)} (\zeta_2 - \zeta_0)^{j-1} \right] A_j \right. \\ &\quad \left. + \left[ \frac{j\mu_2^2 B}{\omega'_2(\zeta_2)} (\zeta_2 - \zeta_0)^{j-1} \right] \bar{A}_j \right\} \\ \sigma_y &= 2 \sum_{j=1}^N \operatorname{Re} \left\{ \left[ \frac{j}{\omega'_1(\zeta_1)} (\zeta_1 - \zeta_0)^{j-1} + \frac{jC}{\omega'_2(\zeta_2)} (\zeta_2 - \zeta_0)^{j-1} \right] A_j \right. \\ &\quad \left. + \left[ \frac{jB}{\omega'_2(\zeta_2)} (\zeta_2 - \zeta_0)^{j-1} \right] \bar{A}_j \right\} \end{aligned} \quad (17)$$

$$\tau_{xy} = -2 \sum_{j=1}^N \operatorname{Re} \left\{ \left[ \frac{j\mu_1}{\omega'_1(\zeta_1)} (\zeta_1 - \zeta_0)^{j-1} + \frac{j\mu_2 C}{\omega'_2(\zeta_2)} (\zeta_2 - \zeta_0)^{j-1} \right] A_j + \left[ \frac{j\mu_2 B}{\omega'_2(\zeta_2)} (\zeta_2 - \zeta_0)^{j-1} \right] \bar{A}_j \right\}. \quad (17)$$

By using conformal mapping and continuation techniques, Equations (17) imply that the stresses satisfy traction-free conditions in the adjacent portion of the entire boundary. However, unlike a classical boundary-value problem where one would typically evaluate the unknown coefficients,  $A_j$ , by satisfying the boundary conditions around the entire shape, one can use some combination of the measured stresses of Equations (17) from the interior of the region  $R_z$  of interest to determine these unknown coefficients. Additional known boundary conditions can also be imposed at discrete locations.

An example of employing some combination of the stresses of Equations (17) is to choose the  $x$ -axis of an orthotropic composite material parallel to its strong, stiff direction (i.e., 1-direction) such that thermoelastic data  $S^*$  can then be expressed as

$$S^* = K_1 \sigma_x + K_2 \sigma_y \\ = 2 \sum \operatorname{Re} \left\{ \left[ \frac{j(K_1 \mu_1^2 + K_2)}{\omega'_1(\zeta_1)} (\zeta_1 - \zeta_0)^{j-1} + \frac{j(K_1 \mu_2^2 + K_2)C}{\omega'_2(\zeta_2)} (\zeta_2 - \zeta_0)^{j-1} \right] A_j + \left[ \frac{j(K_1 \mu_2^2 + K_2)B}{\omega'_2(\zeta_2)} (\zeta_2 - \zeta_0)^{j-1} \right] \bar{A}_j \right\} \quad (18)$$

The  $A_j$  coefficients can now be evaluated from thermoelastically measured input values of  $S^*$  and Equations (18). Thermal mechanical coefficients  $K_1$  and  $K_2$  of Equation (18) are normally determined experimentally.

### 3. Results

Figure 2 shows thermoelastic data throughout an edge section of a vertically-loaded strain-gaged composite ( $E_{11}/E_{22} = 2.4$ ) strip containing symmetrical side notches of radius  $R = 6.35$  mm. These measured values of  $S^*$  were used with Equation (18) to evaluate the  $A_j$  coefficients and hence the stress functions of Equations (14) and (16), from which individual stresses along and adjacent to the notch boundary were obtained from Equations (17). The resulting strain between the side notches is compared in Figure 3 with those from strain gages and FEM. In this case 141 measured interior values of  $S^*$  were used between  $1.2 R$  and  $2.5 R$ , together with  $\sigma_x = \tau_{xy} = 0$  imposed at 13 locations along the traction-free vertical straight edge below the notch and  $\tau_{xy} = 0$  at 20 positions along the vertical and horizontal lines of symmetry to evaluate the 26 unknown coefficients of Equation (16).

Displayed results use measured thermoelastic data. We have also found this general hybrid approach to be advantageous for determining stresses from holographically

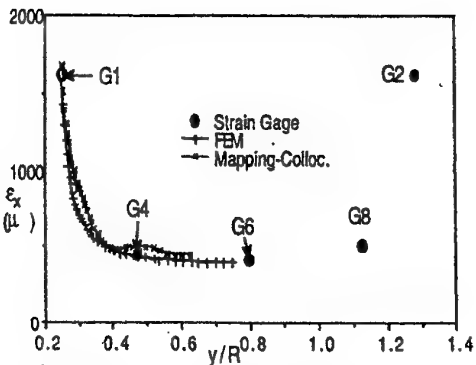


Figure 3: Longitudinal strains between the side notches in the tensile composite strip of Fig. 2 as obtained from strain gages (G), FEM and thermoelasticity.

measured isopachics, pure isochromatics (without the need of isopachics or isoclinics) and moiré [1-9]. Moreover, synergizing such analytical and numerical concept tools enables one to determine accurate stresses at reentry corners using essentially classical FEM but with only a few, very coarse elements [10]. Applications include stress analysis of isotropic and orthotropic structural and machine elements, wood engineering and fracture mechanics. Reference 11 describes a new, nondestructive hybrid experimental-theoretical-numerical method for stress analyzing 3-D components from measured (thermoelastic plus photoelastic) surface information.

#### 4. Summary, Conclusions and Discussion

Whereas individual experimental, theoretical or numerical methods of stress analysis are often lacking, synergizing aspects of the specific approaches can be very advantageous. Space permits emphasizing here only the benefits of combining theoretical and numerical concepts with measured thermoelastic data, but applications to moiré, isochromatics, holography and finite elements are also indicated.

#### 5. Acknowledgement

Ford Motor Co., USDA and NSF funded aspects of the research reported here. I also wish to thank Lynda Litzkow of the ME Department, Univ. of Wisconsin, for preparing this manuscript.

## 6. References

1. Lin, S. T. and Rowlands, R. E. (1995), Thermoelastic Stress Analysis of Orthotropic Composites, *Experimental Mechanics*,35(3), 257-265.
2. Huang, Y. M., Rowlands, R. E. and Lesniak, J. R. (1990), Simultaneous Stress Separation, Smoothing of Measured Thermoelastic Information, and Enhanced Boundary Data, *Experimental Mechanics*,30(4),398-403.
3. Lin, S. T., Miles, J. P. and Rowlands, R. E. (1997), Image Enhancement and Stress Separation of Thermoelastically Measured Data under Random Loading, *Experimental Mechanics*,37(3),225-231.
4. Rauch, B. J. and Rowlands, R. E. (1997), Filtering Thermoelastically Measured Isopachic Data, *Experimental Mechanics*,37(4),387-392.
5. Bauman, B. J., Matthys, D. R., Wolfe, R.W., Lin, C. H. and Rowlands, R. E., Thermoelastic Analysis of Metal-Plate Connected Wood Trusses, in preparation.
6. Lin, C. H. (1994), A New Digital Isopachic Contouring Technique for Stress Analyzing Composite Materials, Ph.D. thesis, Univ. of Wisconsin.
7. Hawong, J. S., Lin, C. H. Lin, S. T., Rhee, J. and Rowlands, R. E. (1995), A Hybrid Method to Determine Individual Stresses in Orthotropic Composites using only Measured Isopachic Data, *Jour. Composite Materials*,29(18),2366-2387.
8. Lin, S. T. and Rowlands, R. E., Hybrid Stress Analysis, to appear in *Optics and Laser Engineering*.
9. Rhee, J. and Rowlands, R. E. (1996), Hybrid Moire-Numerical Stress Analysis around Cutouts in Loaded Composites, *Experimental Mechanics*,36(4) 379-387.
10. Lin, S. T., Lin, C. H. and Rowlands, R. E., Reliable Edge Stresses at Geometric Discontinuities using Large Conventional Finite Elements, accepted for publication in *Jour. Finite Elements in Analysis and Design*.
11. Gao, X. L. (1998), On 2-and 3-D Stress Analyses of Loaded Solids, Ph.D. thesis, Univ. of Wisconsin.

## HYBRID STRESS ANALYSIS WITH INTEGRATED PHOTOELASTICITY

H.ABEN AND L.AINOLA

*Institute of Cybernetics,  
Tallinn Technical University, 21 Akadeemia tee,  
EE0026 Tallinn, Estonia*

**Abstract.** In the case of weak birefringence integrated photoelasticity allows for the determination of the distribution of the normal stress in any section of a 3-D specimen. In the case of axial symmetry distribution of the shear stress can also be determined. The question arises how to determine the other stress components. This problem of hybrid mechanics is especially complicated by investigating residual stresses in glass since residual stresses are caused by incompatibility of residual deformations. Due to that, direct application of the compatibility equations is not possible. In this paper formulas are derived for the complete determination of residual stresses in glass in the axisymmetric case and in the case of plane deformation. Examples of complete residual stress analysis are given.

### 1. The Case of Weak Birefringence

In integrated photoelasticity [1] the specimen is placed in an immersion bath and a beam of polarised light is passed through the specimen (Fig.1). Transformation of the polarisation of light in the specimen is measured on many rays. In certain cases this integrated optical information enables one to determine distribution of some components of the stress tensor.

In the general case, due to the rotation of the principal stress directions on the light rays, optical phenomena are complicated and so are the algorithms for the interpretation of the measurement data. However, if birefringence is weak, photoelastic measurements with a 3-D specimen can be carried out similarly to the 2-D case [2, 3]. That is, on every ray it is possible to measure the parameter of the isoclinic  $\varphi$  and optical retardation  $\Delta$ . The latter are related to the components of the stress tensor on the ray by simple integral relationships

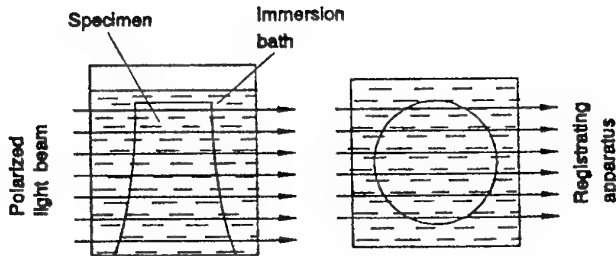


Figure 1. Experimental setup in integrated photoelasticity.

$$\Delta \cos 2\varphi = C \int (\sigma_z - \sigma_x) dy = V_1, \quad (1.1)$$

$$\Delta \sin 2\varphi = 2C \int \tau_{zx} dy = V_2. \quad (1.2)$$

Here  $C$  is the photoelastic constant and  $\sigma_x$ ,  $\sigma_z$  and  $\tau_{zx}$  are components of the stress tensor in the plane  $zx$  which is perpendicular to the wave normal  $y$ .

Using numerical experiments it has been shown [2] that in the case of axial symmetry relationships (1.1) and (1.2) are valid if  $\Delta$  is less than  $3\lambda/4$  ( $\lambda$  denotes wavelength), and rotation of the principal directions is not strong. In the general case Eqs. (1.1) and (1.2) can be used if  $\Delta < \lambda/3$ .

## 2. Axisymmetric Stress Distribution

### 2.1. STRESSES DUE TO EXTERNAL LOADS

In the case of axisymmetric stress distribution, Eqs. (1.1) and (1.2) permit determination of the distributions of the axial stress  $\sigma_z$  and shear stress  $\tau_{rz}$ . The other stress components,  $\sigma_r$  and  $\sigma_\theta$ , can be determined using the equilibrium equation

$$\frac{\partial \sigma_r}{\partial r} + \frac{\sigma_r - \sigma_\theta}{r} + \frac{\partial \tau_{rz}}{\partial z} = 0, \quad (2.1)$$

and the compatibility equation

$$\frac{\partial \epsilon_\theta}{\partial r} - \frac{\epsilon_r - \epsilon_\theta}{r} = 0, \quad (2.2)$$

### HYBRID STRESS ANALYSIS...

3

where  $\epsilon_r$  and  $\epsilon_\theta$  are components of the deformation tensor in cylindrical coordinates. Introducing into Eq. (2.2) the Hooke's law

$$\epsilon_r = \frac{1}{E}[\sigma_r - \mu(\sigma_\theta + \sigma_z)] + \alpha T, \quad (2.3)$$

$$\epsilon_\theta = \frac{1}{E}[\sigma_\theta - \mu(\sigma_z + \sigma_r)] + \alpha T, \quad (2.4)$$

$$\epsilon_z = \frac{1}{E}[\sigma_z - \mu(\sigma_r + \sigma_\theta)] + \alpha T, \quad (2.5)$$

we obtain, taking  $T=\text{const}$ :

$$\frac{\partial}{\partial r}[\sigma_\theta - \mu(\sigma_r + \sigma_z)] - (1 + \mu)\frac{\sigma_r - \sigma_\theta}{r} = 0. \quad (2.6)$$

Here  $E$  is the elasticity modulus,  $\mu$  is the Poisson coefficient,  $\alpha$  is the thermal expansion coefficient and  $T$  is temperature. The algorithm for determining  $\sigma_r$  and  $\sigma_\theta$  from Eqs. (2.1) and (2.6) has been elaborated by Doyle and Danyluk [4, 5].

#### 2.2. THE CASE OF RESIDUAL STRESSES

In the case of residual stresses in glass, in Eqs. (2.3) to (2.5) the term  $\alpha T$  must be included. Since residual stresses in glass have thermal origin, they can be considered as being caused by a fictitious temperature field [6, 7]. Unfortunately, this temperature field is not known. Therefore, the compatibility equation cannot be used when investigating residual stresses in glass and one has to look for other analytical relationships between the stress components.

Thermal stresses in an axisymmetric body can be expressed as [8].

$$\sigma_r = 2G\left(\frac{\partial^2 F}{\partial r^2} - \Delta F\right) + \frac{2G}{1-2\mu}\frac{\partial}{\partial z}\left(\mu\Delta L - \frac{\partial^2 L}{\partial r^2}\right), \quad (2.7)$$

$$\sigma_\theta = 2G\left(\frac{1}{r}\frac{\partial F}{\partial r} - \Delta F\right) + \frac{2G}{1-2\mu}\frac{\partial}{\partial z}\left(\mu\Delta L - \frac{1}{r}\frac{\partial L}{\partial r}\right), \quad (2.8)$$

$$\sigma_z = 2G\left(\frac{\partial^2 F}{\partial z^2} - \Delta F\right) + \frac{2G}{1-2\mu}\frac{\partial}{\partial z}\left[(2-\mu)\Delta L - \frac{\partial^2 L}{\partial z^2}\right], \quad (2.9)$$

$$\tau_{rz} = 2G\frac{\partial^2 F}{\partial r \partial z} + \frac{2G}{1-2\mu}\frac{\partial}{\partial r}\left[(1-\mu)\Delta L - \frac{\partial^2 L}{\partial z^2}\right], \quad (2.10)$$

where  $F$  is stress function and  $L$  Love's displacement function,

$$\Delta F = \frac{1+\mu}{1-\mu}\alpha T, \quad \Delta \Delta L = 0, \quad G = \frac{E}{2(1+\mu)}, \quad \Delta = \frac{\partial^2}{\partial r^2} + \frac{1}{r}\frac{\partial}{\partial r} + \frac{\partial^2}{\partial z^2}. \quad (2.11)$$

Let us assume that a long cylinder or tube is manufactured by solidifying it in an axisymmetric temperature field without gradient in the axial direction. In this case the thermal (and residual) stresses are the same in all cross sections of the cylinder, except the parts near the ends of the latter. Now from Eqs. (2.7) to (2.9) follows the classical sum rule

$$\sigma_r + \sigma_\theta = \sigma_z. \quad (2.12)$$

The classical sum rule (2.12) was in a somewhat different way first derived by O'Rourke [9].

Using the equilibrium equation (2.1) and the classical sum rule (2.12), all the residual stress components can be determined. This method has been widely used for residual stress measurement in glass cylinders, and in axisymmetric fibers and fiber preforms [10, 11].

In the general case, in axisymmetric glass articles stress gradient in axial direction cannot be ignored. Let us try to derive from Eqs. (2.7) to (2.10) a relationship between stress components for that case.

If stress gradient in axial direction is present but smooth, we may write

$$\frac{\partial^2 F}{\partial z^2} = \frac{\partial^2 L}{\partial z^2} = 0. \quad (2.13)$$

Now from Eqs. (2.7) to (2.10) follows

$$\sigma_r + \sigma_\theta = \sigma_z + \frac{2G}{1-2\mu} \frac{\partial}{\partial z} [3(\mu-1)\Delta L]. \quad (2.14)$$

Differentiating (2.10) relative to  $z$  and integrating along  $r$  reveals

$$\int_0^r \frac{\partial \tau_{rz}}{\partial z} d\tau = \frac{2G}{1-2\mu} \frac{\partial}{\partial z} [(1-\mu)\Delta L] + C(z), \quad (2.15)$$

where  $C(z)$  is the integration constant.

From (2.14) and (2.15) follows

$$\sigma_r + \sigma_\theta = \sigma_z - 3 \int_0^r \frac{\partial \tau_{rz}}{\partial z} d\tau + C(z). \quad (2.16)$$

The last relationship is named the generalized sum rule. It is valid when stress gradient in the axial direction is present, with certain restrictions (2.13) upon the functions  $F$  and  $L$ . Actually, Eq. (2.16) is first approximation of the generalized sum rule. By handling Eqs. (2.7) to (2.10) asymptotically, higher approximations of the generalized sum rule can be obtained.

As a practical example, residual stress distribution in a section of an axisymmetric article of optical glass is shown in Fig. 2.

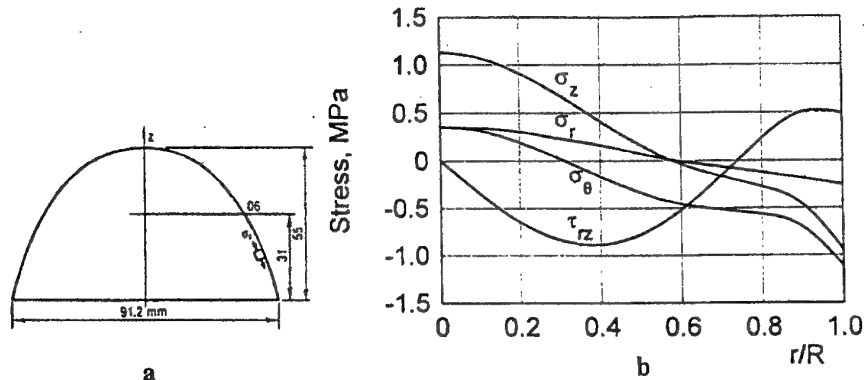


Figure 2. Geometry of the axisymmetric article of optical glass (a), and distribution of residual stresses in section 06 (b).

### 3. Specimens of Arbitrary Shape

In the case of articles of arbitrary shape, measurement of the integrals (1.1) and (1.2) should be carried out scanning two parallel cross sections,  $\Delta z$  apart from each other, under different angles  $\Theta$  (Fig. 3). From the equilibrium condition of the segment ABC one obtains

$$\int_A^C \sigma_z dy' = \frac{1}{2C\Delta z} \left[ \int_l^B V'_2 dx' - \int_l^B V_2 dx' \right] - \frac{V_1}{C}. \quad (3.1)$$

Here  $V'_2$  denotes the value of  $V_2$  for the auxiliary section.

Formula (3.1) enables one to calculate the line integral of  $\sigma_z$  for any light ray. From tomography it is known that if one can measure line integrals of a certain field along many rays then the field can be reconstructed using the Radon inversion [13]. In this respect we are actually dealing with optical tomography of the stress field which has been considered in papers [14, 15].

Unfortunately, in the general case of a 3-D article axial stress  $\sigma_z$  is the only stress component which can be determined directly from the measurements.

### 4. The Case of Plane Deformation

In cylindrical coordinates an algorithm for complete stress determination has been considered by Puro and Kell [16] who have used their method for

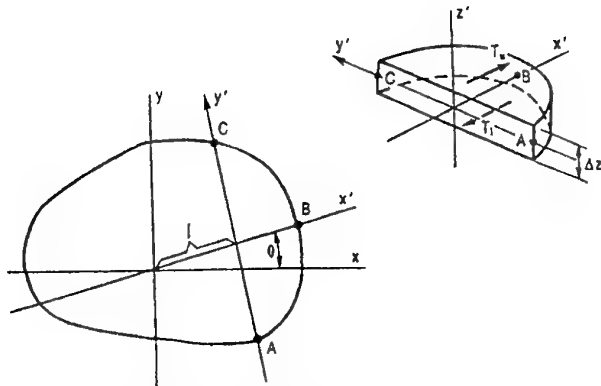


Figure 3. Illustration to the investigation of the general 3-D state of stress.

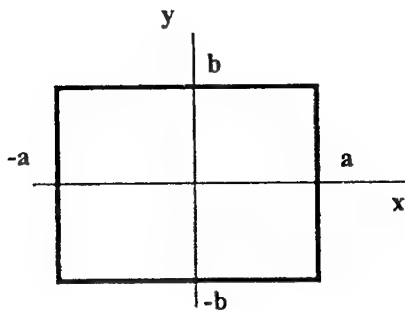


Figure 4. Considering plane deformation in rectangular coordinates.

stress measurement in an optical fiber preform of complicated cross section. Let us consider the same problem in rectangular coordinates (Fig. 4).

Our aim will be to express the stress function  $\varphi$  through the axial stress  $\sigma_z$  which we can determine directly from the measurement data.

Let us express the stress function  $\varphi(x, y)$  in the form

$$\varphi(x, y) = \sum_{i,k=0}^m \alpha_{ik} \varphi_{ik}(x, y), \quad (4.1)$$

where

$$\varphi_{ik}(x, y) = (x^2 - a^2)^k (y^2 - b^2)^i x^{2i} y^{2k}. \quad (4.2)$$

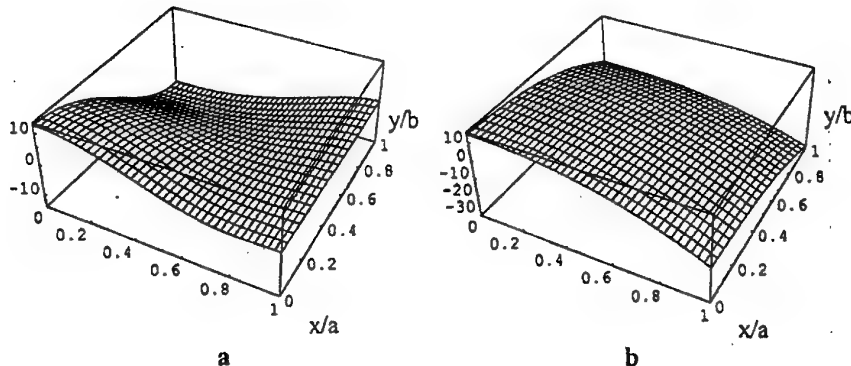


Figure 5. Distribution of the normal stresses  $\sigma_x$  (a) and  $\sigma_z$  (b) in a quadrant of the glass prism.

It can be shown that the coefficients  $\alpha_{ik}$  can be determined if distribution of  $\sigma_z$  is known. Knowing the stress function, the normal stresses  $\sigma_x$  and  $\sigma_y$  are determined as

$$\sigma_x = \sum_{i,k=0}^m \alpha_{ik} \frac{\partial^2 \varphi_{ik}}{\partial y^2}, \quad \sigma_y = \sum_{i,k=0}^m \alpha_{ik} \frac{\partial^2 \varphi_{ik}}{\partial x^2}. \quad (4.3)$$

The method described above has been used for complete determination of the residual stresses in a glass prism of quadratic cross section 40 x 40 mm. Axial stress distribution was determined with an automatic polariscope passing the light through the cross section of the prism in 60 directions (step 3 deg). For every direction of observation optical retardation was recorded at 140 points. Since in the middle of the prism stress gradient in axial direction can be ignored, we have practically the case of plane deformation.

The stress function was approximated in normalized coordinates as

$$\varphi(x, y) = (x^2 - 1)^2(y^2 - 1)^2[\alpha_{00} + \alpha_{10}(x^2 + y^2) + \alpha_{11}x^2y^2]. \quad (4.4)$$

Distribution of the normal stresses  $\sigma_z$  and  $\sigma_x$  is shown in Fig. 5. Macrostatic equilibrium conditions for  $\sigma_x$  and  $\sigma_z$  are well observed.

### 5. Conclusion

It has been shown that after distribution of the normal stress  $\sigma_z$  has been measured experimentally with integrated photoelasticity, axisymmetric thermal stresses (or axisymmetric residual stresses in glass) and stress

distribution in the case of plane deformation can be completely determined using relationships derived from the equations of the theory of elasticity.

### 6. Acknowledgement

The support by the Estonian Science Foundation (grant No. 2248) is greatly appreciated.

### References

1. Aben, H.: *Integrated Photoelasticity*, McGraw-Hill, New York *et al.*, 1979.
2. Aben, H.K., Josepson, J.I., and Kell, K.-J.E.: The case of weak birefringence in integrated photoelasticity. *Optics and Lasers in Eng.* 11 (1989), 145-157.
3. Aben, H., Josepson, J., and Puro, A.: Cases of weak and strong birefringence in integrated photoelasticity. In M.Kh.Akhmetzjanov, S.I.Gerasimov, and K.L.Komarov (eds.), *Photomechanics' 95*. Proc. SPIE, vol. 2791, 1996, pp. 2-7.
4. Doyle, J.F., and Danyluk, H.T.: Integrated photoelasticity for axisymmetric problems. *Exp. Mech.* 18 (1978), 215-220.
5. Doyle, J.F.: Closed-form inversion of the axisymmetric integrated photoelasticity equations. *J. Appl. Mech.* 47 (1980), 431-433.
6. Bartenev, G.M.: *The Structure and Mechanical Properties of Inorganic Glasses*. Wolters-Nordhoff Publ., Groningen, 1970.
7. Gardon, R.: Thermal tempering of glass. In D.R.Uhlmann, and N.J.Kreidl (eds.), *Elasticity and Strength of Glass. Glass: Science and Technology*. 5. Academic Press, New York, 1980, pp. 196-217.
8. Melan, E., and Parkus, H.: *Wärmespannungen infolge stationärer Temperatursfelder*. Springer-Verlag, Wien. 1953.
9. O'Rourke, R.C.: Three-dimensional photoelasticity. *J. Appl. Phys.* 22 (1951), 872-878.
10. Aben, H., and Guillemet, C.: *Photoelasticity of Glass*. Springer-Verlag, Berlin *et al.*, 1993.
11. Urbanczyk, W., and Pietraskiewicz, K.: Measurement of stress anisotropy in fiber preform: modification of the dynamic spatial filtering technique. *Appl. Opt.* 27 (1988), 4117-4122.
12. Timoshenko, S., and Goodier, J.N.: *Theory of Elasticity*, McGraw-Hill, New York *et al.*, 1951.
13. Herman, G.T.: *Image Reconstruction from Projections*. Academic Press, New York, 1980.
14. Aben, H.: Tomographie optique des champs de contraintes. *Rev. Française de Mécanique*, No 1 (1989), 121-130.
15. Aben, H.K., Idnurm, S.J., Josepson, J.I., Kell, K.-J.E., and Puro, A.: Optical tomography of the stress tensor field. In G.Levin (ed.), *Analytical Methods for Optical Tomography*, Proc. SPIE, vol. 1843, 1992, pp. 220-229.
16. Puro, A.E., and Kell, K.-J.E.: Complet determination of stress in fiber preforms of arbitrary cross section. *J. Lightwave Technol.* 10 (1992), 1010-1014.

## D. IMAGE. PROC. BY PHASE SHIFT. M. U. FOURIER TRANS.

1

**DIGITAL IMAGE PROCESSING BY PHASE SHIFTING METHOD  
USING FOURIER TRANSFORM**

Y. MORIMOTO and M. FUJIGAKI

*Department of Opto-Mechatronics, Faculty of Systems Engineering  
Wakayama University  
Sakaedani, Wakayama 640-8510, JAPAN***Abstract**

Phase analysis methods provide accurate results of fringe pattern analysis. A phase shifting method using Fourier transform uses many images obtained by changing the phases of fringe patterns. The phase at each pixel point is analyzed by calculating the argument using Fourier transform of the phase shifted brightness at the pixel point. It is applied to the analysis of fringe patterns obtained by a Twyman-Green interferometer and photoelastic fringe patterns obtained by a linear polariscope. Furthermore it is extended to a phase shifting method using correlation with rectangular functions to measure a 3-D shape by a grating projection method.

**1. Introduction**

Small displacement, stress and optical shape of specimens are able to be measured by using optical interferometry such as moire interferometry, Twyman-Green interferometry, Fizeau interferometry and photoelasticity. The shape of a 3-D object is also measured by grating projection methods. The displacement and the shape are measured by analyzing the images of fringe patterns. The analysis of fringe patterns by hand requires great skill. It is, furthermore, tedious and it consumes much labor and much time because of an enormous amount of two-dimensional data. The images are recently analyzed by a computer using digital image processing technique to perform automated, high speed and accurate analysis [1-3]. In the early stage of fringe pattern analysis using computers, the analysis methods were similar to the method by hand. It required skillful technique to obtain the positions of the center lines of fringe lines and to determine fringe orders.

To analyze interference fringes accurately, phase-measurement techniques [4-19] becomes popular. A fringe pattern obtained by optical interferometry usually has a sinusoidal brightness distribution. If the phase information of the sinusoidal brightness is analyzed at each pixel point on the image, the displacement at each point of the whole interference field is obtained accurately.

There are some methods for the phase analysis. The first is the phase stepping method (PSM) [5-6] using a few images obtained by changing the phase shift amount. The second is the Fourier transform moire and grid methods (FTP, FTM or FTMG) [7-12] using one image. The third is the phase shifting method using extraction of characteristic (PSM/EC) [13-14] using many images obtained by changing the phase shift amount. The method obtains the phase distribution by detecting the maximum brightness on each pixel point of the fringe images while the phase of the images shifts through  $2\pi$ . As the fourth, the authors developed a method using wavelet transform to analyze phase information from one image [16]. The authors also proposed a method using Gabor transform [17].

In the PSM, the accuracy is not good in case that the image input equipment has nonlinearity or the images have noise and phase shift error. In the FTMG, the results include some errors at the both edges of the image if the image has a discontinuity at the both edges of the image. The PSM/EC does not require any complicated processing which the PSM and the FTMG require. It resists the nonlinearity of the image input equipment. But this method is more sensitive to noise such as random noise and phase shift error than the Fourier transform methods. Though the wavelet transform method gives accurate strain distributions, it requires too much time to calculate. The Gabor transform method can be applied to wider frequency region than the FTMG.

Bruning et. al. [4] proposed a phase analysis method using several images obtained by changing the phase shift amount. The authors applied this method to the measurement of beam deflection [14]. The authors also applied it to the photoelastic fringe pattern analysis to separate the isochromatics and the isoclinics from the images obtained by a plane polariscope [15]. The authors call this method the phase shifting method using Fourier transform (PSM/FT). These methods are useful to obtain a wrapped phase distribution using a 3-D image. Huntley et al. [18] introduced a phase unwrapping method using a 3-D image.

Furthermore the authors extend it to a phase shifting method using correlation to measure 3-D shapes by a grating projection method.

In this paper the phase shifting method using Fourier transform applied to Twyman-Green interferometer and a plane polariscope are introduced, and also the phase shifting method using correlation of the rectangular brightness of a projected grating and two rectangular functions to analyze 3-D shapes are explained [19].

## 2. Phase shifting method using Fourier transform applied to Twyman-Green interferometer [14]

### 2.1 THEORY OF PHASE SHIFTING METHOD USING FOURIER TRANSFORM

Let us show the theory of the phase shifting method using Fourier transform, PSM/FT. A fringe pattern obtained by interferometry such as Twyman-Green interferometry, moire interferometry and holographic interferometry has a cosinusoidal brightness distribution.

The fringe pattern is usually produced by the interference between two beams i.e. an object beam and a reference one. If the optical path of one of the beams is moved a little in

## D. IMAGE. PROC. BY PHASE SHIFT. M. U. FOURIER TRANS.

3

the direction normal to the optical path, the phase of the fringe at every point is shifted by a constant value. The brightness distribution  $f(x, y)$ , when the phase shifting is performed, is expressed as follows:

$$f(x, y) = a(x, y) \cdot \cos\{\phi(x, y) - \alpha\} + b(x, y) \quad (1)$$

where  $a(x, y)$  is the amplitude of the brightness,  $b(x, y)$  is the average brightness,  $\phi(x, y)$  is the phase value which we have to analyze at any point  $(x, y)$  on the original fringe pattern, and  $\alpha$  is the amount of the phase shift of the optical path. When the interferometer has an object beam and a reference beam, the phase shifting is usually performed by moving a mirror with a piezoelectric transducer (PZT) or by tilting a glass plate in the reference beam. The phase is shifted little by little until the amount of the phase shift  $\alpha$  covers from 0 to  $2\pi$ , and every 2-D  $(x, y)$  image is recorded. A 3-D  $(x, y, \alpha)$  image consists of the sequentially phase shifted 2-D  $(x, y)$  images. Figure 1(a) shows an example of a 3-D image when the number of the 2-D images is six. Figure 1(b) shows the brightness distributions along an  $x$ -directional line of the 3-D image. In the same pixel point on the  $x$ - $y$  plane of this 3-D image, the  $\alpha$ -directional brightness distribution is one cycle of a sinusoidal form. An example is shown as a thick line in the figure.

In the method PSM/FT, the brightness distribution  $f(x, y)$  expressed in Eq. (1) is regarded as a function of  $\alpha$ . The  $\alpha$ -directional brightness distribution  $f(\alpha)$  is expressed in the Fourier series with respect to  $\alpha$ , because it is a periodic function with a period  $T=2\pi$ . That is

$$f(\alpha) = \sum_{n=-\infty}^{\infty} c_n \cdot \exp(jn\omega_0\alpha) \quad (2)$$

where

$$c_n = \frac{1}{T} \int_{-\frac{T}{2}}^{\frac{T}{2}} f(\alpha) \cdot \exp(-jn\omega_0\alpha) d\alpha \quad (3)$$

$j$  is the imaginary unit and  $\omega_0 (=1)$  is the fundamental frequency.

The  $\alpha$ -directional Fourier transform of Eq. (2) is

$$\begin{aligned} F(\omega) &= \int_{-\infty}^{\infty} f(\alpha) \cdot \exp(-j\omega\alpha) d\omega = \sum_{n=-\infty}^{\infty} c_n \int_{-\infty}^{\infty} \exp(jn\omega_0\alpha) \cdot \exp(-j\omega(n\omega_0 - n\omega)) d\alpha \\ &= \sum_{n=-\infty}^{\infty} 2\pi \cdot c_n \cdot \delta(\omega - n\omega_0) \end{aligned} \quad (4)$$

where  $\omega$  is frequency and  $\delta$  is the Dirac delta function. If the phase shifting is performed perfectly and the 3-D image data have no noise, the frequency spectrum expressed in Eq. (4) appears only at the frequency  $\omega = -1, 0, 1$ . By substituting Eqs. (1) and (3) into Eq. (4) when  $\omega=1$  and  $n=1$ ,  $F(\omega_0)$  is obtained.

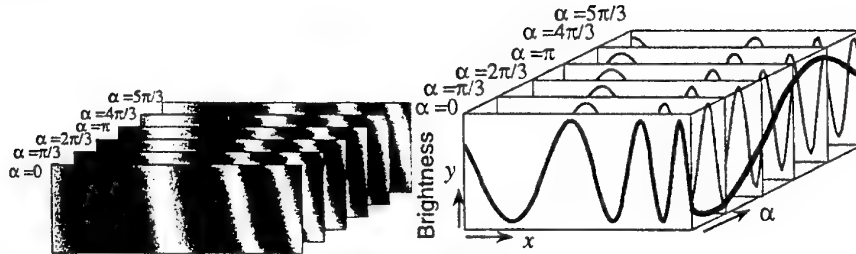
$$\begin{aligned}
 F(\omega_0) &= \frac{2\pi}{T} \delta(0) \int_{-\frac{T}{2}}^{\frac{T}{2}} f(\alpha) \cdot \exp(-j\omega_0\alpha) d\alpha = \delta(0) \int_{-\pi}^{\pi} \{a \cdot \cos(\phi - \alpha) + b\} \cdot \exp(-j\alpha) d\alpha \\
 &= \pi \cdot a \cdot \delta(0) \cdot \exp(-j\phi)
 \end{aligned} \tag{5}$$

This means that the phase value  $\phi$  is obtained by calculating the argument, i.e., the arctangent of the ratio of the imaginary part to the real part of  $F(\omega_0)$ :

$$\phi = -\tan^{-1}\left[\frac{\text{Im}\{F(\omega_0)\}}{\text{Re}\{F(\omega_0)\}}\right] \tag{6}$$

Like this, the phase distribution  $\phi(x, y)$  is obtained. The displacement or the shape of the specimen is calculated from the phase distribution.

In this method, because only the harmonic with frequency 1 is extracted, phase shifting error and the other experimental noise which appears at other frequency components are eliminated.



(a) Phase shifted fringe pattern      (b) Brightness distribution along a line

Figure 1.  $x$ -directional brightness distributions of phase shifted fringe patterns of 3-D image

## 2.2 EXPERIMENT FOR CANTILEVER BEAM

### 2.2.1 Experimental procedure

Figure 2 shows an application of the PSM/FT to the measurement of the out-of-plane displacement distribution of a cantilever beam using a Twyman-Green interferometer. Figure 3 shows the specimen and the measured area of this experiment. The specimen is a glass plate and it has an initial deformation. One end of the plate is fixed on a thick steel plate with a plastic glue and it is deformed at one line near the other end shown as the dashed line in Fig. 3. The displacement value at the loading point is  $2\mu\text{m}$ .

In this study, the phase shifting in the interferometer is performed by moving the reference mirror with a PZT control stage. The resolution of the stage movement is fine in the order of a few nanometer, the stage is moved along the optical path, as shown in the plain arrow line in Fig. 2. A reference mirror is moved little by little, and all the images are recorded in an image grabber system through a CCD camera. The phase at each pixel

## D. IMAGE. PROC. BY PHASE SHIFT. M. U. FOURIER TRANS.

5

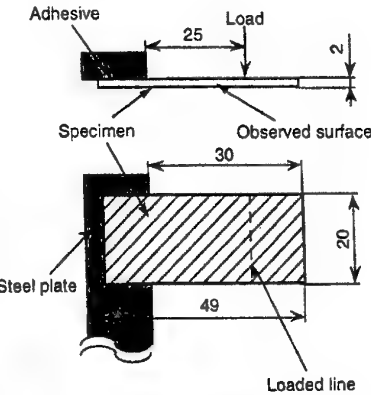
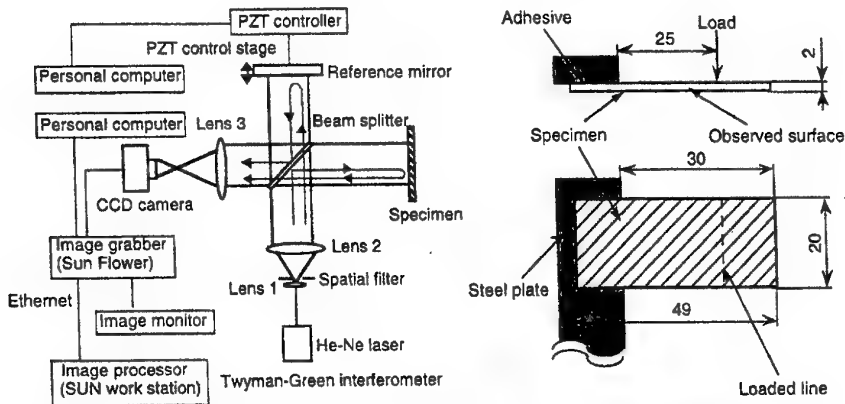


Figure 2. Schematic diagram of experimental system Figure 3. Specimen and measured area (Unit mm)

point of the interference image is analyzed as mentioned in the previous section. In order to calculate displacement, the sequential phase shifted images before and after deformation are recorded respectively. The difference  $\Delta\phi$  of the phases at each pixel point between images before and after deformation is analyzed. The displacement is calculated from the following equation.

$$u = \frac{\lambda}{4\pi} \Delta\phi \quad (7)$$

where  $u$  is the displacement and  $\lambda$  is the wavelength of the laser. In this experiment, a He-Ne laser is used as the light source, the wavelength  $\lambda$  is 633 nm.

### 2.2.2 Experimental results

Fig. 4 shows some parts of the sequential phase shifted fringe patterns before and after deformation respectively. The fringe images before deformation represent the initial deformation of the specimen and the optical system. The amount of one step of the phase shift is  $\pi/15$ . The 3-D image consists of 30 phase shifted 2-D images. Figure 4 shows



Figure 4. Phase shifted fringe patterns of 3-D image;

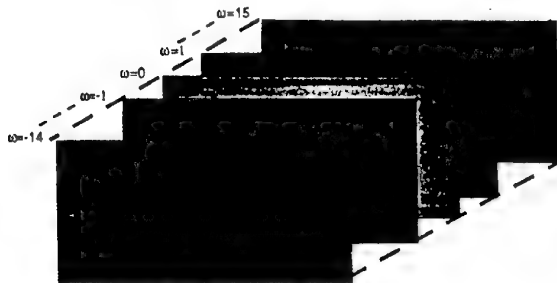
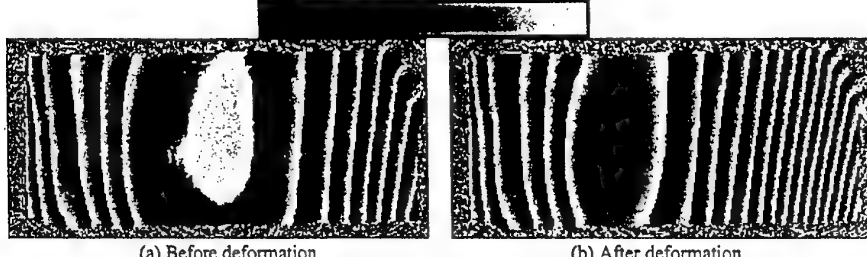


Figure 5. Fourier spectrum (After deformation)

 $\pi$  (rad)

(a) Before deformation

(b) After deformation

Figure 6. Wrapped phase distribution

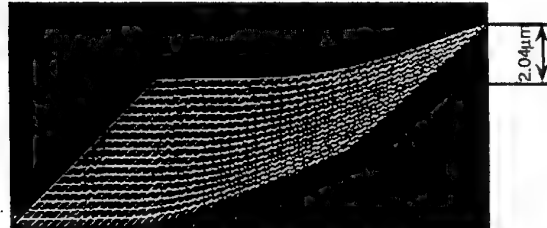


Figure 7. Displacement distribution obtained by the PSM/FT (3-D plot)

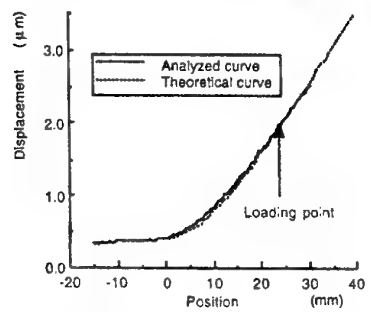


Figure 8. Displacement curve along x-directional center line

## D. IMAGE. PROC. BY PHASE SHIFT. M. U. FOURIER TRANS.

7

only 4 2-D images to understand easily in visualization. After performing the  $\alpha$ -directional Fourier transform on the 3-D image using the mixed radix FFT as used in our previous method [11, 12], the Fourier spectrum for the data after deformation are obtained as shown in Fig. 5. This figure shows only 5 2-D images although there are 30 2-D images. The brightness corresponds to the amount of the real part of the frequency at the pixel point. The brightness is low in the images except the frequency 1, 0 and -1. They are showing the error components. By extracting the frequency with 1 and calculating the argument at every point, the wrapped phase distribution is obtained as shown in Fig. 6. After connecting the wrapped phase distributions smoothly by adding  $\pm 2\pi$  at the discontinuity, the unwrapped phase distributions are obtained. The displacement distribution is calculated from the difference of the phases between before and after deformation. The result is shown in Fig. 7. Figure 8 shows the displacement curve along the  $x$ -directional center line. The theoretical curve is shown in Fig. 8 for comparison.

### 3. Phase shifting method using Fourier transform applied to plane polariscope [15]

In photoelasticity, the image obtained in the field of a plane polariscope consists of isochromatics and isoclinics. In analysis of stress, though it is necessary to separate the isochromatics and the isoclinics, it is difficult. The most popular method is to use the isochromatic fringe image captured in the field of a circular polariscope [20]. The isoclinics are not obtained by a circular polariscope. The positions of the isoclinics obtained by a plane polariscope are not so accurate because of the wide width of the isoclinic lines and the accuracy of quarter wave plates. The authors [13] developed a software of 3-D image processing, and applied it to the analysis of the 3-D ( $x, y, \theta$ ) image data consisted with the spatial coordinates ( $x, y$ ) and the angle  $\theta$  of the crossed polaroids.

In this section, the phase shifting method using Fourier transform applied to the separation of the isochromatics and the isoclinics is shown.

#### 3.1 THEORY OF SEPARATION OF ISOCHROMATICS AND ISOCLINICS

The light intensity obtained in a dark-field plane polariscope, shown in Fig. 9, is expressed by

$$i(\theta) = a^2 \sin^2 \{2(\phi - \theta)\} \cdot \sin^2(m\pi) \quad (8)$$

$$= \frac{a^2}{2} \{1 - \cos 4(\phi - \theta)\} \cdot \sin^2(m\pi) \quad (9)$$

where  $a$  is the amplitude of the incident polarized light,  $\phi$  is the angle of the principal stress and  $\theta$  is the angle of the analyzer and  $m$  is the isochromatic fringe order. The fringe order  $m$  is expressed as follows:

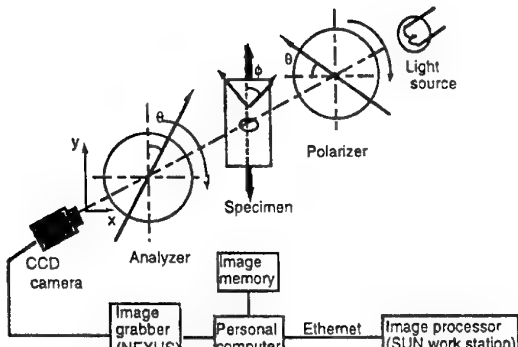


Figure 9. Schematics of polariscope and image processor

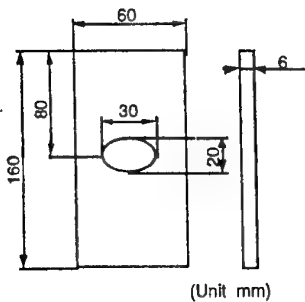


Figure 10. Specimen

$$m = (C/\lambda)d(\sigma_1 - \sigma_2) \quad (10)$$

where  $C$  is the photoelastic constant,  $d$  is the thickness of the specimen,  $\lambda$  is the wavelength and  $(\sigma_1 - \sigma_2)$  is the principal stress difference of the specimen.

Equation (8) is expressed in the Fourier series with respect to  $\theta$ , because it is a periodic function with a period  $T=\pi/2$ . That is

$$i(\theta) = \sum_{n=-\infty}^{\infty} c_n \exp(jn\omega_0\theta) \quad (11)$$

where

$$c_n = \frac{1}{T} \int_{-\frac{T}{2}}^{\frac{T}{2}} i(\theta) \cdot \exp(-jn\omega_0\theta) d\theta \quad (12)$$

and

$$\omega_0 = \frac{2\pi}{T} = \frac{2\pi}{\pi/2} = 4 \quad (13)$$

The Fourier transform of Eq. (11) is

$$\begin{aligned} I(\omega) &= \int_{-\infty}^{\infty} i(\theta) \cdot \exp(-j\omega\theta) d\theta = \sum_{n=-\infty}^{\infty} c_n \int_{-\infty}^{\infty} \exp(jn\omega_0\theta) \cdot \exp(-j\omega\theta) d\theta \\ &= \sum_{n=-\infty}^{\infty} 2\pi \cdot c_n \delta(\omega - n\omega_0) \end{aligned} \quad (14)$$

where  $j$  is the imaginary unit,  $\omega$  is frequency and  $\delta$  is the Dirac delta function.

Equation (14) indicates the discrete frequency spectrum which appears only on the frequency components  $n\omega_0$  ( $n=0, \pm 1, \pm 2 \dots$ ). By extracting the delta functions  $2\pi \cdot c_0 \delta(0)$  and substituting Eq. (9) and Eq. (12) into Eq. (14) when  $n=0$ ,  $2\pi c_0 (n=0)$  is

## D. IMAGE. PROC. BY PHASE SHIFT. M. U. FOURIER TRANS.

9

obtained.

$$\begin{aligned}
 2\pi c_0 &= \frac{2\pi}{T} \int_{-\frac{T}{2}}^{\frac{T}{2}} i(\theta) d\theta = 4 \int_{-\frac{\pi}{4}}^{\frac{\pi}{4}} \frac{a^2}{2} \{1 - \cos 4(\phi - \theta)\} \sin^2(m\pi) d\theta \\
 &= 2a^2 \sin^2(m\pi) \int_{-\frac{\pi}{4}}^{\frac{\pi}{4}} \{1 - \cos 4(\phi - \theta)\} d\theta = \pi a^2 \sin^2(m\pi)
 \end{aligned} \tag{15}$$

$2\pi c_0 = \pi a^2 \sin^2(m\pi)$  is obtained from the amplitude at  $\omega = 0$  of the Fourier spectrum of the  $\theta$  directional brightness distribution. Equation (15) indicates that the isoclinics are eliminated. That is, the image of  $2\pi c_0$  shows the isochromatics in the whole field of the specimen.

In the same way, from Eq. (9), Eq. (12) and Eq. (14) where  $n=-1$ , can be written

$$\begin{aligned}
 2\pi c_{-1} &= \frac{2\pi}{T} \int_{-\frac{T}{2}}^{\frac{T}{2}} i(\theta) \cdot \exp(j\omega_0\theta) d\theta \\
 &= 4 \int_{-\frac{\pi}{4}}^{\frac{\pi}{4}} \frac{a^2}{2} \{1 - \cos 4(\phi - \theta)\} \sin^2(m\pi) \cdot \exp(j4\theta) d\theta \\
 &= 2a^2 \sin^2(m\pi) \left[ \int_{-\frac{\pi}{4}}^{\frac{\pi}{4}} \exp(j4\theta) d\theta - \frac{1}{2} \int_{-\frac{\pi}{4}}^{\frac{\pi}{4}} [\exp(j4(\phi - \theta)) + \exp(-j4(\phi - \theta))] \exp(j4\theta) d\theta \right] \\
 &= -a^2 \sin^2(m\pi) \left[ \int_{-\frac{\pi}{4}}^{\frac{\pi}{4}} \exp(j4\phi) d\theta + \int_{-\frac{\pi}{4}}^{\frac{\pi}{4}} \exp(-j4(\phi - 2\theta)) d\theta \right] \\
 &= -\frac{\pi}{2} a^2 \sin^2(m\pi) \cdot \exp(j4\phi)
 \end{aligned} \tag{16}$$

The argument  $4\phi$  is obtained by calculating the arctangent of the ratio of the imaginary and real parts of  $2\pi c_{-1}$ :

$$4\phi = \tan^{-1} \left| \frac{I_m(2\pi c_{-1})}{R_e(2\pi c_{-1})} \right| \tag{17}$$

Equation (17) indicates that one fourth of the argument is equal to the direction of principal stress.

In this method, by calculating the Fourier transform of the sequential images captured by the rotating the angle  $\theta$  of the crossed polaroids, the isochromatic image is

obtained from only the intensity data of the frequency where  $\omega = 0$ . The direction of principal stress on each point is computed from only the argument where  $\omega = -\omega_0$ . The other frequency components, in other words, experimental noise is completely eliminated.

### 3.2 EXPERIMENT FOR PLATE WITH ELLIPTIC HOLE

The photoelastic experiment system with the crossed plane polariscope is shown in Fig. 9. Figure 10 shows the specimen made of epoxy resin. The rectangular plate has an elliptic hole at the center. The constant tensile load along the y axis yielding on the specimen is 6.5 N. The polaroids are rotated in the crossed position when the angle  $\theta$  is from  $-45^\circ$  to  $44^\circ$ .

Ninety sequential 2-D images recorded at every  $1^\circ$  angle of  $\theta$  from  $-45^\circ$  to  $44^\circ$  with a CCD camera are stored into a hard disk. One mm corresponds to 1.98 pixels. The ninety 2-D images are treated as a 3-D image as shown in Fig. 11. The size of the 3-D image is 128 (width)  $\times$  120 (height)  $\times$  90 (depth) pixels. The 3-D image data are directly processed using the 3-D image processing program including Fourier transform programmed by the authors.

The mixed radix fast Fourier transform (MRFFT) in the  $\theta$  direction yields the 3-D image data, i.e. the Fourier spectrum as shown in Fig. 12. In this figure, the 2-D image at  $\omega = 0$  shows the isochromatics. Figure 13 is the isochromatics.

By calculating the arctangents of the ratios of the imaginary parts and the real parts of the data in the frequency at  $\omega = -\omega_0$ , the directions of principal stresses are determined in the whole field of the specimen as shown in Fig. 14.

This method is insensitive of high frequency noise, because the high frequency components are eliminated using Fourier filter. The positions and angles may have finer resolution than those in the conventional method, because the data obtained using Fourier transform is naturally smooth.

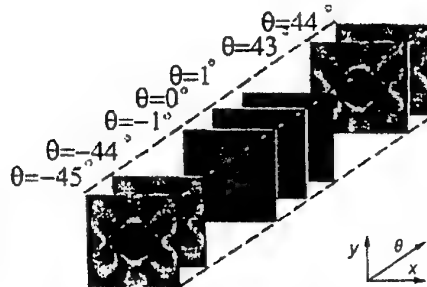


Figure 11. Three-dimensional image data

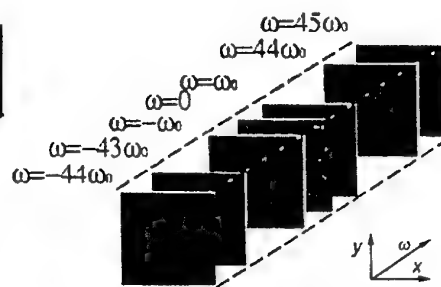


Figure 12.  $\theta$  directional frequency spectrum of image data of Fig. 11

## D. IMAGE. PROC. BY PHASE SHIFT. M. U. FOURIER TRANS.

11

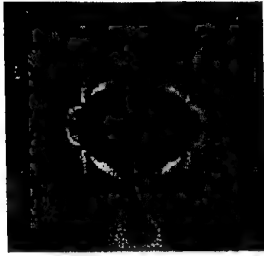


Figure 13. Isochromatics obtained by PSM/FT



Figure 14. Distribution of principal stress direction

#### 4. Phase shifting method using correlation with rectangular function applied to 3-D shape measurement [19]

In this section, we propose a new phase shifting method to analyze phase distribution using the correlation between the brightness of the projected grating and a rectangular function. Figure 15 shows the brightness distributions of the projected grating at a pixel point while the projected phases are shifted. Figures 15(a) and (b) show examples when the initial phases of the grating projected at the points are 0 and  $\phi$ , respectively. The distribution is a rectangular function with a period  $2\pi$ . The upper and lower brightness intensities are mainly depending on the reflection ratio of the object. After normalizing the brightness, the normalized brightness is multiplied by two weight functions  $f_0$  and  $f_1$  shown in Fig. 16 (a) and (b), respectively. Figure 16(a) is a rectangular weight with phase 0. Figure 16(b) is a rectangular weight with phase  $\pi/2$ . The products are integrated from  $\alpha=0$  to  $\alpha=2\pi$ , respectively.

Figure 17(a) shows the relationship between the initial phase  $\phi$  and the integration values  $S$ . From the two integration values  $S_0$  and  $S_1$ , obtained by two weight functions  $f_0$  and  $f_1$ , respectively, the phase  $\phi$  is determined as wrapped phase  $\phi'$  uniquely from the following conditions.

- A:  $\phi' = -S_1/4$  when  $S_0 > S_1$  and  $|S_0| > |S_1|$
- B:  $\phi' = -S_0/4 + \pi/2$  when  $S_0 > S_1$  and  $|S_0| < |S_1|$
- C:  $\phi' = -S_0/4 + \pi/2$  when  $S_0 = S_1$  and  $S_0 < 0$
- D:  $\phi' = S_1/4 - \pi$  when  $S_0 < S_1$ ,  $S_1 \geq 0$  and  $|S_0| > |S_1|$  (18)
- E:  $\phi' = S_1/4 + \pi$  when  $S_0 > S_1$ ,  $S_1 < 0$  and  $|S_0| > |S_1|$
- F:  $\phi' = -S_0/4 - \pi/2$  when  $S_0 < S_1$  and  $|S_0| < |S_1|$
- G:  $\phi' = -S_0/4 - \pi/2$  when  $S_0 = S_1$  and  $S_0 > 0$

The results are shown in Fig. 17(b).

Since this algorithm is very simple, it is easy to perform high-speed processing. Since the grating brightness function is rectangular, the non-linearity of input devices does not affect the results.

This method is applied to shape measurement of a rubber ball and a metal spoon.

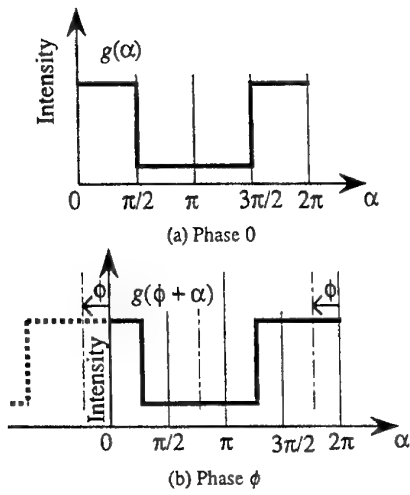


Figure 15. Brightness distribution of projected grating obtained by shifting phase

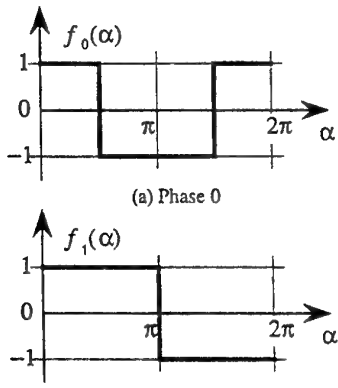
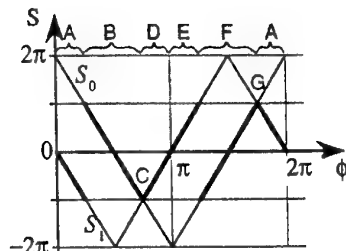
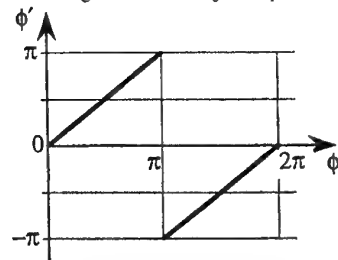


Figure 16. Weight distributions of filters



(a) Relationship between initial phase  $\phi$  and integration values  $S_0$  and  $S_1$



(b) Calculated wrapped phase  
Figure 17. Relationships between initial phase  $\phi$  and integration values and calculated phase

The projected grating is shifted by  $2\pi/32$ , and the 32 products are calculated and added. All the images are used for this analysis. As we use only a conventional personal computer, in this paper, the processing time is a few second. It is, however, possible to make a real-time hardware for this method.

Figure 18(a) shows one of the 32 images. The resultant phase distribution is shown in Fig. 18(b). This method is useful even if the material of an object is metal because the use of a grating with rectangular brightness can detect the brightness change.

## D. IMAGE. PROC. BY PHASE SHIFT. M. U. FOURIER TRANS.

13

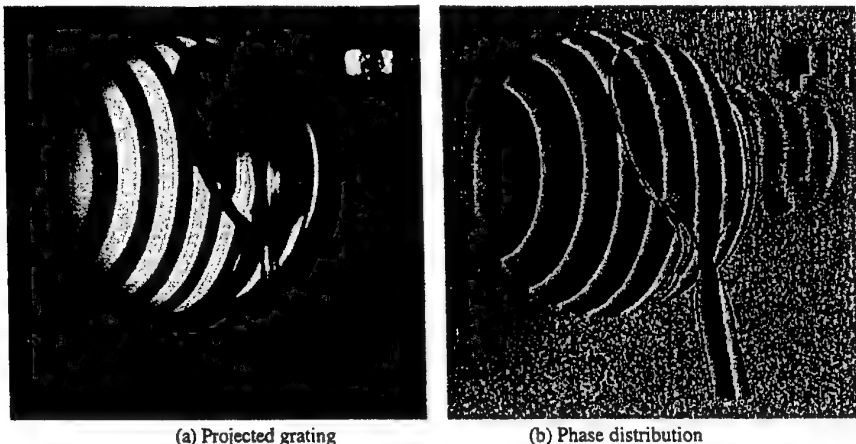


Figure 18. Phase distribution of rubber ball and metal spoon obtained by phase shifting method using correlation with rectangular

## 5. CONCLUSIONS

The phase shifting method using Fourier transform (PSM/FT) has been introduced to analyze the phase distribution of interference fringes. In this method many sequentially phase shifted fringe patterns are required, however, the effect of noise and phase shifting error of the patterns are eliminated by performing the  $\alpha$ -directional Fourier transform and extracting the harmonic with frequency 0, 1 or -1. This method is more insensitive to noise than the other methods and error does not appear at the both edges of the image unlike the results obtained by the conventional 2-D Fourier transform method (FTMGM). If accurate phase shifting is performed, the phase is analyzed from only a few phase shifted fringe images. The PSM/FT has been applied to measurement of the displacement distribution of a cantilever beam using Twyman-Green Interferometer.

The PSM/FT has been applied to the separation of the isochromatics and the isoclinics obtained in the plane polariscope. The isochromatics and the isoclinics are separated almost automatically from the 3-D image data obtained by rotating the crossed polaroids.

Full automated analysis is possible and this method is useful for not only optical interferometric fringe analysis but also the other fringe pattern analysis such as shape measurement by the grating projection method.

The authors have also proposed the real-time phase shifting method using correlation with two rectangular functions. By using this method, the 3-D shapes of a ball and a spoon have been analyzed.

This study is supported by Research Project (Project No. 09555033), the Grant-in-aid for Scientific Research of the Ministry of Education, Science and Culture.

## 6. REFERENCES

1. Sirkis, J. S. Chen, Y., Singh, H. and Cheng, A. Y.: Computerized optical fringe pattern analysis in photomechanics: a review, *Opt. Eng.*, **31**-2, (1992), 304-314.
2. Kujawinska, M.: Automatic fringe pattern analysis in optical methods of testing, *Warsaw Univ. Technol. Sci. Rep.*, **138**, (1990), 1-80.
3. Morimoto, Y.: Chap. 21 Digital image processing, in Kobayashi, A. S. (Ed), *Handbook on Experimental Mechanics, Second Revised Ed.*, , Soc. for Exp. Mech., (1993), 969-1030.
4. Brunning, J.H., Herriott, D. R., Gallagher, J.E., Rosenfeld, D. P., White, A.D. and Brangaccio, D.J.: Digital wave front measuring interferometer for testing optical surface and lenses, *Appl. Opt.*, **13**, (1974), 2693-2703.
5. Hariharan, P. Oreb B. F. and Brown, N.: A digital phase-measurement system for real-time holographic interferometry, *Optics Communications*, **41**, (1982), 393-396.
6. Creath, K.: Phase measurement interferometry techniques, *Prog. Opt.*, **26**, (1988), 350-393.
7. Sciammarella, C. A. and Sturgeon, D. L.: Digital-filtering techniques applied to the interpolation of moire-fringes data, *Experimental Mechanics*, **7-11**, (1967), 468-475.
8. Takeda, M. Ina, H. and Kobayashi, S.: Fourier transform method of fringe pattern analysis for computer-based topography and interferometry, *J. Opt. Soc. Am.*, **72**-1, (1982), 156-160.
9. Macy, W. W. Jr.: Two-dimensional fringe-pattern analysis, *Appl. Opt.*, **22**-23, (1983), 3898-3901.
10. Bone, D. J., Bachor, H. A. and Sandeman, R. J.: Fringe-pattern analysis using a 2-D Fourier transform, *Appl. Opt.*, **25**-10, (1986), 1653-1660.
11. Morimoto Y., Seguchi, Y. and Higashi, T.: Application of moire analysis of strain by Fourier transform, *Optical Engineering*, **27**, (1988), 650-656.
12. Morimoto Y., Seguchi , Y. and Higashi, T.: Two-dimensional moire method and grid method using Fourier transform, *Experimental Mechanics*, **29**, (1989), 399-404.
13. Morimoto, Y., Morimoto, Y. Jr. and Hayashi, T.: Separation of isochromatics and isoclinics using 3-D image processing, *Proc. Japan Soc. for Photoelasticity (in Japanese)*, **13**-1, (1993), 23-28.
14. Morimoto Y. and Fujisawa, M.: Fringe-pattern analysis by phase-shifting method using extraction of characteristic, *Experimental Mechanics*, **20**-4, (1996), 25-29.
15. Morimoto, Y., Morimoto, Y. Jr. and Hayashi, T.: Separation of isochromatics and isoclinics using Fourier transform", *Experimental Technique*, **17**-5, (1994), 13-16.
16. Morimoto, Y. and Imamoto, Y.: Application of Wavelet Transform to Displacement and Strain Measurement by Grid Method, *Proc. of 1995 SEM Spring Conf. on Exp. Mech.*, (1995), 898-903.
17. Morimoto, Y., Inoue, H. and Fujigaki, M.: Application of Gabor Transform to 3-D Shape Analysis Using Grating Pattern Projection Method, *Int. Symp. on Adv. Tech. in Exp. Mech.*, JSME-MMD, (1995), 67-72.
18. Huntley, J. M. and Saldner, H.: Temporal phase-unwrapping algorithm for automated interferogram analysis, *Appl. Opt.*, **32**-17, (1993), 3047-3052.
19. Morimoto, Y. and Fujigaki, M.: Real-time phase-distribution analysis of fringe patterns, *Int. Conf. on Applied Optical Metrology, in Balatonfured, Hungary, SPIE*, submitted, 1998
20. Burger, C.P., "Chap. 5 Photoelasticity," in Kobayashi, A. S. (Ed), *Handbook on Experimental Mechanics, Second Revised Ed.*, , Soc. for Exp. Mech., (1993), 165-266

## DIGITAL IMAGE COMPARATOR FOR EXPERIMENTAL ANALYSIS OF DEFORMATIONS

L. BERKA<sup>1)</sup>, J. KLÍMA<sup>2)</sup>, M. DRUCKMÜLLER<sup>3)</sup>, M. SOVA<sup>4)</sup>  
<sup>1)</sup>*Faculty of Civil Engineering, Czech Technical University, Thákurova  
7, 166 29 Prague, Czech Republic*  
<sup>2)</sup>*Tescan Ltd, Brno*  
<sup>3)</sup>*Faculty of Mechanical Engineering, TU Brno*  
<sup>4)</sup>*SOVAX, Prague*

**Abstract.** Optical methods of deformation measurements represent one of the oldest and the most widespread area of experimental mechanics. The optic methods of strain measurements are generally-interferometry, stereo image analysis and digital image analysis. The above-mentioned optical methods are of particular importance for deformation analysis in microstructures and microobjects, where they are the only possible experimental tools. The basis of the stereoscopic technique of deformation measurements is the taking of pair stereoscopic photographs of objects, using the time base principle, i.e. photographs of objects before and after the deformation under the entirely same conditions are taken. The further step in stereointerimage method of the strain analysis is the stereocomparation of the pair of images. Up to now we have used for it the analog apparatus ZEISS-Stecometr. The paper which is presented describe a digital system of reading and comparation of the pairs of stereointerimages.

### 1. Introduction

Optical methods of deformation measurements represent one of the oldest and the most widespread area of experimental mechanics. The furthest and the most frequently used principle of optical methods is interference [1], and almost a hundred years old history has the stereoscopic principle [2]. Newer are photomethods applying image analysis to calculate coordinates of identification points fields [3].

The above-mentioned optical methods are of particular importance for deformations analyses in microstructures and microobjects, where they are the only possible experimental tool. Evolution of optical methods of deformations measurements in the field of experimental micromechanics commences at the end of 1980s. In the field of interferometry there are contributions of Sciammarella [4], and Michel and Kühnert [5]. Stereoscopic method was employed by Davidson [6], and Berka and Růžek [7]. Image analysis of microidentification point structures was worked-in-progress by Allais [8] and Fischer [9].

At present, the best sophisticated and the most frequently used method in this area is the interference micro-moire' technique of D. Post [10]. In our country, Václavík and Minster [11] are working with this technique. Advantage of it is the full-surface scan of deformations field and the high accuracy, reached by using grids pairs with the density of 1200 lines/mm, positioned both in the interferometer and also in the measured object. Development of the technique was influenced also by the rapid evolution of image analysis and digital technique, enabling measurement in the real time.

Evolution of the stereoscopic method of deformation analysis is connected with the overall development for evaluation of pairs stereoscopic photographs. This results from the fact that taking photographs and their analysis does not take place simultaneously. With regards to specific conditions of taking ground photographs by using special cameras, the evaluation systems are equipped with the high resolution scanners that markedly enhance purchase and operating expenses of these systems, and thus they become hard available. Users of stereoscopic measurement technique, who can work with digital image recording, gained by CCD camera or scanning electron microscope, therefore try to create on-line system enabling record, processing and comparation of images obtained by the time base method (Fig. 1). The system described in the following contribution is a digital image of the hitherto used analog system for recording and evaluation of stereoscopic photographs pairs, that was referred to on the previous conferences EAN [12].

### 2. The deformation analysis by the stereoimage technique

The basis of stereoscopic technique of deformation measurements is the taking of stereoscopic objects photographs pairs, using the time base principle, i.e. photographs of objects before and after the deformation under the entirely same conditions. To fulfil this requirement, it is necessary not only for the image-taking apparatus, a microscope in

our case, but also for the CCD camera to ensure, by their external (sample and apparatus position) and also internal (magnification stability, orientation) a reproducibility of photographs with accuracy attributed on the deformation measurement accuracy. This can be different according to the nature of solved problem (elastic or plastic deformation). According to it, it is also necessary to choose an appropriate method.

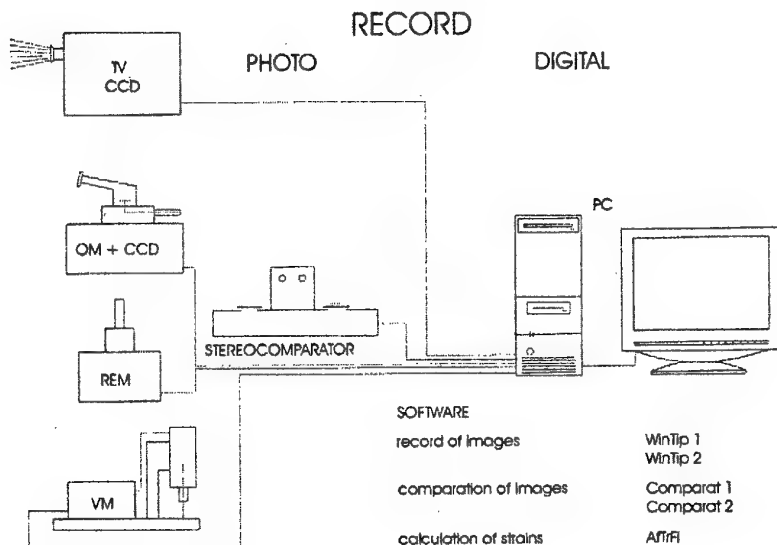


*Figure 1. The schematic drawing of the measuring system*

Taking into consideration deformation measurements in the vicinity of the agreed plasticity limit of steel, having a size of 0.2 % with accuracy 10 %, i.e. value of  $\Delta\epsilon = 0.02 \%$ , the requirement follows on the accuracy of the couple of stereoscopic photographs evaluation of undeformed specimen, obtained by the time base method. It means that after the first image processing, the specimen is undertaken to all necessary measurement operations, and then the second image is performed. Found values of fictive deformations represent faults of measurements that must be lower than the required value of 10 % of plasticity limit. Deviations may result from:

- differences in the position and microscopic identity of sample surface in its taking out and reloading into the vacuum microscope chamber
- differences in the resetting of microscope electronic regime during exchange or the switching the device off.

To minimize these deviations, it is necessary, regardless the type of a microscope, to choose such a method that will limit changes in the setting of device parameters, used in the first photographs processing, at maximum. This is the question of keeping the working distance and set magnification, whose deviations are equal to a relative error in their deformations measurements. Errors in the measured deformation can be caused also by overfocusing and higher differences in the brightness and contrast setting, which change dimensions of microobject image and thus conditions of the photographic comparison.

Further group of errors is connected with the quality of image recording, both photographic and digital. In case of the stereocomparation, besides identity of microsurface images, it is also internal resolution of stereocomparator  $\Delta l$ , which at device ZEISS Stecometr is  $2 \mu\text{m}$ . The necessary precision in the deformation measurement equal to  $\Delta e = 0.0002$  is reached at the photographic distance of compared points  $l$  equal to  $\Delta l/\Delta e = 2/0.0002 = 1.10 \mu\text{m}$ . At the smaller points distance, the error is bigger than presumed 10 %.

At digital system of evaluation of a stereoscopic pair of photographs, the accuracy of a points position is measured mainly by the resolution at which the image is taken.

### 3. The reading and image processing - system TESCAN

TESCAN has developed a device for digitization, preprocessing and recording of electron microscopic image. Hardware of the device is composed of personal computer, digital generator of scan signal and acquisition device of video signal, positioned on the special developed card in the ISA computer bus and converters units D/A and A/D in the separate box, where there are the circuits for an option of input analog signal, signal filters, power supplies and auxiliary circuits.

Signal for electron beam sweeping in the microscope tube is generated in the computer in the digital form. According to the generation principle, it is necessary to resolve fast and slow raster scanning. In the fast raster scanning mode - called "fast" in the program - the step signal is generated mainly by hardware tools - everything is subordinate to reaching the maximum speed of raster scanning. Sweeping is not synchronized with the power supply. This mode serves to the rapid scanning of specimen and to the microscope setting.

Generated sweeping signal is then, in the D/A converters units, transformed from the digital form onto the analog signal, and in the output circuit, it is possible to set its polarity, amplitude and ss level suitable for an appropriate type of microscope (between -10 and +10V). The basic setting of system magnification is carried out here in order that the operating field of system may be concordant with the original field of electron microscope .

Analog video signal generated and strengthened in the microscope is brought via input switching circuits into an A/D converter. Even four signal from different detectors from the microscope is possible to transfer into the input circuits, and one of them to choose for display by means of the program. In the A/D converter, the analog video signal is converted onto the digital form simultaneously with the filtration - all higher frequencies that are not necessary for real image signal transmission are reduced, and thus the image noise is reduced. Digital video signal is then via special interface, located on the same card in the computer as a generator of sweeping, brought into the computer video memory and - as far as an operator commands by means of the control program - the image is set also on the chosen memory medium.

The entire process of sweeping and image acquisition is controlled by the program that operates in the Window 95 environment and uses the standard image format BMP. The program includes also procedures for image preprocessing - brightness and contrast manipulation, image focusing and noise reducing. Program offers ample possibilities in the software calibration field of image magnification on the basis of known objects and measuring of formations in the image.

The big attention in the program creation has been also payed to the comfortable and users-friendly storage system, which enables quick scanning, copying and opening of stored images by means of "album" of their miniatures, sorting according to the data in the head stored with each image etc. Program enables to make images with the resolution of 256x256 up to 4096x4096 of image elements (pixels).

The researchers payed an extraordinary attention to the problem of necessary resolution (i.e. fineness of the raster step) and its fitting with the other requirements on the system. These requirements are rather controversial. As mentioned above, improvement of the signal/noise ratio is possible to reach by the duration of electron beam in each pixel, while in order to reach the higher resolution of optical microscope system, it is necessary to operate with "thinner" and unfortunately less intensive electron beam. Increasing of requirement on the duration in each pixel and simultaneously increasing of numbers of pixels in the given image leads to the disproportionate prolongation of time for one image - above the level, which is usually guaranteed by producers for stability of their devices and after all above the time acceptable for an operator. Thus, the probability is increased that during the long time of photo performing, a random failure of power supply or a shake etc. may happen, which is displayed by the image error. For example, in the size magnification of units of thousands and image division onto the 4096x4096 pixels, which is a requirement for microdeformation measurement with the above mentioned accuracy, at the microscopes with thermoemission electron gun is the time necessary for one pixel about 200  $\mu$ s, which at 4096x4096 pixels represents the time of image processing 60 minutes. During this time, defocusing of image may happen as well as its shifting by device drift or a change of brightness. When solving this problem, the procedure has been developed, which enables in the lower resolution raster regime (as a basic raster regime we consider resolution 512x512 pixels) to choose a window of the chosen size (using the multiple of

two), to place this window on the chosen object decisive for microdeformations evaluations, and then to scan the image in this window with the very fine raster scanning, which corresponds to 4096 image elements on the row throughout the whole image. Thus, scanned chosen parts of image are screened on the display with the full resolution, and can be used for evaluation of microdeformations by digital comparator.

In conclusion, it is necessary to add that the proposed system requires the best quality computer hardware. The necessity is the high quality resolution monitor and a graphic card with the memory 4 MB, fixed disc with the high capacity, or further tools for recording of digitized images sets.

#### 4. The digital comparation of stereoimages - system COMPARAT

To evaluate a stereoscopic pair of raster electron microscope images, the software system has been developed. The system enables an operation with images up to maximum dimension of 2048x2048 pixels. Both compared images are displayed simultaneously on the computer display in complementary colours. The high sensitivity of the human eye on the change of colour tone, which is near to neutral gray, is utilized. Changes in images are shown as garish colour changes. A user marks in an interactive way a certain amount of points corresponding each other in the both images. Thus, the relative shifts in these points are determined. The absolute shifts are possible to determine only after the precise matching of both compared images. Three following methods are possible to employ.

- 1) The precise matching of compared images is guaranteed by the technical solution of experiment. In this case, relative shifts are considered as absolute ones. In practice, it is very difficult to find such a technical solution.
- 2) During images scanning, it is guaranteed that both images have the same scale, i.e. magnification of the raster electron microscope is in both images identical. In this case, such a translation and rotation of the second of the images pair is searched in order that the sum of deviation quadrates in the users tagged points was minimal. Practically it is carried out in such a way that both images are placed into the complex numbers plane and linear transformation

$$w = a.z + b$$

is searched, where  $a, b$  are complex constants and  $\text{abs}(a) = 1$  is valid. After the linear transformation with required attributes has been found, the second of the images is transformed. Shifts between marked point in the first image and transformed second image are considered to be absolute.

- 3) This method is used then, when it is not possible to guarantee that compared images have the same scale. In this case, such a translation, rotation and homotetie (a scale change) is searched in order that the sum of deviation quadrates in the points marked by

the user may be minimal. Analogously with the item 2), the linear transformation is searched in the complex plane with the difference that abs (a) need not to equal to 1. It is possible to employ this method only if we accept an assumption that the size of surfaces has not been changed by deformation. After the linear transformation with required attributes has been found, the second of the images is transformed. Shifts between marked points in the first image and transformed second image are considered to be absolute.

After the absolute shifts have been found, the conform scan, determined by the absolute shifts in the set points is searched. This display is then employed for shifts matrix generation in the sufficiently dense grid of points. For images of 2048x2048 pixels, the grid with the step of 64 pixels is applied. This matrix of shifts is an output of the comparator. The system has also a possibility of graphic output in which the shifts vectors are plotted in the nodal points of a grid. To reach the maximum possible accuracy of printing on all possible types of printers, the system TEX has been chosen. The comparator generates automatically the source set for TEX, and therefore it is sufficient to translate this set using some of the TEX version (quite sufficient is the version Plain TEX) and print out. When employing laser printers 300 dpi or some better, the printing accuracy is comparable or better than an error caused by discretization of the image processed by the comparator.

##### 5. Objects of microstrain analysis

The deformations caused by machining were analysed. The machine technologies give many examples about the influence of machining conditions on the resulting properties of produced parts. The next figure shows the deformation of the plate due to the grinding (Fig. 2).



Figure 2. The plate edge after grinding, 400 x magnification. The mechanically cut grid with the step of 10  $\mu\text{m}$  can be seen on the left hand side.

## 6. References

- [1] Born, M., Wolf, E., Principles of Optics, 4th ed., Pergamon Press, N. Y., London (1970)
- [2] Pantofliček J., Technický obzor ( Technical Survey, Prague ), 21 (1913)
- [3] Hendryks, M. A. N., Identification of the Mechanical Behavior of Solid Materials. PhD. Thesis, TU Eindhoven (1991)
- [4] Sciammarella, C.A., Bhat, G., An electro-optical system to measure strains. Proc. of 9th Int. Conf. on Experimental Mechanics, TU Denmark, Copenhagen, 5(1990), 1924-1933.
- [5] Kühnert, R., Michel, B., Moire' techniques by means of scanning electron microscopy. Phys. State Solids (a) 89(1985), 163-165.
- [6] Davidson, D.L., The observation and measurement of displacements and strain by stereoimaging. Scanning Electron Microscopy 2(1979), 79-86.
- [7] Berka, L.; Růžek, M.: Analysis of microdeformations in a structure of polycrystals. J. Mater.Sci. 19, 5(1984), 1486-1495.
- [8] Alais, L., Bornert, M., Bretheau, T., Caldemaison, D., Experimental characterization of the local strain field in a heterogeneous elastoplastic material. Acta metall.mater. 42(1994) 3865-3880
- [9] Crostack, H.-A., Fischer, G., Deformation measurement at microstructural level by means of object grating method within SEM. Proceedings of the 15th Riso International Symposium on Materials Science, 1994, 275-280
- [10] Post , D., Moire Interferometry for Composites. Manual on Experimental Methods for Mechanical Testing of Composites, Pendleton, R. L. - Tuttle, M. E. Eds., SEM, (1989)
- [11] Václavík, M., Minster, D., Replikace mřížek pro moirovou interferometrii užitím interferenční fotografické matice. Jemná mechanika a optika, 41, 1(1996)
- [12] Berka L., Sova M., Experimental Methods of Strain Measurements in Microstructures. Sborník EAN 1994, 32. konference o experimentální analýze napětí.

## Acknowledgment

Support of the Grant Agency of the Czech Republic (Project No. 106/95/0596) is gratefully acknowledged.

## PRECISE AND ROBUST PHASE MEASUREMENT ALGORITHMS

M. F. KÜCHEL  
*Fachhochschule Aalen*  
*Heinrich-Rieger-Strasse 22/1*  
*D-73430 Aalen*  
email: [mkuech@rzws.fh-aalen.de](mailto:mkuech@rzws.fh-aalen.de)

### 1. Abstract

Explicit analytical expressions for families of 3-point, 4-point, 5-point, and 6-point ( $m$ -point) phase-measurement formulas are presented, which are exactly valid for 1, 2, 3, 4, ( $m-2$ ) different values of the phase-steps, applied in the sequence of intensity-measurements. These values are the "design phase-steps", which can be chosen in accordance with the actual necessity. These formulas are equally suited for the temporal as well as for the spatial case. In the spatial case, the formulas can be used as components to design very compactly two dimensional convolution kernels, which lead to high spatial resolution and minimized sensitive to higher-order miscalibration errors.

We also present formulas with  $m$  points, which have ( $m-2$ ) design phase-steps located symmetrical with respect to  $\pi/2$ . These formulas give the lowest errors over the largest range.

Finally we present formulas which are insensitive to linear phase-shifter calibration errors and at the same time to nonlinearity of the intensity measurement or non-cosine fringe profiles.

The basic theory to derive these formulas and to design two dimensional convolution kernels was established by the author in 1986 and applied during the production of the ESO-NTT primary from 1986 to 1987 within the Carl Zeiss company [1]. It was patented by Carl Zeiss [2], was called the "Direct Measuring Interferometry" (DMI) Method, and implemented in the Laser-Interferometer DIRECT 100, which has real-time wavefront measuring capability on a set of 480 x 480 measurement points [3]. The features of this method have been presented in different papers [4,5,6], the theory behind some of the formulas is given in greater detail in [7].

### 2. Introduction

It is the purpose of this paper, to present phase algorithms, which are robust and precise at the same time: now, before telling how, I want to say, why and give an idea for the benefits!

Measurements are taken in real world conditions, that means, they are prone to harmful influences in many respects. As one cannot expect measurement results with mathe-

matical precision, it makes sense to search for procedures, which give the most precise result in a given situation. So it was the goal, to find methods and the appropriate formulas which are intrinsically "good conditioned", that means, if the error function is plotted against any of the error influences, one should encounter a nearly horizontal tangent around the working point. When you are lucky enough to establish such a procedure, then – may be after some calibrations –, you will end up with a stable, robust and precise method, since precision can be kept high if errors can be kept small! Of course, this is not the only weapon against the undesirable influences of the real world on our measurement results. The others are to protect our measurement set-up as good as we can afford and to relay on the laws of statistics. Doing all together is the key for success.

To explain a little bit what I mean with good condition, I want to give an example from the field of optics. Suppose you have to design some optics which are intended to be used with laser light. At first glance one would guess, that it would not be necessary to correct the optics for more than the working wavelength; but correcting them for a second wavelength will generate a horizontal tangent for the dependence of the focal length from color! Thus, also the tolerances for the index of refraction of the lens material can be lowered, the focal length of the lens will not act very much on changes of the index of refraction induced by temperature and so on. I would say, a bichromat is a "better conditioned creature" than a lens corrected for one wavelength only. In the case that within the experiment the color can change by a significant amount, it would even be preferable to design a trichromat (equal focal length for three colors), since the variation of the focal length between the three design wavelengths will be lowered again!

Phase shifting is the most common technique for fringe evaluation in interferometry, fringe projection, moiré techniques and other fields, where „fringes“ are involved. Two principles have established themselves and are widely used:

- the temporal phase shift techniques have a high resolution in space but suffer from the fact, that several very precise phase steps have to be realized in the (time) sequence of measurements, a demand which is difficult to fulfill in production environment;
- the spatial phase shift technique, where the acquisition of only one fringe-measurement is necessary but where the spatial resolution might be not optimal.<sup>1</sup>

In both cases it is difficult to precisely control the values of the phase steps. Especially for the second case, where the intrinsically given phase variations from one camera pixel to the next are used as the phase steps, there is a systematic deviation of the actual phase step from the nominal value by principle. So, one has to deal with a phase step error (linear or higher order, as described later), which varies across the fringe map and would lead to severe measurement artifacts (reported by others, see for example [9]), unless an algorithm is applied, which is highly tolerant for phase step deviations.

Another source of errors with both, the temporal phase shift technique as well as the spatial phase shift technique, is the nonlinearity of the device, which measures the

---

<sup>1</sup> Our aim was therefore to develop a spatial phase shift technique, which is intrinsically robust against vibrations and has a uniform high spatial resolution, which is not the case with the Fourier-method [8].

## PRECISE AND ROBUST PHASE MEASUREMENT ALGORITHMS 3

fringe intensity (normally a CCD-camera). For instance, when the signal is clipped due to saturation, the intensity values transferred to the computer might not be well described by a function  $a + b \cos(\phi)$ . The same applies in the case of the fringe projection techniques, if a Ronchi ruling is used for projection.

### 3. Phase-shifting formulas with m points, which are valid for m-2 values of the phase-step

#### 3.1 THEORY

The theory of deriving the following phase-shifting formulas is given in greater detail in [6]; the following outline is rather briefly.

In two-beam interferometry, we end up with an equation, given below in different forms:

$$I(\phi + \delta) = B \cos(\phi + \delta) + A \quad (1a)$$

$$I(\phi + \delta) = \cos \delta \cdot B \cos \phi - \sin \delta \cdot B \sin \phi + A = \cos \delta \cdot N - \sin \delta \cdot Z + A \quad (1b)$$

$$I(\phi + \delta) = \operatorname{Re}\{B \exp(i\phi) \cdot \exp(i\delta)\} + A = \operatorname{Re}\{B \cdot \exp(i\delta)\} + A \quad (1c)$$

In (1a)  $A$  is the mean intensity,  $B$  is the modulation of the fringes<sup>2</sup>,  $\phi$  is the phase to be measured and  $\delta$  is the additional phase, which is added to the fringe map for phase shifting purposes. Whereas  $A$ ,  $B$  and  $\phi$  depend on the spatial coordinates  $x, y$  of the camera,  $\delta$  is constant over the whole interferogram and is changed in steps in order to generate additional equations. For (1b) the cos-term is expanded and the products  $B \cos \phi$  and  $B \sin \phi$  are substituted by  $N$  and  $Z$  respectively. For (1c)  $B \cos(\phi + \delta)$  is substituted by the real part of the complex expression  $B \exp(i\phi) \cdot \exp(i\delta)$ . We interpret  $B \exp(i\phi)$  to be a vector  $\mathcal{B}$  in the complex plane, which has the two components  $iZ$  and  $N$  in a Cartesian coordinate system and the magnitude  $B$  and phase  $\phi$  in a polar coordinate system:

$$\mathcal{B} = \begin{pmatrix} N \\ iZ \end{pmatrix} = B e^{i\phi} \rightarrow \phi = \arg(\mathcal{B}) = \arctan \frac{Z}{N} = \arctan \frac{B \sin \phi}{B \cos \phi}; \quad B = \sqrt{Z^2 + N^2} \quad (2)$$

For phase-shifting, three intensity measurements  $I_1, I_2, I_3$  are taken at each pixel of the CCD-camera, with the extra phase-values of  $\delta_1, \delta_2, \delta_3$  applied to the interferogram:

$$I_1 = B \cos(\phi + \delta_1) + A = \cos \delta_1 \cdot N - \sin \delta_1 \cdot Z + A$$

$$I_2 = B \cos(\phi + \delta_2) + A = \cos \delta_2 \cdot N - \sin \delta_2 \cdot Z + A \quad (3a)$$

$$I_3 = B \cos(\phi + \delta_3) + A = \cos \delta_3 \cdot N - \sin \delta_3 \cdot Z + A$$

$$\begin{pmatrix} \cos \delta_1 & -\sin \delta_1 & 1 \end{pmatrix} \begin{pmatrix} N \\ Z \\ A \end{pmatrix} = \begin{pmatrix} I_1 \\ I_2 \\ I_3 \end{pmatrix} \quad (3b)$$

Provided that the determinant

$$\operatorname{DET}_{123} = \sin(\delta_2 - \delta_3) + \sin(\delta_3 - \delta_1) + \sin(\delta_1 - \delta_2) \quad (4)$$

---

<sup>2</sup> The quantity  $C = B/A$  is the „contrast“ according to the definition of Michelson; in some of the literature  $C$  is called the „modulation“.

of this linear system of equations is not zero, we get the solutions for  $N$ ,  $Z$  and  $A$ :

$$N = I_1 \frac{[\sin \delta_3 - \sin \delta_2]}{\text{DET}_{123}} + I_2 \frac{[\sin \delta_1 - \sin \delta_3]}{\text{DET}_{123}} + I_3 \frac{[\sin \delta_2 - \sin \delta_1]}{\text{DET}_{123}} \quad (5a)$$

$$Z = I_1 \frac{[\cos \delta_3 - \cos \delta_2]}{\text{DET}_{123}} + I_2 \frac{[\cos \delta_1 - \cos \delta_3]}{\text{DET}_{123}} + I_3 \frac{[\cos \delta_2 - \cos \delta_1]}{\text{DET}_{123}} \quad (5b)$$

$$A = I_1 \frac{\sin(\delta_2 - \delta_3)}{\text{DET}_{123}} + I_2 \frac{\sin(\delta_3 - \delta_1)}{\text{DET}_{123}} + I_3 \frac{\sin(\delta_1 - \delta_2)}{\text{DET}_{123}} \quad (5c)$$

For us, the equations (5a) and (5b) are the most interesting. Both vector-components,  $N$  and  $Z$ , which establish the vector  $\mathcal{B}$  in the complex plane, is built up as a weighted sum of the three intensity measurements. It is important to notice, that the equations (5) are mathematical identities, provided that the phase constants  $\delta_k$  and the intensity measurements  $I_k$  are known with infinite precision. In this case, the computed quantities  $\text{DET}_{123}$ ,  $N$ ,  $Z$ ,  $A$  are exact; the same is true for the derived quantities  $B$  and  $\phi$ . If under real world conditions, the phase-values  $\delta_k$  deviate from the values which we suppose that they have, but instead have the values  $\delta_k^*$ , then the equations will not deliver the correct results for  $\text{DET}_{123}$ ,  $N$ ,  $Z$ ,  $A$ ,  $B$  and  $\phi$ , but instead the more or less faulty values  $\text{DET}_{123}^*$ ,  $N^*$ ,  $Z^*$ ,  $A^*$ ,  $B^*$  and  $\phi^*$ . So errors occur due to wrong values for the additional phase  $\delta_k$ , especially the phase-error  $\Delta\phi = \phi^* - \phi$ .

Until here, there was nothing really new! Now we will introduce the new and most important idea (see also [1]): the only thing actually said about the values for  $\delta_1$ ,  $\delta_2$ ,  $\delta_3$  is, that the determinant  $\text{DET}_{123}$  should not be zero. If we would use another set  $\delta_2$ ,  $\delta_3$ ,  $\delta_4$ , for the additional phase-values for instance, we should end up with essentially the same vector  $\mathcal{B}$ ! So if we use in total  $m$  different values for the additional phase  $\delta_k$ , performing  $m$  intensity measurements and collect them into  $(m-2)$  packages, each package containing three successive measurements, we will be able to compute  $(m-2)$  vectors  $\mathcal{B}_1$  to  $\mathcal{B}_{(m-2)}$ , which all shell point in the same direction and all shell have equal magnitude. So, we are free to build a new "super-vector"  $\mathcal{B}$ , as a weighted vector-sum of those vectors, using the weighting-factors  $\alpha_1$  to  $\alpha_{(m-2)}$

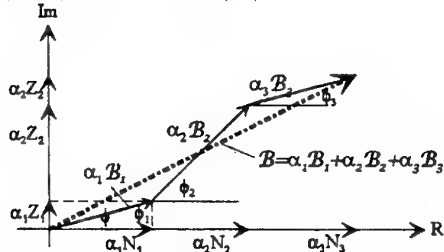


Figure 1: Example of the construction of a 5-point formula: three vectors  $\mathcal{B}_1$ ,  $\mathcal{B}_2$ ,  $\mathcal{B}_3$  added with weighting factors  $\alpha_1=0.25$ ,  $\alpha_2=0.5$ ,  $\alpha_3=0.25$ , to set up the new vector  $\mathcal{B}$ , shown for a case, where the phase-steps  $\Delta\delta$  deviate considerably from their nominal value

$$\mathcal{B} = \alpha_1 \mathcal{B}_1 + \alpha_2 \mathcal{B}_2 + \dots + \alpha_{(m-2)} \mathcal{B}_{(m-2)} = \alpha_1 \left( \begin{matrix} N_1 \\ iZ_1 \end{matrix} \right) + \alpha_2 \left( \begin{matrix} N_2 \\ iZ_2 \end{matrix} \right) + \dots + \alpha_{(m-2)} \left( \begin{matrix} N_{(m-2)} \\ iZ_{(m-2)} \end{matrix} \right) \quad (6)$$

We will show, that this new vector  $\mathcal{B}$  will not only act as the individual components, but can have new characteristics concerning the phase-values  $\delta_k$ , for which the mathematical correct value for  $\phi$  results. Like an achromatic lens has the same focal length for more than one wavelength, the new vector  $\mathcal{B}$  can have the correct argument  $\phi$  for more than one set of phase-values  $\delta_k$  or phase-steps  $\delta = \delta_k - \delta_{(k-1)}$ . Tailoring of the features of  $\mathcal{B}$  is done by calculating and applying the appropriate weighting factors  $\alpha_1$  to  $\alpha_{(m-2)}$ . We do not have the space to explicitly demonstrate the necessary calculations here, but want to point out, that  $\mathcal{B}$  can either be given ultimate robustness against false phase-steps (e.g. the range for  $\delta$  is very large) with reasonable errors  $\Delta\phi$  in between the design phase steps, or can be made to create very small errors  $\Delta\phi$  over a smaller range for  $\delta$ . For reasons of simplicity, we will restrict ourselves to equal phase-steps (linear phase-shift miscalibration). The basic phase-step, for which all the vectors  $\mathcal{B}_k$  will give the exact value  $\phi$  for the argument is named  $\delta$ . Additional phase-steps, for which only the super-vector has the correct argument  $\phi$  are named  $\beta_1, \beta_2, \dots, \beta_{(m-3)}$ .

### 3.2 THE GENERAL 3-POINT FORMULA

We suppose, three measurements are taken with the phase-values increasing by  $\delta$  in each measurement, and having no additional phase for the central measurement (this is an important assumption!):  $\delta_1 = -\delta; \delta_2 = 0; \delta_3 = \delta$ .

$$I_1 = B \cos(\phi - \delta) + A \quad (7a)$$

$$I_2 = B \cos(\phi) + A \quad (7b)$$

$$I_3 = B \cos(\phi + \delta) + A \quad (7c)$$

Then the general 3-point formula (which is only exact for the phase step value  $\delta$ ) is immediately derived from (5a) and (5b):

$$N = -\sin \delta \cdot I_1 + 2 \sin \delta \cdot I_2 - \sin \delta \cdot I_3 \quad (8a)$$

$$Z = (1 - \cos \delta) \cdot I_1 + 0 \cdot I_2 + (1 - \cos \delta) \cdot I_3 \quad (8b)$$

As we expect to get the values for  $Z$  and  $N$  by a convolution of one kernel for the numerator and one kernel for the denominator. In the following we will associate with these kernels the symbols  $z_1, z_2, \dots, z_m$  and  $n_1, n_2, \dots, n_m$  for a  $m$ -point formula. The general form for the computation of  $\phi$  is then:

$$\tan \phi = \frac{z_1 I_1 + z_2 I_2 + \dots + z_m I_m}{n_1 I_1 + n_2 I_2 + \dots + n_m I_m} \quad (9)$$

Rather than to compute absolute values for  $B$ , it is enough in most cases, that a quantity proportional to  $B$  is achieved. Then it is possible to cancel out common factors in the denominator and the numerator of (9), in order to simplify the kernels further. We will do so for the rest of the paper. Then we can present the general form for the 3-point formula as:

$$z_1 = +\sin\left(\frac{\delta}{2}\right) \quad z_2 = 0 \quad z_3 = -\sin\left(\frac{\delta}{2}\right) \quad (10a)$$

$$n_1 = -\cos\left(\frac{\delta}{2}\right) \quad n_2 = +2 \cos\left(\frac{\delta}{2}\right) \quad n_3 = -\cos\left(\frac{\delta}{2}\right) \quad (10b)$$

## 3.3 GENERAL 4-POINT FORMULAS

Due to the limited space, we will give only the results, without any derivation. With our theory, it is possible to derive 4-point formulas, which work exactly for two different values of the phase steps. We have computed two different general 4-point formulas with this feature; the first one has its design phase-steps at  $\pi/2$  and  $\delta$ , the second one has its design phase-steps at  $\delta$  and  $(\pi - \delta)$ . Given are the convolution kernels for  $Z$  and  $N$ :

$$\begin{aligned} Z : & \sin\left(\frac{\delta}{2}\right) - \cos\left(\frac{\delta}{2}\right) & \sin\left(\frac{\delta}{2}\right) + 3\cos\left(\frac{\delta}{2}\right) & -\sin\left(\frac{\delta}{2}\right) - 3\cos\left(\frac{\delta}{2}\right) & -\sin\left(\frac{\delta}{2}\right) + \cos\left(\frac{\delta}{2}\right) \\ N : & -\sin\left(\frac{\delta}{2}\right) - \cos\left(\frac{\delta}{2}\right) & \sin\left(\frac{\delta}{2}\right) + \cos\left(\frac{\delta}{2}\right) & \sin\left(\frac{\delta}{2}\right) + \cos\left(\frac{\delta}{2}\right) & -\sin\left(\frac{\delta}{2}\right) - \cos\left(\frac{\delta}{2}\right) \end{aligned} \quad (11)$$

$$\begin{aligned} Z : & 0 & 2\sin\delta & -2\sin\delta & 0 \\ N : & -1 & 1 & 1 & -1 \end{aligned} \quad (12)$$

## 3.4 GENERAL 5-POINT FORMULAS

In the case of 5-point formulas we present here 3 types, which are different with respect to the location, symmetry and multitude of the design phase-steps. It is possible to have 3 zero-positions in the error function at maximum, but that is not guaranteed in any case.

The following formula (13) is the most simple one, and is related to formula (12) for 4-points. It has a fixed design phase-step at  $\pi/2$  and an other, which can be chosen, at  $\beta_1$ , where zero-positions of the error function are located. Then due to the symmetry of the formula, an additional zero position at  $\beta_2 = \pi - \beta_1$  is generated.

$$\begin{aligned} Z : & -1 & +2(1+\sin\beta_1) & 0 & -2(1+\sin\beta_1) & +1 \\ N : & -1 & -2\sin\beta_1 & +2(1+2\sin\beta_1) & -2\sin\beta_1 & -1 \end{aligned} \quad (13)$$

In the next formula (14) the design phase steps are  $\delta$  and  $\beta_1$ , which can be chosen ad-lib and where zero-positions for the error function are generated! Provided  $2\delta + \beta_1 < 2\pi$ , then there exists another zero-position of the error function at  $\beta_2 = 2\pi - 2\delta - \beta_1$ .

$$\begin{aligned} z_1 &= -z_5 = \cos\delta\sin\beta_1 + (1-\cos\beta_1)\sin\delta - \sin\beta_1 \\ z_2 &= -z_4 = -2(2(1-\cos\beta_1)\sin\delta + \sin\beta_1\cos\beta_1)\cos\delta + 2\cos\beta_1((1-\cos\beta_1)\sin\delta + \sin\beta_1) \\ z_3 &= 0 \\ n_1 &= n_3 = (1-\cos\beta_1)(1+\cos\delta) - \sin\delta\sin\beta_1 \\ n_2 &= n_4 = 2((\cos\beta_1)^2 + 2\sin\delta\sin\beta_1 - 1)\cos\delta + 2(1-\cos\beta_1)\sin\beta_1\sin\delta - 2(1-(\cos\beta_1)^2) \\ n_3 &= 2(\cos\beta_1 - 4\sin\delta\sin\beta_1 + 1 - 2(\cos\beta_1)^2)\cos\delta + 2(2\cos\beta_1 - 1)(\sin\beta_1\sin\delta - \cos\beta_1) + 2 \end{aligned} \quad (14)$$

The third formula has only one design phase-step  $\delta$ , but the error function has a double zero position there. Provided that  $\delta < 2\pi/3$ , a third zero position is at  $\beta_1 < 2\pi - 3\delta$ .

$$\begin{aligned}
 z_1 &= -z_3 = -(1 - \cos \delta) \\
 z_2 &= -z_4 = 4(\cos \delta)^3 - 6(\cos \delta)^2 - 2 \cos \delta + 4 \\
 z_3 &= 0 \\
 n_1 &= n_3 = -\sin \delta \\
 n_2 &= n_4 = -2 \sin \delta(1 - \cos \delta - 2(\cos \delta)^2) \\
 n_3 &= 2 \sin \delta(3 - 2 \cos \delta - 4(\cos \delta)^2)
 \end{aligned} \tag{15}$$

### 3.5 GENERAL 6-POINT FORMULAS

We present here only one 6-point formula, which has the two design phase-steps  $\delta$  and  $\beta_1$ , where zero positions are located. Then the formula generates two more zero-positions for the phase-steps  $\beta_2 = \pi - \delta$  and  $\beta_3 = 2\pi - 2\delta - \beta_1$ . Since the formula is lengthy, we have used abbreviations. Care should be taken when the 4 zero-positions are selected: the formula is not valid for any two-fold zero-position!

$$\begin{aligned}
 z_1 &= -z_4 = -(cld - c3d)(c3b \cdot sld - clb \cdot sld - slb \cdot c3d + slb \cdot cld) \\
 z_2 &= -z_3 = (cld - c5d)(c3b \cdot sld - clb \cdot sld - slb \cdot c3d + slb \cdot cld) \\
 z_3 &= -z_4 = c5b \cdot s3d \cdot c3d - sld \cdot clb \cdot c5d + s5b \cdot cld^2 + s3b \cdot cld \cdot c3d + c5b \cdot sld \cdot cld \\
 &\quad + s3b \cdot c5d \cdot cld + sld \cdot c3b \cdot c5d + sld \cdot clb \cdot c3d + clb \cdot s3d \cdot cld + s5d \cdot c3d + s5b \cdot c3d^2 \\
 &\quad - s3b \cdot c5d \cdot c3d - clb \cdot s3d \cdot c3d - 2 \cdot s5b \cdot cld \cdot c3d + c3b \cdot s5d \cdot cld - c5b \cdot sld \cdot c3d \\
 &\quad - c5b \cdot s3d \cdot cld - c3b \cdot s5d \cdot c3d - clb \cdot s5d \cdot cld - s3b \cdot cld^2 - c3b \cdot sld \cdot cld \\
 n_1 &= n_4 = slb \cdot cld \cdot sld - c3b \cdot sld \cdot s3d - clb + clb \cdot cld^2 + slb \cdot c3d \cdot s3d + c3b \\
 &\quad - c3b \cdot cld^2 - slb \cdot c3d \cdot sld - slb \cdot cld \cdot s3d + clb \cdot sld \cdot s3d \\
 n_2 &= n_3 = clb - s5b \cdot cld \cdot sld - c5b + slb \cdot cld \cdot s5d + c5b \cdot cld + slb \cdot c5d \cdot sld \\
 &\quad - s3b \cdot c5d \cdot sld - slb \cdot cld \cdot sld - clb \cdot sld \cdot s3d - slb \cdot c3d \cdot s5d + s5b \cdot c3d \cdot sld \\
 &\quad + s3b \cdot cld \cdot sld - clb \cdot cld^2 + c5b \cdot s3d \cdot sld \\
 n_3 &= n_4 = c3b \cdot sld \cdot s3d + s5b \cdot cld \cdot sld - c5b \cdot cld^2 - slb \cdot c3d \cdot s3d - c3b - slb \cdot cld \cdot s5d \\
 &\quad + slb \cdot c3d \cdot sld - slb \cdot c5d \cdot sld + s3b \cdot c5d \cdot sld + slb \cdot cld \cdot s3d \\
 &\quad + c5b + slb \cdot c3d \cdot s5d - s5b \cdot c3d \cdot sld - s3b \cdot cld \cdot sld + c3b \cdot cld^2 - c5b \cdot s3d \cdot sld
 \end{aligned} \tag{16}$$

$$\begin{aligned}
 cld &= \cos\left(\frac{1}{2}\delta\right); & c3d &= \cos\left(\frac{3}{2}\delta\right); & c5d &= \cos\left(\frac{5}{2}\delta\right); \\
 sld &= \sin\left(\frac{1}{2}\delta\right); & s3d &= \sin\left(\frac{3}{2}\delta\right); & s5d &= \sin\left(\frac{5}{2}\delta\right); \\
 clb &= \cos\left(\frac{1}{2}\beta_1\right); & c3b &= \cos\left(\frac{3}{2}\beta_1\right); & c5b &= \cos\left(\frac{5}{2}\beta_1\right); \\
 slb &= \sin\left(\frac{1}{2}\beta_1\right); & s3b &= \sin\left(\frac{3}{2}\beta_1\right); & s5b &= \sin\left(\frac{5}{2}\beta_1\right);
 \end{aligned} \tag{17}$$

### 3.6 m-POINT FORMULAS WITH A (m-2)-FOLD ZERO AT $\pi/2$

As a special case of the formulas presented so far, one can compute m-point formulas with a  $(m-2)$ -fold zero at  $\pi/2$  by a very simple rule: in this case, the weighting-factors  $\alpha_1, \alpha_2, \dots, \alpha_{(m-2)}$ , with which the vectors  $\mathcal{B}_1, \mathcal{B}_2, \dots, \mathcal{B}_{(m-2)}$  are multiplied before being added to establish the “super-vector”  $\mathcal{B}$  are simply the binomial coefficients. Another alternative for computing the final values is by a very simple recursion, which we can not present here due to the limitation of space. In the following table, the coefficients for the convolution kernels are given up to a 16-point formula. Every first row shows the kernel for the numerator, every second the kernel for the denominator.

TABLE 1. Convolution kernels for m-point formulas with an  $(m-2)$  fold zero of the error function at  $\pi/2$ .

### 3.7 SYMMETRICAL m-POINT FORMULAS WITH DISTRIBUTED ZERO-POSITIONS

The following formulas are extremely useful, since they produce the smallest errors over the largest region. They are constructed as a superposition of the formulas shown in Table 1. When for instance a new 9-point formula has to be designed, the convolution kernels for the numerator and the convolution kernels for the denominator are established by a weighted sum of the kernels from the 3-point, 5-point, 7-point and 9-point formulas of table 1. Depending on the weighting factors chosen, the new formula will have its zero-positions at different locations. But it is also possible to compute the necessary weighting factors which produce exactly the desired zero-positions. This procedure is best done numerically. I have written a program which delivers the final formula, when I type in the desired number of points and locations of the zero-positions (e.g. the design-phase-steps). As there is a nearly infinite multitude of different formulas, which can be computed, I will only give some examples to demonstrate the superior

PRECISE AND ROBUST PHASE MEASUREMENT ALGORITHMS 9

quality of these new kernels. Since the 9 coefficients have odd and even symmetry, we only give the first 5 of them.

9-point formula with an oscillating error function; useful range  $30^\circ < \theta < 150^\circ$ :

design phase-steps:  $31^\circ, 41^\circ, 61^\circ, 90^\circ, 119^\circ, 139^\circ, 149^\circ$

P/V error smaller than  $1.2 \cdot 10^{-4}$  fringe-numbers<sup>3</sup> over the range  $30^\circ < \theta < 150^\circ$

Z: 1 -6.091 433 622 -7.448 639 941 31.535 820 411 0

N: 1 4.091 433 622 -17.631 507 185 -6.455 673 284 37.991 493 694

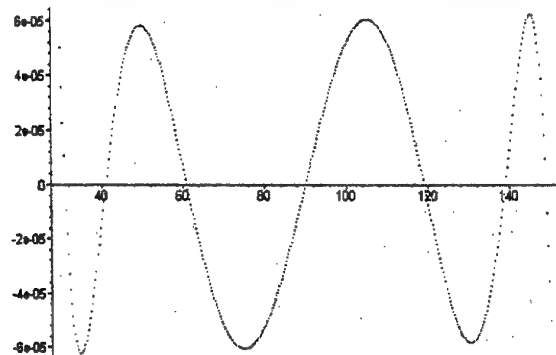


Figure 2: Error function for the 9-point formula given above. The oscillating character is seen clearly, also the location of the design phase-steps, which are the zero-positions of the error function. The units of the abscissa are degrees, the units of the ordinate are fringe-fractions.

9-point formula with an oscillating error function; useful range  $50^\circ < \theta < 130^\circ$ :

design phase-steps:  $51^\circ, 58.4^\circ, 72^\circ, 90^\circ, 108^\circ, 121.6^\circ, 129^\circ$

P/V error smaller than  $4 \cdot 10^{-6}$  fringe-numbers over the range  $50^\circ < \theta < 130^\circ$

Z: 1 -7.159 858 824 -10.844 265 315 44.204 264 421 0,

N: 1 5.159 858 824 -23.163 982 962 -10.196 016 144 54.400 280 564

9-point formula with an oscillating error function; useful range  $67.2^\circ < \theta < 112.8^\circ$ :

design phase-steps:  $67.7^\circ, 72^\circ, 80^\circ, 90^\circ, 100^\circ, 108^\circ, 112.3^\circ$

P/V error smaller than  $7 \cdot 10^{-8}$  fringe-numbers over the range  $67.2^\circ < \theta < 112.8^\circ$

Z: 1 -7.722 147 975 -12.910 753 065 51.920 419 395 0

N: 1 5.722 147 975 -26.355 049 016 -12.654 617 314 64.575 036 709

8-point formula with an oscillating error function; useful range  $71^\circ < \theta < 109^\circ$ :

design phase-steps:  $72^\circ, 80^\circ, 90^\circ, 90^\circ, 100^\circ, 108^\circ$

P/V error smaller than  $4.4 \cdot 10^{-7}$  fringe-numbers over the range  $71^\circ < \theta < 109^\circ$

Z: 0 -5.871 728 539 5.871 728 539 19.236 319 724

N: 1 -1 -14.489 888 400 14.489 888 400

<sup>3</sup> one fringe-period is equivalent to  $2\pi$  or  $360^\circ$  respectively; in interferometry one fringe-period equals  $1 \lambda$

**4. Phase-shifting formulas which are insensitive to a nonlinear characteristic curve of the camera and at the same time to fringes, which deviate from the cos-profile.**

The formulas given so far can compensate linear "phase-shifter" calibration errors to an extend, which is far beyond measurement precision. This feature is absolutely necessary, when the formulas are used for the purpose of extracting the phase from a map of high density fringes (the DMI technique) and high precision is wanted. We have also used the DMI kernels for extracting the phase out of fringe maps, which have been photocopied or published in papers and had been "hard-clipped", that means, they contain only black and white. The technique still works amazingly good, but it is clear, that you will end up with high frequency artifacts. In this case, the fringe intensity is no longer well described by equation (1a), so the formulas cannot give error free results. The same applies in any case, where the fringe intensity deviate from (1a), as in fringe projection technique, when a Ronchi ruling is projected or in the case of a nonlinear characteristic function for the device, with which the intensity is measured.

In all this cases, the resulting intensity pattern can be described to any level of precision by a function, containing higher harmonics of the phase-function  $\phi$ . Making this a new starting point for the phase-shifting formulas, the problem is solved totally!

$$\begin{aligned} I &= A + B_1 \cos(\phi_1 + \delta) + B_2 \cos(2 \cdot (\phi_1 + \alpha_2 + \delta)) \\ &\quad + B_3 \cos(3 \cdot (\phi_1 + \alpha_3 + \delta)) + B_4 \cos(4 \cdot (\phi_1 + \alpha_4 + \delta)) + \dots \\ &= A - \sin(\delta) \cdot Z_1 + \cos(\delta) \cdot N_1 - \sin(2\delta) \cdot Z_2 + \cos(2\delta) \cdot N_2 \\ &\quad - \sin(3\delta) \cdot Z_3 + \cos(3\delta) \cdot N_3 - \sin(4\delta) \cdot Z_4 + \cos(4\delta) \cdot N_4 - \dots \end{aligned} \quad (18)$$

$$\begin{aligned} \phi_1 &= \arctan\left(\frac{Z_1}{N_1}\right); & \phi_2 &= \phi_1 + \alpha_2 = \arctan\left(\frac{Z_2}{N_2}\right) \\ \phi_3 &= \phi_1 + \alpha_3 = \arctan\left(\frac{Z_3}{N_3}\right); & \phi_4 &= \phi_1 + \alpha_4 = \arctan\left(\frac{Z_4}{N_4}\right) \end{aligned} \quad (19)$$

$$\begin{pmatrix} 1 & -\sin(\delta_1) & \cos(\delta_1) & -\sin(2\delta_1) & \cos(2\delta_1) & -\sin(3\delta_1) & \cos(3\delta_1) & -\sin(4\delta_1) & \cos(4\delta_1) \\ 1 & -\sin(\delta_2) & \cos(\delta_2) & -\sin(2\delta_2) & \cos(2\delta_2) & -\sin(3\delta_2) & \cos(3\delta_2) & -\sin(4\delta_2) & \cos(4\delta_2) \\ 1 & -\sin(\delta_3) & \cos(\delta_3) & -\sin(2\delta_3) & \cos(2\delta_3) & -\sin(3\delta_3) & \cos(3\delta_3) & -\sin(4\delta_3) & \cos(4\delta_3) \\ 1 & -\sin(\delta_4) & \cos(\delta_4) & -\sin(2\delta_4) & \cos(2\delta_4) & -\sin(3\delta_4) & \cos(3\delta_4) & -\sin(4\delta_4) & \cos(4\delta_4) \\ 1 & -\sin(\delta_5) & \cos(\delta_5) & -\sin(2\delta_5) & \cos(2\delta_5) & -\sin(3\delta_5) & \cos(3\delta_5) & -\sin(4\delta_5) & \cos(4\delta_5) \\ 1 & -\sin(\delta_6) & \cos(\delta_6) & -\sin(2\delta_6) & \cos(2\delta_6) & -\sin(3\delta_6) & \cos(3\delta_6) & -\sin(4\delta_6) & \cos(4\delta_6) \\ 1 & -\sin(\delta_7) & \cos(\delta_7) & -\sin(2\delta_7) & \cos(2\delta_7) & -\sin(3\delta_7) & \cos(3\delta_7) & -\sin(4\delta_7) & \cos(4\delta_7) \\ 1 & -\sin(\delta_8) & \cos(\delta_8) & -\sin(2\delta_8) & \cos(2\delta_8) & -\sin(3\delta_8) & \cos(3\delta_8) & -\sin(4\delta_8) & \cos(4\delta_8) \\ 1 & -\sin(\delta_9) & \cos(\delta_9) & -\sin(2\delta_9) & \cos(2\delta_9) & -\sin(3\delta_9) & \cos(3\delta_9) & -\sin(4\delta_9) & \cos(4\delta_9) \end{pmatrix} \begin{pmatrix} A \\ Z_1 \\ N_1 \\ Z_2 \\ N_2 \\ Z_3 \\ N_3 \\ Z_4 \\ N_4 \end{pmatrix} = \begin{pmatrix} I_1 \\ I_2 \\ I_3 \\ I_4 \\ I_5 \\ I_6 \\ I_7 \\ I_8 \\ I_9 \end{pmatrix} \quad (20)$$

If the series expansion (18) for the fringe intensity is truncated after the fourth harmonic, as given in the example of equation (20), one can see, that at least 9 intensity measurements are necessary to solve the resulting linear system of equations. Normally one is only interested in the quantities  $Z_i$  and  $N_i$ , from which the phase  $\phi$  can be com-

puted, but nevertheless it is necessary that the rank of the matrix is 9. In order to end up with robust formulas, the magnitude of the determinant of the matrix in (20) should be as big as possible. This is the case, if the phase-steps are properly chosen, for instance in our case of 9 intensity measurements phase-steps of  $\delta = 2\pi/9$  equally to  $(40^\circ)$  would be a good value to be considered. But you can compute the magnitude of the determinant as a function of  $\delta$  and chose the phase-steps with regard to that.

Solving eq. (20) for  $Z_1$  and  $N_1$  in a general (analytical) manner gives the general phase-shifting formula for the case of harmonics up to the 4<sup>th</sup> order; this is then the basis to compute the vector  $\mathcal{B}_1$  as described in section 3.1. If one applies two additional phase-shifts, e.g. in total  $m=11$  measurements in our case, it is possible to compute another vector  $\mathcal{B}_2$ , which can be summed up with the first one in such a way, that the resultant vector  $\mathcal{B}$  will have a zero position of its error function at a second phase-step value, e.g. the formula works with two different design phase-steps. In general, you need  $m=2w+2r-1$  intensity measurements to construct a formula which is valid for  $r$  different design phase-steps and take into consideration an intensity profile up to the  $w^{\text{th}}$  harmonic of the phase  $\phi$ .

I have written another program, with which the kernels for the numerator  $Z$  and the denominator  $N$  are computed, after typing in the design phase-steps and the harmonics to be taken into account. There might be situations, where you know that the fringe profiles are symmetric, and therefore do not want that the odd-harmonics (3, 5,...) are considered. In this case, you can compute smaller kernels, reducing the effort.

Before I give explicit examples, I want to point out an important special case. This is to consider only the second harmonic, which will cover the biggest part of detector non-linearity, see for example [10]. In this case, it is not necessary to establish a new theory, but simply construct a new odd-point kernel out of an even-point and an odd-point kernel, by interlacing the two kernels. If both known kernels have the same design phase-steps (the odd kernel will have one in addition, but this doesn't care), then the new kernel will have the same design phase steps, but divided by two! I will give an example to make things more clear.

If you superimpose the last two kernels given in section 3.7, you end up with the following (9+8)-point=17-point kernels (due to symmetry only the first 9 coefficients!):

17-point formula with an oscillating error function; useful range  $35.5^\circ < \theta < 54.5^\circ$   
 design phase-steps:  $36^\circ, 40^\circ, 45^\circ, 50^\circ, 54^\circ$   
 P/V error smaller than ? fringe-numbers over the range  $35.5^\circ < \theta < 54.5^\circ$   
 Z: 1 0 $\alpha$  -7.722 147 975 -5.871 728 539 $\alpha$  -12.910 753 065  
     5.871 728 539 $\alpha$  51.920 419 395 19.236 319 724 $\alpha$  0  
 N: 1 1 $\alpha$  5.722 147 975 -1 $\alpha$  -26.355 049 016  
     -14.489 888 400 $\alpha$  -12.654 617 314 14.489 888 400 $\alpha$  64.575 036 709

This formula will work for any value of  $\alpha$ , for instance for  $\alpha=1$ , but can be optimized, by applying to  $\alpha$  an optimal value. A total set of error-functions can be computed with different values for  $\alpha$  (having zero-positions as stated) and then the optimal one chosen.

A very interesting new 9-point phase-step function is gained, if you combine the equations (12) and (13) to new kernels:

$$\begin{array}{ccccccccc} -1 & 0\alpha & +2(1+\sin 2\beta_i) & +2\alpha \sin 2\delta & 0 & -2\alpha \sin 2\delta & -2(1+\sin 2\beta_i) & 0\alpha & +1 \\ -1 & -1\alpha & -2\sin 2\beta_i & +1\alpha & +2(1+2\sin 2\beta_i) & +1\alpha & -2\sin 2\beta_i & -1\alpha & -1 \end{array} \quad (21)$$

$\pi/4$  is here the naturally given design phase-step. Therefore  $\delta = \beta_i = \pi/4$  will give very good results, but also  $\delta = \beta_i = 2\pi/9$  equal  $40^\circ$  could be considered for example. In this case there will be a second zero-position of the error function located  $50^\circ$ , due to the symmetry of the formula with respect to  $45^\circ$ . Again, the factor  $\alpha$  is another degree of freedom in this formula, which can be used for optimization.

Now going back to the general case: as an example of the result of my program, I will now give a 17-point formula, which takes into account all higher harmonics till the 4<sup>th</sup> and at the same time has 5 design phase-steps  $36^\circ, 40^\circ, 45^\circ, 50^\circ, 54^\circ$ , the same values as in the example above! These are not totally optimal distributed, but for reasons of comparison I chose them. Fig. 3 shows the error-function for the first harmonic  $\phi$ .

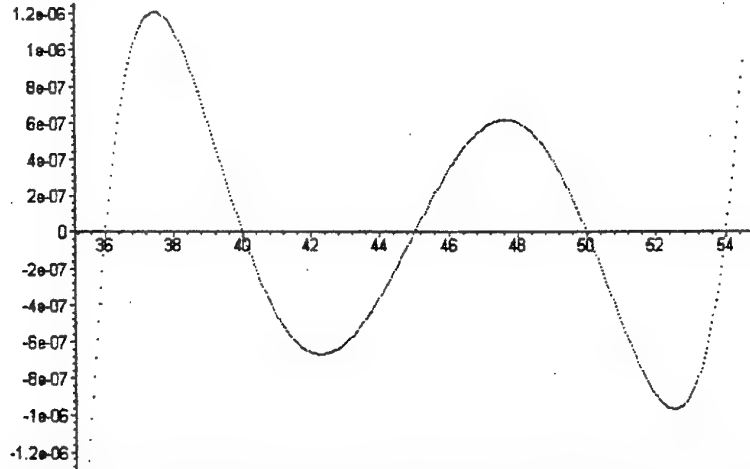


Figure 3: Error function for the 17-point formula given below. The units of the abscissa are degrees, the units of the ordinate are fringe-fractions.

The coefficients for the kernels are:

$$Z: \begin{array}{cccccc} 1. & .277\,370 & -4.482\,025 & 1.060\,792 & -14.159\,974 \\ 11.724\,757 & 10.599\,099 & 10.941\,335 & 0 & \end{array}$$

$$N: \begin{array}{ccccc} .226\,979 & 1.209\,593 & 3.281\,505 & -.540\,325 & -7.540\,562 \\ -10.123\,640 & -3.281\,505 & 9.454\,373 & 14.627\,167 & \end{array}$$

### 5. Miscellaneous

There are some things left, which are important in constructing robust procedures, which I can not consider in detail, but rather would mention it here.

Due to limited space, I can not describe, how to construct two-dimensional convolution kernels, which are based on the new formulas. What I want to do is to give some hints with respect to phase-sifting in time as well as in space.

It is very useful to study the error function  $\Delta\phi = \Delta\phi(\phi, \theta)$  of the formulas as a function of the two variables  $\phi$  and  $\theta$ , where  $\phi$  is the phase to be measured and  $\theta$  is the phase-step value actually applied. As was already pointed out by Schwider et al, this is a periodic function in  $\phi$ . The extreme values of this function are normally found around  $\pi/4 \pm n \cdot \pi/2$ . Our sketches of the error functions are traces computed for values  $\phi = \pi/4$ . Due to the periodic character of the error function with a main period of  $2\phi$ , one can cancel out residual phase-errors by accumulating phase-results from measurements, with a randomly distributed starting phase. Alternatively one can accumulate phase-results and applying a continuously changing starting phase, as is done in the interferometer DIRECT 100 with a measurement frequency of 25 Hz.

My new idea is, to add an odd number  $p=(2n+1)$  of measurements ( $n=1$  or  $2$  or  $3$  all would work perfectly), and changing the starting phase in steps by  $\psi = n \cdot 2\pi/p$ . This is a much better procedure than the "Averaging 3&3" technique, which is reported frequently and was first introduced by Schwider et al [11] and by Koliopoulos [12]. The reason is, that the error function contains mainly terms with an even symmetry with  $\phi$ , which are cancelled out completely by this procedure.

The next point to be considered are higher order phase-calibration errors. I have not dealt with that analytically till now, but numerical simulations showed me, that the zero-positions of the error-functions of my formulas are shifted a little bit away from the design phase-steps, when I apply a higher order calibration error to the phase-steps. Therefore one can conclude, that the robustness of the formulas prevent them from going obsolete, and that higher orders can be taken into account by the design of the formulas, if their values are known a priori.

The last point concerns the number of fringes, which one introduces in an interferogram. It is clear, that with higher numbers of fringes, the test set up is less "common path" and therefore more prone to errors, which are not cancelled out to the same degree, as when the fringes are nulled. This is for the optical side; now we want to consider the phase-measurement side: assuming that you have a phase-measurement error due to any reason, this error by principle will be located between  $0$  and  $2\pi$ . In other words, only fringe fractions are subject to errors, not the integer fringe numbers (it is impossible, that  $2\pi$  is not one period!). Therefore the more fringes you introduce, the higher is the spatial frequency of the errors. These errors are filtered out very easily by any low-pass filtering procedure, as for instance applying a Zernike fit to the phase-

map. Since the most pronounced remaining errors have a period of  $\pi$  which equals half a fringe period, they are nearly completely washed out by averaging 2x2 pixels, if the carrier frequency is chosen to have 4 pixels at one fringe period ( $\rightarrow$  phase-shift of  $90^\circ$ ). With the DMI method, a reproducibility of better than 0.05nm r.m.s. is reached by averaging during one minute, but without any averaging in space!

## 6. References

- /1/ Küchel,M., W.Wiedmann: "In-process metrology for large astronomical mirrors". Invited Paper in *Advanced Optical Manufacturing and Testing*, San Diego, California, 9-11 July (1990), Proc. SPIE Vol. 1333, pp. 280-294.
- /2/ Küchel, Michael (Erfinder), Firma Carl Zeiss (Patentinhaber); Europäische Patentschrift: "Verfahren und Vorrichtung zur Messung eines phasenmodulierten Signals". Pat.Nr. 0 455 218 B1. Anmeldetag: 30.4.1991, Priorität 02.05.90 DE 4014019. Küchel, Michael (Inventor), Carl-Zeiss-Stiftung (Assignee); United States Patent: "Method and Apparatus for Phase Evaluation of Pattern Images used in Optical Measurement". Pat.Nr. 5,361,312. Date of Patent: Nov. 1, 1994.
- /3/ Küchel,M.: "The new Zeiss interferometer". Special Paper in C.P.Grover (ed.) *Optical Testing and Metrology III: Recent Advances in Industrial Optical Inspection*, San Diego, California, 9-11 July (1990). Proc. SPIE Vol. 1332, pp. 655-663.
- /4/ Freischlad,K., M.Küchel, K.H.Schuster, U.Wegmann, W.Kaiser: "Real-time wavefront measurement with  $\lambda/10$  fringe spacing for the optical shop". in C.P.Grover (ed.) *Optical Testing and Metrology III: Recent Advances in Industrial Optical Inspection*, Proc. SPIE Vol. 1332, (1991), pp. 18-24.
- /5/ Küchel,M.F.: "Advances in interferometric wavefront-measuring technology through the Direct Measuring Interferometry method". in Baker (ed.) *Commercial Applications of Precision Manufacturing at the Sub-Micron Level*, Proc. SPIE 1573, London, United Kingdom, 19-21 Nov. (1991), pp.159-162.
- /6/ Küchel,M.F.: "Advanced Interferometry at Carl Zeiss", Invited Paper in *International Symposium on Optical Fabrication, Testing, and Surface Evaluation*, Tokyo, Japan, 10-12 June, (1992), Proc. SPIE Vol. 1720, pp. 452-455.
- /7/ Küchel,M.F.: Some Progress in Phase Measurement Techniques", in W. Jüptner and W. Osten (eds.), *Fringe '97, Automatic Processing of Fringe Patterns*, Bremen, Germany, Sept. 15-17, 1997, Akademie Verlag, Berlin, pp. 27-44.
- /8/ Takeda,M., H.Ina, S.Kobayashi: „Fourier-transform method of fringe-pattern analysis for computer-based topography and interferometry. J. Opt. Soc. Am. 72 (1982) 156-160.
- /9/ Pirga,M., M. Kujawinska: "Errors in two-directional spatial-carrier phase shifting method", in M. Kujawinska, R.Pryputniewicz, M.Takeda (eds.), *Interferometry VII: Techniques and Analysis*, 11-12 July 1995, San Diego, SPIE Proceedings Vol. 2544, pp. 112-121.
- /10/ Creath,K.: "Phase-Measurement Interferometry Techniques", E. Wolf (ed.) in *Progress in Optics XXVI*, Elsevier Science Publishers B.V., 1988, pp. 351-393.
- /11/ Schwider,J., R.Burow, K.-E.Eißner, J.Grzanna, R.Spolaczyk and K.Merkel: „Digital wave-front measuring interferometry: some systematic error sources". Appl. Opt., 22 (1983) 3421-3432.
- /12/ Koliopoulos,Ch.L.: „Interferometric Optical Phase Measurement Techniques“. Ph.D. Thesis, U. Arizona (1981).

**PLOTTING OF ISOCHROMATIC AND ISOSTATICS PATTERNS OF SLICE  
OPTICALLY ISOLATED IN A THREE DIMENSIONAL PHOTOELASTIC  
MODEL**

A. ZENINA

*LMS, Université de Poitiers, CNRS UMR 6610  
SP2MI - Téléport 2 - BP 179, 86960 FUTUROSCOPE CEDEX, FRANCE*

J.C. DUPRE

*LMS, Université de Poitiers, CNRS UMR 6610  
SP2MI - Téléport 2 - BP 179, 86960 FUTUROSCOPE CEDEX, FRANCE*

A. LAGARDE

*LMS, Université de Poitiers, CNRS UMR 6610  
SP2MI - Téléport 2 - BP 179, 86960 FUTUROSCOPE CEDEX, FRANCE*

**Abstract**

We show a non destructive experimental method which gives the isochromatics and isostatics patterns of slice optically isolated in a three dimensional photoelastic model. We used a non destructive method of optical slicing developed in our laboratory. In this method, the photoelastic model is optically sliced by two plane laser beams. The analyze of the scattered light gives fringes equivalent to the ones obtained in a plane polariscope (isochromatic and isoclinic fringes). In order to separate the isochromatic and the isoclinic fringes, we recorded several images for different polarization orientations and we separated the isoclinic and isochromatic fringes using the Fourier transform. Then the isostatics pattern is plotted.

We show a test of a punctual loading on the top of a prismatic specimen and the possibilities of our method in an industrial case of a model realized by stereolithography technique.

**1. Introduction**

Photoelasticity coupled with the stress frozen technique is still used by industrialists. Usually the three dimensional specimens are sliced by a mechanical process to obtain two dimensional models. The slices can be analyzed in a plane or a circular polariscope.

Let us remind that into a plane polariscope, a two dimensional analysis of a beam allows us to visualize two fringes patterns. The direction of principal stresses is obtained from isoclinic fringes, their difference is given by isochromatic fringes.

Different two dimensional automated photoelastic fringe analysis has been recently investigated, there are techniques based on the use of circular polariscope (Voloshin, A., et al. 1983) (Patterson, E.A., et al. 1991) or plane polariscope (Dupré, J.C., et al. 1993) (Mueller, S.A., et al. 1993) (Morimoto, Y., et al. 1994). Other methods use two (Umezaki, E., et al. 1989) or three (Kihara, T., 1994) wavelengths. The mechanical slicing is a destructive procedure, can disturb the measurement and for different planes takes a lot of time. Furthermore it requires the molding of several models for a general study. Three dimensional methods have been developed (Srinath, L.S., et al. 1988) (Ezaki, K., et al. 1996) (Zénina, A., et al. 1997) (Zénina, A., et al. 1998).

In this paper an another experimental solution is proposed, we used a non-destructive method of optical slicing of three dimensional photoelastic model developed in our laboratory (Dupré, J.C., et al. 1997) (Plouzennec, N., et al. 1998). In this method we obtained a fringe pattern like in a light plane polariscope. We could not obtain directly a fringe pattern corresponding to a circular polariscope, then we chose a procedure based on a Fourier transform (Morimoto, Y., et al. 1994) which only used a plane polariscope configuration without modification of the angle between polarizer and analyzer.

To show the possibilities of this method, we present a test of a punctual loading on the top of a prismatic specimen and an industrial case of a model realized by stereolithography technique.

## 2. Principle of the optical slicing experimental method

The basic idea is to use the properties of polarization of the scattered light (Rayleigh's law). If one observes along the  $\vec{Z}$  vector, perpendicular to the direction of the propagated light beam  $\vec{X}$ , the scattered light is polarized rectilinearly along  $\vec{Z} \wedge \vec{X}$ . The principle of the method is to isolate a slice of the studied photoelastic model between two parallel plane laser beams (figure 1) (Plouzennec, N., et al. 1998) (Dupré, J.C., et al. 1997) (Dupré, J.C., et al. 1996). In the direction perpendicular to the plane of the two illuminated sections, we observe a speckle pattern due to the interference of the light beams of each section. Their possibilities of interference depend on the birefringence of the isolated slice.

The correlation factor  $\gamma$  of the two speckle fields is given by :

$$\gamma^2 = 1 - \sin^2 2\alpha \sin^2 \frac{\Phi}{2} \quad (1)$$

$\alpha$  is the angle of one of the principal stresses, the isochromatic parameter  $\varphi$  is expressed by :

$$\varphi = \frac{2\pi Ce}{\lambda} (\sigma' - \sigma'') \quad (2)$$

Where  $e$  is the thickness of the specimen,  $C$  presents the photoelastic constant,  $\lambda$  is the wavelength of the light used and  $(\sigma' - \sigma'')$  is the secondary principal stress difference of the specimen.

## PLOTTING OF ISOCHROMATIC AND ISOSTATICS 3

Expression (1) is similar to the relationship of the light intensity obtained in a plane polariscope. Thus, the analyze of the scattered light gives fringes equivalent to the ones obtained in a plane polariscope (isochromatic and isoclinic fringes).

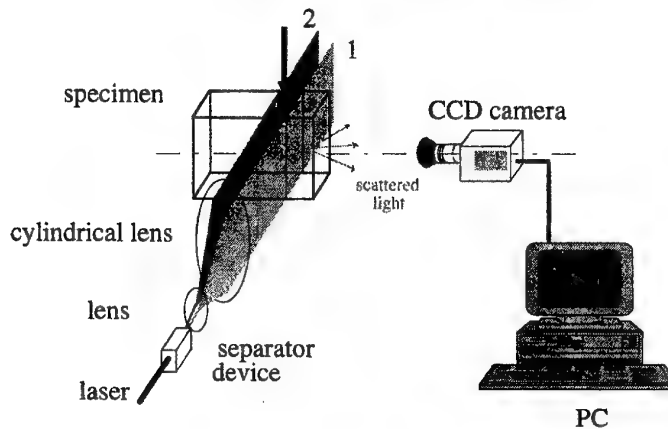


Figure 1 : Experimental set-up

### 3. Separation of isochromatic and isoclinic using Fourier transform

As we obtained fringes pattern from a plane polariscope, we chose a procedure based on the Fourier transform (Morimoto, Y., et al. 1994) which only used a plane polariscope configuration without variation of the angle between analyzer and polarizer.

#### 3.1. PRINCIPLE

If we turn the polarizer and the analyzer direction with an angle  $\theta$ , expression (1) becomes :

$$\gamma^2(\theta) = 1 - \sin^2 2(\alpha - \theta) \sin^2 \frac{\phi}{2} \quad (3)$$

$$\gamma^2(\theta) = [1 - \frac{A}{2}(1 - \cos 4(\alpha - \theta))] \quad (4)$$

In each point of the image  $A$  is constant ( $A = \sin^2 \frac{\phi}{2}$ ).

The signal (4) is a periodic function with a period  $T = \frac{2\pi}{4} = \frac{\pi}{2}$ , thus it is expressed in the Fourier series with respect to  $\theta$  :

$$\gamma^2(\theta) = \sum_{n=-\infty}^{+\infty} C_n e^{jn\omega_0\theta} \quad (5)$$

$$C_n = \frac{1}{T} \int_{-T/2}^{+T/2} \gamma^2(\theta) e^{-jn\omega_0\theta} d\theta \quad (6)$$

With :

$$\omega_0 = \frac{2\pi}{T} = \frac{2\pi}{\pi/2} = 4$$

The Fourier transform of equation (5) is :

$$\begin{aligned} \Gamma(\omega) &= \int_{-\infty}^{+\infty} \gamma^2(\theta) e^{-j\omega\theta} d\theta \\ \Gamma(\omega) &= \sum_{n=-\infty}^{+\infty} C_n \int_{-\infty}^{+\infty} e^{jn\omega_0\theta} e^{-j\omega\theta} d\theta \end{aligned}$$

Using the flowing formulations (Brigham, O.E., 1974) :

$$\begin{aligned} \delta(\omega) &= \int_{-\infty}^{+\infty} e^{j2\pi\omega\theta} d\theta \\ \delta(\omega - a) &= \int_{-\infty}^{+\infty} e^{j2\pi(\omega-a)\theta} d\theta \end{aligned}$$

We obtained :

$$\Gamma(\omega) = \sum_{n=-\infty}^{+\infty} 2\pi C_n \delta(\omega - n\omega_0) \quad (7)$$

With  $\delta$  is the Dirac delta function,  $\omega$  is the frequency and  $j$  is the imaginary unit.

The signal (7) indicates the discrete frequency spectrum which appears only on the frequency components  $n\omega_0$  ( $n = \pm 0, \pm 1, \pm 2, \dots$ ).

**n = 0 :**

From equation (6), we obtained :

$$2\pi C_0 = \frac{2\pi}{T} \int_{-T/2}^{+T/2} \gamma^2(\theta) d\theta$$

PLOTTING OF ISOCHROMATIC AND ISOSTATICS 5

$$2\pi C_0 = 4 \int_{-\pi/4}^{+\pi/4} [1 - \frac{A}{2}(1 - \cos 4(\alpha - \theta))] d\theta$$

$$2\pi C_0 = 2\pi - \pi A = 2\pi(1 - \frac{A}{2}) \quad (8)$$

Equation (8) indicates that the isoclinics are eliminated. The image of  $2\pi C_0$  shows the isochromatic fringes in the whole field of the specimen.

n = +1 :

From equation (6), we obtained :

$$2\pi C_{+1} = \frac{2\pi}{T} \int_{-T/2}^{+T/2} \gamma^2(\theta) e^{-j\omega_0 \theta} d\theta$$

$$2\pi C_{+1} = 4 \int_{-\pi/4}^{+\pi/4} [1 - \frac{A}{2}(1 - \cos 4(\alpha - \theta))] e^{-j\omega_0 \theta} d\theta$$

By using :  $\cos 4(\alpha - \theta) = \frac{1}{2}(e^{j4(\alpha-\theta)} + e^{-j4(\alpha-\theta)})$ , we obtained :

$$2\pi C_{+1} = 4 \int_{-\pi/4}^{+\pi/4} e^{-j4\theta} d\theta - 2A \int_{-\pi/4}^{+\pi/4} e^{-j4\theta} d\theta + A \left[ \int_{-\pi/4}^{+\pi/4} e^{-j4\alpha} d\theta + \int_{-\pi/4}^{+\pi/4} e^{j4(\alpha-2\theta)} d\theta \right]$$

$$2\pi C_{+1} = \frac{\pi}{2} A e^{-j4\alpha} = \frac{\pi}{2} A [\cos 4\alpha - j \sin 4\alpha] \quad (9)$$

Finally , we obtained the isoclinic parameter  $\alpha$  by calculating the arctangent of the ratio of the imaginary and real parts of  $2\pi C_{+1}$  :

$$\alpha = \frac{1}{4} a \tan \left[ \frac{-\Im(2\pi C_{+1})}{\Re(2\pi C_{+1})} \right] \quad (10)$$

The method consist in recording several images for different orientations and in calculating the Fourier transform of the correlation factor of each pixel. Then the isoclinics and isochromatic fringes can be separated using this technique and the isostatics pattern can be plotted.

### 3.2. EXPERIMENTAL PROCEDURE

Experimentally we have to analyze images corresponding to different plane polariscope orientations. Due to refraction and reflection phenomenon's, the models are immersed in a tank of index liquid. The first solution is to turn the two laser beams but it imposes to

have a special tank shape because The edge of the tank must be perpendicular to the incident beams. The second solution is to turn the specimen of  $-\pi/4$  to  $\pi/4$ . Then we record several images for different orientations of the model. Numerical rotation is applied for each image in order to obtain the correct position of the model, as we have turned the laser beams. This procedure is more simple but the common area is a circle so we loose a part of the image.

By calculating the Fourier transform at each point of these images, the isochromatic pattern is obtained from the correlation factor data for the frequency  $\omega = 0$ . The Isoclinic image is obtained for  $\omega = \pm \omega_0$  (figure 2).

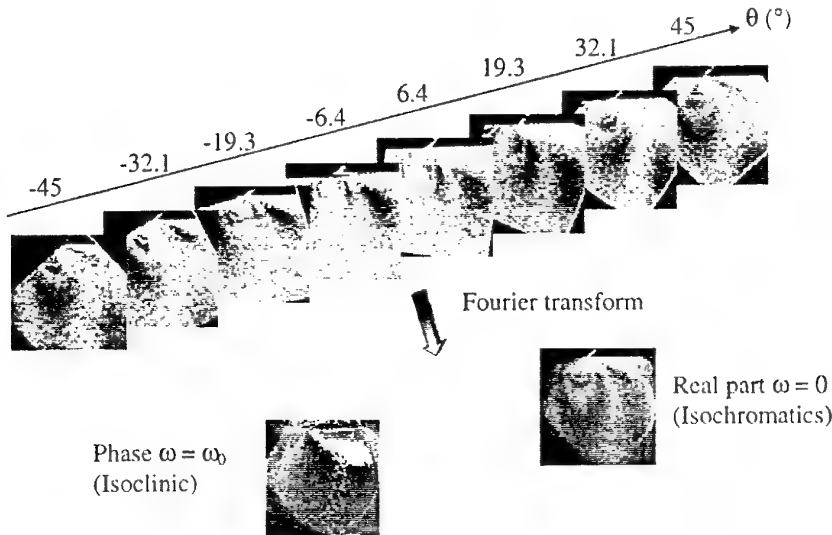


Figure 2 : Recorded images obtained by changing the angle of polarizer and analyzer and a part of the Fourier spectrum given the isoclinic and the isochromatic parameters

#### 4. Experimental results

A three dimensional photoelastic block model adopted in this study is made of an Araldite epoxy-resin. The model is loaded by a concentrated force (figure 1).

The model is placed in a tank of index liquid and illuminate perpendicularly to the observation direction. Several images are recorded for different polarization orientations i.e. for different rotation of the specimen in the interval  $[-\pi/4, \pi/4]$  by a CCD camera with 1024 grey levels of brightness. The minimal number of images recorded is eight (figure 2), but for a best contrast it is necessary to record sixteen images.

When the isoclinic  $\alpha$  is determined for the whole field, the isostatics can be plotted to obtain a better visualization of the principal stress direction (figure 3).

We show in figure 4 an application of our method in an industrial case of a model realized by stereolithography technique. We show a zoom in the particular zone for more details in the specimen.

PLOTTING OF ISOCHROMATIC AND ISOSTATICS

7

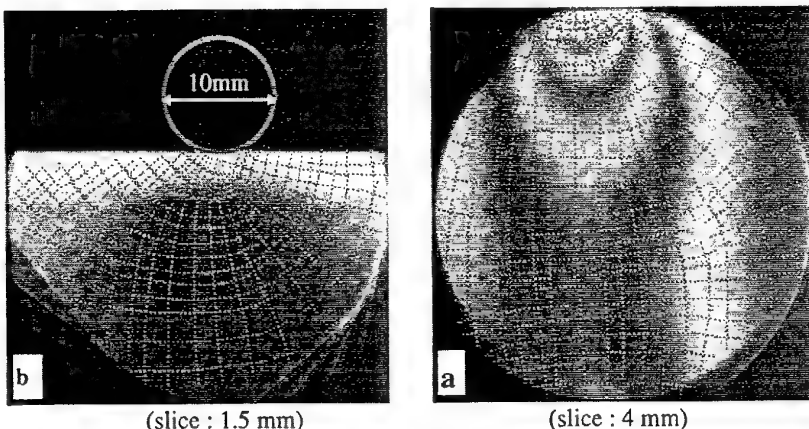


Figure 3 : Isostatics and isochromatics patterns for two thicknesses of slice

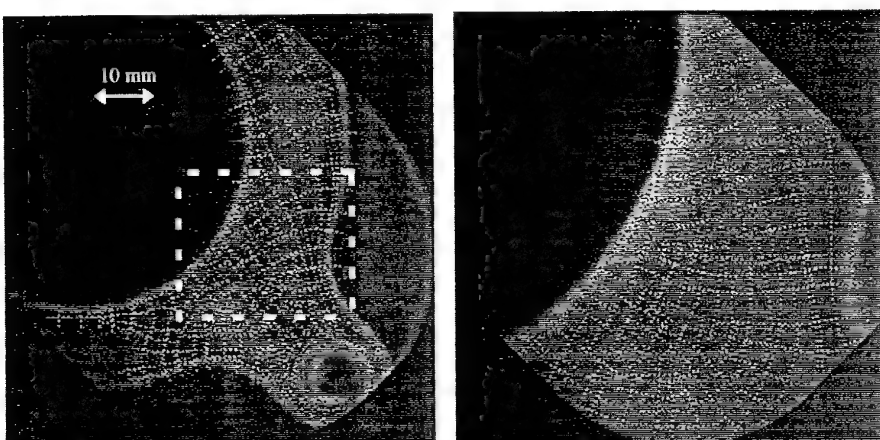


Figure 4 : Isostatics and isochromatic patterns for a model, provided by PSA, realized by stereolithography technique (slice : 2.5 mm).

## 5. Conclusion

We have developed a non destructive experimental technique for the study of the stresses field in a three dimensional photoelastic specimen. This method allows us to separate the isochromatic and the isoclinic fringes and to plot the isostatics pattern.

This method is based on a simple experimental set up with few manipulations and spend a short time.

The numerical procedure associated with the optical slicing method can be used, in industry, for fast investigation for three dimensional specimens realized by molding or stereolithography.

## 6. Acknowledgments

We would like to thank PSA for its support to our work.

## 7. References

Brigham, O.E. (1974) *The fast Fourier transform*, Prentice-Hall Inc.

Dupré, J.C., Brémand, F., and Lagarde, A. (1993) Photoelastic data processing through digital image processing : isostatics and isochromatics reconstruction, International conference on Photoelasticity : new instrumentation and data processing technique, London.

Dupré, J.C., Plouzennec, N., and Lagarde, A. (1996) Nouvelle méthode de découpage optique à champ complet en photoélasticité tridimensionnelle utilisant des moyens numériques d'acquisition et d'analyse des champs de granularité en lumière diffusée, C.R. Acad. Sci, Paris, t. 323, Série II b, pp. 239-245.

Dupré, J.C. and Lagarde, A. (Dec. 1997) Photoelastic analysis of a three dimensional specimen by optical slicing and digital image processing, Experimental Mechanics, Vol. 37., N° 4., pp. 393-397.

Ezaki, K., Ikeda, A., Mawatari, S., and Takashi, M. (1996) Comparison of transmitted and scattered light methods for 3-D photoelastic stress analysis, Post Conference Proceeding of the 1996 VIII International Congress on Experimental Mechanics, SEM, U.S.A, pp. 332-338.

Kihara, T. (1994) Automatic whole field measurement of principal stress directions using three wavelengths, Recent advances in experimental mechanics, J.F. Silva Gomes et al. Editors, pp. 95-99.

Morimoto, Y., Morimoto, Y. Jr., and Hayashi, T. (Sept./Oct. 1994) Separation of isochromatics and isoclinics using Fourier transform, Experimental Techniques, pp. 13-17.

Morimoto, Y. and Imamoto, Y. (1994) Error causes and error reduction in fringe pattern analysis by phase shifting method using Fourier transform, Experimental Mechanics, pp. 379-384.

Mueller, S.A. and Mosleh F.A. (Sept. 1993) An image analysis technique for constructing isostatics from isoclinics in photoelasticity, International Symposium on Optical Tools for Manufacturing and Advanced Automation, SPIE, Boston.

Patterson, E.A. and Wang Z.F. (May 1991) Towards full field automated photoelastic analysis of complex components, Strain, Vol. 27, n°2, pp. 49-56.

Plouzennec, N., Dupré, J.C., and Lagarde, A. (Sept. 1998) Visualization of photoelastic fringes within three dimensional specimens using an optical slicing method, Symposium I.U.T.A.M. « Advanced Optical Methods and Applications in Solid Mechanics », Poitiers, France.

Srinath, L.S., Ramesh, K., and Ramamurti, V. (Mar. 1988) Determination of characteristic parameters in three dimensional photoelasticity, Optical Engineering, Vol. 27, N°3, pp. 225-230.

Umezaki, E., Tamaki, T., and Takahashi, S. (1989) Automated stress analysis of photoelastic experiment by use of image processing, Experimental Techniques, pp. 22-27.

Voloshin, A. and Burger C.P. (Sept. 1983) Half-fringe photoelasticity: a new approach to whole field stress analysis, Experimental Mechanics, pp. 304-313.

Zénina, A., Dupré, J.C., and Lagarde, A. (Sept. 1997) Découpage optique d'un milieu photoélastique épais pour l'étude des contraintes dans un milieu tridimensionnel, 13<sup>ème</sup> Congrès Français de Mécanique, Poitiers, France, vol. 4, pp. 447-450.

Zénina, A., Dupré, J.C., and Lagarde, A. (Sept. 1998) Optical approaches of a photoelastic medium for theoretical and experimental study of the stresses in a three dimensional specimen, Symposium I.U.T.A.M. « Advanced Optical Methods and Applications in Solid Mechanics », Poitiers, France.

## EXPERIMENTAL FRACTURE MECHANICS A MOIRÉ INTERFEROMETRY ANALYSIS

ALBERT S. KOBAYASHI  
*University of Washington*  
*Department of Mechanical Engineering*  
*Box 352600*  
*Seattle, Washington 98195-2600*

### Abstract

Moiré interferometry with a low density grating was used to evaluate the suitability of the  $T^*$ , integral and CTOA as ductile fracture parameters for characterizing low cycle fatigue and dynamic crack growth in thin aluminum fracture specimens. Phase shifting Moiré interferometry with a high density grating was also used to determine the energy dissipation mechanism in brittle alumina ceramics.

### 1.1 Introduction

The gradual acceptance of linear elastic fracture mechanics (LEFM) for assessing failure in the 1960's generated a need to estimate the stress intensity factor (SIF) of a crack in a complex structure and loading. Prior to the dominant usage of finite element (FE) analysis, one of the more commonly used procedure for SIF determination in a laboratory setting was the two- and three-dimensional photoelasticity. While two-dimensional photoelasticity has, for all practical purpose, being replaced by FE analysis, three dimensional photoelasticity is still in use today [1]. Other popular optical techniques of the time include interferometry [2] and caustics [3, 4] with the whole field version of the latter being referred to as the coherent gradient sensor [3]. As research in LEFM evolved beyond the mere compilation of SIF's for different boundary value problems, real structural materials had to be used in place of photoelastic material in order to model their fracture responses. Thus optical techniques, such as caustics and Moiré techniques came into use for studying the dynamic fracture, elastic-plastic fracture and time-dependent fracture responses of steel, aluminum, ceramics and concrete, etc.

One of the earlier application of geometric Moiré in experimental fracture mechanics is a dynamic ductile fracture study [5, 6] using a single frame, ultra-high speed photography. In this study, the transient strain fields in fracturing magnesium, 7075-T6 and 7178-T6 aluminum alloy, center notch (CN) specimens were shown to vary with a strain singularity between 0.4 - 0.6 while the corresponding static strain had a strain singularity of about 0.6 - 0.8. These results suggested that a propagating ductile crack can be modeled, as a first approximation, by dynamic LEFM and thus justified the earlier and extensive LEFM approach to dynamic fracture. This pseudo-elastic response was associated with a relatively high crack velocity of 10 to 20 percent of the Rayleigh wave velocity generated by an overdriven crack at a blunt starter notch. In contrast, most dynamic ductile fracture phenomena are associated with lower crack velocities of 5 to 10 percent of the Rayleigh wave velocity. Reference [7] provides an up to date summary of some of the recent usage of geometric Moiré in elastic-plastic fracture mechanics (EPFM).

The lack of strain sensitivity in the earlier Moiré analysis was removed by the introduction of Moiré interferometry in the late 70's [8]. The specialized optical setups used and selected results obtained since that time are summarized in [9]. In the following, some results obtained by the author and his colleagues using Moiré interferometry over the past ten years are presented.

## 2. Moiré Interferometry

As mentioned previously, many of the popular Moiré interferometry setups are described in [9] and further theoretical and experimental details can be found in [10]. In this paper, only the low-spatial-frequency, steep grating that was developed for elastic-plastic analysis of the crack tip region in ductile material, and a phase-shifting Moiré interferometry of high sensitivity for fracture process zone analysis of structural ceramics are discussed.

### 2.1. LOW-SPATIAL-FREQUENCY STEEP GRATING

The low-spatial-steep grating consists of an ultra-thick, 5-10  $\mu\text{m}$  thick, semi-transparent film which is etched with a deep grating on a mirrored surface of the specimen [11]. In order to enhance the diffraction efficiency of the grating, the specimen surface must be polished to a mirror grade. The film combines the function of a reference grating and a display layer. When the two coherent beams of  $A(x)$  and  $B(x)$  shown in Figure 1 intersect on the specimen surface, the diffraction beams,  $A(i+m, j)$  and  $B(i-m, j)$ , interfere and are projected onto the recording surface. Unlike the standard Moiré interferometric fringes, this interference pattern can be observed clearly from any direction. For example, a grating of  $f=40$  lines/mm in an argon laser field will project  $i = j = (2m)^2 = (2 \cdot 48)^2 = 9216$  visible diffracted beams in all directions. All but the minus or plus first order of the incident  $A(x)$  and  $B(x)$  beams, respectively are blocked

by the steep grating. Good contrast of the displacement patterns is obtained even when the specimen surface is warped due to the large out-of-plane deformation of the crack tip plastic zone. For the low-spatial-frequency of 40 lines/mm used in this study, an incidence angle between the z-axis and the two coherent beams of  $1.176^\circ$  was required. Since the grating spatial frequency of 40 lines/mm requires an incidence angle between the z-axis and the two coherent beams of  $1.176^\circ$ , a special compact Moiré interferometer was built.

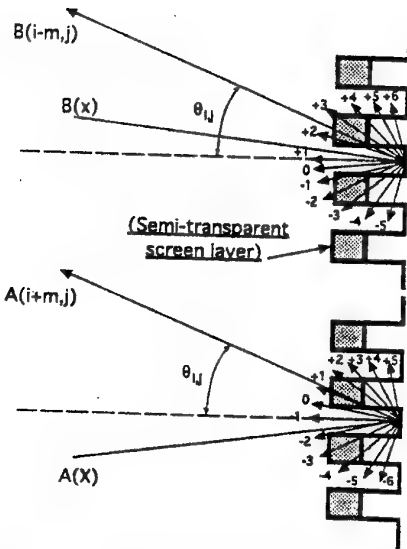
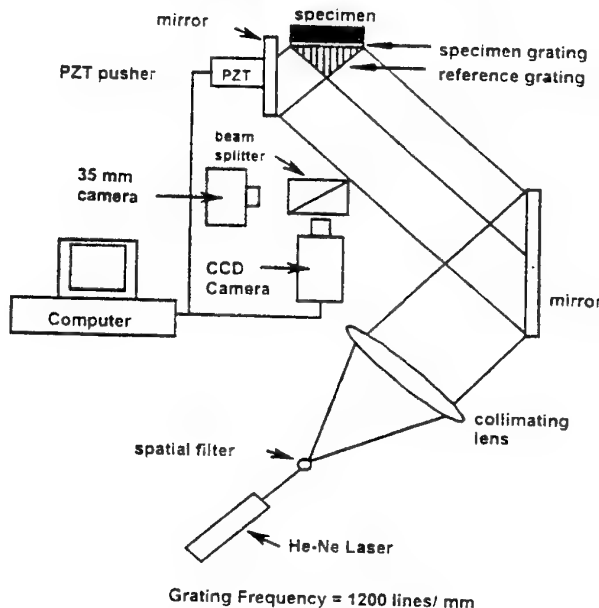


Figure 1. Diffraction angles of a steep grating.

## 2.2. PHASE SHIFTING MOIRÉ INTERFEROMETRY

The specimen grating for Moiré interferometry was affixed by the standard replica technique [10] where the master grating of 1200 lines/mm together with a highly reflective aluminum coating was transferred to a thin half-cured epoxy film coated on the fracture specimen. The specimen grating was then placed in a standard two-beam, phase-shifting Moiré interferometer, as shown in Figure 2, with an appropriate oblique incident illumination that yielded reflected diffraction of the order  $\pm 1$  normal to the grating surface. In this study, only the v-displacement, which is perpendicular to the crack, was recorded. This optical setup effectively doubled the frequency of the specimen grating to 2400 line/mm. The two oblique beams also generated an interference fringe pattern, which becomes the reference grating, of 2400 lines/mm in front of the specimen grating. Phase shifting was accomplished by a piezoelectric transducer which translated one of the oblique beams and effectively shifted the spatial

location of the Moiré reference grating. Four steps in the total PZT displacement generated shifts of  $90^\circ$ ,  $180^\circ$ ,  $270^\circ$  and  $360^\circ$  phase differences. When the specimen grating was distorted by the deformation in the specimen, the distorted diffraction of +/- 1 order interfered with the undistorted reference grating and generated the Moiré fringe pattern in the space in front of the specimen. A CCD camera was focused on this Moiré fringe pattern, which was recorded as a wrapped phase map, in space. A two dimension spatial unwrapping software provided the unwrapped phase distribution which is proportional to the displacement of interest. The estimated accuracy of the entire phase shifting Moiré interferometry procedure is  $\lambda/20$  or  $0.03 \mu\text{m}$ .



*Figure 2. Phase shifting Moiré interferometry setup.*

### 3. Ductile Fracture Parameters

#### 3.1. $T^*_e$ INTEGRAL

For a stably growing crack, Brust et. al. [12] showed that the  $T^*_e$  integral, which is based on the incremental theory of plasticity, reaches a steady state value during stable crack growth and could be an effective stable crack growth parameter. In this integral, the unloading effect is accounted by stretching the integration contour with the extending crack tip. For an integration contour close to the crack tip,  $T^*_e$  represents the

energy inflow to the wake as well as to the frontal crack tip region [13]. In contrast, the J integral represents the energy inflow to a closed contour that moves with the crack tip. Like the J, the  $T^*_e$  is a path dependent integral in the presence of large scale yielding and unloading. Thus it must be evaluated near the crack tip if it is to be considered a crack tip parameter. This near-field  $T^*_e$ , is defined as

$$T^*_e = \int_{\Gamma_e} \left( W n_1 - t_i \frac{\partial u_i}{\partial x_1} \right) d\Gamma \quad (1)$$

where  $t_i$  are the surface tractions on the contour  $\Gamma_e$ , W is the strain energy density and  $n_1$  is the first component of the normal to the curve.  $\Gamma_e$  is an arbitrary small contour immediately surrounding the crack tip and more importantly it elongates together with crack extension.  $T^*_e$ , as defined by Equation (1), is identical in form to the J integral and therefore  $T^*_e$  coincides with J where the deformation theory of plasticity prevails.

In terms of the incremental theory of plasticity,  $T^*_e$  integral at the end of the Nth load steps is the sum of  $\Delta T^*_e$  which is the incremental change of  $T^*_e$  over a load step. The current  $T^*_e$  is thus dependent on the prior loading history, a property that is essential for elastic-plastic analysis under crack growth. Although such incremental analysis can be routinely conducted by finite element (FE) analysis, it is not practical in experimental analysis as the cumulative experimental errors per load step will eventually swamp the sought data. Fortunately Pyo et al [14] have shown, through numerical experiments, that the total  $T^*_e$  integral computed directly by using the stresses and strains based on the incremental theory of plasticity, was for all practical purpose, equal to the summed  $\Delta T^*_e$ . Thus Equation (1) can be used for crack growth study without the cumbersome incremental procedure provided the states of stress and strain are based on the incremental theory of plasticity.

Another series of numerical experiments showed that the numerical integration process along the trailing contour behind the crack tip can be ignored if the contour is very close to the traction free crack, i.e. for a very small  $\epsilon$  [13]. The magnitude of  $\epsilon$  is governed by a characteristic dimension which assures that a plane stress state exists along the integration contour of  $\Gamma_e$ . This distance,  $\epsilon$ , is equated to the plate thickness after [15]<sup>2</sup>. For a plane strain state, this characteristic distance could be several times the crack tip radius.

### 3.2. CTOA CRITERION.

The critical crack opening displacement (CTOA) criterion assumes that stable crack growth occurs when an angle made by a point on the upper surface of a crack surface, the crack tip, and a point on the lower surface reaches a critical angle. For convenience,

---

<sup>2</sup> The three-dimensional elastic-plastic finite element analysis of a flat crack in a plate by Narashimhan and Rosakis (1990) showed that the plane stress state prevailed at one half of the plate thickness from the crack tip. Since a 100 percent shear lip is the norm in ductile fracture, the minimum distance,  $\epsilon$ , was conservatively picked as the plate thickness.

a point 1 mm behind the crack tip has been used. Extensive experimental results from thin aluminum fracture specimens have shown that after an initial transient period, the CTOA remains constant throughout Mode I stable crack growth [16, 17]. Moreover, a two-dimension, elastic-plastic FE simulation of stable crack growth based on the CTOA criterion correctly predicted the load-crack opening displacement (COD) relations and the Mode I crack extension histories of fracture specimens.

#### 4. Low Cycle Fatigue

The objective of this study was to explore experimentally the feasibility of using  $T^*_e$  as a cyclic crack growth criterion

##### 4.1. EXPERIMENT ANALYSIS

The experimental procedure consisted of measuring the two orthogonal displacement fields surrounding a crack extending under low-cycle fatigue in an aluminum 2024-T3 central notched (CN) specimen. Moiré interferometry with a coarse cross diffraction grating of 40 lines/mm was used due to the presence of large scale yielding in the specimen. The stresses corresponding to the total strains were then computed using the equivalent stress-strain relation and the measured uniaxial stress-strain data of the 2024-T3 sheet. This use of the deformation theory of plasticity to compute stresses did not account for the unloading process, which occurred in the trailing wake of the extending crack. By restricting the integration contour very close to and along the extending crack, [13] showed that the contour integration trailing the crack tip can be neglected by virtue of the closeness of the integration path,  $\Gamma_e$ , to the traction free crack surface. This partial contour integration, which was evaluated in the very vicinity of the moving crack tip not only simplifies the integration process but also eliminated the undesirable effects of the deformation theory of plasticity that was used to compute the stresses from the strains derived from the measured displacements.

##### 4.2. NUMERICAL ANALYSIS

A finite element (FE) analysis based on the incremental theory of plasticity using the measured equivalent stress-strain relation was conducted for comparison purpose. Plane stress, FE model of a segment of the CN specimens was driven in its generation mode by the measured, time varying displacements and instantaneous crack length. The  $T^*_e$  integral along the entire elongated contour surrounding the cyclically growing crack of the fracture specimens was computed. Since the FE analysis provided stresses which accounted for the unloading effect in the trailing wake of the extending crack tip, the entire contour with a domain integral [18] was used for the  $T^*_e$  evaluation in order to mask the numerical errors in the FE data surrounding the crack tip. To recapitulate, the  $T^*_e$  evaluation procedures for the Moiré and FE studies differ in that the former used

only the frontal segment of a near-field contour,  $\Gamma_e$ , while the latter involved an equivalent domain integral over much of the crack length.

#### 4.3. RESULTS

Figure 3 shows that the the  $T^*_e$  values, which was determined experimentally and by FE analyses, for  $\varepsilon = 2.0$  mm are in good agreement with the exception of the unloaded  $T^*_e$  values. This discrepancy is due to the use of deformation theory of plasticity in computing the  $T^*_e$  integral at the unloading point. Despite the differences in the load versus loadline displacement curves for the three specimens, all three loading and reloading  $T^*_e$  curves nearly coincide and suggests that crack growth under cyclic loading of thin aluminum fracture specimens could be characterized by a master  $T^*_e$  versus crack extension curve for a given  $\Gamma_e$ .

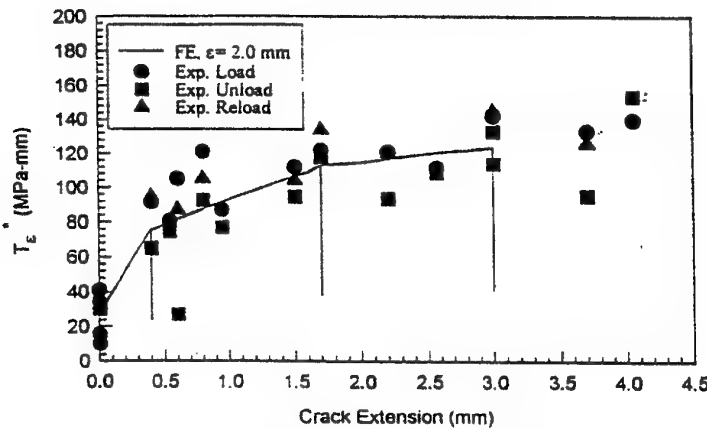


Figure 3. Experimental and FE  $T^*_e$  for cyclically loaded 2024-T3 CN specimens.

Figure 4 shows the experimental and FE CTOA variations with cyclic crack growth. The large differences in the experimental and FE generated CTOA at unloading showed that commercial FE code did not model the loading, unloading and reloading process. Likewise difference between the measured and FE determined  $T^*_e$  at unloading, followed the results of Brust et. al. [12] thus suggesting a possible fundamental modeling error in the commercial computer code used in this study.

#### 5.0 Dynamic Ductile Fracture

Dynamic Moiré interferometry was used in search of a dynamic fracture parameter that control rapid fracture of a somewhat ductile material.

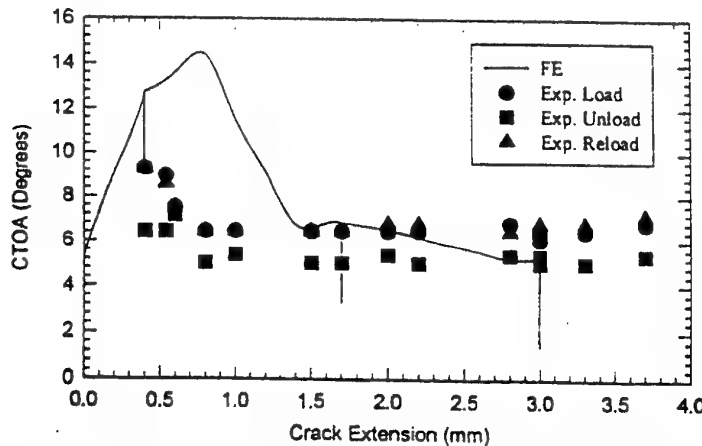


Figure 4. Experimental and FE CTOA for cyclically loaded 2024-T3 CN specimens.

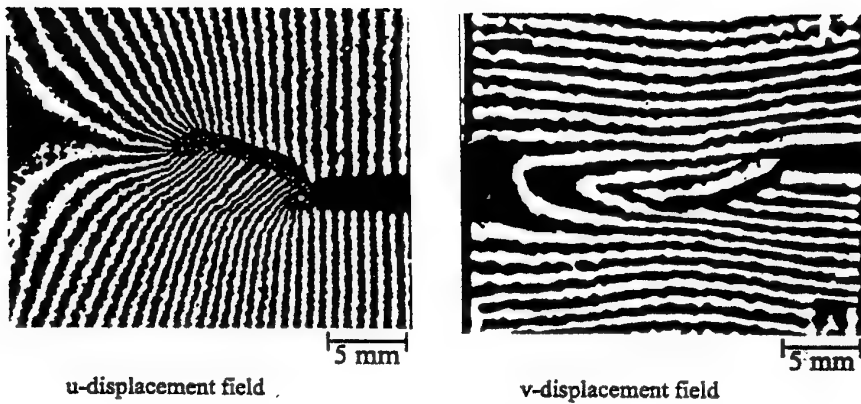
### 5.1. EXPERIMENTAL ANALYSIS

Dynamic Moiré interferometry was used to determine the transient displacement fields perpendicular and parallel to the running crack in 7075-T6 aluminum alloy, SEN specimen, 1.6 mm thick, that was either fatigue precracked or blunt notched for low and high crack velocity tests, respectively. Four frames of the Moiré fringe patterns corresponding to either the vertical or horizontal displacements were recorded by an IMACON 790 camera. This limited number of frames and the fixed framing rate, i.e., 100,000 frames per second, required multiple and separate u- and v-displacement recordings of identically loaded SEN specimens at different delay timings in order to capture the entire fracture event that lasted about 1.2 milliseconds. Despite all efforts to generate reproducible tests, no two dynamic fracture tests were identical and thus the final composite fracture event was constructed with due consideration of the load-time histories and the varying crack opening profiles of each fracture test. The compiled displacement records was then used to compute the  $T^*$ , integral according to the procedure described in Section 3.1.

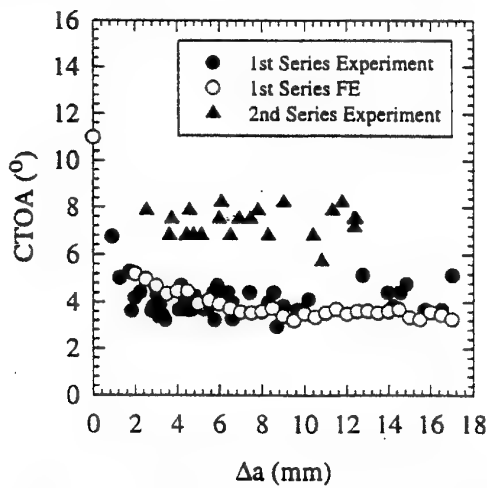
### 5.2. RESULTS

Figure 5 shows typical dynamic Moiré fringe patterns associated with the propagating crack. Crack velocities of about 35 m/s and 300 m/s were observed in the fatigue-precracked and blunt notched specimens, respectively. Figure 6 shows the variations of

CTOA with crack extension. The data identified as the first series is from Lee et. al. [18] using fatigue precracked specimens and the second series refers to the data on the



*Figure 5. Dynamic Moiré patterns of a fracturing 7075-T6 SEN specimen.*



*Figure 6. CTOA variations in a fracturing 7075-T6 SEN specimen.*

blunt notched specimens. Figure 7 shows the  $T^*$  versus crack velocity relations of 7075-T6 and 2024-T3 SEN specimens. The 2024-T3 results [18] are also shown for comparison. For the 7075-T6 specimens,  $T^*$  increased with increasing crack velocity

and eventually leveled off at a terminal velocity of about 300 m/s. In contrast, the crack velocity in the fatigued precracked 2024-T3 specimens did not reach a terminal velocity and arrested at a  $T^*$  higher than its initiation value.

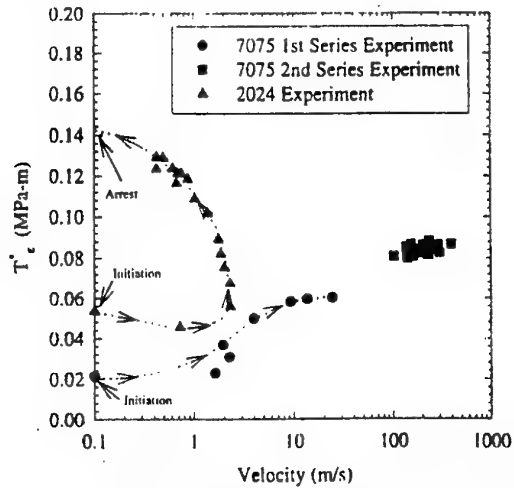


Figure 7.  $T^*$  versus crack velocity relation of a fracturing 7075-T6 SEN specimen.

The dynamic strain energy release rate,  $G_{ID}$ , with respect to crack velocity of 7075-T6, like other somewhat brittle materials, was expected to exhibit the characteristic gamma-shaped curve. To test this postulate, the crack tip opening displacement (CTOD) at a crack tip distance,  $r = 1$  mm, was used to compute  $K_{ID}$ , and the strain energy release rate,  $G_{ID}$ , based on LEFM for the fatigue-precracked (first series) and the machine-notched (second series) 7075-T6 SEN specimens. The same procedure was used to compute  $G_{ID}$  for the blunt-notched 7075-T6 SEN specimens of [6] and the characteristic gamma shaped  $G_{ID}$  versus crack velocity relation was obtained.

### 5.3. DISCUSSIONS

Both the  $T^*$  and CTOA are being considered for stable crack growth criteria and likewise possibilities exist as dynamic ductile fracture criteria. CTOA, by definition, is a local crack tip parameter that exhibited a precipitous drop at the initial phase of rapid crack propagation in fatigue-precracked 2024-T3 and 7075-T6 SEN specimens. Dawicke et. al. [16] attributed this drop to the crack front tunneling prior to crack extension. However, the blunt, machine-notched 7075-T6 SEN specimens in this study did not exhibit the initial high CTOA. Thus the initial high value in CTOA in the fatigue-precracked SEN specimens is probably due to crack tip blunting prior to crack extension.

Both CTOA and  $T^*$  remained constant despite the increasing crack velocity in the 7075-T6 SEN specimens and the decreasing crack velocity in the 2024-T3 specimens.

CTOA in the 2024-T3 SEN specimens at crack arrest was lower than the CTOA's at the initiation of rapid crack propagation and during crack propagation. On the other hand,  $T^*_e$  at crack arrest in the 2024-T3 SEN specimens was higher than its constant value during crack propagation as shown in Figure 7.

The distinct difference in the  $G_{ID}$  and  $T^*_e$  responses at the terminal velocity, suggests that the traditional practice of characterizing dynamic fracture of somewhat ductile material through the  $G_{ID}$  versus crack velocity relation based on LEFM could be misleading. The LEFM approach results in a terminal velocity, which is insensitive to the driving force,  $G_{ID}$ , while the  $T^*_e$  approach, based on elastic-plastic fracture mechanics (EPFM), suggests that the terminal crack velocity is a consequence of the saturation of the dissipated plastic energy.

## 6. Process Zone of Polycrystalline Alumina

A hybrid experimental-numerical procedure was used to determine the crack closing stress (CCS) versus crack opening displacement (COD) relations of a high- and a medium-density polycrystalline alumina.

### 6.1. EXPERIMENTAL ANALYSIS

Wedge-loaded, double cantilever beam (WL-DCB) specimens were machined from high-density (AL23) and medium-density (AD90) commercial alumina. The grain sizes ranged from 5 to 45  $\mu\text{m}$  with an average size of 18  $\mu\text{m}$  for the former and an average grain size of 9  $\mu\text{m}$  for the latter. A 50% side groove was machined to channel the stably growing crack that would otherwise curve away from its intended straight path.

A 1200 lines/mm specimen grating was affixed by a replica technique on the ungrooved surface of the fracture specimen. The specimen grating was then placed in a two-beam, phase-shifting Moiré interferometer with an appropriate oblique incident illumination as described in Section 2.2.

The fracture specimen was loaded in a rigid displacement controlled loading fixture and the Moiré fringes at the peak load of each increment of increasing displacement loading and the stably growing crack were recorded. Load-line displacement was not recorded since the Moiré fringes provided an accurate displacement measurement at the contact point of the loading rod and specimen.

### 6.2. NUMERICAL ANALYSIS

A two-dimensional, linearly elastic, finite element (FE) model of the WL-DCB specimen was used in a propagation analysis with the applied wedge load, wedge-opening displacement, instantaneous crack length and the elastic properties as input conditions. The measured load at the time of recording of the Moiré fringe pattern, instead of the applied displacement, was used to reduce the sensitivity of the numerical analysis to the error in the load-line displacement measurement. The instantaneous

crack tip location was determined from the Moiré data with an accuracy of 0.1 mm. The CCS versus COD relation and the modulus of elasticity were the two disposable parameters in this numerical analysis and the Poisson ratio was assumed to be 0.22. The latter variation in the modulus of elasticity was less than 6 percent of the manufacturer's quoted value and is within accepted tolerance.

### 6.3. RESULTS

A total of four specimens of each alumina, i.e., AL23 and AD90, were analyzed in this study. Moiré fringe patterns obtained from each test provided the crack opening profiles for the two microstructures for several crack lengths and loading. Using the inverse analysis described previously, the crack closing stress (CCS) versus the crack opening displacement (COD) relation, which provided the best fit between the calculated and measured COD profiles, was obtained through an iterative procedure. Figure 8 shows the CCS versus COD relation of AL-23 alumina. For comparison, the CCS versus

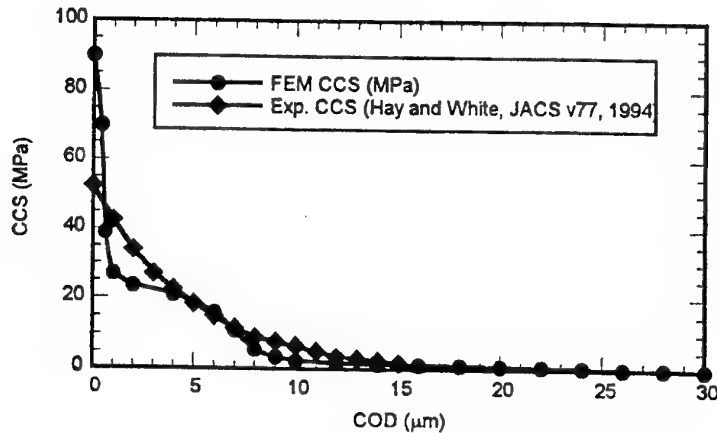


Figure 8. CCS versus COD relation for AL-23 alumina WL-DCB specimen.

COD relation, which was obtained by the post fracture tension (PFT) tests described in [19], is superimposed in Figure 8. The lower CCS near the crack tip, i.e., at a lower COD, is due to the averaging effect over a relatively large distance of 1 mm in the PFT specimen. The CCS versus COD relation of the AD90 specimen also compares well with that reported in [20]. This was expected, as the 11  $\mu\text{m}$  average grain size of the alumina specimen of [20] was very close to the 9  $\mu\text{m}$  grain size of AD90. The CCS

versus COD relation of AD90, however, lacked the trailing tail in Figure 8 due to the lack of the broad grain size distribution of AL23. The smaller average grain of AD90 effectively reduced the bridging distance and hence the bridging force

Figure 9 shows the variation in energy partition with crack extension in the AL23 specimen. The dissipated energy in the FPZ was computed by summing up the work done in the FPZ per incremental crack extension. The rate of energy dissipation is about 95 percent of the energy released which is the difference between the total work and the stored elastic energy. The result of Figure 9 proves that the FPZ is the major energy dissipation mechanism in the brittle alumina.

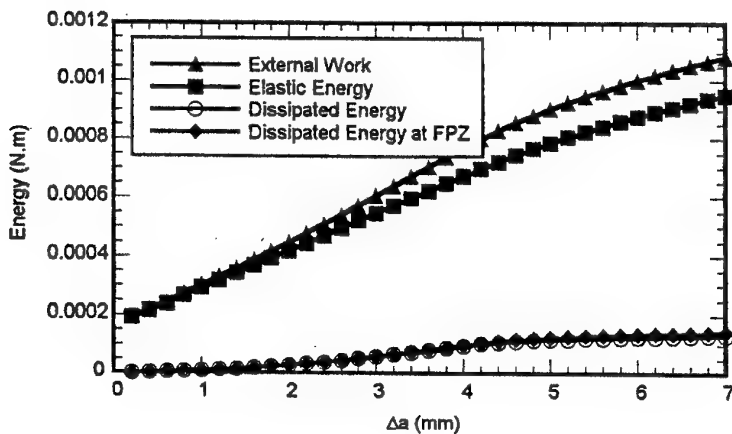


Figure 9. Computed energies for AL-23 alumina WL-123 specimen.

#### 6.4. CONCLUSIONS

The crack closing stress versus crack opening displacement relations governing the fracture process zone, which trails a stably growing crack in the high-density alumina, WL-DCB specimens were quantified.

The fracture process zone trailing the crack tip was shown to be the major energy dissipation mechanism in alumina fracture specimen.

#### 7. Conclusion

The effectiveness of Moiré interferometry for studying the fracture response of real structural material was demonstrated. New and controversial results in low cycle fatigue

of thin 2024-T3 aluminum, dynamic fracture of 7075-T6 aluminum and fracture of AL-23 and AD90 alumina were presented.

## 8. Acknowledgment

This paper summarizes the research conducted by J. H. Jackson, M. T. Kokaly, P. W. Lam, J. Lee, L. Ma, Y. Omori, D.K. Tran of the University of Washington, H. Okada, Kagoshima University and P. W. Tan of the FAA William Hughes Technical Center. This study is supported by FAA Research Grant 92-G-005, DOE Grants DE-FG06-94ER 14490, AFOSR Grant F49620-93-1-0210 and ONR Contract N00014-89-J-1276.

## 9. References

1. Smith, Charles W.: Measurements of three-dimensional effects in cracked body problems, in Jonathan S. Epstein (ed.), *Experimental Techniques in Fracture*, VCH Publishers, 1993, 253-289.
2. Liechti, Kenneth M.: On the use of classical interferometry techniques in fracture mechanics, *ibid. loc. cit.*, 95-124.
3. Rosakis, Ares J.: Two optical techniques sensitive to gradients of optical path difference: the method of caustics and the coherent gradient sensor (CGS), *ibid. loc. cit.*, 327-426.
4. Kalthoff, Joerg F.: Shadow optical method of caustics, in Albert S. Kobayashi (ed.), *Handbook on Experimental Mechanics*, VCH Publishers, 1993, 407-476.
5. Kobayashi, A. S., Harris, D. O. and Engstrom, W. L.: Transient analysis in a fracturing magnesium plate, *Experimental Mechanics*, 7, 10 (1967), 434-440.
6. Kobayashi, A. S. and Engstrom, W. L.: Transient analysis in fracturing aluminum plates, *Proc. 1967 JSME Semi-International Symposium*, 1997, 172-181.
7. Chiang, Fu-pen.: Moiré and speckle method applied to elastic-plastic fracture mechanics, in Jonathan S. Epstein (ed.), *Experimental Techniques in Fracture*, VCH Publishers, 1993, 291-325.
8. Post, D.: Optical interference for deformation measurements - Classical holography and Moiré interferometry, in W.W. Stinchcomb (ed.), *Mechanics of Nondestructive Testing*, Plenum Press, 1980, 1-53.
9. Epstein, J.S. and Dadkhah, M.S.: Moiré interferometry in fracture research, in Jonathan S. Epstein (ed.), *Experimental Techniques in Fracture*, VCH Publishers, 1993, 427-140.
10. Post, D.: Moiré interferometry, in Albert S. Kobayashi (ed.), *Handbook on Experimental Mechanics*, VCH Publishers, 1993, 297-364.
11. Wang, F.X., May, G.G. and Kobayashi, A.S.: Low-spatial-frequency steep grating for use in Moiré interferometry, *Optical Engineering*, 33, 4 (1994), 1125.

1131.

12. Brust, F.W., Nishioka, T., Atluri, S.N. and Nakagaki, M.: Further studies on elastic-plastic stable fracture utilizing the  $T^*$ -integral, *Engineering Fracture Mechanics*, 22 (1985), 1079-1103.
13. Okada, H. and Atluri, S.N.: Further Study on the Near Tip Integral Parameter  $T^*_e$  in Stable Crack Propagation in Thin Ductile Plate, *Proceedings of Aerospace Division, ASME*, AD-Vil. 52, J.C.I. Chang et al. (eds.), 1997, 251-2614.
14. Pyro, C.R., Okada, H. and Atluri, S.N.: An Elastic-Plastic Finite element Alternating Method for Analyzing Wide Spread Fatigue Damage in Aircraft Structures, *Computational Mechanics*, 16 (1995), 62-68.
15. Narashinhan, R. and Rosakis, A.J.: Three-dimensional effects near a crack tip in a ductile three-point bend specimen: Part 1 - A numerical investigation, *ASME Journal of applied Mechanics*, 57 (1990), 607-617.
16. Dawicke, D.S., Newman, J.C. Jr., Sutton, M.A. and Amsstutz, B.E.: Stable tearing behavior of a thin sheet material with multiple cracks, *Fracture Mechanics: 26th Volume*, ASTM STP 1256, W.G. Reuter, J.H. Underwood and J.C. Newman, Jr. (eds.), ASTM, 1995.
17. Dawicke, D.S., Plascik, R.S. and Newman, J.C. Jr.: Prediction of stable tearing and fracture of a 2000-series aluminum alloy plate using a CTOA criterion, *Fatigue and Fracture Mechanics; 27th Volume*, ASTM STP 1296, R.S. Plascik, J.C. Newman, Jr. and N.E. Dowling (eds.), ASTM, 1997, 90-104.
18. Lee, J., Kokaly, M.T. and Kobayashi, A.S.: Dynamic ductile fracture of aluminum SEN specimens: An experimental-numerical analysis, *Advances in Fracture Research, ICF 9*, B.L.I. Karihaloo, Y.W. Mai, M.I. Ripley and R.O. Richie (eds.), Pergamon Press, 1997, 2965-2972.
19. Hay, J.C. and White, K.E.: Grain boundary phase and wake zone characterization in monolithic alumina, *J. of Amer. Ceramic Soc.*, 78 (1995), 1025-1032.
20. Roedel, J., Kelly, J.F. and Lawn, B.R.: In situ measurements of bridged crack interfaces in scanning electron microscope, *J. of Amer. Ceramic Soc.*, 73 (1990), 3313-3318.

### Stress field at crack bifurcation

## STRESS FIELD MEASUREMENT AT BIFURCATION OF FAST PROPAGATING CRACKS BY HIGH-SPEED INTERFEROMETRY

S. SUZUKI, I. INAYAMA, N. ARAI and T. MIZUTA  
*Dept. Mechanical Engineering, Toyohashi University of Technology  
Tempaku-cho, Toyohashi, 441-8580 Japan*

### Abstract

Interferometry with high-speed holographic microscopy is applied to investigate stress field near fast propagating crack tips at the instant of crack bifurcation. It is found that, at the instant of bifurcation, the stress field in the vicinity of fast propagating crack tips deviates from the singular stress field of the dynamic fracture mechanics. Such deviation is due to the existence of bifurcated crack tips.

### 1. Introduction

When brittle materials are broken by external force, fast propagating cracks often appear, whose speed of propagation is at several hundred m/sec or more. If the crack speed is high enough, a fast propagating crack bifurcates into two or more cracks.

Bifurcation is a characteristic feature of fast propagating cracks, accordingly, many researchers have tried to know the bifurcation mechanism [1]-[4]. However, the bifurcation mechanism has not been clearly understood yet, because there are many difficulties in experimental studies on dynamic fracture phenomena.

Recently, Suzuki developed high-speed holographic microscopy which can take three successive microscopic photographs of fast propagating cracks [5]-[8]. High-speed holographic microscopy has the spatial resolution of about 180 lines/mm, which is much higher than the other optical methods used for dynamic fracture research. High-speed holographic microscopy can therefore measure the stress field in the vicinity of fast propagating crack tips with very high accuracy.

The present study applies interferometry to measure stress field in the neighborhood of fast propagating crack tips. High-speed holographic microscopy is utilized to photograph the cracks, their bifurcation process and interference fringes with high spatial resolution. And it is found that, at the instant of bifurcation, the stress field in the vicinity of crack tips deviates from the singular stress field of the dynamic fracture mechanics. Such deviation occurs not only after bifurcation but just before bifurcation.

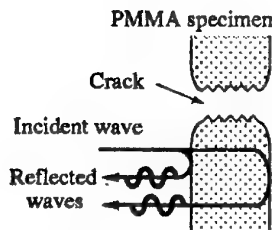


Fig.1 Principle of Interferometry.

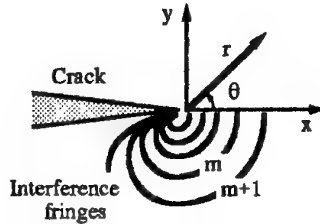


Fig.2 Crack, fringes and coordinates

## 2. Experimental Method

The present study uses transparent PMMA specimens with 3mm in thickness. A crack of the opening mode propagates rapidly in a specimen and bifurcates into two or more cracks in the observation area in the specimen.

### 2.1. INTERFEROMETRY

Figure 1 shows the principle of interferometry to measure stress field near crack tips. A crack propagates perpendicularly to the paper plane. An parallel light beam impinges upon specimen surfaces perpendicularly, and is reflected either by the front surface or by the back one of the specimen. The two reflected light waves interfere with each other and interference fringes appear around the crack tip. The interference fringes are contours of the thickness and refractive index of the specimen, consequently, they represent the contours of the sum of principal stresses.

The dynamic fracture mechanics says that there exists the singular stress field around fast propagating crack tips [9]. Using the formula for the singular stress field, one can obtain the following equation about  $\partial m / \partial r$  as a function of  $r$  and  $\theta$ ,

$$\frac{\partial m}{\partial r} = A K_I(v) r^{-3/2} f(\theta, v) F(v) \quad (1)$$

where  $m$  is the fringe order,  $r$  is the distance from the crack tip,  $\theta$  is the angle measured from the crack propagation direction (Fig.2). And  $A$  is a constant,  $v$  is the crack speed,  $K_I(v)$  is the dynamic stress intensity factor,  $f(\theta, v)$  describes the circumferential variation of the stress field and  $F(v)$  expresses the dynamic effect. When you measure the crack speed  $v$  and  $\partial m / \partial r$  at a certain position ( $r, \theta$ ) in the singular stress field, you can know the dynamic stress intensity factor  $K_I(v)$  through the above equation.

Here it must be noticed that if  $\partial m / \partial r$  is measured within the singular stress field of plane stress, the  $\partial m / \partial r$  measurements always give the unique value of  $K_I(v)$ . But if the singular stress field does not exist around crack tips, the  $\partial m / \partial r$  measurements at different positions give different  $K$  values. Therefore, measuring  $\partial m / \partial r$  at some different positions, one can examine whether the singular field is developed or not.

## Stress field at crack bifurcation

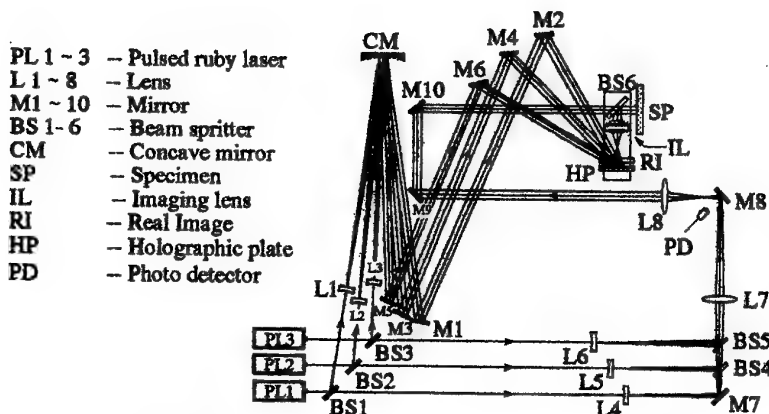


Fig.3 The optical system for high-speed holographic microscopy.

## 2.2. HIGH-SPEED HOLOGRAPHIC MICROSCOPY [5]-[8],[10]

Figure 3 shows the optical system for holographic recording of fast propagating cracks, in plan view [10]. A crack propagates in the specimen SP perpendicularly to the paper plane. When the crack is propagating in the observation area, the three pulsed ruby lasers oscillate successively in the order of PL1, PL2 and PL3. The three laser pulses record the crack as the first, the second and the third hologram, respectively. The frame interval is 1 $\mu$ sec or more.

The light beam emitted from ruby laser PL1 is divided into two parts by beam splitter BS1. The reflected light beam from BS1 is diverged and collimated, and falls upon the holographic plate HP obliquely. This is the reference beam for the first hologram. The light beam transmitted through beam splitter BS1 is reflected by mirror M7, and passes through beam splitters BS4 and BS5. The light beam becomes a parallel light beam, passes through beam splitter BS6 and falls upon the specimen surfaces perpendicularly. The light beam is reflected either by the front surface or by the back one of the specimen, and makes interference fringes on the specimen. The reflected light from the specimen is reflected by beam splitter BS6, passes through imaging lens IL and impinges on the holographic plate perpendicularly. This is the object beam. The object beam is recorded as the first hologram.

The second and the third holograms are recorded similarly. The angles of incidence of the reference beams for the three holograms are different from one another, and the three holograms are superimposed on one holographic plate. That is the angle-multiplexing holography.

At reconstruction, each hologram reconstructs separately the crack image and interference fringes at the position where the specimen existed at the recording. The reconstructed images are photographed through a conventional microscope.

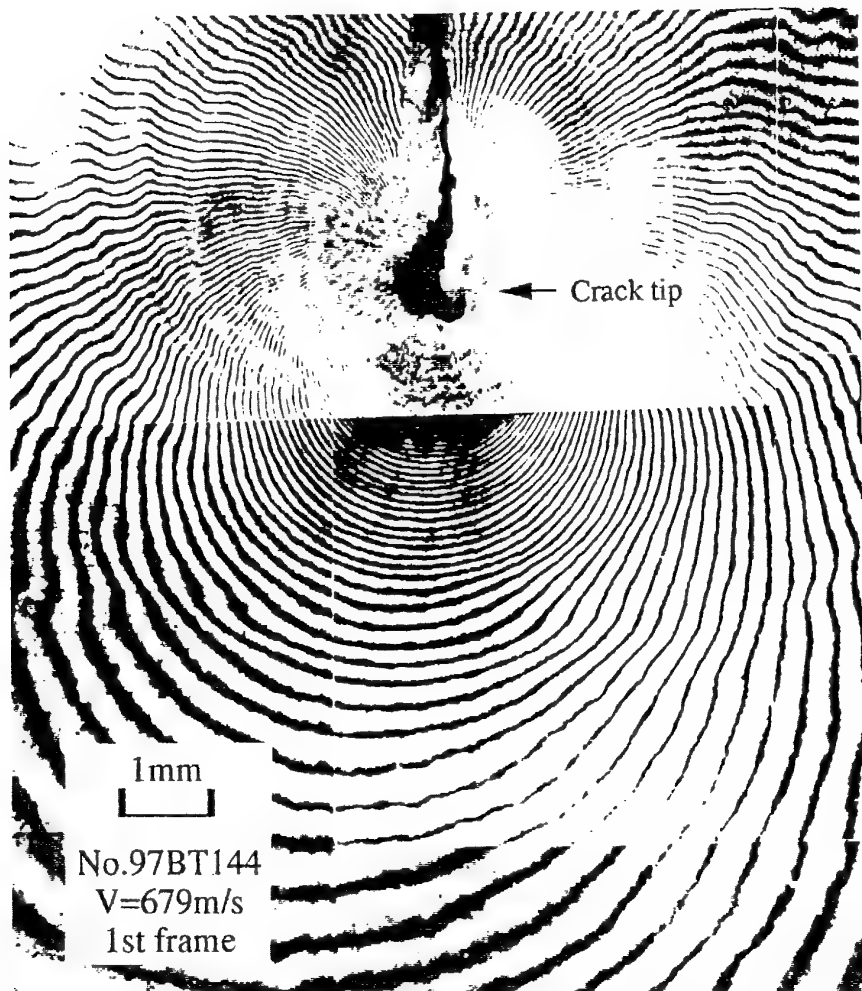


Fig.4(a) A fast propagating crack at  $3.1\mu\text{sec}$  before bifurcation. The first frame.

### 3. Results and Discussions

#### 3.1. MICROSCOPIC PHOTOGRAPHS OF CRACK BIFURCATION

Figure 4(a), (b) and (c) show microscopic photographs of a crack at bifurcation. The crack is of the opening mode and was propagating in a PMMA plate specimen at a speed of  $682\text{m/sec}$ . The frame interval was about  $4.8\mu\text{sec}$ . The first frame in Fig.4(a) was photographed at  $3.1\mu\text{sec}$  before the bifurcation. The second and the third frames in Fig.4(b) and (c) were taken at  $1.8\mu\text{sec}$  and at  $6.5\mu\text{sec}$  after the bifurcation, respectively.

Stress field at crack bifurcation

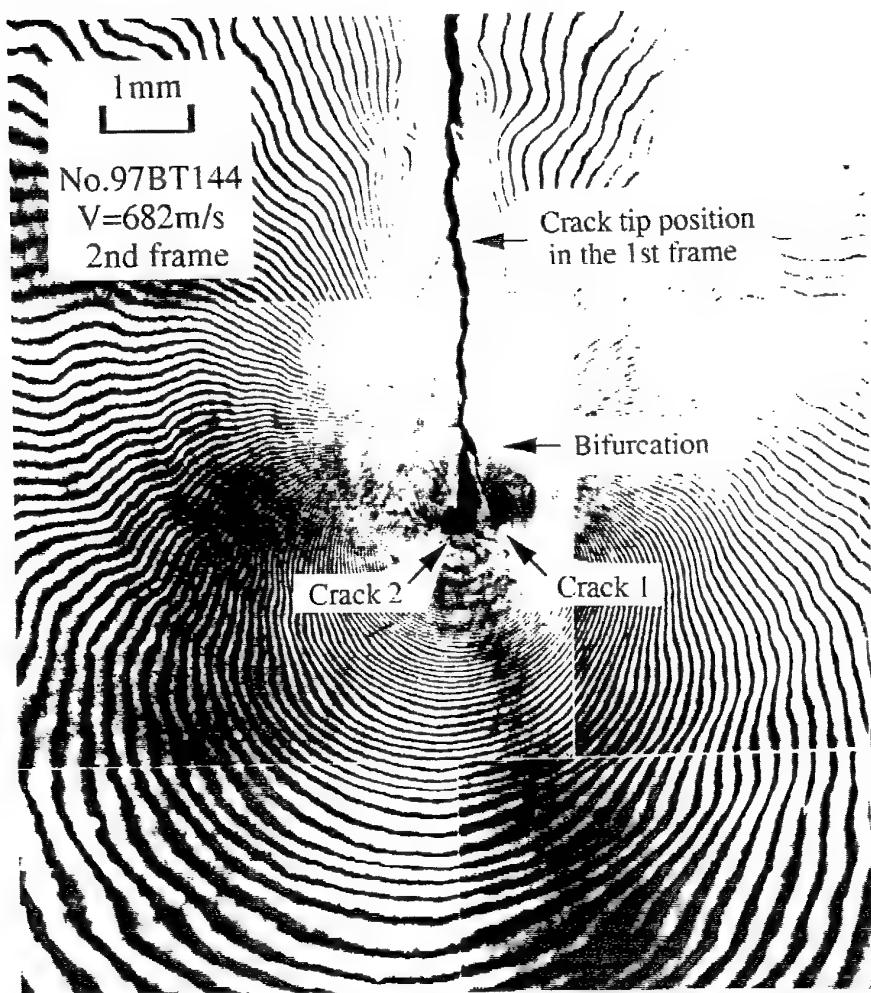


Fig.4(b) The fast propagating crack at  $1.8\mu\text{sec}$  after bifurcation. The second frame.

At first the crack bifurcated into two cracks, Crack 1 and Crack 2. Then Crack 2 bifurcated into Crack 3 and Crack 4. At the right of Crack 1 in the third frame, you can find a crack which has stopped propagating.

One can see many fine interference fringes around the crack tips. Stress field around the crack tips can be examined through the fringe analysis described in the previous section.

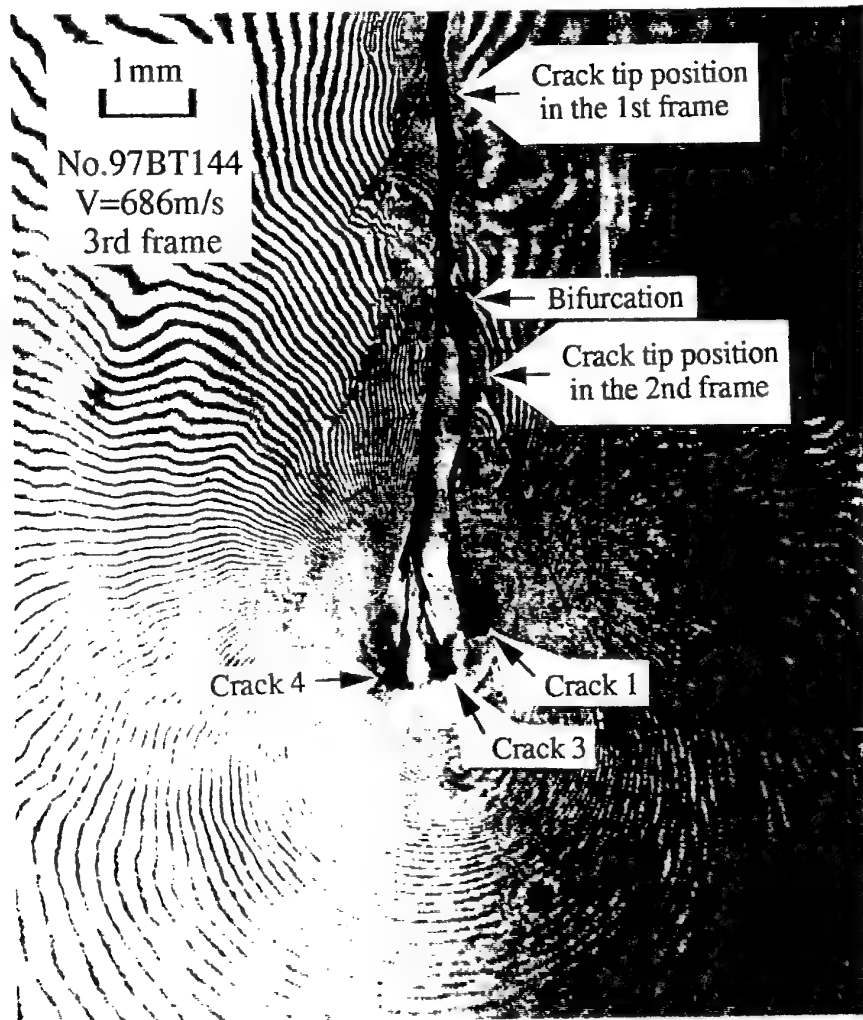


Fig.4(c) The fast propagating crack at  $6.5\mu\text{sec}$  after bifurcation. The third frame.

### 3.2. NEAR-TIP STRESS FIELD AT BIFURCATION

Figure 5(a), (b) and (c) show the results of fringe analysis of the photographs shown in Fig.4(a), (b) and (c), respectively. The horizontal axis indicates the distance  $r$  from a crack tip, and the vertical axis indicates the  $K$  value obtained from the  $\partial m/\partial r$  measurement through Eq.(1). The  $\partial m/\partial r$  measurement was carried out in the direction of  $\theta=0^\circ$ ,  $\pm 72^\circ$  and  $\pm 90^\circ$ . As mentioned in the previous section, the  $K$  values are kept constant if the measurement is carried out within the singular field of plane stress.

## Stress field at crack bifurcation

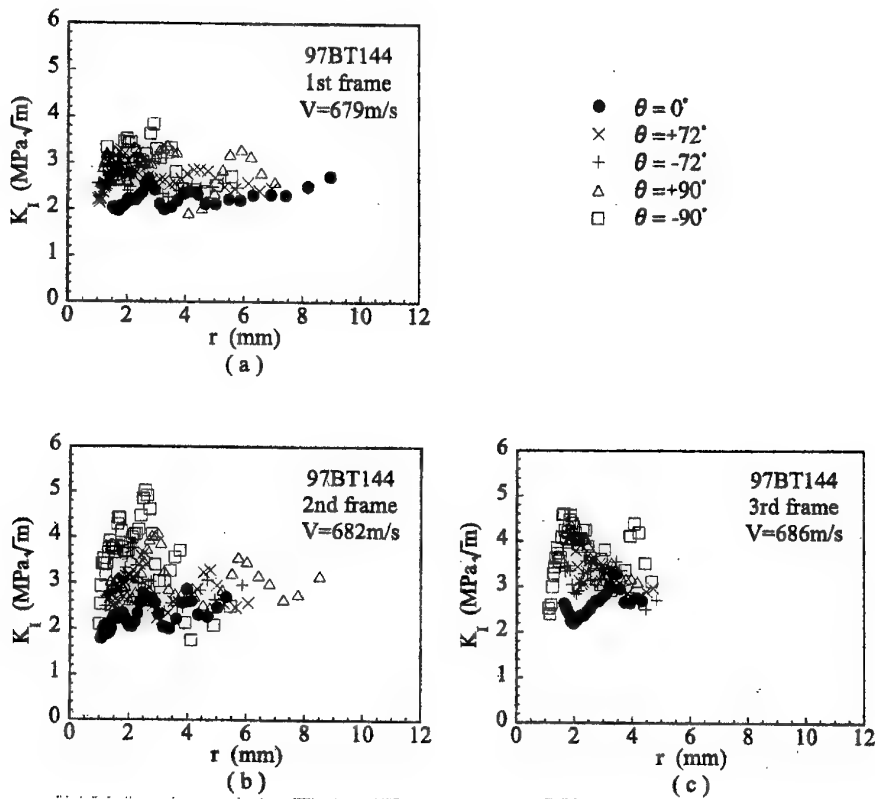


Fig.5 The dynamic stress intensity factor measured by interferometry. (a) At 3.1 $\mu$ sec before bifurcation.  
 (b), (c) At 1.8 $\mu$ sec and 6.5 $\mu$ sec after bifurcation.

### 3.2.1. Near-Tip Field after Bifurcation

Figure 5(b) and (c) show that, the  $K$  values in the direction of  $\theta=\pm 72^\circ$  and  $\pm 90^\circ$  are larger than those in the direction of  $\theta=0$  in the region of  $r$ ,  $1.5\text{mm} < r < 4\text{mm}$ . This fact means that the  $K$  field does not exist in the region,  $1.5\text{mm} < r < 4\text{mm}$ . Figure 5(b) and (c) show the results on the stress field after bifurcation, where there are two or more crack tips. The singular stress field of the dynamic fracture mechanics is for cracks whose tips are not bifurcated. The deviation of the near-tip field from the singular stress field is caused by the bifurcated crack tips shown in Fig.4(b) and (c).

### 3.2.2. Near-Tip Field before Bifurcation

The most interesting thing in the measurement results is that the near-tip field deviates from the singular field in the region of  $r$ ,  $1.5\text{mm} < r < 4\text{mm}$ , not only after bifurcation

S. Suzuki, I. Inayama, N. Arai and T. Mizuta

but also before bifurcation (Fig.5(a)). This may be caused by microcracks and attempted branches which appear near a crack tip just before bifurcation.

Reflection type high-speed holographic microscopy can observe specimen surfaces only. Thus it can find microcracks and attempted branches on specimen surfaces, but cannot find those inside specimens. The deviation of the near-tip field from the singular field measured before bifurcation may be due to microcracks and attempted branches which were not photographed in Fig.4(a), but existed within the specimen. It was reported that many attempted branches appear near crack tips just before bifurcation, and were photographed by high-speed holographic microscopy [10].

#### 4. Conclusions

- (1) Interferometry with the reflection type high-speed holographic microscopy can measure the stress field in the vicinity of crack tips at the instant of crack bifurcation.
- (2) At bifurcation, the stress field in the vicinity of crack tips deviates from the singular field which exists near un-bifurcated crack tips. Such deviation occurs not only after bifurcation but also just before the bifurcation.
- (3) The deviation just before bifurcation may be caused by microcracks and attempted branches which appear near crack tips just before bifurcation.

#### Acknowledgement

The present study was supported by Grant-in-Aid for Fundamental Scientific Research (09650097) of The Ministry of Education, Science and Culture. One of the authors, S.Suzuki, expresses his gratitude for the grant.

#### References

1. Yoffe,E.H.: The moving Griffith crack, *Phil. Mag.* 42 (1951), 739-750.
2. Baker,B.R.: Dynamic stresses created by a moving crack, *Trans. ASME, J.Appl.Mech.* 29 (1962), 449-458.
3. Ravi-Chandar,K. & Knauss,W.G.: An experimental investigation into dynamic fracture: III. On steady-state crack propagation and crack branching. *Int. J. Fracture.* 26 (1984), 141-154.
4. Ramuru,M. & Kobayashi,A.S.: Mechanism of crack curving and branching - a dynamic fracture analysis. *Int. J. Fracture.* 27 (1985), 187-201.
5. Suzuki,S. et al.: Optical measurement of stress waves and rapid crack propagation in the time domain of microseconds, in B.L.Karihaloo, Y-W.May, M.I.Ripley and R.O.Ritchie (eds.), *Advances in Fracture Research*, Proc. 9th Int. Conf. Fracture, Vol.6, Pergamon, (1997), 2925-2932.
6. Suzuki,S. et al.: High-speed holographic microscopy for fast propagating cracks in transparent materials, *Appl. Opt.* 36 (1997), 7224-7233.
7. Suzuki,S. et al.: Application of high-speed holographic microscopy to study on rapid crack propagation, in D.L.Paisley and A.M.Frank (eds.), *Proc. 22nd Int. Cong. High-Speed Photography and Photonics*, SPIE Vol.2869, (1997), 644-650.
8. Suzuki,S. et al.: Resolution of high-speed holographic microscopy for photographing fast propagating cracks. *Proc. Int. Conf. Advanced Technology in Exp. Mech.*: The Japan Society of Mechanical Engineers, Tokyo, (1997), 267-272.
9. Freund,L.B.: *Dynamic fracture mechanics*, Cambridge University Press, Cambridge, 1990.
10. Suzuki,S. et al.: Reflection type high-speed holographic microscopy to photograph crack bifurcation, *Proc. 11th Int. Conf. Experimental Mechanics*, Oxford, UK, August, 1998, (to be published).

**THE STRESS FIELD AROUND TWO PARALLEL CRACKS IN A FINITE GEOMETRY: A HYBRID STUDY COMBINING HIGH-DENSITY GEOMETRIC MOIRE AND PHOTOELASTICITY WITH THE WESTERGAARD APPROACH AND LOCAL COLLOCATION METHODS**

RAVINDER CHONA

*Department of Mechanical Engineering  
Texas A&M University, Mail Stop 3123  
College Station, Texas 77843-3123, USA*

**Abstract**

Finite geometry problems, in which two or more cracks are in close proximity so that their stress fields interact, are generally found to be substantially more challenging than problems involving single or isolated cracks. The present study now, combining optical techniques such as photoelasticity with high density geometric moire, a method of modelling single cracks with similar loadings and geometries, and an elasticity technique well-suited to problems with multiple boundaries, produces an overall solution for the stress field around multiple crack tips in finite geometries.

**Introduction**

The basic approach adopted here is to use the generalized Westergaard equations [1] to represent the stress field around each individual crack tip as if it were an isolated crack and then apply the Schwarz alternating method [2], or method of successive stress removal, to obtain the additional stress fields that must be superposed on the original (isolated) solutions to ensure that the boundary conditions on each of the crack faces are satisfied. The end result of this iterative approach provides the overall stress field for the entire region surrounding both crack tips.

This overall stress field can then be utilized in a local collocation analysis procedure in an analogous manner to that currently followed for single crack problems [3,4]. Photoelastic isochromatic and high density geometric moire fringe patterns for the case of two parallel edge cracks in pure bending were the source for experimental data collection. Additional data was obtained from finite element models of similar geometries for which the calculated in-plane cartesian stress components were converted into isochromatic data and nodal displacement values were used directly.

The objectives of the study can be summarized as being: (a) to utilize the combined Westergaard-Schwarz approach to obtain a full-field representation of the stress field surrounding two parallel edge cracks in a finite body; (b) to use this stress field representation to analyze the case of two parallel edge cracks under pure bending by performing local collocation analyses of experimental and finite-element-generated photoelastic and high-density geometric moire data; (c) to determine the influence of the presence of the other crack on the stress intensity factors for the multiple crack configuration; and (d) to establish guidelines for the separation distances at which the two cracks could be considered to behave as one crack or as two separate cracks which do not interact with one another. Obtaining converged solutions for the local collocation analyses was not always a trivial problem. However, in general, the combined Westergaard-Schwarz method gave satisfactory results for both the experimental and the finite-element-generated data.

The solutions for the experimental analyses were verified by comparing computer generated fringe plots [5] with the original fringe patterns. For the finite-element-generated data, the verification was to compare the J-integral value calculated from the stress intensity factors for each crack tip with the J-integral value calculated directly from the finite element analysis.

### Synopsis of Procedure and Results

The geometry of a four-point bend specimen with two parallel, interacting edge cracks is shown in Figure 1. In all cases, the length of the first crack, denoted  $a_1$  in the figure, was kept constant at a value of  $a_1/W = 0.50$ . The length of the second crack, denoted  $a_2$  in the figure, was then varied from  $a_2/W = 0.25$  to  $a_2/W = 0.625$ , in steps of 0.125. This provided a range of values for the relative crack lengths,  $a_2/a_1$  ranging from  $a_2/a_1 = 0.5$  up to  $a_2/a_1 = 1.25$ , in steps of 0.25. The spacing between the two cracks, denoted  $c$  in the figure, was varied from a value of  $c/a_1 = 0.50$  up to  $c/a_1 = 1.00$ , in steps of 0.25. In this manner, the interaction effects of the two crack tips could be examined as functions of both the relative crack size and the crack plane separation.

Finite-element models of the various geometrical combinations of  $a_2/a_1$  and  $c/a_1$  were generated using a standard pre-processor (PATRAN) and the nodal displacements and element stresses calculated using a commercially-available finite element code (ABAQUS). Eight-noded isoparametric elements were used throughout and no attempt was made to incorporate special crack-tip singularity-type elements. This choice was based on the desire to insulate the results from any kind of assumed singularity-dominance over a finite region since the size and shape of any singularity-dominated zone(s) would not be known *a priori* in a general application. Furthermore, it was desired to simulate the experimental data analysis conditions as closely as possible throughout and it would be necessary to exclude data from a finite region around the crack tip in any experimental arrangement because of a lack of generalized plane stress in the very near vicinity of the crack tip.

The experimental results were obtained using specimens machined from a PSM-1 polycarbonate sheet which was free of residual stresses. For the geometric moire experiments,

## THE STRESS FIELD AROUND TWO PARALLEL CRACKS

moire gratings with a grating frequency of 20 lines/mm (500 lines/inch) were photographically reproduced from a master grating and bonded to the specimens. Since both u-field and v-field information was desired, the specimen grating used was a bi-directional line grating, while the reference gratings employed were uni-directional line gratings of the same frequency. The test specimens were loaded in four-point bending using a displacement-controlled load frame placed within the optical arrangement of a standard, diffused-light polariscope for the photoelastic tests. The same light source was also utilised (without the polarizer-analyzer pairs) for the geometric moire experiments.

The resulting images were captured and stored using a CID camera and a commercially-available digital imaging system with 8-bit resolution. Figure 2 shows the changes observed in the u-field pattern as the relative crack size was increased from  $a_2/a_1 = 0.50$  to  $a_2/a_1 = 1.25$  for a fixed crack plane separation of  $c/a_1 = 0.75$ . Figure 3 shows the corresponding changes in the v-field pattern for the same relative crack sizes and crack plane separation.

Data points for analysis purposes were selected over pre-determined data gathering domains and stored in data files for later analysis by the local collocation programs that had been developed. The unknown coefficients of the series-type stress field representations employed were determined in a least-squares sense from these analyses. The quality of the solution was estimated quantitatively by examination of the average error between the computed and actual fringe orders over the data analysis region and by a visual comparison of the fringe pattern predicted by a solution set with the fringe pattern from which the data had been extracted.

An example of the quality of the comparison between predicted (computed) and actual photoelastic fringe patterns is shown in Figure 4 for the case of two cracks with a separation of  $c/a_1 = 0.54$  and a relative crack length of  $a_2/a_1 = 0.833$ . A similar comparison is shown in Figure 5 for the case of a u-field corresponding to  $c/a_1 = 1.0$  and  $a_2/a_1 = 1.25$ .

Figure 6 shows a comparison of the overall results for the case of two cracks with a crack plane separation of  $c/a_1 = 0.75$ , and relative crack length,  $a_2/a_1$ , varying from 0.50 to 1.25. The figure compares the J-integral value calculated directly (using a contour integral) from the finite element results with the J-value obtained from the stress intensity factors calculated at each crack tip using the local collocation analysis of the finite element data.

### Conclusions

The Westergaard-Schwarz approach was found to be suitable for representing the stress and displacement fields over relatively large regions surrounding the tips of two parallel, interacting cracks in a finite geometry. The resulting model for the stress and displacement fields proved to be useful in interpreting the data for stresses and displacements obtained using the experimental techniques of photoelasticity and geometric moire and the method of finite elements.

The results showed that:

- (a) as the length of one crack increases relative to the length of a second crack of fixed length, the interaction between the two crack-tip fields acts to lower the opening-mode stress intensity factor of the crack of fixed length;
- (b) the opening mode stress intensity factors for the two cracks are not significantly affected by changes in the crack plane separation, at least over the separation range studied; and
- (c) the interaction effect between the two crack-tip stress fields causes shear-mode stress intensity factors to develop in cases that would be under predominantly opening-mode loading in an isolated, single crack situation.

#### References

1. Sanford, R.J.: A Critical Re-examination of the Westergaard Method for Solving Opening-Mode Crack Problems, *Mechanics Research Communications* 6 (1979), 289-294.
2. Ukaudgaonker, V.G., and Naik, A.P.: Interaction Effect of Two Arbitrarily Oriented Cracks - Part I, *International Journal of Fracture*, 51 (1991), 219-230.
3. Sanford, R.J.: Application of the Least-Squares Method to Photoelastic Analysis, *Experimental Mechanics* 20 (1980), 192-197.
4. Chona, R.: Extraction of Fracture Mechanics Parameters from Steady-State Dynamic Crack-Tip Fields, *Optics and Lasers in Engineering* 19 (1993), 171-199.
5. Sanford, R.J., Barker, D.B., and Chona, R.: Computer Generated Fringe Patterns in Speckle Analysis, *International Conference on Speckle SPIE* 556 (1985).

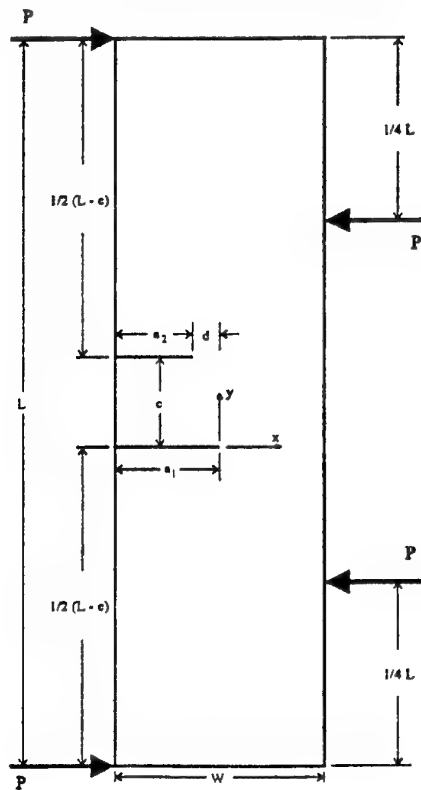


Figure 1 The geometry and loading of a four-point bend specimen with two parallel interacting edge cracks

THE STRESS FIELD AROUND TWO PARALLEL CRACKS

5



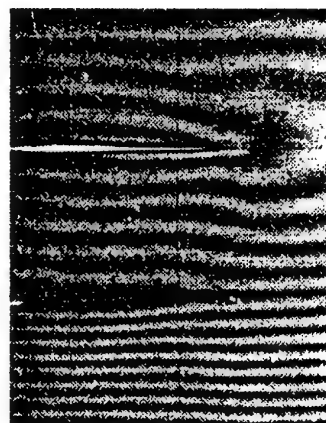
a) EXP 2.1;  $a_2/a_1=0.5$ ;  $M=225 \text{ lb}_f \text{ in}$



b) EXP 2.2;  $a_2/a_1=0.75$ ;  $M=225 \text{ lb}_f \text{ in}$



c) EXP 2.3;  $a_2/a_1=1.0$ ;  $M=225 \text{ lb}_f \text{ in}$



d) EXP 2.4;  $a_2/a_1=1.25$ ;  $M=125 \text{ lb}_f \text{ in}$

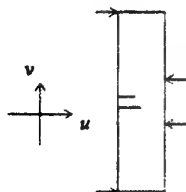


Figure 2 The changes in the u-field pattern observed as the relative crack size was increased from  $a_2/a_1 = 0.50$  to  $a_2/a_1 = 1.25$  for a fixed crack plane separation of  $c/a_1 = 0.75$

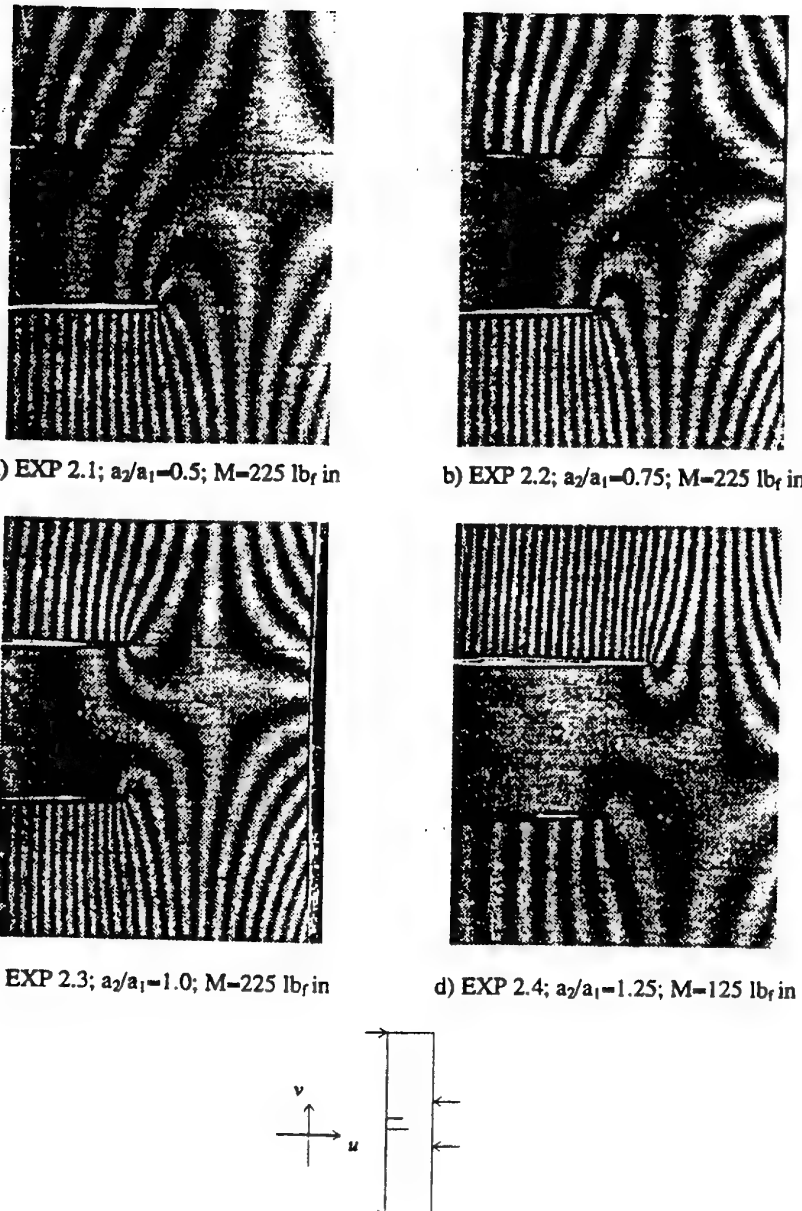


Figure 3 The changes in the v-field pattern observed as the relative crack size was increased from  $a_2/a_1 = 0.50$  to  $a_2/a_1 = 1.25$  for a fixed crack plane separation of  $c/a_1 = 0.75$

THE STRESS FIELD AROUND TWO PARALLEL CRACKS

7

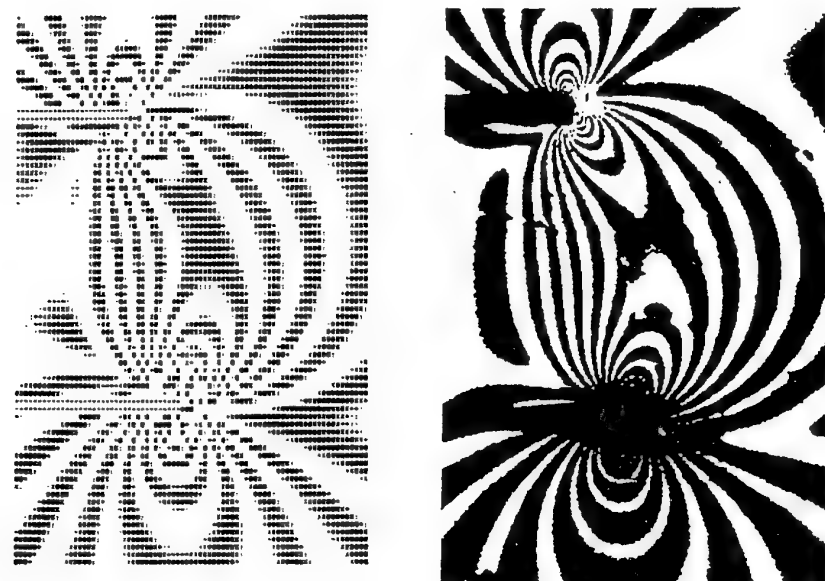


Figure 4 Reconstructed and experimentally recorded photoelastic fringe patterns corresponding to a relative crack size,  $a_2/a_1 = 0.833$ , for a crack plane separation,  $c/a_1 = 0.54$

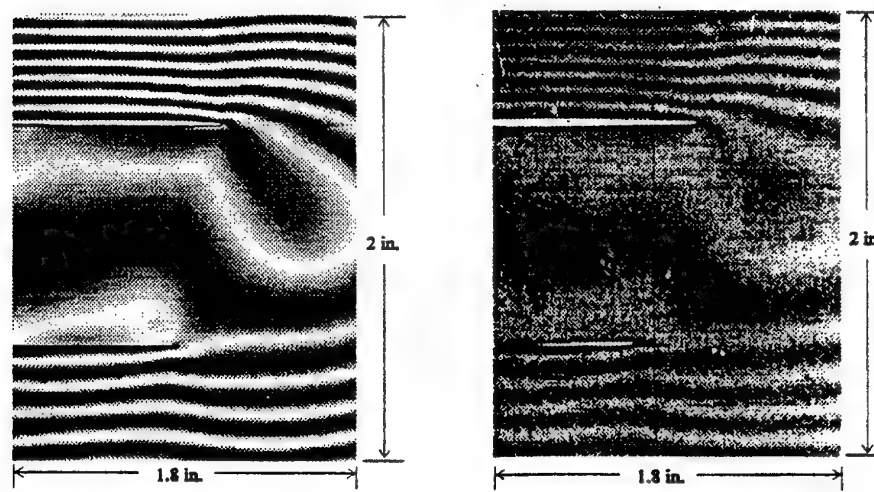


Figure 5 Reconstructed (computer-generated) and experimentally recorded u-field patterns corresponding to a relative crack size,  $a_2/a_1 = 1.25$ , for a crack plane separation,  $c/a_1 = 1.0$

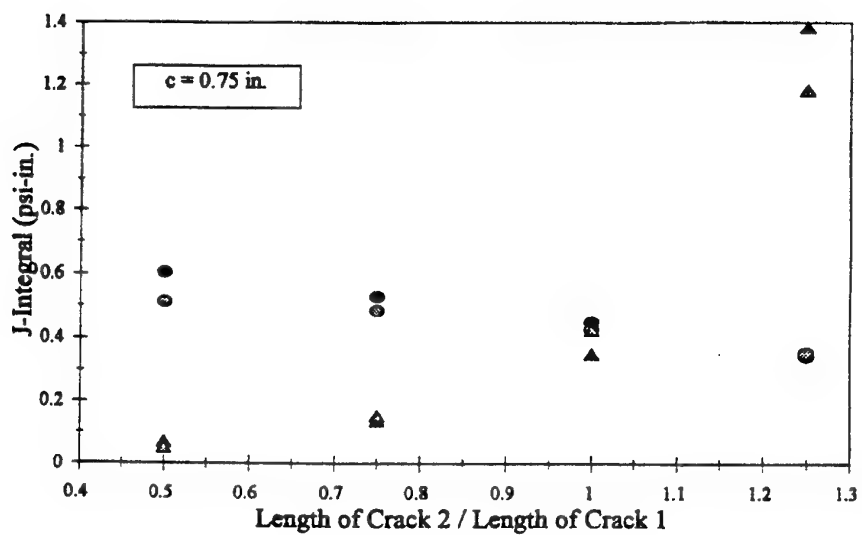


Figure 6 J-integral values calculated from finite element results using a contour integral and the stress intensity values at each crack tip calculated using the local collocation method; shown as a function of the relative crack size,  $a_2/a_1$ , for a crack plane separation,  $c/a_1 = 0.75$

**DYNAMIC BEHAVIOUR OF INTERFACIAL CRACK TIPS  
IN A WEDGE-SHAPED BIMATERIAL SPECIMEN UNDER IMPACT**

**J. FANG, C. Y. XIONG**

*Department of Mechanics & Engineering Science,  
Peking University, Beijing 100871, China*

**X. F. YAO**

*Department of Engineering Mechanics, Tsinghua University,  
Beijing 100084, China*

**ABSTRACT:** A specimen partially bonded by two wedge-shaped plates of dissimilar materials is impulsively loaded. Tip response of a crack along the interface is investigated to the action of stress wave with transmission and reflection. A hybrid technique of combining dynamic photoelasticity with dynamic caustics is used to analyze the wave propagation in media and the singular behavior of crack tips. Based on some characteristic dimensions of the caustic curves belonging to each medium, the complex stress intensity factors of the interfacial crack tips are computed, showing an oscillation history of the modulus with the passing of the compressive wave and the intersection of the reflected tensile pulse.

**1. Introduction**

Debonding of interface between two-phase material has been a typical failure in composite materials. Under impact loading, the interface of the multiphase materials may fracture rapidly due to the action of stress wave. Even in a homogeneous medium of elasticity, in fact, internal fracture may occur resulting from the focusing of the stress wave reflected from the boundaries of a solid body<sup>[1]</sup>. When a specimen of bimaterial is impulsively loaded, the tips of a crack lying along the interface may be initiated to cause a high speed debonding of the dissimilar media<sup>[2]</sup>.

The optical method of caustics is a useful technique to study the singular behavior of crack tip with high stress gradients, as proved by plenty of work by Kalthoff<sup>[3]</sup>, Theocaris<sup>[4]</sup>, et al. For the interface crack in bimaterial, Theocaris<sup>[5]</sup> used the method to determine the complex stress intensity factors at tips under normal and shear loading.

Herrman<sup>[6]</sup> extended the technique to dynamic case to evaluate the caustic patterns for arbitrary curvilinear interfacial cracks. When we investigate the response of interfacial crack tip to stress wave, however, the information provided by caustic shadows is often not enough to understand the dynamic behavior of multiphase media. The reason is that the optical caustics is a local effect of high stress gradient around crack tip, which can not offer a visual image of stress wave propagation in whole field.

A hybrid technique of combining dynamic caustics and dynamic photoelasticity has been proposed by the authors<sup>[7]</sup>, to study the fracture mechanism of crack in homogeneous material, that includes the interaction between the stress wave in a cantilever beam and the crack normal or inclined to the beam edge<sup>[8]</sup>, the curving fracture of a crack in bent beam under impact<sup>[9]</sup>. In this paper, this optical method is applied to the response study of interfacial crack to stress wave focusing. Two kinds of patterns, the isochromatic fringes of photoelasticity and the optical shadows of caustics, are recorded at the same time instants but with separated films. With the help of the isochromatic patterns, the stress wave propagation in the whole field can be visualized through the movement of fringes in the bimaterial specimen, showing the transmitting and superimposing of the wave fringes. Meanwhile, the patterns of caustic shadows provide the local responses at the vicinity of crack tips to the wave action with mixed type of loading.

## 2. Impact Experiment and Dynamic Recording

### 2.1 SPECIMEN AND LOADING

The bimaterial specimen used in impact test is made of epoxy resin and polycarbonate, bonded together with a high speed adhesive. The shape of the specimen is a model easy to produce the focusing of stress wave, consisting of two wedge-shaped plates of angle  $\alpha=22^\circ$ , as illustrated in Figure 1. The mechanical properties of the materials are given in the Table 1, by showing the medium of epoxy resin as Phase 1 and that of polycarbonate as Phase 2, respectively.

A crack with length of 7mm is fabricated along the interface of the dissimilar materials, with its upper-tip U below the top edge AB of the specimen by a distance of  $l=(AB/2) \sin 2\alpha$ . At the center position P of the top edge, an impulsive point load is acted by a bullet of gun, that produces a compressive stress wave propagating in the bimaterial specimen.

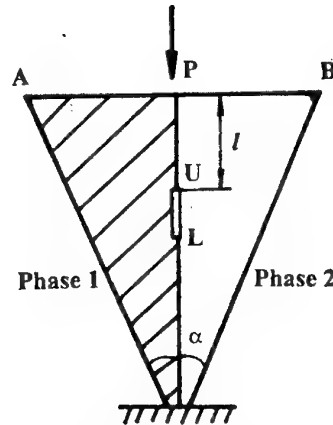


Figure 1, The specimen of bimaterial

TABLE 1 Mechanical properties of the materials

Material	Young's module (N/m <sup>2</sup> )	Poisson's ratio	Thickness (mm)
Phase 1	$E_1=4.7\times10^9$	$\nu_1=0.38$	$t_1=6$
Phase 2	$E_2=2.6\times10^9$	$\nu_2=0.35$	$t_2=5$

## 2.2 HIGH-SPEED RECORDING SYSTEM

A modified Cranz-Schardin camera is used to record dynamic patterns of impact. The light source consists of 16 (4×4) spark gaps that are precharged with high voltage and then flash sequentially by discharge to produce strong point-like light sources.

The light beam is collimated by a field lens  $L_1$  to illuminate the specimen B, as illustrated in Figure 2. The light becomes circularly polarized after passing through a polarizer  $P_1$  and then a quarter wave plate  $Q_1$ . Another field lens  $L_2$  focuses the light beam into an image lens  $l_i$  of small aperture, that corresponds to the  $i$ -th source flash of  $S_i$ . In a dark box, a partially reflecting mirror  $M_p$  separates the light beam into two parts. The reflected part is received by a set of films located on a plane  $I_c$  that is of a distance from the image plane  $I_0$  of the specimen. The off-focusing of this recording plane enables the caustic shadow of crack tip to be recorded with an object distance of  $z_o$  from the specimen. The light transmitting the mirror  $M_p$ , meanwhile, passes another quarter-wave plate  $Q_2$  and then a polarizing analyzer  $P_2$ , to record the isochromatic patterns of moving fringes.

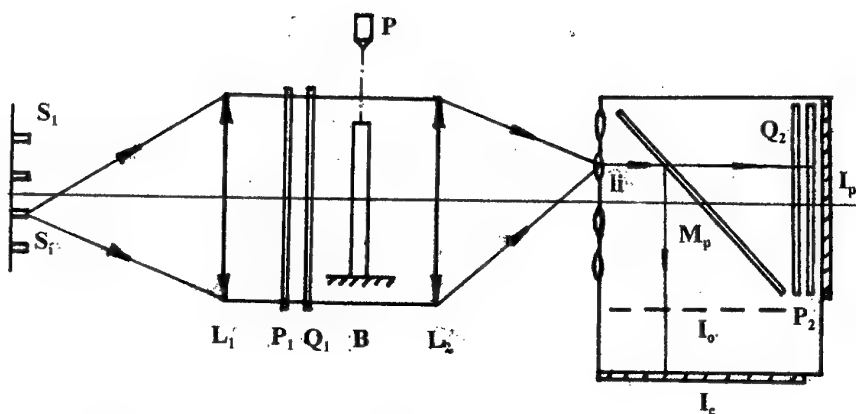


Figure 2. A schematic illustration of high speed recording system of the hybrid method

### 3. Results and Discussions

Figure 3 presents a series of photographs recorded by the camera system mentioned above. With different time sequence, the left column of patterns shows the isochromatic fringes of the specimen, and the right column gives the caustic shadows magnified around the crack tips, presenting the wave motion in whole field and the singular response of the interfacial crack, respectively.

#### 3.1 DATA EVALUATION FROM PATTERNS

The isochromatic fringes result from the transparent specimen with optical property of stress-birefringence. The fringe number  $N$  is related to the difference of principal stresses given by

$$\sigma_1^{(i)} - \sigma_2^{(i)} = Nf_i / t_i \quad (i=1,2) \quad (1)$$

where the index  $i$  means the  $i$ -th medium of bimaterial specimen,  $f_i$  the dynamic stress-fringe value calibrated by impact test, and  $t_i$  is the thickness of the plate as shown in Table 1.

The shadow pattern of caustics represents an optical mapping of the singularity at crack tip to the light distribution of caustic curve on a reference screen. When the bimaterial specimen is illuminated by collimated beams, as schematically illustrated by Figure 4, the light rays transmitting the near region of the crack tip are strongly deviated by the refractive index change of the materials and the thickness change of the specimen, due to the concentrated deformation around tips. Attaching a coordinate system of  $\xi$ - $O$ - $\eta$  to the specimen plane, with the axis  $\xi$  in coincidence with the interface of those two dissimilar materials, the shadow spots surrounded by bright caustic rim can be observed on the screen plane X-O'-Y. The caustic curve consists of points with complex variable  $W_i = X_i + jY_i$ , at which the deviated rays come from the position vector  $\zeta_i = \xi_i + j\eta_i$ , in the specimen plane, with a mapping equation of [10].

$$W_i = \zeta_i - C_i (\frac{1}{i} + j\beta) K_i \zeta_i^{-3/2-j\beta} \quad (2)$$

where  $C_i$  is a constant determined by the optical property of the material and the thickness of specimen, and also by the off-focusing distance  $z_0$  of recording plane,  $K_i$  is the complex stress intensity factor of crack tip, with  $K_i = gK_2$ , whereas  $g$  and  $\beta$  are constants.

An initial curve, surrounding the interfacial crack tip on the specimen plane to correspond to the caustic curve on the screen, satisfies the equation of

$$J = \partial(X, Y) / \partial(\xi, \eta) = 0 \quad (3)$$

Substituting the expression (2) into above equation and letting  $\zeta_i = r_i e^{j\phi_i}$ , the radius  $r_i$  of the initial curve can be written as

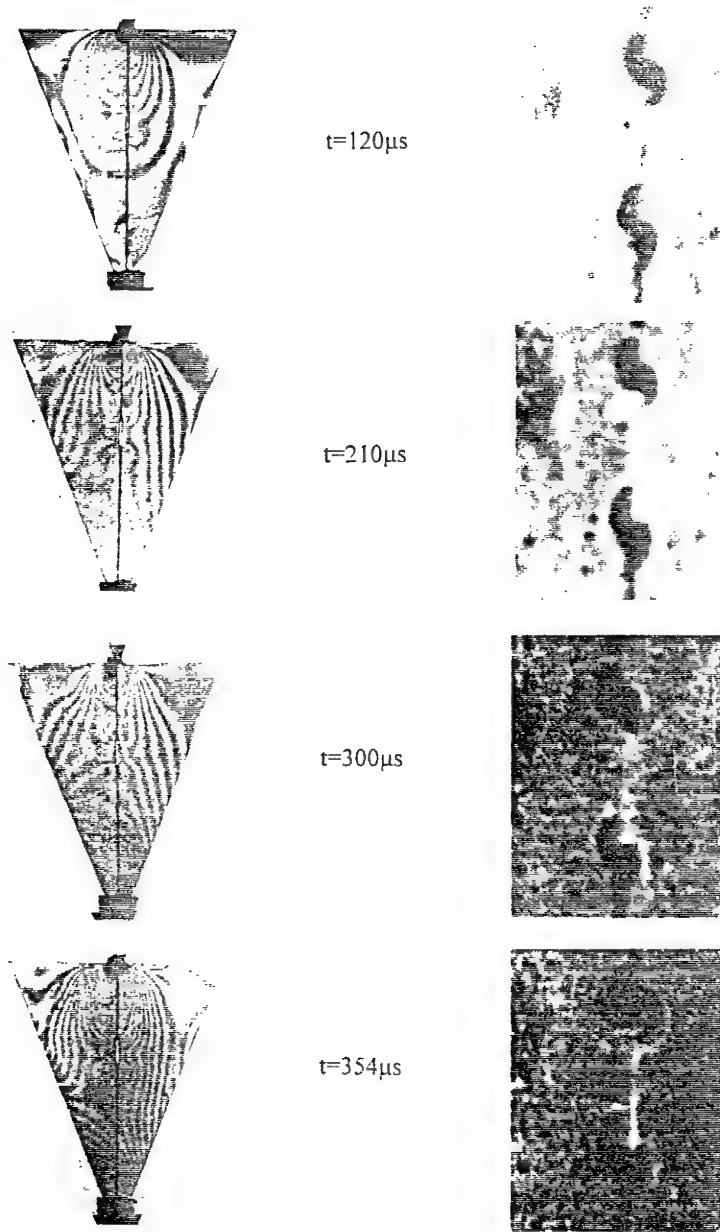


Figure 3, Dynamic patterns of isochromatic fringes and caustic shadows

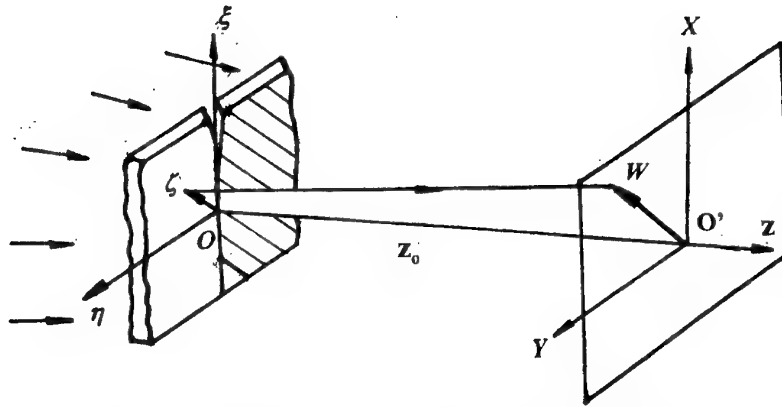


Figure 4, An illustration of caustic mapping for an interfacial crack in bimaterial,

$$r_i = H_i |K_i|^{5/2} \exp^{\frac{2}{5}\beta\phi_i} \quad (4)$$

where  $H_i = |C_i(1/2+j\beta)(3/2+j\beta)|^{2/5}$ . Therefore, the equation (2) of the caustic curves can be expressed as

$$W_i = H_i |K_i|^{2/5} \exp\left(\frac{2}{5}\beta\phi_i\right) \exp(j\phi_i) + C_i \left(\frac{1}{2} - j\beta\right) |K_i| \left[ H_i |K_i|^{2/5} \right]^{\frac{1}{5}+j\beta} \exp\left(-\frac{2}{5}\beta\phi_i\right) \exp\left\{j\left[-\theta_i + \beta \ln(H_i |K_i|^{2/5}) + \frac{2}{5}\beta^2\phi_i + \frac{3}{2}\phi_i\right]\right\} \quad (5)$$

where  $\theta_i$  is the argument of  $K_i$ .

By geometrical measurement of some characteristic dimensions of caustic curves, the evaluation of the stress intensity factors  $K_i$  can be convenient for the interfacial crack tips. The coordinates of the end-point of caustic branches, or  $X^{(0)}_1, Y^{(0)}_1$  and  $X^{(n)}_1, Y^{(n)}_1$ , corresponding to  $\phi=0$  and  $\phi=\pi$  for the medium of epoxy resin, and  $X^{(0)}_2, Y^{(0)}_2$  and  $X^{(n)}_2, Y^{(n)}_2$ , to  $\phi=0$  and  $\phi=-\pi$  for the medium of polycarbonate, respectively, are used to determine the distance  $d_i$  between the end-point of the caustics belonging to material  $i$ , from that the module  $|K_i|$  and the argument  $\theta_i$  can be solved by numerical computation, and thus the values of  $K_2$  can be obtained by  $K_2 = g K_1$ .

### 3.2 DYNAMIC RESPONSE OF CRACK TIPS

Following a concentrated impact at the center position of the specimen top-edge, a compressive pulse radiates from there moving downwards; as shown by the isochromatic patterns of fringe rings in Figure 3. The stress wave propagates in the bimaterial specimen and the dynamic fringes soon reach the upper tip (Tip-U) of the interfacial crack and then the lower tip (Tip-L) by transmission. This action results in an

impulsive loading at the crack tips with stress concentration. The modulus of the dynamic stress intensity factors  $|K_1|$  and  $|K_2|$ , determined by the caustic curves as described in the last section, show the tip response of the crack lying along the interface of those two dissimilar media, as given in Figure 5(a) and 5(b), respectively.

During the beginning period from the instant of  $t=116\mu s$  to  $t=206\mu s$ , the amount of  $K_i$  at the Tip-U varies between  $3.5 \times 10^4 N/m^{3/2}$  and  $6.5 \times 10^4 N/m^{3/2}$ , and that of  $K_i$  at the Tip-L oscillates in a range of  $4.2 \times 10^4 N/m^{3/2}$  to  $10 \times 10^4 N/m^{3/2}$ , respectively. The tendency of those variations is a decrease of  $K_i$  values, corresponding to the passing of the transmitting wave. The amount  $|K_i|$  reaches the minimum at the instant of  $t=242\mu s$ , with  $|K_1^U|=3.83 \times 10^4 N/m^{3/2}$ ,  $|K_2^U|=3.2 \times 10^4 N/m^{3/2}$ , and  $|K_1^L|=4.7 \times 10^4 N/m^{3/2}$ ,  $|K_2^L|=3.84 \times 10^4 N/m^{3/2}$ , respectively, when the main part of the compressive pulse has run over the crack tips towards the lower base and the slop boundaries of the specimen, with fewer fringes around the interfacial crack.

The stress waves reflected from the sloping sides of the wedge move back the interface of bimaterial and produce a tensile pulse intersecting on the crack, that makes the amount of  $|K_i|$  increased rapidly due to a stress wave focusing. Since then, the form of isochromatic patterns has been changed from the fringe rings to those nearly parallel to the interface, as presented by the last part of the isochromatic fringe patterns in Figure 3. This kind of fringes become more and more and reach the highest density at the instant of  $t=296\mu s$ , with the arrival of the wave reflected from the wedge apex. Correspondingly, the module  $|K_i|$  at Tip-L reaches the maximum value at first, with  $|K_1^L|_{max}=14.6 \times 10^4 N/m^{3/2}$  and  $|K_2^L|_{max}=12.1 \times 10^4 N/m^{3/2}$ , respectively. And sequentially, with the movement of the reflected wave upwards, the amount of  $|K_i|$  has the maximum of  $|K_1^U|_{max}=8.8 \times 10^4 N/m^{3/2}$  and  $|K_2^U|_{max}=7.4 \times 10^4 N/m^{3/2}$ , respectively.

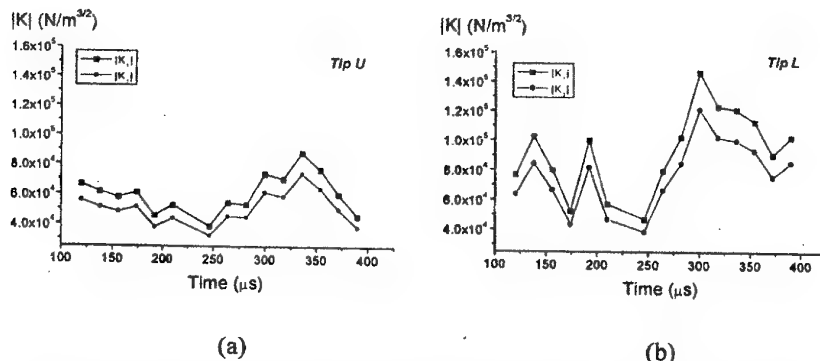


Figure 5, The module of the complex stress intensity factors at the upper-(a) and lower- (b) tip

#### **4. Conclusions**

Under the action of impact load, a bimaterial specimen of wedge-shaped plate can produce a tensile pulse in the interface of two dissimilar materials by stress wave focusing. In the dynamic history, the complex stress intensity factors  $K_i$  of crack tips show to be oscillated with the action of pulse wave. The amount  $|K_i|$  in epoxy resin side is relatively higher than that in polycarbonate, but both of them reach their maximum values when the stress wave reflected from specimen boundaries by focusing at the crack tips.

The experimental results show the hybrid method of combining dynamic photoelasticity and caustics to be a useful technique to study the dynamic behavior of interfacial crack tips under impulsive loading. The isochromatic fringes give the stress wave transmission, reflection and focusing in the specimen of bimaterial. The caustic shadows present the responses of the crack tips to the wave action. The technique offers a visual way to interpret the dynamic stress history in the composite structure, and also a useful tool of quantitative analysis for the wave propagation in bimaterial and singularity behavior of the interfacial crack tips.

**Acknowledgements:** The support of NNSF of China is greatly appreciated.

#### **References**

1. Gomes J.F.S. and Al-Hassani S.T.S. Internal fracture in spheres due to stress wave focusing. *Int.J.Solids Structures*, **13** (1977), 1007-1017
2. Liu C., Lambros J. and Rosakis A.J., Highly transient elastodynamic crack growth in a bimaterial interface, *J. Mech. Phys. Solids*, **41** (1993), 1887-1954.
3. Kalthoff J.F., On the measurement of dynamic fracture toughness-a review of recent work, *International Journal of Fracture*, **27** (1985), 277-298
4. Theocaris P.S. and Papandopolous G.A., Elastodynamic forms of caustics from running cracks under constant velocity, *Engng. Frac. Mech.*, **31**(1980), 683-689.
5. Theocaris P.S. Partly unbonded interfaces between dissimilar material under normal and shear loading, *Acta Mechania*, **24**(1978), 99-115
6. Herrman K.P, Noe A. Analysis of dynamic mixed mode stress fields in bimaterials by the method of caustics. *Theoretical and Applied Fracture Mechanics*, **19**(1993), 49-59
7. Fang J, Qi, Jiang Z.D and Zhao Y.P., An experimental method to investigate the interaction between stress waves and cracks in polycarbonate, *Recent advances in experimental mechanics*, Silva Gomes et al. (ets), Balkema, Rotterdam, 1994, 593-598.
8. Fang J, Qi J, Yao X.F, Zhao Y.P and Jiang ZD. The response and fracture of a crack in epoxy resin beam under the action of bending stress wave. *DYMAT Journal*, **2**(1995), 143-150.
9. Yao Xuefeng, Xiong Chunyang, Yang Zili and Fang Jing, Visualization of fracture behavior in crack curving, *4th Asian symposium on Visualization*, Int. Academic Pub., 1996, 445-450.
10. Theocaris P.S, Stassinakis. Complex stress intensity factors at tips of cracks along interfaces of dissimilar media. *Engineering Fracture Mechanics*, **14**(1981), 363-372.

## RESIDUAL STRESS MEASUREMENT WITH OPTICAL STRAIN ROSETTES

KEYU LI

*Department of Mechanical Engineering  
Oakland University  
Rochester, MI 48309*

### 1. Abstract

Optical strain gages were developed in 1960s and have many advantages over resistance strain gages. For instance, they are noncontacting, have extremely short gage lengths, and can be used to measure large strains. The interferometric strain rosettes are extended from the interferometric strain gages and have recently been developed to measure residual stresses. The technique is quantitative and is expected to be an accurate method of residual stress measurement. The method can potentially resolve many challenging problems which may not be tackled by any other means.

### 2. Introduction

Residual stresses exist in a solid body free from external forces and constraints. They are frequently induced during fabrication operations, such as casting, rolling, welding, stamping and forging. Traditional methods employed for determining residual stresses include hole-drilling, in which the strains relieved by the hole are measured with a resistance strain rosette (Kobayashi, 1993). However, the method has several drawbacks such as being destructive to test objects, attachment requirement to a surface area, and high costs incurred for mounting a rosette, installing a milling guide and gathering data. Nondestructive methods such as X-ray diffraction, ultrasonic and magnetic methods are all highly sensitive to microstructure properties such as texture, working hardening and grain size (Lu et al, 1995). The methods remain semi-quantitative and are only useful for comparative measurements. Recently there has been considerable interest in using optical methods such as moiré, holographic and speckle interferometric methods in measurements of residual stresses (McDonach et al, 1983, Nicoletto, 1991, Dai et al, 1996, Wang and Chiang, 1997, Perry et al, 1997, Nelson et al, 1994, Hung et al, 1996, Antonov, 1983, Goncalves et al, 1996). Some of the limitations of conventional methods can be overcome by using optical methods which are noncontacting and don't require center-hole drilling. However, application of the moiré method can be time consuming and is limited to flat objects (Post et al, 1994). The holographic interferometry method requires strict vibration isolation (Vest, 1976) and thus is not well suited for industrial

settings. Most full-field optical methods require either flat surfaces or rather strict vibration isolation.

In contrast to the full-field optical methods, optical strain gages were developed to measure strain components on one location of a material surface. Grating diffraction strain gage was developed to measure dynamic strains (Bell, 1956; Valle, Cottron and Largarde, 1996), and the diffractographic strain gage was based on laser diffraction from the gap between two blades attached to a specimen surface (Pryor and North, 1971). The interferometric strain/displacement gage technique (ISDG) was based on interference of laser reflected from two grooves (Sharpe, 1968). The interferometric strain rosette technique (ISR) (Li, 1995) was recently extended from the ISDG. Compared with resistance strain rosettes (Dally and Riley, 1991), the ISR is quantitative in nature and has high accuracy for measurements of three strain components. In addition, the ISR possesses a few advantages over resistance strain rosettes. For instance, the ISR has been developed to measure out-of-plane displacement derivatives (Li, 1996) and has a high frequency response to measure vibrations (Li, 1997a). Both the ISDG and ISR have extremely short gage lengths on the order of 100 micrometers so that localized strains can be measured. In fact, the ISDG has been used to measure displacements and strains in miniature specimens (LaVan and Sharpe, 1997).

### 3. Principle of Residual Stress Measurement by ISR

An ISR consists of three micro-indentations and may have the configurations of delta and rectangular rosettes. Fig. 1 shows a typical  $60^\circ$  ISR which has a delta configuration. Fig. 2 shows a typical  $45^\circ$  ISR which has a rectangular configuration. Three in-plane strains in the separating directions of the indentations can be measured. For instance, a  $60^\circ$  ISR can measure normal strains in the directions of 0, 60 and 120 degrees. A  $45^\circ$  rosette can measure normal strains in the directions correlation with 0, 90, and 135 degrees.

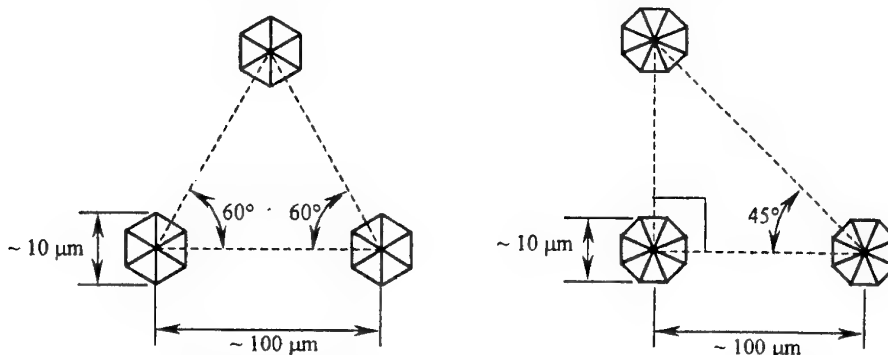


Fig. 1 The schematic diagram of a  $60^\circ$  ISR

Fig. 2 The schematic diagram of a  $45^\circ$  ISR

The ISR may be used in conjunction with the hole-drilling method or ring-core method to measure residual stresses. Three micro indentations of an ISR are depressed on the

surface of an evaluated object. When a micro-hole or a ring core is drilled near an ISR, the residual stresses at the location of an ISR are released. The released stresses cause strains between the three indentations. The relieved strains are measured by the ISR and are used to calculate residual stresses.

### 3.1 RING-CORE METHOD

The basis for ring-core method is to completely remove a ring of the material around an ISR. When a ring-core is cut around a  $60^\circ$  ISR, the measured strains are in the directions of 0, 60 and 120 degrees, namely,  $\varepsilon_0$ ,  $\varepsilon_{60}$  and  $\varepsilon_{120}$ . Then the three strain components  $\varepsilon_x$ ,  $\varepsilon_y$  and  $\gamma_{xy}$  are calculated by using strain transformation equations as follows:

$$\begin{aligned}\varepsilon_x &= \varepsilon_0 \\ \varepsilon_y &= \varepsilon_{60} + \varepsilon_{120} - \varepsilon_0 \\ \gamma_{xy} &= (\varepsilon_{60} - \varepsilon_{120})/\sin 60\end{aligned}\quad (1)$$

Similarly, the strain components can be calculated from the measurements of a  $45^\circ$  ISR by using strain transformation equations. The relieved residual stresses can be calculated by using Hooke's law.

$$\begin{aligned}\sigma_y &= E(\nu\varepsilon_x + \varepsilon_y)/(1-\nu^2) \\ \sigma_x &= E(\varepsilon_x + \nu\varepsilon_y)/(1-\nu^2) \\ \tau_{xy} &= G\gamma_{xy}\end{aligned}\quad (2)$$

where  $E$  is Young's modulus,  $\nu$  is Poisson's ratio,  $\sigma_y$  and  $\sigma_x$  are normal stresses, and  $\tau_{xy}$  is shear stress.

It is assumed that the residual stresses at the location of the ISR are completely relieved. The amount of relieved stresses approximately equals to the amount of real residual stresses. Since the size of the ISR is tiny, the inner diameter of the ring-core can be made very small that the measurement is highly localized. The cutting process should be more convenient than that used with a resistance strain rosette.

### 3.2 HOLE-DRILLING METHOD

A hole can be drilled to relieve residual stresses. In a thin-thickness specimen, a through hole is drilled. The residual stresses are determined by employing Kirsh's equations for an infinite plate subjected to a biaxial stress state (Li, 1997b). In a thick component, a blind hole is drilled (Li et al, 1997). When the residual stress distribution versus depth is of concern, an incremental hole drilling process is employed (Tjhung et al, 1998). For incremental hole-drilling, residual stresses are calculated from the measured strains by employing either calibrated coefficients or finite element methods.

The method of material removal may also be done using other techniques. For example, chemical etching technique may be used to remove layers of materials to study the distribution of the residual stresses with depth. The chemical environment should not interfere with the ISR in contrast to the case of a resistance strain rosette.

#### 4. Two-step Measurement Program and Evaluation Tests

A movable ISR system was constructed. It contains an 8-mw He-Ne laser and six photodiode sensors. The direction and distance between sensors are adjustable. The system is vertical and may be set up in front of any machine for testing purposes. Traditionally, the ISR system is used for real-time measurements. When the specimen is loaded, the ISR records the strain increment for each step of loading. The total strain value is an accumulation of the increments in real time.

When the ISR is used to measure residual stress, a two-step measurement procedure must be developed for taking two sets of data separately. An IBM computer is programmed to record the two measurements and calculate the strain incurred between the two steps of measurements.

To evaluate the measurement procedure and the computer program, various tensile/compressive tests are conducted on a bar specimen. The dimensions of the specimen are: thickness =3.175mm, width=51.2 mm, Length =300mm. The material properties of the specimen are recorded in TABLE 1.

TABLE 1: Material properties of aluminum 6061

E	G	v	$\sigma_y$	$\sigma_u$
70 GPa	26 GPa	0.33	270MPa	310MPa

The ISR movable system is set up at a distance of 44 cm from the specimen. The gage length of the ISR is 250 micrometers. The first group of tests are the so called "zero-shift" tests. When the applied load is zero, two-step measurements are taken within a few minutes. Theoretically, there is zero strain in the specimen and the program should output zero readings. But in real experiments, nonzero strains were recorded. The strain components in x-y coordinates along the transverse and axial directions of the bar are calculated by using equation (1) and shown in TABLE 2. The maximum shift of strain readings between the two steps of measurements is about 7 microstrains. The maximum difference for the stresses calculated from the strains is 0.7 MPa. These nonzero results may be due to the sensitivity of the electrical-optical system to its environment.

TABLE 2: Two step measurements of strain and stress by the ISR at zero load

Test #	Axial strain, $\epsilon_x(\mu\epsilon)$	Transverse strain, $\epsilon_y(\mu\epsilon)$	Shear strain, $\gamma(\mu\epsilon)$	Axial stress, $\sigma_x(\text{MPa})$	Transverse stress, $\sigma_y(\text{MPa})$	Shear stress, $\tau(\text{MPa})$
Test 1	-1.66	-0.31	3.56	-0.14	-0.68	0.09
Test 2	4.08	1.47	-5.38	0.28	0.097	-0.15
Test 3	4.28	-0.1	-0.52	0.33	0.10	-0.013
Test 4	-0.33	-1.34	1.56	-0.11	-0.06	0.04
Test 5	4.28	-0.10	-0.52	0.33	0.10	-0.013
Test 6	1.2	0.34	1.17	0.10	0.057	-0.03
Test 7	2.42	1.51	1.61	0.23	0.18	0.04
Test 8	-0.66	-2.76	-6.25	-0.23	-0.12	-0.16
max value	5	3	7	0.4	0.7	0.2

The second group of tests apply loads to the bar. Two-step measurements are conducted before and after a load is applied. The stress and strain between zero and the applied load can be calculated from the theory of uniaxial loading. The measured strains by the ISR agree well with the results of the calculation and resistance strain gages in TABLE 3 and Figure 3. The maximum relative difference of the axial strain is 6% between the ISR data and the calculated strains.

TABLE 3: The comparison of the results of the ISR measurements with that of the calculation and the resistance strain gage measurements.

Test #	$\sigma_y$ (MPa) Theory	Axial strains, $\epsilon_y$ ( $\mu\epsilon$ )			Transverse strains, $\epsilon_x$ ( $\mu\epsilon$ )			
		Theory	ISR	Strain Gage	Difference between ISR & Theory	Theory	ISR	Difference between ISR & Theory
1	27.64	394.85	385.00	394	-9.85	-130.30	-133.93	-3.63
2	27.37	390.94	383.11	409	-7.83	-129.01	-143.53	-14.52
3	-13.96	-199.43	-201.93	-213	-2.50	65.81	81.88	16.07
4	-16.42	-234.57	-250.52	-249	-15.95	77.41	100.20	22.79
5	-24.90	-355.76	-358.09	-376	-2.33	117.40	126.07	8.67
6	-27.37	-390.94	-381.83	-408	9.11	129.01	137.31	8.30
7	-35.30	-504.32	-524.00	-529	-19.68	166.42	208.04	41.62
8	-41.05	-586.41	-566.77	-592	19.64	193.52	200.49	6.97
9	-42.69	-609.87	-583.35	-611	26.52	201.26	219.15	17.89

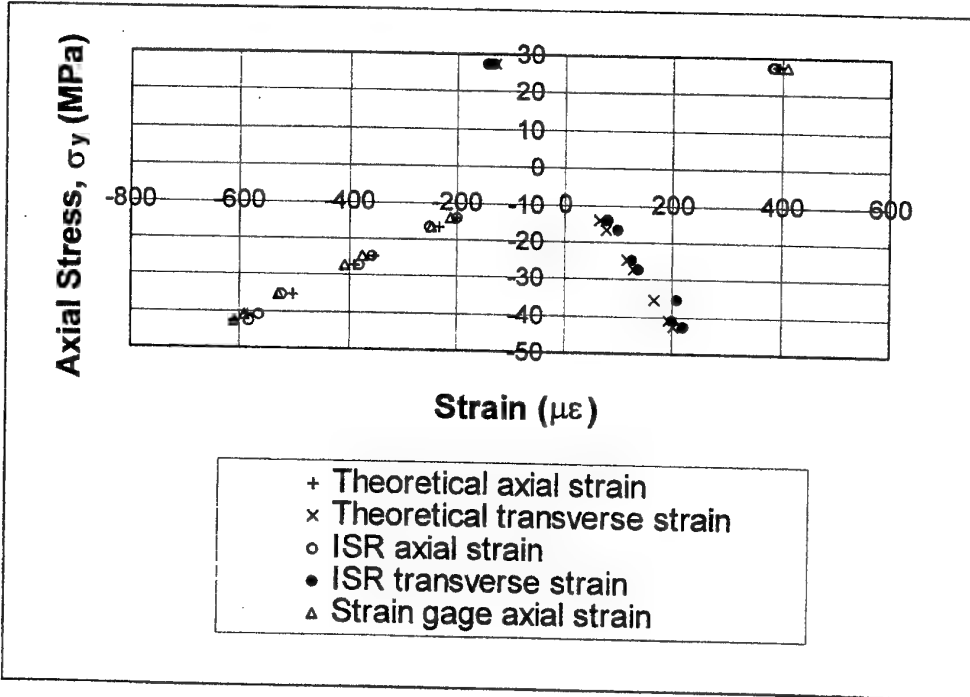


Figure 3. The plots of the ISR data, the resistance strain gage data and the calculated stress-strain.

## 5. Experiments of Residual Stress Measurements by Ring-core and Hole-drilling

Once the two-step measurement procedure is established and evaluated, the ISR method may be used to measure real residual stresses in manufactured components. For example, the aluminum 6061 bar specimen used in the above uniaxial tests contains residual stresses induced during its rolling process. The bar specimen after a heat-treatment is taken as the test sample of the ISR experiment by using the ring-core method. A cutter is specially made and hardened. The inner diameter of the cutter is 2.0 mm and the outer diameter is 4.5 mm. First, a 60° ISR of 250 micrometer gage length was indented on the surface of the bar specimen. Secondly, the ISR system was set up in the same way as the previous uniaxial tests. Then the first step of the measurement is done. A milling guide (model RS-200, Measurement Group, Inc.) was positioned, and a milling rod with a universal joint connected with a hand-drill was used to cut a ring around the ISR. Precaution must be taken to avoid any disturbance to the ISR system. The second step of measurement process was done by measuring the strains relieved during the ring-core cutting. The results are listed in TABLE 4. Strain components in x-y coordinates along the transverse and axial directions of the bar are calculated by using equation (1). The ring has an inner diameter of 2.0 mm and outer diameter of 5.0 mm. The depth of the cutting is about 2 mm, which is supposedly enough to relieve the residual stresses completely. The original residual stresses should take the opposite signs of the stress calculated by using equation (2). In fact, the ring-core cutting relieves positive residual stresses to get negative strains in the center of the remaining materials. The residual stresses are recorded in TABLE 4.

TABLE 4: Measurement of residual stresses in the aluminum bar and titanium block by using the ISR and ring-core cutting method.

Test #	Strains ( $\mu\epsilon$ )						Residual stress (MPa)		
	ISR strains			Strain components					
	$\varepsilon_{60}$	$\varepsilon_0$	$\varepsilon_{120}$	$\varepsilon_{xx}$	$\varepsilon_{yy}$	$\gamma_{xy}$	$\sigma_{xx}$	$\sigma_{yy}$	$\tau_{xy}$
1	-659.4	-569.0	-508.3	-569.0	-588.8	-174.5	94.2	95.9	7.2
2	112.8	155.6	175.3	155.6	140.3	-72	-21.7	-20.6	3.0

The second ring-core cutting experiment was performed on a surface shot-peened titanium block. The material properties of TA6V are:  $E=110$  GPa and  $v=0.3$ . Since the material was extremely hard, drilling was too difficult to cut more than 0.1 mm in depth. The inner diameter of the ring-core is 2 mm, and the outer diameter is 4.5 mm. The strains measured by ISR, the calculated strain components, and the calculated residual stresses are recorded in the second row of TABLE 4. Since the depth of the drilling is very shallow, only a small portion of the residual stresses is relieved. The measurement values should be much smaller than the real values of residual stresses. The measurement results show that the residual stresses on the surface are compressive, as found by using a resistance strain rosette reported in a previous paper (Li et al, 1997).

The hole drilling method is under development for residual stress measurements by the ISR. The size of the hole, and the distance between the center of the hole and the ISR influence the measurement sensitivity. There is no requirement for a center hole

drilling. We have applied the ISR to various manufactured samples including aluminum tubes (Li, 1996), and surface-shot peened titanium alloy blocks (Li et al, 1997). We are currently applying the method to measure residual stresses in welds (Tjhung et al, 1998). The ISR results have shown favorable agreement with the results of resistance strain rosettes. In addition, we are investigating the ISR technique for analyzing and validating analytical models of simulating casting and quenching processes (Li et al, 1998). The study aims to optimize the design of the process parameters. As residual stresses are minimized, distortion during the machining of the materials will be eliminated or reduced.

## 6. Conclusions

Following our previous efforts on developing the interferometric strain rosette technique (ISR), we have extended the method into measurement and evaluation of residual stresses. The measurement system has been reconstructed as a movable structure. A two-step measurement procedure and software have been established. The accuracy of the two-step measurement has been evaluated by the uniaxial tests. The maximum zero shift was found to be 7 microstrains, and the difference between the theoretical and measurement results is less than 6%. Ring-core and hole-drilling methods are under development for use with the ISR technique. The feasibility of the two methods has been verified. The applicability is being studied and evaluated on various manufactured samples. The ISR has the potential to be developed as an accurate method of residual stress evaluation. The deployment of the method will enable resolution of many challenging problems in mechanics and industry.

## 7. Acknowledgment

The author would like to thank Mr. Forrest Wright, a machine specialist, for the design of the ring-core cutter, and Mr. Xi Zhang, a visiting scholar, for the design of the adjustable arms to support the six photodiode sensors of the ISR system. She acknowledges the laboratory assistance received from Ms. Ming Yu and Mr. Liangdao Xia, who were master graduate students. Mr. Tana Tjhung, a research assistant, drew the figures. Financial support for this work and the presentation is provided by the Civil & Mechanical Systems Div. of NSF (Grant CMS-9503621 and an on-coming career award), and Alcoa Foundation's Science Support.

## 8. Reference

- Antonov, A. A. (1983). Inspecting the level of residual stresses in welded joints by laser interferometry, Weld Prod., 30, 29-31.
- Bell, J. F. (1956) Determination of dynamic plastic strain through the use of diffraction grating, Journal of Applied Physics, 27, 1109-1113.
- Dally, J.W., and Rilley, W. F. (1991) *Experimental Stress Analysis*, McGraw-Hill, Inc.
- Dai, F., Shi, L., Huang, L., Tang, X. (1996) Residual thermal strain measurements inside Pb/Sn solder joints, Abstract Proceedings of VIII International Congress on Experimental Mechanics, pp. 33-34.

Kobayashi, A. S. (1993) *Handbook on Experimental Mechanics*, Prentice-Hall Inc., pp. 785-829.

Goncalves, Jr., Kanda, C., Boettger, J., (1996) Residual stress measurement using a radial interferometer - a preliminary analysis, Abstract Proceedings of VIII International Congress on Experimental Mechanics, pp. 27-28.

Hung, Y.Y., Long, K.W., Wang, J.Q., and Hovanesian (1996) Automated measurement of residual stresses by phase-shift shearography, Abstract Proceedings of VIII International Congress on Experimental Mechanics, pp. 122-123.

Joh, D., Byun, K. Y., & Ha, J. (1993), Thermal residual stresses in thick graphite/epoxy composite laminates - uniaxial approach, *Experimental Mechanics*, **33**, 276-80.

LaVan, D. A., and Sharpe, W. N., Jr. (1997) Strain measurement on miniature tension specimen, Abstract Proceedings of the SEM Spring Conference on Experimental Mechanics, June 2-4, Bellevue, WA, pp.116-117.

Li, K. (1995) Interferometric 45° and 60° strain rosettes, *Journal of Applied Optics*, **34**, 6376-6379.

Li, K. (1996) Out-of-plane displacement derivative measurements using interferometric strain/slope gage, *Journal of Applied Mechanics*, **63**, 1033-1038.

Li, K. (1997a) Interferometric strain/slope rosette for static and dynamic measurements, *Experimental Mechanics*, **37**, 111-118.

Li, K. (1997b) Application of interferometric strain rosette to residual stress measurements, *Journal of Optics and Lasers in Engineering, Special Issue on Optical Methods for Residual strain Measurement*, **27**, 125-136

Li, K., Xia, L, and Lu, J. (1997) Residual stress measurements on a surface peened block by resistance and interferometric strain rosettes, Abstract Proceedings of SEM Spring Conference, Bellevue, WA, June 2-6, pp. 259-260.

Li, K., Tjhung, T., Li, N., Pien, J. (1998) Numerical simulation and experimental evaluation of residual stresses in casting and quenched components, Abstract Proceedings of SEM Spring Conference, Houston, TX, 416-418.

Lu, J. (1995) editorial boards: James, M., Lu, J., and Roy, G., *Handbook on Techniques of Measurement of Residual Stresses*, Society of Experimental Mechanics, Inc..

McDonach, A., McKelvie, A., MacKenzie, P., & Walker, C. A. (1983) Improved moiré interferometry and applications in fracture mechanics, residual stress and damaged composites, *Experimental Mechanics*, **7**, 20-24.

Nelson, D., Fuchs, E., Makino, A., and Williams, D. (1994) Residual stress determination by single-axis holographic interferometry and hole drilling - part II: experiments, *Experimental Mechanics*, March 1994, 79-88.

Nicoletto, G., (1991) Moiré interferometry determination of residual stresses in presence of gradients, *Experimental Mechanics*, **31**, 252-236.

Perry K.E., Jr, Epstein, J.S., and Clark D.E. (1997) Phase shift moiré studies of processing-induced residual strains in nickel 200 spot welds, *Journal of Optics and Lasers in Engineering, Special Issue on Optical Methods for Residual strain Measurement*, **27**, 125-136

Pryor, T.R., and North, W. P.T. (1971) The diffractographic strain gage, *Experimental Mechanics*, **11**, 565-568.

Post, D., Han, B., and Ifju, P. (1994) *High Sensitivity Moiré*, Springer Verlag.

Sharpe, W. N., Jr. (1968) The interferometric strain gage, *Experimental Mechanics*, **8**, 164-170.

Tjhung, T., Li, K., Barber, G., Hassan, A. (1998) Measurement of unequal biaxial residual stresses in the vicinity of welds by the interferometric strain rosette technique, Abstract Proceedings of SEM Spring Conference, Houston, TX, pp. 228-231.

Valle, V., Cottron, M., and Lagarde, A. (1996) Grating diffraction for local strain determination under dynamic loading, PD-Vol. **76**, ESDA, Volume 4, ASME 1996, The Third Biennal Conference, Montpellier France, July 1-4.

Vest, M. L. (1976) *Holographic interferometry*, Johns Wiley & Sons, Inc.

Wang, Y.Y., and Chiang, F. P. (1997) Experimental study of three-dimensional residual stresses in rails by moiré interferometry and dissecting methods, *Journal of Optics and Lasers in Engineering, Special Issue on Optical Methods for Residual strain Measurement*, **27**, 89-100.

## APPLICATION OF GEOMETRIC MOIRÉ TO THE ANALYSIS OF LARGE DEFORMATION IN THREE-DIMENSIONAL MODELS

V. CICINELLI, C. PAPPALETTERE, W.M. SUN

*Dipartimento di Progettazione e Produzione Industriale  
Politecnico di Bari - Viale Japigia 182 - 70126 Bari (Italy)*

L. SURACE

*Dipartimento di Ingegneria Strutturale  
Università della Calabria - 87036 Arcavacata di Rende, Cosenza (Italy)*

### Abstract

The application of geometric moiré in large deformation of 3-D models is discussed. Different aspects of the method, such as mismatch technique and mechanical differentiation, are taken into consideration for the measurement. An application of the method is given to the cushion disk of an artificial knee joint in whose axis-symmetric cross section a cross specimen grating of 0.5mm pitch was replicated. The analysis shows the applicability of the geometric moiré, together with its various approaches, in the large deformation measurement giving the whole field quantitative definition.

### 1. Introduction

#### 1.1 GENERAL PROBLEM

The experimental techniques have made a great contribution to the analyses of mechanical behaviour of components and structures. In particular, the optical methods, such as holographic interferometry, moiré and speckle techniques etc., have played a very important role in both qualitative and quantitative determination of mechanical parameters [1]. However, most of them are limited to the application on the surface of models, while the analysis of the internal parts could be needed. Some techniques have been proposed by researchers to solve such problem, for instance, the white light speckle method where some form of inhomogeneity was formed within a cast block of model for interior strain measurement [2].

On the other hand the optical methods have been found their applications not only in traditional mechanical structures but also in a widespread fields (e.g. in biomechanics) where large deformation and non-linearity are present. Some of the optical techniques, such as grid analysis [3,4], have played a successful role in the measurements of large deformation.

This research is aimed to apply geometric moiré in the analysis of an internal section of a model with large deformation to obtain directly whole field displacement measurement and strain field by means of mechanical differentiation.

### 1.2 APPLICATION TO KNEE JOINT

Arthroprosthesis design is based on the analogy existing between the human joint and the mechanical motion system. In general a knee joint is considered as mechanical contact structure in which mechanical actions are originated by muscles.

The first artificial joint was made by substituting a part of the knee with an inert material and the results obtained have lead to the utilisation of biocompatible materials. Then the total substitution of the human joint rather than some singular parts was preferred [5,6,7].

According to the mechanical kind of joints the prosthesis are classified (Fig. 1) in: 1) constrained prosthesis, where the motion is allowed only in one plane by a joint, 2) semi-constrained prosthesis, where the motion is allowed in two planes by a spherical joint between the femur and tibia, and 3) un-constrained prosthesis, where there is no connections between its components and any kind of motion is allowed. A good shape design must assure large stability to this last kind of knee prosthesis, which perfectly simulates the human motion of the knee.

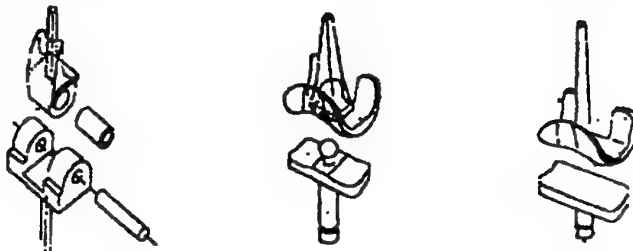


*Fig. 1: Prosthesis classifications: constrained, semi-constrained and non-constrained prosthesis.*

The artificial knee joint actually used (Fig. 2) is made of an inox steel structure inserted into the femur, a polyethylene disk and a tibial metal plate linked to the human tibia bone.

The characteristics of this prosthesis is the presence of the cushion part, the disk, actually made of UHMPEPE. Here a disk made of a more soft material, the polyurethane, is investigated.

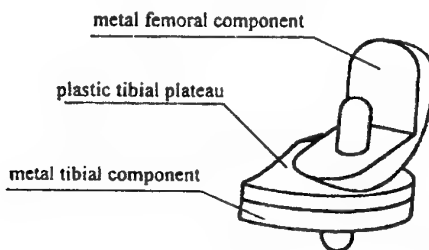


*Fig. 2: Typical structure of an actual artificial knee joint.*

## 2. In-plane geometric Moiré

### 2.1. GENERALS

In-plane moiré is typically carried out by gratings of equispaced, parallel lines [1]. One grating set is applied to a flat surface of the specimen to be analysed, and a second set (reference grating) can be put in contact with the specimen grating or more conveniently recorded by an image processing system. The gratings can be x- or y- or cross oriented.

The strain can be determined by using the four derivatives of the fringes in the two reference grating directions:

$$\varepsilon_{xx} = p_0 \frac{\partial N_x}{\partial x}, \quad \varepsilon_{yy} = p_0 \frac{\partial N_y}{\partial y}, \quad \gamma_{xy} = p_0 \left( \frac{\partial N_x}{\partial y} + \frac{\partial N_y}{\partial x} \right) \quad (1)$$

where respectively  $p_0$  is the reference grating pitch,  $N_x$  and  $N_y$  are fringe orders of x and y displacements.

Despite the source of these equations, they are strictly geometric equalities and do not require elastic behaviour of the specimen; this allows a wide range of their applications. The superposition of specimen gratings and reference gratings can be done by digital logical operations of grabbed images by an image processing system [8,9].

In relation to the subject of this paper, three aspects of in-plane geometric moiré were considered here: (1) large deformation measurement; (2) mismatch method to increase (decrease) fringe numbers; (3) mechanical differentiation.

All these aspects were carried out using an image processing system.

#### 2.1.1. Large deformation measurements

The sensitivity of the in-plane geometric moiré is equal to the reference grating pitch  $p_0$ , which is the non-deformed one. However, in the case of large deformation the applied grating pitch is relatively high and must be taken into consideration in strain calculation.

Between two fringes, spaced  $d$ , the average tension and compression strains may be calculated respectively by [10]:

$$\varepsilon_{tension} = +\frac{p_0}{d - p_0}, \quad \varepsilon_{compression} = -\frac{p_0}{d + p_0} \quad (2)$$

#### 2.1.2. Mismatch method for non-uniform deformation

The choice of the grating pitches is always based on the strain range to be measured. For a 3-D model the specimen gratings are always replicated during its modelling, thus a change of grating pitches is not practicable. In addition, in many cases where the non-linear and non-uniform strains are present, such as contact, material discontinuity and non-linear materials etc., a single pitch cannot satisfy the measurement of whole field.

In the case of large deformation, it is difficult to consider an application of very fine gratings since the large tension/compression deformation may destroy such fine gratings. Moreover, a fine grating may provide the fine measurement in one zone, but becomes ineffective or over-effective in other zones.

The mismatch method, in providing different carrier fringes (tension or compression) to different measuring zones, is a very efficient way in the measurement of large and non-linear deformation.

The mismatch is carried out by taking some new reference gratings with the pitches different from that of original one. If the pitches of these new gratings are greater than that of original one, the number of fringes will be increased over the original fringes at the zone where the compression deformation goes on, while decreased the tension deformation. Inverse effect is present when the pitches of these new gratings are less than that of original one. In general, at least two new reference gratings are used, one with slightly greater pitch and one with slightly less pitch than that of the original one. If the deformation has a very large range, more reference grating with different mismatch pitches may be taken to suit each strain level.

Using the mismatch technique the equations (1) become:

$$\varepsilon_{xx} = p_0 \left( \frac{\partial N_x}{\partial x} - \frac{\partial N_0}{\partial x} \right), \quad \varepsilon_{yy} = p_0 \left( \frac{\partial N_y}{\partial y} - \frac{\partial N_0}{\partial y} \right), \quad \gamma_{xy} = p_0 \left( \frac{\partial N_x}{\partial y} + \frac{\partial N_y}{\partial x} \right) \quad (3)$$

where  $\partial N_0/\partial x$  and  $\partial N_0/\partial y$  are the fringe derivatives of the mismatch fringes before loading, in the x and y displacement.

### 2.1.3. Mechanical differentiation

The moiré method, as many other optical interferometry, provide directly the measurement of displacement field, while the structure is characterised by stress distribution. Nevertheless, the mechanical differentiation can give proportional strain distribution, proportional strain value and, in some cases, particular characteristics, for example contact area in contact problems, like in this study.

The mechanical differentiation is the superposition of two identical moiré patterns, one of which is shifted by increments  $\Delta x$  and  $\Delta y$ . In this way, the contour maps  $\Delta N_x/\Delta x$ ,  $\Delta N_x/\Delta y$ ,  $\Delta N_y/\Delta x$  and  $\Delta N_y/\Delta y$  can be obtained. To obtain strains, the basic displacement can be written in the form:

$$\Delta u_x = p_0 \Delta N_x, \quad \Delta u_y = p_0 \Delta N_y \quad (4)$$

Then the strain can be defined as:

$$\varepsilon_{xx} = p_0 \frac{\Delta N_x}{\Delta x}, \quad \varepsilon_{yy} = p_0 \frac{\Delta N_y}{\Delta y}, \quad \gamma_{xy} = p_0 \left( \frac{\Delta N_x}{\Delta y} + \frac{\Delta N_y}{\Delta x} \right) \quad (5)$$

In practice, mechanical differentiation can be obtained by shifting directly two identical deformed grating images without generating ordinary moiré fringes. It should be noted that the above relationships are correctly applicable for small strain, i.e. the finite increment reasonably represent the true derivatives if the shifts  $\Delta x$  and  $\Delta y$  are small.

## 2.2. IMAGE PROCESSING

The specimen gratings need to be grabbed before and after loading. The software available to the purpose, IMAGEPRO by CORECO - USA provided the following image processing operators:

1. *horizontal and vertical edge filters*, to separate the crossed gratings respectively into vertical and horizontal lines for superposition of x and y displacement fields;
2. *contrast enhancement operators*, such as *stretching and equalising*, to obtain high contrast gratings and fringes (the image processing system also provides the

binarization of images which gives images with only two grey levels);

3. *arithmetic and logical operators* to obtain the superposition of two grating patterns, for instance, to get average value of two images in each pixel;
4. *scaling operator* to generate mismatch reference gratings reducing or increasing the image scale;
5. image shifting for mechanical differentiation carried out by digitally positioning the gratings.

### 3. Preparation of the specimen analysed and the optic system applied

In order to evaluate the internal strains of the polyurethane tibial plateau, a 0.5mm pitch grid was engraved in a diametrical section of it. The elastomeric disk, 10mm thick with a diameter of 80mm, was made by sequential polymerisation of two half of it, casting the resin in a circular steel mould. The casting procedure was realised in a vacuum oven with controlled temperature (60°C). After the polymerisation of the first half of the cylinder a master grating was replicated onto the flat specimen section by a xerographic technique, which was decided to be adopted to produce a good quality cross grating. The master grating was drawn by a CAD system and printed on a film. After the replication of the grating, the specimen was cast into its complete form.

Three specimens for each of three different ratios of the polyurethane resin to its hardener (1:1; 1:0.7; 1:0.5) were produced, plus another one, on whose section a 10 grid strain-gauges chain was bonded.

The mechanical load of 800 N was applied in 100N steps by a steel sphere with a diameter of about 130mm, which simulated the femoral component (Fig. 3). The load was centrally applied on the diametrical plane of the sphere, then a three-dimensional axis-symmetric problem occurred.

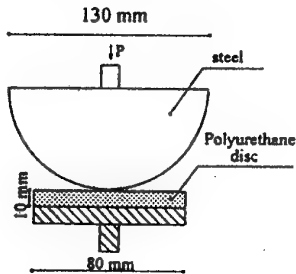


Fig. 3: Mechanical rig

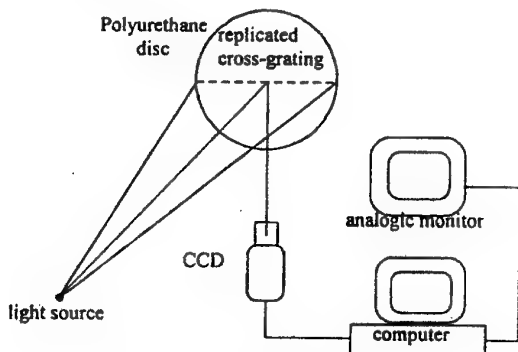


Fig. 4: In-plane moiré set-up

The optical set-up of in-plane geometrical moiré method is shown in Fig. 4. A white light was used. A laser light is not necessary for the illumination since it may produce unwanted speckles in the specimen surface. By recording and superposing the grating patterns before and after loading, some digital imaging operations are carried out to obtain the x- and y-displacements and their corresponding strain distributions.

#### 4. Results

The results obtained for the model with a ratio 1:1 of the polyurethane resin to the hardener are reported in the following.

Figs. 5 report for a load of 800N the grating image as grabbed (Fig. 5a) and after it was transformed respectively by vertical (Fig. 5b) and horizontal (Fig. 5c) filtering provided by the image processing system.

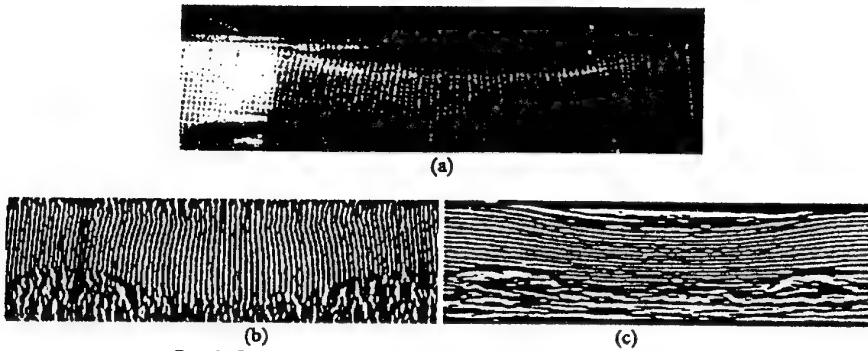


*Fig. 5: Gratings imaging and processing at the loading of 800 N  
(a) original; (b) vertical filtering and (c) horizontal filtering.*

The superposition of the deformed and non-deformed gratings were obtained for each loading step (100N). The horizontal,  $u_x$ , and vertical,  $u_y$ , displacement fringes under loading of 800 N are shown respectively in Figs. 6a and 6b.

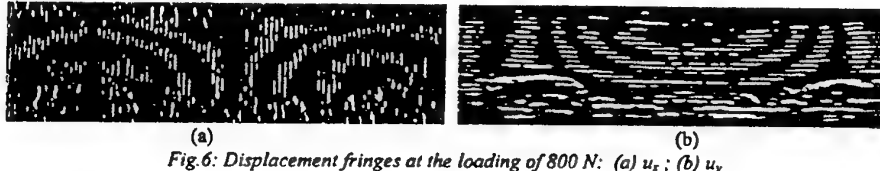


*Fig. 6: Displacement fringes at the loading of 800 N: (a)  $u_x$ ; (b)  $u_y$*



*Fig. 7: Mismatch fringes of  $u_x$  at the loading of 800 N*

Close to the contact area, very few number of fringes were observed in the x displacement field due to its low deformation level. Then a mismatch reference grating

with 15% reduction of the non-deformed grating (i.e.,  $p_0' = 0.375$  mm) was superposed onto the gratings to get more fringes. Fig. 7 gives the result of this operation in the case of a 800 N loading for another specimen.

Based on the above displacement measurement the strain distribution  $\varepsilon_{xx}$  and  $\varepsilon_{yy}$  along the different sections have been calculated as reported in Figs. 8, which shows that the strain  $\varepsilon_{xx}$  decreases going away from the contact centre, while the maximum strain  $\varepsilon_{yy}$  is located in the middle of the y section as stated in previous work.

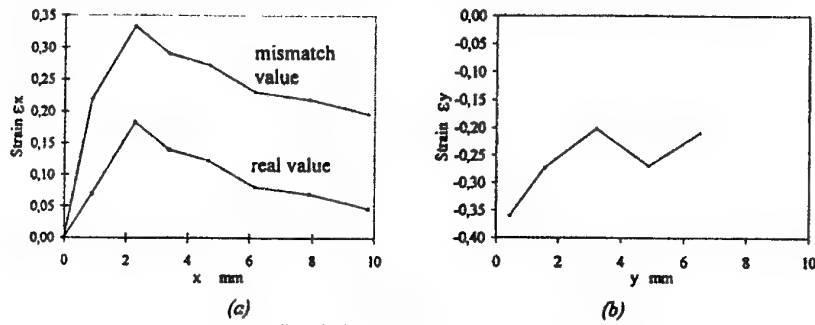


Fig. 8: Strain distribution: (a)  $\varepsilon_{xx}$  (b)  $\varepsilon_{yy}$

Maximum average strains and maximum vertical displacements are given in Figs. 9 for the loads applied. Their behaviours were confirmed by the numerical results obtained in other research works under study.

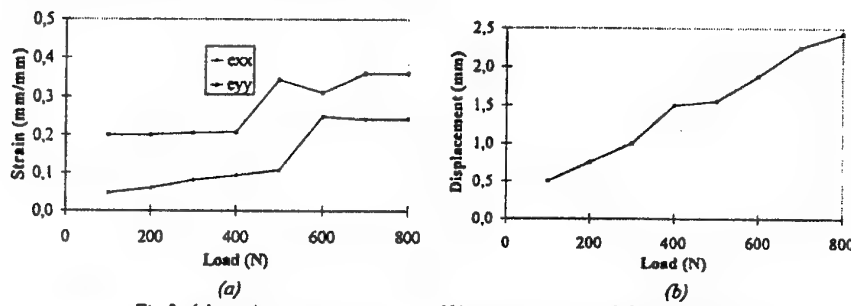


Fig. 9: (a) maximum average strains; (b) maximum vertical displacements

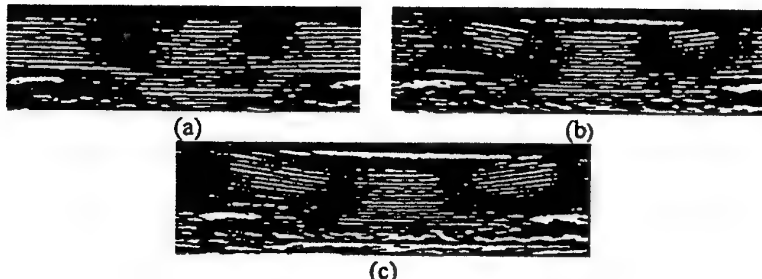


Fig. 10: Mechanical differentiation fringes of  $\Delta N / \Delta x$  with  $\Delta x = 3$  mm  
(a) 100 N; (b) 400 N and (c) 800 N.

The extension of the contact area is a very important factor in the present analysis. It may be measured directly by the image observation and more precisely, by mechanical differentiation to obtain the shear component. Figs. 10 show the mechanical differentiation fringes respectively for loads of 100 N, 400N and 800N. These fringes represent the  $\Delta N_y/\Delta x$  component with shifting  $\Delta x=3$  mm. The contact extension is given versus load increasing in Fig. 11.

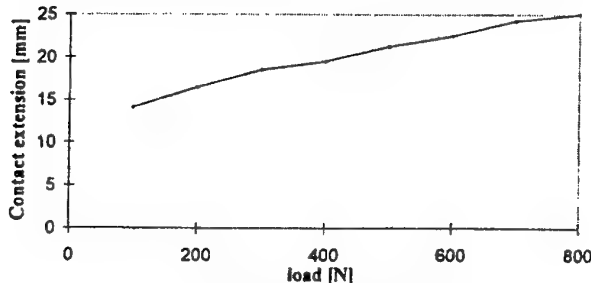


Fig. 11: Contact area extension.

## 5. Conclusions

Geometrical moiré technique was applied to the study of internal large strains of transparent models.

The results obtained for a biomechanical application showed the good feasibility of the technique.

Further researches are in progress on the refinement of the grating, automation of stress calculation and study of wear disk contact surface.

## 6. References

- [1] A.S., Kobayashi & Parks, V.J., *Handbook on Experimental Mechanics*, Prentice-Hall, Inc., 1987.
- [2] A. Asundi & Chiang , F.P., Applications of the white light Speckle method to interior displacement measurement, *Journal of Strain Analysis*, Vol. 18, No.1, 1983, 23-26.
- [3] J. Dupré, F. Brémard & Lagarde, A., Numerical spectral analysis of a grid: Application to strain measurements, *Optics and Lasers in Engineering*, 18, 1993, 159-172.
- [4] H. T. Goldrein, S.J.P. Palmer & Huntley, J. M., Automated fine grid technique for measurement of large-strain deformation maps, *Optics and Lasers in Engineering*, 23, 1995, 305-318.
- [5] D.D., Auger and Dowson,D., Cushion form bearings for total knee joint replacement. Part 1: design, friction and lubrication. Proc.Instn. Mechan. Engrs, Part H, Journal of Engineering in Medicine, Vol.209, 1995.
- [6] D.D., Auger and Dowson,D., Cushion form bearings for total knee joint replacement. Part 2: wear and durability. Proc.Instn. Mechan. Engrs, Part H, Journal of Engineering in Medicine, Vol.209, 1995.
- [7] E.G., Little, R.S., Olivito & Surace, L., A numerical analysis of the contact problem of artificial knee joints, Proceedings of XXV AIAS National Conference/International Conference on Material Engineering, Gallipoli, Italy, 1996.
- [8] A. Asundi and Yung, K.H., Logical moiré and its application, *Experimental Mechanics*, 31(3), 1991.
- [9] A. Asundi, Computer aided moiré methods, *Optics and Lasers in Engineering*, 18, 1993, 213-238.
- [10] Bray & Vicentini, V., *Meccanica Sperimentale: misure ed analisi delle sollecitazioni*, Levrotto&Bella, Turin, 1975.

## DEVELOPMENT OF A STEREOSCOPIC OPTICAL STRAIN MEASUREMENT TECHNIQUE : APPLICATION OF MAIZE ROOTS

S. DENIS

*LMS, Université de Poitiers, CNRS UMR 6610*

*SP2MI - Téléport 2 - BP 179, 86960 FUTUROSCOPE CEDEX, FRANCE*

F. BREMAND

*LMS, Université de Poitiers, CNRS UMR 6610*

*SP2MI - Téléport 2 - BP 179, 86960 FUTUROSCOPE CEDEX, FRANCE*

### **Abstract**

The main goal of this work concerns the experimental measurement of the rigidity modulus of a vegetal material in order to numerically simulate the mechanical behavior of a maize root system in soil. Due to the complexity of a such material, non-contact and non-disturbing optical methods of strain measurement have a big advantage over classical extensometers. Among all these techniques, the tracking of two markers constitutes the best choice. Since a maize root is not rectilinear, a tension test introduces two important perturbations given by the transverse and the out-of plane displacements. To avoid this non suitable strains, we have used two CCD cameras allowing the determination of the spatial coordinates of the two markers. Then the longitudinal strain can be easily extracted. With stress evaluated form a special testing machine, the rigidity modulus for three genotypes of maize is finally shown.

### **1. Introduction**

Beating down of maize by wind and storms is an accident which causes the destruction of the plants. Our common goal with the INRA (National Institute of Agronomic Research) is to evaluate the influence of each parameters governing the embedding of the root system in soil. Agronomists from INRA (Lusignan, France) are specially studying the biological observations (lignin rate...) and some geometrical aspects as length, radius of roots... In our side, we carry out experimental analysis on the mechanical behavior root system for various maize genotypes. The correlation between both approaches will be made by Finite Element Method with a numerical evaluation of the mechanical behavior of each genotype [Denis, S. and Brémand, F. 1998]. In a first step, the soil is simulated by a stiffness depending on the humidity rate and a linear

constitutive law is assumed for this complex material. Furthermore we suppose that roots on one inter-node have the same rigidity coefficient (Figure 1). In this paper, we present the experimental technique used for the evaluation of this parameter.

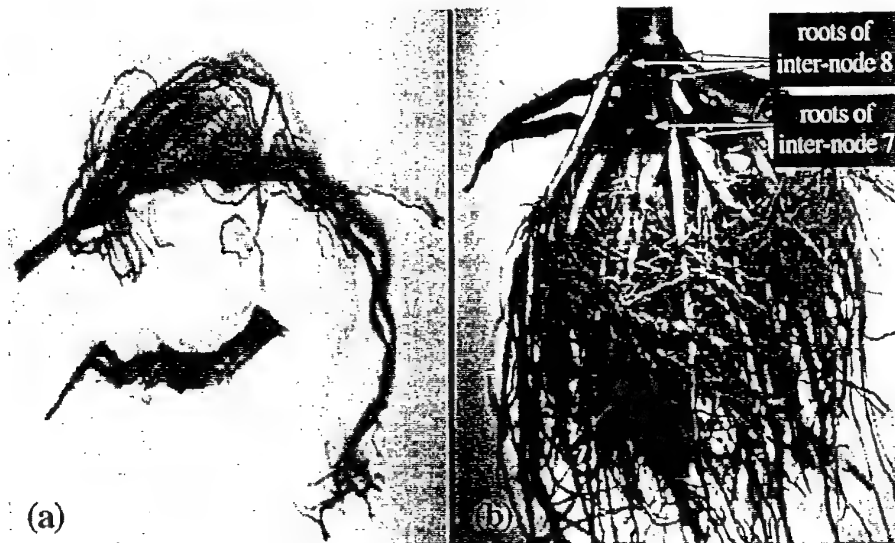


Figure 1 : (a) maize roots, (b) root system

A tensile test is performed on a 50 mm long specimen extracted from the more rectilinear part of the root. Since this complex material is non-homogeneous with a surface who can present some roughness or some important irregularities (Figure 1), classical extensometers as strain gauges are not adapted. The choice of optical methods of strain measurement appears very important because they perform non contact and non-disturbing strain evaluation. Several methods are available as optical diffraction of a laser beam by a grating marked on the surface [Brémand, F. and Lagarde, A., 1986], numerical spectral analysis by FFT [Dupré, J.C., et al. 1993] or white light speckle by numerical correlation [Sutton, M.A., et al. 1986], but they need either to stick or to engrave a grid on the surface which is not possible with maize roots [Denis, S., 1996]. To obtain the longitudinal elongation only two points should be identified. These points are drawn with black ink. With the help of imaging system, the method consists in recording images of the specimen for each loading step [Brémand, F. et al. 1995]. Thus, the x and y coordinates are obtained by the calculation of the center of gravity of each marker.

During the tests, we have noticed different displacements. The longitudinal one is due to the tensile force, whereas the transverse and the out-of plane displacements come from the irregular geometry of maize roots [Denis, S. et al. 1998]. The latter induces variations in the enlargement ratio leading to false strains. To avoid these variations, a stereoscopic experimental set-up is used.

## DEVELOPMENT OF A STEREOSCOPIC OPTICAL

3

## 2. Stereoscopic method for strain evaluation

In order to quantify the transverse and the out-of plane displacements, two identical CCD cameras are used. They are located perpendicularly (Figure 2) in such manner that the transverse displacements of one camera corresponds to the out-of plane displacements of the other. The physical referential is determined as follows :

- X-axis is parallel to the line passing by the focal points  $I_1(-L, L)$  and  $I_2(-L, -L)$  of each camera,
- Y-axis goes from cameras to specimen,
- Z-axis is vertical,
- the origin O is defined as the intersection of the two optical axis which are located at  $45^\circ$  related to Y-axis.

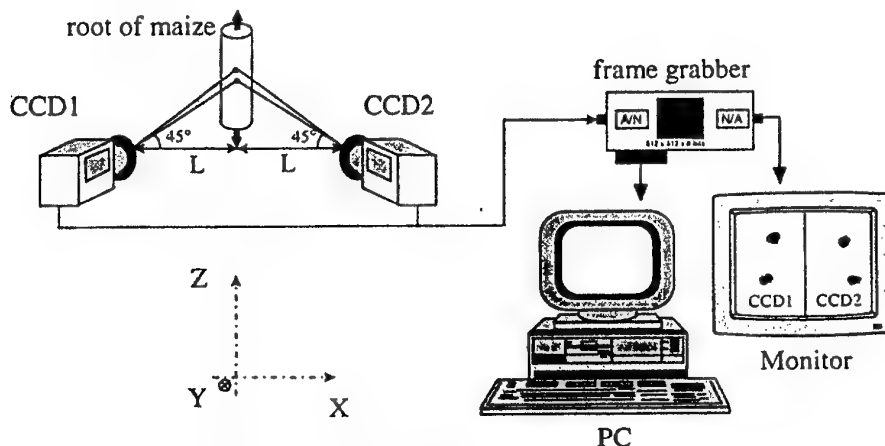


Figure 2 : Experimental apparatus using two CCD cameras

Cameras are adjusting such that the images of the point O should correspond to the center  $(x_0, z_0)$  of each camera (Figure 3). In our case,  $x_0=z_0=256$  pixels. The physical coordinates  $(x, y, z)$  of a point M are obtained by triangulation with the two corresponding points  $M_1$  and  $M_2$  (images of M respectively by CCD1 and CCD2). Let us call  $a_1$  and  $b_1$  the coordinates of  $M_1$  and  $a_2$  and  $b_2$  the coordinates of  $M_2$ , these quantities are expressed in pixels and are obtained from the calculation of the gravity center by a classical interpolation [Brémand et al., 1992]. Since the two cameras have identical lenses with a focal length f, the same enlargement ratio G can be deduced for both cameras. The numerical technique consists in calculating in millimeters the two shifts  $\delta_1$  of  $M_1$  and  $\delta_2$  of  $M_2$  related to the center  $(x_0, z_0)$  of each image.

The x and y values of M should be firstly obtained from the x-components  $dx_1$  of  $\delta_1$  and the x-components  $dx_2$  of  $\delta_2$ . Then the third coordinate z of M (Figure 4) can be determined from the z-component  $dz_1$  of  $\delta_1$  (or  $dz_2$  of  $\delta_2$ ).

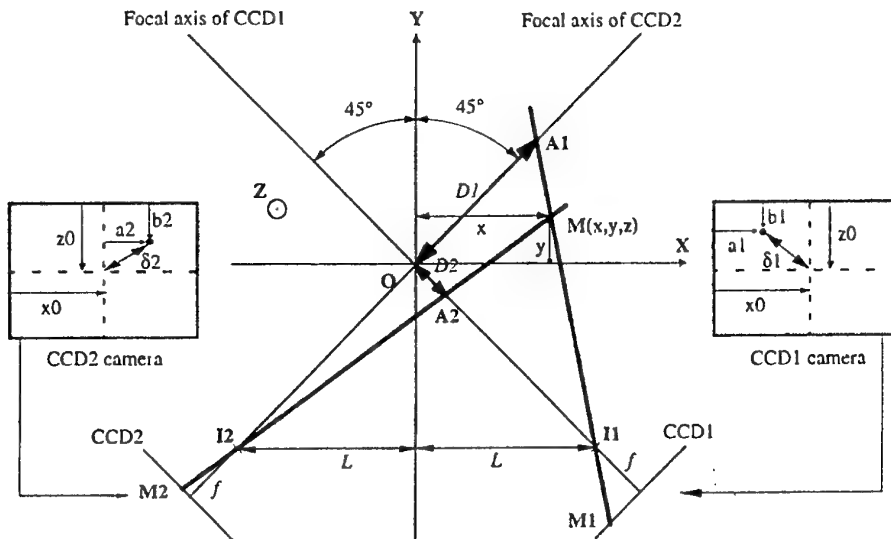


Figure 3 : Schematization of the experimental device

The two straight lines passing by each focal points  $I_1, I_2$  and point  $M$  intersect each optical axis in  $A_1$  and  $A_2$  (Figure 3). The coordinates of these points are :

$$A_1\left(\frac{D_1\sqrt{2}}{2}, \frac{D_1\sqrt{2}}{2}\right) \quad A_2\left(\frac{D_2\sqrt{2}}{2}, -\frac{D_2\sqrt{2}}{2}\right) \quad (1)$$

where the distances  $D_1$  and  $D_2$  are obtained by :

$$\frac{D_1}{dx_1} = \frac{D_2}{dx_2} = \frac{L\sqrt{2}}{f} \quad (2)$$

with the two shifts given by :

$$dx_1 = G(a_1 - x_0) \quad \text{and} \quad dx_2 = G(a_2 - x_0) \quad (3)$$

The  $x$  and  $y$  coordinates of  $M$  can be determined by the calculation of the intersection of the two straight lines  $(A_1, I_1)$  and  $(A_2, I_2)$ . Hence :

$$x = \frac{L * f * (dx_1 + dx_2)}{dx_1 * dx_2 + f^2} \quad (4)$$

$$y = \frac{L * f * (dx_1 + dx_2)(dx_1 + f) - 2 * dx_1 * L * (dx_1 * dx_2 + f^2)}{(dx_1 * dx_2 + f^2)(dx_1 - f)} \quad (5)$$

## DEVELOPMENT OF A STEREOSCOPIC OPTICAL

5

The last coordinate  $z$  is obtained from  $x$  and  $y$ . Only one camera is sufficient to determine  $z$ . For example, we use the CCD1 camera (Figure 4).

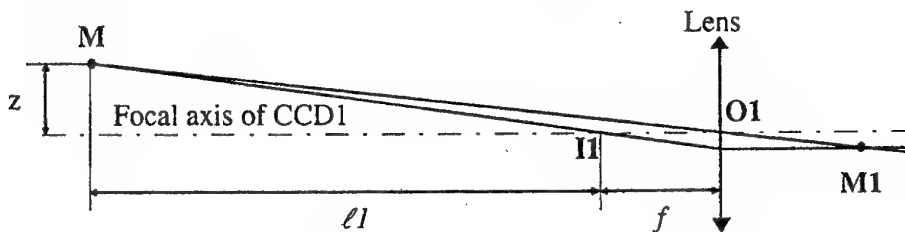


Figure 4 : Determination of the third coordinate  $z$

So one can write :

$$z = -dz_1 * \frac{l_1}{f} \quad (6)$$

where

$$\ell_1 = MI_1 = \sqrt{(x-L)^2 + (y+L)^2} \quad (7)$$

$$dz_1 = G(b_1 - z_0)$$

Now the knowledge of the three-dimensional coordinates leads to longitudinal strain  $\epsilon_{zz}$  by deriving the displacements  $(u_x, u_y, u_z)$ .

$$\epsilon_{zz} = \frac{1}{2}(2 * u_{z,z} + u_{x,z}^2 + u_{y,z}^2 + u_{z,z}^2) \quad (8)$$

Usually we consider that the error made on the location of one marker is the tenth of pixel. For our experiments (with  $L = 370$  mm and  $f = 50$  mm), an accuracy around one hundredth of millimeter has been obtained for each coordinate. As the distance between the two points is around 5 mm, the strain accuracy is estimated to  $10^{-3}$  which is more than enough for our purpose.

### 3. Application

For the measurement of the rigidity modulus of each root, our colleagues from INRA have chosen three genotypes (5, 7 and 16) of maize relative to their very different agronomic behavior. For each variety inter-nodes 6, 7, 8 (when existing) have been studied (Figure 1). Roots have been selected with respect to some important geometrical conditions. First of all we must chose the part of the root close to the stem because it is the more rectilinear. Furthermore its length should be at least 50 mm and its section the more possible constant. In fact, if our roots are too curved, we do not realize a pure tensile test but a combined tension bending test which does not correctly solicit the rigidity modulus.

### 3.1. EXPERIMENTAL APPARATUS

In order to perform these tests, a specially designed low charge testing machine is used. Its stepper motor is controlled by a PC. The loading is made at imposed displacement speed (1 mm/min) and is recording by an acquisition card at regular interval,  $\Delta_t = 2$  s, chosen by user (Figure 5). Stress  $\sigma$  is obtained in dividing the load by the section area. A second PC is charged of the image acquisition. It contains a frame grabber Matrox PIP 1024 (512\*512 pixels, 8 bits). This card receives pictures of the two CCD cameras with the same time interval  $\Delta_t = 2$  s.

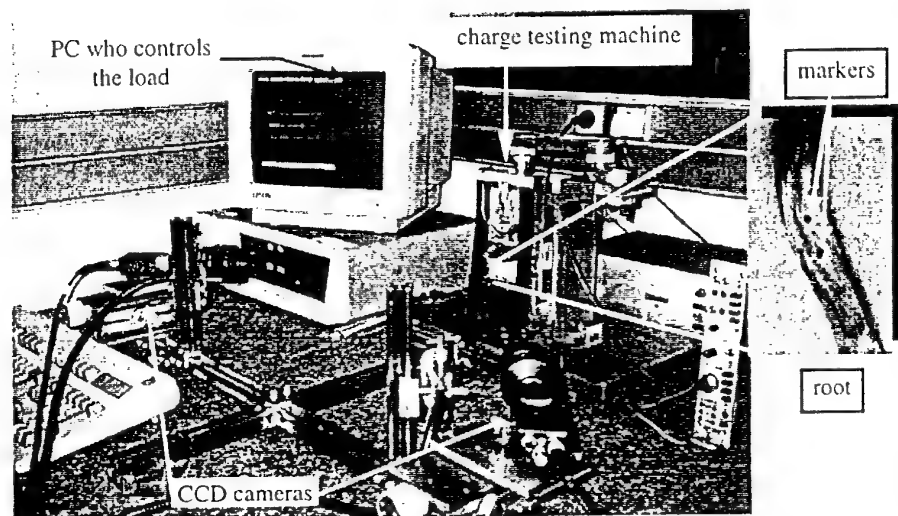


Figure 5 : View of testing machine

### 3.2. RESULTS

A hundred tests have been performed. For each of them, we have plotted the stress  $\sigma$  versus the longitudinal strain  $\epsilon$ . We have chosen only two representative tests which are presented on Figure 6. We have also plotted the curves  $\sigma = f(\epsilon_{\text{ccd}1})$  and  $\sigma = f(\epsilon_{\text{ccd}2})$ , where  $\epsilon_{\text{ccd}1}$  and  $\epsilon_{\text{ccd}2}$  are respectively the longitudinal strains obtained by CCD1 and CCD2. Due to the nature of maize roots (non homogeneous...), experimental curves are not exactly linear. We notice, Figure 6, in some cases, that the longitudinal strains obtained by one of the two cameras are irregular and negative. It is the result of out-plane displacements where specimen moves to opposite direction from CCD camera. Since curves obtained by CCD1 and CCD2 are very different a stereoscopic method for the study of maize roots is absolutely required. It gives a curve obtained from a complex function of CCD1 and CCD2 signals (Figure 6b and equation (8)), but does not lead to the average between CCD1 and CCD2 as shown on Figure 6a. We can also remark that the new curve is smoother than CCD1 and CCD2 curves.

DEVELOPMENT OF A STEREOSCOPIC OPTICAL

7

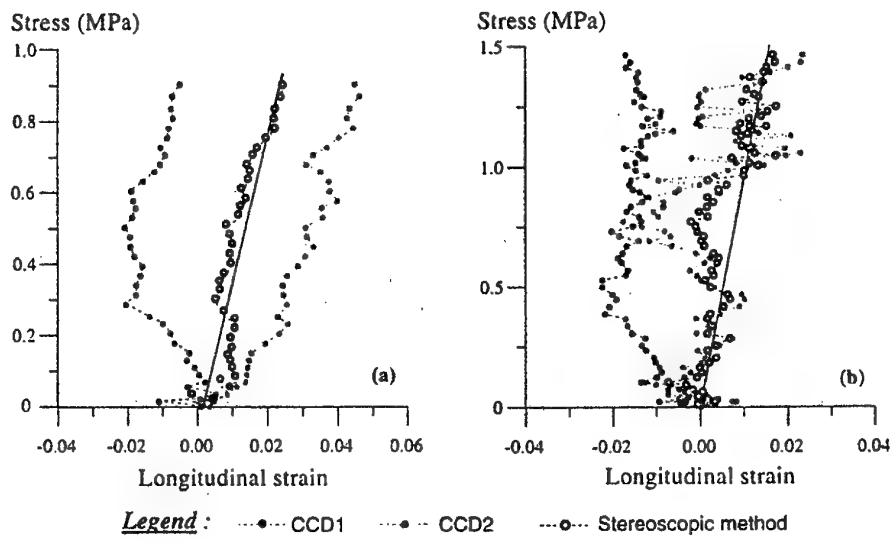


Figure 6 : experimental curves

In order to get the rigidity modulus for each curve  $\sigma = f(\varepsilon)$ , a linear interpolation passing through origin is calculated by a least square method consisting in minimizing the normal distance between experimental results and their fitting curve. We have sum up rigidity modulus on Figure 7 obtained from the slope :

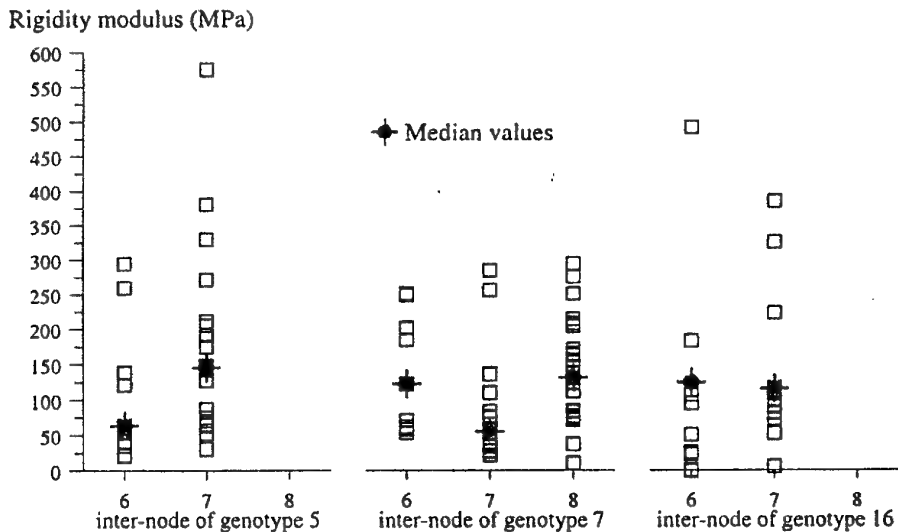


Figure 7 : rigidity modulus for each inter-node of each genotype

For each inter-node of each variety, we have a disparity in the rigidity modulus due to the nature of material. In fact, biological and geometrical studies, realized in parallel by agronomists from INRA such as lignin rate or radius of roots, also show disparities in results. That is why the median of rigidity modulus of each inter-node will be used in order to numerically simulate the mechanical behavior of a maize root system in soil.

#### 4. Conclusion

The utilization of a non contact and a non-disturbing optical method allows us to test vegetal materials. In fact, the study on the mechanical behavior of a maize root system have been required the tracking of two markers associated with a stereoscopic method to determine the three spatial coordinates of the points for each loading step. We obtain coordinates with an accuracy around  $10^{-2}$  mm and longitudinal strain accuracy is estimated to  $10^{-3}$ .

Now a mesh of a maize plant, stem and roots, by finite element method is realized according to geometrical data and rigidity modulus of each genotype. A root is simulated by around 50 cylindrical segments with a decreasing radius. The determination of the influence of each parameter is in progress.

#### 5. Acknowledgments

We would like to thank Region Poitou-Charentes for the financial support and Yannick HEBERT from INRA for his biological work realized in parallel.

#### 6. References

Brémand, F., Lagarde, A., 1986, A new method of optical strain measurement with applications, Proceeding of the 1986 SEM Spring Conference on Experimental Mechanics, pp 686-694.  
Brémand, F., Dupré, J.C., Lagarde, A., 1992, Non-contact and non-disturbing local strain measurement methods. Part 1: Principle, European Journal of Mechanics. vol : 11 A, n° 3, pp 349-366, 1992.  
Brémand, F., Dupré, J.C., Lagarde, A., 1995, Mesure des déformations sans contact par analyse d'images, Photomécanique 95, Cachan, Eyrrolles, pp 171-178.  
Denis, S., 1996, Etude des propriétés mécaniques du système racinaire et de ses organes chez le maïs, DEA, Université de Poitiers.  
Denis, S., Belkadi, S., Brémand, F., 1998, Mesure des déformations par stéréoscopie sur surface quelconque - Application aux racines de maïs, Photomécanique 98, Marne la Vallée, pp 73-80.  
Denis, S., Brémand, F., 1998, Experimental study on the mechanical behaviour of maize root system : soil-root interface evaluation and rigidity modulus determination, Les racines principales: structures et fonctionnement colloque de l'International Union of Forestry Research Organizations, Bordeaux.  
Dupré, J.C., Brémand, F., Lagarde, A., 1993, Numerical spectral analysis of a grid. Application to strain measurements, Optics and Lasers in Engineering. vol 18, n° 3, pp 159-172.  
Sutton, M.A., Cheng, M., Peters, W.H., Chao, Y. J., Mc Neill, S.R., 1986, Application of optimized digital correlation method to planar deformations analysis, Image and Vision Computing vol. 4 n°3, pp 143-150.

ANALYSIS OF THE DEGRADATION MECHANISMS  
IN COMPOSITE MATERIALS THROUGH A  
CORRELATION TECHNIQUE IN WHITE LIGHT

Y. BERTHAUD

*LMSGC, UMR 113 LCPC / CNRS  
F-77420 Champs sur Marne, France*

AND

S. CALLOCH, F. COLLIN, F. HILD AND Y. RICOTTI  
*LMT-Cachan, ENS de Cachan / CNRS / Université Paris 6  
F-94235 Cachan, France*

**Abstract** — The analyzed material is a vinylester matrix reinforced by randomly oriented continuous fibers. The degradation mechanisms are determined from tensile tests on coupons and SEM observations. Notched specimens and plates with central holes are then studied when loaded in remote uniaxial tension. Cross-shaped specimens are then studied. The evolution of the strain field is computed through a correlation technique in white light. In particular, the initiation location can be measured.

## 1. Introduction

The aim of this study is first to evaluate the effect of the fiber orientation of a composite material made by a Resin Transfer Molding (RTM) technique. Second, the notch sensitivity of this material is assessed for specimens loaded along one and two directions. The strain fields are evaluated by using a correlation technique. The initiation sites are determined by this technique coupled with a finite element computation.

## 2. Studied Material

The composite material is made of a vinylester matrix reinforced by continuous E glass fibers (see Fig. 1). The RTM process induces a random in-plane fiber bundle orientation (Fig. 2). The fiber volume fraction is equal to 30%.

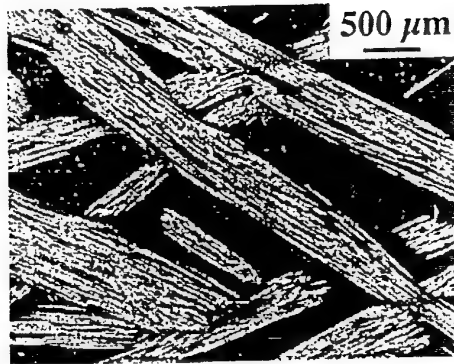


Figure 1. Surface of the composite.

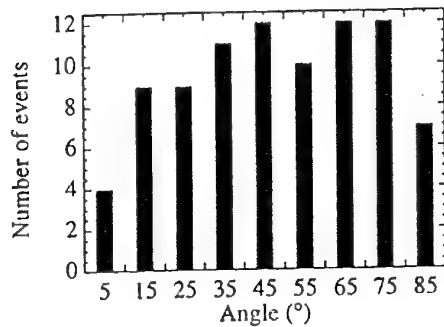


Figure 2. Angular distribution of fiber bundles in the material.

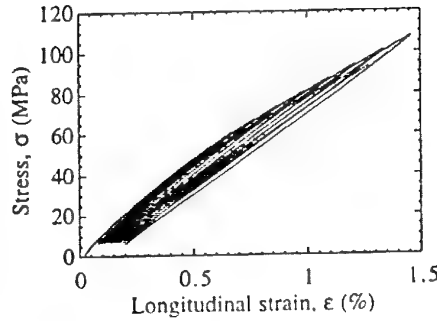


Figure 3. Stress/strain curve of a coupon specimen.

### 3. Uniaxial Loading

#### 3.1. COUPONS

Tensile tests have been carried out on  $25 \times 3 \times 150$  mm<sup>3</sup> coupons (Fig. 3). To analyze the effect of fiber orientation, the coupons were cut in two perpendicular directions. There is no effect on the stress/strain response of the composite [1]. A microscopic analysis of the degradation mechanisms shows multiple matrix cracks (Fig. 4). Furthermore, single fiber pull-out has been observed. More importantly, fiber bundle pull-out is systematically present at the fracture surface (Fig. 5). The fiber bundle behaves like a fiber with a large cross-sectional area rather than the sum of single fibers of small diameters.

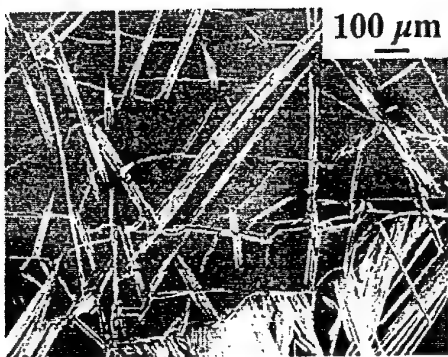


Figure 4. Cracking of the vinylester matrix.

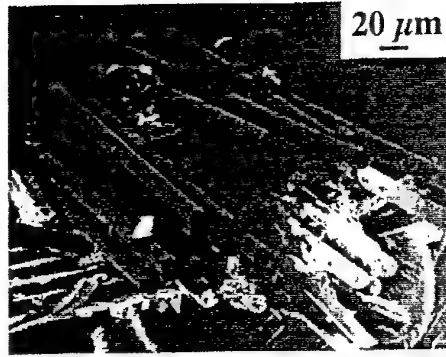


Figure 5. Fiber bundle failure and pull-out.

### 3.2. PLATES WITH NOTCHES OR HOLES

A series of experiments has been carried out on plates with holes (of radius  $R$ ) and doubled edge-notched specimens (the total notch size is  $2a$ ). The total width  $L$  is identical to that of the coupons. Two ratios  $2a/L$  and  $2R/L$  have been considered: 1/2 and 1/4. These specimens are loaded in remote uniaxial tension. To compare the load levels of different configurations, the net section stress is computed. Figure 6 shows the net section stress vs. the strain measured in the vicinity of a notch by a  $1 \text{ mm}^2$  strain gauge. The shape of the curve is comparable to that obtained with coupons (Fig. 3).

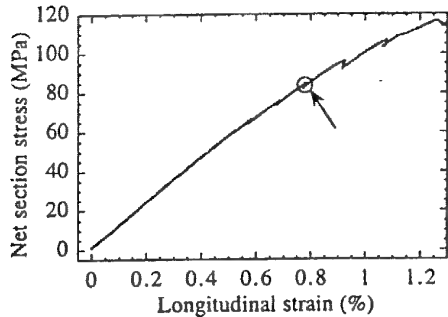


Figure 6. Tensile curve of a notched specimen ( $2a/L = 0.25$ ). The arrow shows the level corresponding to the strain measurements of Fig. 9.a.

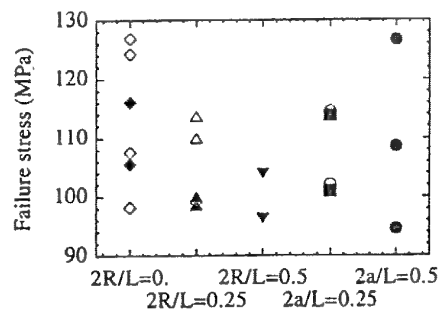


Figure 7. Net section stress at failure for different orientations ( $0^\circ$ : filled symbols,  $90^\circ$ : open symbols) and different types of specimens.

Figure 7 shows the net section stress levels at failure for different specimens. One can see a scatter for all types of specimens. This scatter is

probably linked to the randomness of the bundle failure stress and orientation (Fig. 5). It is worth noting that the stress levels cannot be distinguished within each scatter. Furthermore, the effect of orientation is negligible. All these results tend to show that there is no influence of the presence of stress concentrators on the net section stress level at failure. Therefore the material is notch-insensitive in 'uniaxial' tension.

Figure 8 shows various shapes of the fracture surface. It can be noted that there is always a shear-type of failure (with an angle of  $45^\circ$  wrt. the loading direction). However sometimes a tensile-type of failure can be observed (perpendicular to the loading direction). In the following, the initiation sites will be determined by using the measured strain field through a correlation technique.

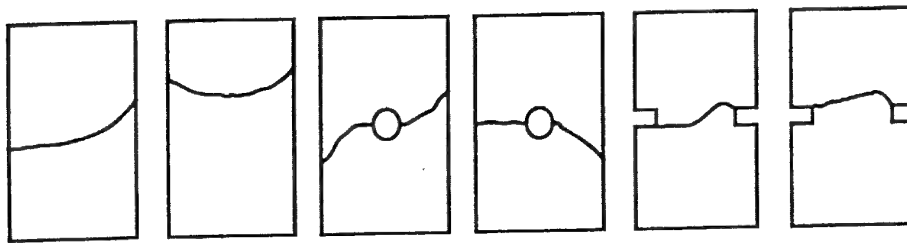


Figure 8. Examples of fracture surfaces.

### 3.3. CORRELATION TECHNIQUE

To locate the initiation site(s), the strain field is evaluated during the experiment. The specimen is polished and then coated by a random black and white pattern. By using a fixed CCD camera, pictures at different stages are recorded. The in-plane displacement map is computed by using a correlation technique between an initial picture (with no applied load) and a subsequent one (when the load is applied). This technique has been applied to different situations [2, 3, 4] even in the presence of finite strains [5].

The specimen is divided into a regular array of zones (cells), the size of which is equal to  $32 \times 32$  pixel. The displacement vector is obtained by maximizing a correlation function between corresponding cells of the two pictures. This cross-correlation is computed in the Fourier space. A local parabolic interpolation about the peak allows a sub-pixel evaluation of its position. The second image is then shifted by the previous computed displacement to get the next value. An iterative scheme is used to get an auto-correlation function. With two or three iterations on  $32 \times 32$  pixel cells, an accuracy of  $3/100$ -th of pixel is obtained [6]. The main advantages

of this technique is its insensitivity to lighting variations and lack of focus. It is well suited for small strain evaluations (of the order of 5% so that the hypothesis of solid displacement of the cells is fulfilled). To compute the strain field, the displacement map is prescribed on the same Finite Element (FE) mesh as the one used in the image analysis. This procedure allows a direct comparison between experiments and model predictions (usually obtained by non-linear FE analyses). The commercial FE code ABAQUS [7] has been used in the present study.

### 3.4. INITIATION SITE

The evolution of the strain field as a function of the load level is obtained by using the above-described method. In particular, the macrocrack initiation locus can be observed. In a double edge-notched specimen, the initiation mechanism is of shear nature (even though another tensile macrocrack is forming with some delay: Fig. 9.a). The two directions are also present on the fracture surface (Fig. 9.b). Figure 9.a shows that the longitudinal strains start to localize in a 45° direction. The corresponding levels are of the order of the failure strains given in Fig. 6. Therefore, this level will be referred to as initiation. In Fig. 6, the stress level at 'initiation' is shown: it occurs prior to reaching the peak level.

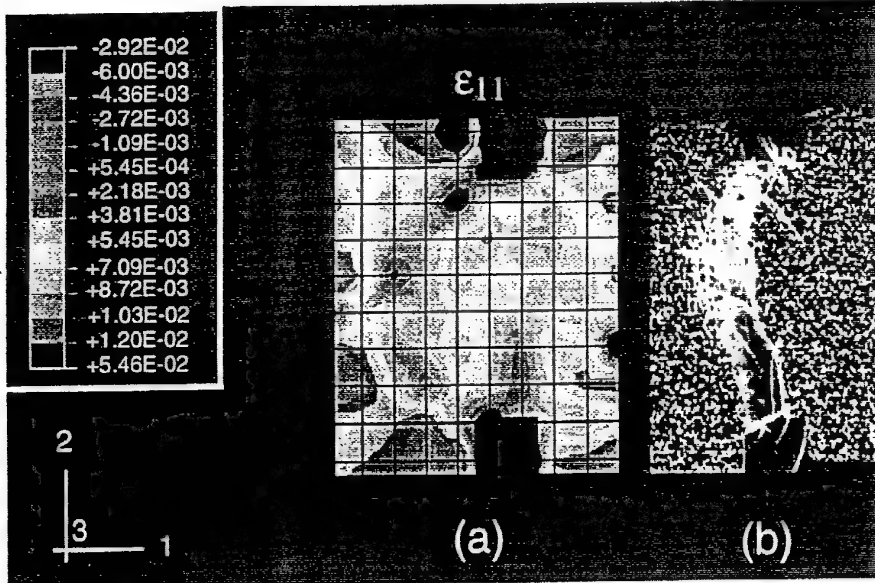


Figure 9. Strain field at 'initiation' (a), specimen surface after failure (b).

#### 4. Biaxial Loading

##### 4.1. SPECIMEN GEOMETRY AND EXPERIMENT

To investigate the effect of biaxial loading conditions, a cross-shaped specimen has been designed (Fig. 10). The ligament length is equal to 36.5 mm and the connecting radius is equal to 5 mm. This specimen is mounted in a triaxial testing machine ASTREE equipped with six servohydraulic actuators [8] (jointly developed by LMT-Cachan and Schenck AG, Darmstadt, Germany). To avoid the coupling between the different loading axes, the actuators are linked two by two along the three axes so that the central point of the specimen is motionless. The specimen fixed in the grips is shown in Fig. 11: four out of six servohydraulic actuators are used.

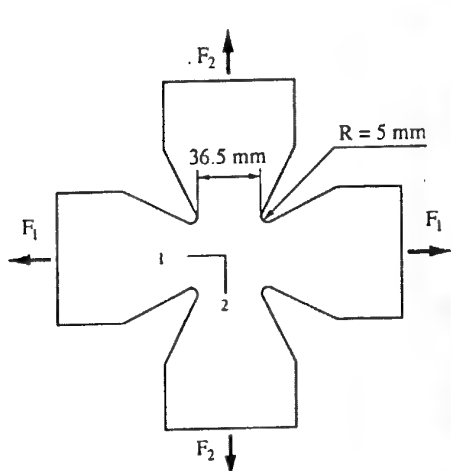


Figure 10. Specimen geometry.

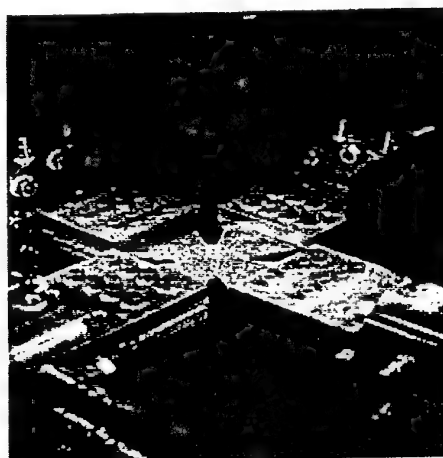


Figure 11. Specimen in the testing machine ASTREE.

##### 4.2. TEST RESULTS

The testing machine allows non-proportional load histories: a squared loading cycle has been prescribed (Fig. 12). The effect of non-proportionality is a motion of the stress concentration zone along the connecting radius. The load level at failure (12 kN) corresponds to a net section stress of 101 MPa. This stress level is close to those observed previously (Fig. 7). This result seems to indicate that the notch-insensitivity is also observed for a non-proportional load history.

The broken specimen is shown in Fig. 13. The correlation technique is used to predict the initiation sites. To determine the location, it is assumed that a strain greater than 1.7% is likely to produce macrocracking (this

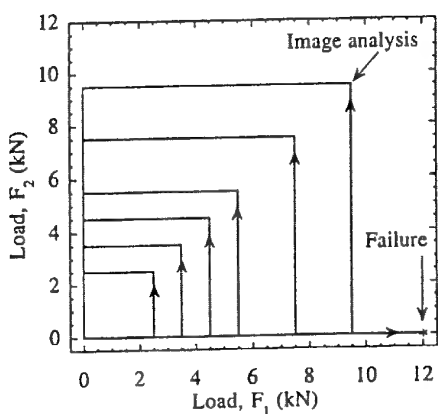


Figure 12. Load history.

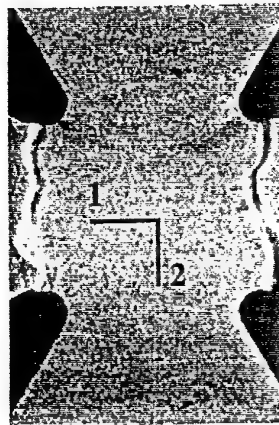


Figure 13. Failure surface.

strain level corresponds to the average failure strain of coupons). The force level for the present analysis is such that  $F_1 = F_2 = 9.5$  kN. For this situation the strain field  $\epsilon_{11}$  and  $\epsilon_{22}$  is symmetrical about the first and second bisector. Any lack of symmetry is a probable indication of initiation. The longitudinal strains  $\epsilon_{11}$  and  $\epsilon_{22}$  determined from the displacement measurements are plotted in Fig. 14. It can be noticed that the strain levels are higher for the strains  $\epsilon_{11}$  than those of the strains  $\epsilon_{22}$ . Furthermore, when the strains  $\epsilon_{11}$  are analyzed, one can see that the highest levels are almost identical on all stress concentration zones. This leads us to assume that initiation occurred independently on all sides along the 1-direction for a load level of the order of 9.5 kN.

### 5. Summary

The results presented herein show that the overall composite behavior is isotropic. A scatter in failure stress has been observed for different specimen geometries and configurations. It is related to a bundle failure. A correlation technique in white light has been used to predict the initiation site(s). This method is applicable even in the presence of macrocracks. In all cases the initiation is predominantly of shear nature, even though tensile initiation may be present simultaneously. Lastly, in the experiments reported in this paper, it is shown that the composite material is notch insensitive when the net section stresses at failure are compared for notched specimens, plates with central holes and cross-shaped specimens. These experimental results will allow us to develop, identify and discriminate different mechanical models describing the behavior of these composites with a randomly

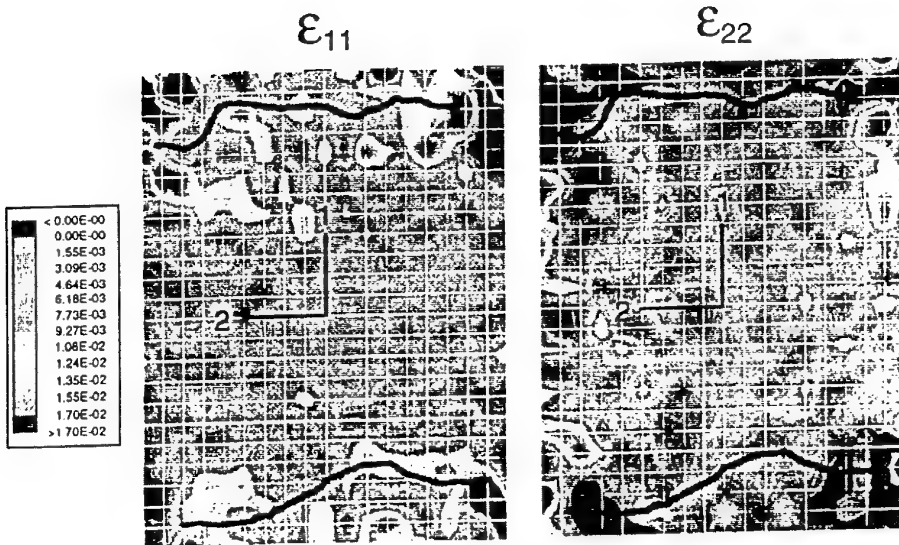


Figure 14. Longitudinal strain field  $\epsilon_{11}$  and  $\epsilon_{22}$  when  $F_1 = F_2 = 9.5$  kN. The observed macrocracks are drawn in black.

oriented microstructure.

## References

1. F. Collin, Y. Berthaud and F. Hild, in Y. Berthaud, M. Cottron, F. Morestin, P. Moucheront and M. Taroni (eds.), in Proceedings Photomécanique 98, Marne-la-Vallée (France), GAMAC, (1998) 241.
2. M.A. Sutton, M.A., W.J. Wolters, W.H. Peters, W.F. Ranson and S.R. McNeill, *Im. Vis. Comp.* 1 [3] (1983) 133.
3. T. C. Chu, W. F. Ranson, M. A. Sutton and W. H. Petters, *Exp. Mech.* 3 [25] (1985) 232.
4. S. Choi and S. P. Shah, *Exp. Mech.* 3 [43] (1997) 307.
5. S. Mguil, F. Morestin and M. Brunet, in Y. Berthaud, M. Cottron, F. Morestin, P. Moucheront and M. Taroni (eds.), in Proceedings Photomécanique 98, Marne-la-Vallée (France), GAMAC, (1998) 361.
6. J. Thesing, Report, LMT-Cachan, 1996.
7. H. D. Hibbit, B. I. Karlsson and P. Sorensen, Abaqus, User's Manual, version 5.6, 1996.
8. S. Calloch and D. Marquis, *Int. J. Plast.* [accepted] (1998).

## MEASUREMENT OF RESIDUAL DEFORMATIONS INDUCED BY HIGH TEMPERATURE LOAD

N. CAVALLO<sup>1</sup>, F. MORESTIN<sup>2</sup>, J.F. JULLIEN<sup>1</sup>  
*INSA de Lyon, 20 avenue Albert Einstein, 69100 Villeurbanne*  
*URGC Structures, "LMSO"*

**Abstract :** Validation of models introduced to simulate the thermo-mechanical consequences of phase transformations in the Heat Affected Zone (H.A.Z.) during welding is a difficult task because of the multiple effects that take place such as heat transfer and the convection of the melting zone. There is also a tridimensionnality induced by the geometry of the pieces to be welded and by the melting zone and displacement of the heat source.

This work treats the development of a specific device to validate thermo-mechanical models describing the H.A.Z.. All the « parasitic phenomena » that occur in reality do not take place under the conditions for the wanted validation : there is no melting zone and the problem is axisymmetric. However, all thermo-mechanical consequences of phase transformations occur. Many measurements are taken to validate each step of the simulations : thermal, metallurgical and mechanical.

An original software for the strain field measurement has been developed to high temperature measurement. This software used the correlation principle and is limited nowadays to the plane surface measurement. This method is particularly well adapted to measure small deformations with high gradients. This new high temperature measurement method without contact can be another tool for validating numerical simulations of the Heat Affected Zone during welding.

### 1. Introduction

The prediction of residual stresses is a particularly difficult task in the case of welding, where structural transformations take place. In order to validate the models generally used to simulate the thermo-mechanical consequences of phase transformations (difference of volume of the phases and dilatation coefficients, transformation plasticity, hardening recovery and multiphased behaviour), a large program is investigated by *Électricité de France* and the *Bureau de Contrôle des Chaudières nucléaires* on a carbon manganese steel (16MND5 in the AFNOR norm). This program is divided into two

main parts as described by Cavallo (1997-I and II). The first one concerns the identification and validation of each model on specimens without thermal gradients. The second one concerns the validation on specimens with thermal gradients and structural effects.

This paper only deals with the second part. A specific device has been developed and realised. It consists of applying an axisymmetric thermal load and in acquiring the maximum quantity of measurements used to validate numerical simulations. To avoid the problems induced by the melting zone and the tridimensionnality due to the displacement of the heat source and specimen geometry which occur in reality, the analysis is limited to the Heat Affected Zone (H.A.Z.), which is the zone where structural transformations happen in a solid state, and the thermal load and the geometry are chosen to be axisymmetric. By keeping only the creation of H.A.Z. phenomena, even if the thermal cycles are slower than the welding ones, the model's validation taking into account phase transformations becomes easier.

To validate strain calculations, a new application of the correlation method has been developed. It permits to measure the plane strain load of the front side of the specimen which is submitted to a high temperature load.

In this paper, the device and the correlation method results are presented.

## **2. Experimental device**

### **2.1.DISK SIZE DEFINITION**

The thermal load is chosen to produce a totally martensitic transformation during the cooling process in the centre of the disk and through its thickness. Therefore, the maximum temperature must be higher than 850°C which is the temperature of the end of austenization for the considered steel, and every point of the disk which maximum temperature is higher than 750°C must have a minimum cooling rate of 10°C/s between 850°C and 390°C (temperature of the beginning of the martensitic transformation). Knowing that the thermal load is applying by a CO<sub>2</sub> laser which produces a flow assumed to be axisymmetric and have a defined form, numerical simulations are performed to estimate the thickness and the diameter of the disk and to produce measurable strains and stresses. Then, the disk is defined to be 5 millimetres thick and to have a diameter of 160 millimetres.

### **2.2.DISK ELABORATION**

Dilatometry tests have shown that internal stresses take place in the steel because of lamination, therefore the samples are taken to be larger than the defined geometry. They are submitted to a preliminary thermal cycle to relax internal stresses.

Disk are manufactured, rectified and polished to reduce the hardening of the disk sides as much as possible.

### 2.3.BOUNDARY CONDITIONS

The disk support is made of three alumina shafts which extremities are pointed to reduce the contact surface. The shafts are placed to be in contact with the parts of the disk which are assumed to stay cold. All the surfaces of the disk are supposed to be cooled by free convection and radiation.

### 2.4.MEASUREMENT METHODS

#### *2.4.1. Temperature measurements*

Temperature measurements are done on both faces of the disk.

On the side submitted to the thermal flow (front side), the temperature is measured by an infrared camera and pyrometers which permit measurements without contacting the disk. On the back side, thermocouples 78  $\mu\text{m}$  diameter type K are welded every two millimetres along a diameter.

The number and the positions of the thermocouples have been determined to allow the use of the inverse method as described in Blanc (1998) to estimate the thermal load in the entire specimen. The measurements done on the front side of the disk which are less precise, are only made to verify the thermal load estimated.

#### *2.4.2. Displacement measurements*

Three displacement sensors LVDT type are equally distributed around the circumference ( $3 \times 120^\circ$ ) to measure the specimen's diameter variation and verify the axisymetrie of the thermal load without preventing the free dilatation of the disk.

Seven other sensors type LVDT measure the axial displacement of the inferior side along a diameter every 5 millimetres.

#### *2.4.3. « Post-mortem » measurements*

Final shapes of the two sides are measured by LVDT sensors along four diameters. Residual stresses are measured at the *Ecole Nationale Supérieure des Arts et Métiers (ENSAF France)* by X-ray diffraction after the test and before the microstructure analyses. Finally, the disk is divided into two parts. It is polished and chemically attacked. Then, microstructure observations are made, completed by micro-hardness and hardness measurements.

#### *2.4.4. Plane strain measurements on the front side by the correlation method*

*Correlation method* The correlation method of numerical images is used to estimate the plane displacement of a fuzzy motif « speckle type » deposited on the disk surface.

This method consists in taking pictures of the specimen before and after it is submitted to the thermal load, and estimating the displacement of each pixel of the picture between the two states using the *SIFASOFT 3.0 code* developed by the *Laboratoire de mécanique des solides* of INSA Lyon (see Mguil 1997). Knowing the displacements of the points of the surface, deformations can be estimated using interpolation.

*Pattern definition* The correlation method requires a special equipment and few precautions. The analysed picture must have the most random aspect as possible : each pattern of the image must be different from each other. Usually, the speckle aspect is obtained by pulverisation of white and black painting. In our case, the pattern must be high temperature resistant, permit the absorption of the laser beam, and provide the lamination. The fuzzy pattern chose is composed of a first fine layer of graphite powder and a second one of bore nitrate.

*Experimental apparatus* The pictures are obtained with a numeric camera Kodak Mega Plus (1024\*1024 pixels). This high definition camera with square contiguous pixels is linked to an acquisition card Matrox PIP1280 connected by a PC 486 DX50. The axial displacement is not taken into account by the use of a telecentric lens Melles Griot, Invaritar Pin 59LGL 428 model.

### 2.5.DISK POSITIONNING

A preliminary test is done on a A33 disk, 1.5 millimetre thick. In this test, differential thermocouples are welded on the back side of the disk. Those thermocouples directly measure the difference of temperature between each couple of points located symmetrically from the centre. Numerically controlled machine allowed in plane disk positioning in order to assure that the centre of the disk lies in the axis of the laser, providing this way an axisymmetric heating.

### 2.6. SCHEME OF THE DEVICE

The experimental device permits the application of an axisymmetric heating load on the front side of the disk. Temperature measurements are done to determine the thermal load in the whole specimen. Deformations are measured during the test on the back side of the specimen. The final deformations of two faces are measured as well as the in-plane deformations of the front side and the superficial residual stresses. Final microstructures are determined by microstructure analyses and hardness measurements.

A simplified scheme of the device is presented on *Figure I*.

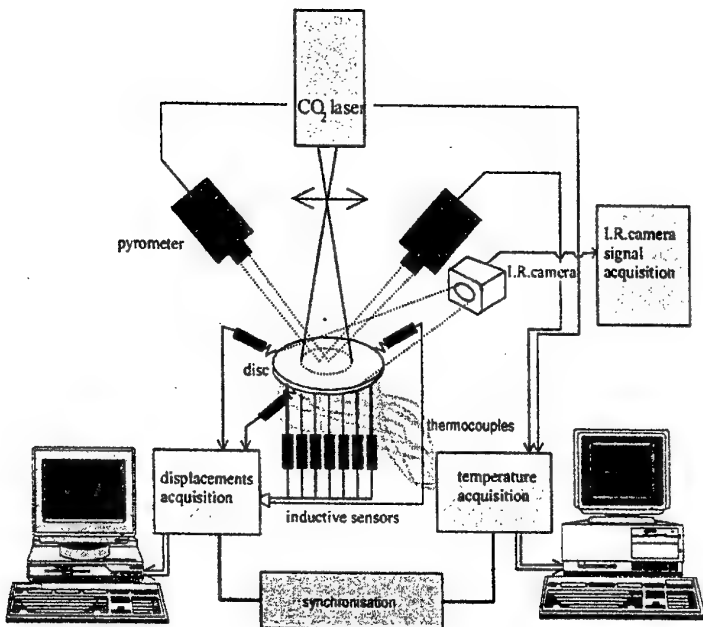


*Figure I : Scheme of the device*

### 3. Results

Only few results are presented here to discuss more about the correlation method results. The maximum temperature reached during the test is 950°C on the front side of the disk. Microstructure analyses and hardness measurements are taken to estimate the metallurgical phases in the different zones of the disk. A diagram of the different zones is presented figure 6. Three particularly zones are determined : a totally austenized one during the heating (1), a partially transformed (2) one and the non thermally affected one (3).

The displacements measured on the back side on the specimen present the same evolution in different proportions. To facilitate its analysis, only one curve is plotted and its evolution is compared to that of the temperature (Figure 3) for two points placed at 10 millimetres from the centre of the disk (which is a point of the H.A.Z.). The disk is heated by the front side. It is noticed that the phase transformations occurring during the cooling do not produce important displacements and therefore produce stresses.

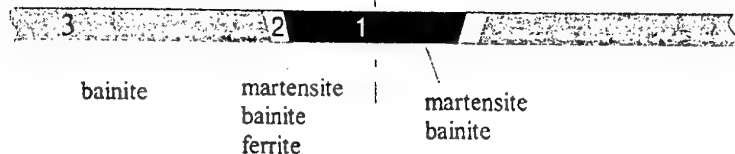


*Figure 2 : Material zones*

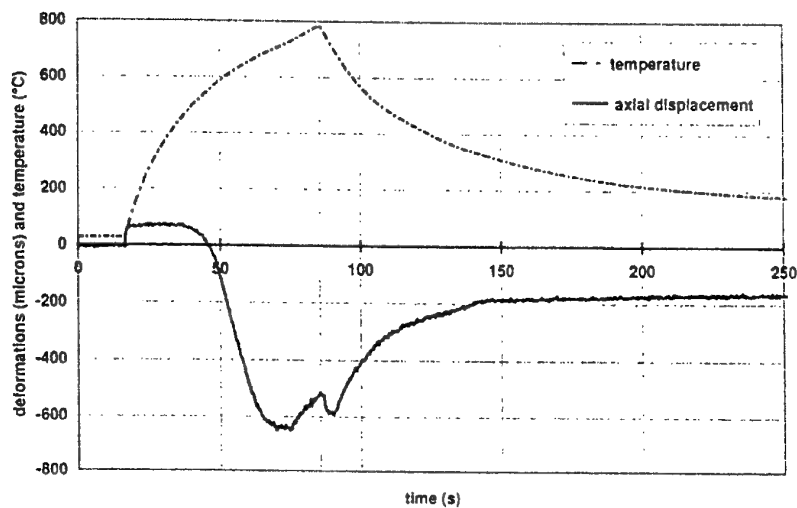


*Figure 3 : Temperature and displacement measured at 10 mm from the centre on the back side*

Figure 4 presents the main directions estimated by the correlation method on the front side of the disk. The grey levels and the crosses represent the direction of the main deformation : they show the strain load is axisymmetric. The Figures 5 shows the loads of the plane main strains. Main strain  $\epsilon_{11}$  and  $\epsilon_{22}$  are estimated to be equal to the circumferential and radial ones because of the principle directions.

All the measurements done enable to validate each step of the calculation : thermal, metallurgical and mechanical (displacements, strains and stresses).

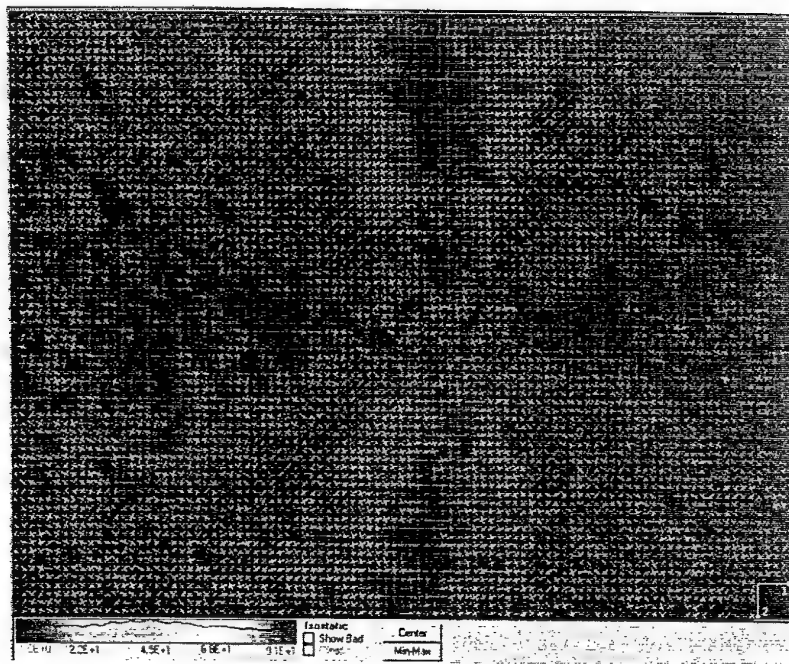


Figure 3 : View of the main directions

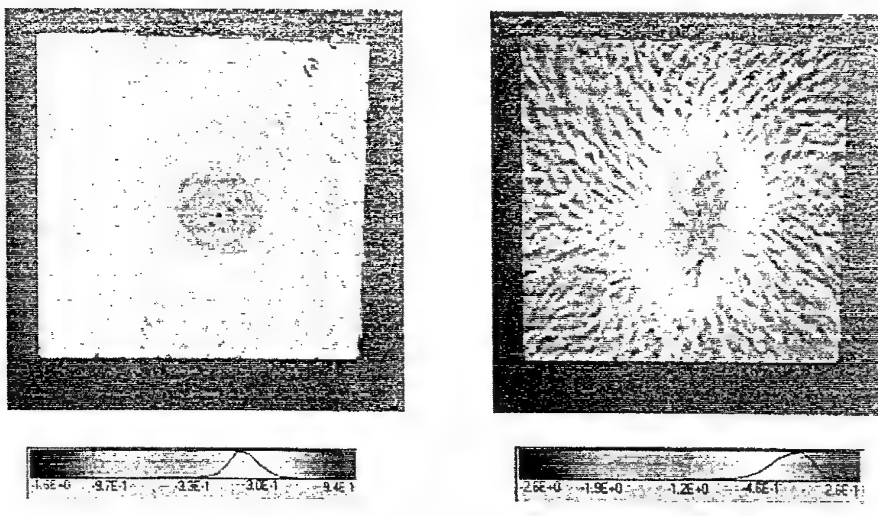


Figure 4 : Plane main strains

#### **4. Conclusion**

The experimental developed permits the application of an axisymmetric thermal load on a disk to measure :

- during the test, temperature and axial displacements along a diameter of the back side of the disk
- after the test, residual stresses, microstructures and final geometry and the residual plane strains on the front side *by a new use of the correlation method*

All of these measurements permit the validation of each calculation step and particularly the capacities of codes to estimate residual strains and stresses in the case of phase transformations. This test can also be used with various loads corresponding to the thickness of the disk and the power of the laser. H.A.Z. gradients can also be reproduced and multicycles can be applied as in the H.A.Z. to validate the stresses relaxation estimated by models.

#### **Acknowledgements**

Authors wish to thank *Électricité de France* and *le Bureau de Contrôle des Chaudières Nucléaires* for financial and technical supports.

#### **5. References**

Cavallo, N., Taleb, L., Jullien , J.F., Wadier, Y., Waeckel, F., Moché, L., Dubois, D., Devaux, J. (1997-I)  
Phase transformation effects on mechanical behaviour of steel vessel, SMIRT Lyon, August 97, pp. 698-  
I\_698-3.

Cavallo, N., Taleb, L., Jullien, J.F., Waeckel, F., Wadier, Y., Moché, L. (1997-II) Thermomechanical  
behaviour of a carbon manganese steel under martensitic transformation, The Firth International  
Conference on Residual Stresses, edited by T.Ericsson, M. Odén and A. Anderson, I, pp.238-243.

Blanc, G., Raynaud, M., Schau, T.H. (1998) A guide for the use of the function specification method for 2D  
inverse heat conduction problems, *Int. J. of heat and mass transfers*13, 703-716.

Mguil-Touchal, S., Morestin, F., Brunet, M. (1997) Various experimental applications of digital image  
correlation method. CNEN97, Rhodes, pp. 45-48.

## APPLICATION OF INFRARED THERMOGRAPHY FOR CONTACT PROBLEMS

T. SAKAGAMI

*Graduate School of Engineering, Osaka University  
2-1 Yamadaoka, Suita, Osaka 565-0871 Japan*

K. OGURA

*Graduate School of Engineering Science, Osaka University  
1-3 Machikaneyama, Toyonaka, Osaka 560-8531 Japan*

S. KUBO

*Graduate School of Engineering, Osaka University  
2-1 Yamadaoka, Suita, Osaka 565-0871 Japan*

T. N. FARRIS

*School of Aeronautics and Astronautics, Purdue University  
1282 Grissom Hall, West Lafayette IN 47907-1282 USA*

### 1. Introduction

Investigation of tribological phenomena such as friction, wear and fretting fatigue is important in evaluating the reliability and safety of structures and mechanical components. In investigating these phenomena, though, it is often difficult to estimate physical parameters such as real contact area, friction coefficient, and contact stress distribution, because of the lack of robust experimental methods. Yet most tribological phenomena are usually accompanied with the generation of heat due to either friction-induced heat flux or plastic deformation at the contact surface. Small temperature changes arising from the thermoelastic effect are also associated with cyclic contact stress and strain fields. Thus measuring near-surface temperature fields offers an encouraging approach for characterizing the mechanics and physics of tribological phenomena. This paper will describe results from several experimental investigations of contact problems through the use of infrared thermography. First, a new technique using infrared thermography combined with infrared-transmitting materials is proposed for direct monitoring of the surface temperature of two contacting solids. This technique is applied to the frictional temperature measurement on the contact surface under dry sliding conditions, as well as the contact stress measurement based on thermoelasticity. Further a newly available infrared thermographic system is used to characterize the near-surface conditions associated with fretting contact.

## 2. Tribological Measurement Using Infrared Transmitting Solid

Consider a contact problem, in which a ball is in contact with a disk, as illustrated in figure 1. When an infrared transmitting solid is employed as the disk material, the distribution of the infrared energy emitted from the contact surface can be measured by thermography since the infrared radiation generated at the contact surface passes through the infrared transmitting disk with a small amount of absorption and scatter. Therefore the temperature distribution on the contact surface of the ball can be visualized by thermography through the infrared transmitting disk. This enables us to continuously monitor tribological parameters, such as frictional temperature rise and the shape and size of the contact area, during the processes of friction and wear [1]. Further, the contact stress field can be measured directly using an infrared stress measurement system based on the thermoelastic effect [2].

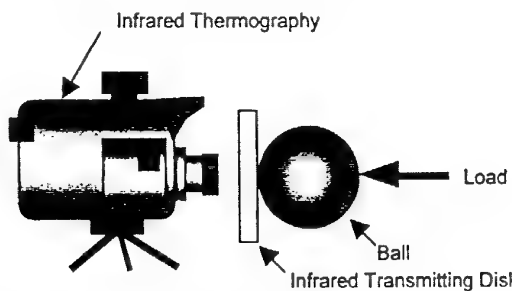


Figure 1. Thermographical measurement of contact surface using infrared transmitting materials.

### 2.1 MEASUREMENT OF DRY SLIDING CONTACT TEMPERATURE

Contact temperature distribution was measured under dry sliding contact using a pin-on-disk type testing system. A cylindrical pin with a spherical contact surface was brought into contact with the rotating disk and loaded. Then the temperature distribution on the contact surface was measured by infrared thermography. Figure 2 is an example of the thermal images, which shows steady state temperature distributions on the contact surface of the plastic pin sliding against an alumina ceramic disk, taken for several combinations of the sliding velocity and the load. The plastic pin was made by machining a PEEK (polyetheretherketone) rod. The curvature of the spherical contact surface,  $R$ , was 25mm. PTFE (polytetrafluoroethylene) was coated on the contact surface of the alumina disk to prevent the pin from excessive wear. Scanning infrared thermography with a magnification lens was employed in this experiment. The sliding direction is indicated by the arrow in the figure.  $\Delta T_{\max}$ ,  $v$ ,  $a$  and  $W$  are the maximum value of the frictional temperature rise, the sliding velocity, radius of contact area and the applied load, respectively. The circle in the figure shows the theoretical contact area, which is calculated by Hertz theory [3]. It is seen from figure 2 that a discrete temperature rise is observed in a restricted area with a maximum temperature rise at the center of the area. The area is circular in shape for low sliding velocity, but changes into elliptical for a higher sliding velocity. The length of the minor axis of the ellipsoidal high temperature area is in a good accordance with the diameter of the theoretical

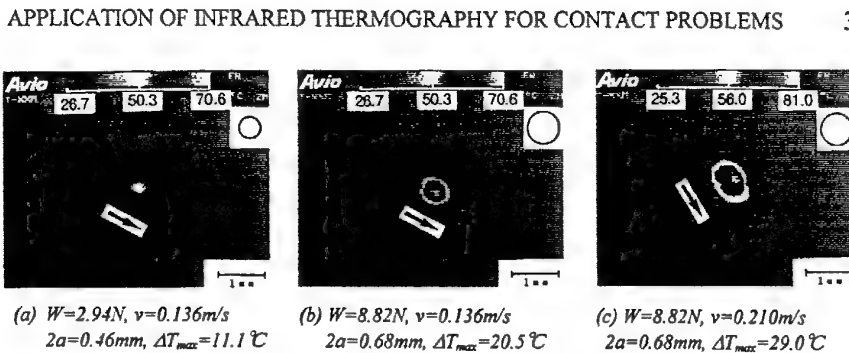


Figure 2. Temperature images of contact surface measured by infrared thermography.

contact area, which is indicated by the circle in figure 2. It is found that the contact area is accurately analyzed from the thermal images.

The observed temperature distribution along the minor axis of the elliptical high temperature area normalized with the maximum temperature rise  $\Delta T_{\max}$  was compared with the contact pressure distribution. The values of normalized temperature rise,  $\Delta T / \Delta T_{\max}$ , and normalized contact pressure,  $p / p_{\max}$ , are plotted along the normalized distance from the center of the contact surface,  $x/a$ , in figure 3, when the load and the sliding velocity were selected as  $W=5.88N$  and  $v=0.2m/s$ , respectively. The contact pressure  $p$  and the maximum contact pressure  $p_{\max}$  were obtained from Hertz theory. It is found from the figure that the  $\Delta T / \Delta T_{\max}$  versus  $x/a$  relation agrees quite well with the  $p / p_{\max}$  versus  $x/a$  relation. This fact may indicate that the temperature distribution on the sliding contact surface is controlled mainly by the heat generation rate, which is in proportion to the product of the friction coefficient, the contact pressure and the sliding velocity.

## 2.2 CONTACT STRESS MEASUREMENT BASED ON THERMOELASTICITY

Consider a spherical contact under cyclic compressive load, in which an infrared transmitting lens with spherical convex surface is in contact with a plate sample as shown in figure 4. The thermoelastic temperature change ( $\Delta T$ ) due to the cyclic stress on the contact surface of the plate can be measured by differential thermography, since the infrared emission from the contact surface passes through the infrared transmitting lens. The range in sum of the principal stresses ( $\Delta\sigma$ ) is determined by a relation of  $\Delta\sigma = -k\Delta T$ , where  $k$  is a thermoelastic constant. The load signal was monitored by a load cell and was employed as the reference signal for differential thermography. A spacer ring for magnification was mounted for the measurement of the stress distribution in a small area. The imaging area was 8.7mm square and the spatial resolution of the stress measurement was 70μm. Sapphire was chosen as the infrared transmitting lens, because

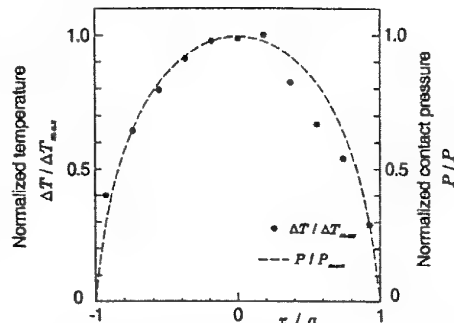


Figure 3. Distribution of normalized temperature and normalized contact pressure on contact surface.

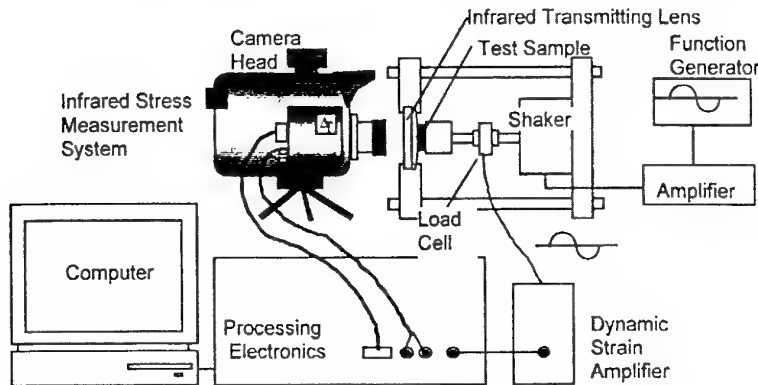


Figure 4. Schematic illustration of apparatus used for contact stress measurement

it transmits infrared well in the 3-5 $\mu\text{m}$  range which is the sensible range for the InSb infrared sensor used in the thermography system.

Stresses caused by spherical Hertz contact were measured for several kinds of commercially available plastics. A flat plate sample (15mm  $\times$  15mm, 1.6mm in thickness) was mounted on the loading stage and was brought into contact with a sapphire convex lens that has a spherical contact surface with a radius of curvature of 150mm. Sand blasting was done on the contact surface of the plastic sample to prevent reflections and to obtain high emissivity. Cyclic compressive loads (45Hz) were applied in several combinations of mean and amplitude values. In this paper, polypropylene is selected as the flat plate sample and the analytical and experimental results obtained for three loading conditions are compared. Table 1 describes the loads and Hertz theory predictions for these cases.

Table 1. Loading conditions and ranges in sums of principal stresses by Hertz theory.

Exp. No	Applied load $P$ (N)	$a_{\min}$ (mm)	$a_{\max}$ (mm)	$\Delta\sigma_{\max}$ (MPa)	$\Delta\sigma_0$ (MPa)
A7-09	$29.0 \pm 11.8$	1.17	1.56	14.1	5.4
A7-11	$29.0 \pm 19.9$	0.95	1.65	18.6	9.7
A7-19	$45.8 \pm 11.7$	1.47	1.75	12.9	3.8

Theoretical analysis for the contact area and contact stress distribution was done based on Hertz theory for spherical contact [2,3]. Distributions of  $\Delta\sigma$  were calculated for the loading conditions shown in Table 1, and plotted in figure 5.  $a_{\max}$  and  $a_{\min}$  are the radius of the contact area at maximum and minimum compressive loads in the cycle, respectively. It is found that  $\Delta\sigma$  shows an axisymmetric distribution, where  $\Delta\sigma$  is increasing from its central value  $\Delta\sigma_0$  up to the maximum value  $\Delta\sigma_{\max}$  at  $r=a_{\min}$ , then  $\Delta\sigma$  is decreasing to zero at  $r=a_{\max}$ .

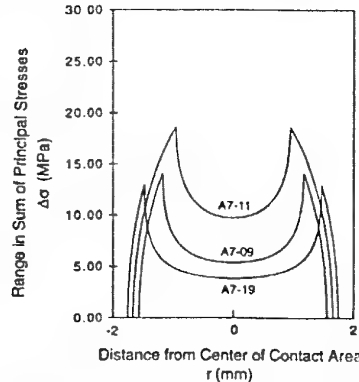


Figure 5. Distribution of range in sum of principal stresses by Hertz theory.

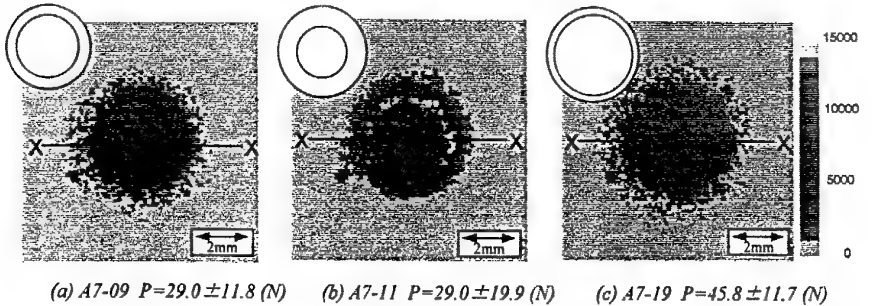


Figure 6. Images of contact stress distributions for Hertz contact between polypropylene sheet and sapphire convex lens obtained by infrared stress measurement system.

The contact stress distributions represented by the distribution of the intensity  $\Delta V$  of infrared emission from the contact surface due to the thermoelastic effect are shown in figure 6. The circles indicate the maximum and minimum contact areas. Line profiles obtained along the lines x-x in figure 6 are plotted in figure 7. An excellent correspondence is found between the contact stress distributions measured by the infrared system and those obtained by Hertz theory.  $\Delta V$  is increasing from the center of the contact area up to the maximum value at  $r=a_{\min}$ , then  $\Delta V$  is decreasing to near zero at  $r=a_{\max}$ . Figures 5 and 7 show that a comparison for the magnitude of  $\Delta\sigma$  can be made among different loading conditions. The asymmetric peaks in figure 7 are probably caused by inhomogeneous geometry of the surface in contact. Calibrations will be needed to obtain absolute values of contact stresses. The calibrations should involve reliable values of the thermal conduction from the plastic sample to the sapphire lens, the infrared transmittance in the sapphire lens, and the thermoelastic constant of the plastic sample.

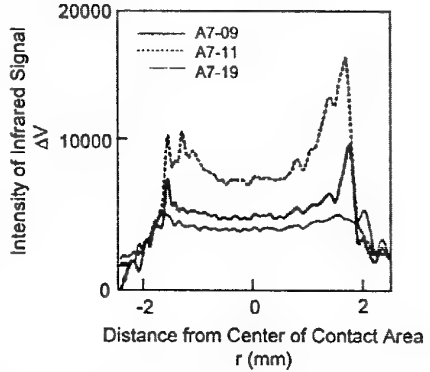


Figure 7. Distribution of intensity  $\Delta V$  of infrared emission along lines X-X in figure 6.

### 3. Evaluation of Fretting Stresses through Full-Field Temperature Measurements

It is very important to analyze the mechanics of crack nucleation under the influence of fretting to secure the reliability and the safety of the any clamped components subjected to vibrations or oscillatory loading such as riveted lap joints and turbine blades. Mechanism of crack nucleation under fretting contact is thought to be associated with the near-surface tangential stress generated by the interfacial frictional traction and the applied bulk load. Computational evaluations [4] showed the presence of a tensile peak in the tangential stress at the trailing edge of contact, where most of the fretting fatigue cracks nucleate in the experiments. The focus of the present study is to obtain experimental results capturing the evolution of friction and characterizing the stress field under fretting conditions. A newly developed multi-element infrared camera was

employed to measure near-surface temperature distribution due to both frictional heating and thermoelastic effects under fretting condition [5].

### 3.1 EXPERIMENTAL SETUP

A schematic of fretting contact and a photograph of the experimental setup are shown in figure 8. Temperature distribution was examined for 2024-T351 aluminum specimen and cylindrical pads. Cylindrical pads with the curvature radius  $R$  ( $R=178\text{mm}$ ) were brought into contact to the specimen and applied normal load  $P$  ( $P=6.41\text{kN}$ ). A cyclic bulk load with amplitude,  $\Delta L$  ( $\Delta L=16.1\text{kN}$ ), fully-reversed in tension and compression, was applied to the specimen using a servo-hydraulic load frame. Then fretting contact between the specimen and pads was induced due to the oscillatory tangential load  $\Delta Q$ .

The temperature distribution on the side surface of the specimen and pads were measured by the high speed and high resolution infrared thermography with an InSb focal plane array to convert thermal radiation into temperature values with a maximum sensitivity of  $0.025\text{ K}$ . A thin coating of flat black paint was applied to the exposed surfaces of the pads and specimen to increase the emissivity of the metallic surfaces. Thin reference lines were etched mechanically on the exposed faces of both the pads and specimen to mark the centerline of contact. A 2024-T3 aluminum plate with an E-type thermocouples was used to obtain a calibration relation between infrared intensity and temperature. Temperature reading from the thermocouples was correlated with the infrared intensity value near by the thermocouple measured by thermography. A fretting experiment was conducted at a frequency of  $2\text{ Hz}$  under fully-reversed loading conditions

### 3.2 EXPERIMENTAL RESULTS

Ten frames per cycle ( $20\text{ Hz}$  sampling rate) were captured for the first 150 cycles of the test, with subsequent images taken at cycles of 1000, 2000, 3000 and 4000. Infrared intensity data were converted to temperature data using the calibration relation and then filtered using a pixel-wise adaptive Wiener method.

Figures 9 and 10 show sequential temperature images taken at the 16th loading cycle and the 151st loading cycle, respectively, in the fretting experiment. The imaging area around the interface of the right pad and the specimen is indicated by the shaded area in figure 11. In figures 9 and 10, the top row of images shows temperature images during

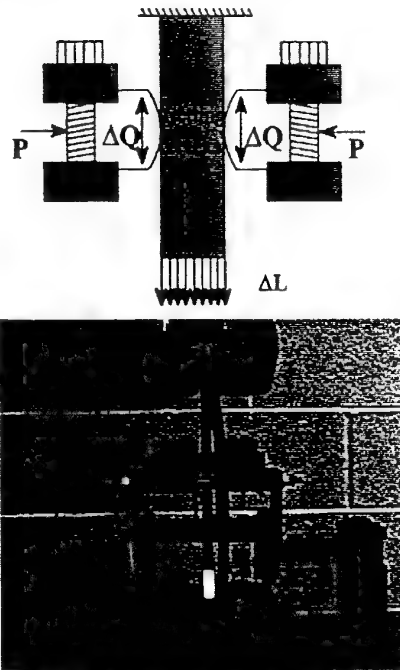


Figure 8. Schematic of fretting contact and photograph of fretting fatigue test fixture.

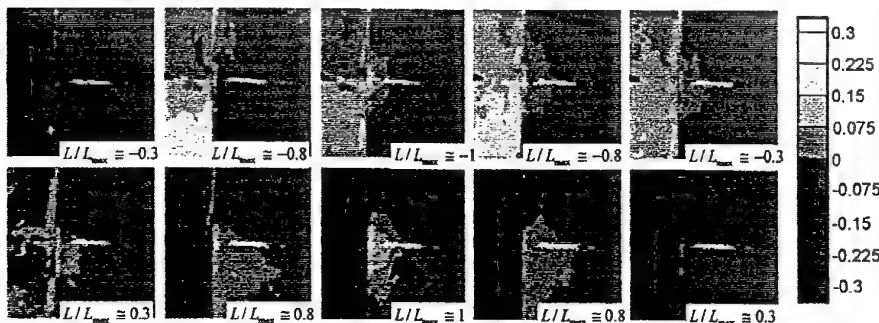


Figure 9. Sequence of thermal images near contact surface taken at the 16th loading cycle.

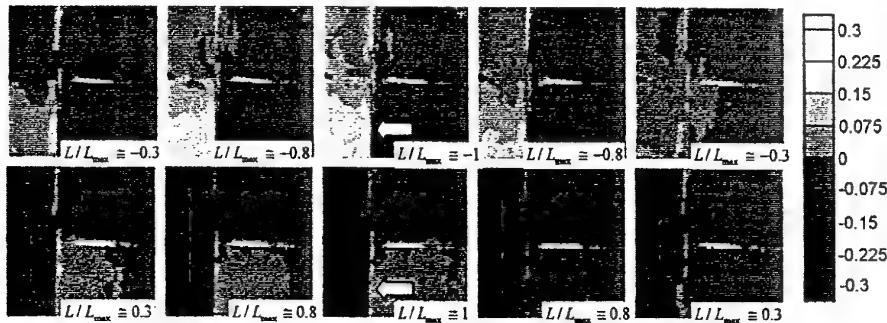


Figure 10. Sequence of thermal images near contact surface taken at the 151st loading cycle.

the compressive bulk loading in the loading cycle ( $L < 0$ ). Conversely, the lower row of images shows temperature images during the tensile bulk loading in the loading cycle ( $L > 0$ ). The gray scale bar indicates temperature changes from room temperature. The horizontal bright line on the pad, found in the temperature images, is caused by the mechanically etched mark indicating the nominal center of contact.

It is seen from figure 9 that the temperature distribution changes at the same frequency as that of the applied bulk load waveform on the specimen surface. This implies that the temperature change is caused by the thermoelastic effect induced by the cyclic bulk loading. The temperature distributions due to the thermoelasticity are nearly homogeneous in the entire specimen, and this indicates that the stress distribution in the specimen is also homogeneous at this stage. On the other hand, a localized near-surface heating spanning the width of the contact area is found in the pad. This heat generation can be observed twice in each loading cycle. This fact means this heat generation is caused by friction between the specimen and pad. It was found that in the beginning stage of fretting loading, gross sliding conditions due to the low frictional coefficient are dominant on the contact surface.

It is found from figure 10 that no frictional temperature rise due to the gross sliding can

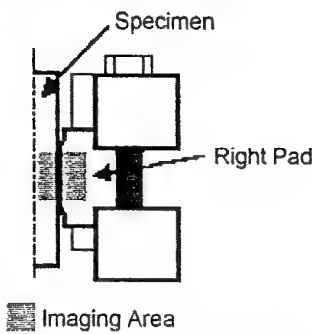


Figure 11. Schematic of imaging area by infrared thermography.

be observed any more at the 151st loading cycle. This implies that the friction coefficient increased and partial slip conditions are dominant at this stage. It was also found that temperature distributions on the specimen was not homogeneous at this time. When tension is applied, lower temperature was observed near the lower trailing edge of contact in the specimen (indicated by arrow in figure 10). This means that higher tensile stress was generated at the lower trailing edge of contact. This indicates that contact tensile stress due to the partial slip condition was applied to the specimen in addition to the bulk tensile stress. Conversely, at compression, higher temperature was observed at the lower trailing edge of contact in the specimen (also indicated by arrow in figure 10). This means higher compressive stress was generated at the lower trailing edge of contact due to the contact compressive stress by the partial slip condition in addition to the bulk compressive stress.

Consequently, it was found that the maximum amplitude in cyclic temperature change, i.e., maximum amplitude in stress, was observed at the trailing edge of contact. This result agrees very well with the results from FEM computations [6] and also the fact that fretting fatigue cracks nucleate from the trailing edge of the contact.

#### 4. Conclusions

Several experimental investigations of contact problems were made by the use of infrared thermography. A new experimental technique using infrared thermography combined with infrared transmitting materials was applied for continuous monitoring of the temperature distribution on the contact surface. Contact temperature measurement was examined for dry sliding contact of a plastic pin with an infrared transmitting disk. It was found that steady state contact surface temperature distribution was accurately monitored by thermography. Contact stress field was measured by an infrared stress measurement system based on the thermoelasticity through an infrared transmitting solid. It was found that the contact stress field was successfully visualized by the proposed method. Finally, a newly available infrared thermography system was used to characterize the near-surface conditions associated with fretting contact. It was found that both frictional temperature rise due to the interfacial global slip and the temperature fluctuation due to thermoelasticity can be measured to evaluate the nature of the contact stress field and the mechanics of partial slip fretting contacts.

#### 5. References

1. Sakagami, T., Ogura, K. and Shoda, M.: Thermal sensing and imaging of the dry sliding contact surface using IR thermo-microscope, *SPIE Proceedings*, **2473** (1995), 263-272.
2. Sakagami, T., et al.: Visualization of contact stress distribution using infrared stress measurement system, *SPIE Proceedings*, **3056** (1997), 250-259.
3. Johnson, K. L.: *Contact Mechanics*, Cambridge University Press, 1985.
4. Szolwinski, M. P. and T. N. Farris.: Mechanics of fretting fatigue crack formation, *Wear* **198** (1996), 93-107.
5. Szolwinski, M.P., Harish, G., Farris, T. N. and Sakagami, T.: In-situ measurement of near-surface fretting contact temperatures in an aluminum alloy, *ASME Journal of Tribology*, (1998), In-Press.
6. McVeigh, P.A. and Farris, T. N.: Finite element analysis of fretting stresses, *ASME Journal of Tribology*, **119**, #4, (1997), 797-801.

## **Applications of Optical Methods of Stress Analysis to Study Fracture Phenomena**

F. Ferber, K.P. Herrmann and K. Linnenbrock

*Laboratorium für Technische Mechanik,  
Paderborn University, Pohlweg 47-49,  
D-33098 Paderborn, GERMANY*

### **1. Introduction**

An overview about the numerical simulation and experimental modelling of cracks arising in homogeneous and nonhomogeneous solids will be given. Shadow optical and photoelastic data were collected from digitally sharpened caustics and isochromatic fringe patterns by using a digital image analysis system. The geometry of the caustics is proportional to the stress field gradient and therefore the caustic contour can be taken as a quantity for experimental measurements.

The solutions of the corresponding mixed boundary value problems of the thermoelasticity were not only obtained by using the FE-method but also by applying the experimental method of photoelasticity as well as the shadow optical method of caustics.

A photoelastic analysis for cracked two-phase compounds has been performed by using the image analysis of isochromatic fringe loops. A combination of the so-called phase-stepping method, an automatic polariscope and the multiple point method results in an automatic method for the determination of stress intensity factors.

Based on the caustics equations measuring algorithms can be formulated in order to determine stress intensity factors from experimentally gained caustics. The numerical simulation of shadow spots and isochromatic fringe patterns, respectively, is based on the fundamental equations of optics. By applying a generated finite element mesh numerically simulated caustics at the tips of straight matrix and interface cracks, respectively, extending quasistatically in the matrix material or in the inclusion matrix interface of a circular composite unit cell were obtained.

In this research contribution, an overview about the experimental and numerical modelling of crack systems arising in thermomechanically loaded models of two-phase composite structures will be given [1-5].

## 2. Photoelastic and Shadow Optical Crack Tip Analysis

A method for a determination of stress intensity factors from isochromatic fringe patterns by using numerous appropriate measuring points has been provided for the first time by Sanford & Dally [6]. By using the stress components near a crack tip as well as the basic equation of the photoelasticity the function  $g_k$  for a photoelastic data point k can be expressed as follows

$$g_k(K_I, K_{II}, a_1, \dots, a_N) = \left( \frac{\sigma_{rr}(r_k, \varphi_k) - \sigma_{\varphi\varphi}(r_k, \varphi_k)}{2} \right)^2 + \tau_{r\varphi}^2(r_k, \varphi_k) - \left( \frac{S n_k}{2 d_{eff}} \right)^2 = 0 \quad (1)$$

After taking a Tailor's series expansion of  $g_k$  and retaining only the linear terms a system of algebraic equations can be obtained

$$\begin{aligned} g_{k,i} &= g_k + \left( \frac{\partial g_k}{\partial K_I} \right)_i \Delta K_I + \left( \frac{\partial g_k}{\partial K_{II}} \right)_i \Delta K_{II} \\ &\quad + \left( \frac{\partial g_k}{\partial a_1} \right)_i \Delta a_1 + \dots + \left( \frac{\partial g_k}{\partial a_N} \right)_i \Delta a_N \end{aligned} \quad (2)$$

where i refers to the ith iteration step. A standard Newton-Raphson procedure can be used to calculate the stress intensity factors  $K_I$  and  $K_{II}$  for a set of proper input data points. By utilizing digital-image-processing and computergraphics techniques, a set of menu-driven software has been developed for interactively implemented fringes processing [7]. The stress components in the vicinity of a crack tip under mixed-mode-loading are given as functions of the seven parameters  $K_I$ ,  $K_{II}$  and the non-singular terms  $\sigma_{ox}$ ,  $a_1$ ,  $a_4$ ,  $b_3$ , and  $b_4$ .

$$\begin{aligned} \sigma_{rr} &= \frac{K_I}{\sqrt{2\pi r}} \frac{1}{4} \left( 5 \cos \frac{\varphi}{2} - \cos \frac{3}{2} \varphi \right) + \frac{K_{II}}{\sqrt{2\pi r}} \frac{1}{4} \left( -5 \sin \frac{\varphi}{2} + 3 \sin \frac{3}{2} \varphi \right) \\ &\quad + \sigma_{ox} \cos^2 \varphi \end{aligned} \quad (3a)$$

$$\begin{aligned} \sigma_{\varphi\varphi} &= \frac{K_I}{\sqrt{2\pi r}} \frac{1}{4} \left( 3 \cos \frac{\varphi}{2} + \cos \frac{5}{2} \varphi \right) + a_4 r (\cos \varphi + 3 \cos 3\varphi) \\ &\quad - b_3 \sqrt{r} \frac{1}{4} \left( 9 \sin \frac{\varphi}{2} + 15 \sin \frac{5}{2} \varphi \right) - b_4 r 2 (\sin \varphi + \sin 3\varphi) \end{aligned} \quad (3b)$$

$$\begin{aligned} \tau_{r\varphi} &= \frac{K_I}{\sqrt{2\pi r}} \frac{1}{4} \left( 3 \cos \frac{\varphi}{2} + \cos \frac{3}{2} \varphi \right) - \frac{K_{II}}{\sqrt{2\pi r}} \frac{1}{4} \left( 3 \sin \frac{\varphi}{2} + 3 \sin \frac{3}{2} \varphi \right) \\ &\quad + \sigma_{ox} \sin^2 \varphi \end{aligned} \quad (3c)$$

$$\begin{aligned} &\quad + a_4 \sqrt{r} \frac{1}{4} \left( 5 \cos \frac{\varphi}{2} - \cos \frac{5}{2} \varphi \right) + a_4 r 3 (\cos \varphi - \cos 3\varphi) \\ &\quad - b_3 \sqrt{r} \frac{1}{4} \left( 15 \sin \frac{\varphi}{2} - 15 \sin \frac{5}{2} \varphi \right) + b_4 r 3 \left( \frac{5}{4} \sin \varphi - \frac{5}{12} \sin 3\varphi \right) \end{aligned}$$

$$\begin{aligned} &\quad - \frac{1}{2} \sigma_{ox} \sin 2\varphi \\ &\quad + a_4 \sqrt{r} \frac{1}{4} \left( \sin \frac{\varphi}{2} - \sin \frac{5}{2} \varphi \right) + a_4 r (\sin \varphi - 3 \sin 3\varphi) \\ &\quad + b_3 \sqrt{r} \frac{3}{4} \left( \cos \frac{\varphi}{2} - 5 \cos \frac{5}{2} \varphi \right) + b_4 r 2 (\cos \varphi - \cos 3\varphi) \end{aligned} \quad (3c)$$

STRESS ANALYSIS TO STUDY FRACTURE PHENOMENA

3

The principle and the experimental set-up of the phase-stepping method from Hecker and Morche [8] by using an automatic polariscope are shown in Figure 1. The determination of the principle stress directions and the isochromatic fringe order is possible by a mathematical combination from 10 images of different angle positions of the polariscope, namely: linear polariscope;  $\alpha/\beta$ ;  $0/90$ ;  $30/120$ ;  $60/150$ ;  $45/135$ ;  $0/0$  [ $^\circ$ ] and circular polariscope:  $\alpha/\beta$ ;  $0/0$ ;  $60/60$ ;  $120/120$ ;  $0/45$ ;  $0/-45$  [ $^\circ$ ]. A combination of the phase-stepping method and the multiple point method results in an automatic method for the determination of stress intensity factors.

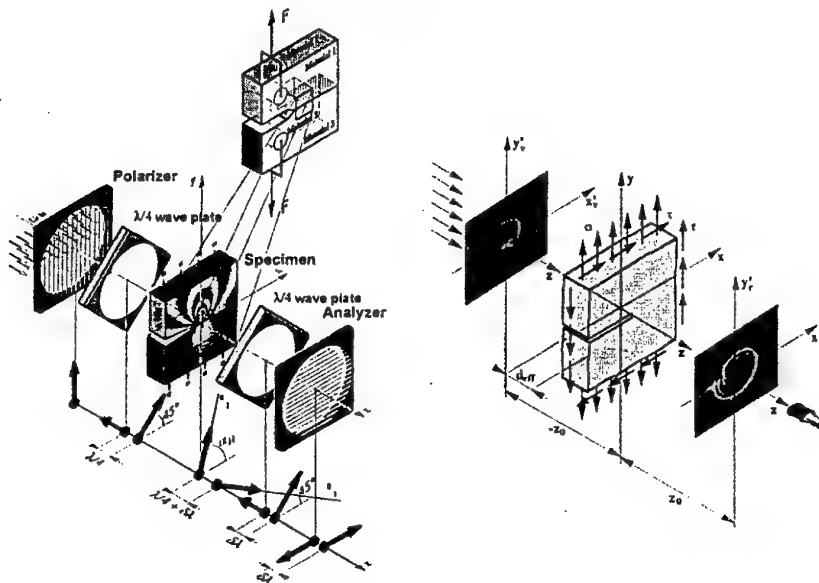


Figure 1. The principle and the experimental set-up of the phase-stepping method.

Figure 2. Experimental set-up for the shadow optical method of caustics.

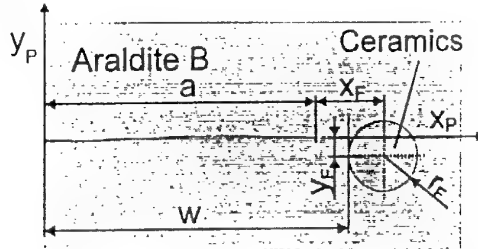
The shadow optical method represents an important tool for the experimental determination of stress intensity factors at the tips of quasistatically extending and fast running cracks, respectively. The physical principle underlying the method of shadow patterns is illustrated in Figure 2. A specimen containing a crack is illuminated with light generated by a point light source. In this case, a specimen of a transparent composite material is considered. The stress intensification in the region surrounding the crack tip leads to a reduction of both the thickness of the specimen and the refractive index of the material. As a consequence, in the transmission case, the light passing through the specimen is deflected outwards. On an image plane at any distance  $z_0$  behind the specimen, therefore, a dark shadow spot is formed. The spot is bounded by a bright light concentration, the caustic. The geometry of the caustic is proportional to the stress field gradient and therefore the caustic contour can be taken as a quantity for experimental measurements [9-13]. In the scope of an experimental failure analysis of brittle composites the method of caustics is applied to determine stress intensity factors or related quantities at crack tips situated in homogeneous components or at the interfaces of composites.

### 3. Material models of fibrous composites

#### 3.1 MATERIAL MODEL OF A CRACKED MATRIX

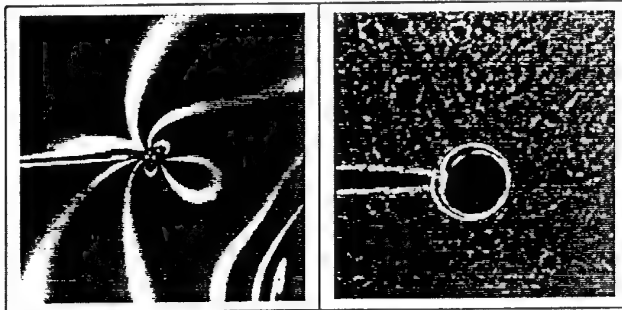
Figure 3 shows a material model of a cracked matrix with an asymmetrically situated inclusion with respect to the crack under thermal load due to a cooling process.

Figure 4 shows experimentally obtained isochromatic fringe patterns and caustics for a straight crack near such an inclusion. Thereby the isochromatic fringes and caustics were obtained for a material combination of Araldite B and ceramics. The definition of a ring region in combination with different angle regions can also be used for the determination of the mixed-mode stress intensity factors  $K_I$  and  $K_{II}$  in relation to the selected crack tip areas.



*Figure 3. Model of a cracked matrix with an asymmetrically situated inclusion under thermal load  
(matrix: Araldite B; inclusion: Ceramics)*

*Specimen geometry:  $a=80$  mm,  $x_F=25$  mm,  $y_F=-14$  mm,  $r_F=12.75$  mm*



*Figure 4. Experimentally obtained isochromatic fringe patterns and caustics.*

A typical result is given in Figure 5. It has been demonstrated, that the values of the mixed-mode stress intensity factors  $K_I$ ,  $K_{II}$  and of the parameter  $\sigma_{oc}$  obtained experimentally by the method of photoelasticity show a very good coincidence with the corresponding numerical values determined by a finite element calculation.

STRESS ANALYSIS TO STUDY FRACTURE PHENOMENA

5

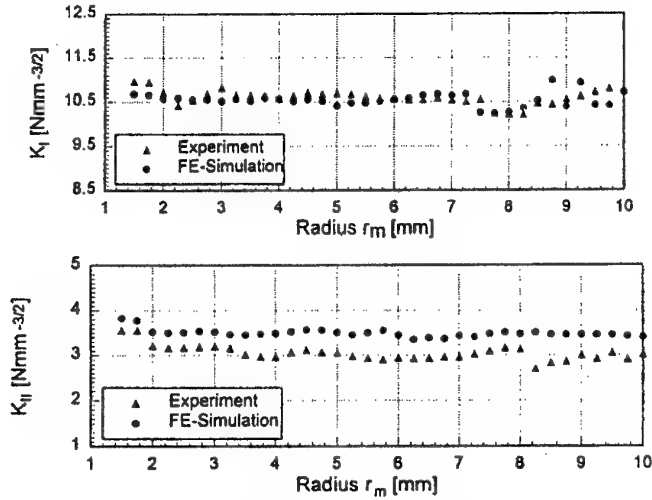


Figure 5. Stress intensity factors  $K_I$ ,  $K_{II}$  in dependence on the crack tip distance  $r_m$ .

An accurate determination of the parameters from isochromatic fringe patterns is given within the range  $2.5 \text{ mm} < r_m < 7.5 \text{ mm}$  of the radius  $r_m$ .

Figure 6 gives a comparison of stress intensity factors from experimentally obtained isochromatic fringe patterns and caustics, where a good agreement can be stated. Shown are typical results from specimens under different thermal loads.

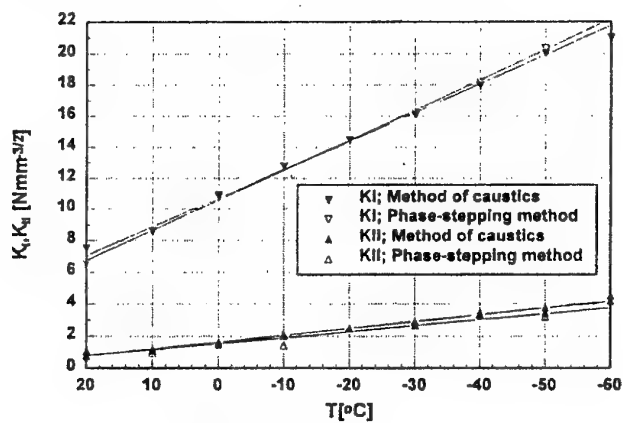


Figure 6. Stress intensity factors  $K_I$ ,  $K_{II}$  in dependence on temperature ( $y_F=8\text{mm}$ ;  $x_F=32\text{mm}$ ).

Figure 7 gives a comparison of stress intensity factors from experimentally obtained isochromatic fringe patterns with a corresponding finite element calculation, where a good agreement can be stated. Shown are typical results from specimens under different thermal loads [14, 15].

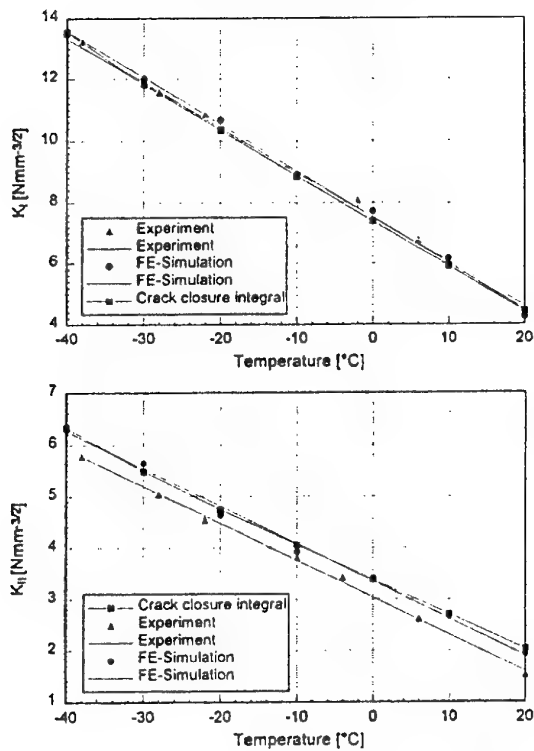


Figure 7. Stress intensity factors  $K_I$ ,  $K_{II}$  in dependence on temperature.

### 3.2 BIMATERIAL MODEL

The experimental determination of stress intensity factors at the tip of a curvilinear thermal crack propagating in the matrix material, Araldite B, of a disk-like bimaterial model (cf. Figure 8 and 9) has been performed. Thereby a ring region can be used to calculate the stress intensity factors in dependence on the crack tip distance  $r_m$ .

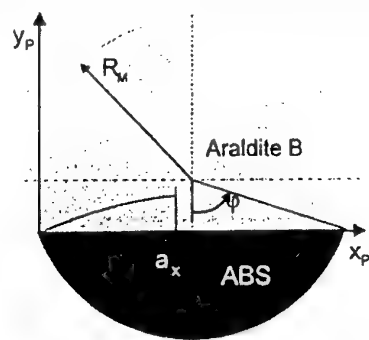


Figure 8. Model of a cracked disk-like bimaterial.

STRESS ANALYSIS TO STUDY FRACTURE PHENOMENA

7

Figure 10 gives a comparison of the stress intensity factors  $K_I$  and  $K_{II}$  gained from experimentally obtained isochromatic fringe patterns by using the multiple point method of photoelasticity. In this case an accurate determination of the parameters  $\sigma_{ox}$ ,  $a_3$ ,  $a_4$ ,  $b_3$ , and  $b_4$  from isochromatic fringe patterns is given within the range  $2\text{mm} < r_m < 11\text{mm}$  of the radius  $r_m$ . This thermal loading process produces a pure mode-I loading, which can also be seen from the  $K_{II}$ -values.

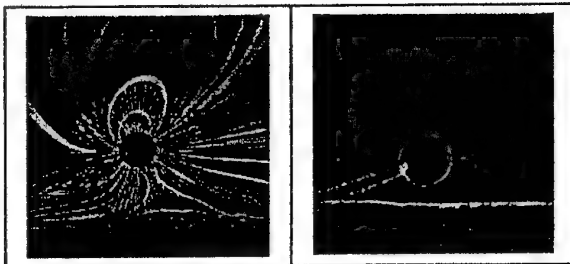


Figure 9. Experimentally obtained isochromatic fringe patterns and caustics

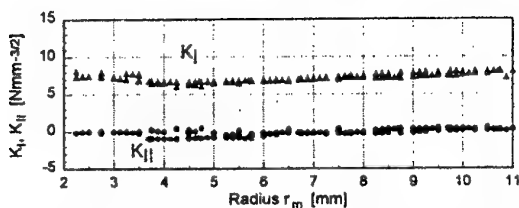


Figure 10. Comparison of stress intensity factors  $K_I$  and  $K_{II}$  gained from experimentally obtained isochromatic fringe patterns by using the multiple point method of photoelasticity.

Figure 11 gives a comparison of stress intensity factors from experimentally obtained isochromatic fringe patterns and caustics in dependence on projected crack length  $a_x$ .

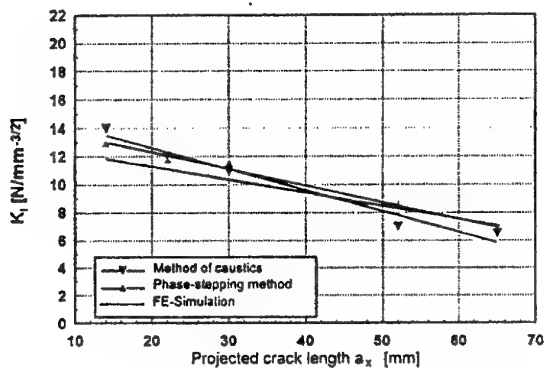


Figure 11. Stress intensity factors  $K_I$  and  $K_{II}$  gained from experimentally obtained isochromatic fringe patterns and caustics in dependence on projected crack length  $a_x$

### Conclusion

Shadow optical and photoelastic data were collected from digitally sharpened isochromatic fringe patterns and caustics by using a digital image analysis system. A photoelastic analysis for cracked two-phase compounds has been performed by using the image analysis of isochromatic fringe loops. A combination of the so-called phase-stepping method, an automatic polariscope and the multiple point method result in an automatic method for the determination of stress intensity factors. An overview about the experimental modelling of cracks arising in plane disk-like models of two-phase composite structures is given.

### References

- 1 Ferber, F. (1986) Ph. D., Dissertation, Paderborn University
- 2 Ferber, F. and Herrmann, K.P. (1991) *Brittle Matrix Composites 3*, eds. A.M. Brandt and I.H. Marshall, Elsevier Applied Science Publishers, London/New York, 403-412
- 3 Dong, M. (1993) *Fortschritt Berichte*, VDI-Reihe 18, No 138
- 4 Noe, A. (1994) Ph. D., Dissertation, Paderborn University
- 5 Ferber, F. and Herrmann, K.P. (1994) *Brittle Matrix Composites 4*, eds. A.M. Brandt, V.C. Li and I.H. Marshall, IKE, Warschau/Woodhead Publ. Ltd., Cambridge, UK., 190-199
- 6 Sanford, R.J. and Dally, J.W. (1979) A general method for determining mixed-mode stress intensity factors from isochromatic fringe patterns. *Engineering Fracture Mechanics* 11, pp. 621-633
- 7 Hinz, O. (1993) Ph. D., Dissertation, Paderborn University
- 8 Hecker, F.W. and Morche, B. (1986) *Computer-aided measurement of relative retardations in plane photo-elasticity*. In: Wieringa, H. (Ed.), *Experimental Stress Analysis*, 535-542, Martinus Nijhoff Publishers, Dordrecht, Boston, Lancaster
- 9 Manogg, P. (1964) Ph. D., Dissertation, Freiburg University
- 10 Kalthoff, J.F. (1985) *The Shadow Optical Method of Caustics*. In: A.S. Kobayashi (ed.), *Handbook of Exp. Mech.*, 430-500. Englewood Cliffs, Prentice Hall
- 11 Theocaris, P.S. (1976) Partly unbonded interfaces between dissimilar materials under normal und shear loading. *Acta Mechanica*, 24, pp. 99-115
- 12 Rossmanith, H.P. (1982) The method of caustics for static plane elasticity problems. *Journal of Elasticity*, 12, pp. 193-200
- 13 Rossmanith, H.P. (1979) Determination of stress intensity factors by the dynamic method of caustics for optically isotropic materials. *Ingenieur-Archiv*, 48, pp. 363-381
- 14 Ferber, F., Herrmann, K.P. and Linnenbrock, K. (1996) *Elementary failure analysis of composite models by using optical methods of stress analysis and modern digital image systems*. In: ESDA 1996, (Eds. A. Large and M. Raous) ASME, New York, Vol. 4, pp. 55-68
- 15 Ferber, F., Herrmann, K.P. and Linnenbrock, K. (1997) *Study of fracture phenomena in thermomechanically loaded composites by using optical methods of stress analysis and digital image systems*. In: Thermal Stresses '97 (Eds. R.B. Hetnarski, N. Noda and H. Ghoneim), Rochester Institut of Technology, pp. 523-526

## ACTIVE CONTROL OF STRESS INTENSITY FACTOR K UNDER MIXED MODE STRESS IN THE SMA-FEC

AKIRA SHIMAMOTO 1, YASUBUMI FURUYA 2 and EISAKU UMEZAKI 3

1. Department of Mechanical Engineering, Saitama Institute of Technology, Okabe-cho,  
Saitama 369-02 Japan

2. Department of Materials Processing, Tohoku University, Sendai 980-77, Japan

3. Department of Mechanical Engineering, Nippon Institute of Technology, Miyashiro-machi, Saitama, Japan

### Abstract

Shape memory TiNi fiber reinforced /epoxy matrix composite (SMA-FEC) is fabricated to demonstrate the suppression effect of crack-tip stress concentration and the fracture toughness ( $K$  value) under mixed mode stresses in the composite. The test specimens have the two types of angled-notches to the transverse direction of the tensile-type specimen, i.e.  $\theta = 45^\circ, 90^\circ$  with several crack lengths. The stress intensity at the notch-tip is experimentally determined by photoelastic fringes. The decreases of  $K$ -value are attributed to the compressive stress field in the matrix which is induced when the prestrained TiNi fibers contract to the initial length upon heating above austenitic finish temperature of TiNi fiber ( $T > Af$ ). The dependencies of  $K$  value on the prestrain value of TiNi fibers as well as on the compressive stress domain size between a crack-tip and fiber are discussed.

### 1. Introduction

The active control of the material degradation (i.e. damage accumulation, crack, delamination etc.) in service time and then elongation of failure life of the material components become more and more important in recent years owing to the increasing demands for the more safety design of various engineering devices and structures. Furthermore, the development of an artificial prevention system of sudden failure of machinery and structures also become one of the worthy and attractive research subjects to create a new design concept of the intelligent/smart material systems and structures.

As one of the works concerning to the active control of the strength and fracture of material system, Rogers [1] proposed the active control method for retardation of fatigue crack propagation from a notch-root by utilizing the contractions of embedded SMA line-type actuator. In his approach, SMA actuator is heated by means of direct current joule heating, and then, the large compressive stresses in the matrix associated with the shrinkages of TiNi actuator acts to reduce the mean stress level of cyclic loading. This enhances the crack-closure phenomena and retardation of the fatigue crack propagation. Rogers also tried to discuss about an experimental result on the suppression of the crack-tip stresses in a pre-cracked TiNi fiber/epoxy resin matrix composite specimen by using photoelastic fringe pattern. However, the change of stress intensity value  $K$  has not been clarified yet in detail as well as systematically.

Concerning this problem, the authors have recently studied the improvements of mechanical strength as well as the active control of stress intensity value  $K_I$  under a uniaxial stress condition (i.e. mode 1) on the basis of the basic experiments of by direct current joule heating of TiNi fibers embedded in photoelastic epoxy matrix composite, (TiNi)<sub>f</sub>/epoxy. [3] [4] [5] However, in general, multi-mode stresses work in the machinery or structural components and it results in failure of the whole structures, therefore, in the present study, the suppression effect of crack-tip stress concentration and the fracture toughness ( $K$  value) under mixed mode stresses in the composite is studied. The test specimens have the two types of angled-notches to the transverse direction of the tensile-type specimen, i.e.  $\theta = 45^\circ, 90^\circ$  with several crack lengths. The stress intensity at the notch-tip is experimentally determined by photoelastic fringes. The decreases of  $K$ -value are attributed to the compressive stress field in the matrix which is induced when the prestrained TiNi fibers contract to the initial length upon heating above austenitic finish temperature of TiNi fiber ( $T > Af$ ). The

dependencies of mixed-mode K values(i.e.KI and KII) on the prestrain value of TiNi fibers as well as on the compressive stress domain size between a crack-tip and fiber are discussed systematically.

## 2. Design concept of shape memory composite

Thermoelastic shape memory effect (i.e. shape memory and recovery phenomenon) takes place during martensite(M) to austenite(A) phase transformation in SMA with increasing temperature. Therefore, material functional properties of SMA changes clearly depending on the changes of temperature [2] as summarized in Fig. 1. It should be noticed as a unique property that SMA shows more higher stiffness (2-3 times) and large recovery stress at the higher temperature region due to inversely thermoelastic phase transformation in opposition to weakening of those properties in the general metals. In consequence, SMA natively has the smart functions , i.e., (1)sensor (thermal), (2)actuator (shape memory deformation) and (3) memory and shape recovery (namely, processor function). These unique properties natively with SMA can be utilized to strengthen the composite. The design concept of enhancing the mechanical properties of the SMA composite is schematically shown in Fig. 2. TiNi fibers are heat-treated to shape-memorize their initial length at higher temperatures ( $>A_f$ ), then quenched to room temperature(nearly ,martensite start temperature  $=M_s$ ),given tensile prestrain  $\epsilon_T(>0)$  and embedded in the matrix material to form a composite. The composite is then heated to temperature( $>A_f$ ) at which the TiNi fibers tend to shrink back to their initial length by the amount of prestrain  $\epsilon_T$ , then the matrix is subjected to compressive stress. It is this compressive stress in the matrix that contributes to the enhancement of the tensile properties of the composite and fracture toughness.

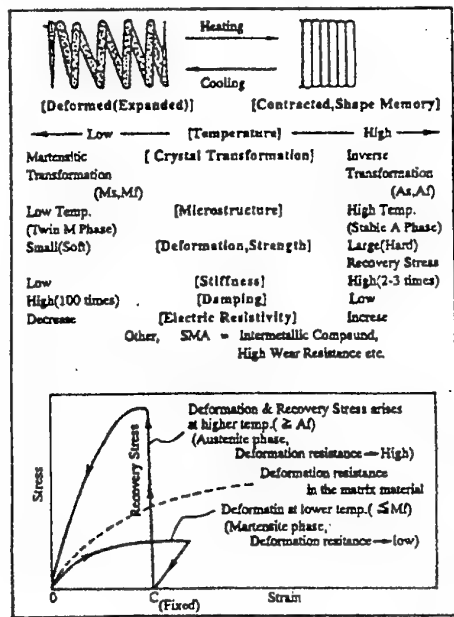


Fig.1 Material properties of shape memory alloy with increasing temperature.

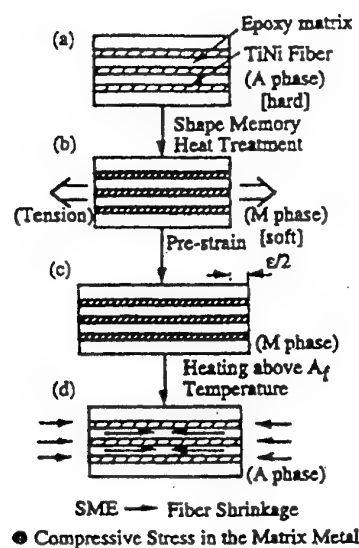


Fig.2 Design concept of SMA smart composite.

### 3. Experiment

#### 3.1 Test specimen

Experimental processing, mechanical testing of TiNi/epoxy composite is described. The shape memorized TiNi fibers(Ti-50.2at%Ni) of 0.4mm diameter supplied by Kantoc Ltd, Fujisawa, Japan are arranged in a mold to which photoelastic epoxy and specified amount of hardener were poured and then kept at 130°C for 2hours for curing. The TiNi fibers were first annealed for 30min at 500 °C,then quenched in ice-water. Four transformation temperatures of TiNi fiber were determined: martensitic start  $M_s=31^{\circ}\text{C}$ ,martensite finish  $M_f=15^{\circ}\text{C}$ , austenitic start  $A_s=57^{\circ}\text{C}$ , and austenitic finish  $A_f=63^{\circ}\text{C}$  from the relationship between strain vs. temperature at constant stress of 94MPa. The photoelastic sensitivity constant of this epoxy resin matrix was  $\alpha =0.116 \text{ mm/N}$ . After curing, as-molded composite was cooled to room temperature. During the process, TiNi fibers were kept in tension with four different prestrains of 0,1,3 and 5%. A center notch which had different angle( $\theta$ ) and length(a) were then cut into the as molded composite specimen by spark-cutting and thin knife-edge. In the case of the specimen with angled crack ,  $\theta =90^{\circ}$  (i.e. mode I), four different crack lengths , $a=3.8,5.0,7.0$  and  $8.8\text{mm}$  were introduced, on the other hand, in the case of  $\theta =45^{\circ}$ (i.e. mode II), $a=7.5,8.8$  and  $12.2\text{mm}$  in mixed-mode test specimens for changing the domain size (D) between a crack-tip and a fiber. The geometries of the composite specimens and pre-crack lengths are shown in Fig.3.

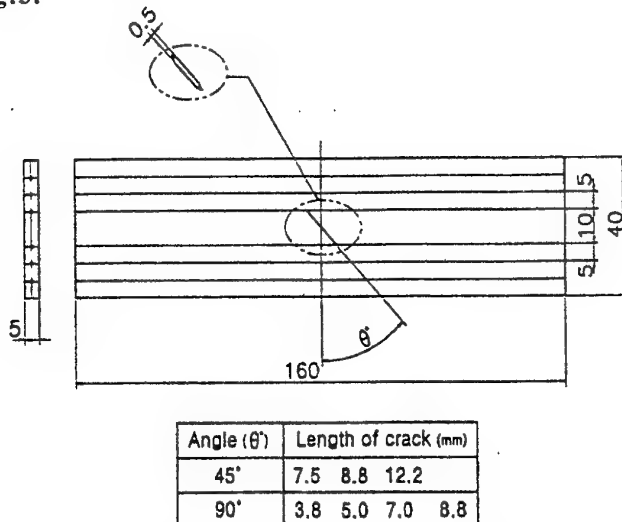


Fig.3 Geometry of TiNi/epoxy composite specimen with a center crack with angle  $\theta$ .

#### 3.2 K-value determination

The composite specimens were loaded by Tensilon/RTM-1T machine in which constant temperature controllable furnace and photoelastic analysis apparatus were combined. A constant load of  $P=1078\text{N}$  was applied to TiNi/epoxy specimen with angled crack  $\theta =90^{\circ}$  , on the other hand,  $P=1274\text{N}$  ,  $\theta =45^{\circ}$  for the controlled tensile test machine to form the third or fourth photoelastic fringe pattern . The changes of number of fringe pattern lines developed around the notch tip were measured at different constant temperatures of 20,30,40,50,60,70,80,90 and  $100^{\circ}\text{C}$  through the plane glass window fixed on the wall of the electric heating furnace. The photographs of the changes of fringe patterns around a crack-tip with increasing temperature were continuously taken by camera, and then, stress intensity factor  $K_I$  and  $K_{II}$  can be calculated from the following formula respectively, i.e.,  $K_I$  of mode I (tensile-type) by Irwin's method, and  $K_{II}$  of mixed-mode by Smith's method.

$$K_I = \frac{n\sqrt{2\pi r_m}}{\alpha t \sin \theta_m} \left[ 1 + \left( \frac{2}{3 \tan \theta_m} \right)^2 \right]^{-0.5} \times \left[ 1 + \frac{2 \tan(3\theta_m/2)}{3 \tan \theta_m} \right] \quad \text{Eqn(1)}$$

$$\left. \begin{aligned} K_I &= \frac{N_m (2\pi r_m)^{1/2}}{\alpha t \left\{ (\sin \theta_m + 2A \cos \theta_m)^2 + A^2 \sin^2 \theta_m \right\}^{1/2}} \\ K_{II} &= \frac{AN_m (2\pi r_m)^{1/2}}{\alpha t \left\{ (\sin \theta_m + 2A \cos \theta_m)^2 + A^2 \sin^2 \theta_m \right\}^{1/2}} \end{aligned} \right\} \quad \text{Eqn(2)}$$

where

$$A = \frac{K_{II}}{K_I} = \frac{2}{3} \left( \cot 2\theta \pm \sqrt{\cot^2 \theta_m + \frac{3}{4}} \right)$$

$n$  is the number of the fringe,  $t$  is the composite plate thickness,  $\alpha$  is the epoxy photoelasticity sensitivity constant,  $r$  and  $\theta_m$  are, respectively, the distance and angle in polar coordinates at point M, shown schematically in Fig.4.

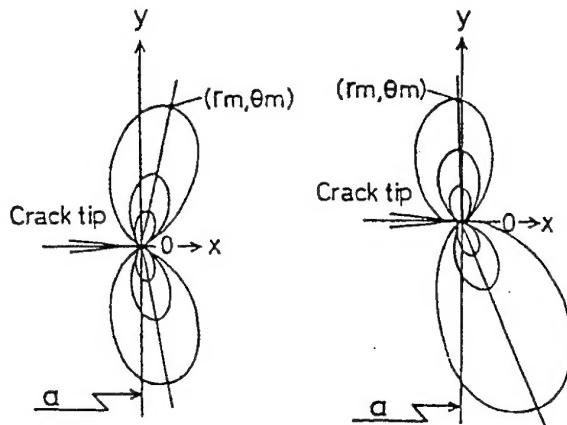


Fig.4 Photoelastic fringe pattern schematically developed around a crack (size: a) in the pole figure. (mode I and mixed mode II)

#### 4. Results and discussion

The Experimental results of the photoelastic fringe patterns are shown in Fig.5 for TiNi/epoxy specimen with angled crack  $\theta=45^\circ$  at  $P=1274\text{N}$  in Fig.5(a), and angled crack  $\theta=90^\circ$  at  $P=1078\text{N}$  in Fig.5(b) respectively. It should be noticed from Fig.5(a), (b) that the photoelastic fringes decrease abruptly with the increasing temperature, especially, at above  $A_f (=63^\circ\text{C})$  temperature. Concerning the active control of the stress intensity at the crack-tip ,as an example, the dependencies of  $K_I$ -value on environmental temperature ( $T$ ) at the crack length of 8.8mm in the specimen with  $\theta=90^\circ$  are shown in Fig.6.  $K_I$ -value of the specimen with pre-strained TiNi fibers decreases clearly above  $50\text{--}60^\circ\text{C}$ , where the decreasing rate of  $K_I$ -value depends on the pre-strain value. Although the

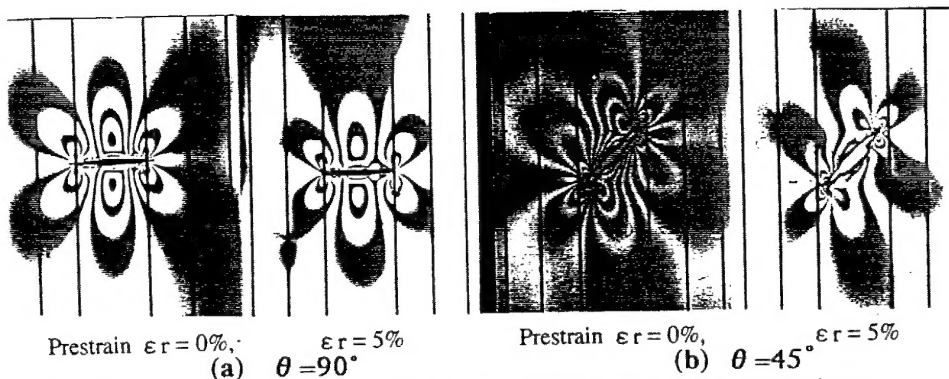


Fig.5 Photoelastic fringe pattern around a center crack in the test TiNi/epoxy specimen

initial absolute K-value differs by the inevitable effect by initially introduced residual stresses in the matrix during the fabrication process of TiNi/epoxy composite. The decrease of K-value scarcely is recognized in the case of pre-strain=0, but, the drop of K-value increases as the pre-tensile strain of TiNi fiber increases. These facts surely suggest that shape memory effect of the embedded TiNi fibers can effectively reduce the stress concentration with increasing prestrain value.

The experimental result of the reduction in mode I stress intensity factor,  $K_I$ , at 80 °C(>Af) is plotted versus pre-strained values  $\varepsilon = 0, 1, 3$  and 5%, for several crack-lengths in Fig.7(a) and similarly shown for mode II, $K_{II}$ , in Fig7(b) in the test specimen with angled crack of  $\theta = 45^\circ$ . The stress intensity factor ratio,K-value ratio, in Y axis means the normalized value of K which can be calculated from dividing absolute K value in a certain prestrained specimen by the K value of zero-prestrained specimen. It can be noticed that all K-values decreases with increases of pre-strain value ,and these decreasing rate(  $\Delta K$ ) becomes much more high depending on crack-length( $a$ ). For instance, in the case of the specimen with 5% prestrain and  $\theta = 45^\circ$  crack , the decreased values by shape memory effect are  $\Delta K_I = 36\%$ ,  $\Delta K_{II} = 21.4\%$  at  $a = 7.5\text{mm}$ ,  $\Delta K_I = 45.4\%$ ,  $\Delta K_{II} = 46\%$  at  $a = 8.8\text{mm}$ , and  $\Delta K_I = 48.7\%$ ,  $\Delta K_{II} = 58.2\%$  at  $a = 12.2\text{mm}$  respectively. The same trend can be

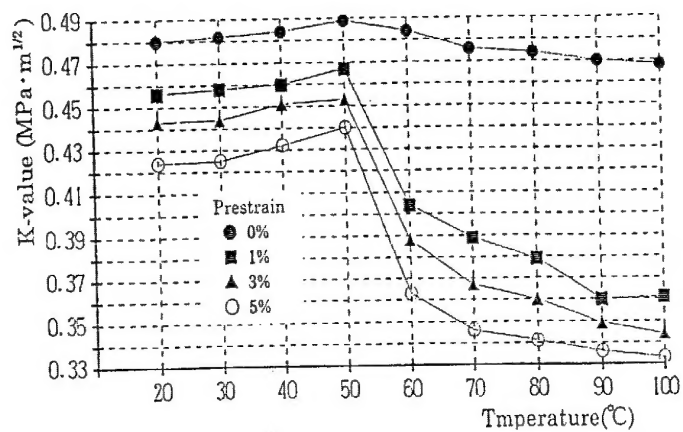
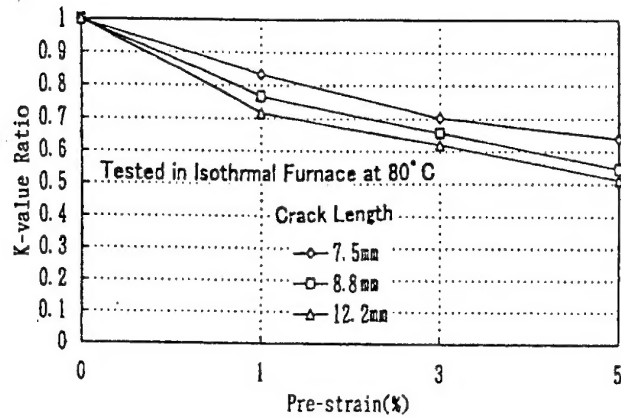


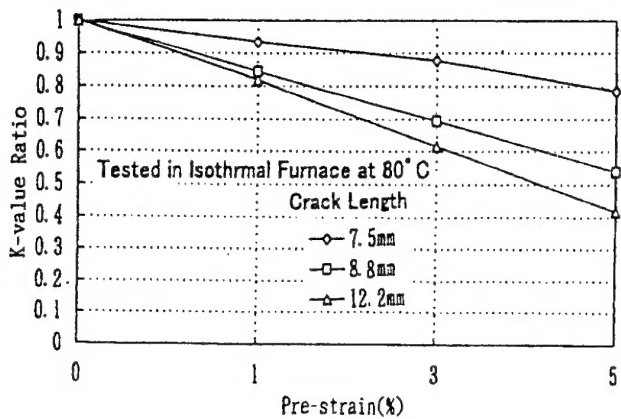
Fig.6 Stress intensity factor KI-ratio as a functions of temperature under three different prestrains in a case of the specimen with crack length  $a=8.8\text{mm}$  and angle  $\theta=90^\circ$ .

recognized in the case of single mode KI in the specimen with angled crack  $\theta = 90^\circ$  as shown in Fig. 7(c), i.e. the decrease range,  $\Delta KI=27.6\%$  at  $a=3.8\text{mm}$ ,  $\Delta KI=29.5\%$  at  $a=5\text{mm}$ ,  $\Delta KI=30.7\%$  at  $a=7\text{mm}$  and  $\Delta KI=82.8\%$  at  $a=8.8\text{mm}$  respectively. These results with decreasing dependencies of K-value ( $\Delta K$ ) on the crack-length( $a$ ) suggest that the decrease of K experimentally seems to become most intense as the domain size between the crack-tip and fiber surface in front of a crack. The same trend of the dependency of drop of K-value on the domain size was previously discussed by the authors using Eshelby's equivalent inclusion method. As to the relationship between K ratio and prestrain value, the analytical model explains the same trend as the experimental results, i.e., K -value decreases with increase in prestrain, however, the predictions are apt to show larger values than those of the experiment.



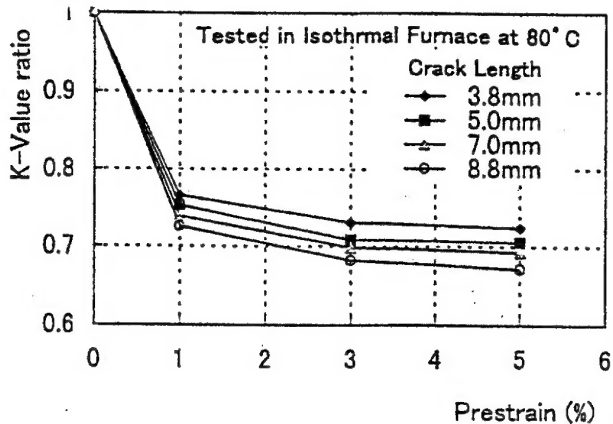
(a) mode KI for  $\theta = 45^\circ$

Fig.7(a) Normalized stress intensity factor K-value ratio vs. prestrain in different crack lengths:



(b) mode KII for  $\theta = 45^\circ$

Fig.7(b) Normalized stress intensity factor K-value ratio vs. prestrain in different crack lengths:



(c) mode KI for  $\theta=90^\circ$   
Fig. 7(c) Normalized stress intensity factor K-value ratio vs. prestrain in different crack lengths:

From the experimental evidences of this study, our proposed "new material system for active failure prevention by using SMA composite" will become a promising idea for active control of the material degradation (i.e. damage accumulation, crack, delamination etc.) in service time and then elongation of failure life of the material components in the near future. Furthermore, the development of an artificial prevention system of sudden failure of machinery and structures also become one of the worthy and attractive research subjects to create a new design concept of the intelligent/smart material systems and structures.

## 5. Conclusion

Following the previous study on active suppression of crack-tip stress concentration and the increase of fracture toughness (K value) by using shape memory strengthening in shape memory TiNi fiber reinforced /epoxy matrix composite (SMA-FEC), in the present paper, the control of crack-tip stress concentration and the fracture toughness (K value) under mixed mode stresses, KI and KII mode, are investigated. The test specimens have the two types of angled-notches to the transverse direction of the tensile-type specimen, i.e.  $\theta=45^\circ, 90^\circ$  with several crack lengths. The stress intensity at the notch-tip is experimentally determined by photoelastic fringes. The decreases of KII value in the mixed mode were also experimentally confirmed similarly as the former mode I type (KI) specimen when the prestrained TiNi fibers contract to the initial length upon heating above austenitic finish temperature of TiNi fiber ( $T > Af$ ). The dependencies of K value on the prestrain value of TiNi fibers and crack length (i.e., compressive stress domain size between a crack-tip and fiber) are recognized as previously predicted by the authors.

## References

- [1] C.A.Rogers ,C,Liang and S.Lee(1991) : Active damage control of hybrid material systems using induced strain actuator. Proc.AIAA/ASME /ASCE/AFS/ASC 32nd Structure, Structure Dynamics and Materials Conference (AIAA, Washington, 1991, Part II) 1190-1203
- [2] Y.Furuya,A.Sasaki and M.Taya,(1993) "Enhanced Mechanical Properties of TiNi Shape Memory Fiber/Al Matrix Composite",Mater.Trans. JIM,Vol.34(3),224-227
- [3] A. Shimamoto and M.Taya (1997) "Reduction in KI by shape memory effect in a TiNi shape memory fiber reinforced epoxy matrix composite" J. JSME ,63-605-A(1997-1),26-31
- [4] A. Shimamoto,Y.Furuya and M.Taya (1997) : "Active control of crack-tip stress intensity by contraction of shape memory TiNi fibers embedded in epoxy matrix composite: Dependency of stress intensity factor on crack-tip domain size", Proc. ICCM-11(Gold-coast,Australia,July,1997) Vol.5,493-499.
- [5] S.Takahashi and S.Nagata(1986) : Science of machine(in Japanese),38-1 ,82-86